CRANFIELD UNIVERSITY

SCHOOL OF ENGINEERING

Numerical Investigation of Recess Casing Treatments in Axial Flow Fans

Ph.D Thesis

ABDURAZAG M. GHILA

February 2003

CRANFIELD UNIVERSITY

SCHOOL OF ENGINEERING

Department of Power, Propulsion & Aerospace Engineering

Ph.D Thesis

Academic Year 2002-2003

Numerical Investigation of Recess Casing Treatments in Axial Flow Fans

ABDURAZAG M. GHILA

Supervisors

Dr. Antonios Tourlidakis Professor Robin L. Elder

This thesis is submitted in partial fulfilment of the requirements for the degree of Doctor of Philosophy

FEBRUARY 2003

Abstract

The casing treatment technique for the axial fan has never been more significant since its potential applications were recognized in gas turbines, tunnel ventilation and many other industrial applications where the axial fan would benefit from the casing treatment. In the last two decades experimental investigations were carried out at Cranfield University to examine the influence of recess casing treatment on stall margin, operating efficiency and flow field of a low-speed axial flow fan. They showed more than 50% improvement in the stall margin with a negligible loss in the efficiency. However, a little work has been done on the numerical simulation of casing treatments due to its complexities, even though in recent years computational fluid dynamics [CFD] analysis has been very active in the prediction of various phenomena in turbomachinery.

This work presents numerical investigation of flow in a single axial-flow fan with and without recess casing treatment. It involves the detailed effect of the recess casing on stall margin improvement as well as its influence on global performance parameters. The project offers a contribution to the understanding of the physical processes occurring when approaching stall and the working mechanism by which recess casing treatments improve stall margin. A Reynolds-Averaged Navier-Stokes CFD code was used for the analysis using steady and unsteady simulations. The numerical investigation of the overall performance, efficiency and work-input characteristics of the fan were found to agree very well with the previously reported experimental results.

The effect of casing treatment was investigated using two types of configurations, vaneless and vaned casing. The vaneless casing treatment produced a sizeable stall margin improvement with a measurable loss in both pressure rise and efficiency. The recess was fitted later with vanes and was shown to offer both a further stall margin improvement and an increase in the pressure rise coefficient without any significant drop in efficiency at design conditions. The effect of number of vanes inside the recess was also investigated by doubling and halving the number of vanes originally adopted. The predicted results highlighted the importance of the vane inside the casing.

Unsteady simulations for the fan with solid and treated casing were carried out. The solid casing simulated for a single blade passage as well as for the entire fan containing all 27 blades highlighted the flow physics of the tip stall growth process, as a large amount of radial flow injected from the hub at the blade suction side near the trailing edge towards the outer casing and occupy this through a mechanism of radial low momentum flow transport. This transport process is the main contributor to the very large separation observed in the shroud region in addition to the locally induced separation due to high blade loading and tip clearance. Although the examination of the unsteady simulation of the recess treatment cavities does not offer an image of large scale unsteady activity at the flow condition investigated, this is on itself quite significant and enables the drawing of an important conclusion namely that large casing treatments rely primarily on a steady-state flow process. The corollary of this conclusion is of course that a steady-state simulation should then be sufficient to capture the essential features of the recess treatment.

Acknowledgements

My ultimate thanks to Allah almighty who created me and gave me strength and knowledge.

I would like to express my greatest gratitude and sincere thanks to my supervisors DR. ANTONIOS TOURLIDAKIS and PROFESSOR ROBIN L. ELDER for their guidance and support throughout the course of the investigation. Also, I would like to thank all my colleagues and members of staff of the school of engineering those directly or indirectly helped me during my studies at Cranfield.

I would like to thank my Father, Mother, brothers and my sister for their continued support and encouragement. Also, I would like to express my deepest appreciation and thanks to my wife and our children HAJER, MOHAMED and AHMED to whom this work is dedicated.

Contents

List of Tables

List of Figures

Nomenclature

Geometry Dimensions

β	blade angle.
θ	camber angle.
ξ	stagger angle.
C	blade chord.
f	fraction distance along the camber line.
h_r	height of the recess.
r	radius.
S/C	space to chord ratio.
t	blade thickness.
t_{max}	maximum thickness.
x_e	axial chord length exposed to the recess.
x_r	width of the recess.
x_s	length of the shroud ring.
x_{in}	inlet of the recess.
x_{out}	outlet of the recess.

Greek Characters

α	absolute flow angle.
ΔH	work-input.

Δn_j discrete outward normal surface vector.

Δt time interval.

δ_{ij} Kronecker delta, $\delta = 0$ for $i \neq j$ & $\delta = 1$ for $i = j$.

ℓ length scale.

ℓ_m turbulent length scale in Prandtl's mixing length turbulence model.

ℓ_t turbulent length scale.

ϵ dissipation rate of turbulent kinetic energy.

ϵ_{ij} rate of dissipation of R_{ij}.

η total to total efficiency.

γ non-dimensional strain rate.

Γ_ϵ diffusion coefficient for ϵ-equation.

Γ_k diffusion coefficient for k-equation.

κ Von Karman constant for smooth walls.

μ dynamic viscosity.

μ_{eff} effective viscosity.

μ_t turbulent viscosity.

Ω_{ij} transport of R_{ij} by rotation.

$\overline{\phi}$ time-average mean value of ϕ.

ϕ flow coefficient.

ϕ general scalar quantity.

ϕ' fluctuating component of area-averaged scalar quantity ϕ.

ϕ'' fluctuating component of mass-averaged scalar quantity ϕ.

Π_{ij} transport of R_{ij} due to turbulent and pressure strain interactions.

ψ total to static pressure rise coefficient.

ρ fluid density.

τ_ω wall shear stress.

τ_{ij} viscous stress tensor.

$\times$ vector cross-product.

ϵ strain rate.

$\vec{\Omega}$ rotational speed.

$\widehat{\phi}$ standard deviation of ϕ.

$\widetilde{\phi}$ mass-weighted mean value of ϕ.

Roman Characters

$\check{r}$ ratio between old and new implicit time steps.

Δn distance from the wall in near-wall function.

$\dot{m}$ mass flow rate.

$\vec{r}$ location vector.

C_μ constant in the k-ϵ turbulence model.

C_P pressure coefficient.

D_{ij} transport of R_{ij} by diffusion.

dn_i Cartesian components of the outward normal surface vector.

k turbulent kinetic energy.

N rotor speed.

N shape function.

n^+ non-dimensional distance from wall in near wall region.

P static pressure.

P_k production rate of turbulent kinetic energy.

P_{ij} rate of production of R_{ij}.

R_{ij} Reynolds stress tensor.

S_i volumetric source term in i-direction.

t time.

T_q torque.

U blade velocity.

u^* friction velocity in near-wall function.

u^+ non-dimensional velocity in near wall region.

u_i velocity in the i-direction.

u_j velocity vector.

U_t velocity tangential to the wall in near-wall function.

u_t velocity turbulence scale.

V flow velocity.

x_j coordinate direction vector.

Subscripts

1 inlet.

2 outlet.

a axial.

e east node.

m mean blade height.

n number of iterations.

p profile.

R reference.

r radial.

S static.

T total.

t tangential.

w west node.

ip integration point.

ss steady simulation.

var variation.

Superscripts

o old time level.

Abbreviations

2-D	Two-Dimension coordinate.
3-D	Three-Dimension coordinate.
ACM	Additive Correction Multigrid.
AMG	Algebraic Multigrid.
ATM	Algebraic Turbulence Models.
BSL	Baseline Turbulence Model.
CDS	Central Difference Scheme.
CFD	Computational Fluid Dynamics.
CFX	Computational Fluid Dynamics Software & Services.
CPU	Central Processing Unit.
CTAN	Comprehensive TEX Archive Network.
DNS	Direct Numerical Simulation.
FDM	Finite Difference Method.
FEM	Finite Element Method.
FVM	Finite Volume Method.
GGI	General Grid Interface.
GMG	Geometric Multigrid.
GRD	GRiD Coordinate file.
IGV	Inlet Guide Vanes.

LES	Large Eddy Simulation.
LPS	Linear Profile Skewed Scheme.
MLPS	Modified Linear Profile Skewed Scheme.
MP	Monitor Point.
MWS	Mass Weighted Skewed Scheme.
NASA	National Aeronautics and Space Administration.
PAC	Physical Advection Correction.
RANS	Reynolds-averaged Navier-Stokes.
RNG	Re-normalization Group.
RSM	Reynolds Stress Models.
SGS	Subgrid-Scale model.
SOU	Second Order Upwind Scheme.
SST	Shear Stress Transport Turbulence Models.
SUDS	Skew Upstream Differencing Schemes.
UDS	Upstream Difference Scheme.
UWDS	Upstream Weighted Differencing Schemes.

"The simplest form of axial compressor is the single stage fan. The distinction between a fan and a compressor has been defined by describing the fan as an air mover, whereas the purpose of a compressor is to increase the pressure and density of the air or other working gas. While this definition is substantially true, nevertheless the specification of a fan usually calls for a pressure rise, even if this is only a centimeter or two of water gauge."

McKenzie (66)

1

Introduction

The fan/compressor market becomes more and more competitive and sensitive to low manufacturing cost and high overall performance, particularly a high operational efficiency with a wide operating range. However, an operational constraint on flow range, which often limits the pressure rise capability of the fan, is the occurrence of stall and/or surge. In fact stall is a disturbance of the rotor region of the fan, which may tiger surge to occur. However, rotating stall in fans and/or compressors can be associated with the initiation of several types of aerodynamic instability, which limit the performance.

Due to the large scale pressure fluctuations involved, the stall phenomena may cause a large fall in pressure rise with aerodynamic instability, blade vibration, noise and even mechanical failure as a result of the periodic loading and unloading of the fan blades. Also, the occurrence of surge causes plant shutdown leading to a loss in production and possible costly damage when used in a process environment. Therefore, preventing these instabilities to occur would benefit the large community of users of turbomachines.

The phenomena of stall and surge in compression systems have been studied almost continuously since rotating stall was first discovered in 1938. The objective of the work has always been the same, namely to obtain the widest possible operating range for the fan and/or compressor, provided that it does not compromise other

aspects of the performance too seriously. Several techniques have been developed in the past in order to control the stall phenomenon in compressors; the two basic approaches used to delay stall inception are the active and passive stall control.

Active stall control, such as variable inlet guide vanes and bleed valves or blow off, achieves its purpose by introducing further dynamics into the compression process to dissipate any tendency for an instability to develop. The passive stall control which has been adopted with some success is known as casing treatment, which usually involves modification of the outer casing design of the compressor with the aim of providing a continuous increase in the pressure characteristic. It has mainly been applied to fans and axial compressors and it is usually installed in the casing over the rotor tip. However, it can be also installed in the rotating hub under the stators for hub critical machines. Within these anti-stall devices a practical division can be made to small and large casing treatments according to their relative size to the adjacent blade, as small and large scale casing treatments.

1.1 Potential applications

The potential of casing treatment for improving safety margins, reliability and running costs are all of considerable interest to fan manufacturers. There are a number of applications where industrial fans would benefit from the installation of such devices. In smoke venting fans where a flow with continuously rising pressure characteristic is usually specified, a casing treatment may enable a higher blade angle to be used than hitherto with consequent advantages to fan size, sound level and in some cases efficiency. Many smoke-venting fans have also to provide good performance in reversed flow during counter-rotation of the impeller. Casing treatments could significantly help the achievement of these demanding design requirements.

Jet fans installed in restricted rail tunnels can experience considerable pressure pulses during the passage of trains. The breakdown may cause by the influence of abrupt changes in cross-sectional area of a railway tunnel on the propagation of pressure waves caused by passing trains. A casing treatment, by reducing the degree of blade flutter set up by the pressure pulses, would reduce or remove cumulative fatigue damage suffered by the fan blades.

In a gas turbine engine, rotating stall will seriously restrict the flow into the combustion chamber resulting in overheating and deceleration of the engine. Restarting of the stalled engine is then often not possible until the stall cell has been cleared and normal flow conditions restored. This usually requires an almost complete shutdown

of the engine. Fans are being installed in air handling units and plenum chambers where space is restricted. They consequently experience a distorted inlet flow, not just due to lack of space in the installation but also due to air flow entering, in varying proportions, from directions other than straight ahead. Casing treatments have been shown to reduce a fan's sensitivity to inlet distortion with consequent improvements in fan operation and noise level.

1.2 Background

The benefits of casing treatment seem to have been discovered by accident around 1970 on a transonic fan, which was used for many of the subsequent studies mainly at NASA Lewis center, Cumpsty (21). Extensive experimental works were conducted on the small casing treatment type by many researchers such as Bailey and Voit (11), Fabri and Reboux (26), Osborn and Moore (74), Prince et al. (78), Smith and Cumpsty (88), Takata and Tsukuda (92) and Greitzer et al. (36). These treatments included axial, skewed and circumferential slots, tapered or straight holes and honeycomb. These devices altered the flow conditions near stall and led to a limited but valuable stall margin[†] improvement, between 4-28%, accompanied most often with a loss in efficiency of around 2-4%.

The large casing treatment also called vaned recess has shown experimentally a remarkable effect on stall margin improvement. The concept goes back to the patent by Ivanov et al. (49) and further researches conducted by Azimian (7), Bard (13, 14), Basharhagh (15), Hill (44), Kang (51), Miyake et al. (69) and more recently by Akhlaghi (4). This type of treatment usually consists of a ringed cavity or recess, with a vaned and a vaneless region, situated outside, but open to, the outer annuls wall of the fan or the compressor. The treatment has shown a remarkable effect on stall margin improvement and pressure rise for negligible losses in efficiency.

An extensive experimental work to examine the influence of the recess casing treatment on stall margin, operating efficiency and flow field of a low-speed axial-flow fan with aerospace type blade loading were carried out at Cranfield University initially by Azimian (7). This work showed more than 50% improvement in the stall margin and over twice increase in the pressure rise coefficient with insignificant peak efficiency penalties. Later, Basharhagh (15) demonstrated that these casing treatments were capable of improving stall margin for a range of machines and also increasing tolerance to inlet distortion.

[†]Stall margin is a measure of the range between the compressor operating point and the onset of system instability.

Kang (51) examined different geometrical designs of the vaned recess and concluded that elimination of flow blockage is the essential part of the stall delay mechanism, where the flow measurements obtained inside the recess showed that the treatment effectively reduced the whirl velocity component. The radial flow vectors and flow blockage found at rotor tip in the stalled regime can be removed by entering the cavity. This annular cavity then diffuses the rotational element of the flow by means of turning vanes, in the process raising the static pressure above its mainstream value, and thus permitting it to return to the mainstream in a completely axial sense. The result of this process is that in the blade tip region a larger amount of axial flow will be present thus offering a contribution to maintaining the stability of the flow. Kang's experimental results and basic geometrical features of both rotor blade and recess are employed for the present numerical investigation.

1.3 Present study

Experimental processes can be extremely useful and for years have been the dominant sources of flow information and their conclusions have been used to design and improve turbomachinery. They are capable of producing good quality data with incorporation of new techniques, such as laser methods, and more accurate measurement devices. Unfortunately their cost is quite high and there are not very robust when it comes to study different geometrical configurations. This is where the computational techniques are more favorable providing an efficient tool for the analysis and the design of fluid machinery. Of course this depends on the experience of the user and the quality of the hardware and the software in use.

Even though a considerable amount of work has been conducted in the past to understand and control the stall phenomena on the compressors and/or fans using recess casing treatment. The mechanism by which the stall margin is improved by casing treatments is not yet fully elucidated. Various hypotheses have been proposed but none of them are able to explain all the observed phenomena satisfactorily. However some important observations were mentioned in the literature, such as removal of whirl component and the interaction between casing treatment flow and main flow, which appeared to be closely related to the mechanism being sought.

A little work has been carried out on numerical simulation of casing treatments in general and specifically the recess casing treatment due to its complexities, even though computational fluid analysis has been very active in the prediction of various phenomena in turbomachinery in recent years. It is promising as a tool to aid in understanding the complexities of the phenomena associated with casing treatments.

The main aim of this project is to numerically investigate the improvement in stall delay produced on a typical industrial axial-flow fan by the use of a passive stall control device fitted at the outer casing. An important aspect of the work is to analyse the effect of the recess casing treatment on stall margin improvement as well as its influence on global performance parameters. Also, the study seeks to offer a contribution to the understanding of the physical processes occurring when approaching stall as well as the working mechanism by which casing treatments improve stall margin. A Reynolds-Averaged Navier-Stokes CFD code, CFX-TASCflow, was used for the analysis and the predicted result of the overall performance, efficiency and work-input characteristics of the fan with and without casing treatment were compared with previously reported experimental results carried out at Cranfield University by Kang (51).

1.4 Thesis structure

Following this brief introduction, Chapter 2 presents some introductory remarks about stall and the various methods used to prevent it. Subsequently review of the work undertaken previously in this field in theoretical, experimental and numerical aspects is presented. A detailed review on the use of the passive control devices to delay the stall will be given with concentration on the recess casing treatment and its working mechanism.

Chapters 3 and 4 present a brief description of the commercial code CFX-TASCflow used in the present study. In Chapter 3, the governing equations for the conservation of both mass and momentum are described for compressible and incompressible flows, and also the most common turbulence models are classified and discussed. Chapter 4 gives a general introduction to the subject of grids used in CFD, their classes, their quality measures, and their generation methods. It also presents a brief description to the discretization method and some of the boundary conditions implemented by the code and used in the present work.

Chapter 5 describes the various approaches taken to numerically model the axial flow fan similar to that experimental rig in which the flow measurements were performed. It also provides the predicted results for three study cases performed, one is a mesh independence study and the other two are carried out to investigate different turbulence models and discretization schemes available within the code.

The numerical simulations of the axial-fan with solid casing are presented in Chapters 6 and 7. Steady state simulations of the fan were carried out for single blade

passage and presented in Chapter 6. For all simulations, the overall performance of the fan in terms of pressure rise coefficient, efficiency, and work-input characteristics are estimated and compared to the experimental work carried out at Cranfield University by Kang (51). Chapter 7 presents the predicted results for two unsteady flow simulations carried out for the fan, one with single blade passage and another with the entire fan blade row.

The steady state simulations of the fan with treated casing are presented in Chapter 8. In these simulations, a stage interface is used between the recess and the blade grids. The predicted results were compared to the solid casing findings well as the experimental data available from Kang (51). The interaction between the recess and the rotor blade was investigated by performing unsteady simulations of the fan with a treated casing. The results of this investigation is presented in Chapter 9.

Finally, the conclusions from the present work and proposals of possible future research are made in Chapter 10.

"It is not yet possible, on the basis of these tests and previous work on similar configurations, to offer more than a very general hypothesis for the means by which the treatment functions. Both this and minimal loss of efficiency, despite massive rotor tip clearance, remains to be explained by further, more detailed, investigations."

Basharhagh (15)

2

Review of Previous Work

The single stage fan is the simplest form of axial compressor. Turner et al. (97) stated that there was no accepted definition to distinguish between a fan and a single stage compressor. McKenzie (66) defined the difference between them by describing the fan as an air mover, whereas the purpose of a compressor is to increase the pressure and density of the air or other working gas. While this definition is substantially true, nevertheless the specification of a fan usually calls for a pressure rise, and in even if this is only a centimeter or two of water gauge. In turbofan aero-engines the fan may develop a pressure ratio in the region of 2:1, but it is still an air mover in that the majority of the airflow passes directly to a propulsion nozzle where the pressure energy is converted directly to kinetic energy in the propulsive jet.

A familiar form of axial-flow fan is the domestic ventilator. This consists of a single row of blades driven by an electric motor. An example is shown diagrammatically in Figure 2.1. However, this kind of fan is usually a stage having considerably higher stagger and/or space chord ratio than generally found in single stage compressors or multi-stage machines. The fan industry has the tendency to favor the use of only a small number of blades in any one row for simplicity and cost. Therefore, when the size of the unit is reduced for a given space chord ratio, the chord length will also reduce if the same number of blades are used.

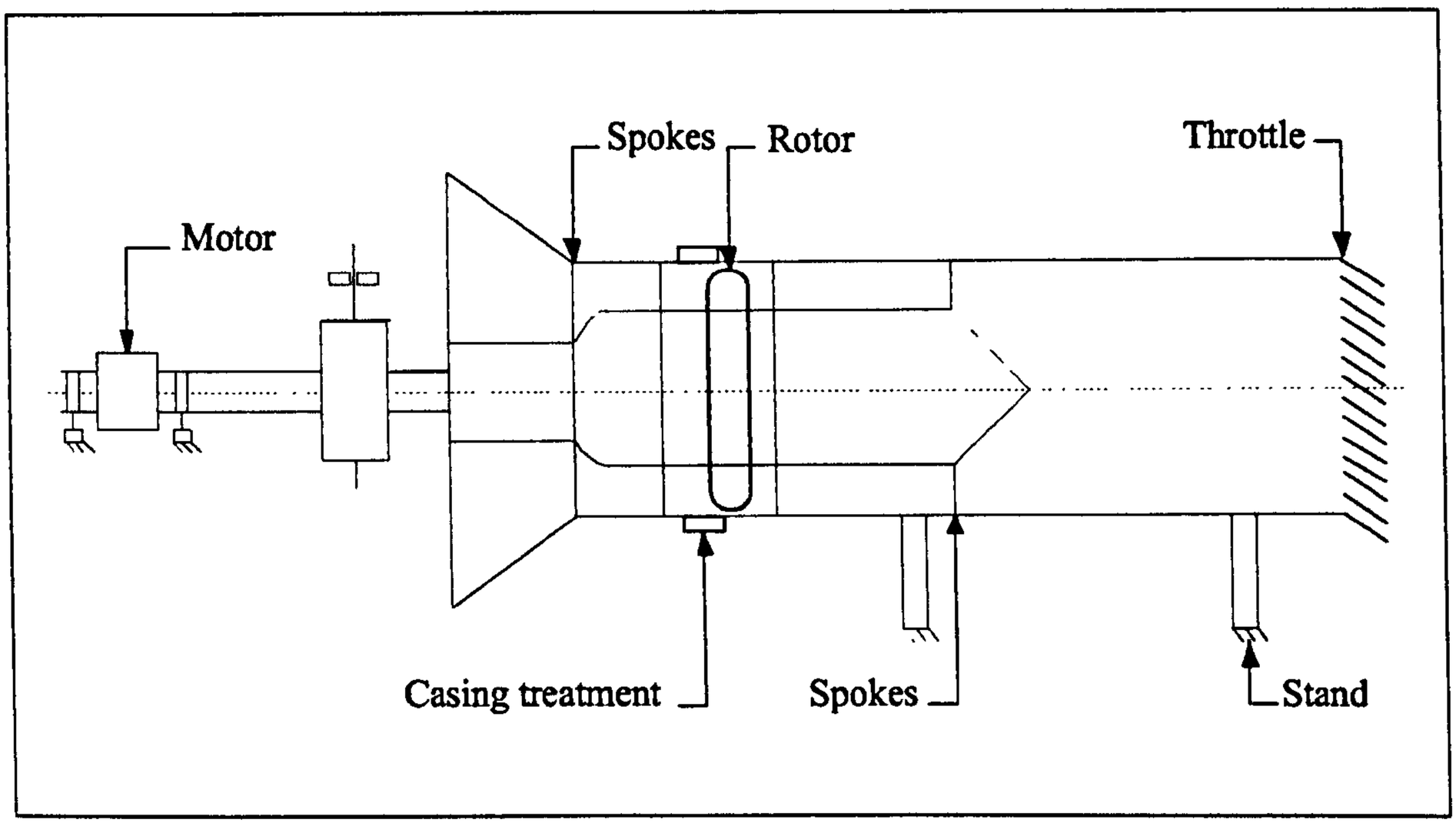

Figure 2.1: Sketch of the low-speed single stage fan rig

To counteract the difficulties associated with the manufacture of airfoils of small chord and thin trailing edge, the number of blades is reduced to increase chord length. This, at a fixed blade height, results in a reduction of the blade aspect ratio[†], and also has the effect of increasing the chord Reynolds number. However, the effects of low aspect ratio blading in the aerodynamic behavior of turbomachinery in an area of some controversy. Wennerstom (104) stated that within the gas turbine industry low aspect ratio is considered to be less than 2, whereas high aspect ratio is greater than 4.

2.1 Stall

The past experimental work and analyses have shown the existence of many types of stall during the operation of a compressor. Rotating stall is the most commonly observed type of stall and will be discussed in detail later. It could be regarded as local instability of the system since its effects are stronger upstream of the rotor with a rapid decay occurring on the downstream side. There are three other phenomena:

[†]Ratio of the blade height to blade chord

Individual blade stall: Aerodynamic stall in which all the blades around the compressor annulus stall simultaneously without the occurrence of a stall propagation mechanism. It is characterized by the development of large separated flow regions or zones of low-flow in the wake of each blade.

Stall Flutter: It takes place at high incidence and it is associated with individual stall blade.

Axi-symmetric stall: It is the reverse flow area, located axi-symmetrically in the annulus and covers part of the blade-span.

2.2 Classification of rotating stall

Rotating stall is the mechanism that allows the compressor to adapt to a mass flow, which is too small. The flow shared unequally, instead of trying to share the limited flow over the whole annulus, so that some blade passages have quite large flow and some have very little. It was firstly observed in 1938, when Sir Frank Whittle's group was developing centrifugal compressors. They constructed a low-speed research rig with an observation window to study the flow pattern at the diffuser entrance with wool tufts.

Grant (33) was the first researcher to label this flow phenomenon as propagating or rotating stall in his study of the stalling characteristics of an axial flow compressor in which the rotating stall patterns were detected by the use of high frequency response hot wire anemometers. Stall initiated by either wall or blade stall in most cases creates a stall cell, which causes a flow blockage in the annulus. This blockage or stall zone can range from covering only part of the span, either at the tip or in rear cases at the root, to the full span.

It is normal with compressors that as the mass flow rate is reduced the pressure rise increases, Figure 2.2. Generally a point is reached at which the pressure rise is maximum and further reduction in mass flow rate leads to an abrupt definite change in the flow pattern in the compressor. Beyond this point the compressor enters into stall.

Rotating stall cells may be singular or several in number depending upon flow conditions and compressor geometry and propagate at some percentage of the rotor speed, usually between 20-70%. Inside the stall cells the axial or through flow velocity is

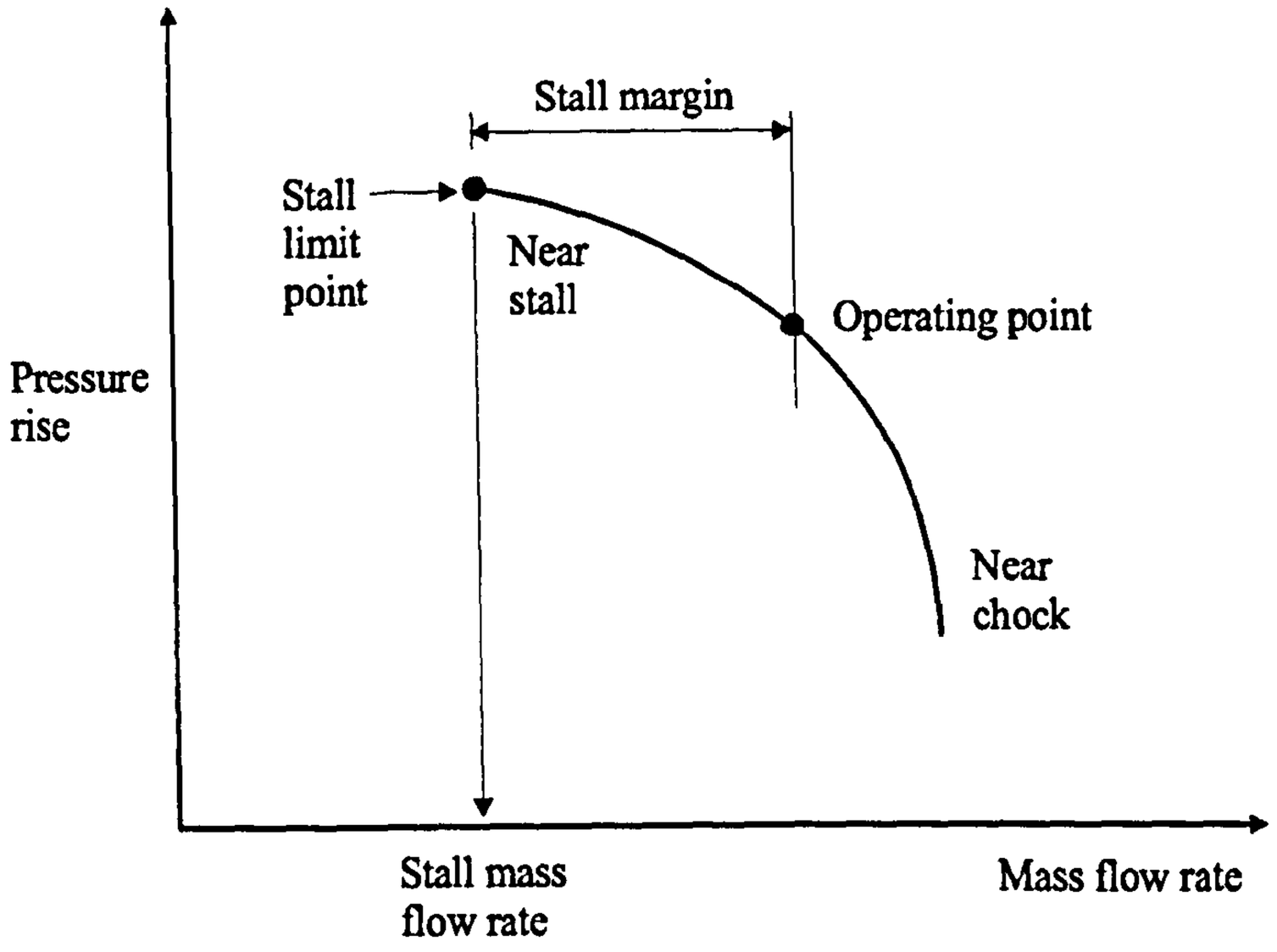

Figure 2.2: Compressor operating characteristic at constant speed

less than the unstalled flow but the circumferential component can be very large. Rotating stall may be also classified by the type of stage performance characteristic associated as progressive or abrupt, which is probably the best way to denote stall type. Also, stall can be classified according to the geometry of the stall zone as part or full-span, or the periodicity of the stall zone as steady or intermittent.

2.2.1 Progressive or abrupt stall

A smooth continuous stage performance characteristic in the stall region, Figure 2.3(a), shows a gradual increase in blocked annulus area due to stall and is therefore referred to as *progressive stall.* The drop in overall performance is quite small and often the presence of stall is indicated only by a change in noise. A discontinuous stage performance characteristic is also possible. Generally for this type of performance curve a single stall zone covering as much as half the annulus area and extending over the entire blade span has been observed. Because of discontinuity in the pressure curve, this type of stall is called *abrupt stall.*

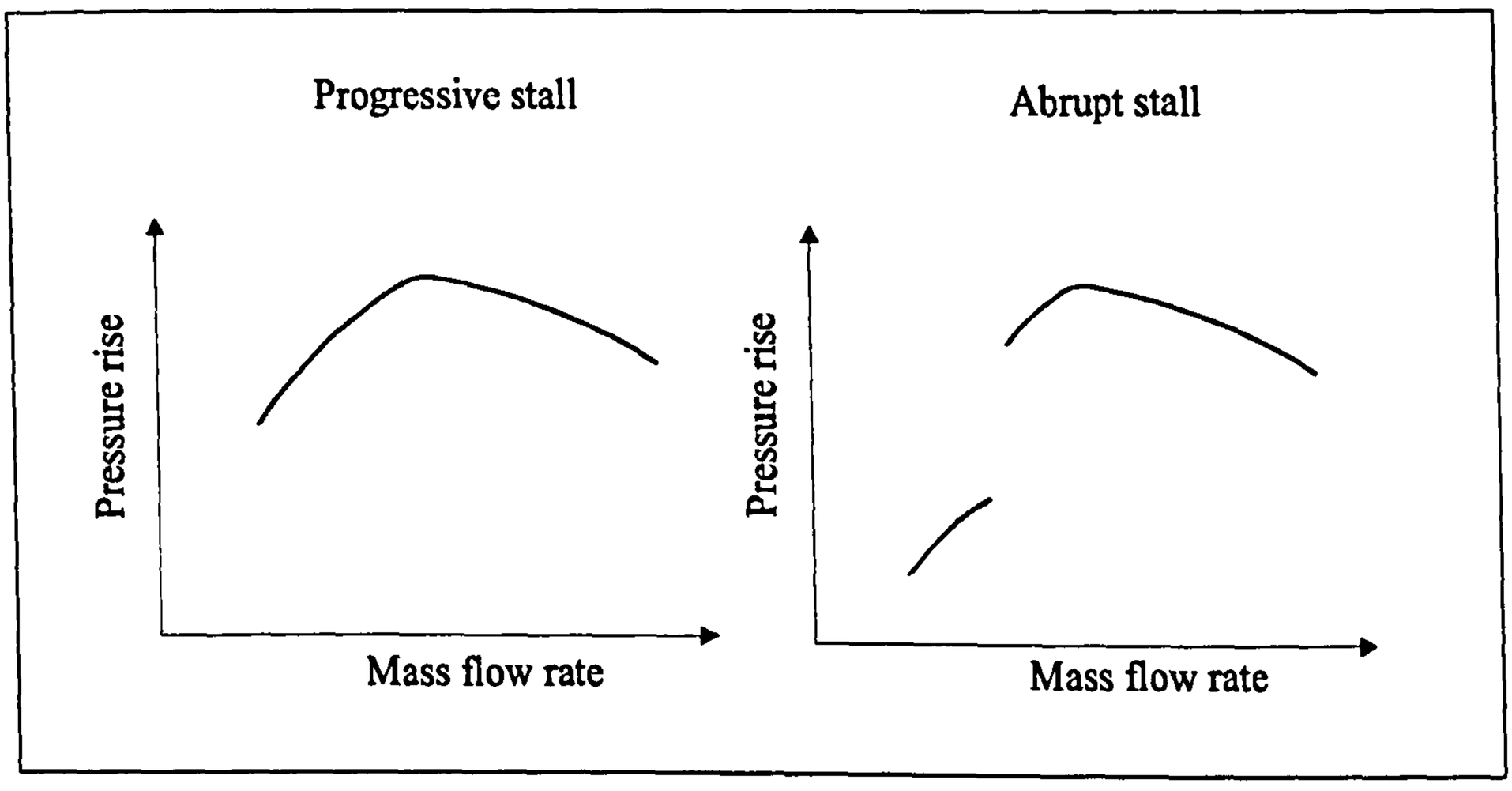

(a) Progressive and abrupt stall

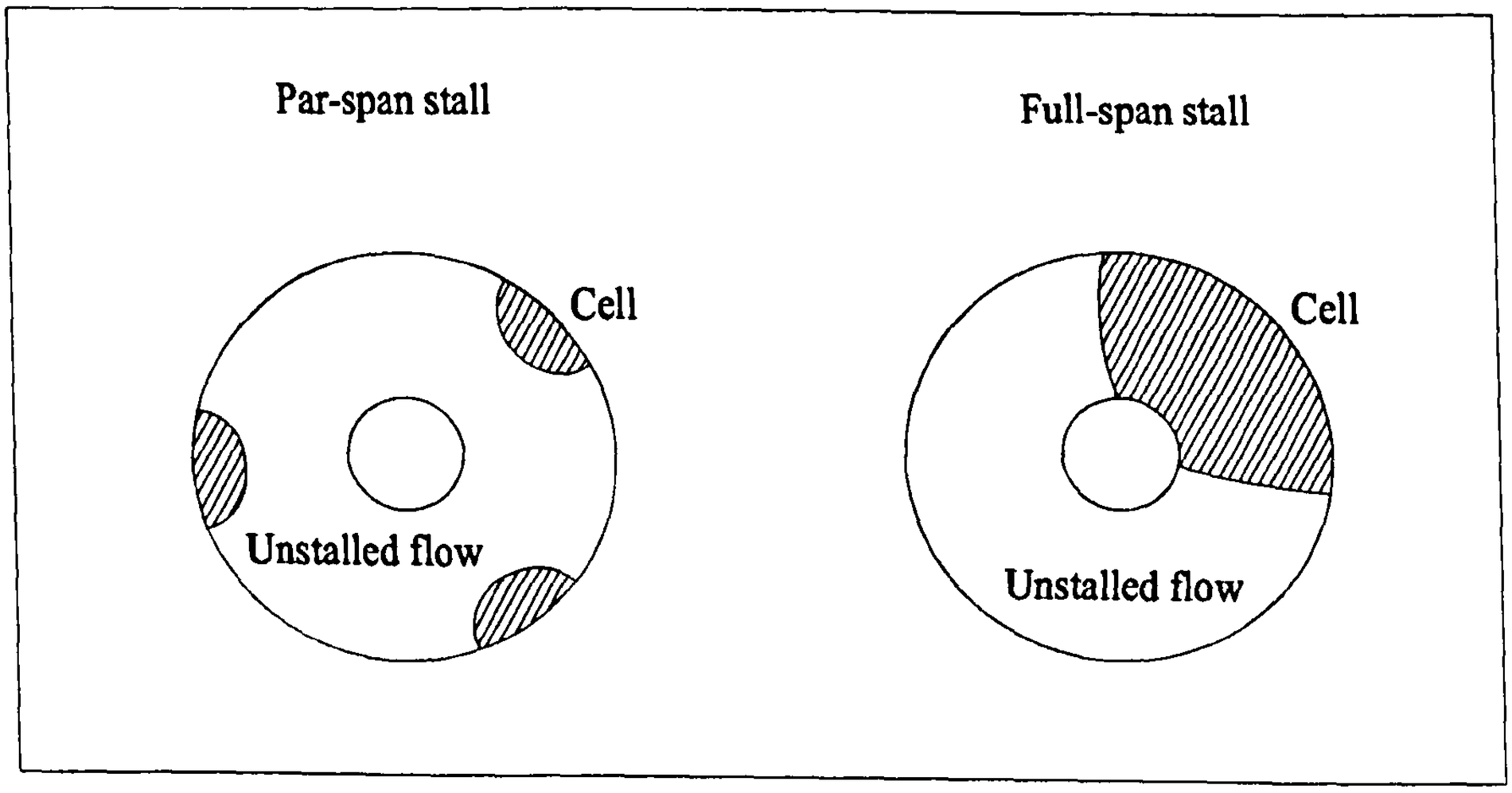

(b) Part- and full-span stall

Figure 2.3: Classification of rotating stall

2.2.2 Part or full-span stall

The term *part-span stall* refers to stall covering part of the blade span only, and the term *full-span stall* to stall covering the whole blade length, Figure 2.3(b). Normally, there seems to be only one cell at full-span stall, whereas at part-span stall there can be multiple cells. The abrupt type characteristic, which gives a large drop in pressure rise, is usually accompanied by full-span stall. The progressive type characteristic, which produces small or moderate drops in pressure rise, indicates part-span stall.

2.2.3 Steady or intermittent stall

Compressors may also have an intermittent stall pattern at a given operating point. In this case one stall pattern exists for an instant before changing to a new stall pattern.

2.3 Stall control techniques

Considerable effort has been expended in the past to understand and control the stall phenomena. A large number of conventional stall control techniques employ the basic concept of restricting the operation of the compressor to the 93-94% of the stall limit by predetermined safety margin. This will limit the operating range of the compressor and prevent it from operating at maximum efficiency point, which may lie very close to the stall line. The alternative is to delay the stall inception allowing operation at normally stalled flow rate. There are basically two approaches to achieve that active and passive stall controls.

2.3.1 Active stall control

It achieves its purpose by introducing further dynamics into the compression process to dissipate any tendency for an instability to develop. The additional dynamics introduced to the system is usually that of variable inlet guide vanes and bleed valves or blow-off.

2.3.1.1 Variable inlet guide vanes

When the incidence angle on the blades is increased as the flow rate is reduced, the flow separates from the suction surface of the blades and eventually causes the associated stages to stall. By using variable inlet guide vanes, the incidence angle can be reduced when the flow rate is reduced and this will prevent the separation of the flow thus delaying the inception of stall for axial compressors working at low speeds.

2.3.1.2 Bleed valves or blow-off

This method is often used in multi-stage compressors operating at low mass flow rates and speeds. In these cases an insufficient pressure rise in the stages leads to an insufficient density rise in the rear stages, and the flow coefficient there becomes large due to the controlling annulus area. This leads to chocking of the rear stages, which limits the flow rate through the front stages resulting in their stalling. To increase the flow rate in the front stages, air can be discharged from some intermediate stages through a valve. The increased flow will shift the operating point of the inlet stages to the right on the compressor pressure rise against mass flow rate characteristic and therefore delays the inception of stall in the front stages.

2.3.2 Passive stall control

This technique usually involves modifying the outer casing design of the compressor. This would provide an extended continuously increasing pressure characteristic, which peaks at a much lower flow rate with a comparatively small efficiency penalty. Such anti-stall device would also reduce the operational and maintenance costs, reduce or remove cumulative fatigue damage that fan blades often suffer, and increase the level of safety of operation. Although an additional production cost may be involved, it could often be recovered by the potential gains in overall performance and safety. These anti-stall devices include small casing treatment, large casing treatment, hub treatment and dynamic control.

2.3.2.1 Small scale casing treatment

These are devices can be described as small in the scale of treatment relative to blade dimension. NASA Lewis Research Centre was the driving force in the de-

velopment of small scale casing treatments for axial flow compressors in the 1970's. The treatments alter the flow conditions near the stall and can improve stall margin, between 4-28%, accompanying most often with loss in efficiency.

2.3.2.2 Large scale casing treatment

A relatively new kind of casing treatment developed by the low-pressure fan industry called vaned recess casing treatment. It is also known as large scale casing treatment, since the dimensions of the treatment are of the same order of the blade. It usually consists of a ringed cavity or recess, with vaned and vaneless regions, situated outside, but open to, the outer annulus wall of the fan. This type of treatments has shown a remarkable effect on stall margin improvement, between 50-67%, and pressure rise for negligible losses in efficiency.

2.3.2.3 Hub treatment for stators

These are similar techniques to small scale casing treatments and have the same working mechanism. They have been used in hub critical machines rather than tip critical ones[†]. In this technique, the stall margin improvement is achieved not directly by reducing the blade incidence but by suppression of the onset of rotating stall.

2.4 Work on rotating stall

Rotating stall first observed in 1938, when Sir Frank Whittle's group was developing centrifugal compressors. They constructed a low-speed research rig with an observation window to study the flow pattern at the diffuser entrance with wool tufts. One of the earliest references to rotating stall available in the open literature appeared in a report on the performance of a centrifugal compressor by Cheshire (19). A ten-vane diffuser system discharging to a common reservoir was brought to the surging condition by closing the throttle, one channel would first break down as indicated by wool tufts, then the next one with the first one regaining normal flow. This reversal travelled round the system at about one-sixth of the rotational speed

[†]Tip critical means the stall initiates at the tip region of the blade.

of the impeller in the direction of the rotation. This is the first recorded example of the phenomena now know as rotating stall.

Another early study by Shulze et al. (87) on axial flow turbojet engine, published by NASA reported the occurrence of an asymmetric flow pattern, detected by the means of wool tufts, in an impulse axial flow compressor. Grant (33) was the first researcher to label this flow phenomenon as propagating or rotating stall in his study of the stalling characteristics of an axial-flow compressor in which the rotating stall patterns were detected by the use of high frequency response hot wire anemometers. Marble (62), Huppert and Benser (46) were also amongst the earliest researchers who reported experimental investigations of propagating or rotating stall phenomena.

The first major investigation into rotating stall was conducted by Iura and Rannie (48). They tested a low-speed single and three stage axial flow compressors, both with hub to tip ratio of 0.6. They noted an efficiency as low as 20%, and two principle types of stall were observed one with the stall regions extending over part of the blade height, the other with a single stalled region over the full blade height. Important findings were noted when changes to the blading of the two compressors were made:

- When removing blades from the third stator row in the three stage compressor, the mode of stall changed from multiple part-span patterns to unstable part-span pattern at the hub.
- By removing alternate blades from each blade row, the effect of a change in solidity was observed on the stall propagation. The multiple part-span stall was not found in this lower solidity configuration, instead a single part-span stall cell appeared at the rotor tip.
- In case of single stage compressor, the stall cells exhibited similar behaviour for the two different blading configurations. It seems that the blading was not an important factor for the stall performance.

Tanaka and Murata (93) conducted experiments on a single stage compressor with different hub to tip ratio of 0.5 and more. They highlighted the importance of the distance between the rotor and stator as the stalled performance affecting both the number of the cells and the propagating velocity. They also noted that the removal of the stator resulting in an increase in rotating stall cell speed. Stall cells were of the part-span type only in the 0.5 hub to tip ratio, and it was concluded that part-span was associated with low hub to tip ratios and full-span type more with the high hub to tip ratios.

A similar finding was reported by Yu and Mckenzie (111) who conducted experiments with an axial-flow fan of low hub to tip ratios of 0.32-0.4, and for the builds tested, only part-span stall was observed. They also concluded that, in low hub to tip ratio fans, the rotating stall was related to flow separation on the casing rather than flow separation on the suction surface of the blade.

Soundranayagam and Elder (90) investigated the stalled flow in an isolated axial impeller with hub to tip ratio of 0.5 and showed that the stagger angle of the impeller was a factor with no rotating stall appearing at high stagger angles. Their result differ from those of Tanaka and Murata (93) with two part-span cells changing to a single full-span cell after the sudden drop in the pressure rise performance characteristics.

Blanco-Marigorta et al. (17) tested a variable pitch axial-flow fan with 0.6 hub to tip ratio and 8 blades. They detected no rotating stall for the smallest pitch and two rotating stall cells for the highest pitch whereas for other pitches a part-span rotating stall was detected. They concluded that the tip blockage plays a main role in the inception and disappearance of rotating stall.

In additional to the experimental work carried out to investigate the rotating stall, several theories of rotating stall in compressors appear in the literature. The objective of all these analyses is to determine a criterion for the onset of rotating stall, the velocity of propagation and the number of stall cells. None of the proposed models can be used to predict propagation rates with any appreciable degree of reliability. However, these theories are useful in evaluating the significance of parameters pertinent to the stall propagation mechanism and thus in planning experimental research programs. All those theories were applied to a single blade row and are therefore doubtful when applied to a single stage including guide vanes, rotor and stator yet alone to multi-stage compressor.

Emmons et al. (25) who were the first to put forward a theoretical study, investigated the flow conditions in an axial flow compressor using hot wire anemometers. When the compressor was throttle, they found that low-speed velocity regions appeared to travel around the annulus in the direction of rotor rotation at lower speed lead to a large loss of compressor performance. They showed that for the most part, stalling occurs in well-defined regions over the compressor annulus. Two principle types of rotating stall were observed, one with two or more stall cells over part of the blade height and others with a single stall cell over the full range of blade height.

Later, Fabri (27) provided a simple mathematical relationship for the propagating speed of stall cells in which the velocity of the stall cells is always less than 50% of

rotor speed, which is not true for most full-span stall cells. More refined analysis was presented by Greitzer (35) who suggested non-linear approaches to the same problem.

Another theoretical study on the inception of rotating stall was provided by Day (22), whose result suggested that the onset of rotating stall is occurring at the peak point of the total to static pressure characteristic. This may be true for most of high hub to tip ratio single stage compressors and some multi-stage compressors but not necessarily so far for low hub to tip ratio machines.

A more recent stall inception model was proposed by Moore and Greitzer (70), in which a small amplitude sinusoidal model or rotating waves appear prior to stall and rotate around the circumference of the compressor annulus. As the stage is throttled towards stall, the rotating waves grow smoothly until a fully developed rotating stall cell is formed. In theory, the frequency of the model wave and the fully developed stall cell should be the same. The conclusions from their work were confirmed experimentally by Garnier et al. (31).

2.5 Small casing treatments

These devices can be described as small in the scale of treatment relative to blade dimension. They consist of axial, skewed and circumferential slots, tapered or straight porous and honeycomb placed over the tip of the rotor, covering 70-100% of the blade chord, in an axial compressor. However, the slot type treatment has been the most common type used in multi-stage axial compressors and adopted also in aircraft design. NASA Lewis Research Centre was the pioneering group in the development of small scale casing treatment techniques for axial flow compressors.

The concept goes back to the research on the outer casing blowing or bleeding method, which was initiated by NASA in the 1960's. The work conducted by Griffin and Smith (37), Koch and Smith (54) and involved studies on blowing and bleeding at the tip of an isolated high aspect ratio rotor found to improve the stall line significantly, with the maximum benefits coming at or near the maximum blow/bleed flow rates, and there was a substantial stall line improvement compared to the smooth casing even when no air was blown or bled. This finding led NASA to initiate an extensive research on casing treatments during the 1970's.

Bailey and Voit (11) are one of the first investigators in NASA to study the effect of various types of small casing treatment on a high aspect ratio single stage axial-flow

compressor. Their experiments involved the application of tapered holes, honeycomb and radial drilled holes casing treatment configurations. They noted no improvement on the stable operation range for the radial drilled holes configuration, Figure 2.4(a), and improvement up to 7% with approximately 2% loss in performance for both tapered holes and honeycomb configurations.

With honeycomb configuration, Figure 2.4(b), a small plenum volume provided the best improvement in stall margin, though zero plenum volume produced no improvement whatsoever. Re-circulation did not seem to be a controlling factor on the stall delay and the authors suggested instead that the large open area in the honeycomb casing treatments might permit equalization of the static pressure in adjacent blade passage and thus delaying the formation of rotating stall cells.

For the tapered holes configuration, Figure 2.4(c), the re-circulation seemed to be necessary for stall margin improvement. The potential for re-circulation was indicated by pressure gradient and temperature rises, difference in plenum temperature to rotor discharge temperature, were used to indicate if re-circulation was present. A positive temperature difference resulted from air flowing through the plenum and receiving additional energy as it passes through the blade row again, while a negative temperature difference would have indicated that no re-circulation was present.

Osborn et al. (73) tested a number of small casing treatment configurations on the performance of an axial flow compressor with an isolated rotor, with hub to tip ratio of 0.5. These included perforated shown in Figure 2.5, honeycomb, circumferentially grooved, axially slotted, skewed slotted and blade angle slotted configurations. They obtained up to 17% stall margin improvements with no efficiency loss for blade angle configurations. The best configuration of those tested was the skewed slotted casing, which gave a stall margin improvement of up to 20%, but suffered from a loss in efficiency of up to 7%.

Moore et al. (71) used the same rig of Osborn et al. (73) to conduct experiments on six different treatments such as circumferential grooves, skewed and blade angle slots, Figure 2.6. Radial surveys of pressure, temperature and flow angle indicated that the entire radial span of the blade is affected by the casing treatment across the rotor tip. All casing treatments tested improved the stall margin and enlarged the losses of the compressor. They concluded that the phenomenon associated with casing treatment is one of flow stabilization rather than one of the loss reduction, and that the casing treatment slots should not extend pass the trailing or leading edges of the blade if both high efficiency and pressure ratio are to be achieved.

Bailey (10) tested a single stage axial flow compressor with different circumferential grooves, shown in Figure 2.7, over the rotor tip region. He examined the number,

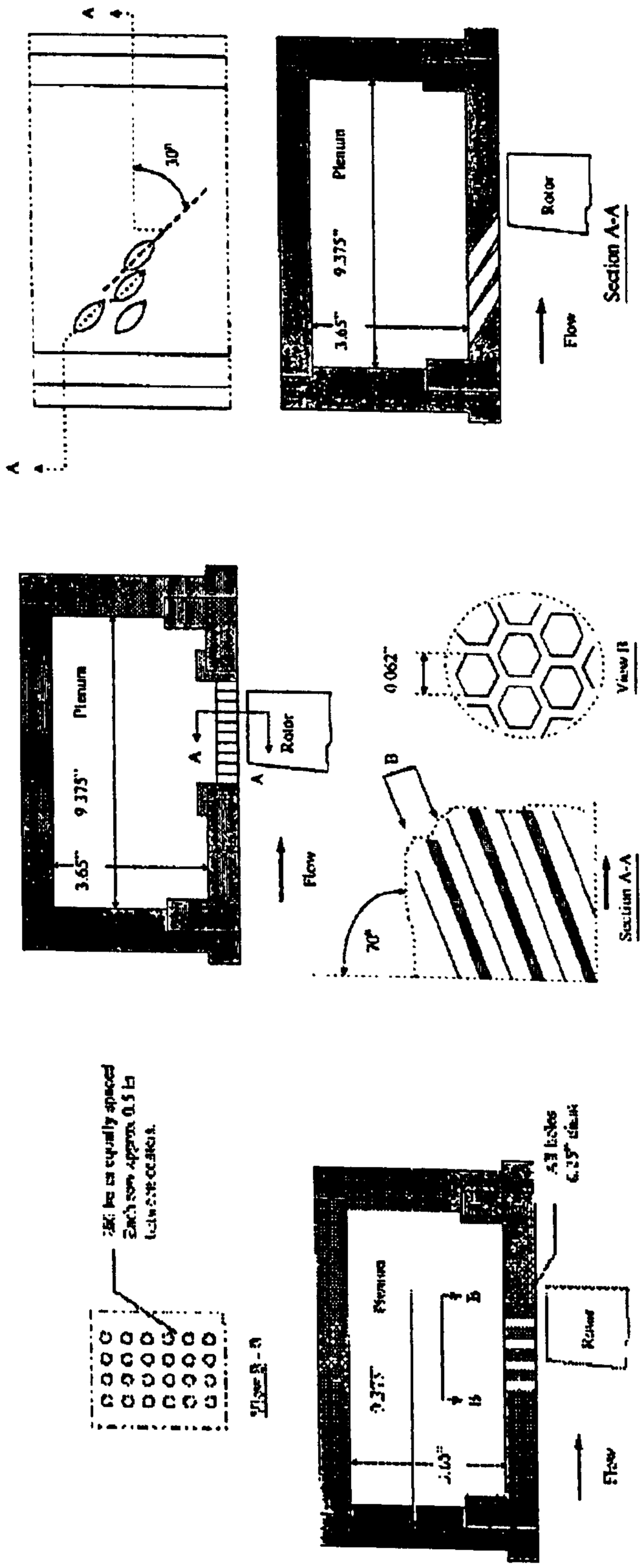

Figure 2.4: Small casing treatment configurations tested by Bailey and Voit (11)

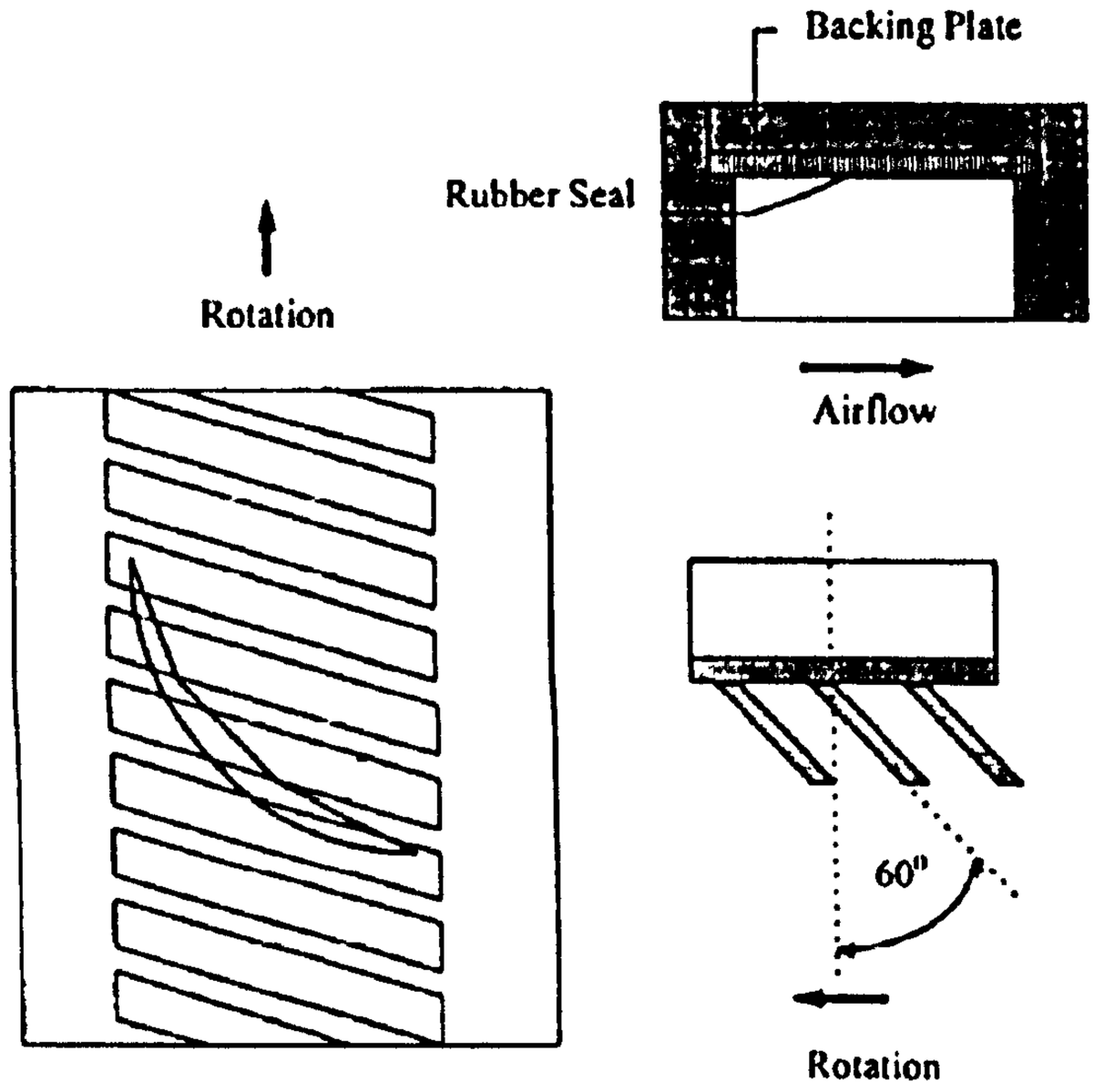

Figure 2.5: Sketch of perforated casing treatment, Osborn et al. (73)

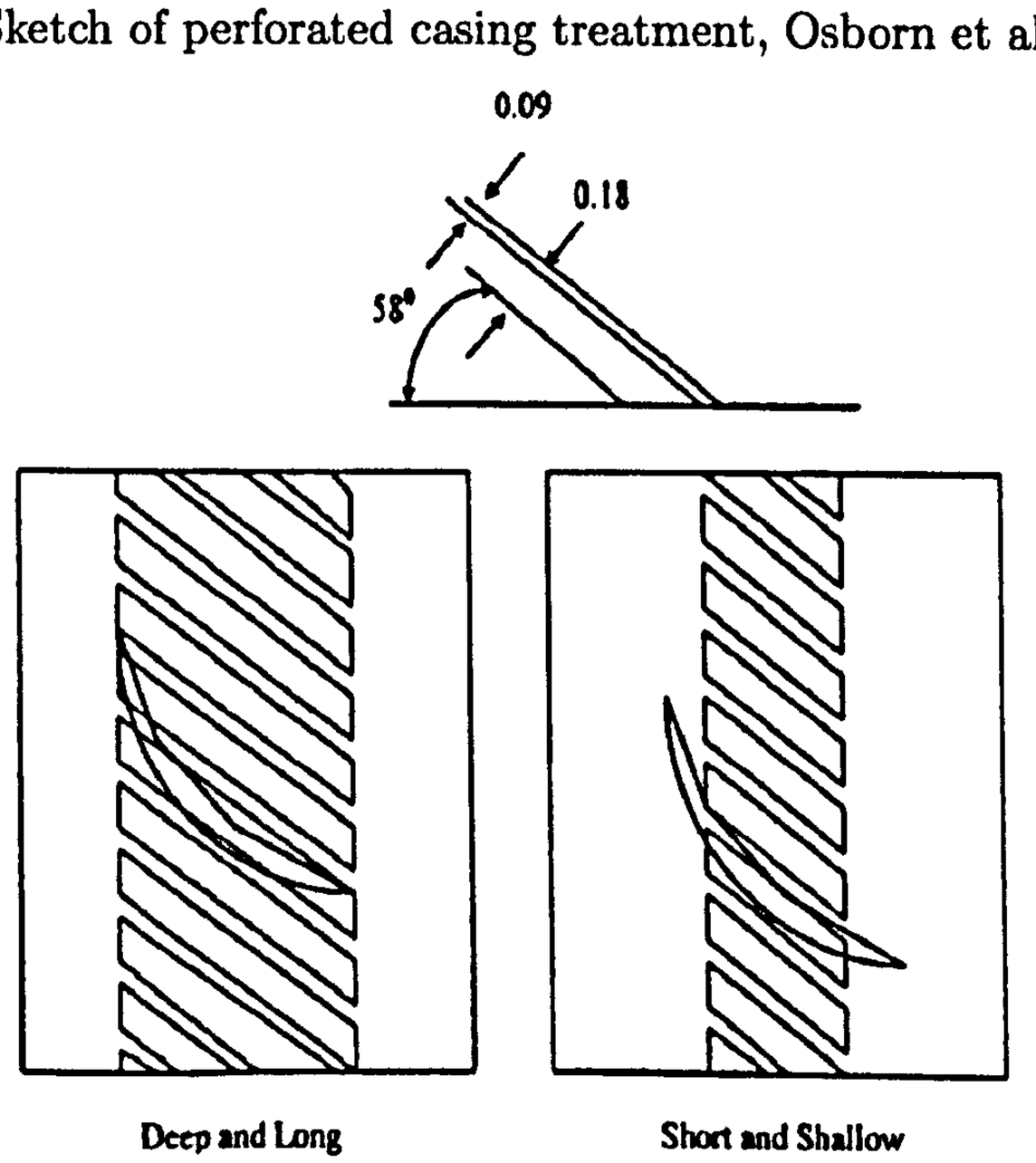

Figure 2.6: Sketch of blade angle casing treatment, Moore et al. (71)

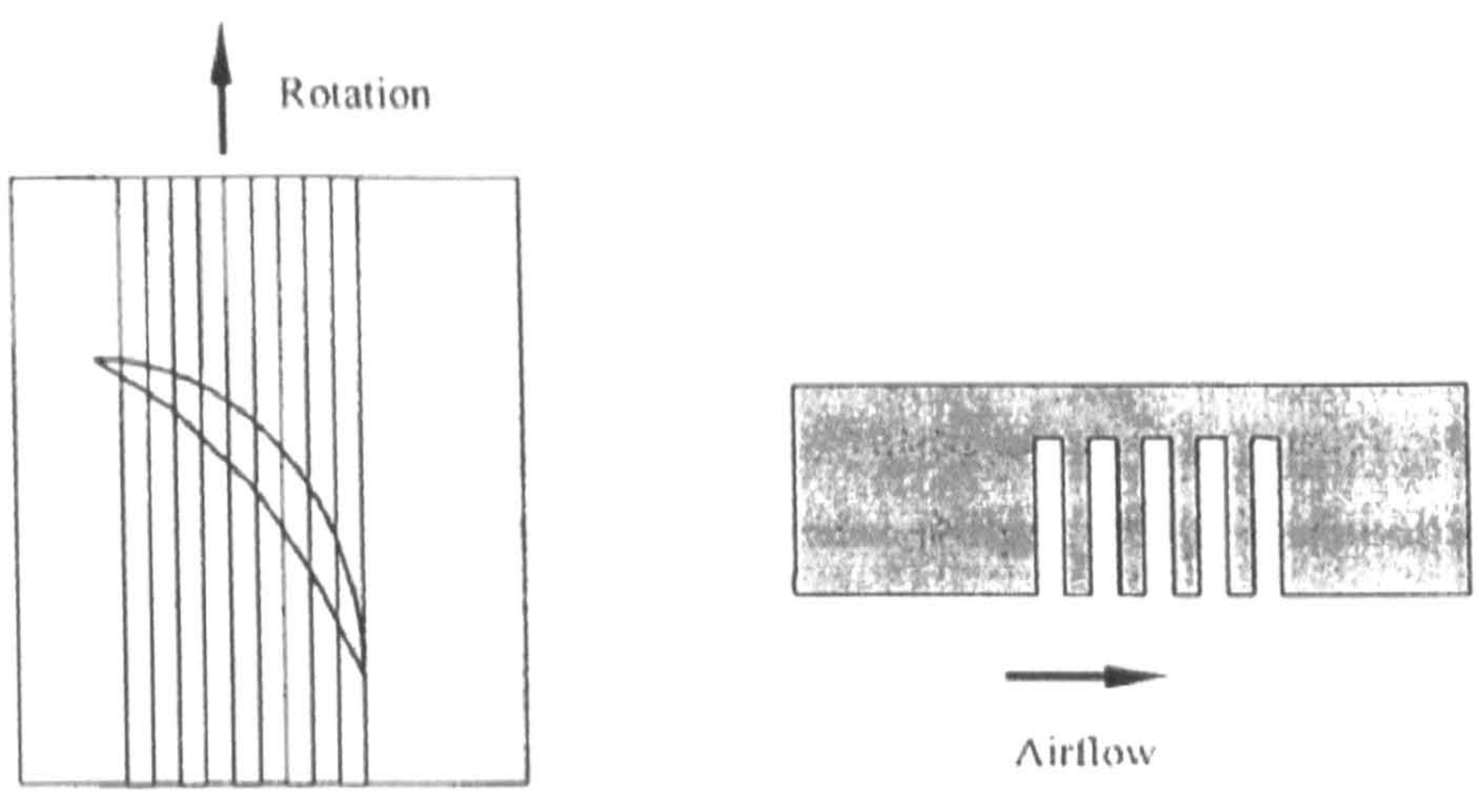

Figure 2.7: Sketch of circumferentially grooved casing treatment, Bailey (10)

depth, and location of the grooves and found that the deepest grooves showed the best stall margin improvement with no significant reduction in efficiency. He noted that stall margin improvement was the best when the forward or rear grooves were not used, therefore he proposed that the mid-chord of the blade is the critical part with respect to the inception of rotating stall.

The first investigation on the effect of casing treatments upon supersonic compressors was conducted by Fabri and Reboux (26). They tested an annular cascade with tangentially grooved outer casing and unusually low aspect ratio blades of 1/6. They noted a stall margin improvement up to 20% at low speed and more than 40% at high speed. The pressure ratio was not effected in the low speed region but an approximately 10% pressure rise was attained at high speed. They also studied the effect of tip clearance on that compressor at moderate speed of rotation, and found a limited improvement in stall margin around 15% with reduced tip clearance, accompanied though by up to 6% decrease in pressure ratio. Two years later, Takata and Tsukuda (92) concluded that the casing treatments overcome any associated effects.

The effect of 8 variations of skewed slot casing and a new teardrop casing configuration on a transonic single stage compressor was tested also in NASA by Osborn and Moore (74). Their results showed that the best stall margin improvement of 23.5% was gained by using the short, mid, open skewed slot configuration, and only 21% improvement was gained by using the long, forward, opened slot configuration. They also noted no improvement on stall margin with the teardrop casing configuration.

Greitzer et al. (36) studied the effect of casing treatment on different rotor builds to simulate the two different modes in which compressor stall could be initiated; near the wall-region, knowing as *wall stall*, or mid-blade region, knowing as *blade stall.* Their results showed that the casing treatment markedly improved the stall range for wall stall rotor, but a little change in stall point for the rotor exhibiting blade stall. A similar conclusion was pointed out by McDougall (65). However, in most compressors it is difficult to determine whether wall or blade stall is the initiator of stall without detailed measurements. They found also the use of a casing treatment caused a large decrease in the total relative pressure defect at the rotor exit when used with wall stall blades, but little change when used with the blade stall rotor.

Whithead et al. (106) used circumferential grooves and baffles at the trailing edge of the blades without success. Ping et al. (76) conducted experiments on a transonic axial compressor together with simulations using a water tunnel. They suggested that because of stall inception usually takes place at the tip or hub of a blade, the onset of stall in compressors has to do with complicated three dimensional flows emanating from the casing or hub treatments. Smith and Cumpsty (88) concluded increasing the clearance would increase the stall margin owing to casing treatment, they achieved 20-28% improvements in stall margin by increasing the tip clearance from 1-6% of blade height. Though no indication was given in the results whether or not this caused a loss in efficiency.

2.6 Hub treatments

Similar techniques to small casing treatment applied to hub critical machines. Wisler and Hilvers (109) did unsuccessful experimental work on hub treatments using a hub critical compressor. They modified the compressor by removing the stator hub shrouds and replace them with a rotating hub spool, which incorporated the stator hub treatment. Their performance results for the base line and the two treatment configurations tested, showed that stator hub treatment did neither delay the stall point nor modified the performance of the compressor. However, many other investigations have demonstrated that the hub treatment is as effective as casing treatment and has similar working mechanism.

Takata and Tsukuda (92) applied axial slots to the hub in order to simulate the effect of discharged jet on the main stream. They obtained an improvement in stall margin with rotating hub and no improvement what so ever if the hub remains stationary. Cheng et al. (18) applied skewed axial slots to an axial compressor hub that rotated underneath a set of cantilevered stator blades, as shown in Figure 2.8.

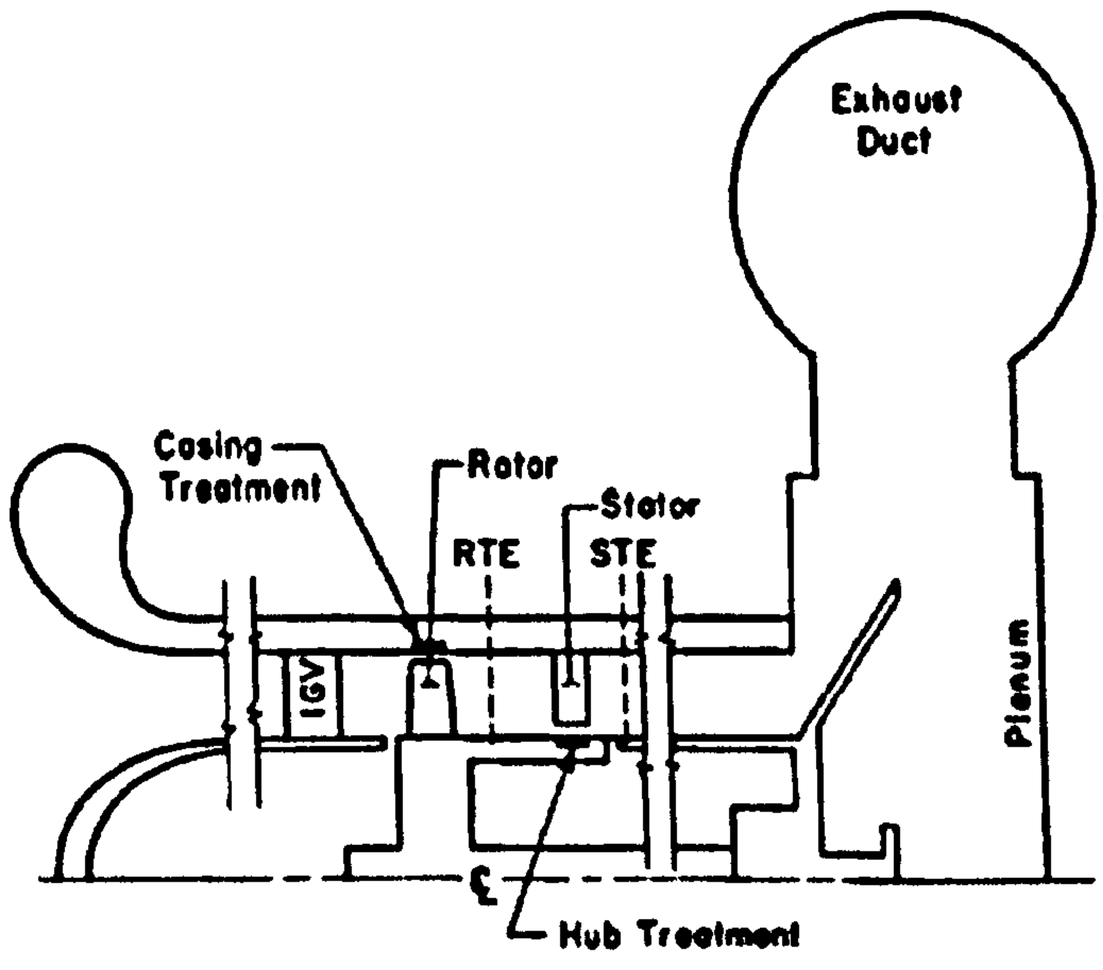

(a) Schematic of compressor cross section

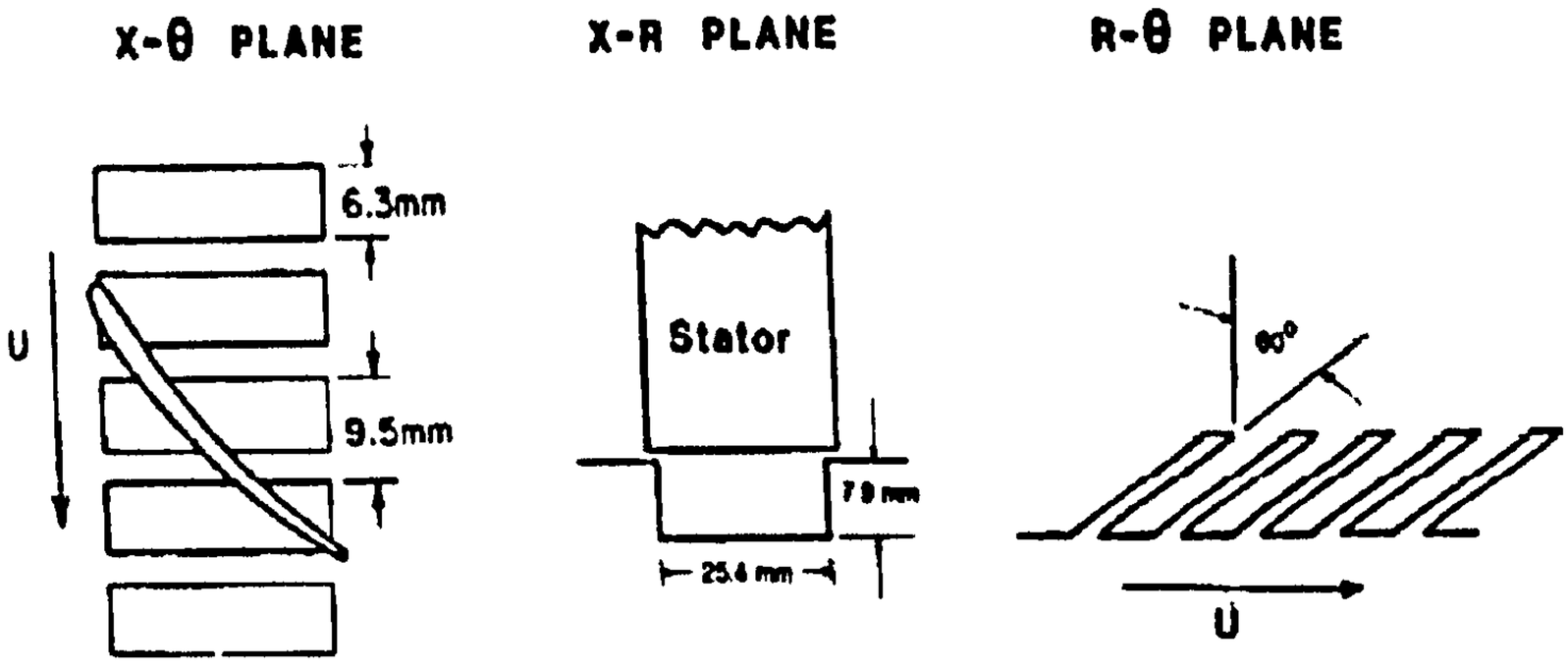

(b) Hub treatment geometry (high stagger stator)

Figure 2.8: Hub treatment tested by Cheng et al. (18)

They used two stators, one with high stagger and one with low stagger. The low stagger angle stator gave a small improvement, only 2%, in stall margin and 5% increase in stator pressure rise characteristics at the peak. On the other hand, the high stagger angle stator gave up to 10% improvement in stall margin with 50% increase in stator pressure rise characteristics at the peak. They suggested that the improvement achieved was due to suppression of wall stall at the hub, and noted that the hub treatment is only effective when wall stall exists, as did Greitzer et al. (36) for small casing treatment.

2.7 Large casing treatments

A relatively new kind of casing treatment developed by the low-pressure fan industry called vaned recess casing treatment. It is also known as large scale casing treatment, since the dimensions of the treatment are of the same order of magnitude as the blade. It usually consists of a ringed cavity or recess, with vaned and vaneless regions, situated outside, but open to, the outer annulus wall of the fan. This type of treatments has shown a remarkable effect on stall margin improvement, between 50-67%, and pressure rise for negligible losses in efficiency.

This type of treatment was first introduced in a patent by Ivanov et al. (49) from work undertaken on an axial-flow ventilation fan. The geometrical design, shown in Figure 2.9, was rather arbitrary with different results obtained for varying vane-setting angles. However, no details were given on its working mechanism. The patent work by Russell and Mahmoud (85) was principally similar apart from radially extended vanes at inlet. Bard (13) studied the flow behavior in devices similar to that of Ivanov et al. (49), and noted that they completely eliminate the stalling cycle without affecting the peak efficiency.

This technique has been applied in industrial applications with much success, one of which for tunnel ventilation is also reported by Bard (14). In this case the treatment was placed just upstream of the tips of the rotor blades, and not over them such as the arrangement of Ivanov et al. (49). He discussed the use of casing treatments in fans for the channel tunnel which use double casing treatment, one on either side of the impeller, providing stable flow conditions and continuously rising fan performance characteristics in both flow directions and for all blade pitches.

Azimian (7) was the first researcher to apply recess vaned casing treatment to an aero-engine type compressor, Figure 2.10, which had much higher blade loading in terms of the work coefficient $\Delta H/U^2$ than industrial fan do. He used a single stage

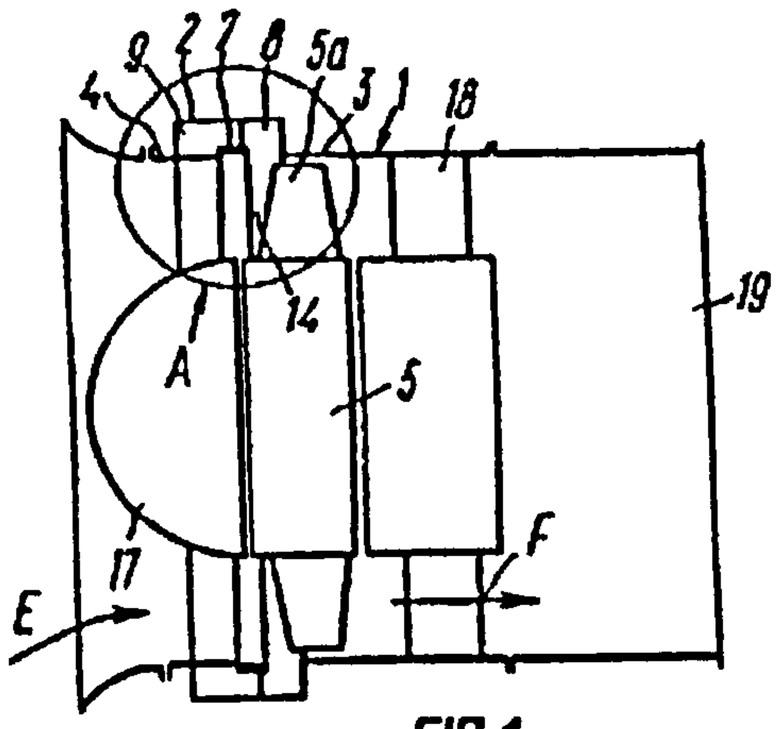

FIG.1

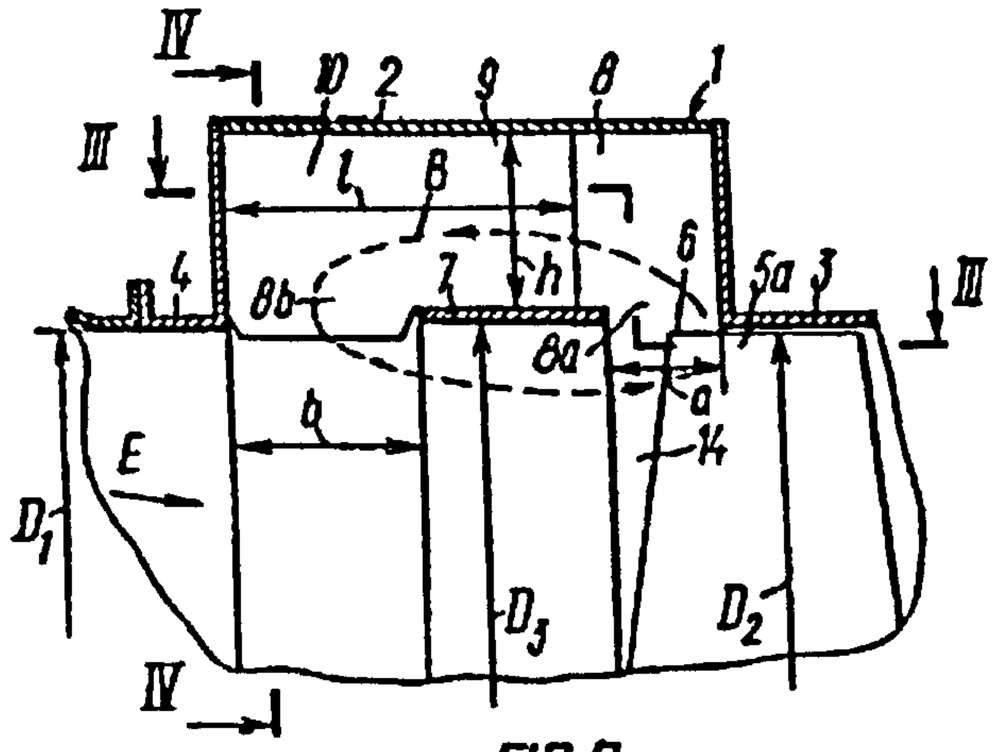

FIG.2

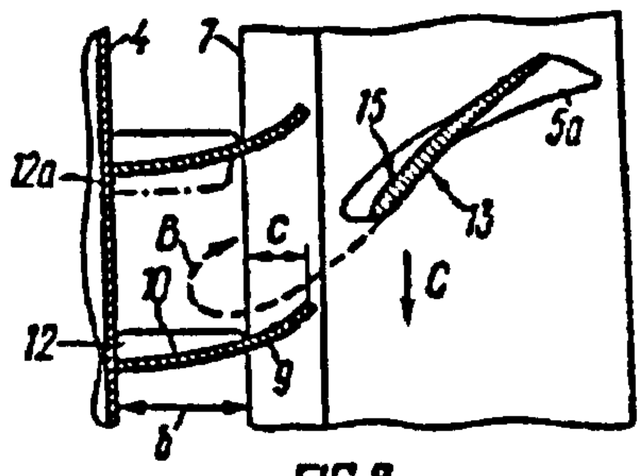

FIG.3

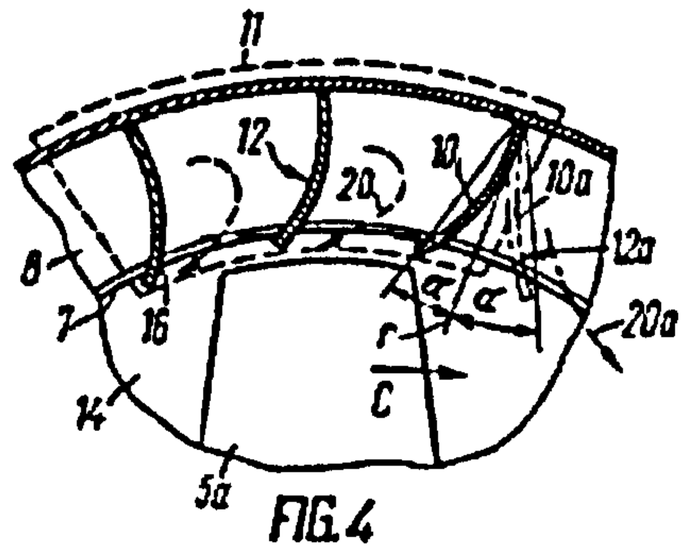

FIG.4

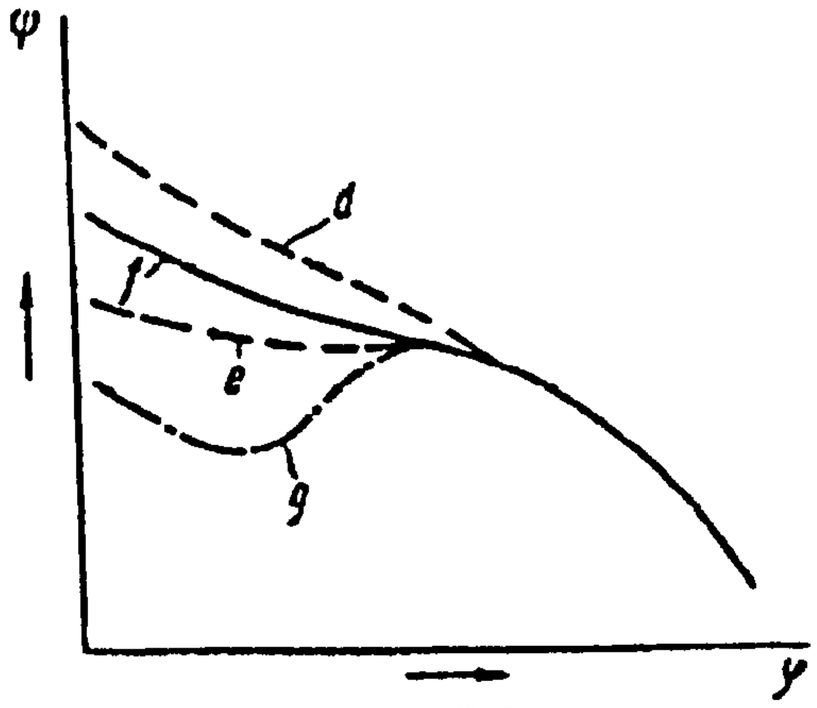

FIG.5

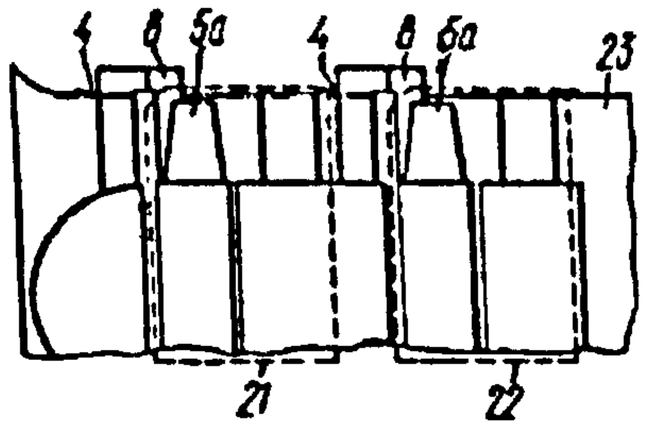

FIG.6

Figure 2.9: Sketch of casing treatment proposed by Ivanov et al. (49)

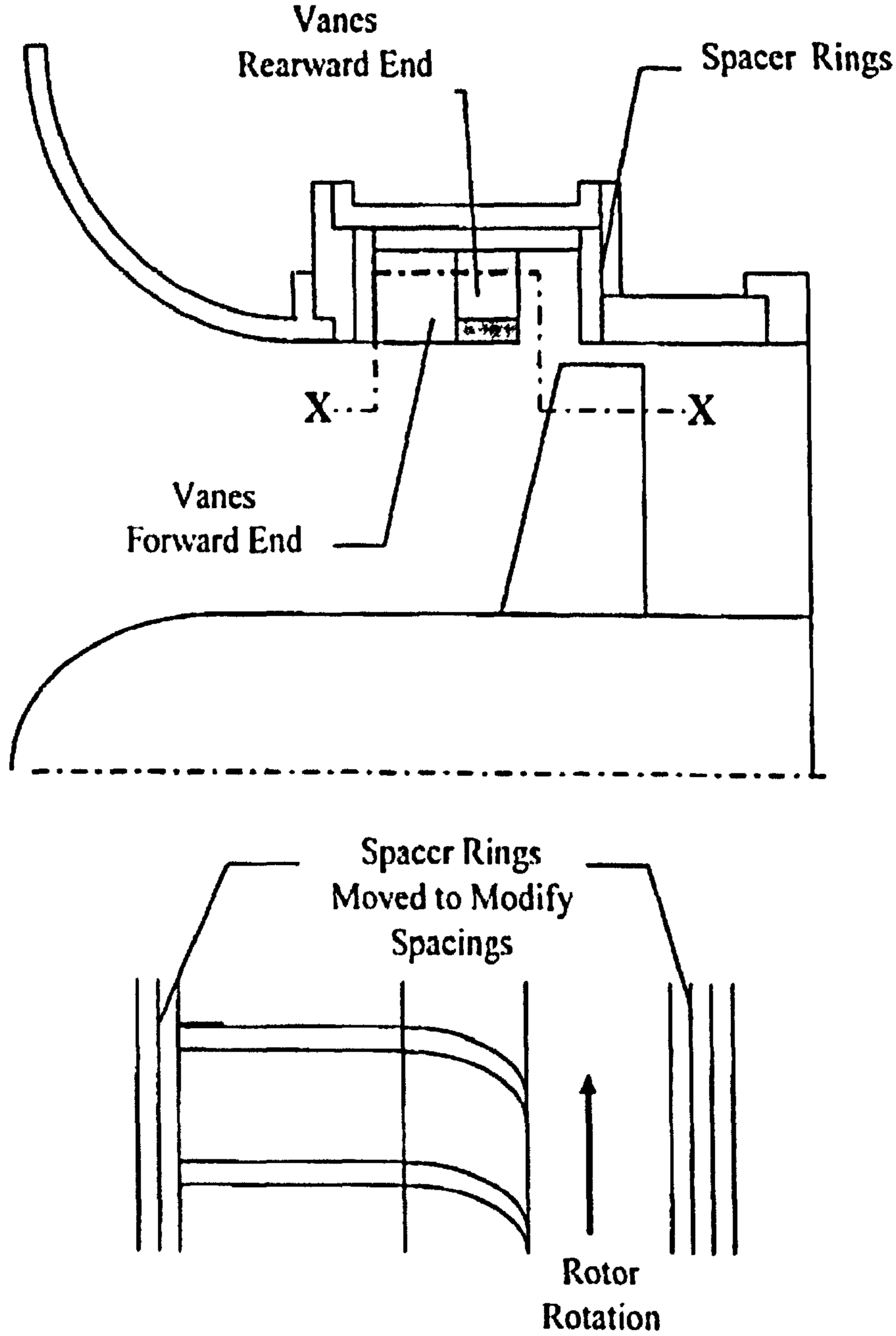

Vane Number = 48 and 24
X - X Section of Recess Vane

Figure 2.10: Recess and vane arrangements test by Azimian (7)

axial-flow fan with hub to tip ratio of 0.5 operating at low-speed of 1 500 rpm. A great number of experiments with up to 40 builds were made to examine the effect of both the rotor axial exposure* and the vanes on stall margin improvement. His results published in Azimian et al. (8, 9) showed more than 50% improvement in stall margin with insignificant efficiency penalties.

The treatment recess used 48 vanes and was tested at different exposure and the best stall margin improvement of 60.8% was achieved at 67% rotor exposure. The results showed that the amount of exposure is a very critical parameter with more than 50% exposure of blade chord required for achieving an improvement in stall margin. This amount is in disagreement with that of Bard (13), whose optimum exposure was zero or negative; though no data was provided for the fan and treatment dimensions and the operating speed. This could indicate that optimum exposure of the blade axial chord to casing treatment might be dependable on blade loading.

They found that the casing treatment gave a much smaller stall margin improvement for stage, rotor and stator builds than rotor only. For low hub to tip ratio stages, the stator hub most often the first section to stall, and also the rotor tip but at lower flow rate. Perhaps both stator hub treatment and rotor casing treatment should combined for the maximum effect. The 48 vane builds gave a much better improvement than vaneless builds, and the best improvement was achieved with an airfoil section at the inner side of the recess as shown in Figure 2.11. They also tested the fan with 24 vanes inside the recess and it produced a further improvement. However, not only number of vanes was changed but also other geometrical parameters were significantly changed. This made it difficult to simply conclude which modification was the major contributor to the improvement.

Basharhagh (15) used the same test rig as Azimian, together with another rig of the same diameter and tip speed but with adjustable hub to tip ratio for values of 0.7 and 0.9. His results showed that the best stall margin improvement for different hub to tip ratios was dependent on the size of the recess. Roy and Agrawal (83) used a recess vaned casing treatment for low-speed contra-rotating axial flow fan unit with low aspect ratio blades. The aim was to remove the casing boundary layer flow from near the second rotor tip and then to inject this flow back into the main annulus near the tip of the first rotor, as shown in Figure 2.12. This arrangement yielded significant improvements in the fan unit performance as well as stall margin.

Kang et al. (52) used the same experimental rig as Azimian to test three different geometrical designs of recess casing treatment, as shown in Figure 2.13, all had 24 vanes in the recess, half of those used by Azimian. More than 65% of stall margin

*Rotor axial exposure is the axial position of the casing relative to the rotor leading edge.

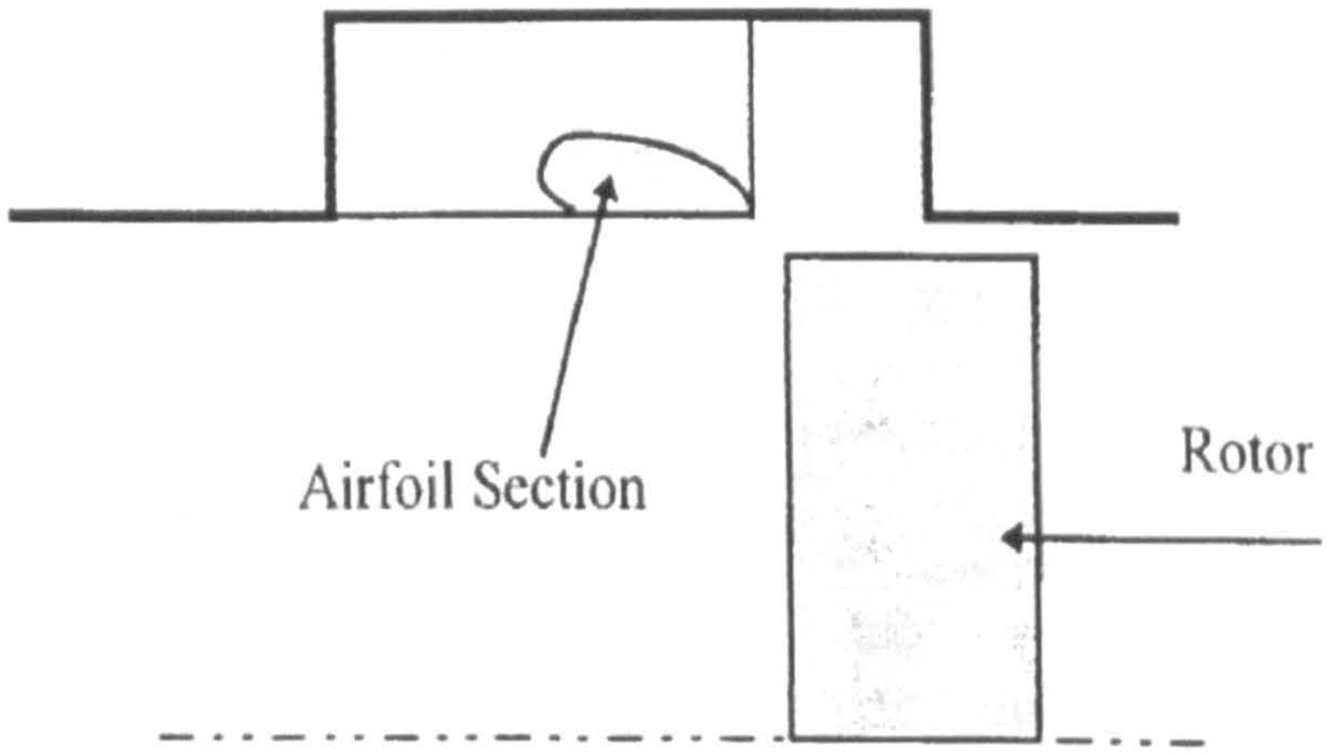

Figure 2.11: Recess casing treatment with an airfoil section, Azimian (7)

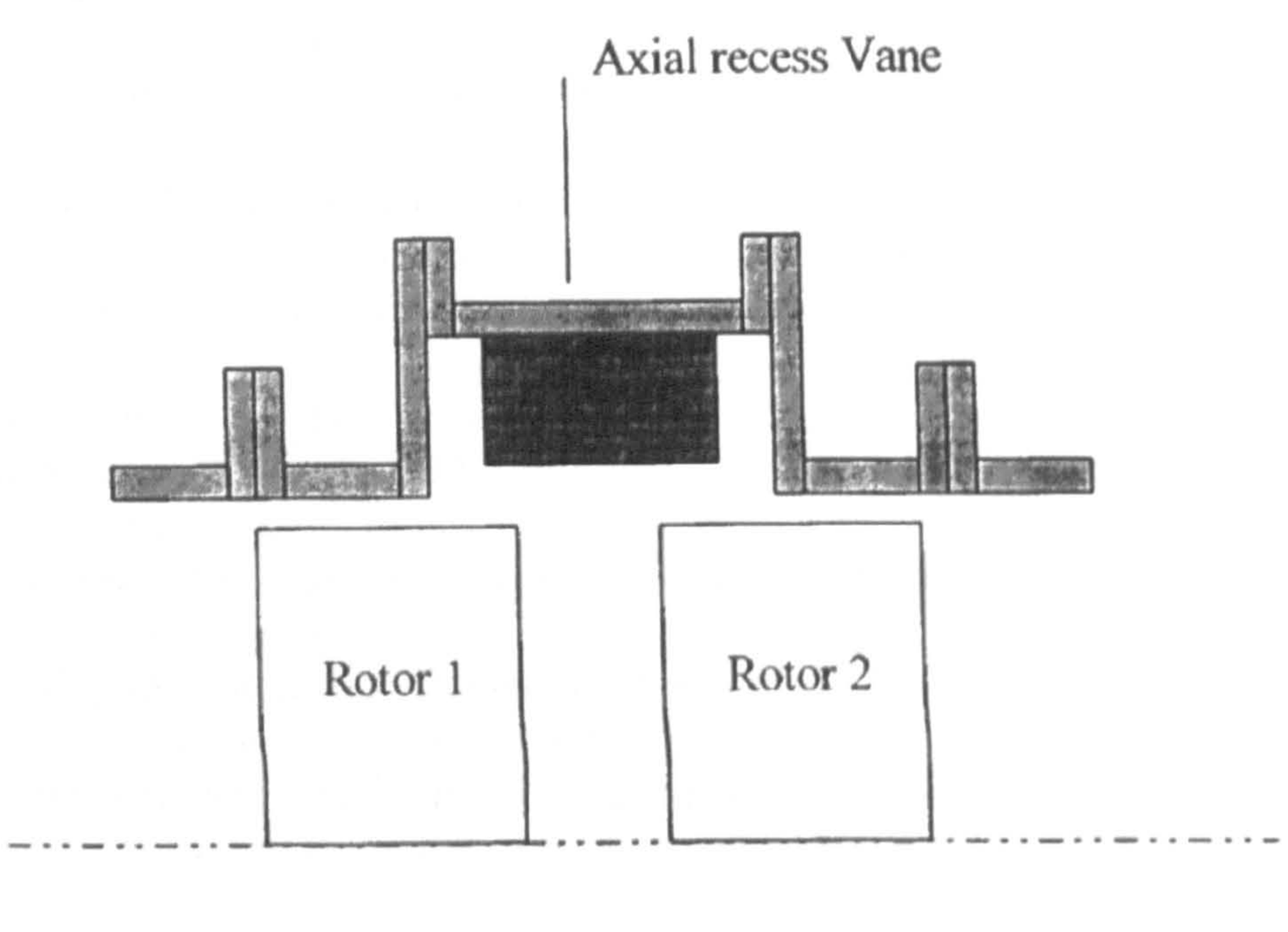

Figure 2.12: Arrangement for contra-rotating unit

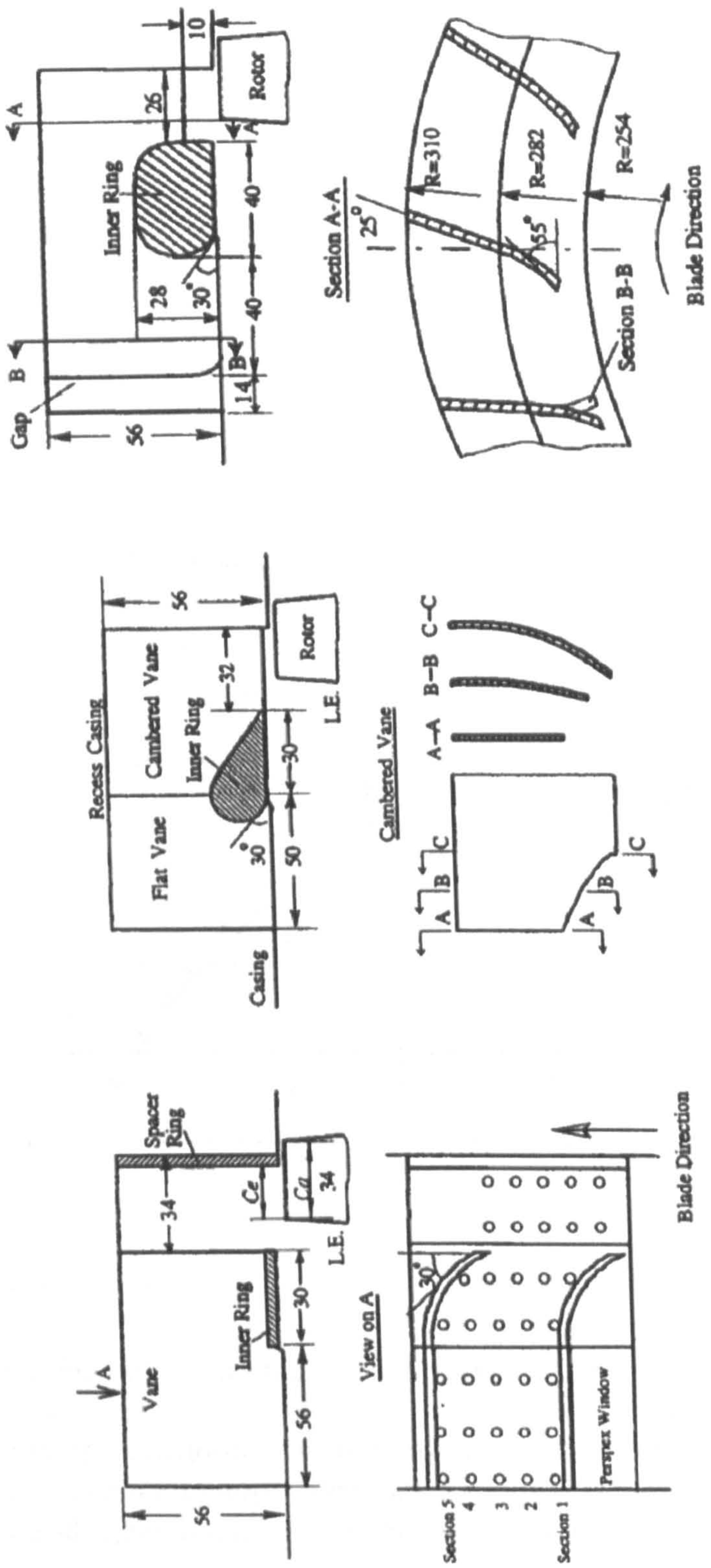

(a) Configuration 1 (b) Configuration 2 (c) Configuration 3

Figure 2.13: Sketch of casing treatment design tested by Kang (51)

improvement and over twice the pressure rise were obtained with insignificant peak efficiency penalties. The research suggested that it is difficult to gain any further improvement of this rig by casing treatment since the stall or separation at the rotor hub sets a new limit to the operating range.

The different configurations tested had only a marginal effect on the fan overall performance, Figure 2.14. The treatments did not significantly alter the efficiency curve, which is a great advantage over the slot type casing treatment, and the work-input was lower at solid casing than at the treated builds due to the reduction of the flow into the stall region. The blade axial exposure was once again found to be a critical parameter and it was suggested that more than 50% of rotor axial chord exposure was favorable choice for a medium load fan or compressor.

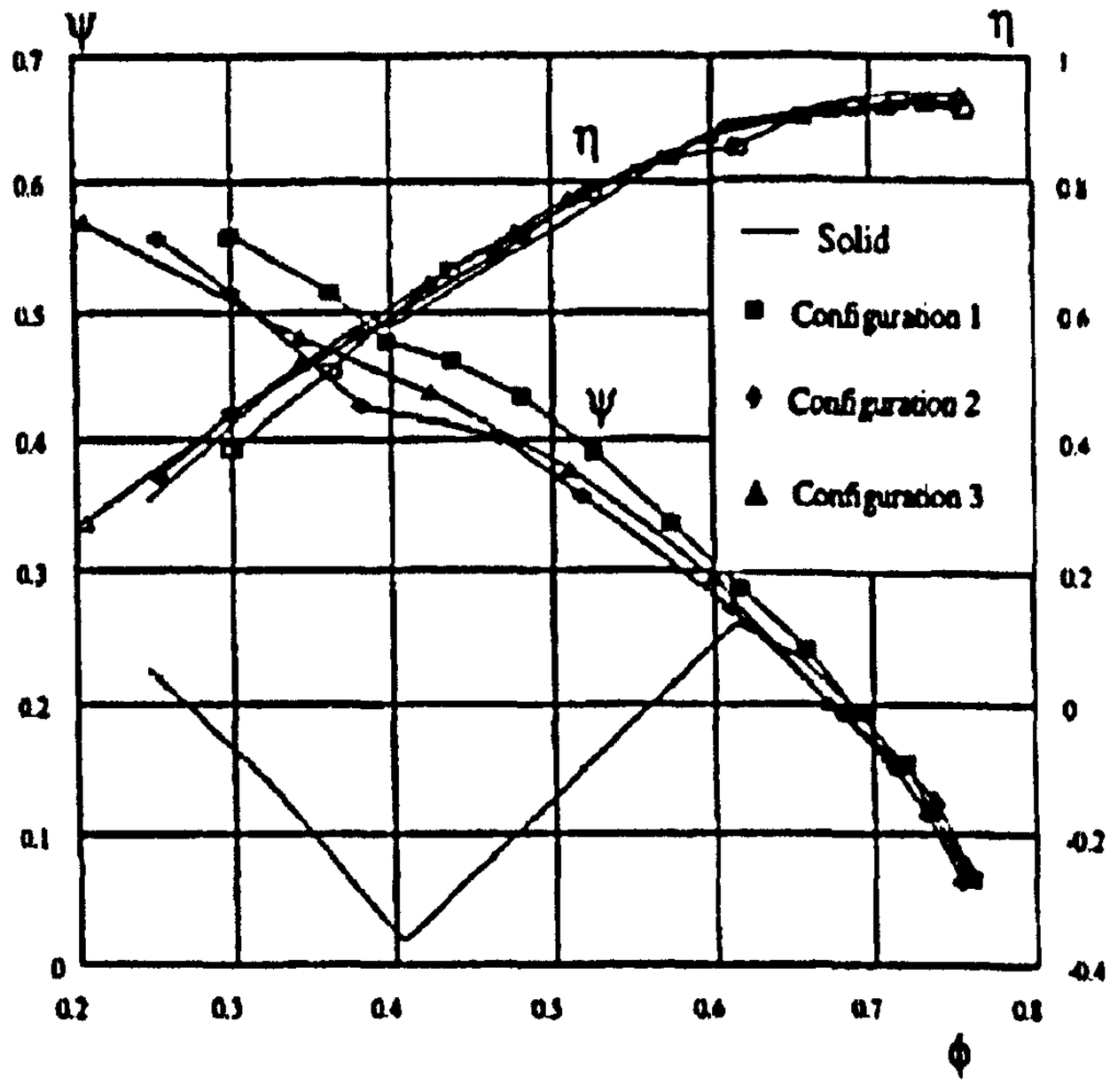

Figure 2.14: Overall performance with various casing treatment, Kang et al. (52)

Figure 2.15 presents the results of several investigations of the effect of rotor axial chord exposure taken from Hill (44), who conducted experiments on 0.5m diameter axial-flow fan with 0.4 hub to tip ratio to study the improvement in stall-free flow range produced on the fan by the use of the recess vaned casing treatment fitted to the outer casing. He also investigated the advantages in reducing the blade vibration stresses and the relation between the improved flow range and the loss of efficiency.

For solid casing treatment, he observed that the stalling for the tested fan is independent of blade profile. For treated casing, he noticed a continually rising performance characteristic with no evidence of rotating stall detected, and when the stall did occur it was of the axi-symmetric type. Stall margin improvements of up to 42% were obtained and this figure was found to be very dependent upon the amount of rotor axial chord exposure. The optimum exposure was found to be 60% of the rotor axial chord, with less stall margin improvements for lower rotor exposure and no benefit at all for very low or no exposure.

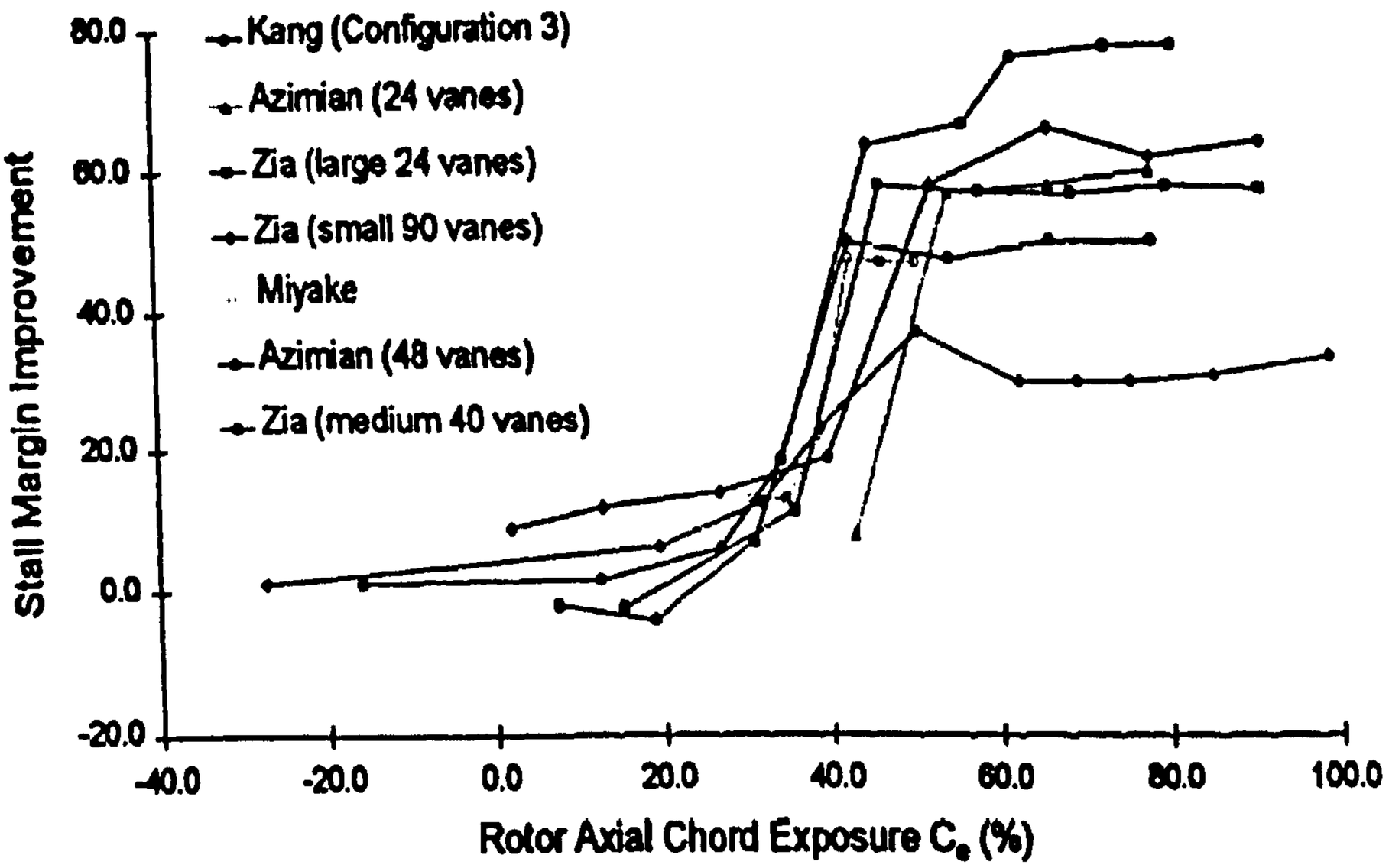

Figure 2.15: The effect of rotor axial chord exposure

Akhlaghi (4) investigated a range of issues related to the use of a vaned-recessed tubular-passage casing treatment as a passive stall control technique in a multistage axial-flow compressor. The configuration of the treatment used consisted of an outer casing ring, a set of 120 evenly spaced curved vanes, and a shroud or inner ring. The treatment was positioned following the inlet guide vanes [IGV] upstream and partly covering the tip of the rotor blades on the first stage of a low-speed three stage axial flow compressor with 0.7 hub to tip ratio. His results showed significant improvements in stall margin in all treated casing configurations along with insignifi-

cant efficiency sacrifices in some compressor builds. Within all configurations tested, the best improvement in stall margin, about 28.56%, was achieved using a casing treatment with 33.3% rotor exposure, and the maximum improvement in efficiency, about 1.81%, was achieved using a casing treatment with 53.5% rotor exposure, but only with 22.54% improvement in stall margin.

Two other types of large scale casing treatment, shown in Figure 2.16, were tested. First was a suction ring upstream of the rotor blades tested by Tanaka and Murata (93), it supposedly removes low energy flow from the blade tip region, providing some stall margin improvement, but this is reduced in the case of a heavily loaded axial-fan. The second type is the blade separator tested by Ushakov (99), which is similar to Ivanov prototype, except it contained with the standard annulus. It was found to have significant stall delay effects and improvement can be large when the fan load is small, with the most important geometrical dimension being the outlet angle of the fins.

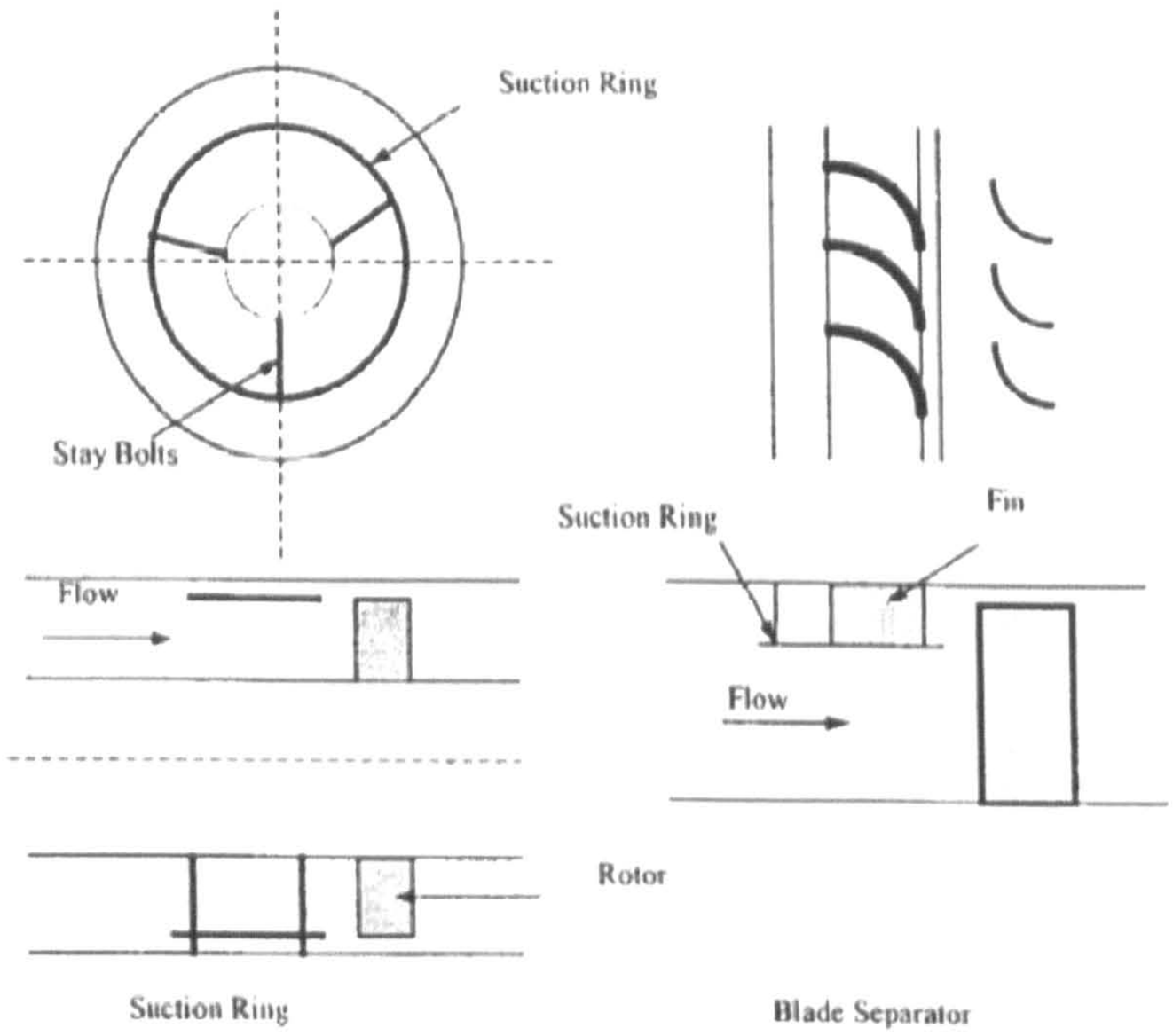

Figure 2.16: Blade separator and suction ring casing treatments

Miyake et al. (69) studied two large-scale devices, a blade separator and an air-separator. They obtained similar result of that Fujita and Takata (29), which revealed that an air-separator could eliminate the unstable characteristics of an axial flow fan even for a build, which originally exhibited a heavy rotating stall.

2.8 Casing treatment mechanism

Casing treatment of various configurations have been proven to be valuable for stall margin improvement and increase of rotor and stage pressure rise. However, there was a little knowledge about the working mechanism by which these devices improve the stall margin. Most of the past investigations of casing treatments concentrated on their effect on stall margin improvement without any further investigating the flow phenomena occurring inside and outside of the treatment. This section will outline research conducted on the casing treatment mechanism and flow phenomena involved.

Bailey and Voit (11) described some observations of flow phenomena associated with the casing treatment they tested. With tapered holes configuration, re-circulation appeared to be necessary for any improvement in stall margin, whereas the equalization of the static pressure in the tip region seemed to be the controlling factor in the honeycomb configuration. The porous casing surrounded by a plenum presents paths for both re-circulation and flow interchange between main flow and plenum.

The work by Prince et al. (78) was probably the first detailed investigation into the mechanism by which the casing treatment improve the stall margin. They tested circumferential, skewed axial, and blade angle slots on low-speed compressor. They attempted analytical modelling of the flow patterns in the treatment cavities in conjunction with experimental investigations utilizing wool tuft visualization and hot wire techniques. They suggested that the interaction of cavity flow with mean stream flow and compliant wall absorption of pressure disturbances are the most important features of the casing treatment effects.

Takata and Tsukuda (92) conducted a set of experiments with a low-speed axial-flow compressor using several casing treatment configurations derived from NASA. They measured the unsteady flow within the treatments using hot wire techniques in order to understand the mechanism through which the casing treatment improves the stall margin. They noted that there is a jet like flow being discharged from the inside of the slots into the main stream periodically at blade passing frequency. The magnitude of this jet also seemed to be depending strongly on the treatment configurations, and the jet velocity or flow in-charge is also well correlated with the amount of stall margin improvement obtained by any particular casing treatment.

A further experiment was carried out to study the effect of the discharged jet from the hub treatment on the main stream using another compressor, Figure 2.17. From both set of experiments two models were proposed; the momentum intercharge model based on the dynamic effect of the high speed jet and the mass intercharge

model which modifies the regions in which low energy fluid collects. The former was thought to be the dominant mechanism for the slot type while the second was thought to be more important as far as the circumferential groove treatment configurations are concerned.

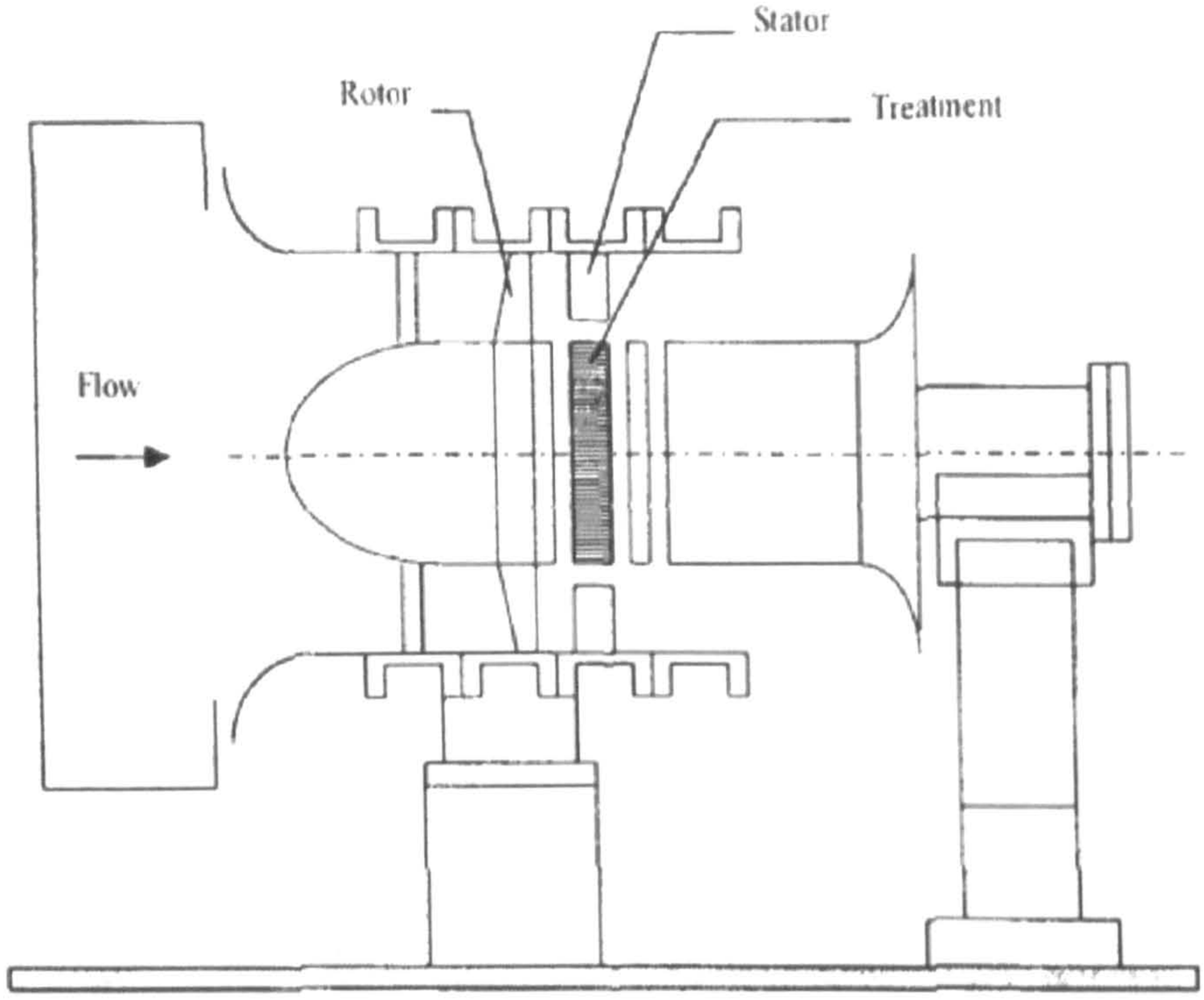

Figure 2.17: One stage test compressor, Takata and Tsukuda (92)

Their studies also included an investigation of tip clearance with results confirming that casing treatments overcome any associated effects. They suggested that, the stall margin improvement, owing to casing treatment, is achieved not by reducing the incidence angle at a particular critical section of the blade row, but by the suppression of the occurrence of rotating stall until the incidence angle attains very large values. They observed also that, the existence of a back chamber or plenum is not essential, which is contrary to most work conducted by NASA in high-speed compressors, though Osborn et al. (73), Urasek and Lewis (98) reached the same conclusions. They also noted that the loss in efficiency from use of the skewed slots can be substantially decreased using baffles at mid-slot axial location, although some decrease in stall margin improvement occurs, as noted by Prince et al. (78).

Another study on the mechanism of casing treatment was conducted by Smith and Cumpsty (88) who tested an axial skewed slot casing treatment over the tips of

an isolated low-speed rotor. The essential feature of the design of this slot was the inclination of the slots so that flow emerging from them possesses swirl in the opposite sense to the rotor motion. Takata and Tsukuda (92) showed that if the inclination was reversed so that flow emerging from the slots in the rotor direction, the compressor would actually stall at higher mass flow rate than with solid casing. Smith and Cumpsty came to the conclusion that unsteady effects in the slots were of secondary importance. Of primary importance was the selective removal of high absolute swirl, high loss fluid, from the end-wall near the trailing edge of the pressure surface of the blade and re-introduction of this, with absolute swirl direction reversed, near the blade leading edge. They also studied the effect of tip clearance on casing treatment performance and concluded, as did Fabri and Reboux (26), Takata and Tsukuda (92), that the larger the clearance the more effective the casing treatment, as the improvement in stall margin increased from 20% to 28% with the increase in tip clearance from 1% to 6% of blade height respectively.

Fujita and Takata (29) conducted a series of experiments similar to those of Prince et al. (78) and obtained the same result. Their analysis showed conclusively that for small scale casing treatment a loss in efficiency is inevitably required for any stall margin improvement. On the mechanism of the slotted casing Johnson and Greitzer (50) conducted experiments on a compressor stator passage end-well and suggested that the suction of the high blockage fluid at the rear of the passage is more important than the jet or flow interaction suggested by Takata and Tsukuda (92).

Lee (59) attempted to quantify the influence of flow removal suggested by Johnson and Greitzer (50) and jet flow suggested by Takata and Tsukuda (92) in an experiment in which the two effects were imposed separately. He found that both removal of high blockage flow from the rear of the slot and high velocity injections at the front increased the stall margin, but neither was effective for a complete treatment. This implies that both of them are responsible for stall improvement in casing or hub treatment. For injection though, a strong correlation was found between the change in stalling pressure rise capability and the stream-wise component of momentum of the injected flow. The degree of stability enhancement achieved with suction did not depend strongly on the location, either at the rear or at front of the stator; the passage was equally effective. However, in general the stall pressure rise increased with the amount of flow removal.

Little work has been carried out on the mechanism of recess casing treatment. Bard (13) proposed that the stalling is eliminated because the radial flow vectors, which become more prominent as the flow is throttled, can be removed from the tip region

by entering the cavity. This annular cavity then diffuses the rotational element of the flow by means of turning vanes, in the process raising the static pressure above the mainstream, and thus permitting it to return to the mainstream in a completely axial sense. The result being that the blade tip region still receives the necessary high axial flow vector.

Similar to Bard (13), Basharhagh et al. (16) from their flow studies with wool tufts, concluded the following hypothesis for the working mechanism of casing treatment, a sketch of the proposed operation is shown in Figure 2.18. Low momentum fluid, associated with stalling flow on the blade, is centrifuged towards the tip. Without the treatment, Figure 2.18(a), the centrifuged flow reaching the casing must be deflected forward or backward or both by the casing as well as being entrained by the mainstream. The casing treatment recess provides an alternative path for the centrifuged air, Figure 2.18(b), and the vanes reduced the whirl velocity to near zero for air which is returned to the normal annulus at the forward end of the recess. Thus, when the mass flow rate falls below the value at which rotating stall cells would normally appear the reversed flow from the rotor does not dramatically upset the incoming flow to the rotor. By this means the rotor is able to continue pumping to higher pressures and lower flows. Eventually, as the mass flow rate is further reduced, so much flow is centrifuged that the recess is too small to cope, and some of the reversed flow starts to occupy the outer region of the normal annulus ahead of the rotor. This may cause rotating stall to be established as when there is no casing treatment.

A study of the three-dimensional flow field in the tip region of moderately loaded axial-flow compressor was carried out by Lakshminarayana et al. (56). They found that tip leakage flow originates near the quarter chord and peaks around the mid-chord of the blade, and there is a strong radial flow from the rotor tip into the treatment recess, which may significantly modify the leakage flow, possible by eliminating the tip leakage vortex.

The detailed flow measurements taken by Kang et al. (52) inside the recess vaned showed that the treatment did not alter the radial pressure profile, whereas the radial distribution velocity upstream of the rotor was altered radically by the recess treatment. They suggested that the recess effectively reduced the whirl velocity component and removed flow blockage found at rotor tip in the stalled regime and then re-introduced the treated flow back into the mainstream. The authors concluded that eliminating flow blockage is the essential part of the stall delay mechanism, neither by reducing the incidence nor by increasing the total pressure in the upstream tip region such as slot type treatment.

Finally, Hill (44) concluded that the treatment operation is dependent upon several

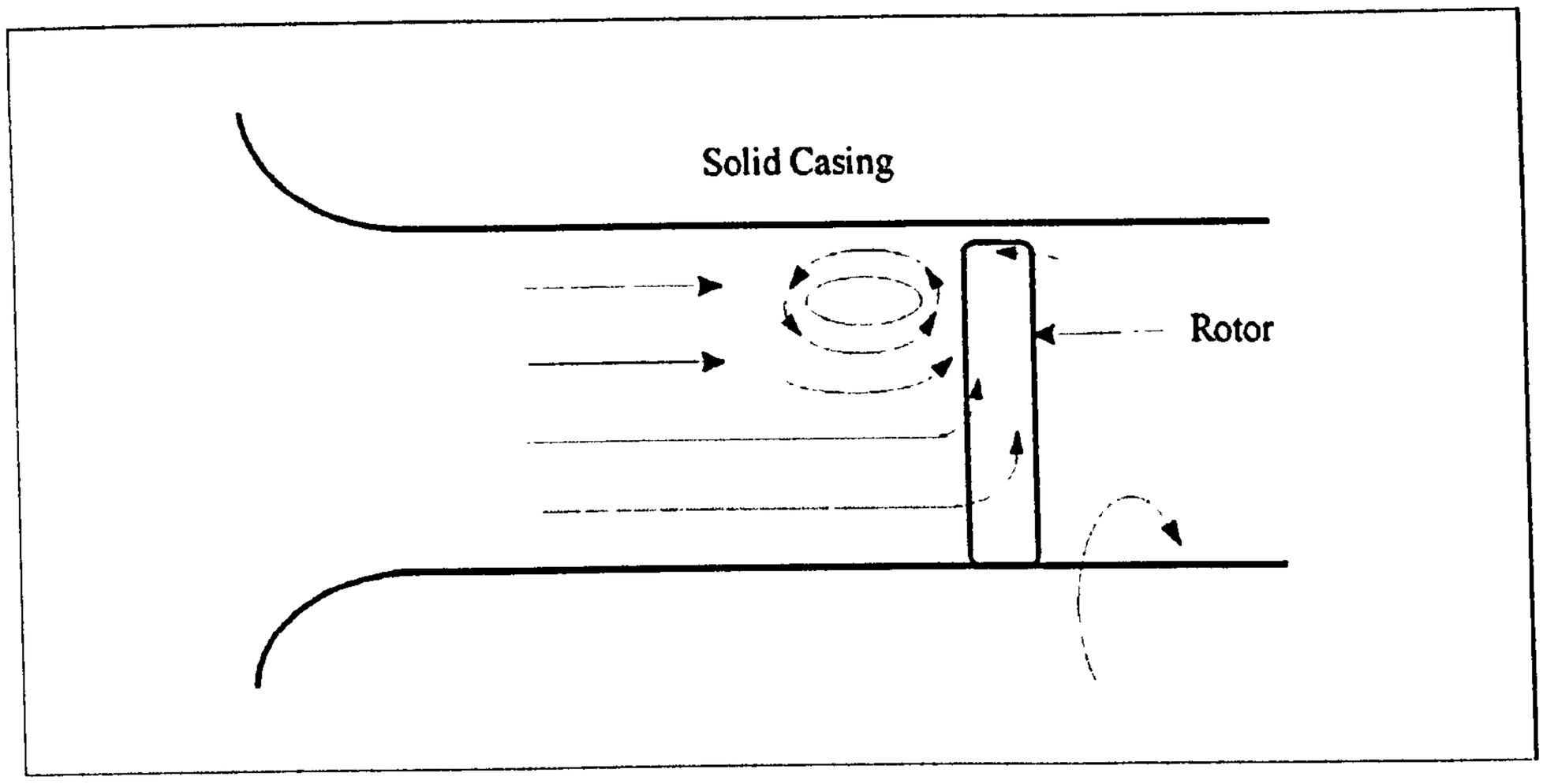

(a) Stall with solid casing

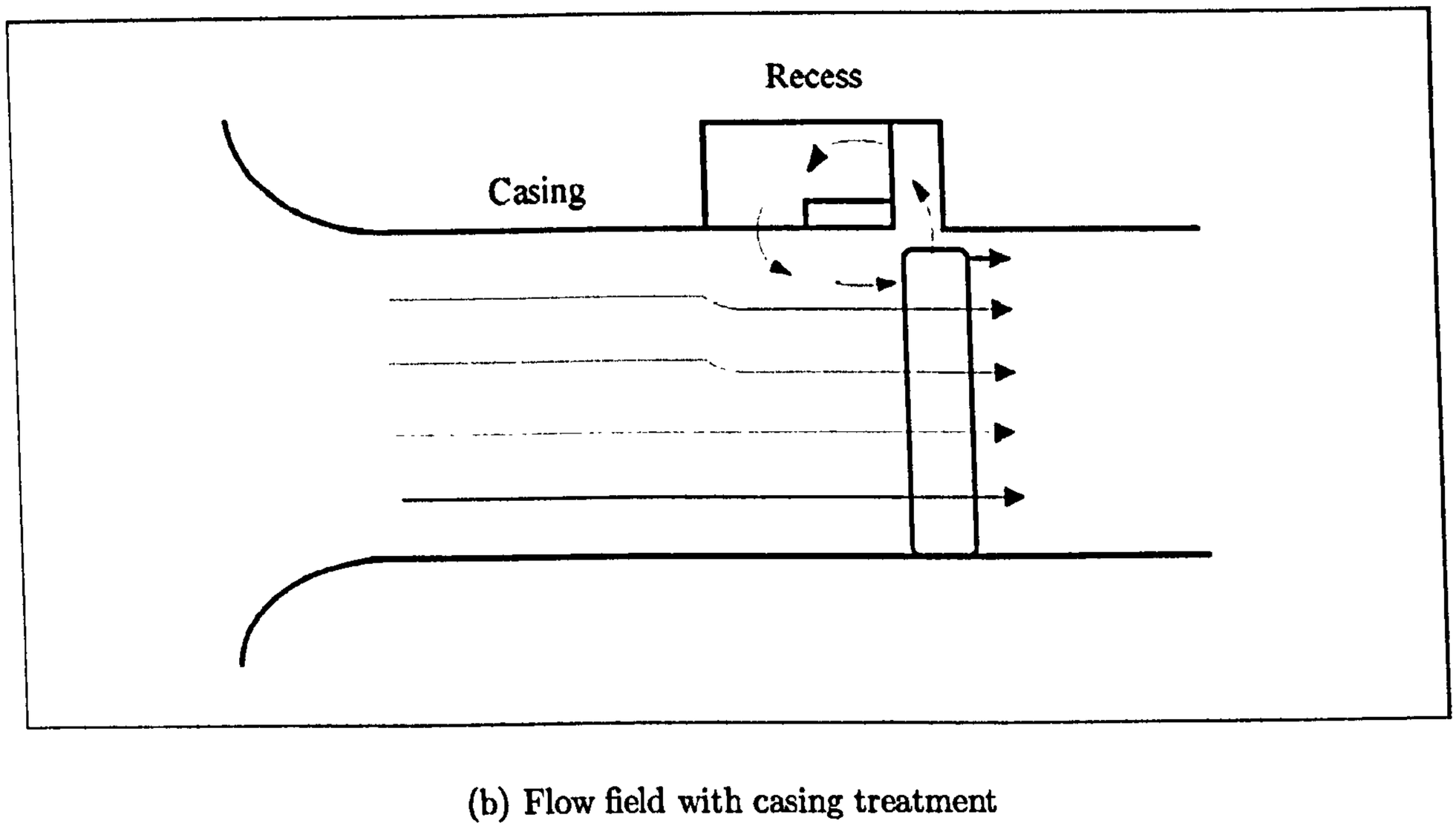

(b) Flow field with casing treatment

Figure 2.18: Sketch of the operation of the recess casing treatment

factors. The most important of these is the elimination of the tangential or whirl velocity component at the inlet, which was clear from the radial traverse results obtained with hot wire and pressure probes. Also, the modification of the tip clearance flows and inward radial flow from the recess play a considerable part in the stall margin improvement.

2.9 Numerical simulations

Computational fluid analysis has been very active in the prediction of various phenomena in turbomachinery in recent years. However, a little work has been done on the numerical simulation of casing treatments due to the complexities associated with casing treatments. One of the earlier studies undertaken was by Snyder and Blade (89), who reported results of simulation of casing treatment effects on multistage compressor. Their simulation model was based on individual stage-by-stage steady-state characteristics. They pointed out that the casing treatment of the front stages could improve only the low-speed operation of the compressor. This is not a global conclusion since many researchers such as Urasek and Lewis (98) demonstrated that the inlet stage treatments are effective.

Amann et al. (5) employed a simplified 2-D analytical model of the flow at the rotor-diffuser interface of a centrifugal compressor, and found that flow relief in the third dimension should delay the onset of stall. Crook et al. (20) attempted the simulation of a grooved hub treatment flow using a 3-D steady viscous flow model. Hub treatments have an area of flow removal over the downstream portion and an area of flow injection over the upstream portion of the treatment. This combination of flow removal and injection was simulated numerically by modelling the treatment area as a second inlet/exit to the flow field domain. Computation results showed that there were two main actions of hub or casing treatment on the leakage flow;

(i) The suction of the low total pressure fluid at the rear of the passage.

(ii) The suppression of the blockage in the core of the leakage vortex due to the energizing of the leakage flow by high velocity injection at the front of the passage.

Another research conducted by Hall et al. (38) on a modern fan rotor with a recess vane casing treatment. Their work involved a time dependent treatment/rotor aerodynamic interaction analysis using a 3-D Navier-Stokes solver. Although it did

not give a detailed description of the final result, it was a big step forward in the numerical solution of the flow in casing treatments. Later, Hall et al. (40) used a 3-D Navier-Stokes analysis technique, Hall et al. (39, 40), to perform a series of detailed numerical predictions to assess the effectiveness of various casing treatments for enhancing the efficiency and stall margin of a modern high-speed fan rotor, with particular attention to examine the effects of inlet distortion.

The primary effect of the axial slot, blade-angle slot, and recess vane treatment types was found to be the sweeping of the clearance flow downstream, thus eliminating much of the blockage associated with the clearance flow in the forward part of the blade passage. The circumferential groove predictions showed some of the same clearance flow behavior, but to a lesser extent. However, from their results it was unclear to them whether the primary stall margin enhancement afforded by the treatment is a result of the clearance flow manipulation or the change in shock structure and location. The vaned recess casing results predicted a much large flow stall margin than the other configurations, and suggested that due to the unconventional nature of this geometry a further study would be required.

An unsteady numerical simulation was carried out by März et al. (63) to understand the mechanisms of rotating stall instabilities in a low-speed axial-flow compressor. The steady-state simulation did not provide converged solutions below a flow coefficient of 0.2. Therefore, the steady single-passage solution at a flow coefficient of 0.2 was used as an initial solution for the unsteady full-annulus calculation. The total pressure, total temperature, and two velocity components are specified at the inlet of the computational domain, while the rotor exit pressure at the casing was gradually raised by an increment of $6.9\,\mathrm{N/m^2}$ to obtain a flow rate of 0.18. They found that the calculated flow field becomes unsteady at mass flow rates below 0.2 due to unsteady movement of tip vortex, which is the result of interactions among the classic tip clearance flow, axial reversed endwall flow, and incoming flow, and this vortex travels from the suction side to the pressure side of the passage at roughly half of the rotor speed. They concluded that the formation and the movement of this vortex seem to be the main causes of unsteadiness when rotating instability develops.

2.10 Summary

Considerable effort has been put in the past to understand and control the stall phenomena on the compressors. Large amount of experimental work was conducted

to delay the stall inception using casing/hub treatments, allowing operation at normally stalled flow rate.

In general, the various types of small casing treatment tested were effective in improving stall margin for tip critical axial and centrifugal compressors, and similar effects were noted with hub treatments for hub critical compressors. However, stall margin improvement for those treatments ranges between 4-28% with a loss of efficiency equivalent to 2-4% is usually incurred. Circumferential grooves configurations cause a little decrease in efficiency for moderate improvement in stall margin, whereas skewed slot ones give a larger improvement in stall margin at the cost of measurable efficiency penalties.

Although the recess casing treatments are more expensive in structure, they offered a much larger improvement in stall margin than the small scale types. More than 65% of stall margin improvement and over twice the pressure rise were obtained with no measurable loss in efficiency in some configurations. The optimum number of vanes inside the recess is yet to be quantified. Azimian et al. (9) used 48 vanes whereas Kang (51) used 24 vanes without any appreciable difference in results. However, there was a little improvement in stall margin with no vanes at all in the recess. The blade axial chord exposure was found to be a critical parameter with more than 50% exposure of blade chord required for achieving an improvement in stall margin and no benefit at all for very low or no exposure.

It seems that the mechanism by which the stall margin is improved by casing treatments is not yet fully elucidated. Various hypotheses have been proposed but none of them is able to explain all the observed phenomena satisfactorily. However some important observations mentioned in this chapter, such as removal of whirl component, interaction between casing treatment flow and main flow, appeared to be closely related to the mechanism being sought.

CFD has been a reasonable predictor of turbo-machine flow fields, and can be seen as a tool to aid in understanding the complexities of casing treatment flow phenomena. Previous attempts to compute fan/compressor casing treatment flow fields are few in number specially for recess casing treatment.

"Most CFD solutions of turbulent flows now contain turbulence models which are just approximations of the real physics, and which depend on empirical data for viscous constants that go into the turbulence models. Therefore, all CFD solutions of turbulent flows are subjected to inaccuracy, even though some calculations for some situations are reasonable."

Wendt (103)

3

Flow Governing Equations

CFX-TASCflow is the commercial CFD code used in the present work. It is a 3-D Reynolds-Averaged Navier-Stokes [RANS] solver based on a fully implicit pressure correction scheme. The code solves the RANS equations for the conservation of mass, momentum, and energy in terms of the independent variables velocity, pressure and enthalpy. It can solve the equations for steady and unsteady state problems as well as for both incompressible and compressible flows. The problem being investigated in the present work is a low-speed case in which the flow can be considered incompressible, where the density and viscosity are assumed to be constant. Through these assumptions, the energy equation can be decoupled completely from the equation system since the continuity and momentum equations are all that necessary to solve for the velocity and pressure fields. This can be applied for all incompressible flows even when the system being solved involves heat transfer, and hence temperature gradients exit in the flow, then the temperature field can be calculated directly from the energy equation after the velocity and pressure fields are obtained from continuity and momentum equations alone, Anderson (6).

In the present study, there is no heat transfer and temperature gradients do not exit, so the problem is reduced to solving for velocity and pressure fields. This chapter presents the flow governing equations for the conservation of both mass and momentum, which are first described for laminar flows, and then are extended to

include turbulent fluctuations, which arise additional stress terms in the momentum equation. These non-linear stress terms must be related to the velocity field using a turbulence model before any closed solution to the mean flow equation system becomes possible. CFX-TASCflow modelling approach of these extra stress terms and their implementations will be presented in detail throughout this chapter.

3.1 Instantaneous equations

The code models the conservation equations of mass and momentum in terms of the dependent variables velocity and pressure. In laminar flows, the instantaneous value of a variable at any given position and time in space is equal to its mean, and the conservation equations for mass, also called the continuity equation, and momentum in a Cartesian coordinate system expressed in tensor notation are:

Continuity equation:

$$\frac{\partial \rho}{\partial t} + \frac{\partial}{\partial x_j}(\rho u_j) = 0 \tag{3.1}$$

***i*-momentum equation:**

$$\frac{\partial}{\partial t}(\rho u_i) + \frac{\partial}{\partial x_j}(\rho u_i u_j) = -\frac{\partial P}{\partial x_i} + \frac{\partial \tau_{ij}}{\partial x_j} + S_i \tag{3.2}$$

where, the viscous stress tensor τ_{ij} is given by:

$$\tau_{ij} = \mu \left(\frac{\partial u_i}{\partial x_j} + \frac{\partial u_j}{\partial x_i} \right) - \frac{2}{3}\mu \, \delta_{ij} \frac{\partial u_l}{\partial x_l} \tag{3.3}$$

where μ is the dynamic viscosity and δ_{ij} represents the Kronecker delta. Further detailed information on the derivation of these equations is given in White (105) and Wendt (103). For flows in rotating frames of reference, the effects of the Coriolis and Centrifugal forces are modelled in CFX-TASCflow code by

$$\vec{S}_i = -\left[2\vec{\Omega} \times \vec{U} + \vec{\Omega} \times \left(\vec{\Omega} \times \vec{r} \right) \right] \tag{3.4}$$

where vector notation has been used, $\times$ is a vector cross-product, $\vec{\Omega}$ is the rotation speed, and $\vec{r}$ is the location vector.

3.2 Turbulence and its modelling

The majority of flows through, in or around engineering equipment are turbulent. By turbulent it is implied that when the flow velocity at a point is continuously sampled the signal is constantly changing in an irregular, non-repeating, and chaotic way. One of the earliest approaches to investigate turbulent flows is the concept of averaging variables over time, where the instantaneous scalar values of velocity, pressure, and stresses in the conservation equations are expressed in terms of their mean and fluctuating components through a process of averaging. Two different averaging procedures are used; time-averaging known as the Reynolds-averaging is used mainly for incompressible flows where the density is constant, and mass-weighted averaging named Favre-averaging for compressible flows. In this chapter the equations of mean flow are first described for compressible flows, and are then simplified for incompressible flows by assuming a constant fluid density.

3.2.1 Averaging procedure

Consider an arbitrary function ϕ such as velocity, pressure and/or density; the instantaneous value of the function is the summation of a mean value $\overline{\phi}$ and a fluctuating component ϕ' as:

$$\phi(x_i, t) = \overline{\phi}(x_i, t) + \phi'(x_i, t) \tag{3.5}$$

The time-average mean component $\overline{\phi}$ of the function at a point in space is formally defined as:

$$\overline{\phi}(x_i, t) = \lim_{\Delta t \to \infty} \frac{1}{\Delta t} \int_0^{\Delta t} \phi(x_i, t) dt \tag{3.6}$$

where the time interval Δt is long compared to the time scale of the turbulent fluctuations. For compressible flows, a mass-weighted decomposition, Favre-averaging, is assembled as:

$$\widetilde{\phi}(x_i, t) = \frac{\overline{\rho\phi}(x_i, t)}{\overline{\rho}} \tag{3.7}$$

with this form of mean function, each dependent variable in the conservation equations is decomposed into a time mean component and fluctuating component as:

$$\phi(x_i,t) = \widetilde{\phi}(x_i,t) + \phi''(x_i,t) \tag{3.8}$$

However, for incompressible flows the fluid density is constant ($\rho' = 0$) and the time-average of a variable is the same as the mass-averaged one, which means

$$\widetilde{\phi}(x_i,t) = \overline{\phi}(x_i,t) \tag{3.9}$$

and,

$$\phi''(x_i,t) = \phi'(x_i,t) \tag{3.10}$$

The following rules are used to simplify the derivation of the mean flow equations for turbulent flow, Versteeg and Malalasekera (101). They govern both the time and mass-weighted averages of the fluctuating properties, their derivatives and combinations.

(i) The time averaging of the fluctuating component of ϕ is equal zero.

$$\overline{\phi'} = 0 \tag{3.11}$$

(ii) The time averaging of n^{th} derivative of the function ϕ is equal to the known n^{th} derivative of the averaged function itself.

$$\overline{\frac{\partial^n \phi}{\partial x^n}} = \frac{\partial^n \overline{\phi}}{\partial x^n} \tag{3.12}$$

(iii) The averaged linear combination (addition) of two quantities, ϕ_1 and ϕ_2, results in the corresponding linear combination of their averaged values.

$$\overline{\phi_1 + \phi_2} = \overline{\phi_1} + \overline{\phi_2} \tag{3.13}$$

(iv) The time averaging of the product of the two instantaneous quantities, ϕ_1 and ϕ_2, produces an additional term containing the correlation between their fluctuating quantities.

$$\overline{\phi_1\,\phi_2} = \overline{(\overline{\phi_1} + \phi_1')(\overline{\phi_2} + \phi_2')} = \overline{\phi_1}\,\overline{\phi_2} + \overline{\phi_1'\phi_2'} \tag{3.14}$$

3.2.2 The Reynolds-averaged equations

The general procedure of obtaining the averaged equations is to substitute the mean and fluctuating component of the instantaneous value of the function in the exact flow equations (3.1) and (3.2). All the terms in those equations contain a single fluctuating quantity only, except the second term on the left-hand side of the momentum equation. Therefore, the mass-weighted averaging procedure results in replacing the instantaneous variables in those instantaneous equations by their mean value, except the non-linear convective term in the momentum equation (3.2), where the last rule, equation (3.14), is applied and produces an additional term involving products of fluctuating velocities. Hence, the flow equations for turbulent flows in terms of Favre-averaging quantities can be written as:

$$\frac{\partial \overline{\rho}}{\partial t} + \frac{\partial}{\partial x_j}(\overline{\rho}\widetilde{u_j}) = 0 \tag{3.15}$$

$$\frac{\partial}{\partial t}(\overline{\rho}\widetilde{u_i}) + \frac{\partial}{\partial x_j}(\overline{\rho}\widetilde{u_i}\,\widetilde{u_j}) = -\frac{\partial \overline{P}}{\partial x_i} + \frac{\partial}{\partial x_j}\left(\overline{\tau_{ij}} - \overline{\rho}.\overline{u_i'' u_j''}\right) + \overline{S}_i \tag{3.16}$$

These equations are generally known as the Reynolds equations and they are different from those describing laminar flow given in equation (3.1) and equation (3.2) only by the presence of additional term $(\overline{\rho}.\overline{u_i'' u_j''})$ involving second-order moments of the fluctuating velocity field. It is not truly part of the fluid stress, but rather represents the average momentum flux due to turbulent motion. This term has the mathematical form of a second-order tensor and so called the turbulent stress or more usually the Reynolds Stress tensor. Because of the non-linearity of this term, the mean flow equations are not closed. To close the problem, the simplest approach is to express the Reynolds stress tensor in terms of the mean velocity itself, which can be done through the eddy-viscosity assumption, Mathieu and Scott (64).

3.2.3 Boussinesq eddy viscosity assumption

Many turbulence models utilize the Boussinesq eddy viscosity concept in which the Reynolds Stresses can be assumed to be proportional to the mean velocity gradient via a turbulent viscosity as:

$$\widetilde{\rho}.\overline{u_i'' u_j''} = -\mu_t\left(\frac{\partial \widetilde{u_i}}{\partial x_j} + \frac{\partial \widetilde{u_j}}{\partial x_i}\right) + \frac{2}{3}\delta_{ij}\left(\mu_t \frac{\partial \widetilde{u_l}}{\partial x_l} + \widetilde{\rho}\widetilde{k}\right) \tag{3.17}$$

This assumption can be simplified for incompressible flows where density is constant and velocity divergence is zero to:

$$\rho.\overline{u_i' u_j'} = -\mu_t \left(\frac{\partial \overline{u_i}}{\partial x_j} + \frac{\partial \overline{u_j}}{\partial x_i} \right) + \frac{2}{3} \rho k \, \delta_{ij} \tag{3.18}$$

Two more unknowns are introduced to the equation system, the turbulent viscosity μ_t and the turbulent kinetic energy k. However the introduction of the eddy viscosity concept by itself is not a turbulence model, rather than the emphasis of the problem has been moved to the determination of the turbulent viscosity and kinetic energy distributions which can be achieved using a turbulence model.

3.2.4 Modelled mean flow equations

Since all the variables in the mean flow equations (3.15) and (3.16) are mean flow quantities, then it is customary to drop the superscripts time and Favre-averaging symbols, and the final form of the mean flow equations can be written as:

The conservation of mass equation:

$$\frac{\partial \rho}{\partial t} + \frac{\partial}{\partial x_j}(\rho u_j) = 0 \tag{3.19}$$

The conservation of i-momentum equation:

$$\frac{\partial(\rho u_i)}{\partial t} + \frac{\partial(\rho u_i \, u_j)}{\partial x_j} = -\frac{\partial P^*}{\partial x_i} + \frac{\partial}{\partial x_i} \left[\mu_{\text{eff}} \left(\frac{\partial u_i}{\partial x_j} + \frac{\partial u_j}{\partial x_i} \right) - \frac{2}{3} \mu_{\text{eff}} \frac{\partial u_l}{\partial x_l} \delta_{ij} \right] + S_i \tag{3.20}$$

where the effective viscosity is given by:

$$\mu_{\text{eff}} = \mu + \mu_t \tag{3.21}$$

In these two mean flow equations (3.19) and (3.20), density is a time-average and mean velocity is a mass-average for compressible flows, and density is constant and

velocity is a time-average for incompressible flows, while the pressure and source term in the momentum equation (3.20) are always a time-average. However, in CFX-TASCflow, the term $(2/3\rho\kappa\delta_{ij})$ in equation (3.17) is grouped with the thermodynamic pressure from equation (3.16) to produce P^* as shown in equation (3.20).

3.3 Turbulence models

For most engineering purposes, only the effects of the turbulence on the mean flow are usually sought, rather than resolving the details of the turbulent fluctuations. For a turbulence model to be useful in the frame work of a general purpose CFD code, it must have a wide applicability, be accurate, simple, and economical to run. The most common turbulence models are classified as shown in Table 3.1.

Table 3.1: Turbulence models

- ▷ **Classic models:**
  - Transport equation models:
    - Zero-equation models†
    - One-equation models
    - Two-equation models:
      - The standard k-ϵ model
      - The RNG k-ϵ model
      - Kato-Launder model
      - The k-ω models
  - Reynolds stress models
  - Algebraic turbulence models
- ▷ **Near-wall models:**
  - Standard Log-law model
  - Two-layer models
- ▷ **Advanced turbulence models**

† Also knowing as mixing length models.

The mixing length scale and the k-ϵ are presently by far the most widely used and validated. The mixing length scale models attempt to describe the stresses by means of simple algebraic formula for turbulent viscosity as a function of position.

On the other hand, two transport equations are solved in the k-ϵ models, one for the turbulent kinetic energy k and a further one for the rate of its dissipation ϵ. In the following sections the mixing length scale and the k-ϵ models will be discussed in details, the main features of the Reynolds stress equation and algebraic stress models will be outlined and other advanced turbulence models will be briefly considered.

3.3.1 Transport equation models

These models employ an eddy viscosity like concept and are commonly classified by the number of equations used with the model:

(i) Zero-equation or mixing length models.

(ii) One-equation models, where a transport equation for turbulent kinetic energy is solved.

(iii) Two-equation models, where an other equation for turbulent length scale is solved in addition to the transport equation for the turbulent kinetic energy.

3.3.1.1 Zero-equation turbulent models

The turbulent viscosity μ_t is expressed as a product of velocity turbulence scale u_t and turbulence length scale ℓ_t,

$$\mu_t = C\rho\,\ell_t\,u_t \tag{3.22}$$

where C is a dimensionless constant. The mixing length model, first proposed by **Prandtl in 1925**, relates the eddy viscosity directly to the mean field. It was derived from thin shear layer flows, where there is only a single significant velocity gradient normal to the flow direction. For such flows;

$$u_t = c\,\ell\left|\frac{\partial U}{\partial y}\right| \tag{3.23}$$

where c is a dimensionless constant, $\partial U/\partial y$ is the velocity gradient normal to flow direction and the absolute value is taken to ensure that the velocity scale is a positive

quantity irrespective of the sign of the velocity gradient. Combining equation (3.22) and equation (3.23) and absorbing the constants c and C into a new length scale ℓ_m results in **Prandtl's mixing length model**;

$$\mu_t = \rho \ell_m^2 \left| \frac{\partial U}{\partial y} \right| \tag{3.24}$$

The mixing length models are well established, very easy to implement and cheap in terms of computing resources. Even though, they give good predictions for thin shear layers such as mixing layers, wakes, and boundary layer they are incapable of describing flows with separation and re-circulation. Also, they are not very suitable when convective and diffusive transport of turbulence or history effects are important since they only calculate mean flow properties and turbulent shear stress, Versteeg and Malalasekera (101). A very popular mixing length type of model is the **Baldwin-Lomax** model, Baldwin and Lomax (12).

3.3.1.2 One-equation turbulent models

In one equation models, a transport equation for the turbulent kinetic energy k is solved, while the distribution of the length scale is specifies empirically in a similar manner to mixing length scale models. However, these empirical relations are satisfactory for simple shear flows but not in more complex flows where the length scale is not very easy to prescribe. Therefore, the trend has been shifted to use two-equation models, in which the length scale is determined from an other transport equation, Rubini (84). A very popular one-equation model is the **Spalart-Allmaras** model, Spalart and Allmaras (91), which solves a transport equation for eddy viscosity rather than, as in the conventional approach in one-equation models, computing initially the turbulent kinetic energy k.

3.3.1.3 Two-equation turbulent models

The turbulent length scale in two-equation turbulent models is usually estimated from two properties of the turbulence field, the turbulent kinetic energy k and its rate of dissipation ϵ, from the solution of their respective transport equations. Some of these models are outlined in the following sections.

3.3.1.3.1 The standard k-ϵ model: It is the most widely used and validated turbulence model, Launder and Spalding (58). It was first derived for incompressible flows where density fluctuations can be ignored, which is valid for the present study. The turbulent velocity scale and the turbulent length scale are given by:

$$u_t = \sqrt{k} \tag{3.25}$$

$$\ell_t = \frac{\sqrt{k^3}}{\epsilon} \tag{3.26}$$

Substitution the above two equations into the turbulent viscosity equation (3.22) results in the **Kolmogrov-Prandtl** relation;

$$\mu_t = \rho C_\mu \frac{k^2}{\epsilon} \tag{3.27}$$

The following transport equations are used to model k and ϵ in standard turbulence model:

k-equation:

$$\frac{\partial(\rho k)}{\partial t} + \frac{\partial(\rho u_j k)}{\partial x_j} = \frac{\partial}{\partial x_j}\left(\Gamma_k \frac{\partial k}{\partial x_j}\right) + [P_k - \rho\epsilon] \tag{3.28}$$

ϵ-equation:

$$\frac{\partial(\rho \epsilon)}{\partial t} + \frac{\partial(\rho u_j \epsilon)}{\partial x_j} = \frac{\partial}{\partial x_j}\left(\Gamma_\epsilon \frac{\partial \epsilon}{\partial x_j}\right) + \frac{\epsilon}{k}[C_{\epsilon 1} P_k - C_{\epsilon 2}\rho\epsilon] \tag{3.29}$$

where the diffusion coefficients Γ_k and Γ_ϵ are given by:

$$\Gamma_k = \mu + \frac{\mu_t}{\sigma_k} \tag{3.30}$$

$$\Gamma_\epsilon = \mu + \frac{\mu_t}{\sigma_\epsilon} \tag{3.31}$$

P_k is the production rate of turbulent kinetic energy and is given by:

$$P_k = \mu_t \left(\frac{\partial u_i}{\partial x_j} + \frac{\partial u_j}{\partial x_i} \right) \frac{\partial u_i}{\partial x_j} - \frac{2}{3} \left(\rho k + \mu_t \frac{\partial u_l}{\partial x_l} \right) \frac{\partial u_m}{\partial x_m} \tag{3.32}$$

For incompressible flows, the velocity divergence vanishes and the production rate of turbulent kinetic energy is reduced to:

$$P_k = \mu_t \left(\frac{\partial u_i}{\partial x_j} + \frac{\partial u_j}{\partial x_i} \right) \frac{\partial u_i}{\partial x_j} \tag{3.33}$$

The five constants employed in the model are presented in Table 3.2, the values of these constants are arrived at by comprehensive data fitting from a wide range of turbulent flows.

Table 3.2: The standard k-ϵ turbulence model constants

C_μ	σ_k	σ_ϵ	$C_{\epsilon 1}$	$C_{\epsilon 2}$
0.09	1.00	1.30	-1.44	1.92

The accuracy of the k-ϵ model is limited by two factors. Firstly, the modelling assumptions made in the derivation of the transport equation for the dissipation rate of the turbulent kinetic energy. Secondly, the natural limitations of the Boussinesq assumption, where many flows have structures too complex to be described by Boussinesq assumption. In addition to the model is so oblivious to the body forces due to rotation of the frame of reference, the model is reported not to perform well in weak shear layers, swirling flows, and flows with large, rapid, extra strain such as highly curved boundary layers and diverging passages since it does not contain a description of the effects of streamline curvature on turbulence, Versteeg and Malalasekera (101).

Despite its deficiencies the k-ϵ model has a well established regime of prediction capability and performs particular well in a wide range of flows with industrial engineering applications, which explains its popularity and its implementation in many general purpose CFD software packages. In addition to that, the ease with which it may be incorporated into existing codes with relatively small overheads, in terms of computational expense.

3.3.1.3.2 The RNG k-ϵ model: For flows with high rate of deformation, the ϵ-equation has been long suspected as one of the main sources of accuracy limitations in the standard version of the model. Yakhot et al. (110) applied the re-normalization group RNG theory to the RANS equations and produced similar equations to the standard k-ϵ model with a strain-dependent correction term in the constant, where the coefficient $C_{\epsilon 1}$ in equation (3.29) becomes a function of the production and the dissipation rate as:

$$C^*_{\epsilon 1} = C_{\epsilon 1} - \frac{\gamma}{\gamma_o}\left(\frac{\gamma_o - \gamma}{1 + \zeta\gamma^3}\right) \tag{3.34}$$

where γ_o= 4.38, ζ= 0.012, and the non-dimensional strain rate γ is given by

$$\gamma = \frac{\varepsilon\, k}{\epsilon} \tag{3.35}$$

and the strain rate ε is given by

$$\varepsilon = \left[\left(\frac{\partial u_i}{\partial x_j} + \frac{\partial u_j}{\partial x_i}\right)\frac{\partial u_i}{\partial x_j}\right]^{\frac{1}{2}} \tag{3.36}$$

3.3.1.3.3 Kato-Launder model: One of the problems with the two-equation models is the behaviour near the stagnation point where very high levels of turbulence are predicted upstream of a stagnation point and then transported around the body. Kato and Launder (53) proposed an improvement to the standard k-ϵ model by adding a new term to the turbulent production rate, the equation for the new turbulent production rate is given in AEAT (2).

3.3.1.3.4 The standard k-ω models: In many technical applications, the stall characteristics are controlled by the flow separation, and in general the standard turbulence models based on the ϵ-equation predicts the onset of separation too late and also under-predict the amount of separation later on. New turbulence models developed to solve this problem, have shown more accurate prediction of separation in a number of industrial applications. In these models two-transport equations are solved, one for the turbulent kinetic energy k and a second for the turbulent

frequency ω. The starting point for the present formulation of k-ω model was developed by Wilcox (107). Although, the model has shown a significantly accurate prediction of separation in a number of industrial cases especially for low Reynolds number, it is strongly sensitive to inlet condition value of ω. To overcome this problem, Wilcox (108) developed a new version of k-ω model by introducing a new term into ω-equation which make the freestream value of ω to have no effect on the solution.

Also to avoid the problem of strong sensitivity of the original k-ω model of Wilcox to the inlet condition, Menter (67, 68) developed two new turbulence models. The first model, known as the baseline model [BSL], utilizes the original k-ω model of Wilcox in the inner region of the boundary layer and switches to the standard k-ϵ model in the outer region and in free shear flows. The second model, called the Shear Stress Transport model [SST], results from a modification to the eddy-viscosity in the BSL model, which accounts for the effect of the transport of the principle turbulent shear stress.

3.3.2 Reynolds stress models [RSM]

Several major drawbacks of the standard k-ϵ model emerge when it is used to predict flows with complex strain fields or significant body forces. In order to obtain a greater accuracy than it is possible with two-equation models, six transport equations are introduced, one for each Reynolds tensor component, and solved in conjunction with the turbulent kinetic energy dissipation ϵ-equation. The exact form of the Reynolds stress transport equation, Versteeg and Malalasekera (101), is given by:

$$\frac{\partial R_{ij}}{\partial t} + u_l \frac{\partial R_{ij}}{\partial x_l} = P_{ij} - \epsilon_{ij} - D_{ij} - \Pi_{ij} - \Omega_{ij} \tag{3.37}$$

This transport equation describes six partial differential equations one for the transport of each of the six independent Reynolds stresses $R_{ij} = \overline{u_i' u_j'}$, by convection, production, dissipation, diffusion, turbulent pressure-strain interactions and rotation respectively. The RSM models are the most general of all classical turbulence models and present a very accurate calculation of the mean flow properties since six partial differential equations are solved along with an equation for rate of dissipation. They are not validated as well as the mixing length and k-ϵ models and are not widely used in industrial flow calculations due to their high computational expense.

3.3.3 Algebraic turbulence models [ATM]

These consist a reduced form of the RSM models, where the stress components are individually related to the mean flow by six algebraic equations for the six unknown Reynolds stresses. Many authors have made proposals of multi equation models, among others Hanjalic (41), Harlow and Hirt (42). These models are solved either by matrix inversion or by iterative techniques in conjunction with the two-transport equations of the k-ϵ models. However, they are slightly more expensive and not widely validated as the mixing length and k-ϵ model. Also, they are known to encounter problems in flows where the transport assumptions for convective and diffusion do not apply.

3.3.4 Near-wall turbulence models

The boundary layer thickness in turbulent flows is much less than that in laminar flows. Thus , in order to adequately resolve the very large gradients that exist in near wall boundary, a quite large number of nodes would be required. In order to analyze the flow in a more economical way, the near wall region is modelled using an empirically based wall function approach.

3.3.4.1 Standard wall approach

The standard implementation of the k-ϵ turbulence model in CFX-TASCflow employs wall function approaches to model the viscous near-wall layer, a qualitative diagram of this region is shown in Figure 3.1. This approach assumes the universality of a logarithmic velocity profile in the near-wall region, where the near-wall tangential velocity is related to the wall shear stress by means of a logarithmic relation, which in a standard form can be written as follows:

$$u^+ = \frac{1}{\kappa} ln(n^+) + C^* \tag{3.38}$$

where κ is the Von Karman constant for smooth walls, C^* is a constant depending on wall roughness, u^+ and n^+ are non-dimensional velocity and distance respectively

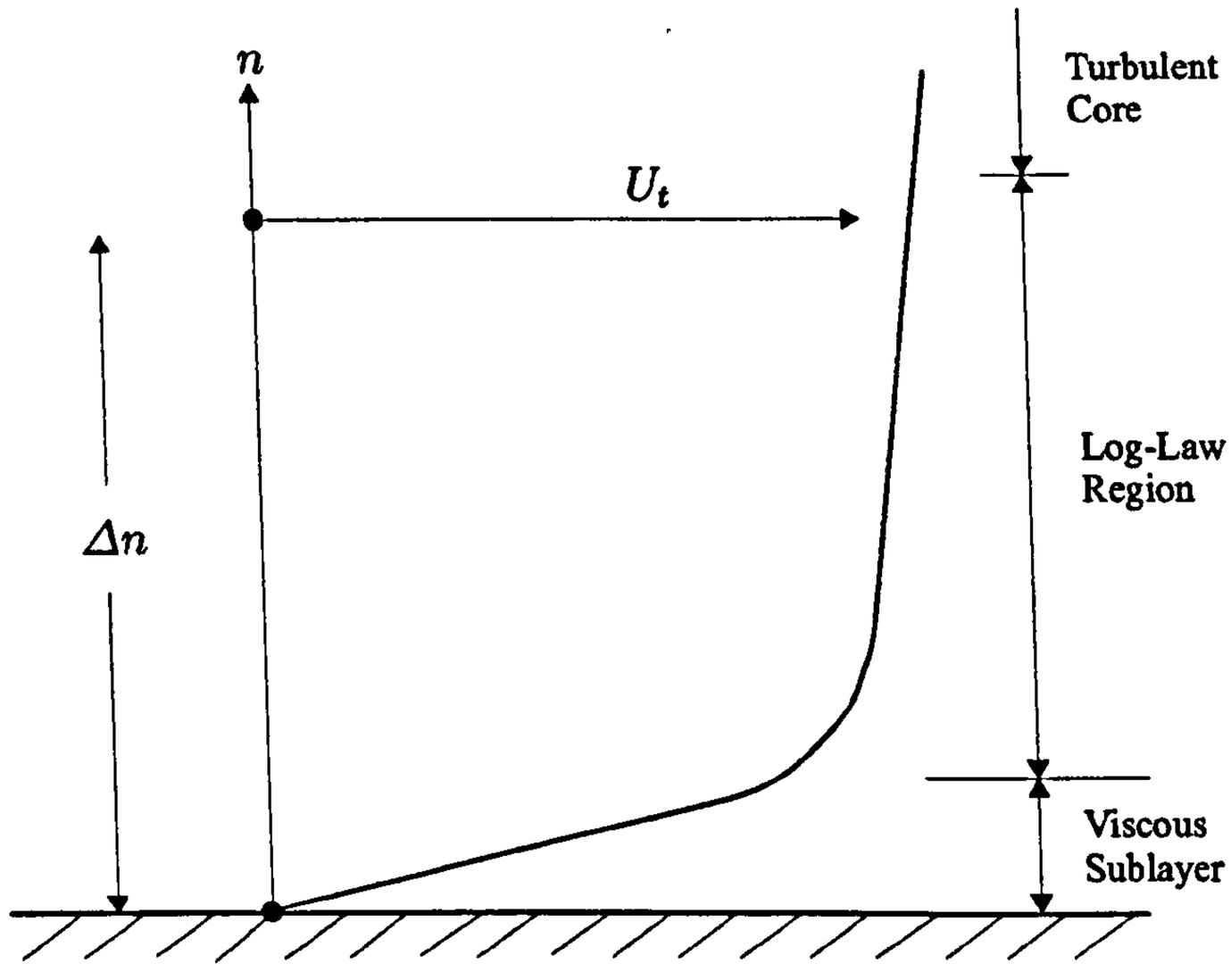

Figure 3.1: Near-wall region

given by:

$$u^+ = \frac{U_t}{u^*} \tag{3.39}$$

$$n^+ = \frac{\rho \Delta n u^*}{\mu} \tag{3.40}$$

where the friction velocity u^* is defined in terms of the wall-shear stress τ_ω as:

$$u^* = \left[\frac{\tau_\omega}{\rho}\right]^{\frac{1}{2}} \tag{3.41}$$

By assuming a local equilibrium, production is equal to dissipation, a relation between the wall-shear stress and turbulent kinetic energy can be written as:

$$\tau_\omega = \rho k \sqrt{C_\mu} \tag{3.42}$$

Substituting equation (3.42) into equation (3.41), the friction velocity u^* can be written in terms of turbulent kinetic energy k as:

$$u^* = \left(k\sqrt{C_\mu}\right)^{\frac{1}{2}} \tag{3.43}$$

This form of wall function used by CFX-TASCflow based on a function of n^+, the recommendation is to locate the near-wall nodes such that n^+ is in the range of 30 to 500 for smooth walls. However, due the fact that some nodes may located closer to the wall than a value of 30, the code divides the near-wall region into 3 sections in which n^+ is defined for each section by:

$$u^+ = \begin{cases} n^+ & n^+ \leqslant 5 \\ d_1 n^{+3} + d_2 n^{+2} + d_1 n^+ + d_4 & 5 \leqslant n^+ \leqslant 30 \\ \frac{1}{\kappa} ln(n^+) + C^* & 30 \leqslant n^+ \leqslant 500 \end{cases} \tag{3.44}$$

The coefficients above are determined such that all 3 relations are continuous in value and first derivative. The coefficients depend on the values of n^+ at which the relations are matched. For $5 \leqslant n^+ \leqslant 30$, the coefficients are given in Table 3.3.

Table 3.3: Near-wall region model constants

κ	C^*	d_1	d_2	d_3	d_4
0.41	5.2	16.4264×10^{-4}	-5.2113×10^{-2}	1.4729	-1.1422

3.3.4.2 Two-layer models

Two-layer models can be used to resolve more closely the near-wall region. These models divide the computational domain into away and near wall regions. The standard k-ϵ model is used away from the wall, and in the near-wall region, a one-equation model is employed to establish the turbulent kinetic energy with the length scale is specified by algebraic equations. Rodi (82) provides a summary of

experience with two-layer models that combine the k-ϵ model with a one-equation in the near-wall region. The setback of these models is the lack of convergence due to the switching problem between the one and two-equation models cased by iteration to iteration oscillations in the location, AEAT (2).

3.3.5 Advanced turbulence models

A recent advance in the field of turbulence modelling is the development of Direct Numerical Simulations [DNS] and Large Eddy Simulations [LES]. The DNS approach to turbulent flow computation resolves all relevant space and time scales and permits high-fidelity flow simulations without using any turbulence model assumptions. Due to the wide range of scales present in turbulent flows of practical interest and the corresponding immense numerical resolution requirements, the application of DNS is presently restricted to prototype flows at low and moderate Reynolds numbers.

LES models are based on space-filtered equations where the time-dependent flow equations are solved for the mean flow and the large eddies while the effect of the small ones is modelled through a subgrid-scale model [SGS]. Since the small scales tend to be more homogeneous and universal, and less affected by the boundary conditions than the large ones, these models can be simpler and required fewer adjustments when applied to different flows than similar models for the RANS equations, Piomelli (77).

Computationally, supercomputer power is of vital importance for DNS, as it requires numerical solutions of the Navier-Stokes equations that resolve the evolution of all scales of motion. LES can be much less expensive than DNS, and since only the largest scales of motion must be computed, LES can be used at much higher Reynolds number than DNS. By contrast, the conventional approach to turbulent flow computation, which for cost reasons still is the workhorse in industrial flow computations, is based on the RANS equations, which need to be closed by some turbulence model. Deficiencies of currently existing turbulence models remain a key problem of CFD. However, the outlook for these techniques is reasonably bright. The notable advancement in SGS modelling over the last few years, and the increasing number of researchers that are applying their talents in this area are both a measure of past achievements, and a reason for optimism for the future.

3.4 Summary

For practical computations, turbulent flows are commonly computed using the Navier-Stokes equations in an averaged form, Reynolds or Favre-averaging. The averaging process gives rise to new unknown terms representing the transport of mean momentum by fluctuating quantities. These undetermined terms are the Reynolds stresses and they lead to the well known closure problem for turbulent flow computations. In order to determine these quantities, turbulence models are required which consist of a set of algebraic or differential equations.

Several turbulence models have been developed which can be broadly classified into the following two categories; eddy viscosity models which are based on the assumption that the Reynolds stresses are a local property of the mean flow and are related to the mean flow gradients via a turbulent viscosity, and RSM models which assume that the Reynolds stresses are dependent variable quantities which can be solved directly from their own transport equations derived from the Navier-Stokes equations along with some modelling equations. The derivation of these models has been largely based on intuition, empirical correlation, and to some extent, constraints set forth by physical realizability. More recently, turbulence models have been developed with more rigor and mathematical formalism based on the Re-Normalization Group RNG theory.

Among the eddy viscosity models, a further classification can be made based on the number of differential equations utilized. Thus, zero, one and two-equation eddy viscosity models have been developed. Among these, the k-ϵ model is one of the most widely used for practical applications. The standard k-ϵ model is only valid in fully turbulent regions and, for wall-bounded flows, requires additional modelling of near-wall regions. Within the family of k-ϵ models, various techniques have been employed to resolve the near-wall flow structure for wall-bounded flows. These include; wall functions, low Reynolds number modifications, and algebraic or one-equation models in the wall region, Rodi (82). The oldest and perhaps the most common of these is the wall functions approach, and although it is not accurate in some flow situations, such as flow separation, it has been shown to yield satisfactory results in complex flow-fields. Moreover, the wall functions approach is very beneficial in complex 3-D geometries due to a large saving in the total number of grid points required and hence a saving in computer memory and Centeral Processing Unit [CPU] time compared to the other two approaches, Viegas and Rubesin (102).

"Over the years, the term CFD has come to embrace a rich variety of methods and techniques. We have, for instance, finite difference, finite volume and finite element methods, time-marching and iterative schemes, density and pressure-based methods, staggered and co-located grid approaches, upwind and central-differenced schemes and numerous other variations."

Venkateswaran and Merkle (100)

4

Computational Methods

The mean flow governing equations for compressible and incompressible flows have been described in the previous chapter. In order to solve these equations numerically, they have to be transformed from their differential form to an algebraic form through a discretization process. Then, they are subsequently solved at discrete points within the domain of interest. Therefore, a set of grid points within the volume as well as the boundaries of the domain must be specified. This process can be considered as the space discretization. The equation system can be discretized by one of three methods; Finite Difference Method [FDM], Finite Element Method [FEM], or Finite Volume Method [FVM]. In the latter, used by CFX-TASCflow code, the mesh of points are arranged so that they can be grouped into a set of control volumes and then the algebraic equations are solved by equating various flux terms through the faces of the control volumes.

This chapter gives a general introduction to the subject of grids, their classes and their quality measures. It also presents a brief description to grid generation methods with some details to CFX-TASCflow grid generation approach. Then, the chapter focuses into the FVM implemented by CFX-TASCflow code to discrete the differential equations to linear algebraic equations, and the treatment of each term in the resulting momentum equation. Finally, the chapter describes the CFX-TASCflow method of solving these linear algebraic equations in addition to some of the boundary conditions implemented by the code and used in the present work. The material

of this chapter draws heavily upon the material in the code accompanying documentation.

4.1 Grid generation

A grid is a foundation on which physical continuous quantities are described by discrete functions and on which the differential equations are approximated by algebraic relations for discrete values that are then numerically analyzed by the application of computational codes. Hence, grids are a very important element of any numerical solution as the quantitative and qualitative properties of any grid plays a significant role in the accuracy and efficiency of the numerical solution, regardless of the flow solver used, and also the solver will be more robust and efficient when using a well constructed mesh. In fact, grid generation is often quoted as the most important and most time consuming part of CFD analysis. It is the phase of the analysis process that determines the total time required to obtain results from a simulation, as all other phases, including the actual computation of the results, can be carried out quite quickly. Similarly the overall cost of the analysis can be totally dominated by the costs of the labor required to build the mesh. Hence, the grid optimization is a worthwhile investment of time and cost.

Most turbomachinery flows involve complex geometry such as tip clearance and leading and trailing edges shape, and a wide variety of flow features in the domain such as vortices, boundary layer and separation regions, and all of these features need to be modelled by the CFD simulation. At these critical regions the gradients of the flow variables in space are high, and a large number of grid points are needed in order to produce a mesh that is capable of modelling these features. This is due to the fact that most numerical methods assume a linear variation of the flow variables between the grid points or within a volume. Consequently, if the flow varies rapidly in space, as it does in the critical regions of the flow, a finer grid will be needed to describe the variation accurately. However, in order to simulate the governing equations, it is extremely important to have accurate values of the variables and their derivatives, and any error in one of them can lead to the numerical solution of the equations being in error. A typical example of this is that flow separation on the surface of an object may not be predicted if the mesh is too coarse near the surface of the object, Shaw (86).

4.1.1 Grid classes

Two fundamental classes of grid are popular in the numerical solution of CFD problems: structured and unstructured. These two classes differ in the way in which the grid points are locally organized along grid lines on regular or an irregular manner. If the grid points can be identified easily with reference to the appropriate grid lines, the grid is known as structured grid. In the other hand, if the grid points cannot be associated with orderly defined grid lines, the grid is known as unstructured grid. Consequently, the connectivity in a structured grid is implicitly taken into account, while in unstructured grids it must be implicitly described by an appropriate data structure procedure. These two fundamental classes of grids give arise to another grid type knowing as hybrid grid, which can be obtained by combining both structured and unstructured grid.

The grid system may also be categorized as fixed or adaptive. A fixed grid system is generated prior to the solution of the governing equations of fluid motion and it remains fixed independent of the solution. In the other hand, if the exact position of the regions of high flow gradients are determined from the actual results of a simulation and this information is used to modify the grid for better numerical result, then the technique is known as an adaptive meshing.

4.1.1.1 Unstructured grids

Unstructured grids have irregularly distributed nodes and their cells are not obliged to have any standard shape. The connectivity of neighboring grid cells is not subject to any restrictions where the cells can overlap or enclose one another. Thus, an unstructured grid concept is considered as one of the appropriate solutions to the problem of producing grids in regions with complex shapes that are not easily amenable to the framework of the pure structured grid concept. Additionally, unstructured grid methods are well suited to inexperienced users because of the little input require by the user and under most circumstances they will generate a valid grid. Also, unstructured grids enable the solution of very large and detailed problems in a relatively short period of time. Figure 4.1 illustrates an example of unstructured grid for aircraft wing.

The major drawback of unstructured grids is the lack of user control when laying out the mesh, where the user involvement is limited only to the boundaries of the mesh while the grid generation code automatically filling the interior. Consequently, when trying to refine the mesh in a local area, the entire grid must be made much

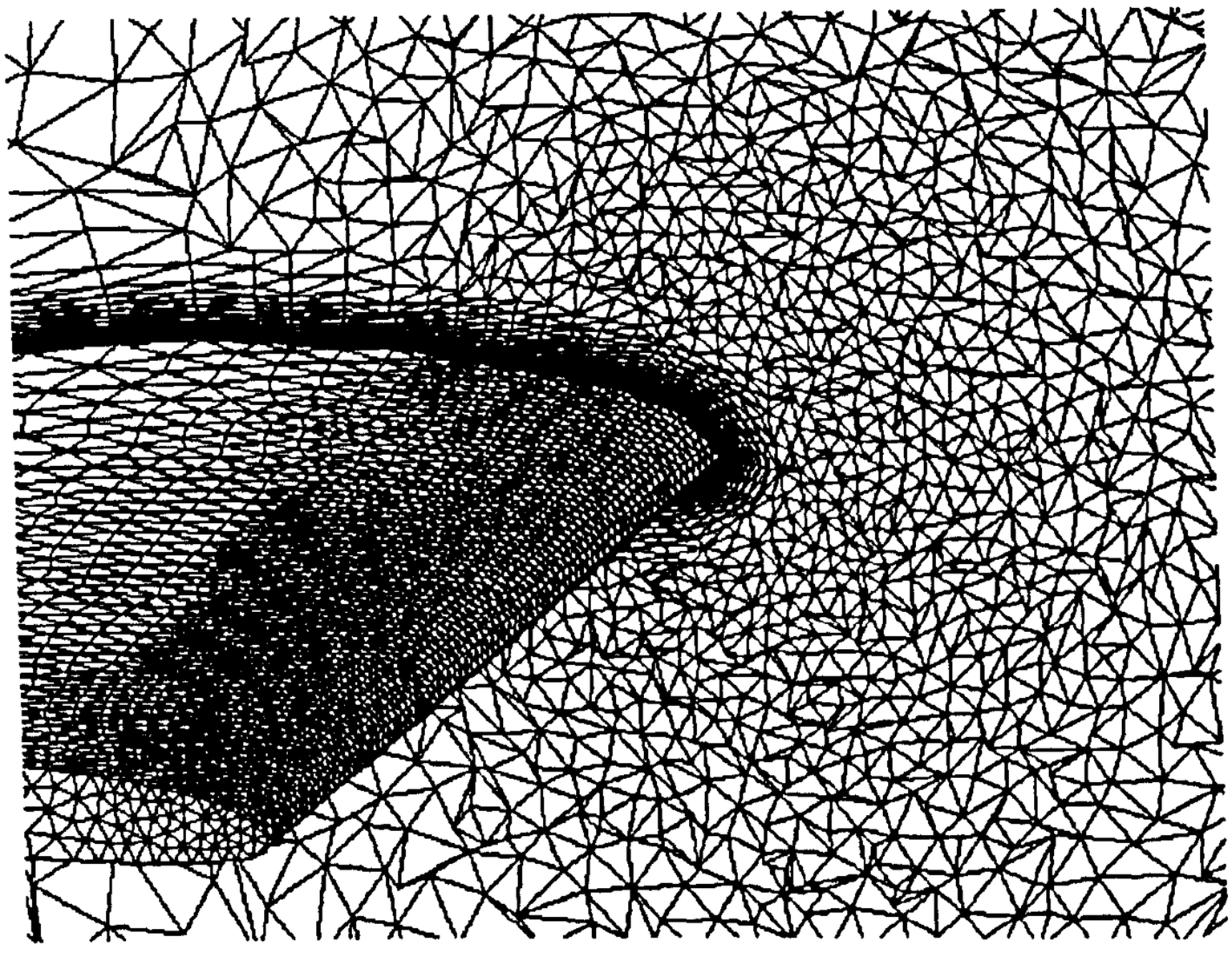

Figure 4.1: Unstructured grid around an aircraft wing

finer in order to get the point densities required locally. An other disadvantage is that the unstructured grid flow solvers typically require more memory and have longer execution times than structured grid solvers on a similar mesh density due to the demands of a special program to number and order the nodes, edges, faces, and cells of the grids. This is in addition to the extra memory required to store the information about the connections between the cells of the mesh.

4.1.1.2 Structured grids

Structured grids take their name from the fact that the mesh is laid out in a regular repeating pattern called a block. They utilize quadrilateral elements in 2-D and hexahedral elements in 3-D in a computationally rectangular array. Although, the element topology is fixed, the grid can be shaped to be body fitted through stretching and twisting of the block. They could be used with a single-block or multi-block, in which several blocks are connected together to construct the whole domain. Single-block structured grids may lack the required flexibility and robustness for handling domains with complicated boundaries, and using them may result in the grid cells may become too skewed and twisted, which prohibiting an efficient

numerical solution. In contrast, multi-block structured grids are considerably more flexible in handling those complex geometries.

Even though, multi-block grids give the user more freedom in constructing the mesh, the block connection requirements can be restricting and are more often difficult to construct. Several block-to-block connection methods are available within CFX-TASCflow code. These include:

(i) Point to point connection, where the blocks must match topologically and physically at the boundary.

(ii) Many points to one point connection, where the blocks must be topologically similar, but not the same at the boundary.

(iii) Arbitrary connections, where the blocks must be physically similar at the boundary, but can have significant topology differences.

Structured grids enjoy a considerable advantage over other unstructured grids in that they allow a high degree of user control, since placing control points and edges are done interactively. The ability to control the shape and distribution of the grid locally is a powerful tool which can yield excellent meshes, and often the mesh will be a flow-aligned resulting in a greater accuracy within the solver. In addition to that, the hexahedral and quadrilateral elements typical of structured grids are very efficient at filling space and support a high amount of skewness and stretching. This allows the user to naturally condense points in regions of high gradients in the flow field and expand out to a less dense packing away from these areas.

Another advantage of structured grids is that the flow solvers using these type of mesh execute faster and typically require the lowest amount of memory for a given mesh size. However, the major drawback of structured block grids is the time and expertise required to lay out an optimal block structure for an entire model, and since some geometries do not lend themselves to structured block topologies, the user is forced to stretch or twist the elements to a degree which may significantly affects the solver accuracy and performance.

Three different types of structured meshes are currently in use; H-type, C-type, and O-type grids. The correct choice depends on the geometry of the computational domain and whereabouts of the most highly skewed region of the grid as well as ease of assembly of the mesh. The H-type grid is appropriate for thin blades and for combination with other grids. However, they suffer from a lack of mesh orthogonality in regions with large contour deflections such as at blade leading edges. The trailing

edges geometry also affects the choice and a much better flow field discretization can be obtained by C-type and O-type grids around those regions, Niestroj and Came (72). Figure 4.2 presents examples of structured grids of C-type and O-type around airfoil.

4.1.1.3 Hybird grids

Hybrid grids are designed to take advantage of the positive aspects of both structured and unstructured grids. Their main advantage is that they can utilize the positive properties of structured grid elements in regions which need them the most and use automated unstructured grid techniques where there is no change in the flow field. The disadvantages of hybrid grids are that they can be difficult to use and require user expertise in laying out the various structured grid locations and properties to get the best results. Also, hybrid grids are typically less robust than unstructured methods and the generation of the structured portions of the mesh will often fail due to complex geometry or user input errors.

The computation of flow-fields requires a uniform rectangular computational domain, and since the majority of the physical domains of interest are non-rectangular, a transformation from physical space to computational domain is needed. This transformation is accomplished by specifying a generalized coordinates system which will map or transform the non-rectangular grid system in the physical (x, y, z) space to a rectangular uniform grid spacing in the computational (ξ, η, ζ) domain. One of the advantages of this transformation is that the body surfaces in the physical space can be selected as a boundary in the computational domain permitting easy application of surface boundary condition. Details for this coordinate transformation can be found in Fletcher (28), Liseikin (61), Wendt (103), Hoffmann and Chiang (45).

The main methods used in generation of structured meshes can be divided into algebraic methods that employ partial differential equations and variational methods. Algebraic methods are the simplest and fastest grid generation technique, in which the interior points of the grid are commonly computed through formule of transfinite interpolation. However, using these methods in regions with complicated shape can cause the cells to be overlapped or cross the boundary, hence they are commonly used to generate grids in regions with smooth boundary that are not highly deformed, or as an initial approximation in order to start the iterative process of an elliptic solver.

They are based mainly on the solution of elliptic, parabolic, or hyperbolic equations. For regions with arbitrary boundaries, elliptic and parabolic methods are commonly

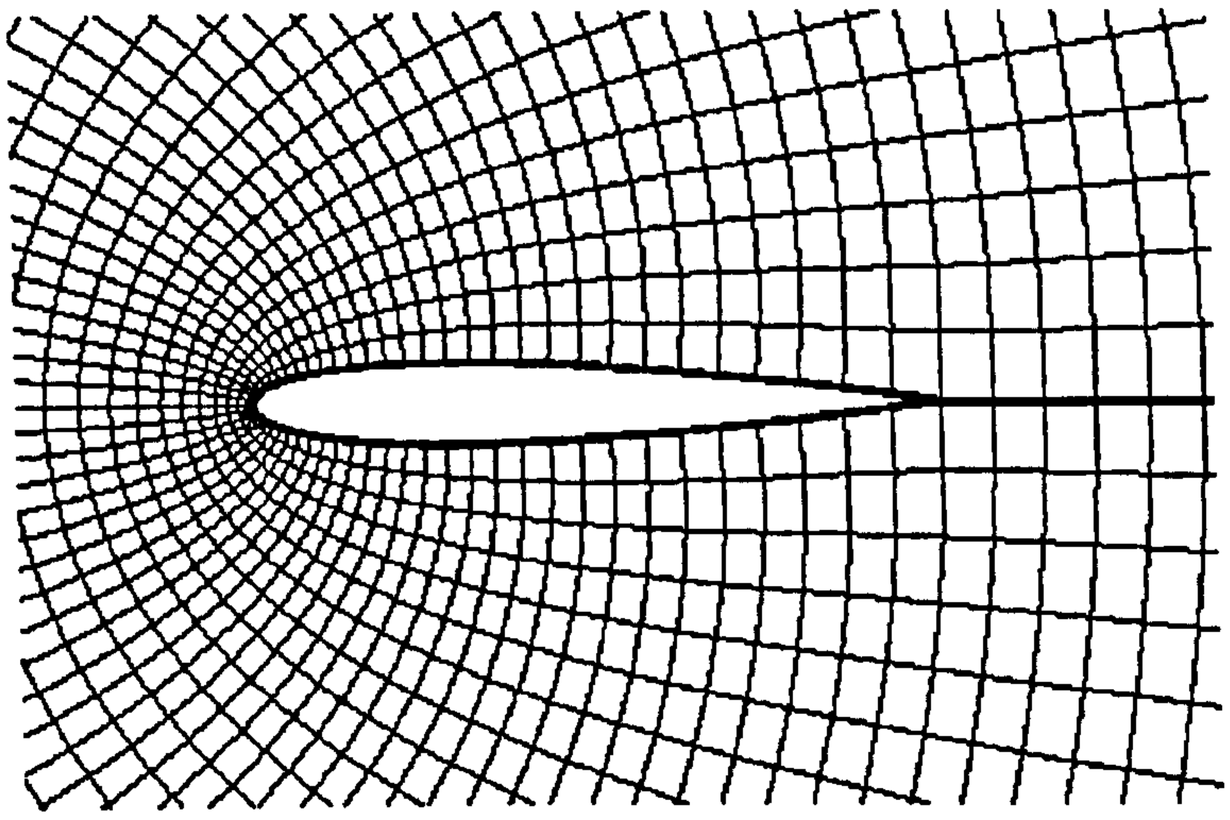

(a) C-type

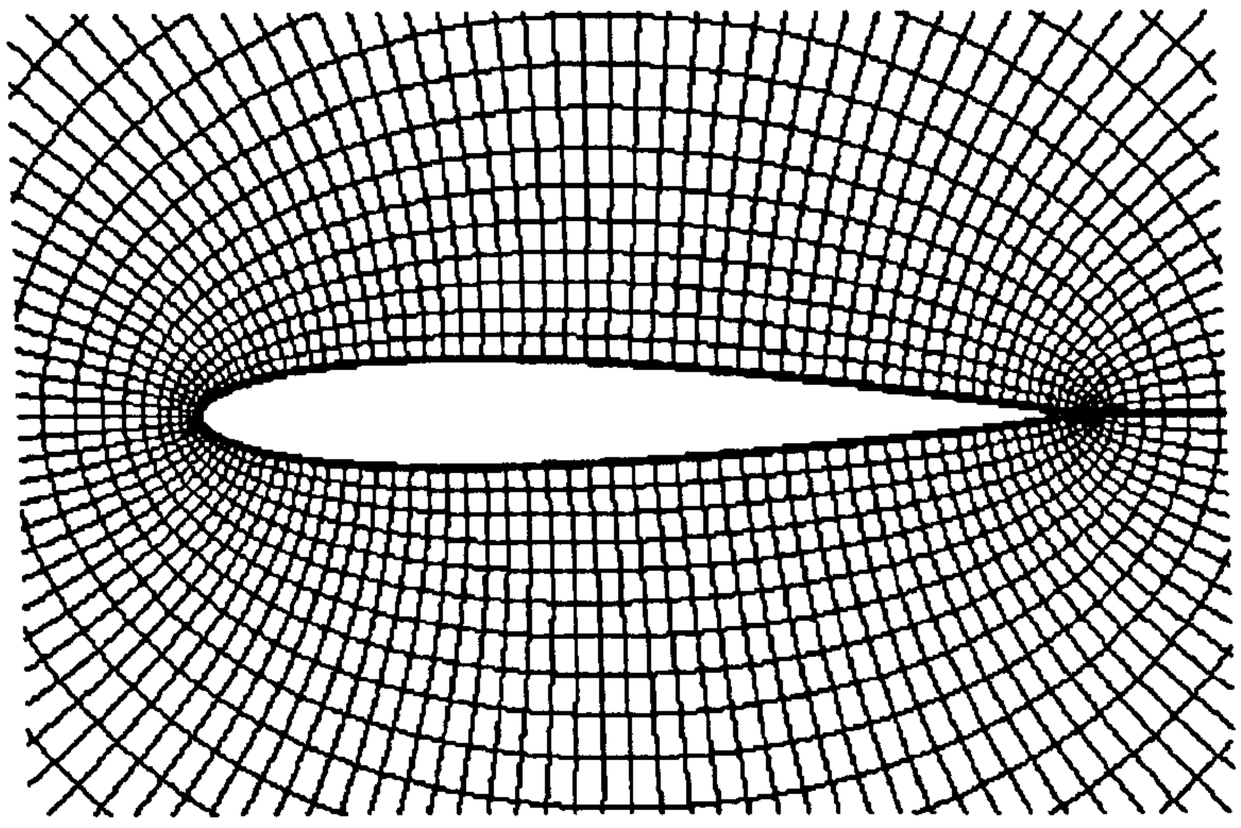

(b) O-type

Figure 4.2: Examples of structured grid

used since the interior coordinate lines derived through these methods are always smooth, and thus discontinuities on the boundary do not extend into the region. Elliptic methods are also used to smooth out algebraic, hyperbolic and unstructured grids. Hyperbolic system is very effective for external flows where the wall boundaries are well defined such as in airfoil, wing, and wing-body, whereas the far field boundary is left arbitrary. This situation also eliminates the need to specify point distribution on some of the edges of the flow domain, and makes it handier than for example the transfinite interpolation methods.

Variational methods are used to generate grids which are required to satisfy more than one condition, such as smoothness, uniformity, or near orthogonality which cannot be achieved simultaneously with algebraic or differential techniques. Even though, at the present they are not widely applied to practical grid generation, mainly because of their formulation that does not always lead to well-defined mathematical problem, they are cited as the most promising method for the development of the future of grid generation techniques.

4.1.2 Grid quality measures

There are a number of measures that are largely used in CFD to determine the grid quality. These measures ensure that the available grid can be used with a CFD code to get the best result possible without any computational errors. One of the most important measures of grid quality is the skewness of the grid. If the angle between two adjacent flux element surfaces is used as a measure of orthogonality, it is strongly recommended in CFX-TASCflow code that the angle has a value between 0° and 180° and preferably between 20° and 180°. Angles outside the former range will likely result in unacceptable Jacobian evaluations, and negative values of Jacobian can result in negative values for the volume of octant, which can be viewed as nonphysical flux element geometry. Also, for angles less 20° a degradation of accuracy could result as well as increase in CPU time required to obtain a solution. The difficulty increases as the angle approaches 0°, where 0° is an unacceptable angle. However, negative Jacobian can occur also from inconsistent mesh orientation. To avoid that the handedness of the i, j, and k indices must agree with the x, y, and z Cartezian coordinates and preferably both following the right-hand-rule.

The other important measure is the aspect ratio, which can be defined as the ratio of the flux element edge lengths. CFX-TASCflow software has been designed so that the performance of the solver is not particularly sensitive to flux element aspect ratio. However, a computer round-off degradation will occur as the aspect ratio

exceeds 100:1 for a single precision machine and the limit is much higher on a double precision machine. In addition to that, aligning the grid lines with flow streamline is recommended by the code to maintain the false diffusion as low as possible.

4.1.3 CFX-TASCflow grid generation approach

The code is a structured grid solver and accepts a single-block or multi-block structure grids generated by the TASCgrid software included into the CFX-TASCflow package or by an external grid generation package. In the present work, CFX-TurboGrid software was used to generate the grid for the main blade of the axial fan while TASCgrid code was used to generate the grid for the recess casing treatment. Both of these codes are briefly described in this section.

4.1.3.1 TASCgrid software

The TASCgrid software generates 2-D and 3-D structured computational grids that can be used in the numerical solution of fluid flow problems. The grids generated are boundary-fitted single-block and in general non-orthogonal and curvilinear suitable for use with the rest of the CFX-TASCflow software. The grid is generated through four basic programs which run sequentially, where the result of each program is used as input for the next program. However, each of these programs requires some form of user input. These programs are:

1. TASCgridg: a program for domain geometry creation, where geometrical data can be created in the form of points, lines and curves, ...etc.
2. TASCgridc: a program for geometry definition, where the nodes are distributed on the lines of the domain.
3. TASCgrids: a program for domain surface definition, where the nodes are distributed over the domain surfaces.
4. TASCgridi: a program for a mapped mesh generation, where a mesh with regular structure is created within the domain by distributing the nodes within the interior volumes. At the end, this program will write a grid data file named GRD, which contain all the information about the geometry and will be read by TASCbob3D, the pre-processor program of CFX-TASCflow code.

4.1.3.2 CFX-TurboGrid software

A grid generation program that combines the four basic programs of grid generation described before in TASCgrid. It is designed for the creation of periodic blade geometry meshes with a minimum of user intervention, where:

- A number of pre-defined grid topology templates are available, each well suited for a certain class of turbo-machines, Figure 4.3.
- Periodic boundaries are managed automatically by ensuring both physical and topological boundaries.
- Grid attachment between sub-grids of multi-block domain and between corresponding periodic boundaries is automatically performed during the mesh creation.

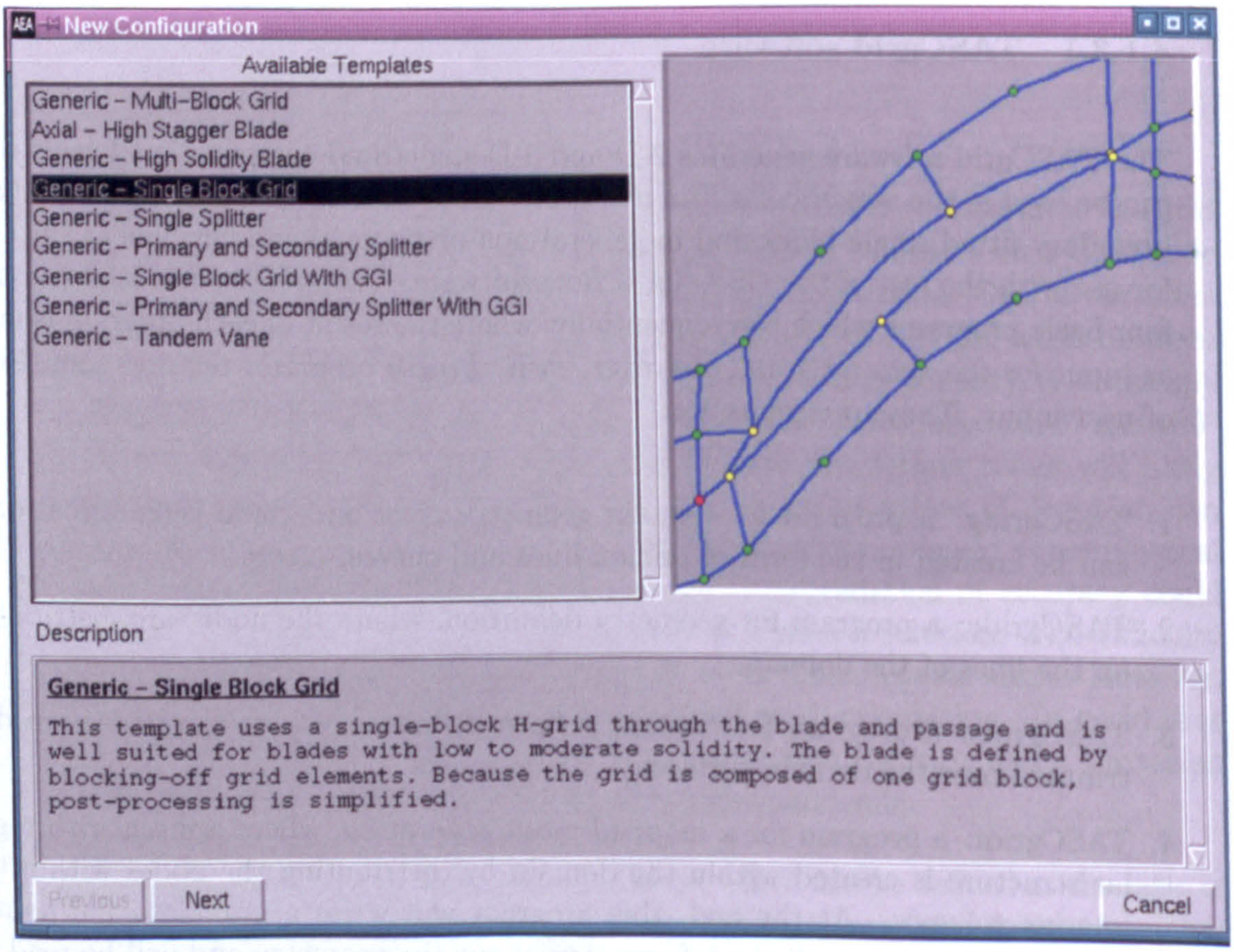

Figure 4.3: CFX-TurboGrid template selection panel

CFX-TurboGrid requires the input of three data files to define the flow-path and blade geometry. These files contain data points in Cartezian (x, y, z) coordinates for the blade profile, hub and shroud curves and a minimum of two blade profiles are required. Both hub and shroud curves must be extended upstream of the blade leading edge and downstream of the blade trailing edge. In addition to the data files, the user has to specify a few other parameters before starting the grid creation such as topology template, axis of rotation, number of blades, tip clearance and grid size.

CFX-TurboGrid checks the grid for negative grid volumes at the completion of the grid generation. A negative volume is reported if the grid is left-handed or a grid element is twisted upon itself. Grid with negative volumes will not be accepted by the solver and needs to be corrected by flipping the topology if the grid is left-handed or by adjusting the control point positions if a grid element is twisted upon itself.

The minimum and maximum grid angles are also reported at the completion of the grid generation. If the minimum angle is below 20°, recommended value by the code solver, the position of the control points has to be modified especially at the periodic boundary or leading and trailing edges to overcome this skewness problem. A detailed guide for the placement of the control points at these positions for each topology template is given in the CFX-TurboGrid Software Documentation, AEAT (3). Indeed, to achieve high quality grid even with an automatic grid generation software may take a fair amount of user interaction and time.

4.2 Discretization

A discretized equation is an algebraic relation connecting the values of an arbitrary function ϕ for a group of grid points, which is derived from the differential equation governing ϕ and thus expresses the same physical information as the differential equation. The value of ϕ at a grid point influences the distribution of ϕ only in its immediate neighbourhood. As the number of grid points becomes very large, the solution of the discretized equations is expected to approach the exact solution of the corresponding differential equation. The three essential discretization approaches are Finite Difference Method FDM, Finite Element Method FEM, and Finite Volume Method FVM.

In the FVM formulation, the computational domain is subdivided into a set of non-overlapping control volumes cover the whole domain such that there is only one

control volume surrounding each grid point. On each control volume the conservation laws are applied to determine the flow field variables in some discrete points of the control volume, called nodes. Two principal methods for defining the boundaries of the control volumes and the location of the nodes within the control volume; node centered or cell vertices as shown in Figure 4.4. The most attractive feature of this formulation is that the resulting solution would imply that the integral conservation of mass and momentum is exactly satisfied over any group of control volume and of course over the whole calculation domain since the flux that leaves one control volume enters the next. This characteristic exists for any number of nodes resulting that even the coarse grid solution exhibits exact integral balances, Patankar (75).

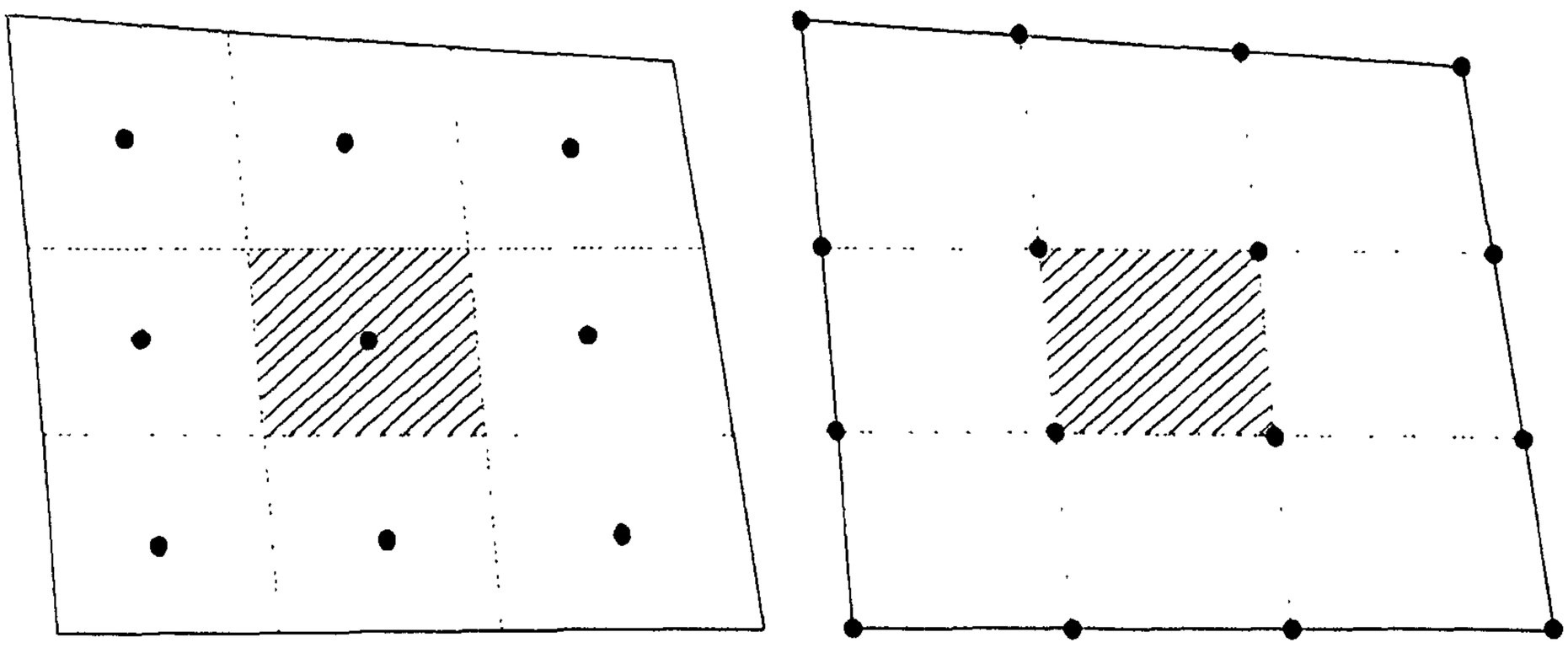

(a) Cell centered approach

(b) Cell vertex approach

Figure 4.4: Typical choice of nodes in Finite Volume Method

CFX-TASCflow uses the finite volume formulation but is based on a finite element approach of representing the geometry, as the computational domain is discretized into elements and the control volume surfaces are defined by element mid-planes. The procedure creates a control volume for each node, with the boundary of each interior control volume defined by 8 line segments in 2-D and 24 quadrilateral surfaces in 3-D. This arrangement is shown in 2-D in Figure 4.5.

The mean flow continuity equation (3.19) and momentum equations (3.20) (without the velocity divergence term) are transferred to algebraic equations by integrating them over each control volume, and applying the Gauss's Theorem and they result

in the following integral equations:

$$\frac{\partial}{\partial t}\int_v \rho dv + \int_s \rho u_j dn_j = 0 \tag{4.1}$$

$$\frac{\partial}{\partial t}\int_v \rho u_i dv + \int_s \rho u_i u_j dn_j = -\int_s P dn_i + \int_s \mu_{\text{eff}}\left(\frac{\partial u_i}{\partial x_j} + \frac{\partial u_j}{\partial x_i}\right) dn_j + \int_v S_i dv \tag{4.2}$$

where v and s denote volume and surface integrals respectively, and dn_i are the differential Cartesian components of the outward normal surface vector. However, the volume integrals are relatively easy to transform into a discrete form, but the surface integrals are complex and need to be evaluated at integration points ip. The flux element and location of these integration points for one flux element into 2-D is illustrated in Figure 4.6. The discrete form of the integral equations are written as:

$$\rho V\left(\frac{\rho - \rho^{\circ}}{\Delta t}\right) + \sum_{\text{ip}} (\rho u_j \Delta n_j)_{\text{ip}} = 0 \tag{4.3}$$

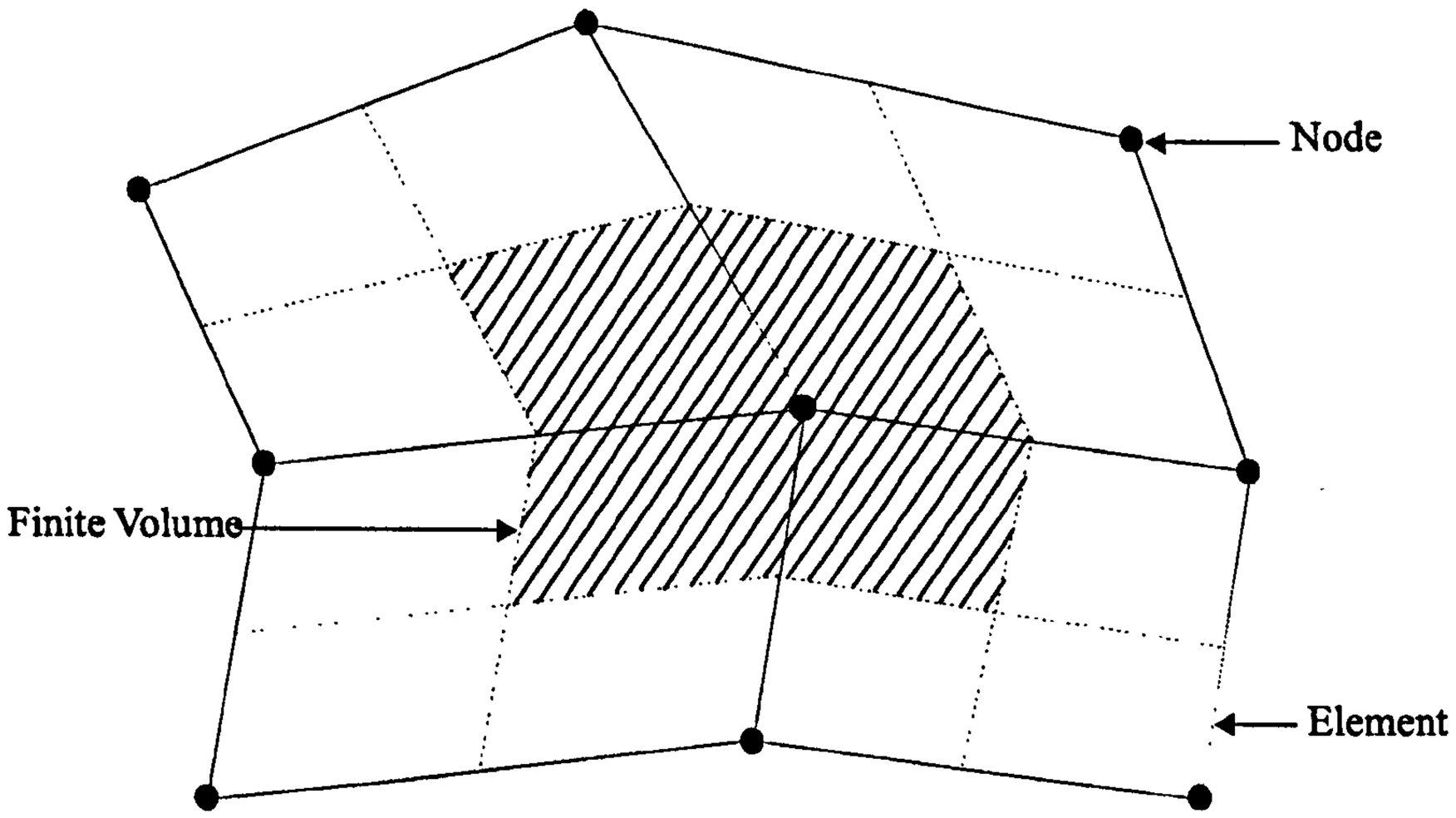

Figure 4.5: Control volume definition

$$\rho V\left(\frac{u_i - u_i^{\circ}}{\Delta t}\right) + \sum_{\text{ip}} \dot{m}_{\text{ip}}(u_i)_{\text{ip}} = \sum_{\text{ip}} (P\Delta n_j)_{\text{ip}} + \sum_{\text{ip}} \left(\tau_{ij_{\text{eff}}} \Delta n_j\right)_{\text{ip}} + \overline{S}_i V = 0 \quad (4.4)$$

where;

$$\dot{m}_{\text{ip}} = \left(\rho u_j \Delta n_j\right)_{\text{ip}}^{\circ} \quad (4.5)$$

$$\tau_{ij_{\text{eff}}} = \mu_{\text{eff}} \left(\frac{\partial u_i}{\partial x_j} + \frac{\partial u_j}{\partial x_i}\right) \quad (4.6)$$

and V is the volume of the control volume, Δn_j is the discrete outward surface vector, Δt is the time step, the superscript $\circ$ means at the previous time level, and the over-bar on the source terms indicate an average value for the control volume.

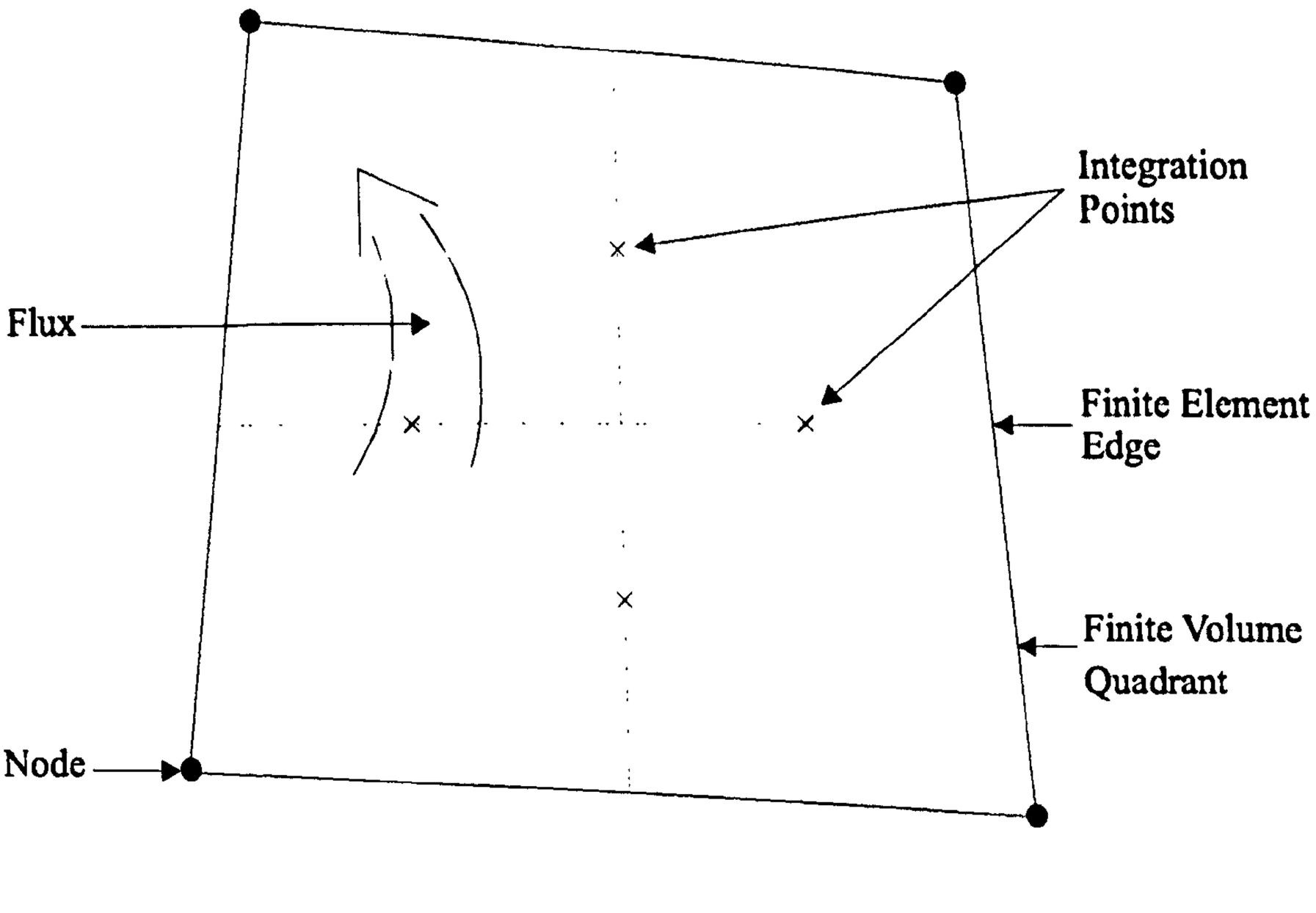

Figure 4.6: Flux element layout

4.2.1 Time term treatment

CFX-TASCflow code employs for steady-state computations a transient formulation as a convenient means of introducing relaxation into the iterative nonlinear solution. If only the steady-state solution is of interest, the time step Δt is used as a free parameter through which the convergence rate is optimized. Relaxation introduced via the time step is preferable to other relaxation schemes such as E factor, Raithby and Schneider (80), or steady formulations with explicit under-relaxation, Patankar (75), because it ensures that the linear momentum and energy equation solutions advance the dependent variables by a consistent amount in each cycle, Galpin and Raithby (30).

The first-order accurate backward Euler approximation employed in the code to represent the time term for the steady-state analysis is also the default implementation used for the formulation of the unsteady simulation. In this approximation,

$$\frac{\partial \phi}{\partial t} \approx \frac{1}{\Delta t}\left[\phi - \phi^{\circ}\right] \tag{4.7}$$

This is the default implementation in CFX-TASCflow for transient simulations. With the above implementation, the error in the transient representation reduces linearly as the time step is linearly refined. In latter versions, the code incorporated an alternative formulation of the transient term in the form of a second-order-accurate backward Euler scheme.

$$\frac{\partial \phi}{\partial t} \approx \frac{1}{\Delta t}\left(\frac{1}{\check{r}(\check{r}+1)}\right)\left[(2+\check{r})\check{r}\phi - (1+\check{r})^2\phi^{\circ} + \phi^{\circ-1}\right] \tag{4.8}$$

where $\check{r}$ is the ratio between old and new implicit time steps

$$\check{r} = \frac{\Delta t^{\circ}}{\Delta t} \tag{4.9}$$

In the case of constant time step, $\check{r} = 1$, equation (4.8) can be simplified to

$$\frac{\partial \phi}{\partial t} \approx \frac{1}{2\Delta t}\left[3\phi - 4\phi^{\circ} + \phi^{\circ-1}\right] \tag{4.10}$$

When expressed as above the error in the transient representation reduces quadratically as the time step is refined linearly. The method remains fully implicit as sufficient iterations are employed to resolve all non-linear terms in ϕ at the new time level.

4.2.2 Diffusion term treatment

The scalar derivatives in the diffusion terms are evaluated using the standard Finite Element approach of shape functions

$$\left.\frac{\partial \phi}{\partial x_j}\right|_{\text{ip}} = \sum_n \left.\frac{\partial N_n}{\partial x_j}\right|_{\text{ip}} \phi_n \tag{4.11}$$

The summation is over all the shape function N. The shape function definition can be found in AEAT (2).

4.2.3 Pressure gradient term treatment

The value of P_{ip} in the surface integration of the pressure gradient term in the momentum equation (4.4) is again evaluated using the shape functions

$$P_{\text{ip}} = \sum_n N_n P_n \tag{4.12}$$

4.2.4 Advection term treatment

The advection terms are more difficult to model and very much responsible for the accuracy and robustness of the solution. The CFX-TASCflow flow code employ advection discretization schemes called Mass Weighted [MWS] and Linear Profile Skewed upstream differencing schemes [LPS] with Physical Advection Correction [PAC]. These schemes are based on the conservative finite volume approach with

special care taken to minimize the errors normally associated with Upstream Differencing Scheme [UDS]. Examining just the advection term, it is represented discretely as,

$$\int_s (\rho u_i \phi) dn_j \approx \sum_{\text{ip}} \dot{m}_{\text{ip}} (u_i)_{\text{ip}} \tag{4.13}$$

This is a second order accurate discrete approximation to the above integral as the integration points are located at the center of their respective line segments, mid-point-rule, Figure 4.7. To achieve algebraic closure, each integration point term, in this case the ϕ_{ip}, must be related to the nodal variables. The closure relation is determined by the advection scheme, which estimated ϕ_{ip} with two components; upstream term and an optional stream-wise correction term,

$$\phi_{\text{ip}} = \phi_{\text{upstream}} + \Delta\phi \tag{4.14}$$

The first component is provided by the upwind scheme, the simplest possible is the Upwind Difference Scheme UDS, which for a mass flow in the indicated direction

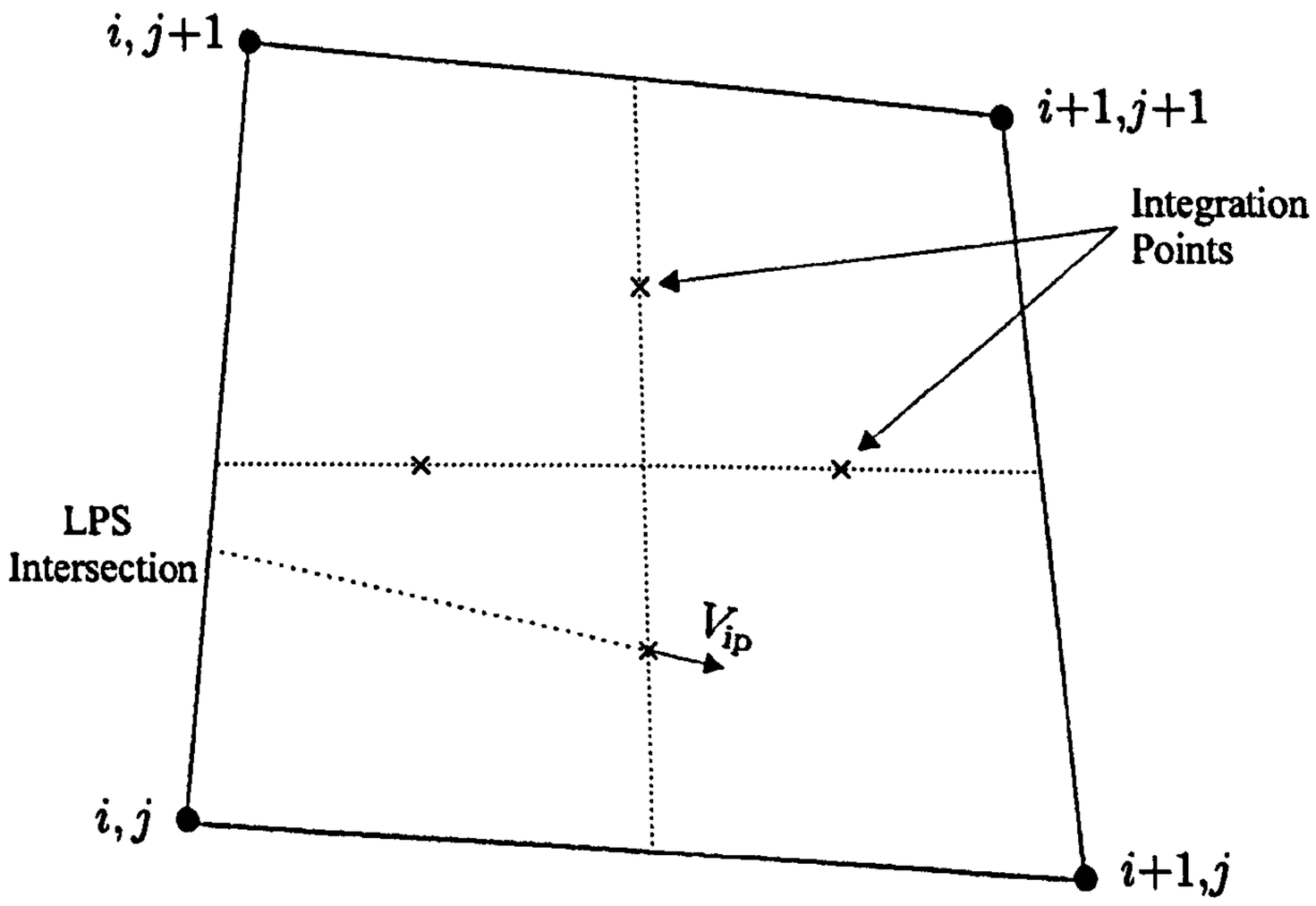

Figure 4.7: Integration points and LPS intersection

would set,

$$\phi_{ip} = \phi_{i,j} \tag{4.15}$$

where $\phi_{i,j}$ is the value of ϕ at node (i,j). UDS is a first-order accurate and its simplicity and robustness has made it widely used in early CFD applications. The major drawback of this scheme is the tendency to produce incorrect results when the flow is not aligned with the grid lines, which is referred to as false diffusion, which leads to excessive smearing and numerical total pressure losses when used in momentum equation.

An improved upwind scheme is the Mass Weighted Skewed Scheme MWS, which brings in influences from other nodes in the element in a manner that models the local directionality of the flow. It reduces the levels of false diffusion present in the basic UDS by including the effects of neighbouring nodes, where the convective value of the function is taken to be equal to the average of the surrounding nodal values weighted according to the mass passing through the control volume faces. It is as robust as UDS and first order accurate too. It reduces the level of smearing, but still has high artificial total pressure losses when used in momentum equations. In order to obtain second-order-accurate upwind scheme, $\Delta\phi$ can be approximated by,

$$\Delta\phi \approx \frac{\Delta x}{2}\left[\frac{\partial\phi}{\partial x}\right] \tag{4.16}$$

where $(\partial\phi/\partial x)$ must at least account for the variation of ϕ between nodes i and $i+1$ in Figure 4.7. Therefore, equation (4.14) becomes,

$$\phi_{ip} = \phi_i + \frac{\Delta x}{2}\left[\frac{\partial\phi}{\partial x}\right] \tag{4.17}$$

Using a finite difference representation

$$\frac{\partial\phi}{\partial x} = \frac{\phi_{i+1} - \phi_i}{\Delta x} \tag{4.18}$$

Substituting this equation into equation (4.17) leads to the Central Difference Scheme [CDS] approximation for ϕ,

$$\phi_{ip} = \frac{\phi_{i+1} + \phi_i}{2} \tag{4.19}$$

The accuracy of this linear profile is satisfactory, but the physical influence is incorrect. For high velocity, equation (4.19) implies that a change in ϕ_{i+1} has just as strong an influence on ϕ_{ip} as does the same change in ϕ_i, where in fact ϕ_{ip} should be independent of ϕ_{i+1} in the limit where advection dominates. This poor physical influence results in difficult convergence for many iterative solver, the need for special boundary condition treatment, non-physical wiggles in the prediction, and high errors, although the truncation error is second order.

One way of eliminating the wiggles in the solution is by blending of CDS and UDS as in the Upstream weighted differencing schemes [UWDS], Raithby and Toorance (81), and Hybrid schemes, Patankar (75). However, for high Peclet numbers, high ratio of advection to diffusion, the truncation error is first order and the inaccuracies of UDS prevail. Instead of blending CDS and UDS to improve physical influence and suppress wiggles in the solution, an alternative method for correcting UDS is to use a different finite difference representation for $(\partial\phi/\partial x)$, Doormaal et al. (24) and AEAT (2). A general form may be

$$\frac{\partial\phi}{\partial x} = a\frac{(\phi_i - \phi_{i-1})}{\Delta x} + b\frac{(\phi_{i+1} - \phi_i)}{\Delta x} + (1-a-b)\frac{(\phi_{i+2} - \phi_{i+1})}{\Delta x} \tag{4.20}$$

By choosing different values of a and b, different schemes can be recovered. For instance CDS is equivalent to $a = 0, b = 1$. The Second Order Upwind scheme SOU is equivalent to $a = 1, b = 0$, as a result,

$$\phi_{ip} = \frac{3\phi_i - \phi_{i-1}}{2} \tag{4.21}$$

The QUICK scheme of Leonard (60) can also be obtained when $a = 0.25, b = 0.75$, as a result,

$$\phi_{ip} = \frac{3\phi_{i+1} + 6\phi_i - \phi_{i-1}}{8} \tag{4.22}$$

However, all these schemes are corrections to UDS based on local finite difference representation of $(\partial\phi/\partial x)$ in equation (4.17). They may lead to higher order discretization schemes but will not have the correct physical influence. Alternatively, the physical influence schemes can be used to ensure that the resulting algebraic equations are correctly imitate the transport properties of the physical processes, which required that the estimation of the function properly reflect the interactions

between the physical processes of advection, diffusion and source terms. Consider an advection dominated transport equation as

$$\frac{\partial}{\partial x}(\rho u\phi) + \frac{\partial}{\partial y}(\rho v\phi) + \frac{\partial}{\partial z}(\rho w\phi) = \dot{S}^{\phi} \tag{4.23}$$

In non-conservative form, this equation becomes,

$$\rho u\frac{\partial \phi}{\partial x} + \rho v\frac{\partial \phi}{\partial y} + \rho w\frac{\partial \phi}{\partial z} = \dot{S}^{\phi} \tag{4.24}$$

Upon rearranging

$$\frac{\partial \phi}{\partial x} = \frac{1}{\rho u}\left[\dot{S}^{\phi} - \rho v\frac{\partial \phi}{\partial y} - \rho w\frac{\partial \phi}{\partial z}\right] \tag{4.25}$$

This equation is clearly illustrates that the derivative $(\partial\phi/\partial x)$ can be determined from the physical influences of the source term and the component of advection along y and z coordinate directions. Substituting equation (4.25) into equation (4.16), the result approximation of the correction

$$\Delta\phi = \frac{\Delta x}{2\rho u}\left[\dot{S}^{\phi} - \rho v\frac{\partial \phi}{\partial y} - \rho w\frac{\partial \phi}{\partial z}\right] \tag{4.26}$$

is referred to as a Physical Advection Correction PAC term and is used instead of a term such as that in equation (4.20). One of the schemes employing PAC is the Linear Profile Skew scheme LPS, which represents an enhancement of Raithby (79) Skew Upstream Differencing Schemes [SUDS]. LPS uses the local flow vector and intersects the upstream direction with element edge. Figure 4.7 shows a sample intersection. A linear variation is assumed between the nodes. Thus, for the sample intersection

$$\phi_{\mathrm{ip}} = a\phi_{i,j} + (1-a)\phi_{i,j+1} \tag{4.27}$$

where a is a function of the intersection point location. LPS ia second-order-accurate. However, when source terms are presented it reverts to first-order. To

achieve second-order-accuracy the variation of the advected variable in the streamwise direction must be taken into account in the advection schemes, which is addressed by the second component, Thomas et al. (95).

A pure version of LPS is implemented in CFX-TASCflow, corresponding to the most accurate but also least robust of the code discretization schemes. A more robust scheme Modified Linear Profile Skewed [MLPS] is also implemented in the code. In this scheme the value of function is initially calculated as for the LPS scheme and then the interpolation coefficients modified such that the value of the function is more evenly dependent on the nodal values upstream and downstream of the integration point.

4.2.5 Pressure-velocity coupling treatment

The control volume formulation used in CFX-TASCflow code store the primitive variables at the nodes. However, if the pressures and velocities are both defined at the nodes of an ordinary control volume, a highly non-uniform pressure field can act like a uniform one in the discretized momentum equations, which is known as pressure-velocity decoupling or checker boarding. This can be demonstrated with the simple one-dimensional incompressible flow in a duct of constant area A as shown in Figure 4.8. The continuity equation can be discretized as:

$$\rho A u_e - \rho A u_w = 0 \tag{4.28}$$

$$\frac{(u_{i+1} + u_i)}{2} - \frac{(u_i + u_{i-1})}{2} = 0 \tag{4.29}$$

$$u_{i+1} - u_{i-1} = 0 \tag{4.30}$$

and the momentum equation is discretized as:

$$\rho A\,(u_e - u_w) + A\,(P_e - P_w) = 0 \tag{4.31}$$

$$\frac{\rho A}{2}(u_{i+1} - u_{i-1}) + \frac{A}{2}(P_{i+1} - P_{i-1}) = 0 \tag{4.32}$$

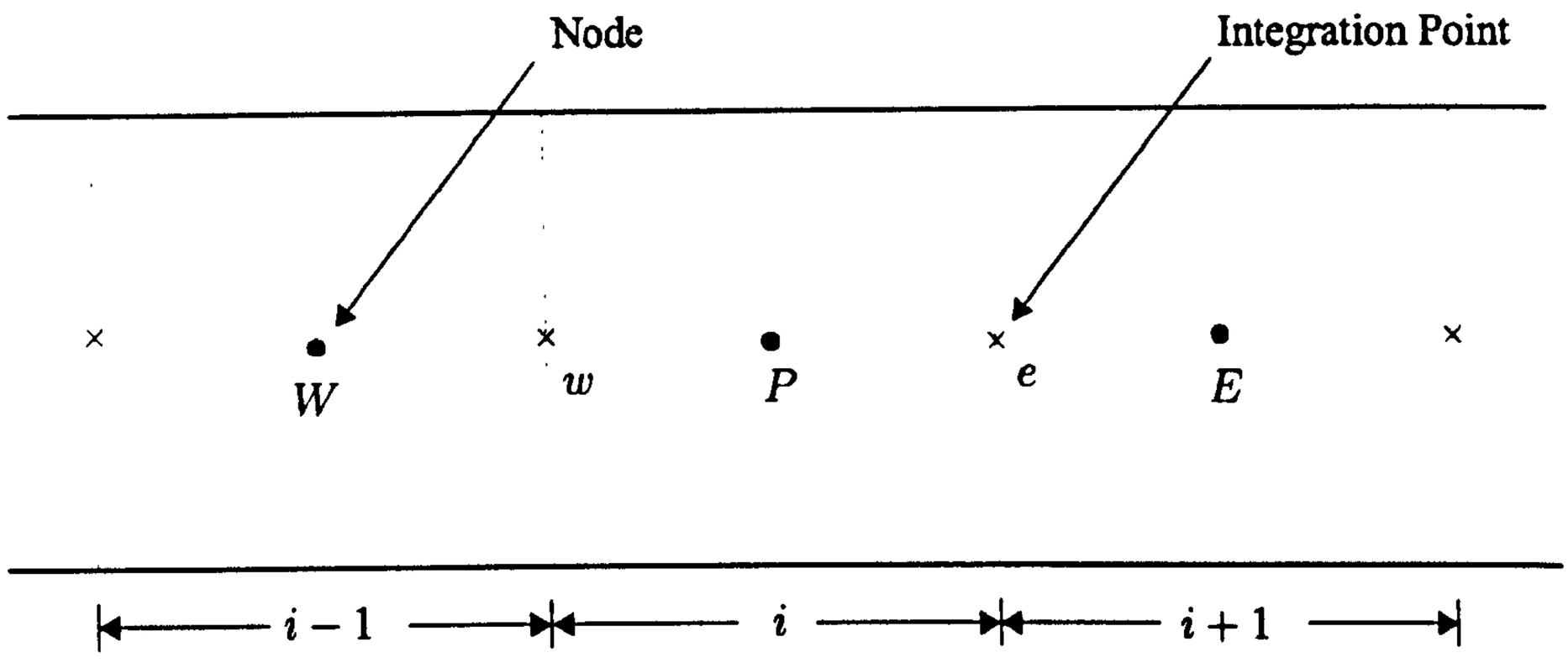

Figure 4.8: One-dimensional duct layout

Substituting equation (4.30) into equation (4.32), yields to:

$$P_{i+1} - P_{i-1} = 0 \tag{4.33}$$

This equation means that the momentum equation will contain the pressure difference between two alternate nodes, and not between adjacent ones. This clearly can be satisfied by zigzag pressure field such as ($P_{i-2} = P_i = P_{i+2} = 50$) and ($P_{i-1} = P_{i+1} = 100$). Such a pressure field would give the same zero momentum source in the discretized equation (4.33) as a uniform pressure field. Thus , a highly non-uniform pressure field would be treated as a uniform one by the discretized momentum equation. This can be overcome by using a staggered grid for the velocity component. The idea is to calculate the velocity components on staggered grids centered around the cell faces, while evaluating other variables such as the pressure and density at ordinary nodal points. This is explained in detailed in Patankar (75) and Versteeg and Malalasekera (101).

CFX-TASCflow code introduces the pressure-velocity coupling by modifying the definition of the integral point velocities in the continuity equation. This is done by involving the local pressure difference instead of simply using a difference of the nodal velocity values. This nodal pressure influence is introduced through an algebraic representation of momentum conservation for the integration point velocities. To

illustrate this, consider a control volume momentum equation of the form:

$$(A_p)_i\, u_i = \left(\sum_n A_n u_n\right)_i - V\left(\frac{\partial P}{\partial x}\right)_i + b_i \tag{4.34}$$

where V is the volume of the control volume about node i. This control momentum equation can be simplified to:

$$u_i = c_i + d_i\left(\frac{\partial P}{\partial x}\right)_i \tag{4.35}$$

where the two new variables c_i and d_i are given by:

$$c_i = \frac{1}{(A_p)_i}\left[\left(\sum_n A_n u_n\right)_i + b_i\right] \tag{4.36}$$

$$d_i = -\frac{V}{(A_p)_i} \tag{4.37}$$

Equation (4.35) applies at a node i, but a similar equation can be written for the integration point e;

$$u_e = c_e + d_e\left(\frac{\partial P}{\partial x}\right)_e \tag{4.38}$$

which can be approximated by averaging the values at the neighboring nodes by;

$$u_e = \frac{1}{2}(c_{i+1} + c_i) + \frac{1}{2}(d_{i+1} + d_i)\left(\frac{P_{i+1} - P_i}{\Delta x_e}\right) \tag{4.39}$$

The connectivity of nodal velocities is large and complicated when c_i and c_{i+1} are expanded, and to reduce that, equation (4.35) is rearranged as:

$$c_i = u_i - d_i\left(\frac{\partial P}{\partial x}\right)_i \tag{4.40}$$

Substituting values c_i and c_{i+1} by their values at the nodal location from this equation into equation (4.39) yield to:

$$u_e = \frac{1}{2}(u_{i+1} + u_i) + \frac{1}{2}(d_{i+1} + d_i)\left(\frac{\partial P}{\partial x}\right)_e - \frac{1}{2}\left[d_{i+1}\left(\frac{\partial P}{\partial x}\right)_{i+1} + d_i\left(\frac{\partial P}{\partial x}\right)_i\right] \quad (4.41)$$

similarly one can produce a similar equation for the integration point w, and by substituting the values of both u_e and u_w into equation (4.28) and also value of d_i from equation (4.37) yields to a new one-dimensional continuity equation

$$(u_{i+1} - u_{i-1}) - \frac{A}{2\dot{m}}(P_{i-2} - 4P_{i-1} + 6P_i - 4P_{i+1} + P_{i+2}) = 0 \quad (4.42)$$

The first term in this equation is identical to equation (4.30) and the remaining are pressure terms and hence pressure-velocity decoupling can no longer occur.

4.3 CFX-TASCflow solver

The previous section outlines the process of discretization and linearization of the continuous governing differential equations which resulted in a system of linear algebraic equations that must be solved, which can be done by simple relaxation methods. However, those are good at reducing error components that have short wavelengths with respect to the grid spacing, but the longer the wavelength of the error, the less effective they become. This observation forms the basis for multigrid methods.

4.3.1 Multigrid solution

The simple relaxation method on a fine grid will reduce only the short wavelength components of error. However, if the equations that are being solved on this fine grid could somehow be represented on a coarse grid, then those wavelengths that are relatively long on the fine grid will be short wavelengths components of error on the coarse grid and will be reduced by applying the simple relaxation method on

the coarse grid. Thus, both long and short wavelengths are addressed. Multigrid methods follow a similar process.

A level of grids is constructed, each one is coarser than the previous, with the finest grid at one end and a coarsest grid at the other. The relaxation method on any given grid addresses its relatively short wavelength component of error. Taking the solution on all the grids together thus causes a reduction of all the components of error. Figure 4.9 demonstrates in a one-dimensional case how the various grids together cover all wavelengths of the error. Details of how the coarse grid equations are constructed and how the information is passed between the grids in CFX-TASCflow code are presented in AEAT (2).

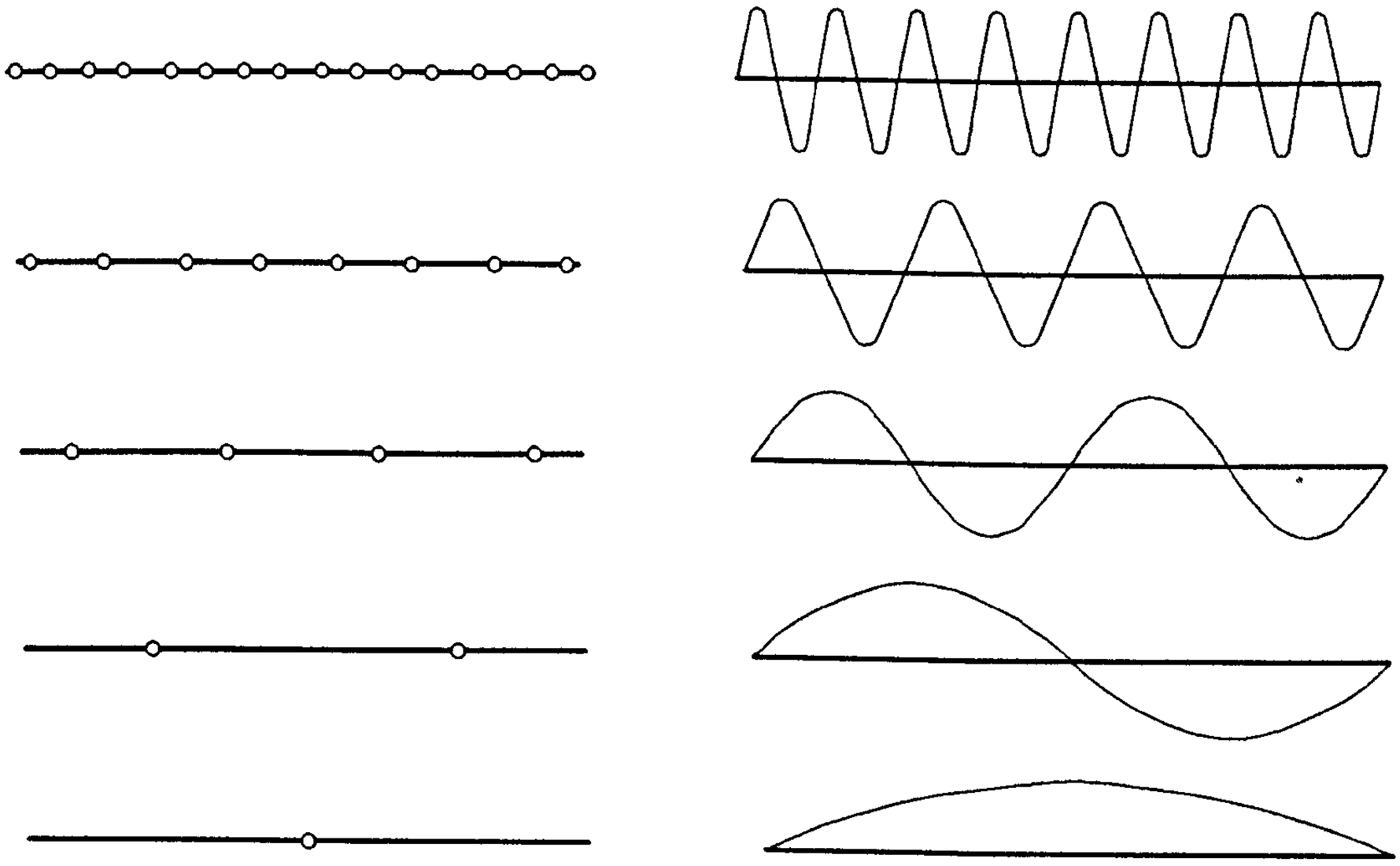

(a) Grid (b) Error Component

Figure 4.9: Multigrid error reduction

The multigrid solver employed by CFX-TASCflow is an Algebraic Multigrid method [AMG] based on the Additive Correction Multigrid [ACM] strategy, Hutchinson and Raithby (47). AMG methods create coarse grid equations from the fine grid

equations without any use or knowledge of the actual geometry or grid structure, while the conventional multigrid techniques are based upon the geometry or grid structure and hence are called Geometric Multigrid methods [GMG].

The ACM strategy is fully coupled, continuity and momentum equations are solved simultaneously, and forms its blocks based on an evaluation of the relative strengths of the coefficients connecting a node to its neighbors, rather than a fixed blocking. This adaptive approach means that one multigrid algorithm is sufficient to reduce all error modes in the solution. The purpose of the additive correction is to get a correction to the current un-converged solution so that the flux balance is satisfied over a group of touching finite volumes.

4.3.2 The relaxation scheme

The relaxation scheme used in CFX-TASCflow code is based upon an incomplete Lower Upper factorization solver, where any non-singular matrix can factored into the product of a lower and upper triangular matrix. To illustrate this, consider the general system of equations being solved as:

$$Ax = b \tag{4.43}$$

The equations are solved for n iteration to become;

$$x = x_n + x' \tag{4.44}$$

where x_n is the last approximation to x after n iteration, and x' is the correction required to get the correct solution. Substituting equation (4.44) into equation (4.43) yields to:

$$R = b - Ax_n \tag{4.45}$$

where R is the residual of the current solution, and can be written in terms of the required correction as;

$$R = Ax' \tag{4.46}$$

If A is factored into a product of lower and upper triangular matrices as;

$$A = LU \tag{4.47}$$

Substituting equation (4.47) into equation (4.46), the equation of the correction becomes,

$$Ux' = L^{-1}R \tag{4.48}$$

$$x' = U^{-1}(L^{-1}R) \tag{4.49}$$

If the factorization of A is approximate, this gives an improved approximation to the solution

$$x^{n+1} = x^n + x' \tag{4.50}$$

The process can be repeated until the residuals are sufficiently lower.

4.4 CFX-TASCflow boundary conditions

The present work presents numerical simulations of axial flow fan with both solid and treated casing which involving more than just one grid. This section will present the different approaches in CFX-TASCflow used to attach two or more grids together for one or more frame of reference.

4.4.1 General grid interface [GGI]

The general grid interface is implemented in CFX-TASCflow to define attachments and/or periodic conditions between grid regions, where the grid regions on either side of the connection can be arbitrarily different in terms of grid dimensions, point distributions and even the physical shape and size of the regions. A control surface approach and a general intersection algorithm are designed and implemented in such a way as to provide for maximum robustness and accuracy. Details on these

numerical algorithms are given in AEAT (1). In the present work, general grid interface was used to attach two grids in the same rotating frame of reference as well as to define periodic conditions between the grid regions when a single passage is solved.

4.4.2 Stage averaging interface

Steady-state predictions can be obtained for multi-stage machines using circumferential averaging between rotating and stationary components. In this stage interface the parameters are passed from one grid to the next incurring a one-time mixing loss. It accounts only for time-average interaction effects and not the transient interaction effects. An application of stage averaging interface is presented later in steady-state simulation for treated casing.

4.4.3 Frozen rotor interface

A steady-state solution is obtained to a multiple frame of reference problem, with some account of the interaction using frozen rotor interface between the moving and stationary grids. The two frames of reference connect in such a way that they each have a fixed relative position throughout the calculation, but with the appropriate frame transformation occurring across a sliding interface.

4.4.4 Sliding interface

The sliding interface is implemented in CFX-TASCflow to account for the transient interaction of a computational domain consists of two or more distinct regions which are in relative motion to each other. It is an extension to Frozen Rotor interface but with the relative grid positions are updated at each time step of the simulation. This sliding interface condition has the following properties:

1. The interface accounts for the change in the frame of reference.
2. Strict conservation is maintained across the interface, for all fluxes of all equations, after accounting for changes in pitch.
3. The interface treatment is fully implicit, so that the presence of an interface does not adversely affect overall solution convergence.

4. The interface is applicable to incompressible, subsonic, transonic and supersonic flow conditions.

5. The interface accounts internally for pitch change by scaling up or down, as required, the local flows as they cross the interface.

6. Any number of frame change interfaces are possible within a computational domain.

A fully detailed description of the implementation procedure of this interface within the code is given in AEAT (2). In the present study, the sliding interface was used to investigate the interaction between the blades of the fan and the vanes inside the recess casing and will be presented later in the unsteady simulations.

4.5 Summary

CFX-TASCflow is a 3-D Navier-Stokes equations solver. It was initially developed for incompressible and subsonic flows, then extended to supersonic flows. The code is a fully implicit, co-located, FVM with a flux element based discretization of geometry. This combines the well-known geometry flexibility of FEM and with the desirable conservation properties of FDM. The term flux element is used to distinguish the approach from the classic FVM.

The governing equations for the conservation of mass, energy and the Cartesian components of momentum are used in strong conservation form. The principle independent variables are pressure, temperature and the Cartesian components of momentum, with the other solution variables, such as density, being evaluated as function of these. The Reynolds stresses and thermal diffusion are evaluated using a turbulence model with wall-functions. Several new turbulence models are incorporated into the code.

The approach taken to model advection is to use a physical corrected skew Upwind scheme. This is broken in two components; the skew scheme itself, of which there are four options, and the PAC term. The skew scheme tends to influence the accuracy in the transverse direction to the flow, such as false diffusion levels, whereas the PAC term tends to influence accuracy in the streamwise direction, such as the conservation of total pressure.

LPS upwind scheme plus the PAC term is formally second-order-accurate and has very good accuracy per grid node characteristics, though it can produce small wiggles

in the presence of very large gradient. A similar but more robust is MLPS upwind scheme. The MWS upwind scheme is designed to minimize the occurrence of wiggles and with the PAC term, maintains excellent streamwise accuracy, but it has higher levels of false diffusion and is formally only first-order-accurate in the transverse direction. The most robust and least accurate is UDS scheme. It is usually run without PAC terms as it is a method of last resort, when the maximum robustness is required to converge a difficult problem.

Finally, the approach employed by the code to solve the set of linear and coupled algebraic equations is an AMG methods based on the ACM strategy. AMG methods create coarse grid equations from the fine grid equations without any use or knowledge of the actual geometry or grid structure. The ACM strategy is fully coupled, continuity and momentum equations are solved simultaneously, and forms its blocks based on an evaluation of the relative strengths of the coefficients connecting a node to its neighbours.

5

Numerical Modelling Approach

This chapter describes the various approaches taken to model the axial-flow fan similar to the experimental rig in which the flow measurements were performed. Throughout this work, the predicted results of the numerical simulations were examined and compared with the available experimental data using pressure rise coefficient, efficiency, work-input characteristics, and radial pressure, velocity and flow angle distributions. The various calculations and procedure used to investigate these are outlined in this chapter.

The number of grid points has a huge effect on the numerical simulation, where a coarse grid may not correctly predict the flow field, on the other hand using a finer grid is time consuming and needs large computational resources to carry out the simulations. Consequently, a sufficient grid number has to be used to produce good results with the available computational resources. A grid independence study was carried out at design flow condition to ensure that the predicted results are independent of the grid size and will be presented in this chapter.

The standard k-ϵ two-equation turbulence model has a well established regime of prediction capability and performs particularly well in a wide range of flows with industrial engineering applications. A study case to see the effect of using another turbulence model RNG k-ϵ model on the predicted result was carried out and will be presented with comparison to the experimental work in this chapter. In addition

this chapter presents another case study in which the four methods available within CFX-TASCflow, to descretize the convective term in the momentum equation, are investigated to check their effect on the predicted results. The simulations of both cases were carried out at design flow condition.

5.1 Axial-fan modeling

The experimental facility is a single stage, isolated rotor, low-speed axial flow fan with design speed of 1 500 rpm, outer tip diameter of 508 mm, hub to tip ratio of 0.5 and near unity blade loading at the hub. The rig has a short inlet section without Inlet Guide Vanes IGV. The rotor was equipped with 27 blades of C4 cross-sections, circular arc profiles, with a fixed tip clearance of 1.2% of the blade height and with maximum thickness to chord ratio of 12%. The geometrical details of the rotor blade at 8 cross-sections are given in Table 5.1.

Table 5.1: Rotor blade geometry

Profile	r(mm)	$\beta_1{}^*$	$\beta_2{}^*$	ξ^*	θ^*	S/C
Hub	127.0	34.9	-18.8	8.0	53.5	0.611
1st	129.540	35.4	-16.9	9.2	52.4	0.623
2nd	158.242	40.9	2.2	21.6	38.6	0.761
3rd	185.420	45.7	16.1	30.9	29.6	0.898
4th	190.500	46.1	17.5	31.8	28.6	0.917
5th	216.154	49.9	26.6	38.3	23.3	1.040
6th	246.380	53.5	36.6	45.0	17.0	1.180
Shroud	254.0	54.2	38.8	46.4	15.5	1.216

Maximum thickness/chord = 12%
Tip clearance/blade height = 1.2%

* In degree

where for each profile r is the radius, β_1 and β_2 are the inlet and outlet blade angles respectively, ξ is stagger angle, θ is camber angle, and S/C is space by chord ratio. The CFX-TurboGrid package was used to generate the grid for the blade domain employing a single-block grid template shown in Figure 4.3, which is designed to produce a high quality mesh for low-blade stagger using one H-type grid block to mesh the blade and the passage with the grid elements inside the

blade being blocked-off in order to form the blade surface. The files required by the CFX-TurboGrid containing data points in Cylindrical coordinates (r, θ, z) for the hub, shroud, and the 6 other blade profile curves in between, are computed from the geometrical details of the rotor blade given in Table 5.1. Details of these calculations are presented in detail in Appendix A.

The resulting files from the calculations contain data points in Cylindrical coordinate (r, θ, z) for 8 blade profiles are imported into CFX-TurboGrid in addition to the hub and shroud curves. Both hub and shroud curves are extended upstream of the blade leading edge and downstream of the blade trailing edge. The calculation of inlet and outlet conditions are taken at stations similar to those where the measurements were taken in the experimental rig. As shown in Figure 5.1, the inlet station is located at 48 mm upstream of the blade leading edge and the outlet station is located at 56 mm downstream of the blade trailing edge.

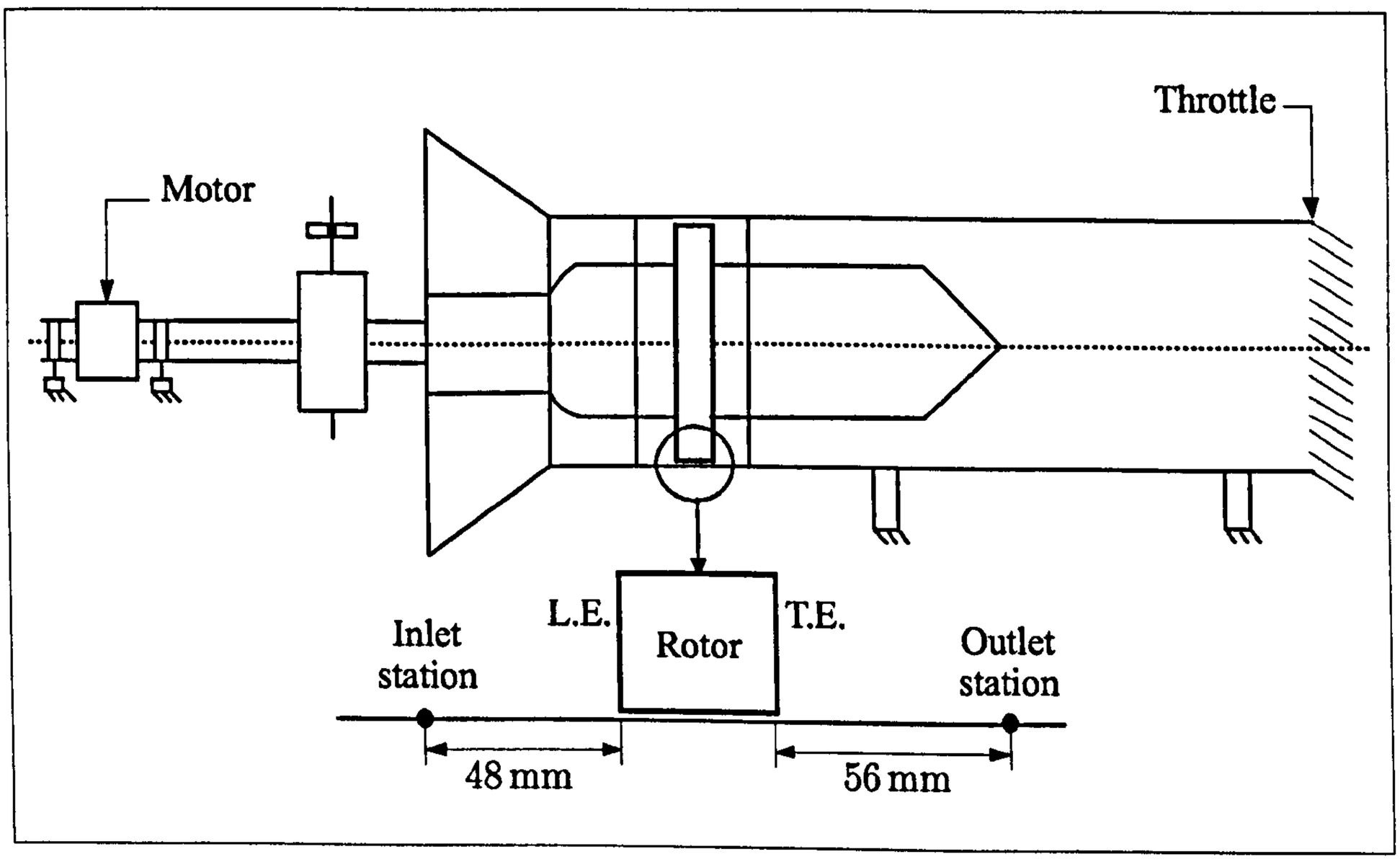

Figure 5.1: Inlet and outlet stations

The computational domain, shown in Figure 5.2, has a fixed tip clearance of 1.2% of the blade height, and consists of $100 \times 40 \times 50$ mesh points, where 100 points are used in the axial direction, 40 points in the blade-to-blade direction, and 50 points in the radial direction. The grid was checked for minimum and maximum skew angle, aspect ratio and negative volume, and the necessary adjustments were made

to satisfy the conditions required by the CFX-TASCflow solver. The resulting mesh at different views of the computational domain is presented in Figure 5.3. This computational domain, shown in Figure 5.2, was used to perform initial steady-state simulations of the fan with solid casing for several study cases to investigate the effect of using different mesh density, different turbulence models and different discretization methods on the flow prediction. The result of each study was in each case presented together with the experimental results from Kang (51).

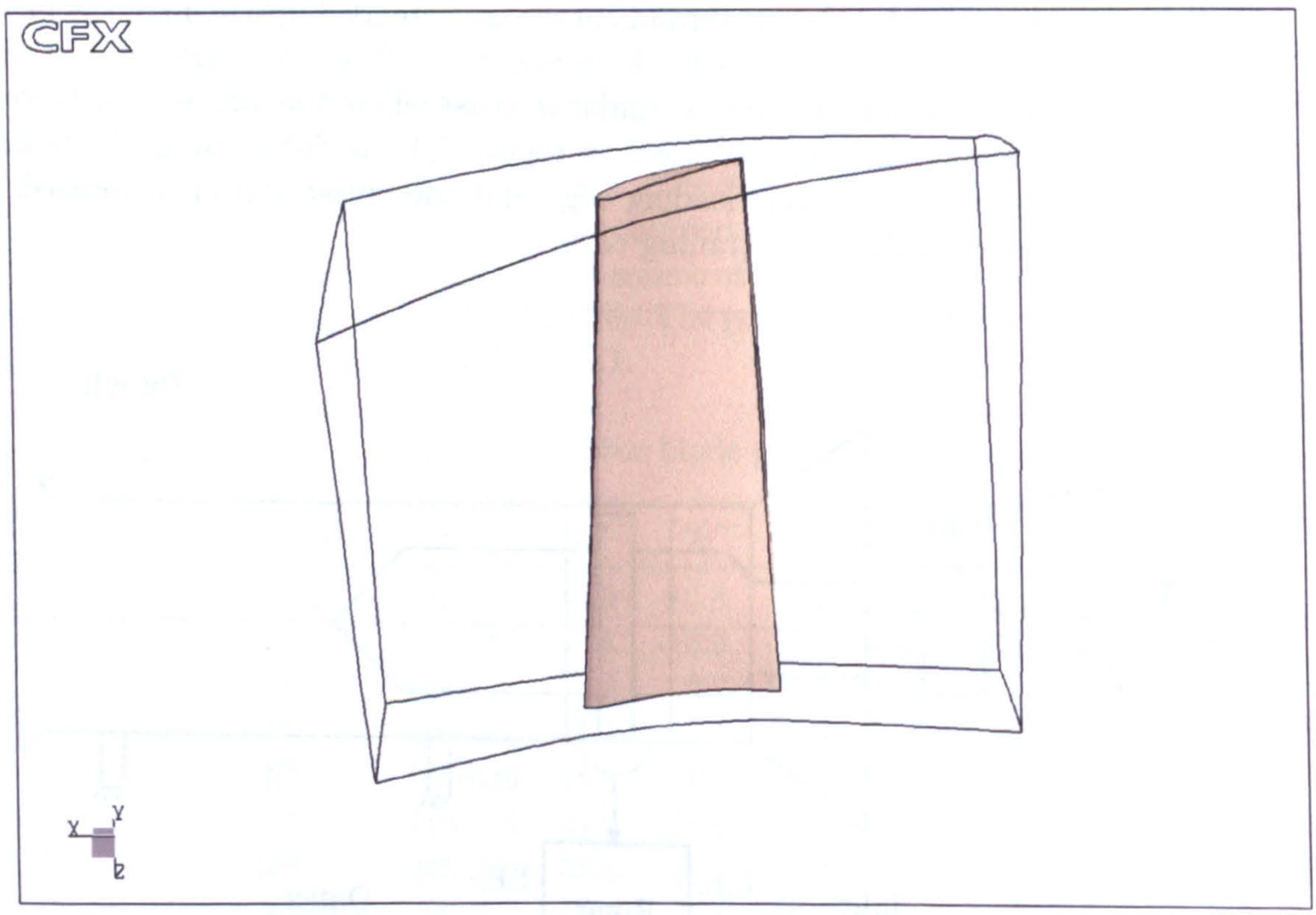

Figure 5.2: Study cases computational domain

5.2 Results analysis approach

The performance of the axial flow fan is usually represented through pressure flow characteristics and efficiency. Total and static pressure rise across the fan, mass flow, rotational speed and work input must be computed to carry out a performance investigation. This section will discuss the general techniques used in the present work to calculate the parameters mentioned above.

5.2.1 Fan overall performance

The overall performance of the fan for all types of simulations throughout the present work was examined and compared to the experimental data as both the total to static pressure rise coefficient ψ and total to total efficiency η are presented as a function of the flow coefficient ϕ, which is defined as the ratio between the axial flow velocity V_a to the blade velocity at the mean blade height U_m;

$$\phi = \frac{V_a}{U_m} \tag{5.1}$$

where

$$U_m = \Omega r_m \tag{5.2}$$

where Ω is the rotational speed and r_m is the radius at mean blade height.

5.2.1.1 Pressure Rise Coefficient

Total to static characteristics are widely used, since they are generally true when the total pressure at the inlet and static pressure at the outlet are uniform over the fan annulus at a given operating point. The total to static pressure rise coefficient ψ is defined by:

$$\psi = \frac{P_{S2} - P_{T1}}{\frac{1}{2}\rho U_m^2} \tag{5.3}$$

where P_{S2} is static pressure downstream of the rotor, obtained through area-averaging of all the static pressure values at the outlet station 56 mm downstream the trailing edge of the blade, and P_{T1} is the total pressure upstream of the rotor, obtained by area-averaging of all the total pressure values at the inlet station 48 mm upstream the leading edge of the blade, see Figure 5.1.

5.2.1.2 Fan efficiency

Total to total efficiency η is defined as:

$$\eta = \frac{60\,\dot{m}\,(P_{T2} - P_{T1})}{2\pi\,N\,\rho\,T_q} \tag{5.4}$$

where $\dot{m}$ is mass flow rate, N is rotor speed, T_q is the computed torque, and P_{T2} is the total pressure downstream of the rotor, obtained by area-averaging of all the total pressure values at the outlet station 56 mm downstream the trailing edge of the blade. CFX-TASCflow computes the torque T_q by integrating over the blades span the product of the tangential component of the blade force due to the pressure and shear stress contributions and the local value of the radius.

5.2.2 Fan work-input

The work-input characteristics of the fan in terms of the work coefficient $\Delta H/U_m^2$ is calculated and presented as a function of flow coefficient ϕ. The work-input ΔH is calculated from the computed torque T_q, mass flow rate $\dot{m}$, and rotor speed N by:

$$\Delta H = \frac{2\pi\,N\,T_q}{60\,\dot{m}} \tag{5.5}$$

5.2.3 Radial pressure profile

In many cases the flow is rotational in the axial flow fans, which causes non-uniform static pressure changes. Consequently, it is very useful to determine the pressure variation of the static and total pressure distribution in the span-wise direction. Throughout the present work, this variation was presented at 25 locations along the span from hub to shroud for both inlet and outlet stations, where the static pressure coefficient C_{P_S} is calculated by:

$$C_{P_S} = \frac{P_S - P_R}{\frac{1}{2}\,\rho\,U_m^2} \tag{5.6}$$

and the total pressure coefficient C_{P_T} is calculated by:

$$C_{P_T} = \frac{P_T - P_R}{\frac{1}{2}\rho U_m^2} \tag{5.7}$$

where static pressure P_S and total pressure P_T are the area-average value of all the pressure values at that span location, and the reference pressure P_R is the area-averaged value of the total pressure at the inlet station.

5.2.4 Absolute velocity profile

The radial profiles of the absolute axial V_a, radial V_r and tangential V_t velocities at the inlet and outlet stations are calculated and compared to the experimental data. They were area-averaged at 25 locations along the span from hub to shroud.

5.2.5 Absolute flow angle

Similarly, the area-averaged absolute flow angles at the inlet α_1 and at the outlet α_2 are calculated and compared to the experimental data at 25 locations along the span from hub to shroud. The flow angle is calculated by:

$$\cos\alpha = \frac{V_a}{(V_a^2 + V_t^2)^{\frac{1}{2}}} \tag{5.8}$$

5.3 Study cases results

Three different study cases were carried out to investigate the effects of different grid size, turbulence model, and discretization scheme on the fan performance. The results of these study cases are discussed in brief in the next sections.

5.3.1 Grid independence study

A grid independence study was carried out at design flow condition to ensure that the predicted results are independent of grid size. This was done by performing simulations with three different grid sizes, 100 000 grid points, 200 000 grid points, and 400 000 grid points. All grids were generated by CFX-TurboGrid and were checked for minimum and maximum skew angle, aspect ratio and negative volume, and the necessary adjustments were made to satisfy the conditions required by the CFX-TASCflow solver. Details of the number of grid points in each direction for the three simulations are presented in Table 5.2.

Table 5.2: Grid details in grid Independence study

Case No.	Inlet to outlet	Blade to blade	Hub to shroud	Total
1	80	25	50	100 000
2	100	40	50	200 000
3	125	50	64	400 000

5.3.1.1 Boundary conditions

For all three simulations, one for each grid size, the boundary condition at the inlet of the computational domain was set as the standard day atmospheric pressure, while the design mass flow rate value of 4.0 kg/s corresponding to flow coefficient of $\phi = 0.72$ was set at the outlet boundary condition. The standard k-ϵ turbulence model with wall functions was employed as a turbulence model, and the MLPS discretization scheme was used for the treatment of the convective term together with the PAC scheme. The initial conditions for turbulence intensity and the eddy length scale were set at the inlet as 0.03.

The shroud of the domain was made stationary while the blade, hub and the rest of the domain were rotating at 1 500 rpm. The numerical solution was assumed to be a fully convergent solution when the residual from the non-satisfaction of the discretized continuity and momentum equations falls below 10^{-5}.

5.3.1.2 Results and discussion

The predicted result of total to static pressure rise coefficient ψ, total to total efficiency η, and work-input coefficient $\Delta H/{U_m}^2$ are presented respectively in Figures 5.4, 5.5 and 5.6. The differences between the predicted results are very small, which implies that predicted results are independent of grid size. A similar conclusion can be drawn from the radial profile of the pressure, velocities, and flow angles presented respectively in Figures 5.7-5.10. However, it can be noted from Table 5.3 that increasing the number of grid points does not improve the predicted results with comparison to the experimental data.

Table 5.3: Grid Independence study results

Case No.	Total Grid Points	ψ	η	$\Delta H/{U_m}^2$
1	100 000	0.1497	0.8755	0.5548
2	200 000	0.1407	0.8709	0.5463
3	400 000	0.1297	0.8660	0.5448
Experimental data*		0.1487	0.9337	0.5920

* Taken from Kang (51)

Therefore, choosing the coarser grid will guarantee the accuracy of the predicted results in additional to the economic and time saving advantages. However, a grid size of 200 000 nodes was chosen for all simulations in the present work due to the fact that the inlet section of the domain had to be extended to accommodate the recess casing treatment, which will be discussed in detail in Chapter 6.

5.3.2 Turbulence modelling study case

The effect of using a different turbulence model on the predicted results was investigated by performing two simulations for the fan with different turbulence models, one with the standard k-ϵ model and another with RNG k-ϵ model.

5.3.2.1 Boundary conditions

For both simulations, the computational domain of 200 000 grid points was used with the inlet boundary condition set as the standard day atmospheric pressure, and the

design flow rate of $\phi = 0.72$ was set as the outlet boundary condition. The MLPS discretization scheme was used for the treatment of the convective term together with PAC scheme. The initial conditions for turbulence intensity and the eddy length scale were set at the inlet as 0.03. The shroud of the domain was made stationary while the blade, hub and the rest of the domain were rotating at 1 500 rpm. The numerical solution was assumed to be a fully convergent solution when the residual from the non-satisfaction of the discretized continuity and momentum equations fall below 10^{-5}.

5.3.2.2 Results and discussion

The predicted result of total to static pressure rise coefficient ψ, total to total efficiency η, and work-input coefficient $\Delta H/{U_m}^2$ are presented respectively in Figures 5.4, 5.5 and 5.6, as well as in Table 5.4. The predicted results are very similar for both turbulence models, which also can be concluded from the radial profile of the pressure, velocities, and flow angles presented respectively in Figures 5.11-5.14. This is due to the fact that the RNG k-ϵ model is a modification to the standard one for flows with high rate of deformation, which is low in the axial fan. However, the standard k-ϵ turbulence model was used for all simulations in the present work and the initial conditions for turbulence intensity and the eddy length scale were always set at the inlet as 0.03.

Table 5.4: Turbulence study case results

Case No.	Turbulence model	ψ	η	$\Delta H/{U_m}^2$
1	Standard k-ϵ	0.1407	0.8709	0.5463
2	RNG k-ϵ	0.1719	0.8878	0.5571
Experimental data*		0.1487	0.9337	0.5920

* Taken from Kang (51)

5.3.3 Discretization study case

These simulations were carried out to investigate the various discretization schemes available within the code for the treatment of the convective term in the momentum equation. These are UDS, MWS, LPS and MLPS.

5.3.3.1 Boundary conditions

For all these simulations, the computational domain consisting of 200 000 grid points was used. The standard k-ϵ turbulence model with wall functions was employed as a turbulence model. The initial conditions for turbulence intensity and the eddy length scale were set at the inlet as 0.03.

The inlet boundary condition was set as the standard day atmospheric pressure, and the design flow rate $\phi = 0.72$ was set as the outlet boundary condition. The shroud of the domain was made stationary while the blade, hub and the rest of the domain were rotating at 1 500 rpm. The numerical solution assumed to be fully converged when the residuals fall below 10^{-5}.

Table 5.5: Discretization schemes study case results

Case No.	Discretization scheme	ψ	η	$\Delta H/{U_m}^2$
1	UDS	0.1493	0.8599	0.5611
2	MWS	0.1426	0.8638	0.5580
3	LPS	0.1433	0.8635	0.5552
4	MLPS	0.1407	0.8709	0.5463
	Experimental data*	0.1487	0.9337	0.5920

* Taken from Kang (51)

5.3.3.2 Results and discussion

The predicted result of total to static pressure rise coefficient ψ, total to total efficiency η, and work-input coefficient $\Delta H/{U_m}^2$ are presented respectively in Figures 5.4, 5.5 and 5.6, as well as in Table 5.5. The predicted results are very similar for all discretization schemes, which also can be concluded from the radial profile of the pressure, velocities, and flow angles presented respectively in Figures 5.15-5.18. However, the MLPS scheme was used for all simulations in the present work.

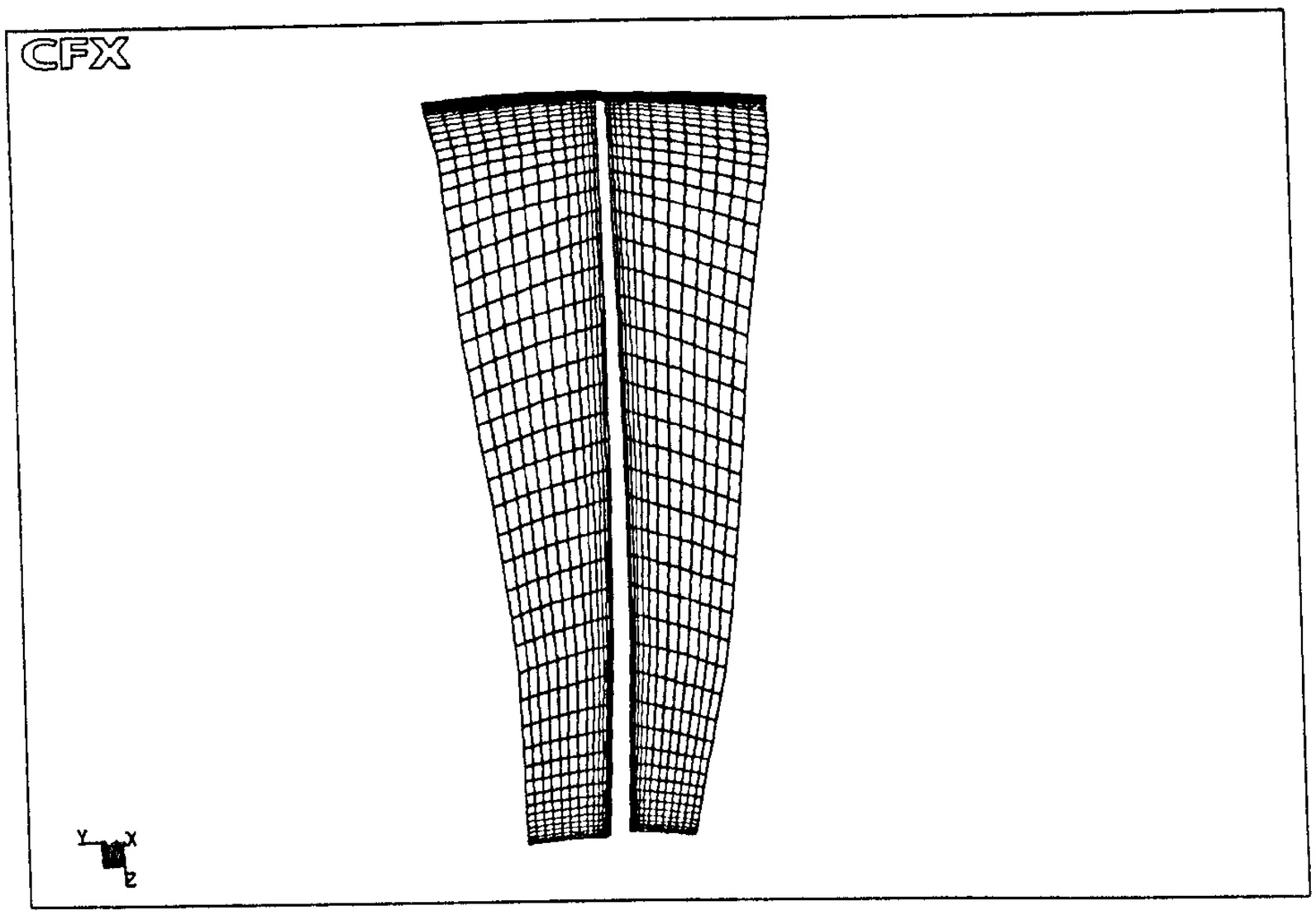

(a) Pitchwise view near the blade leading edge

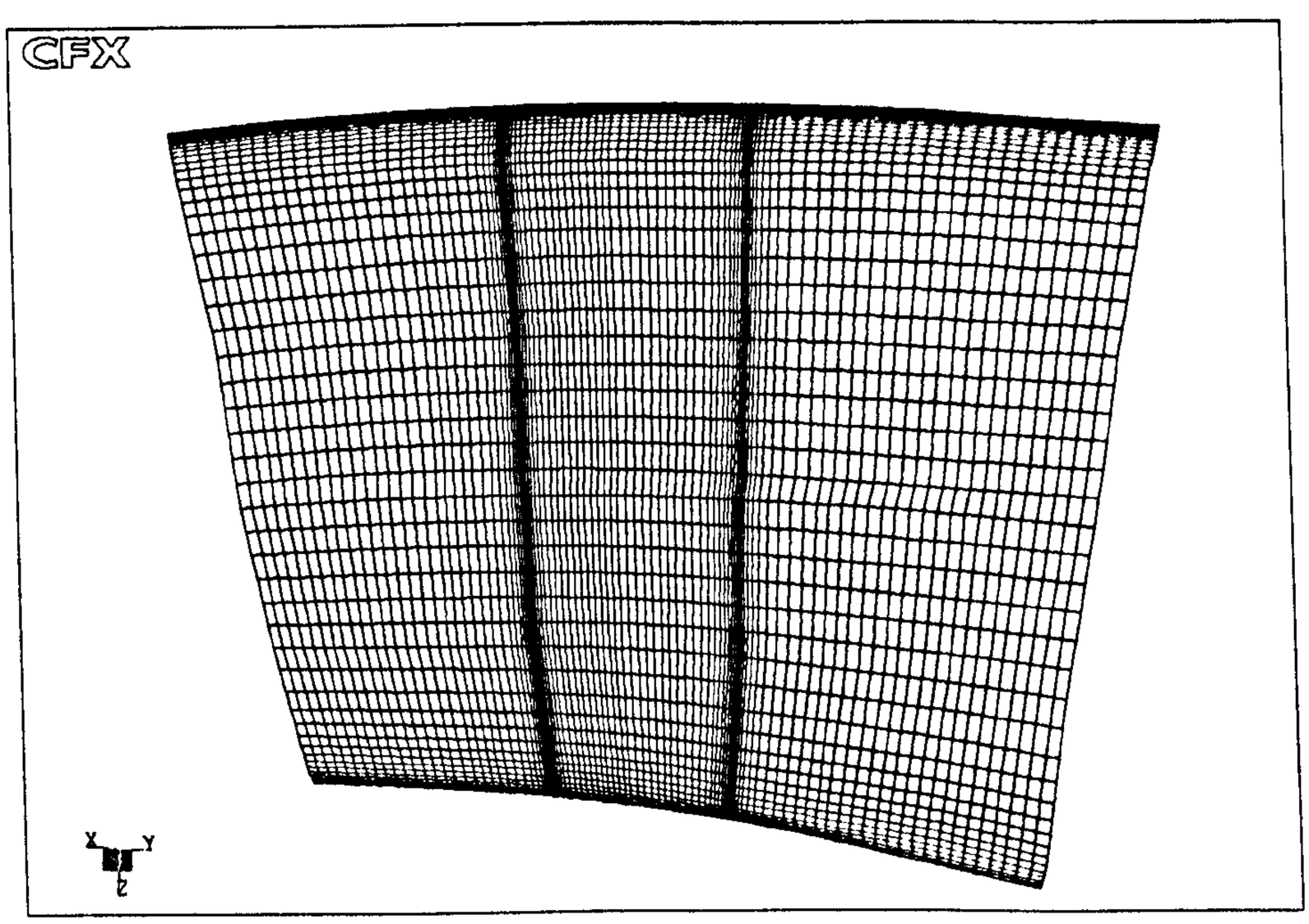

(b) Meridional view

Figure 5.3: Views of the computational domain mesh

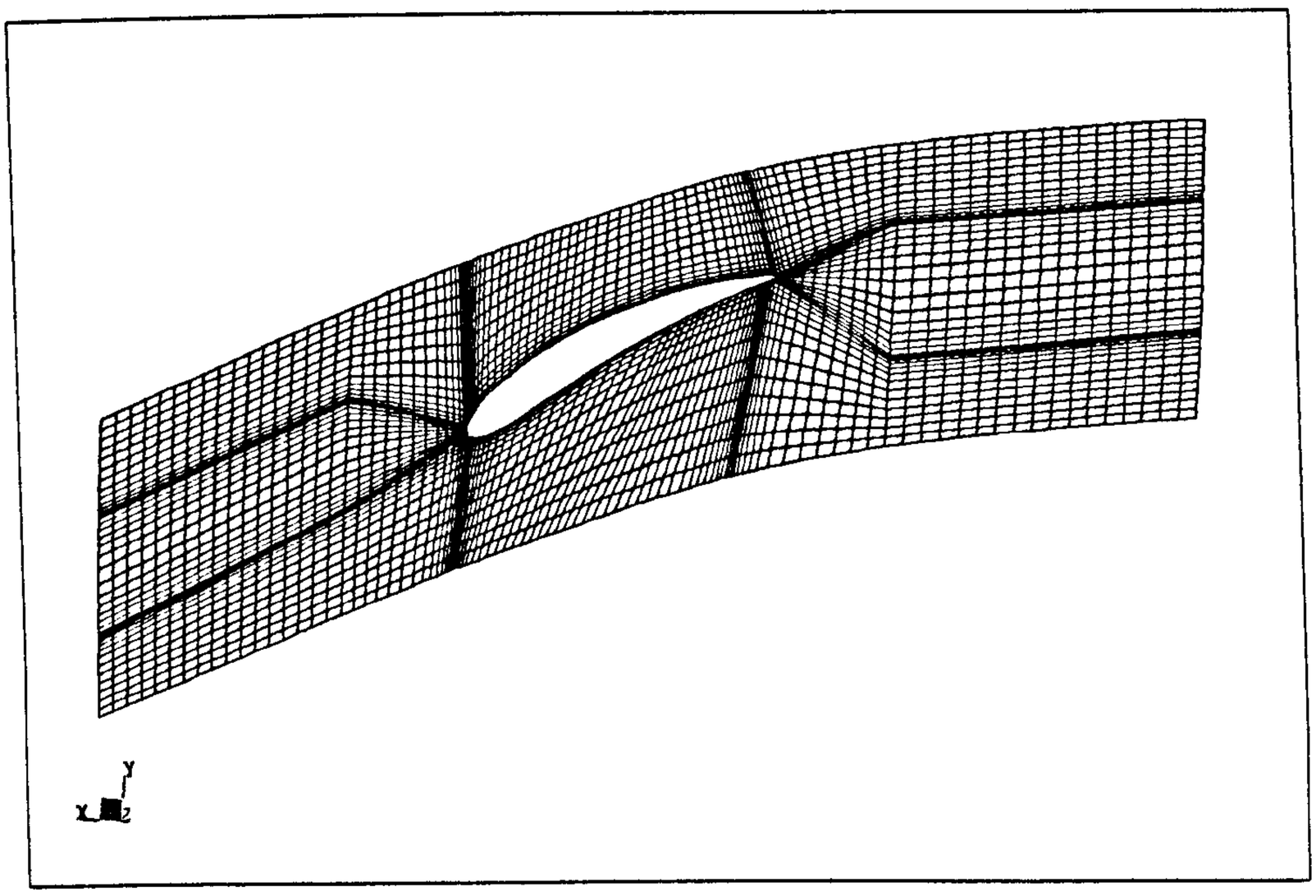

(c) Blade-to-blade view at mid-span

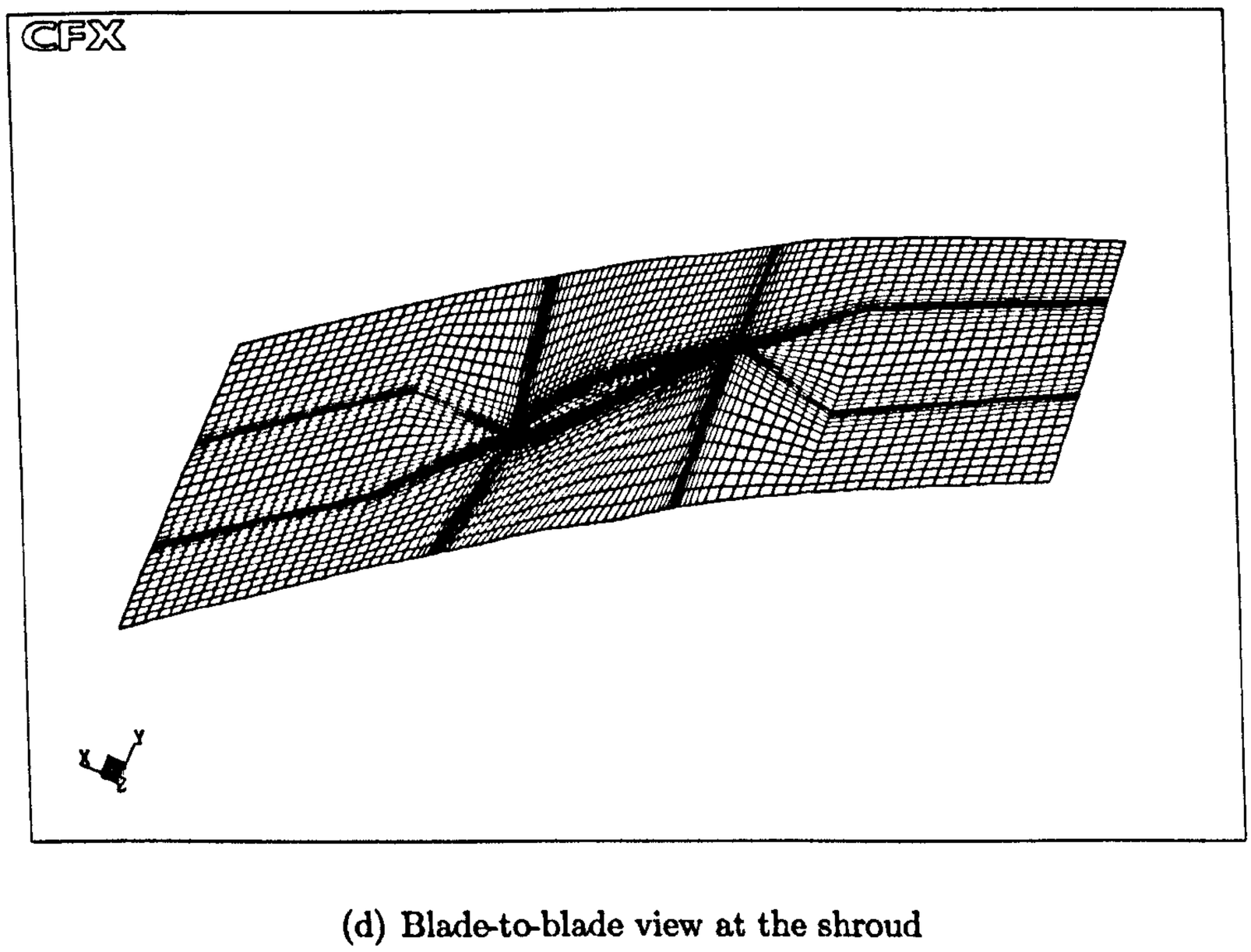

(d) Blade-to-blade view at the shroud

Figure 5.3: Views of the computational domain mesh (cont.)

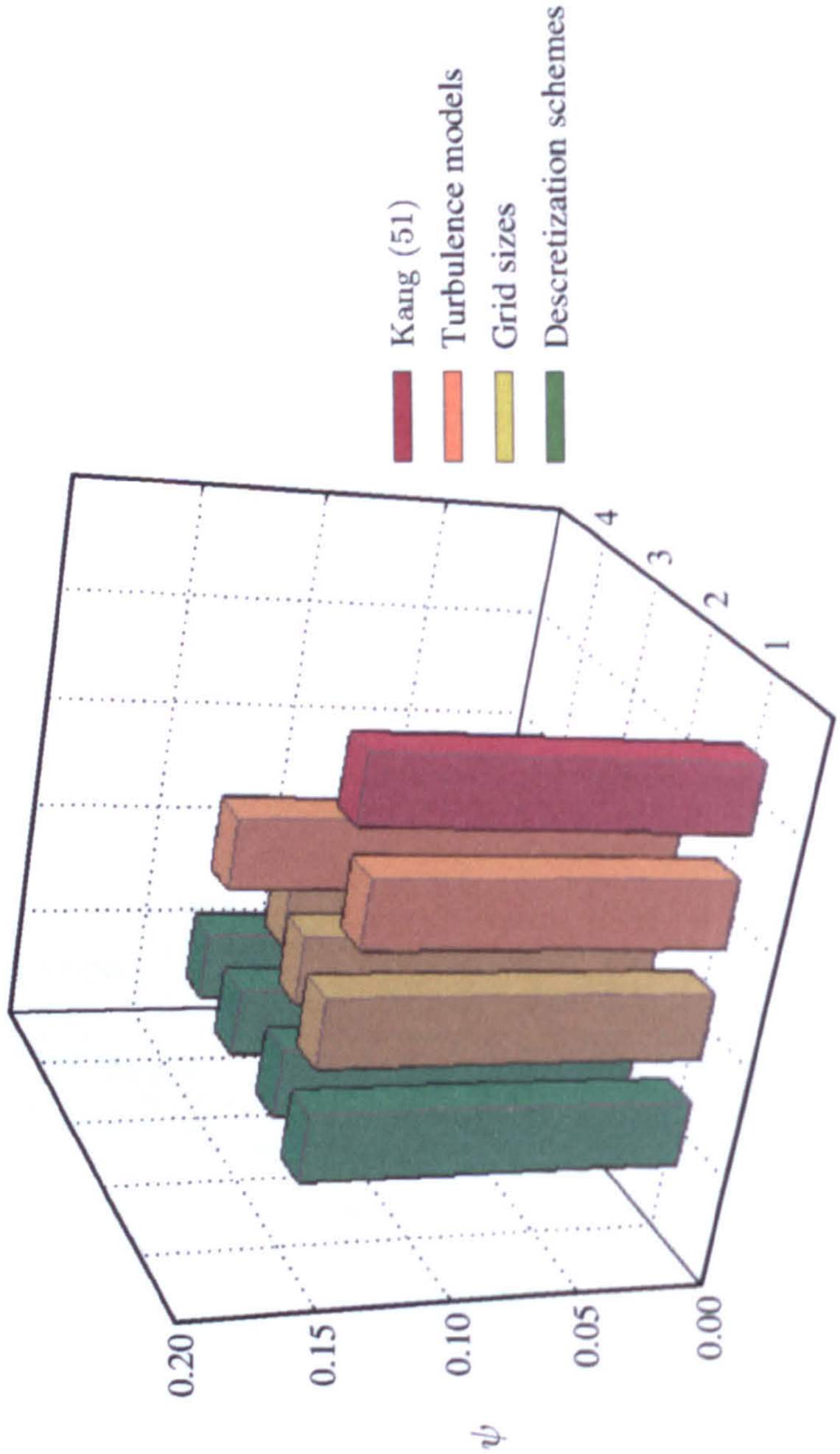

Figure 5.4: Pressure rise coefficients for the study cases

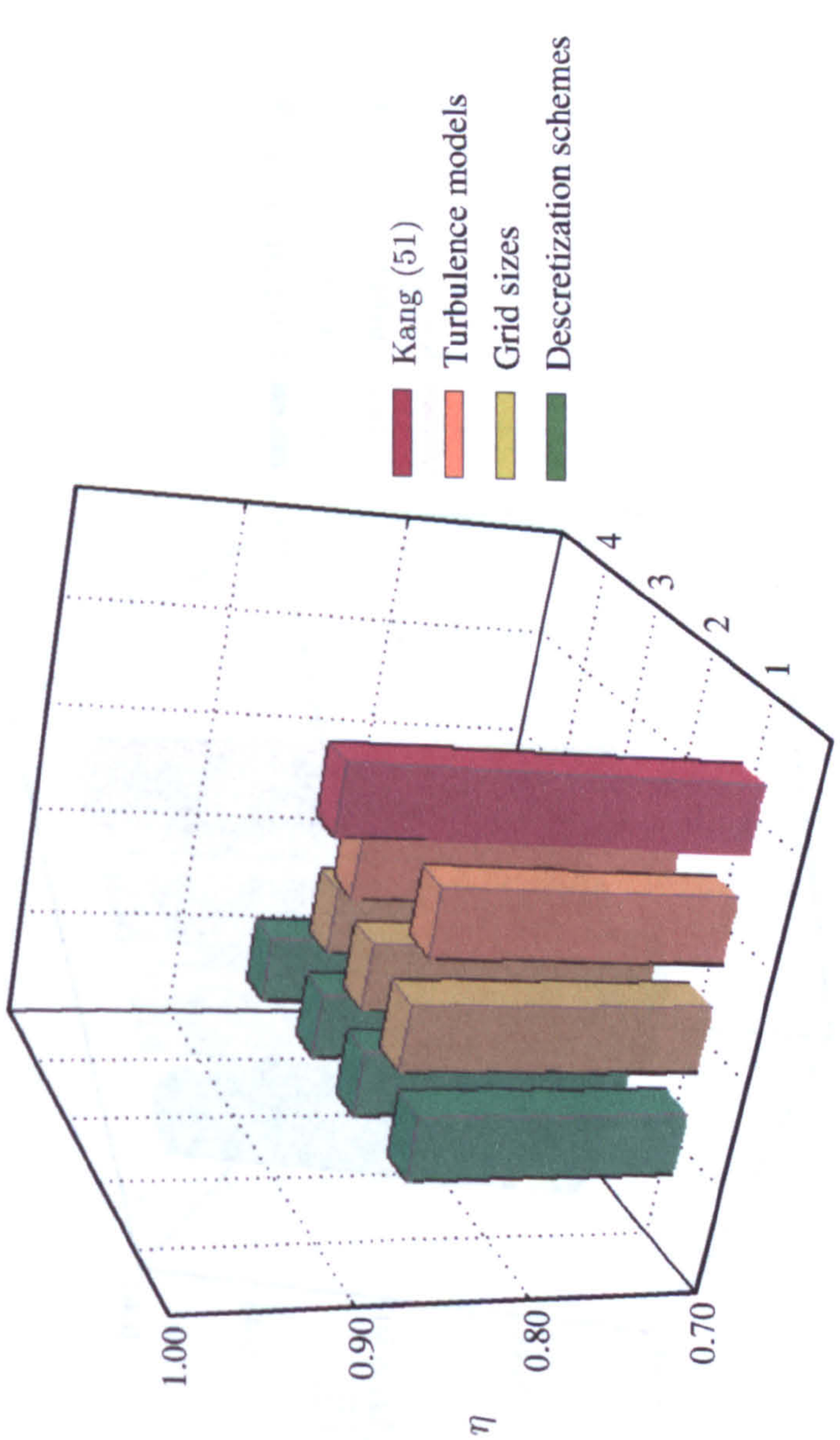

Figure 5.5: Total to total efficiency for the study cases

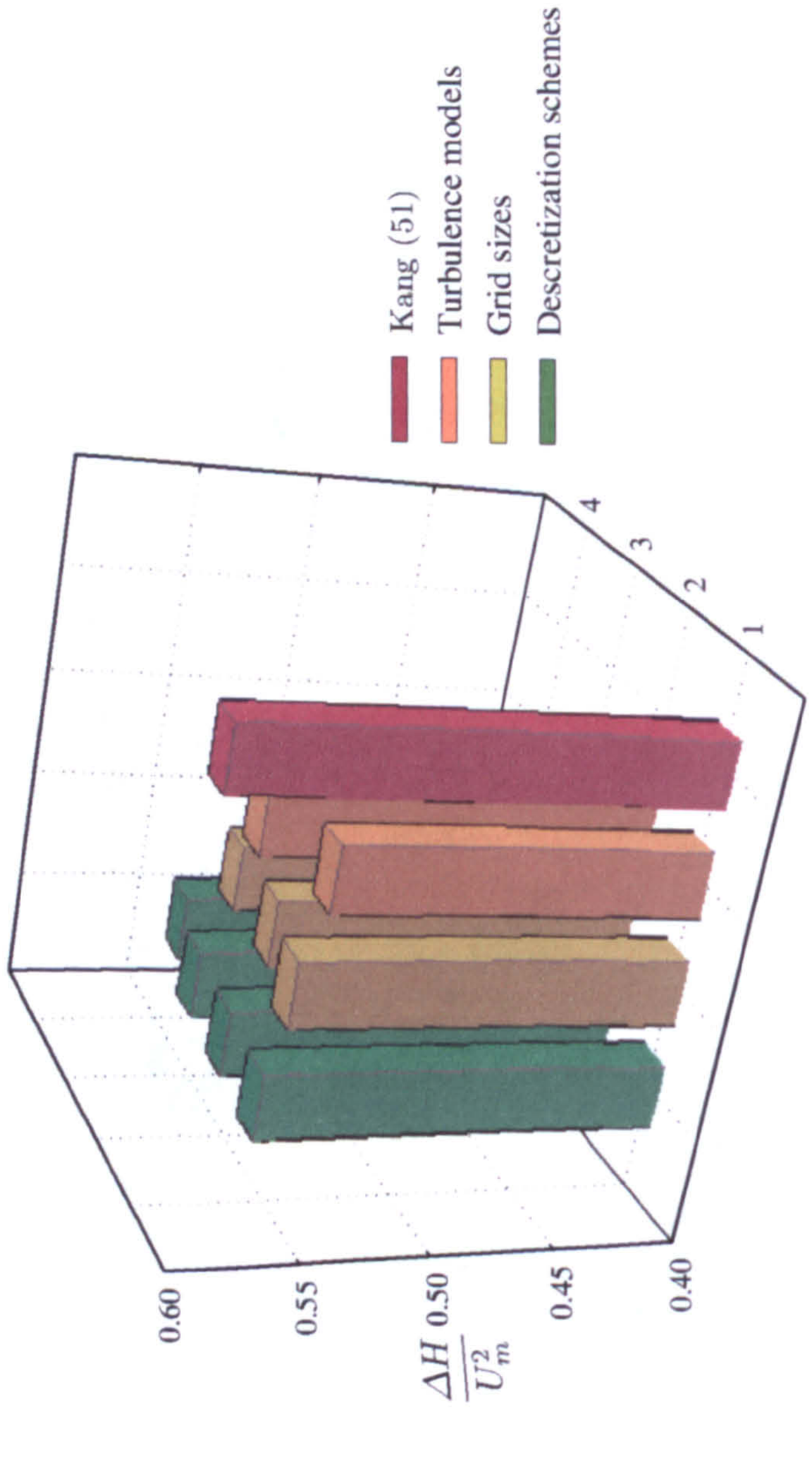

Figure 5.6: Work-input characteristics for the study cases

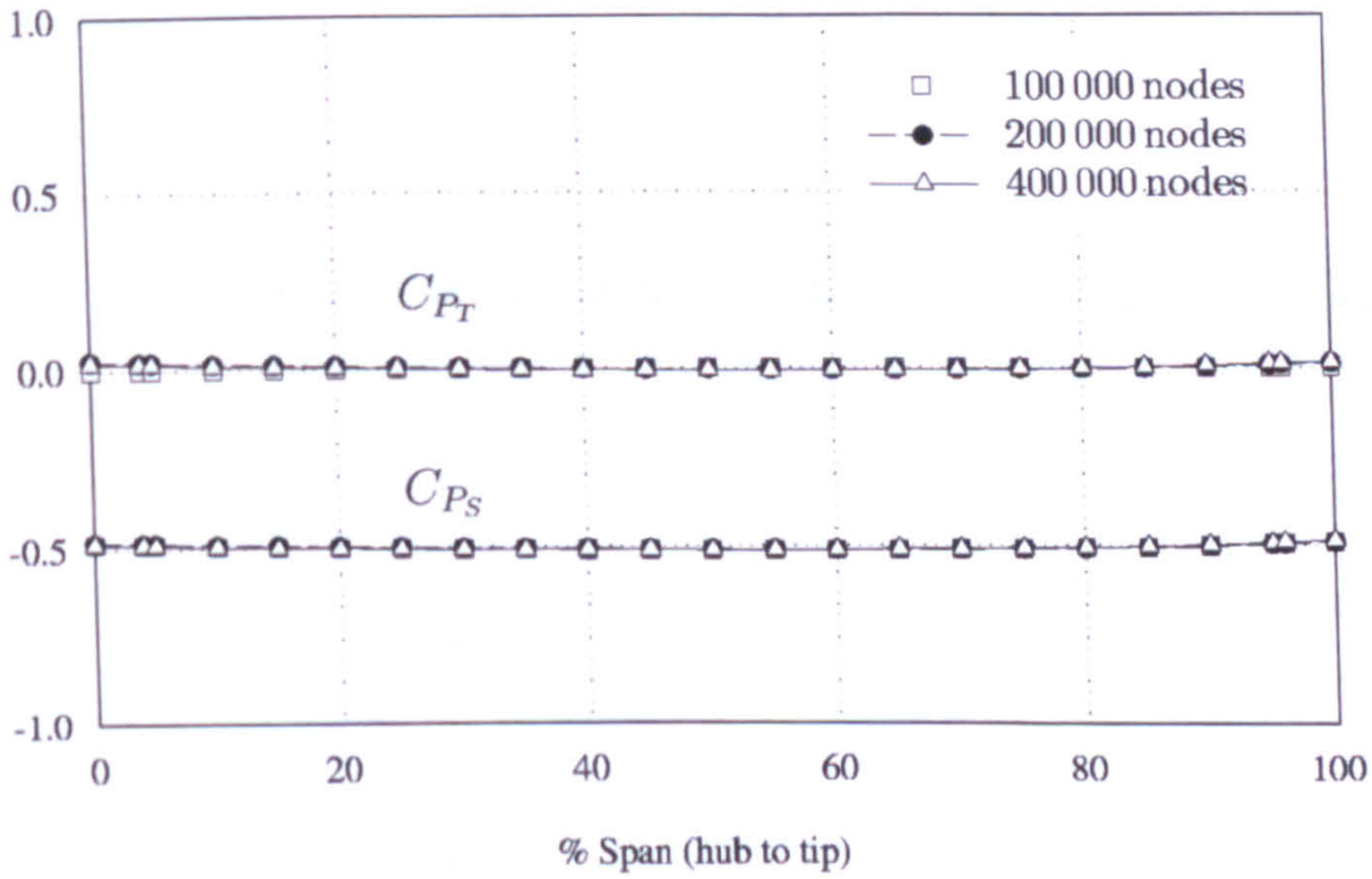

(a) Inlet station

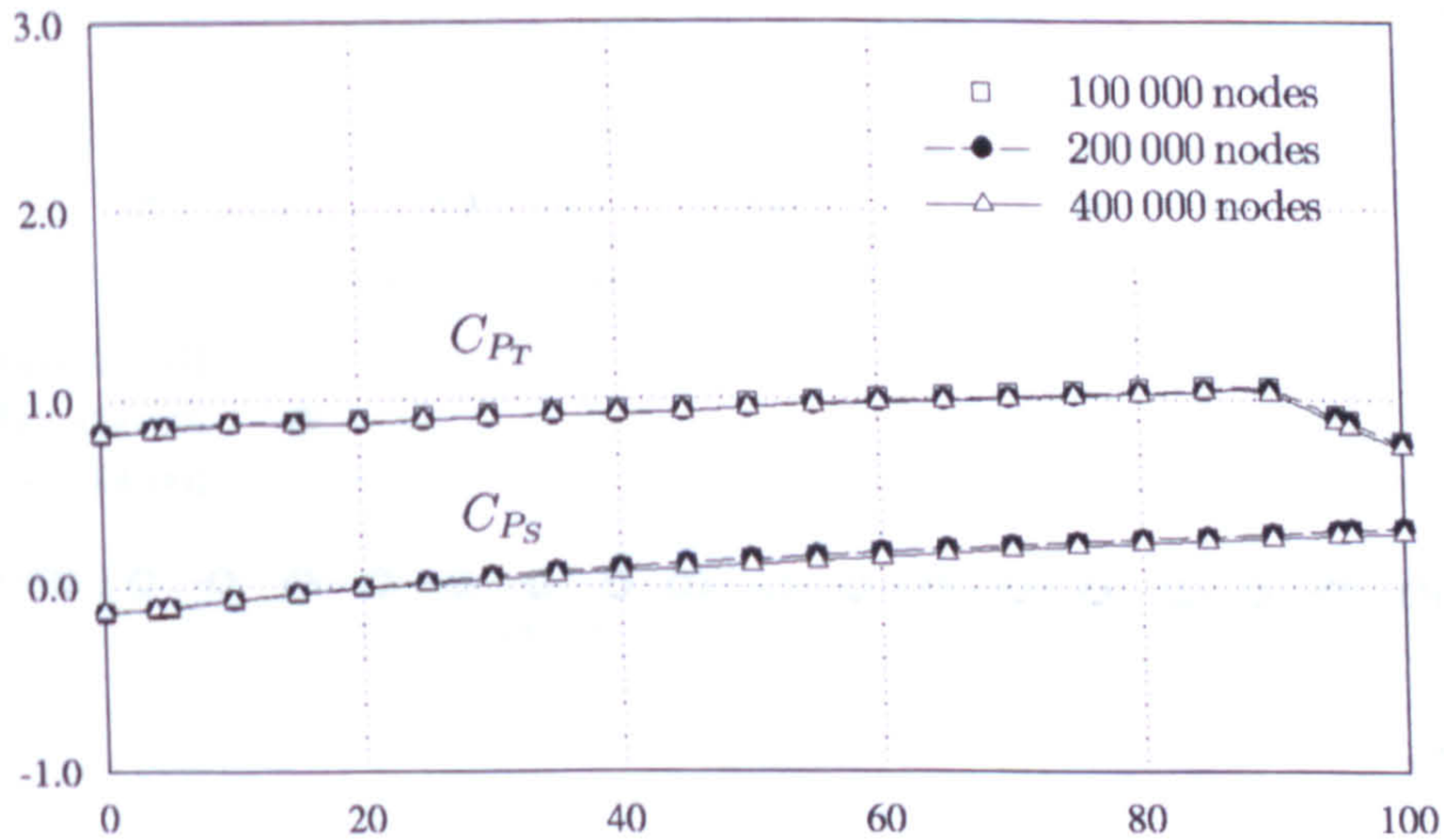

(b) Outlet station

Figure 5.7: Radial profile of the pressure for different grid sizes

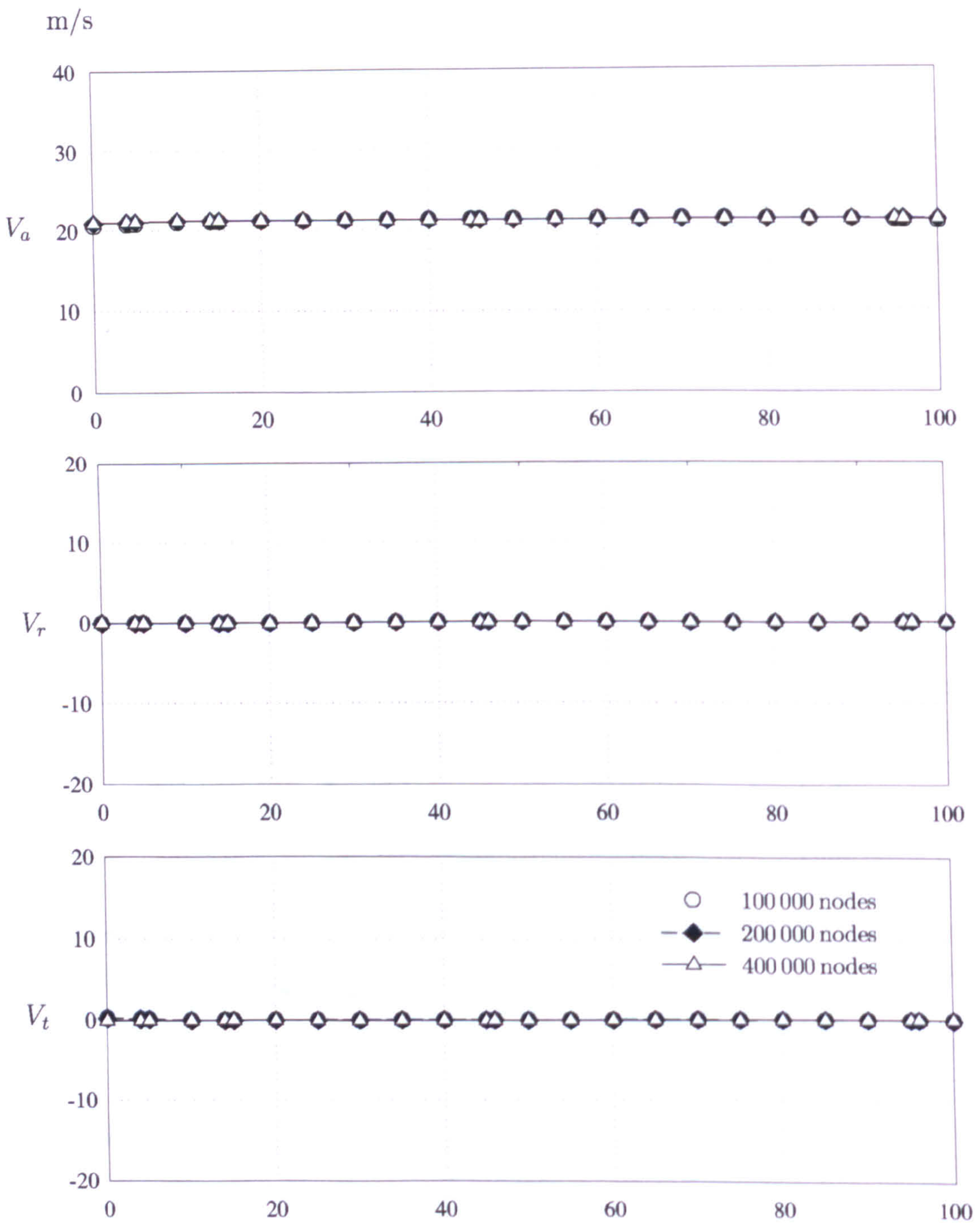

Figure 5.8: Radial profile of inlet velocity for different grid sizes

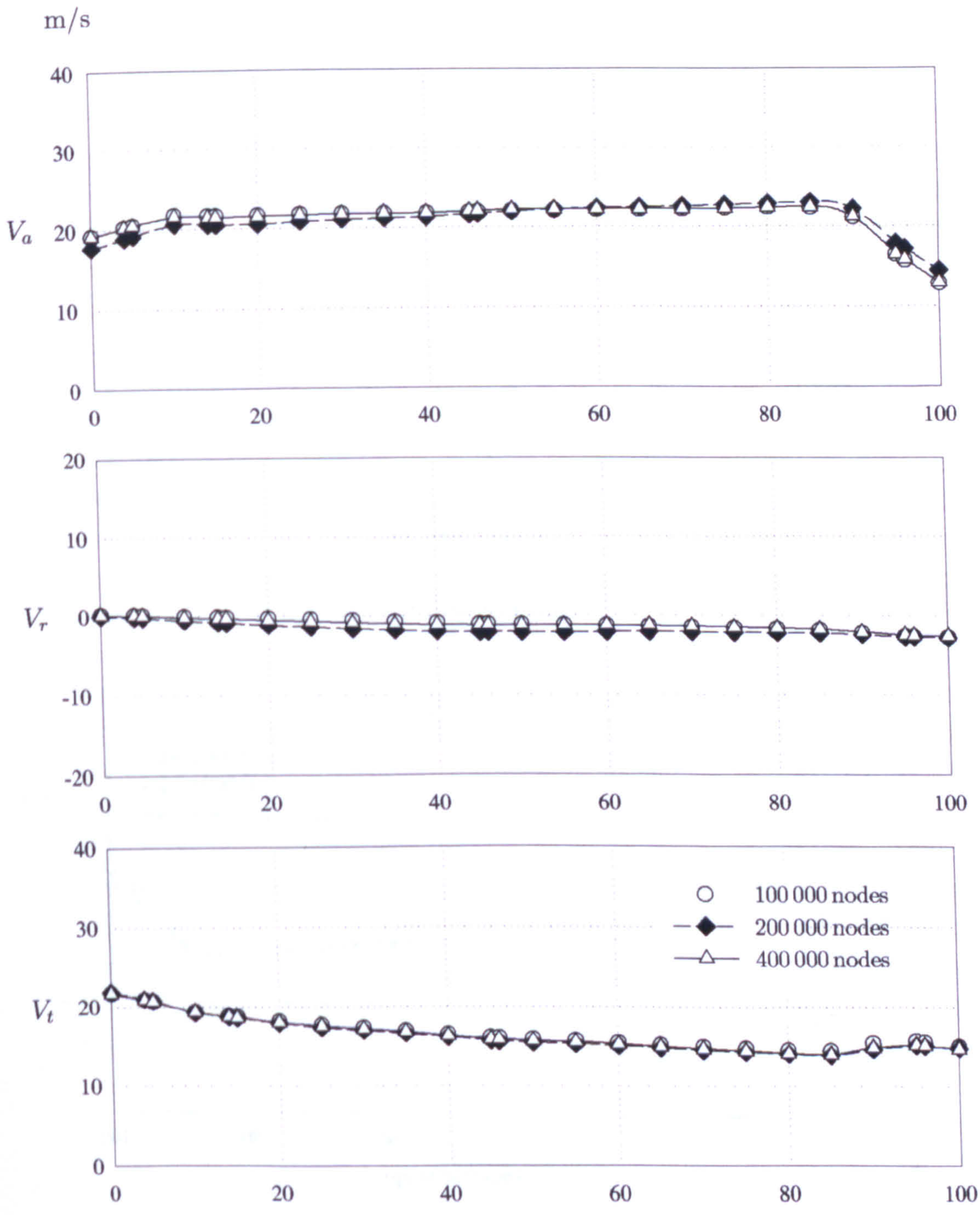

Figure 5.9: Radial profile of outlet velocity for different grid sizes

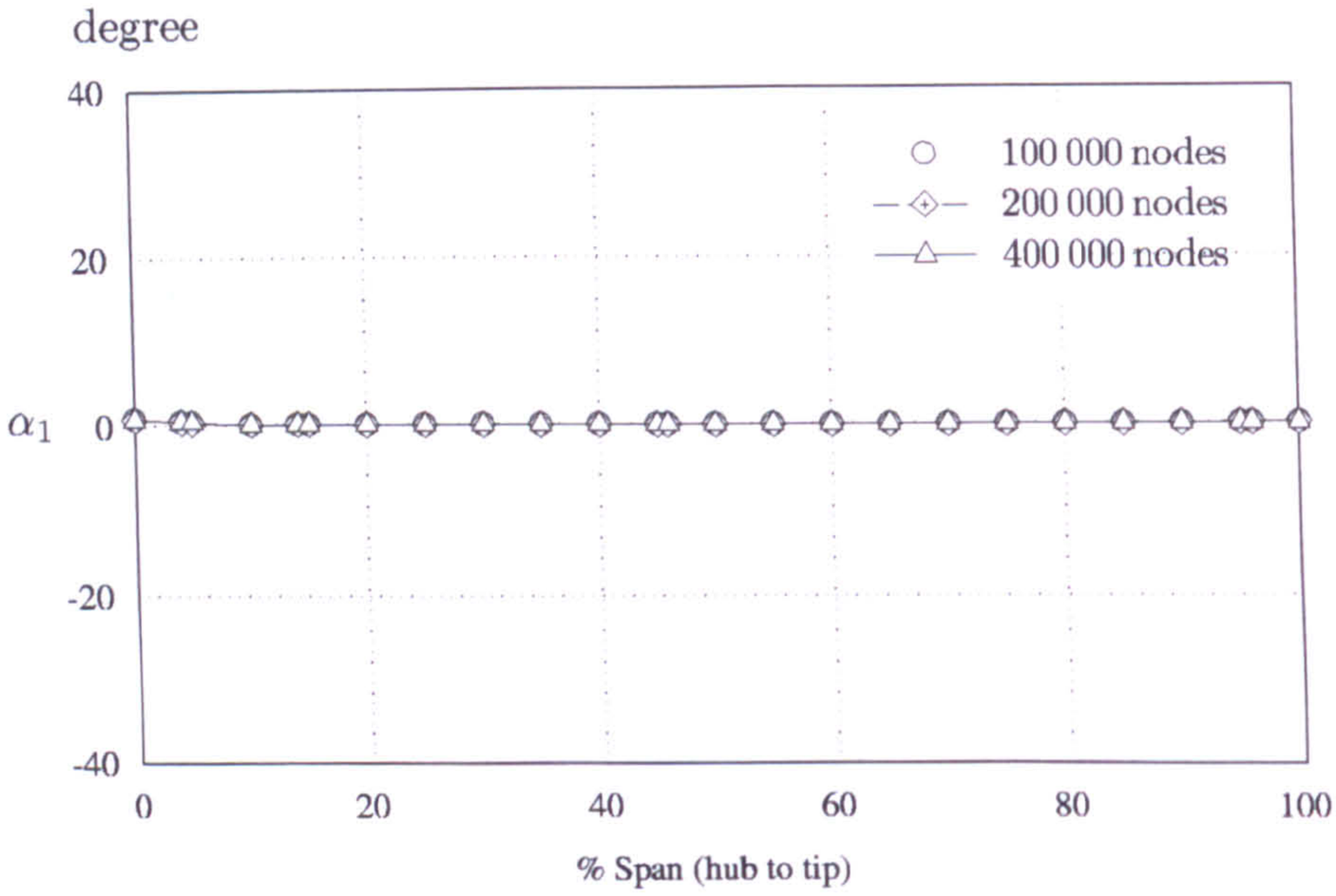

(a) Inlet station

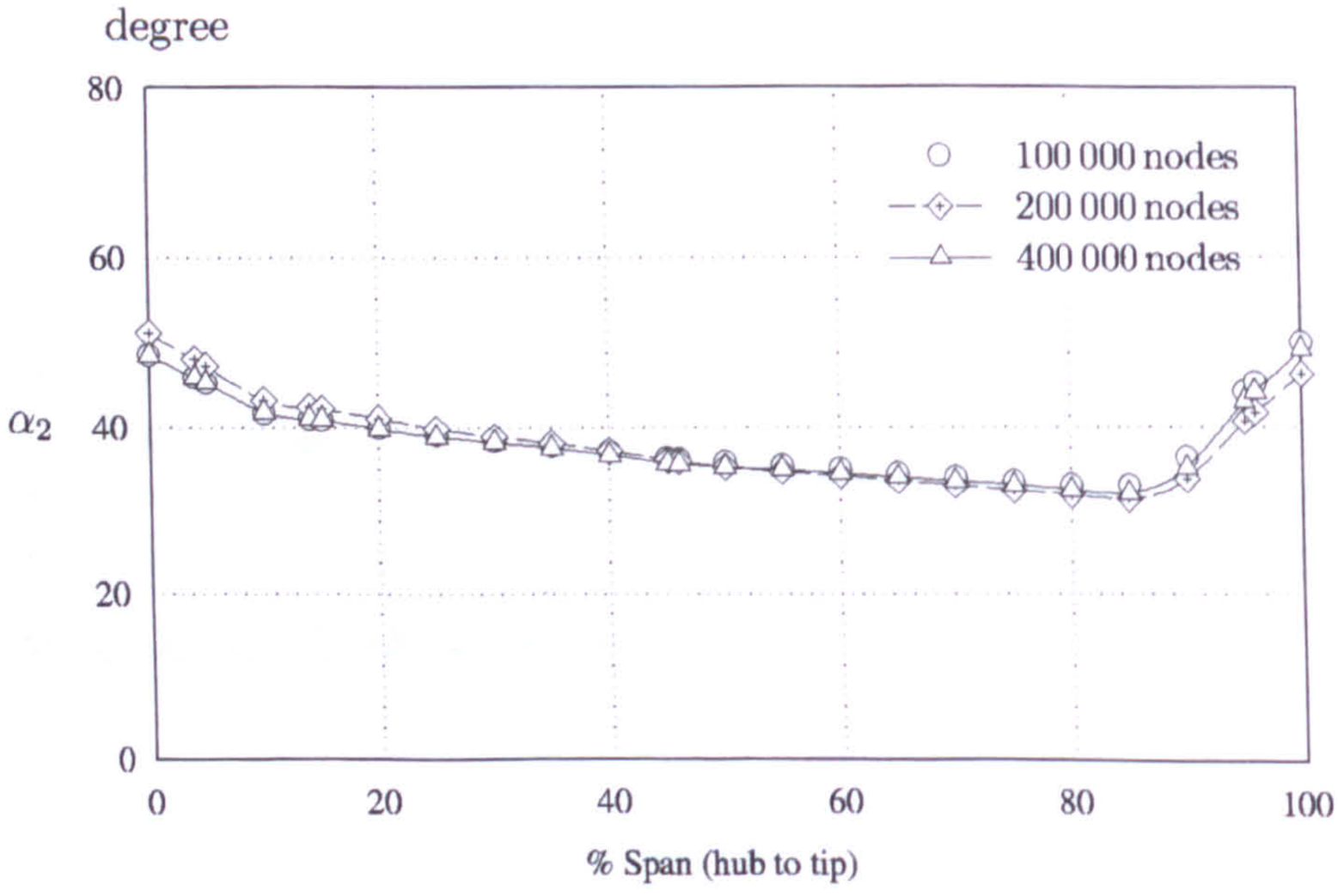

(b) Outlet station

Figure 5.10: Absolute flow angles for different grid sizes

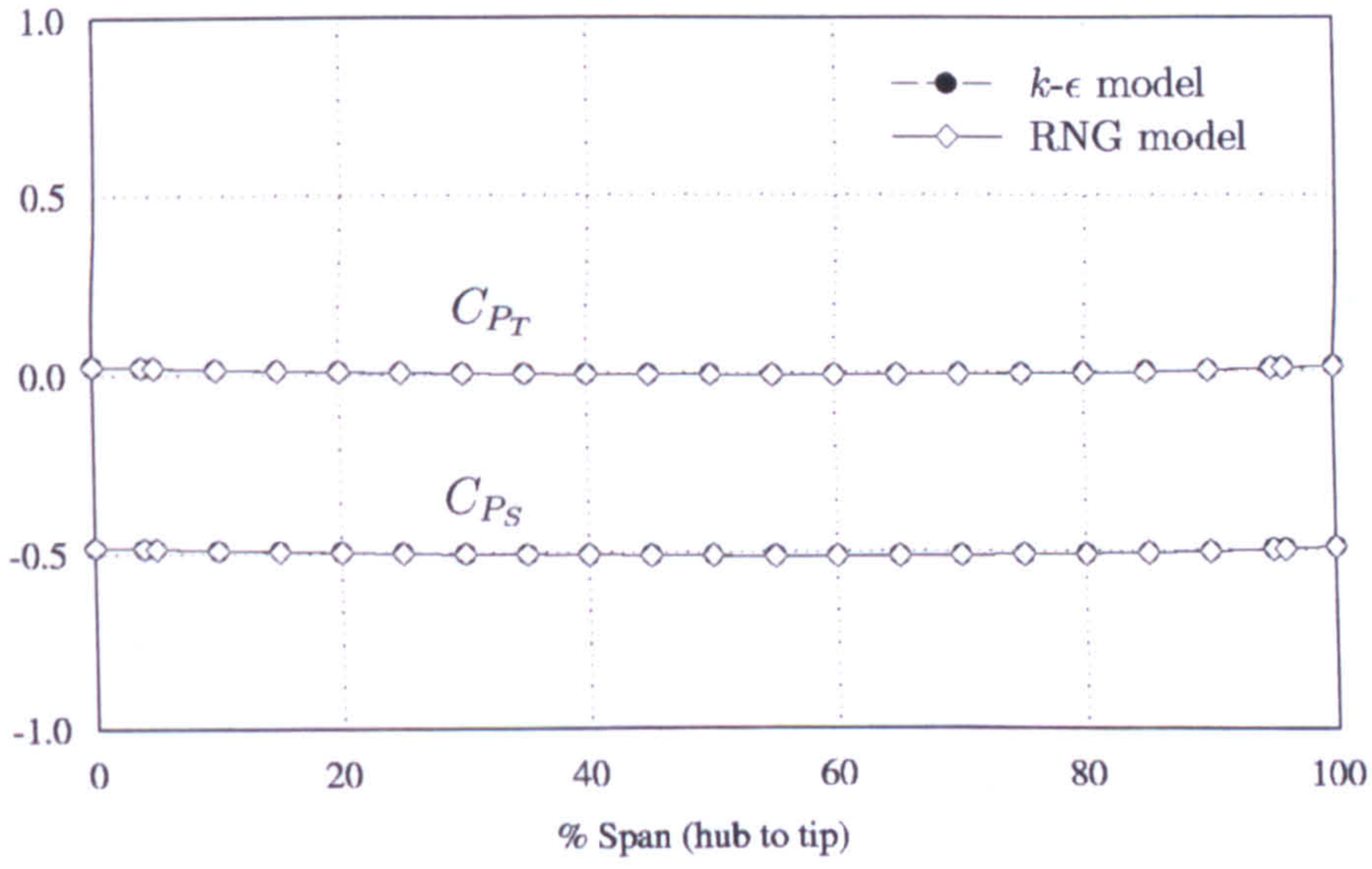

(a) Inlet station

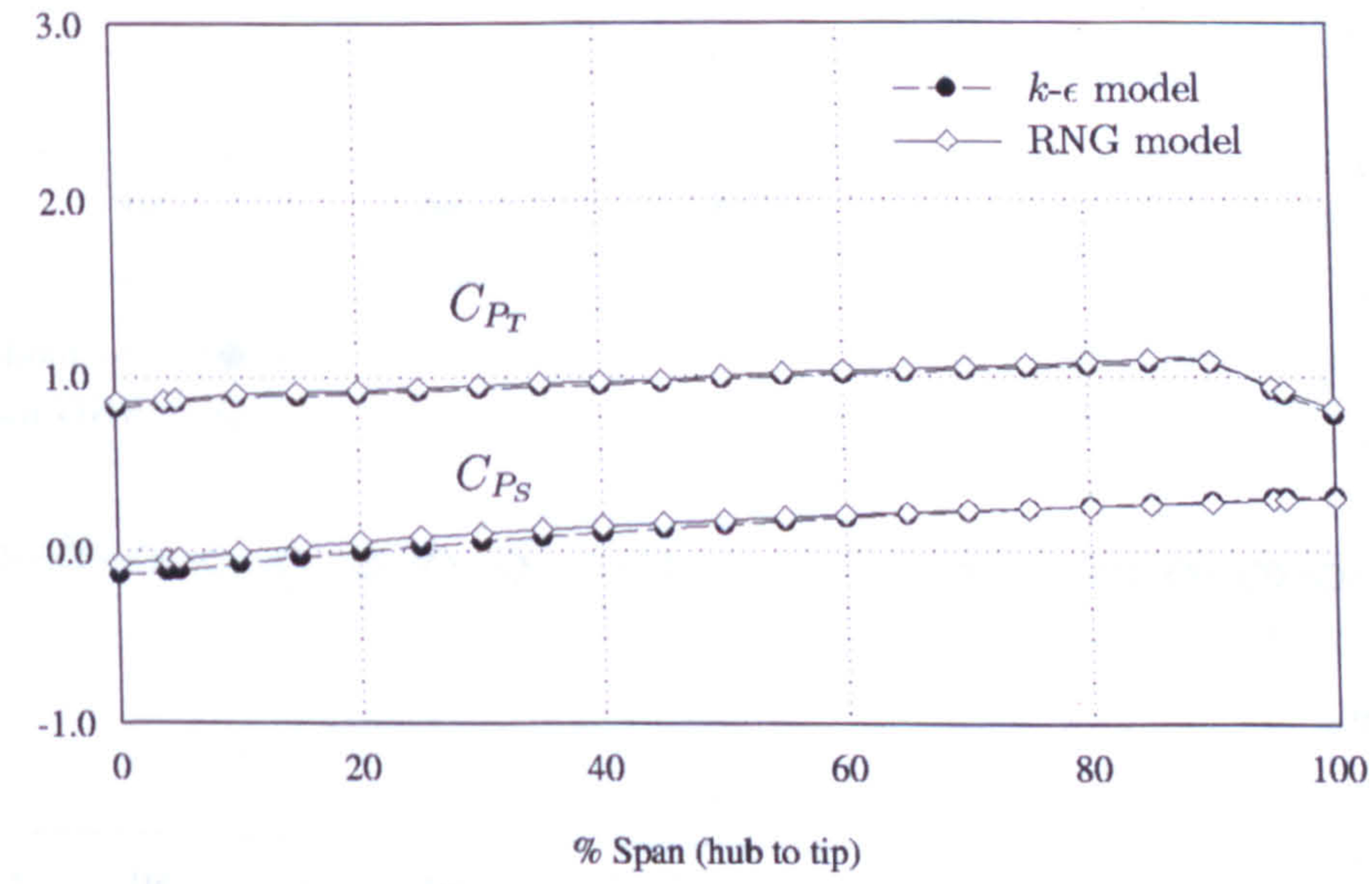

(b) Outlet station

Figure 5.11: Radial profile of the pressure for different turbulence models

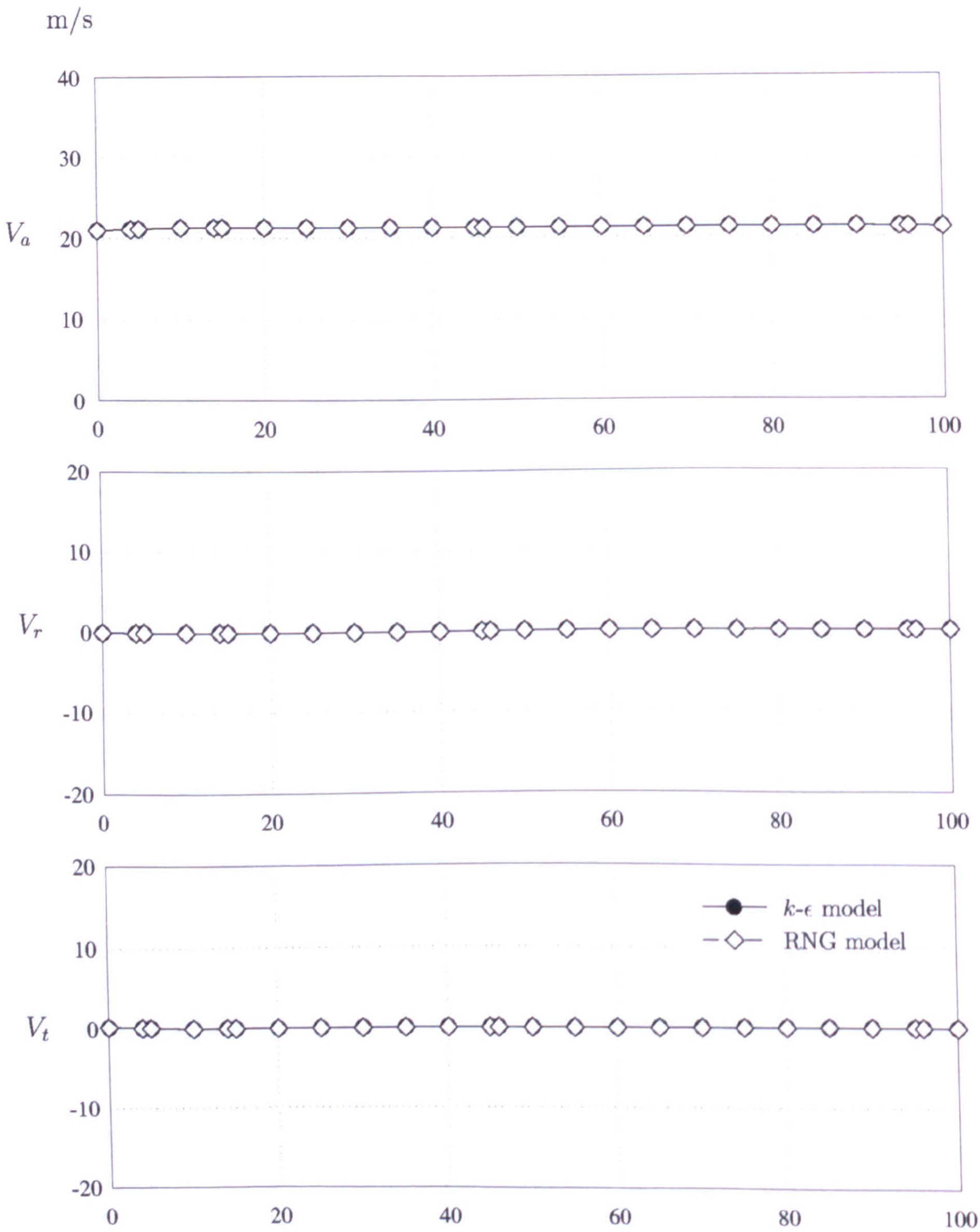

Figure 5.12: Radial profile of inlet velocity for different turbulence models

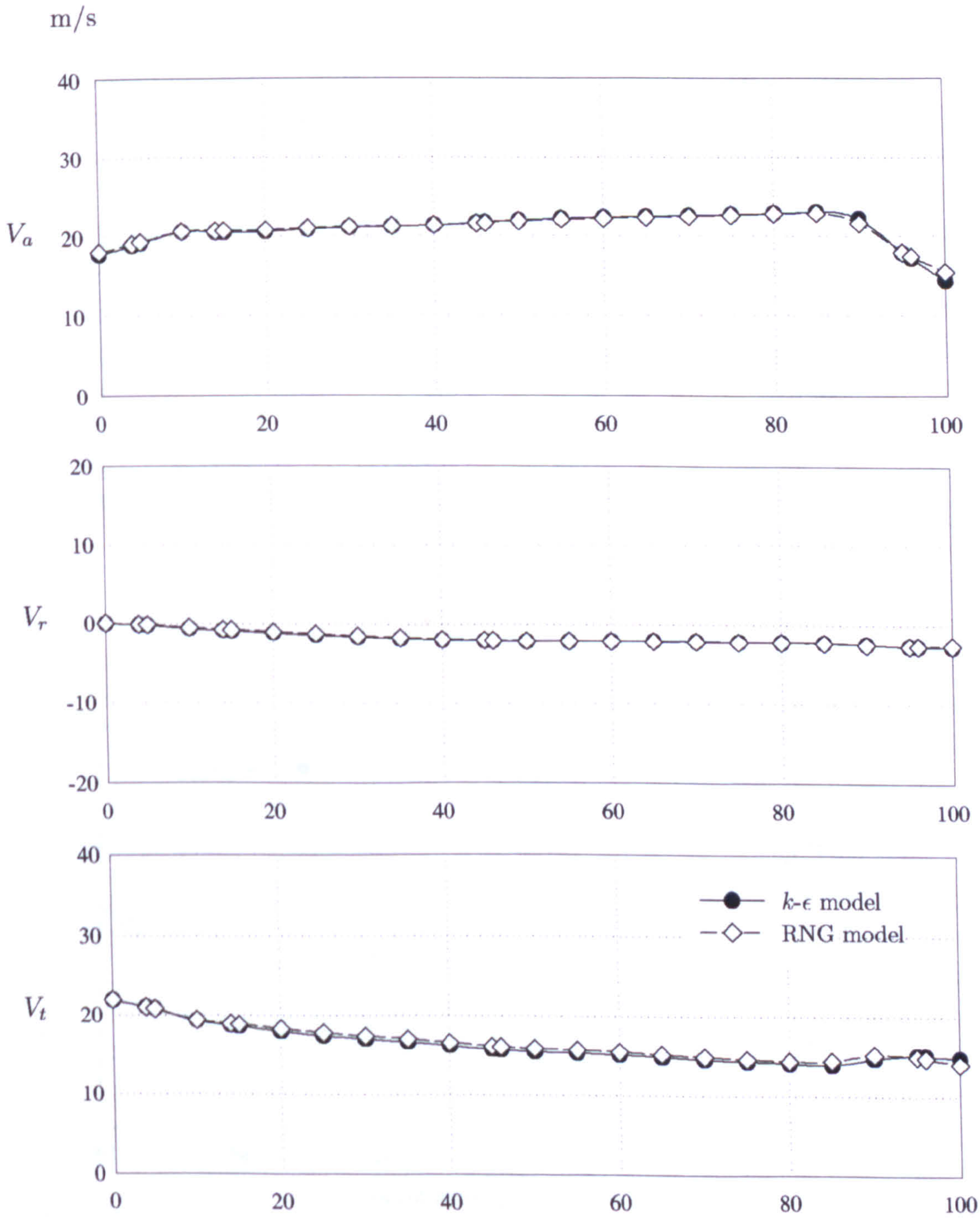

Figure 5.13: Radial profile of outlet velocity for different turbulence models

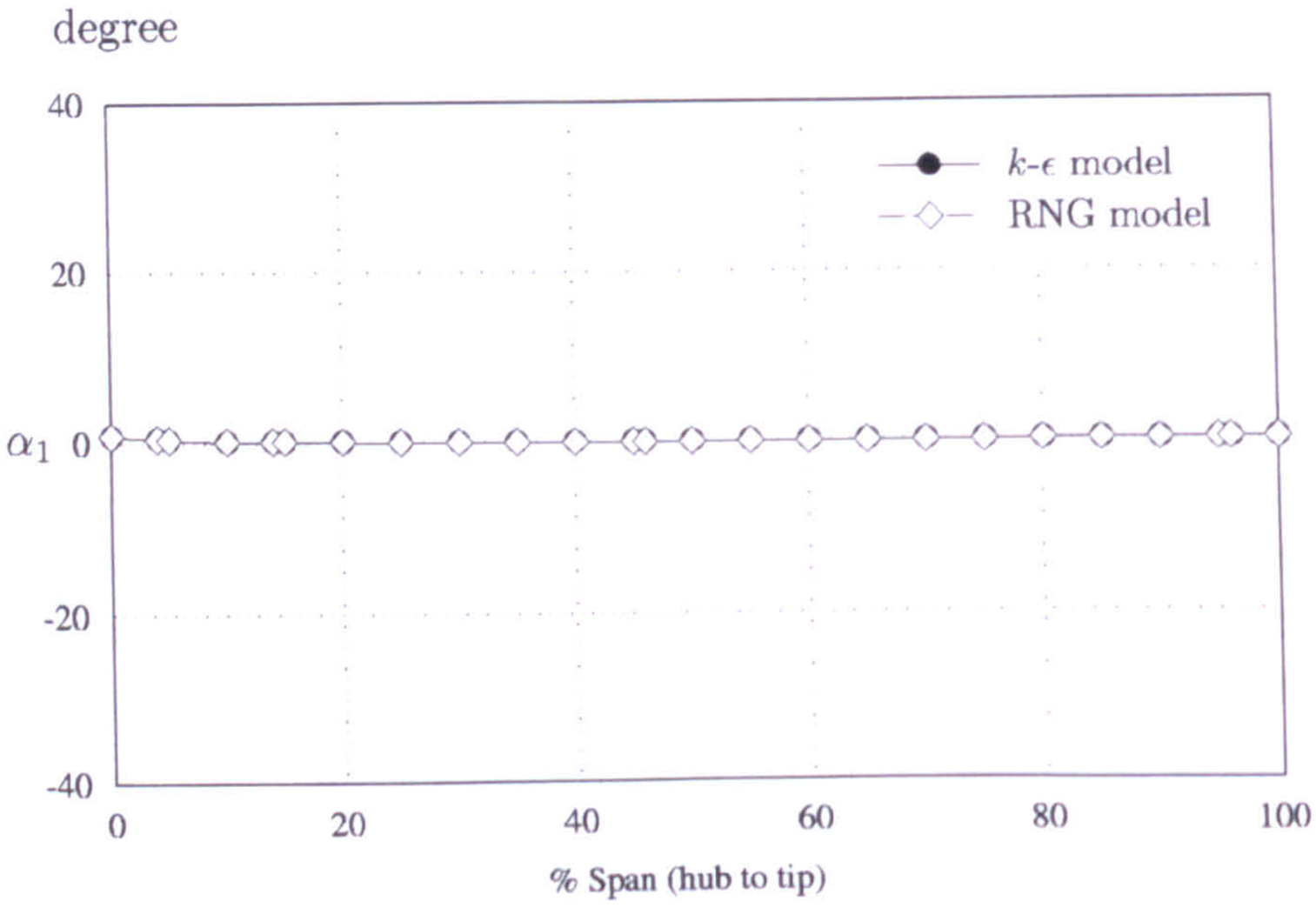

(a) Inlet station

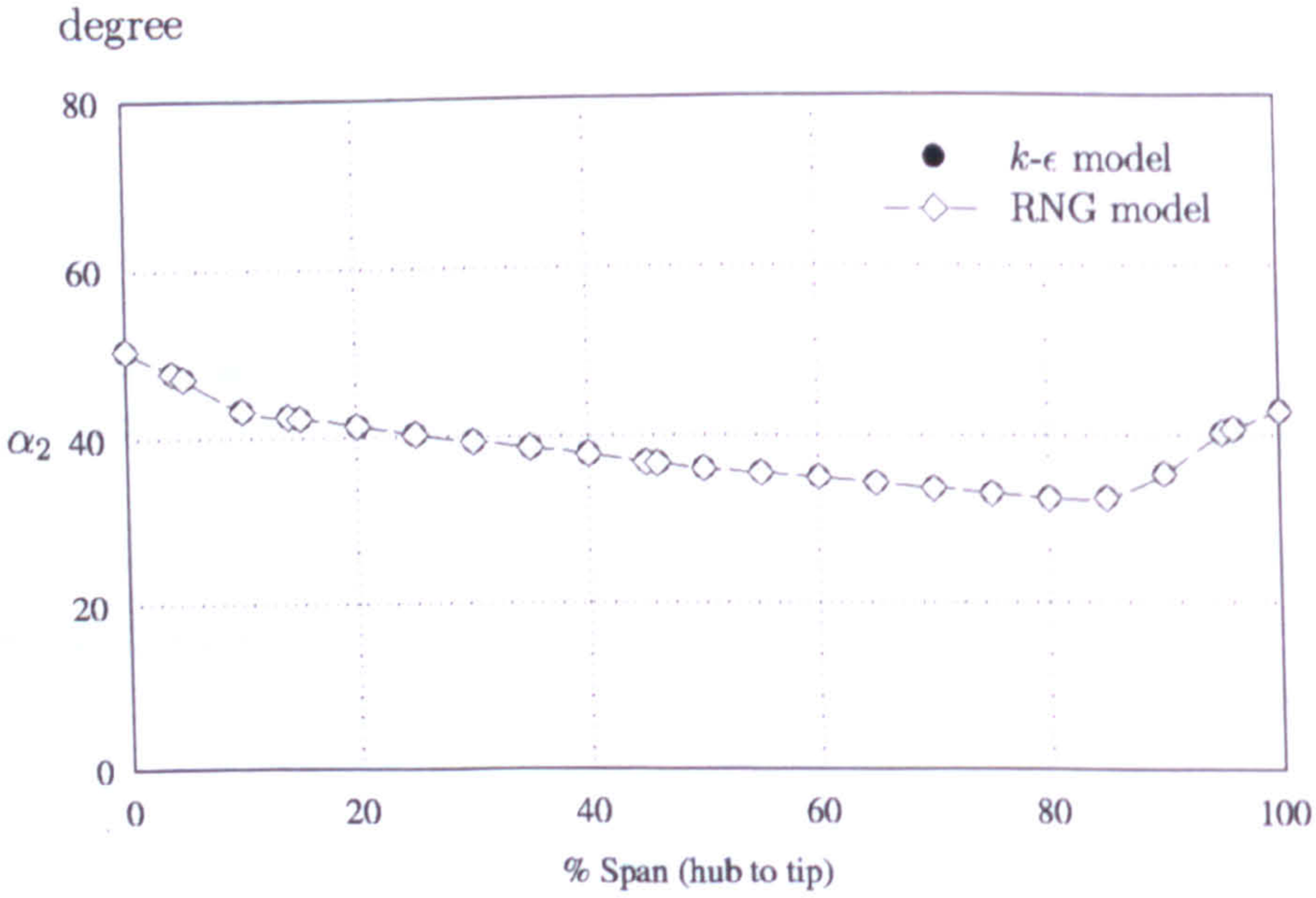

(b) Outlet station

Figure 5.14: Absolute flow angles for different turbulence models

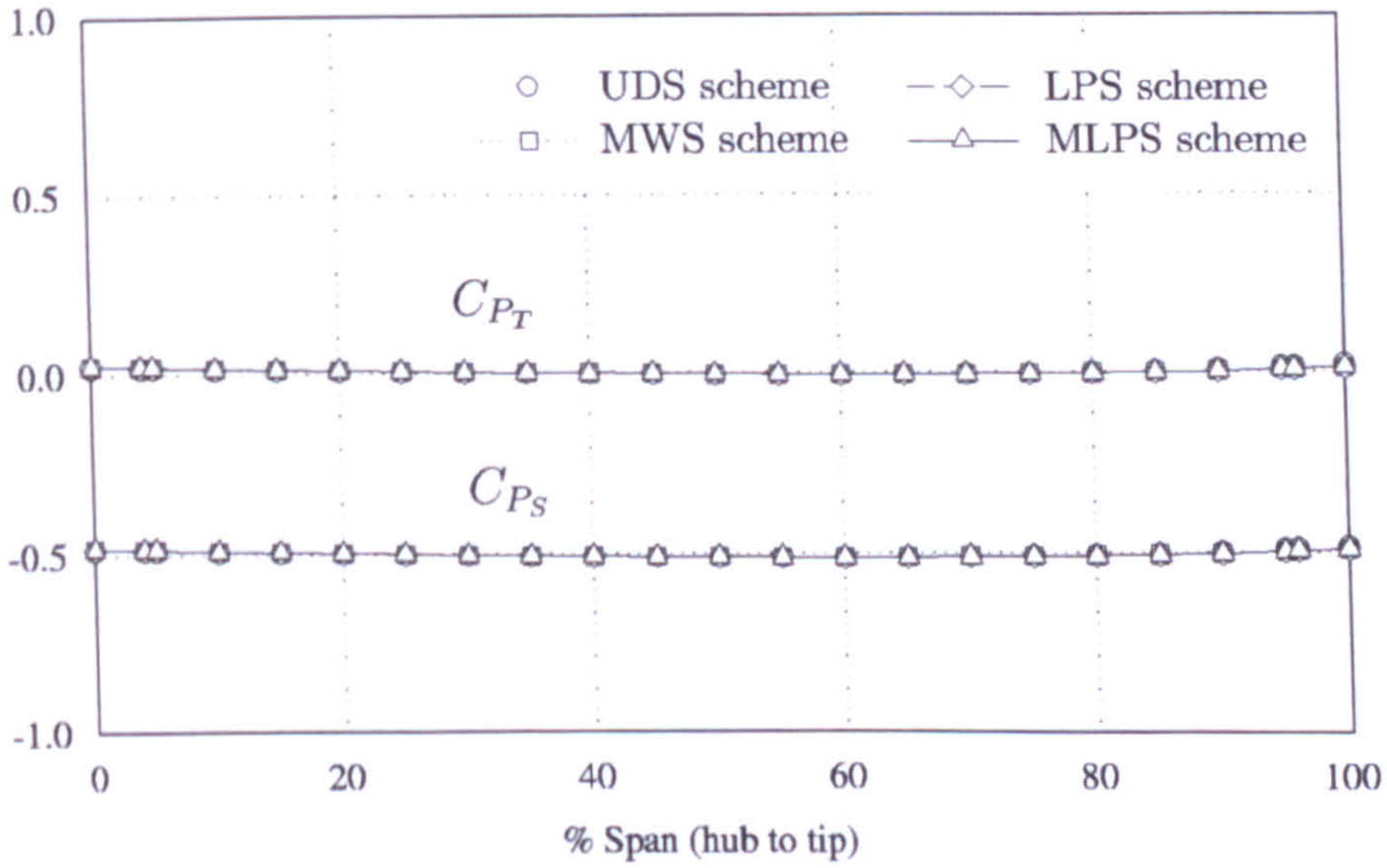

(a) Inlet station

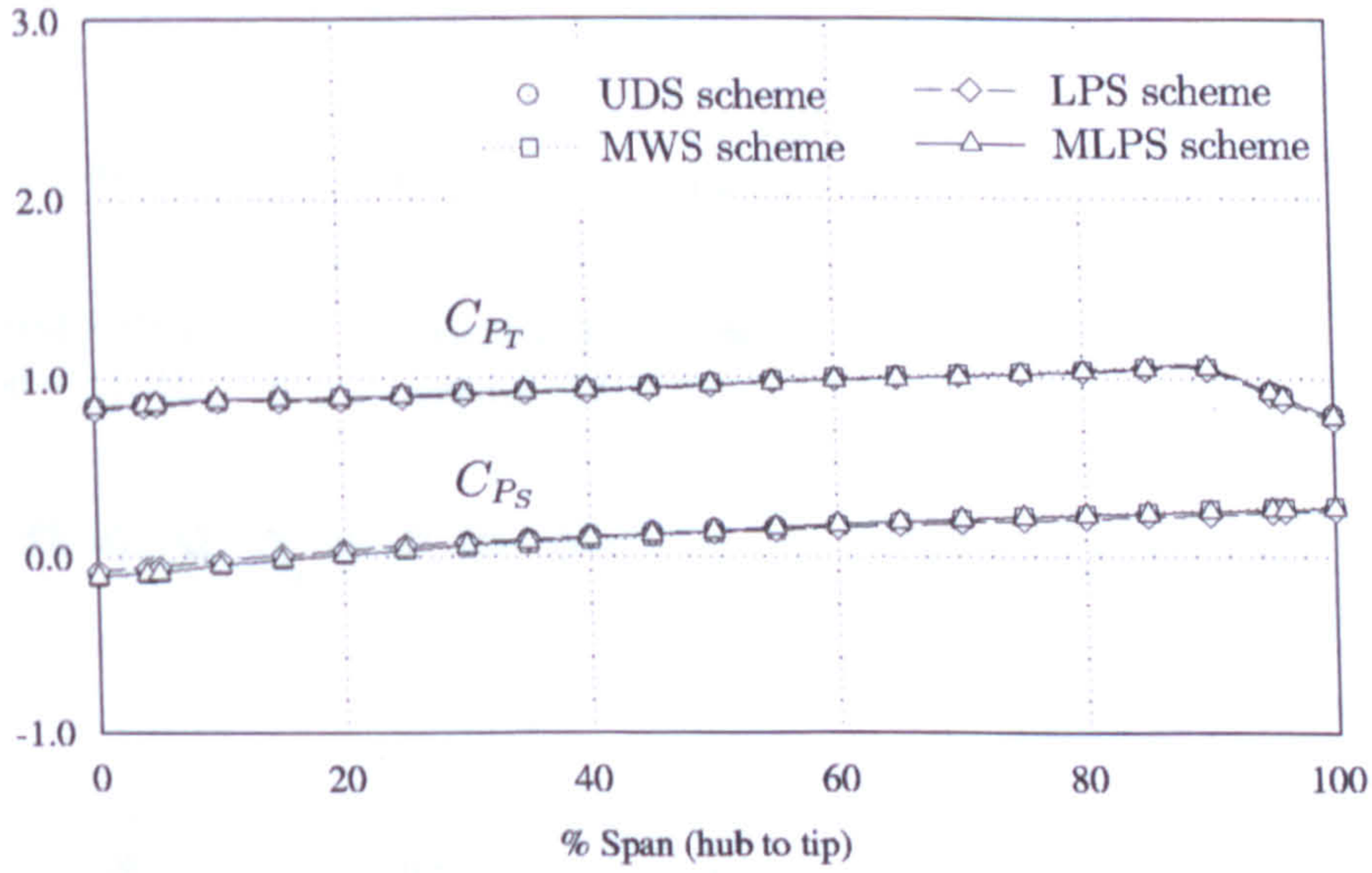

(b) Outlet station

Figure 5.15: Radial profile of the pressure for different discretization schemes

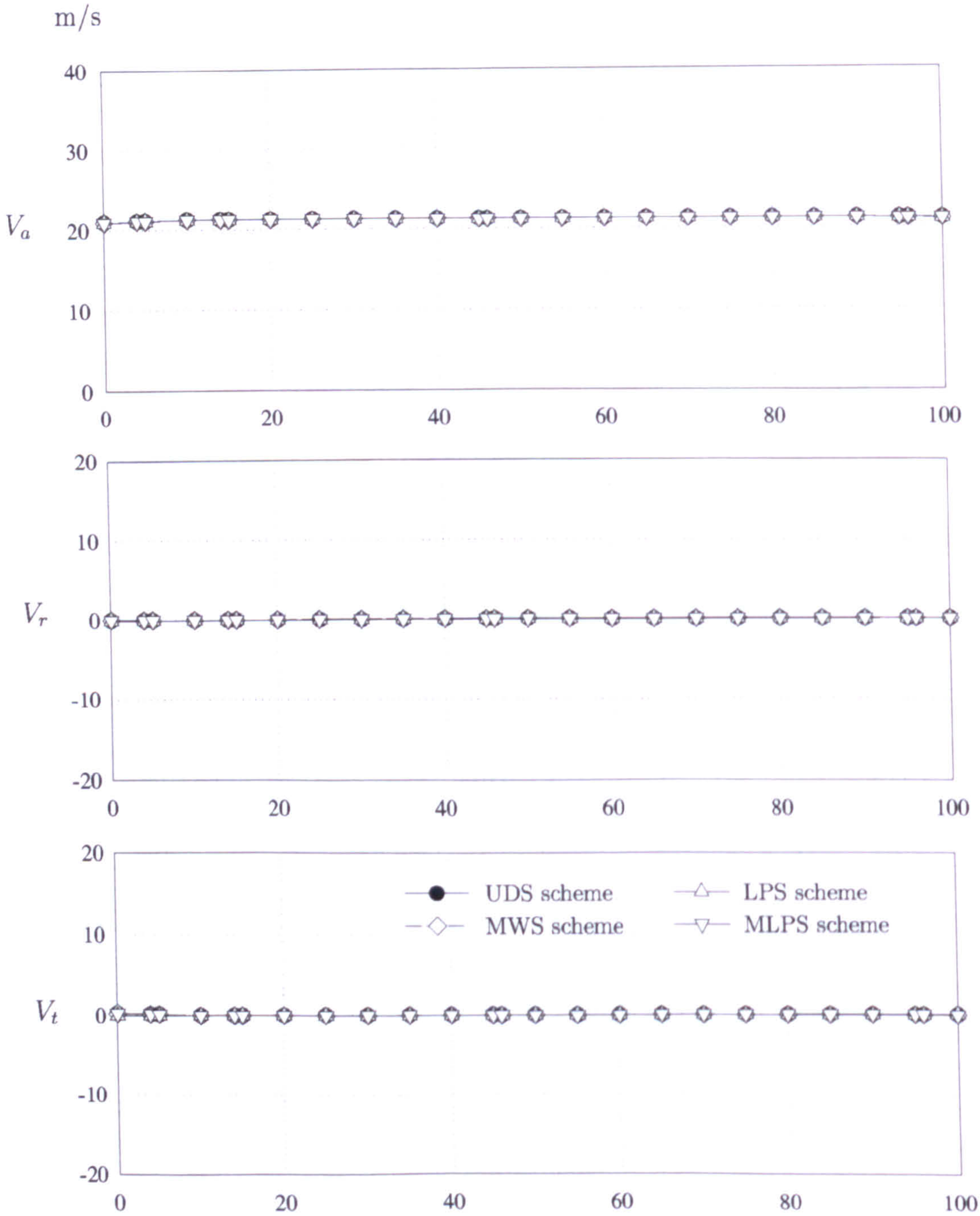

Figure 5.16: Radial profile of inlet velocity for different discretization schemes

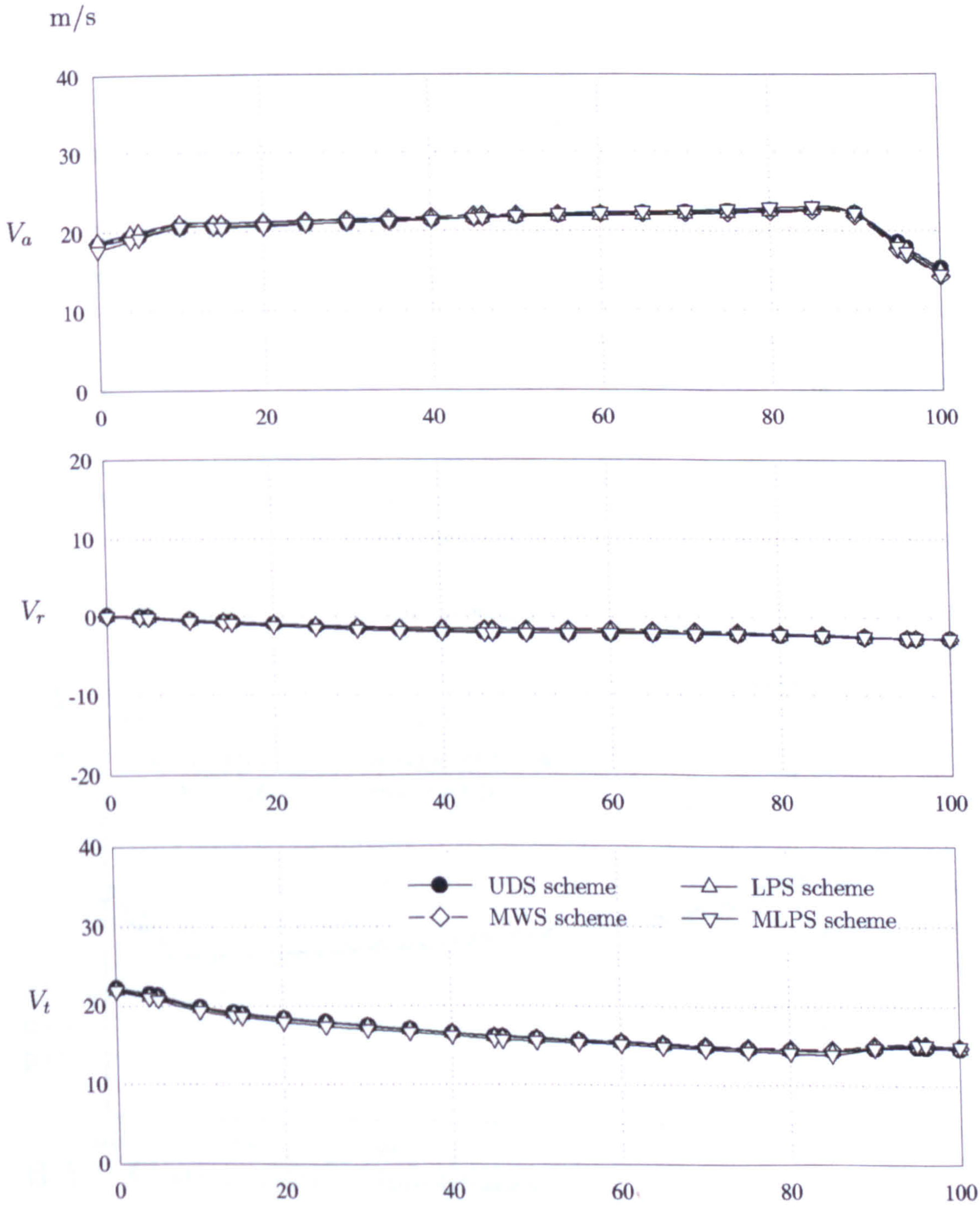

Figure 5.17: Radial profile of outlet velocity for different discretization schemes

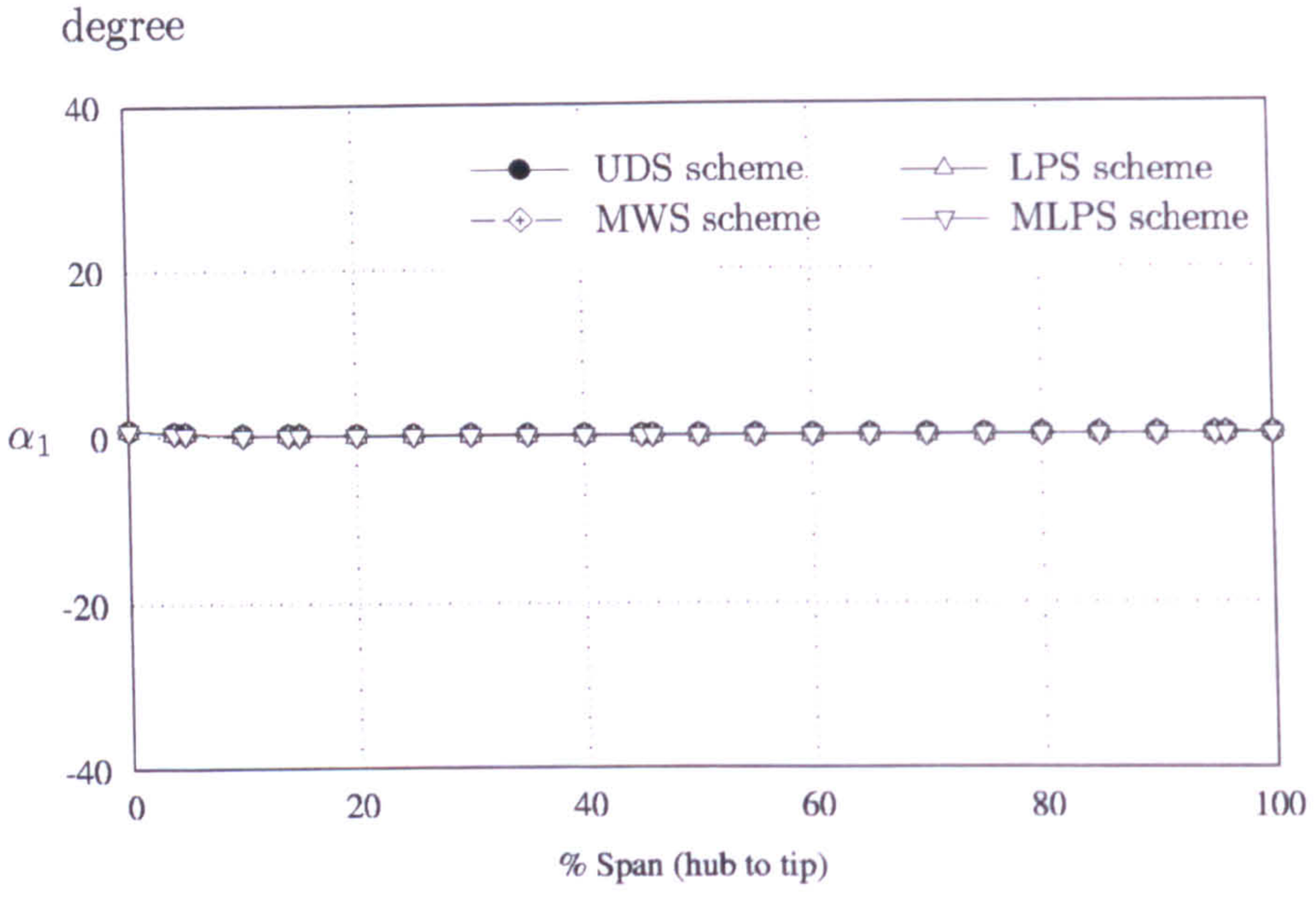

(a) Inlet station

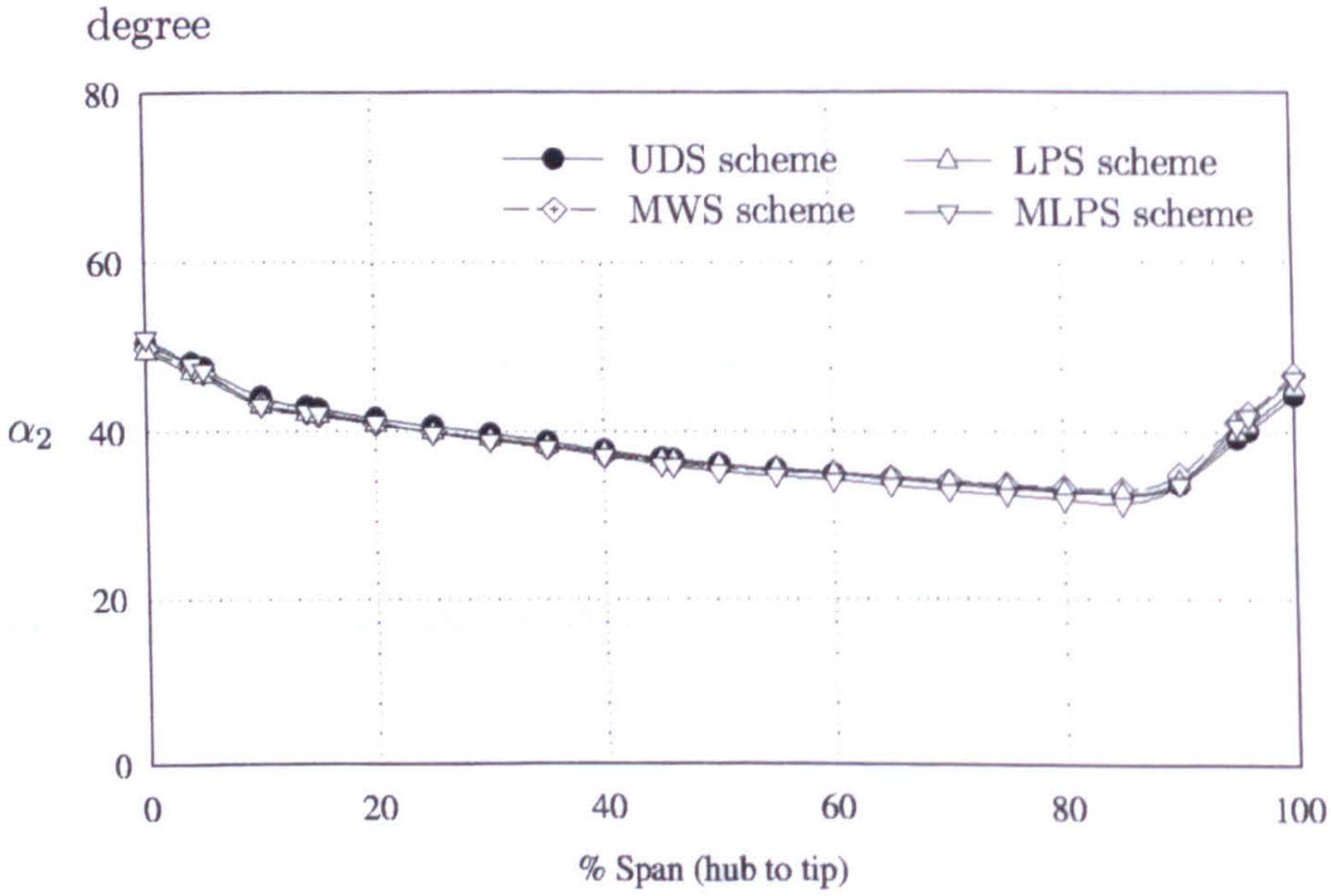

(b) Outlet station

Figure 5.18: Absolute flow angles for different discretization schemes

"There is no reliable method to define the stall point using a steady Reynolds-Averaged Navier-Stokes solver based on physical criteria. Usually the numerical procedure becomes unstable or diverges when approaching stall and this usually consists an indication of stall based on purely numerical basis."
Ghila and Tourlidakis (32)

6

Steady Simulations for Solid Casing

The numerical simulations of the axial flow fan with solid casing are presented in this chapter. The simulations were carried out for one blade-row with steady-state boundary conditions. For each simulation a different flow coefficient was specified at the outlet and the atmospheric total pressure was considered at the inlet. The overall performance of the fan in terms of pressure rise coefficient, efficiency, and work-input characteristics was estimated at each flow coefficient and compared to the experimental work carried out at Cranfield University by Kang (51). The spanwise variations of the pressure, velocity, and flow angle were evaluated at 25 span locations and also compared to the experimental data. There are no experimental data available for the pressure and velocity contours across the fan for any flow coefficient, so the flow field inside the fan was discussed with contour plots produced only numerically by the code.

6.1 Computational domain

The computational domain used in the study cases carried out in Chapter 5, shown in Figure 5.2, has a short inlet section and can not accommodate the large recess casing tested in the experiments, which will be used later in this work to carry

out the treated casing simulations. In addition to that, the shape of the mesh at the shroud surface of the domain especially above the blade, Figure 5.3(d), is not aligned in straight lines which makes it impossible to identify the boundaries, where the casing has to be fitted. However, in order to study the effect of the treatment, the predicted results for the simulation of the fan with solid and treated casing will be compared. For better comparison, the domain shown in Figure 5.2 is modified to perform the simulation of the fan with solid casing and then with treated casing after fitting the recess at the top of the domain.

The inlet section of the domain is extended further by modifying the value of the z-coordinate in the hub and shroud data curves. However, the inlet and outlet flow conditions will still be computed at the same stations shown in Figure 5.1. Also, the value of the shroud radius in the shroud data curve is modified, so that the new blade domain will only include half of the tip clearance, 0.6% of blade height, while the other half will be used to design a single-block grid, *tip* grid, which will be attached at the top of the blade main grid. The result will be a multi-block grid with full tip clearance consisting of two single-blocked grids.

The mesh for the blade domain was generated using CFX-TurboGrid with the same 8 data profiles used before, but with the modified hub and shroud data curves, which include an extension of the inlet section and half of the tip clearance as discussed before. The domain , as previously discussed, consists of $100 \times 40 \times 45$ mesh points, where 100 points were used in the axial direction, 40 points in the blade-to-blade direction, and 45 points in the radial direction. The grid was checked for its quality and the necessary adjustments were done to satisfy the requirements of the CFX-TASCflow solver.

The tip grid is designed so that it has a height equal to half of the tip clearance and the same periodic boundaries as the blade grid. This is done by importing the blade grid to CFX-TASCbob3D, the code pre-processor, and the periodic boundaries curves at the top of the blade grid are extracted and used as the periodic boundaries at the bottom of the tip grid. The periodic boundaries of the top surface of the tip grid are then calculated by adding half of the tip clearance to the z-coordinate values of the bottom surface.

The tip grid was generated with a H-type mesh using TASCgrid, and consists of $100 \times 40 \times 5$ mesh points, where 100 points were used in the axial direction, 40 points in the blade-to-blade direction, and 5 points in the radial direction. Figure 6.1 shows the mesh of the tip grid at the shroud surface, where the red colored mesh shows where the recess casing will be fitted later for the simulation of the fan with the casing treatment.

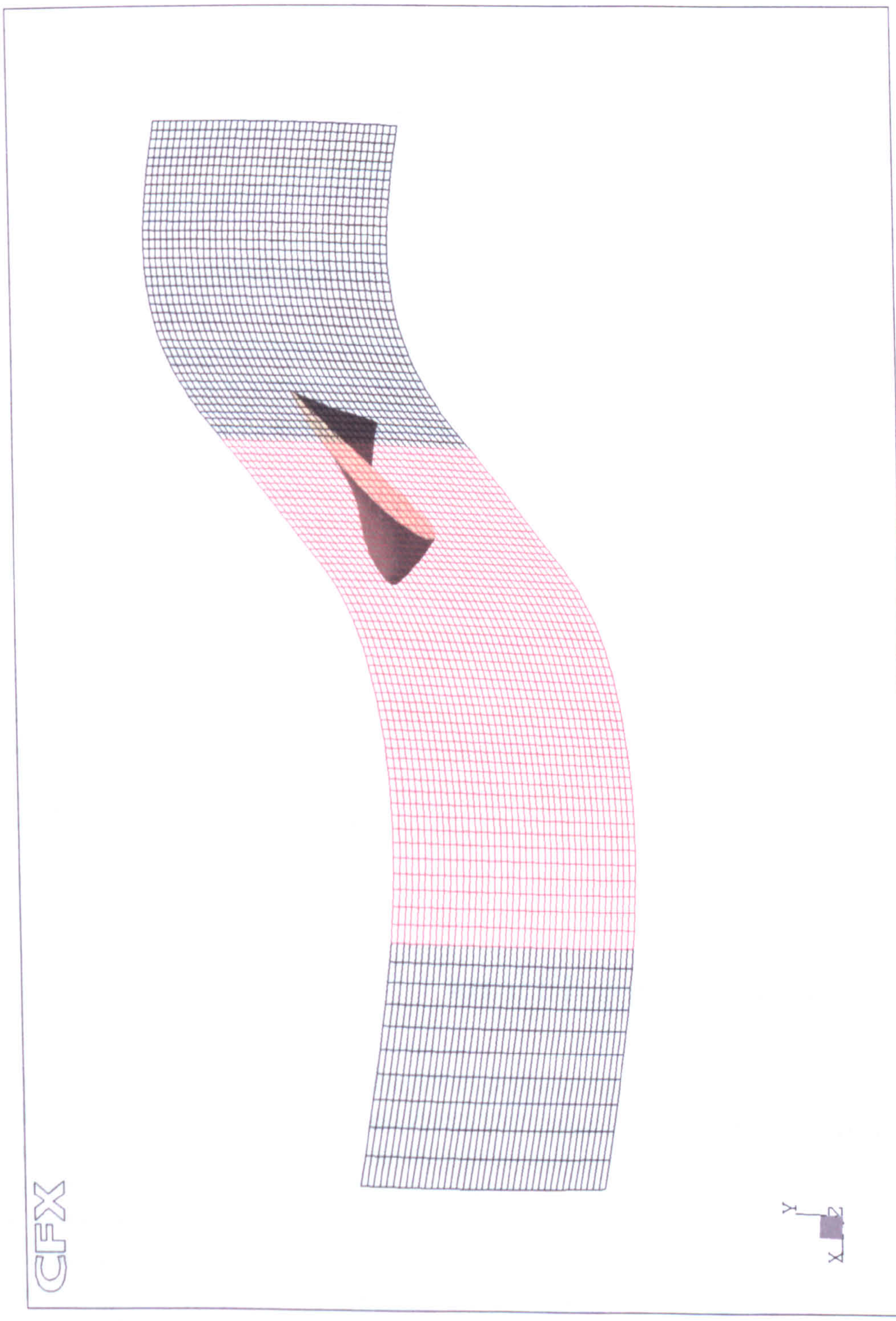

Figure 6.1: Shroud surface mesh of the solid casing computational domain

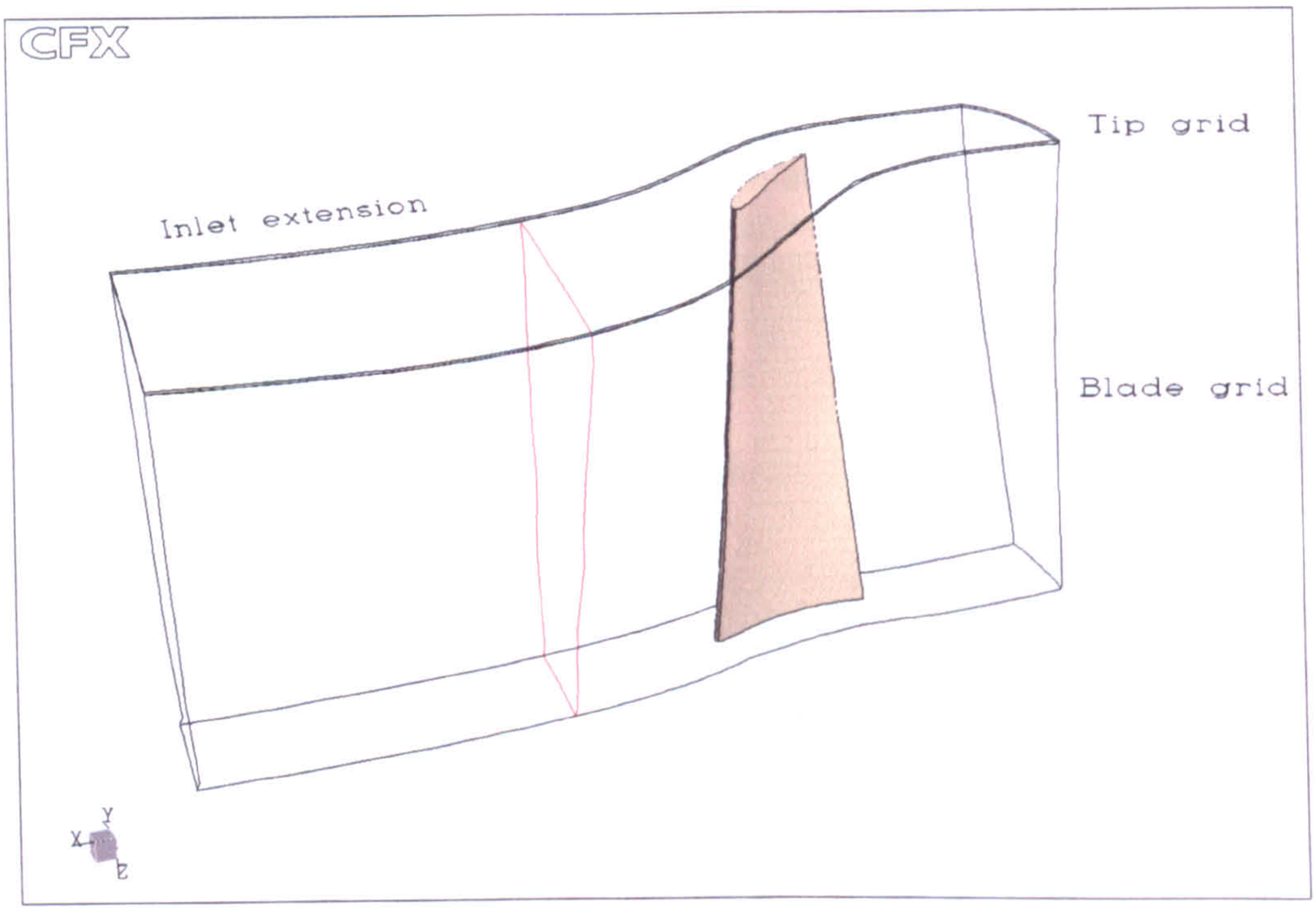

Figure 6.2: Solid casing computational domain

The two grids, blade and tip grid, are imported into CFX-TASCbob3D and attached together using General Grid Interface [GGI], explained in Chapter 4, to build the new modified computational domain, Figure 6.2. This domain has $100 \times 40 \times 50$ mesh points, 100 points in the axial direction, 40 points in the blade-to-blade direction, and 50 in the radial direction.

6.2 Boundary conditions

For all the simulations the inlet boundary condition of the domain was set as the standard day atmospheric pressure, $101\,325\,\mathrm{N/m^2}$, and a different flow coefficient was used for each simulation at the outlet boundary condition. The standard k-ϵ turbulence model with wall functions was employed as a turbulence model, and MLPS discretization scheme was used for the treatment of the convective term together with PAC scheme. The shroud of the domain was made stationary while the blade, hub and the rest of the domain were rotating at 1 500 rpm. The numerical solution assumed to be a fully convergent solution when the residual from the non-satisfaction of the discretized continuity and momentum equations fall below 10^{-5}.

6.3 Results and discussion

The predicted results of the overall performance and the work-input characteristics of the fan with solid casing were examined, and the spanwise variation of the pressure, velocity, and flow angle were evaluated and compared to the experimental data. The flow field inside the fan was visualized and discussed with plots produced numerically.

6.3.1 Fan overall performance

The predicted total to static pressure rise coefficient ψ and total to total efficiency η are presented as a function of the flow coefficient ϕ in Figure 6.3 together with the measured data given in Kang (51). From the experimental work it is apparent that three distinct regimes of flow can be identified in the fan performance chart. An unstalled region stretching from the throttle is being fully open to the peak pressure rise, flow coefficient from 0.76 to 0.61 respectively. A fully stalled region from a flow coefficient of 0.61 to 0.41, shown in the performance plot as a dotted line, where the fan suffers deep stall and the flow breaks down with an abrupt fall in pressure rise. The operation in this flow regime is unstable and no accurate measurements are available. The final region is encountered as the mass flow rate is further reduced below a flow coefficient of 0.41, where the fan operation despite a deep stall becomes more stable with pressure steadily increasing.

In the present work, numerical simulations were performed beyond the first of these flow regimes into the stalled region but as is to be expected from the limitation of a steady code, these were accompanied by increasing convergence difficulties. Although these runs were carried out as far as flow coefficients of 0.33, no numerical results below 0.56 are presented given the uncertainty associated with these. However the numerical result for mass flow coefficient just below 0.61 showed that there were drops in pressure rise coefficient as well as efficiency due to the stall inception.

The numerical simulation and the experimental work for the unstalled region exhibit similar trends for pressure rise as well as efficiency. Quantitatively the code showed a slight overestimation of pressure rise coefficient and a sizeable underestimation of the efficiency by about 5% with the experimental results. A note of caution must be sounded on account of this discrepancy though, in view of the fact that Kang's experimental efficiency results were themselves recognized by that author to be the subject of some uncertainty, Kang (51). This may explain the inconsistency between the two results as the code overestimated the pressure rise coefficient with underestimation of the efficiency for lower work-input coefficient.

6.3.2 Work-input characteristic

The work-input characteristics are cast in terms of the work coefficient $\Delta H/U_m{}^2$ and presented as a function of the flow coefficient ϕ in Figure 6.4 together with the measured data given in Kang (51). From the experimental work the three distinct regimes of flow discussed previously can be easily identified in the chart. The numerical simulation and the experimental work for the unstalled region exhibit similar trends for the work coefficient. Quantitatively the code showed an excellent agreement with the experimental results of the work coefficient data.

6.3.3 Radial pressure profile

The radial profile of the total pressure coefficient C_{P_o} and the static pressure coefficient C_P are evaluated at two different flow coefficients; design flow rate $\phi = 0.72$ and flow rate $\phi = 0.61$. They were area-averaged at 25 span locations and presented with the measured data from Kang (51) in Figure 6.5 for the inlet station and in Figure 6.6 for the outlet station. In general, the predicted pressure coefficients for the inlet and outlet at both flow coefficients agreed very well with experimental results along most of the span locations except near the shroud, where there is a slight difference between them. This may be caused by the use of the $k - \epsilon$ turbulence model with wall function used in the present work, which has certain limitations and may cause errors especially at low Reynolds numbers.

6.3.4 Absolute velocity profiles

The spanwise variation of the absolute axial V_a, radial V_r, and tangential V_t velocity components at the inlet and outlet stations of the domain were computed at the same flow coefficients. They were area-averaged at 25 span locations and presented with the experimental data from Kang (51) in Figure 6.7 for the inlet station and in Figure 6.8 for the outlet station. Both the numerical and experimental results produced similar velocity distributions at both flow coefficients. Similar plots presented at 8 mm upstream the blade leading edge, Figure 6.9, and at 6 mm downstream the blade trailing edge, Figure 6.10, show a slight increase in the tangential velocity and a sizeable drop in the axial velocity near the tip region due to the large separated flow especially at flow coefficient 0.61.

6.3.5 Absolute flow angles

The absolute flow inlet α_1 and outlet α_2 angles of the fan were calculated at 25 span locations for design flow rate $\phi = 0.72$ and for near stall flow rate $\phi = 0.61$, and presented in Figure 6.11. The numerical simulation produces similar results to experimental data except near the shroud, where a slight difference can be seen. This may be caused as discussed before by the k-ϵ turbulence model with wall function used in the present work.

6.3.6 Flow field visualization

The blade loading of the blade is presented in Figure 6.12 for flow coefficients of 0.739, 0.654 and 0.56. The static pressure coefficient around the blade are presented near the blade hub at 5% of the span and near the blade tip at 95% of the span. A much more uniform blade loading is demonstrated at the blade hub, Figure 6.12(a), than at the tip, Figure 6.12(b). The lift force produced from the pressure difference between the pressure and suction sides of the blade is much larger at the tip than at the hub due to the larger stagger at the tip. As the flow coefficient is reduced more lift is produced at the tip, flow coefficient 0.654, until near stall where there is no any further increase in the lift, flow coefficient 0.56.

Blade-to-blade relative velocity magnitude contours are shown in Figure 6.13 for flow coefficient of 0.56 at four different blade-to-blade span locations. The low-speed region seen behind the blade trailing edge in the near hub plot, Figure 6.13(a), is increased and moved toward the suction side of the blade in the mid-span plots, Figures 6.13(b) and 6.13(c). This region is increased further and occupied some three-quarters of the pressure and suction sides of the blade as can be seen in the plot near blade tip, Figure 6.13(d). It seems that the large separated flow at the shroud responsible for the stall of the fan is not because of the tip clearance only, but due to the radial flow injected from the hub to the shroud at the blade suction side near the trailing edge.

The extent of flow separation inside the domain at the flow coefficients of 0.72 and 0.56, is presented in Figure 6.14. For the two pictures, the direction of the flow is from right to left with the blade suction side displayed uppermost. The blue shaded areas of these isotimic[†] plots depict the presence of axial velocities, whose direction is the opposite of that of the main stream, reverse flow. A comparison between

[†]Isotimic is a 3-D surface of constant value for the selected variable field, AEAT (1)

the isotimic plots show that fairly similar amounts of flow separation are present near the blade trailing edge for the two flow conditions and the extent of the stalled region at the tip is much more affected by the reduction in mass flow rate.

The propagation of this flow separation inside the domain as the flow coefficient reduces from design point $\phi = 0.72$ to 0.56, is presented in Figure 6.15. The streamlines correspond to fluid particles released upstream of the blade root leading edge, region [25,1:40,2:3]. These streamline plots highlight the flow physics of the tip stall growth process. In the high flow rate condition, Figure 6.15(a), the near hub seeded fluid particles roll into a vortex extending to some three-quarters of the blade height. At low flow rate, Figure 6.15(b), the bulk of these particles can be seen to have been ejected towards the outer casing and occupy this through a mechanism of radial low momentum flow transport. This transport process is thought to be a large contributor to the very large separation observed in the shroud region in addition to the locally induced separation due to high blade loading and tip clearance, which was already seen at high flow rate in Figure 6.14(a). These plots, Figures 6.14 and 6.15 provide evidence that the tested fan is prone to the tip stall behaviour, which characterizes tip critical machines for which the large recess casing in particularly suitable.

The extent of flow separation inside the domain demonstrated by the isotimic and streamlines plots is also shown in the relative total pressure contours just behind the blade trailing edge presented in Figures 6.16(a) and 6.16(b) for the flow coefficients $\phi = 0.72$ and 0.56 respectively. A comparison between these two plots shows that at the tip region the extent of the stalled region is much more affected by the reduction in mass flow rate and that small amount of separated flow is present elsewhere for the two flow conditions. The plots of Figure 6.17 depicted the flow radial velocity for these flow coefficients at the same plane shows clearly that the amount of separated flow is larger and with higher radial velocity for the flow coefficient of 0.56 than of 0.72.

The relative total pressure contour at low-flow coefficient of 0.56 is also presented in Figure 6.18 for the blade pressure side and suction sides. A comparison between these two pictures shows clearly that at the blade tip much more separated flow is found at the blade suction side, Figure 6.18(b), than at the pressure side, Figure 6.18(a). This is clearly due to the fact that the separated flow is ejected from the hub to the outer casing at the blade suction side near the trailing edge as was highlighted by the streamlines plots.

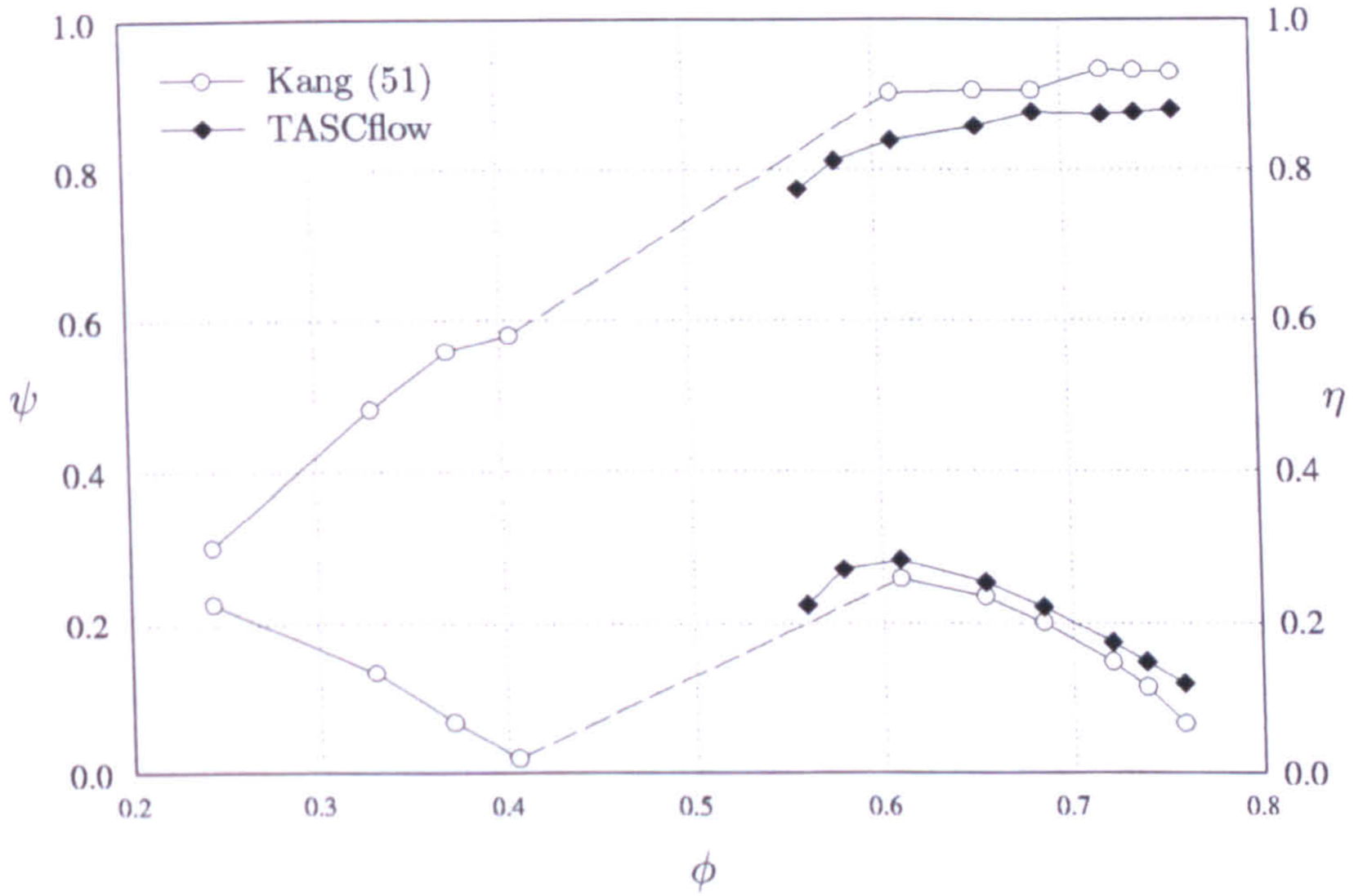

Figure 6.3: Overall performance of the fan with solid casing

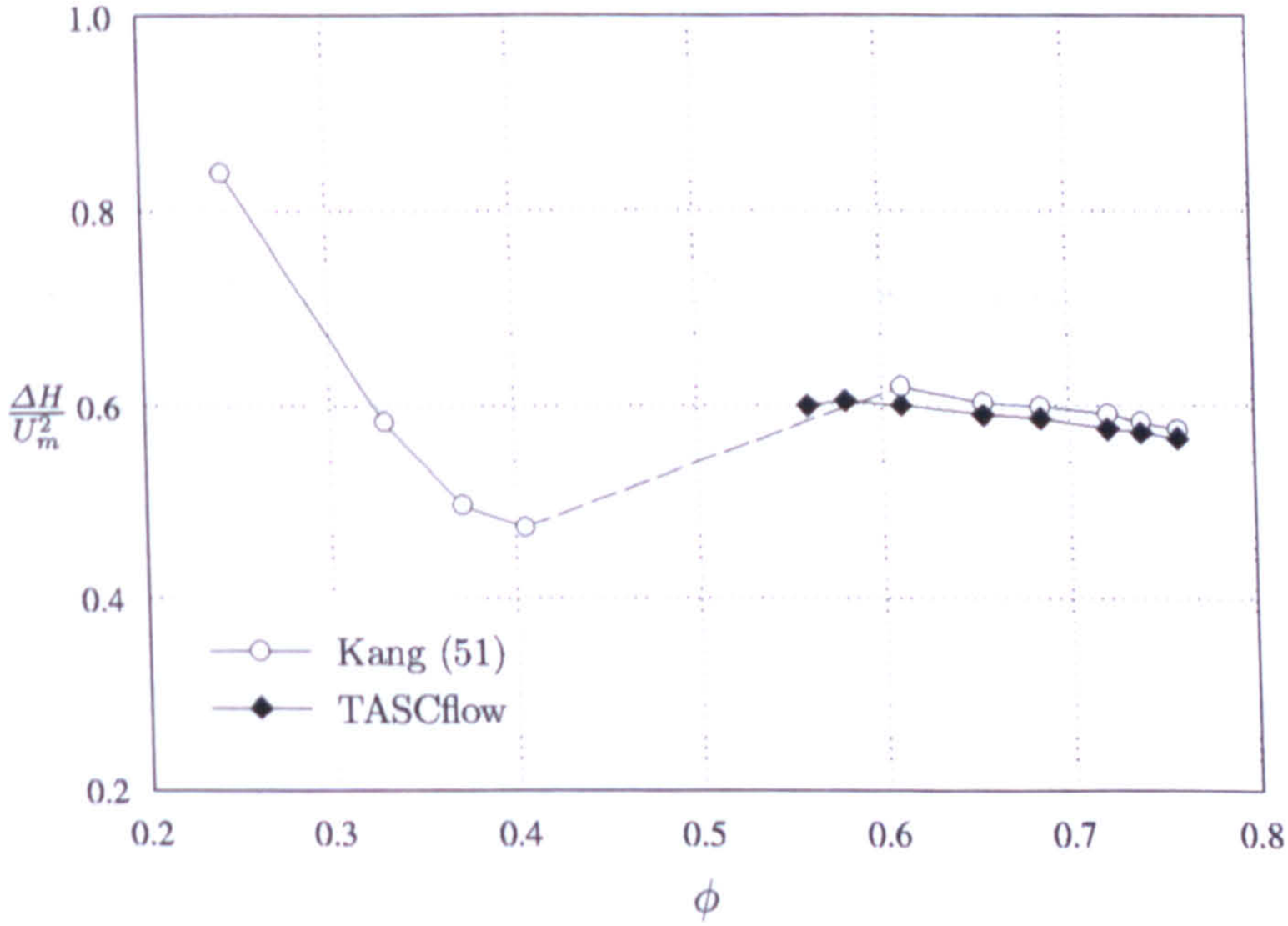

Figure 6.4: Work-input characteristics of the fan with solid casing

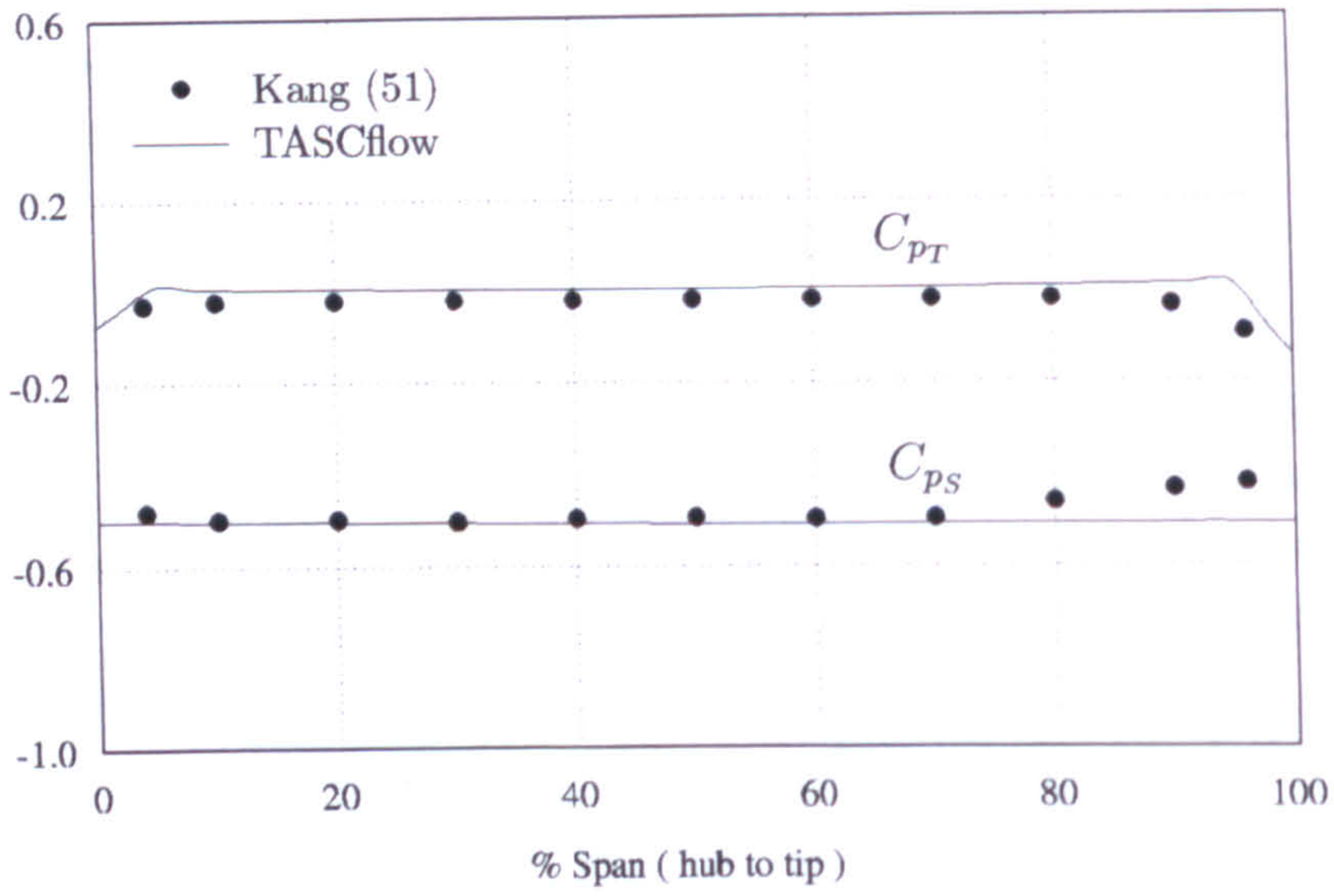

(a) At $\phi = 0.72$

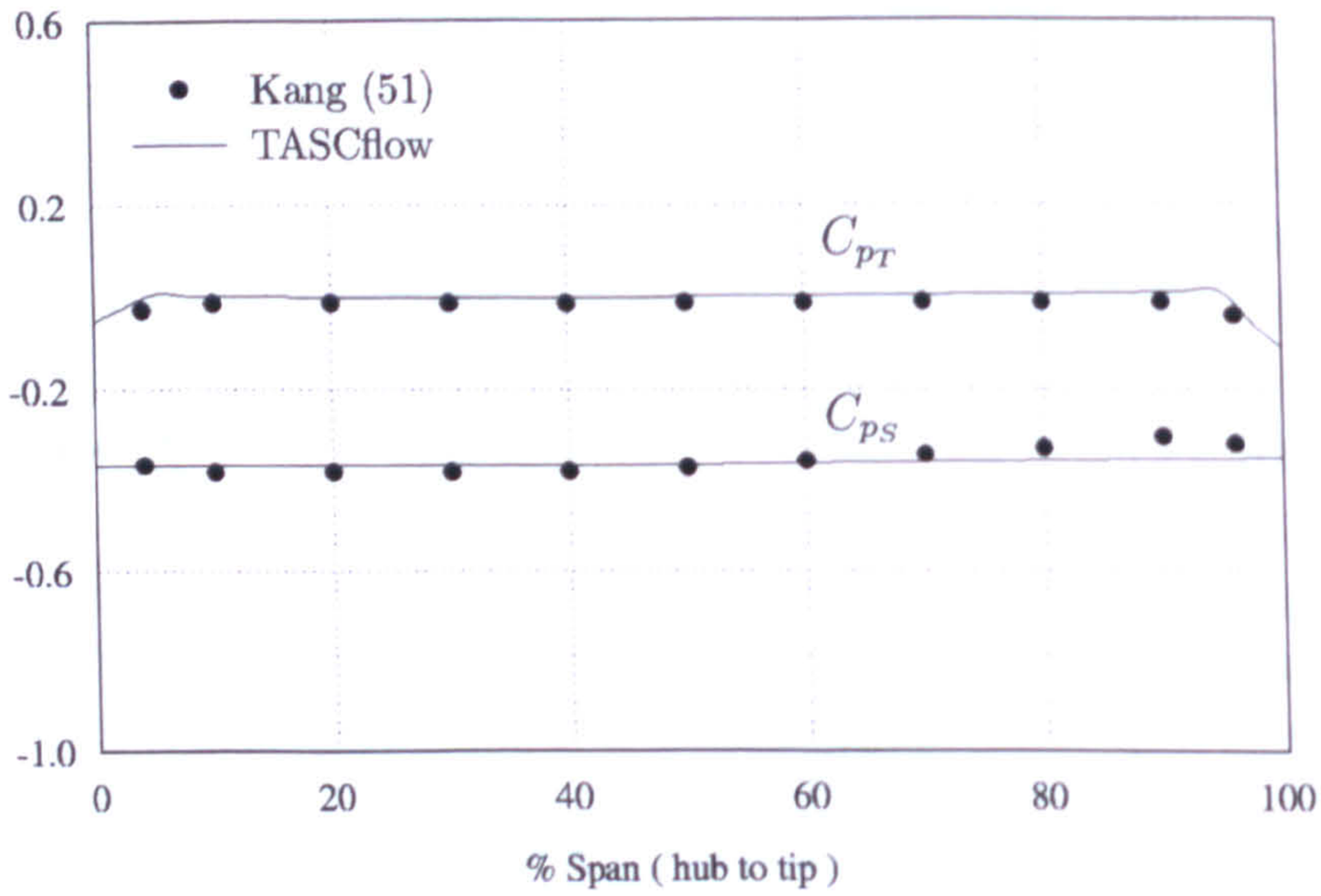

(b) At $\phi = 0.61$

Figure 6.5: Radial profile of the pressure coefficients at the inlet

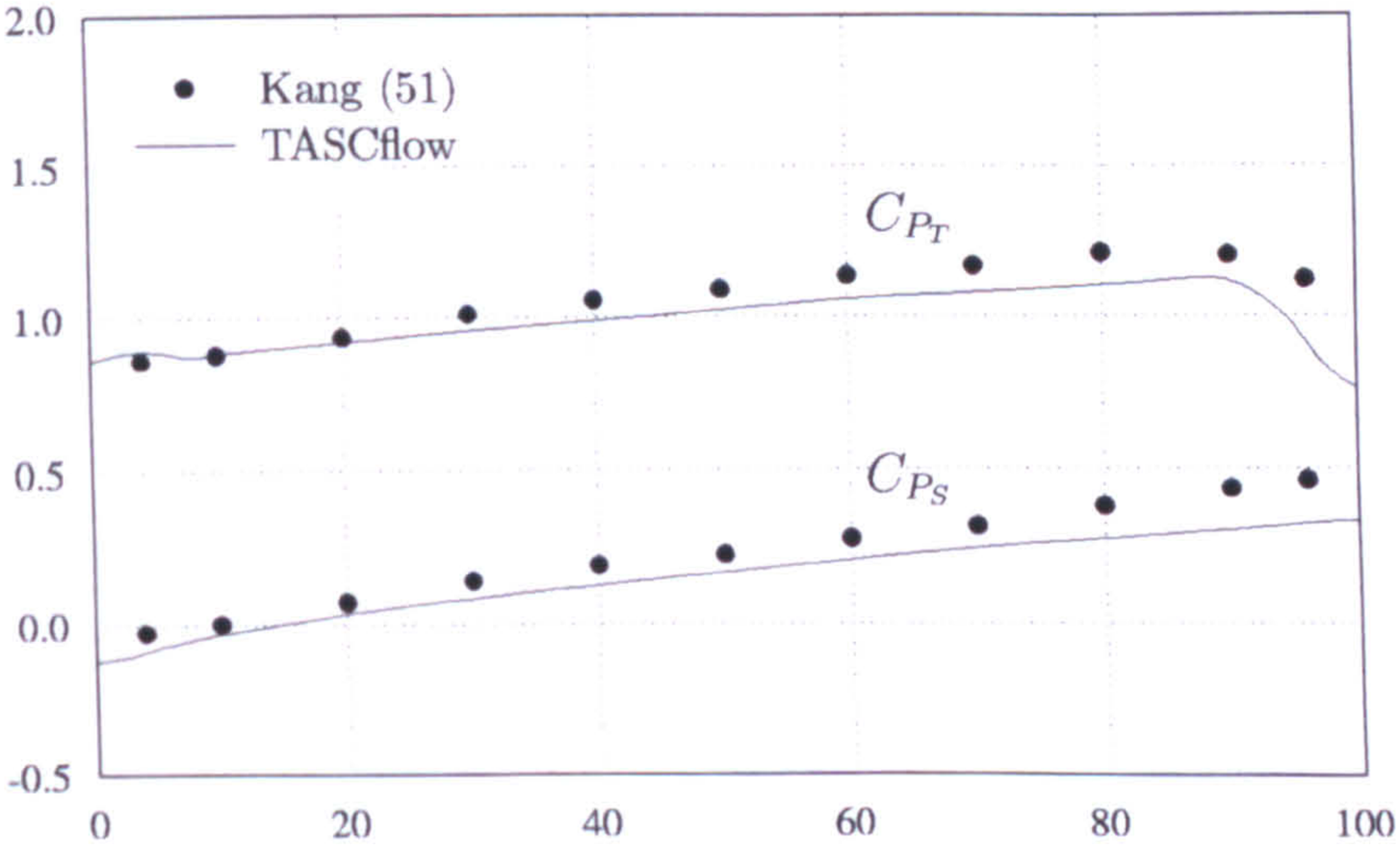

(a) At $\phi = 0.72$

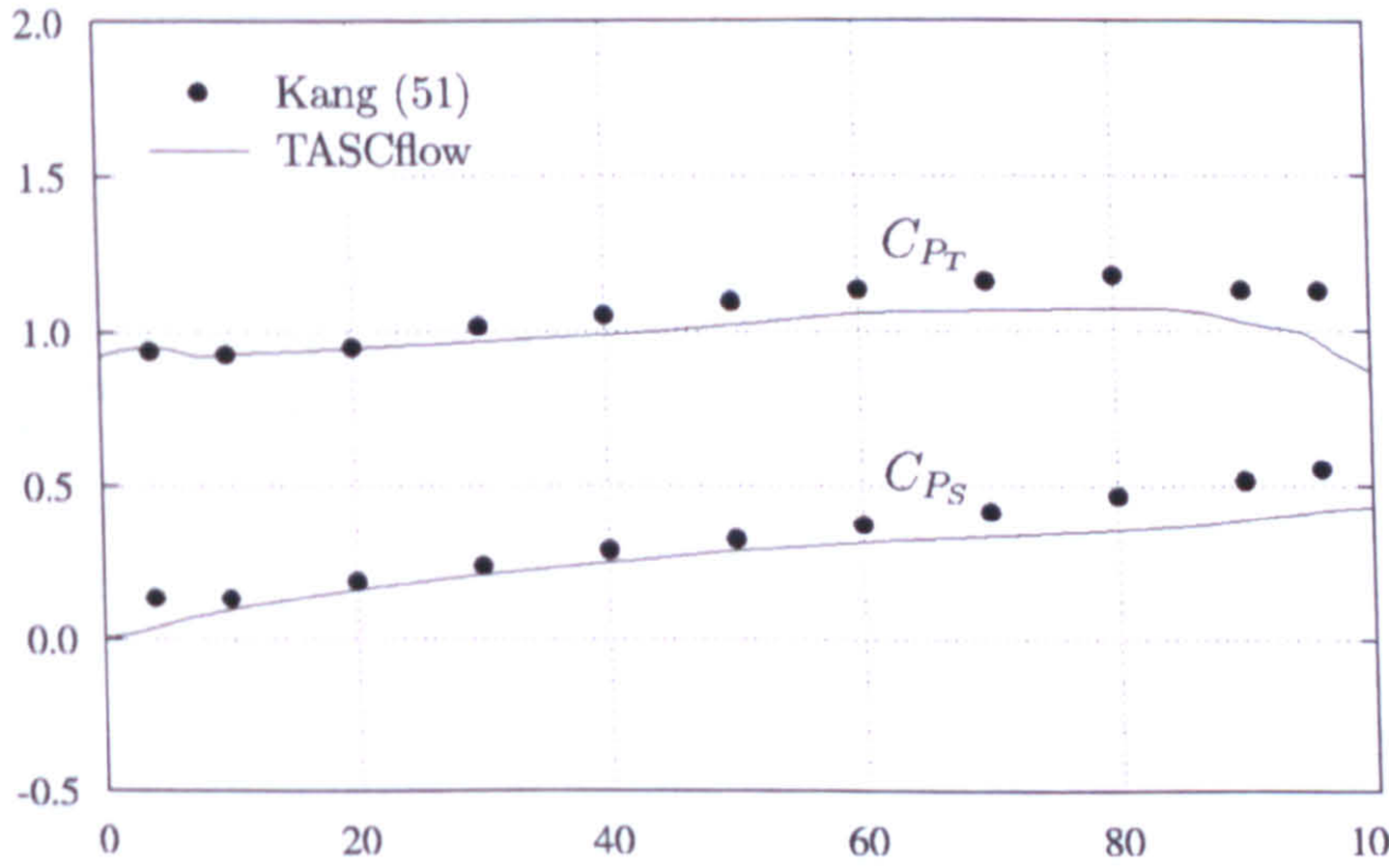

(b) At $\phi = 0.61$

Figure 6.6: Radial profile of the pressure coefficients at the outlet

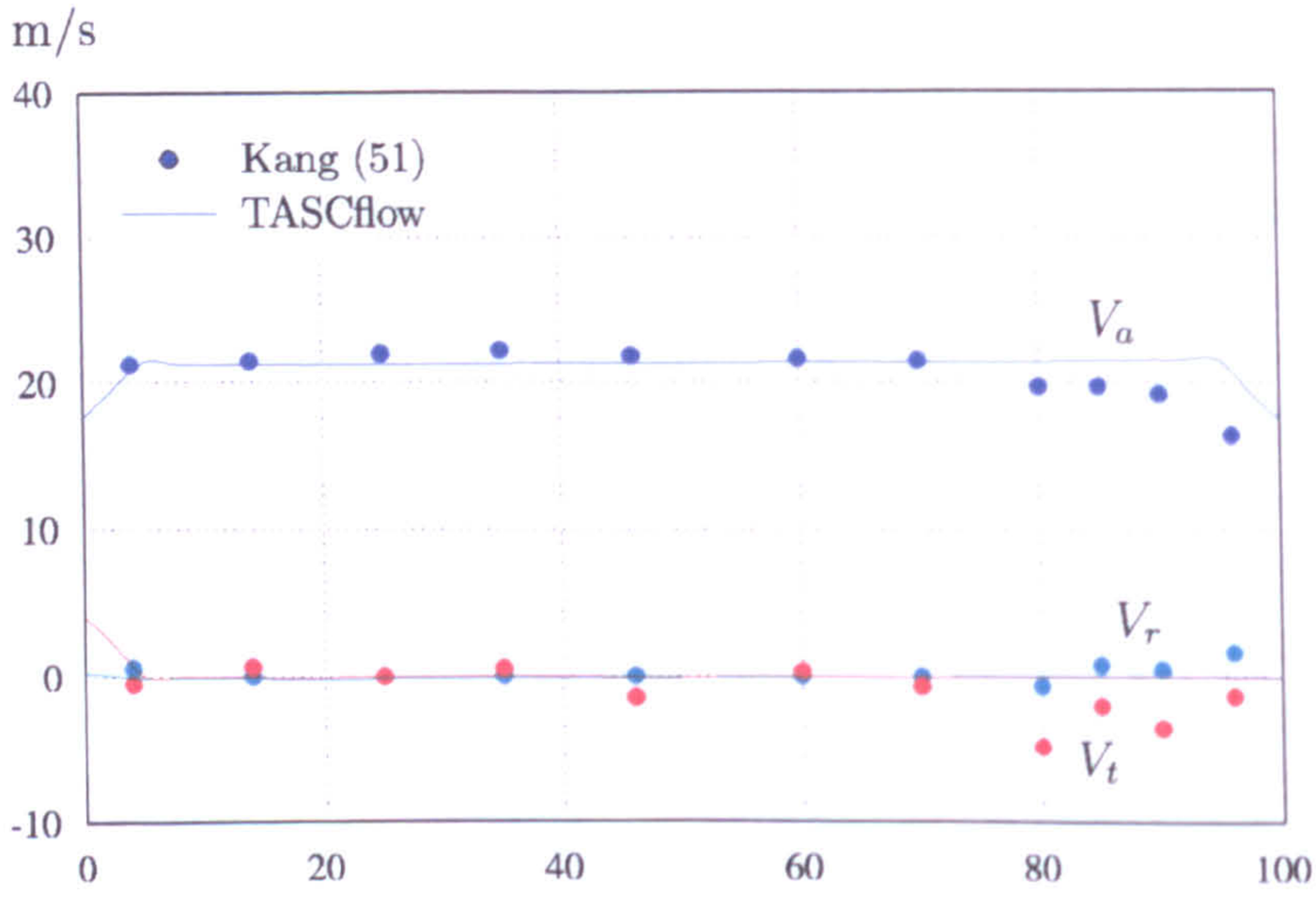

(a) At $\phi = 0.72$

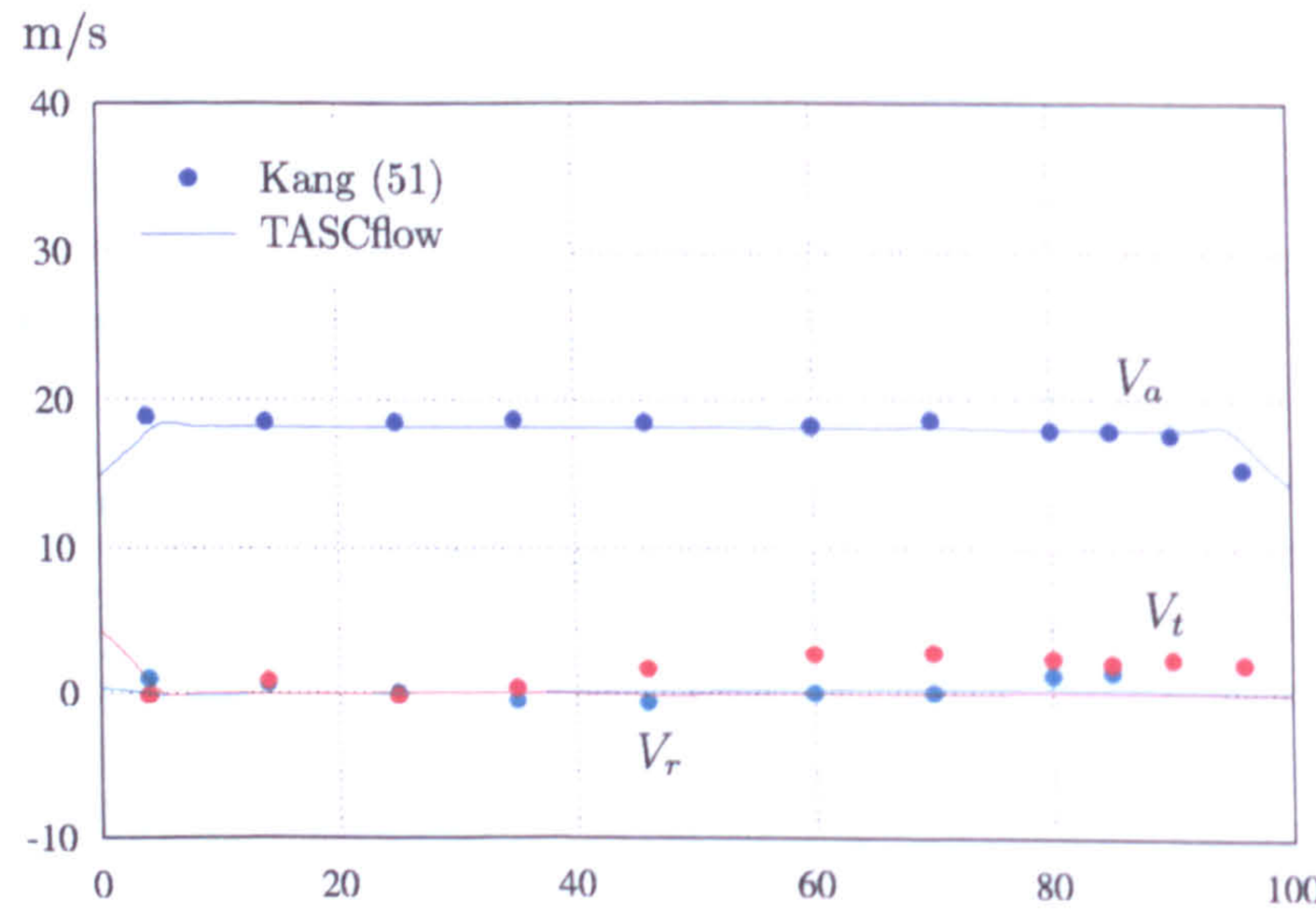

(b) At $\phi = 0.61$

Figure 6.7: Radial profile of the absolute velocity components at the inlet

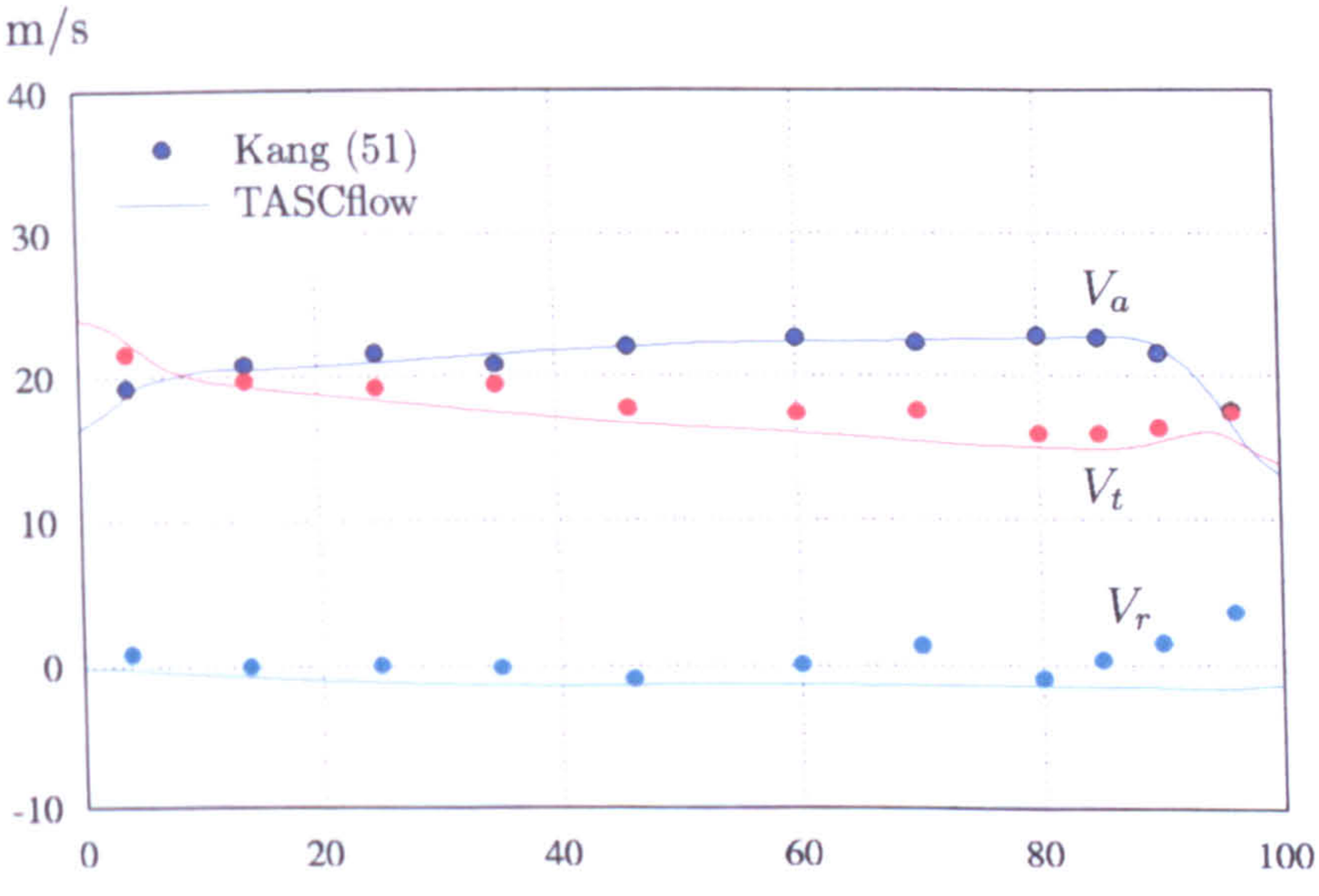

(a) At $\phi = 0.72$

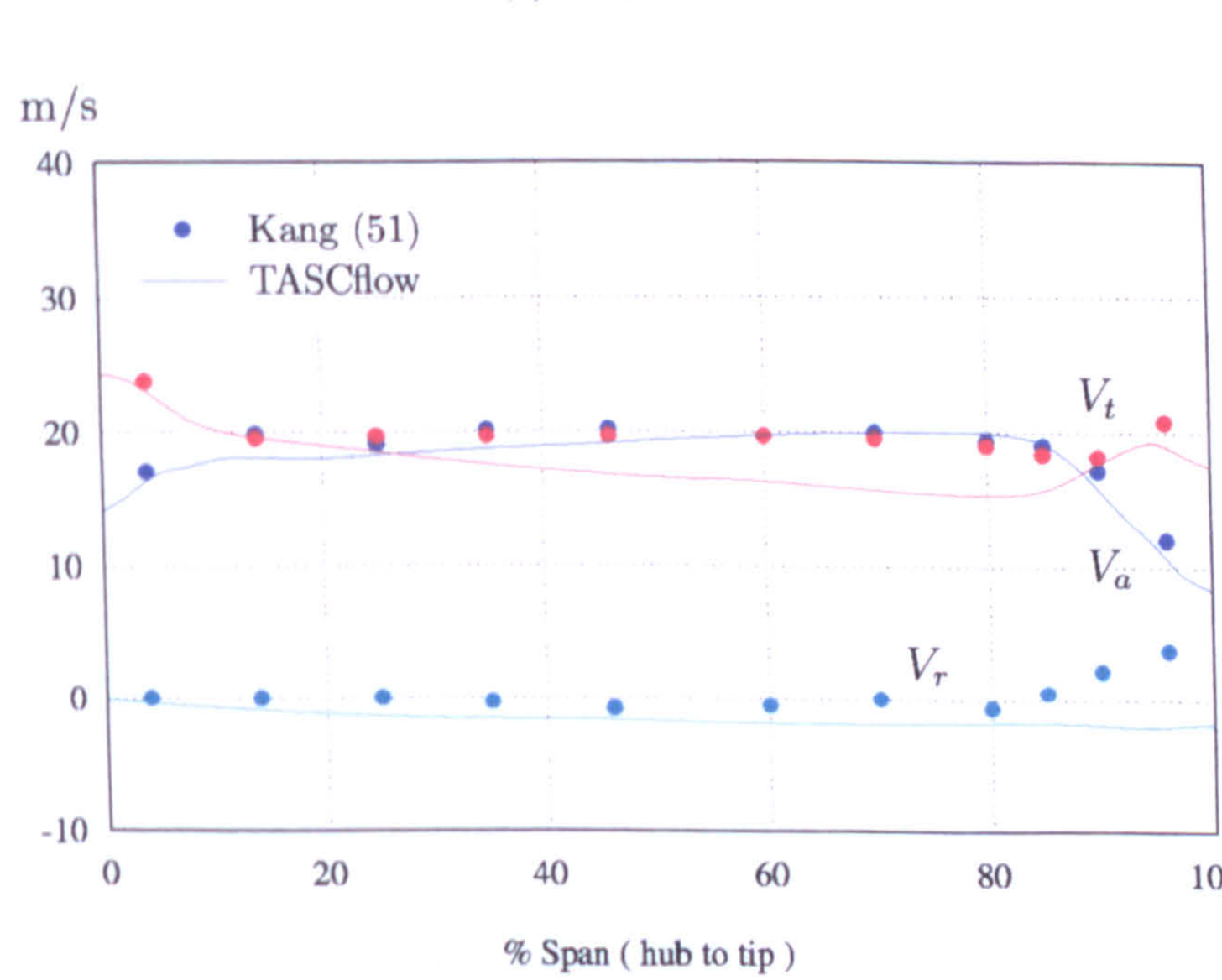

(b) At $\phi = 0.61$

Figure 6.8: Radial profile of the absolute velocity components at the outlet

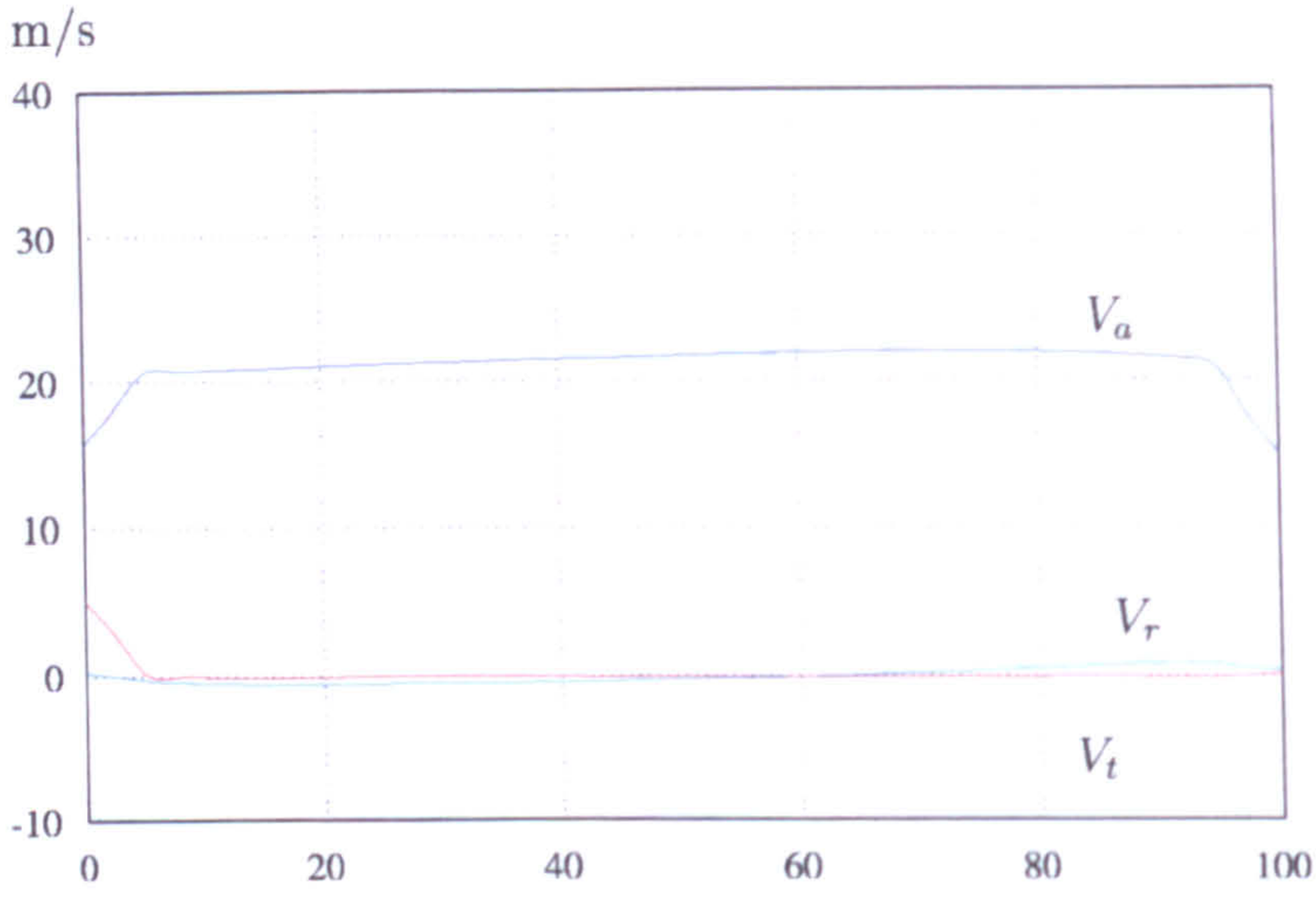

(a) At $\phi = 0.72$

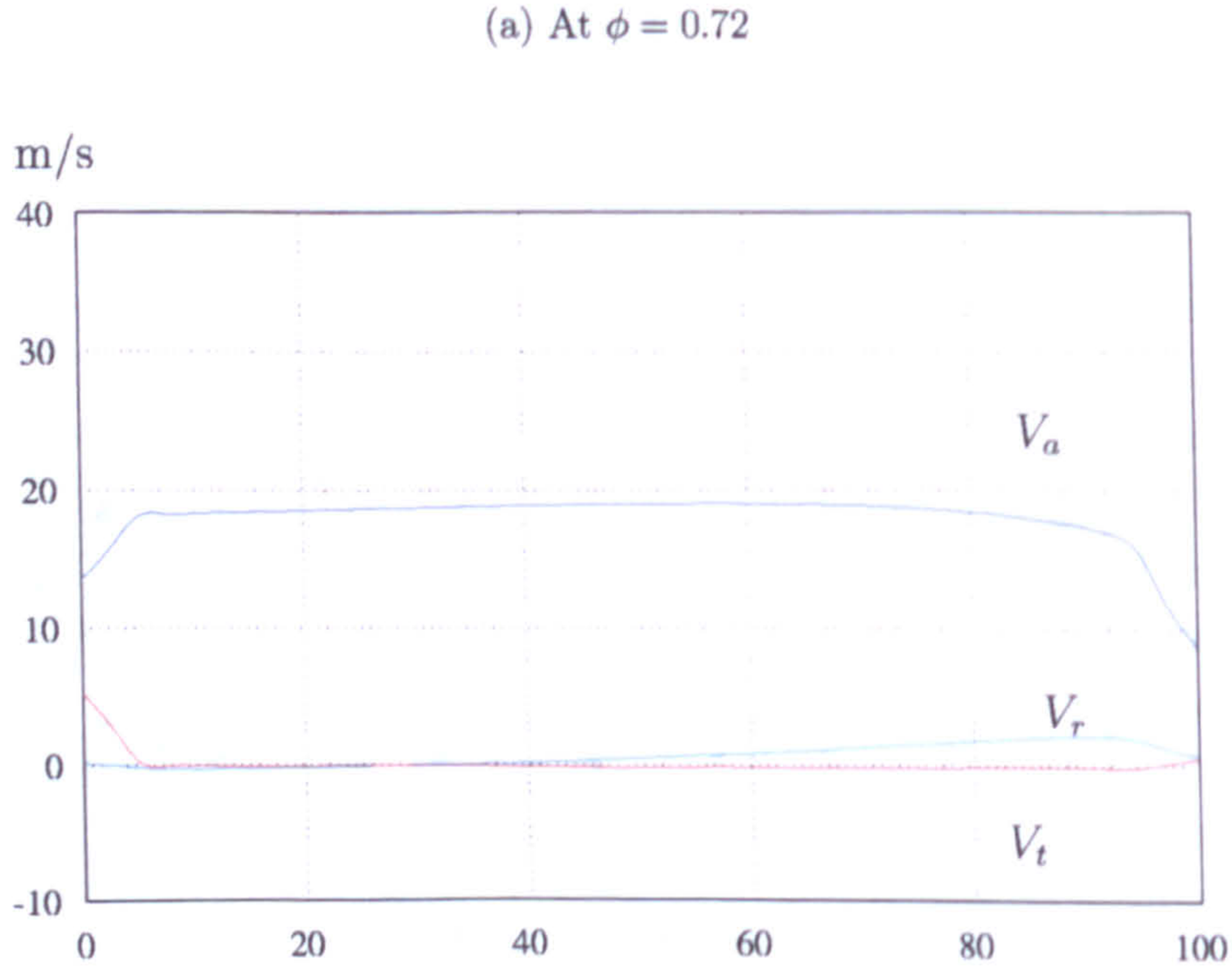

(b) At $\phi = 0.61$

Figure 6.9: Radial profile of the velocity components near the blade leading edge

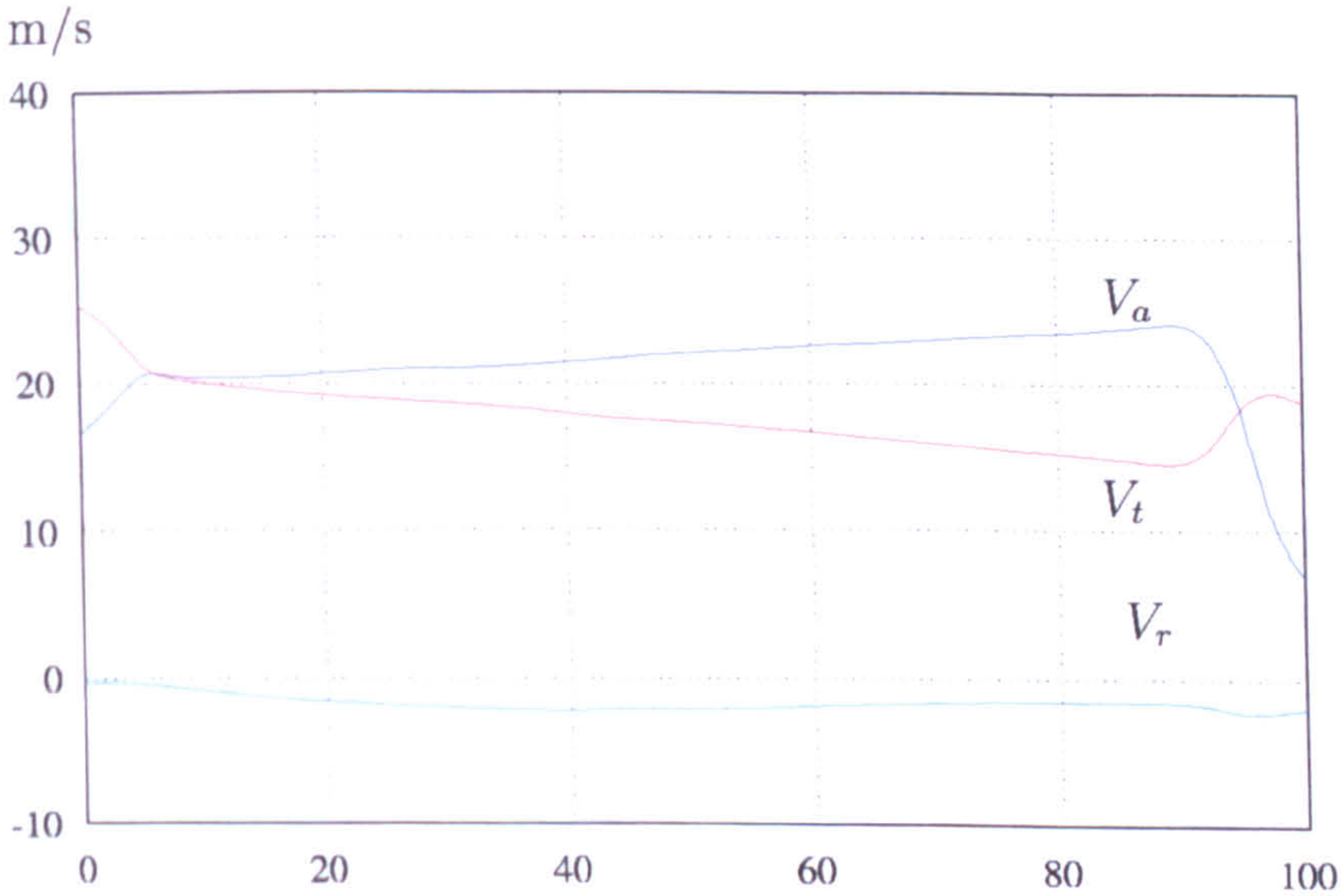

(a) At $\phi = 0.72$

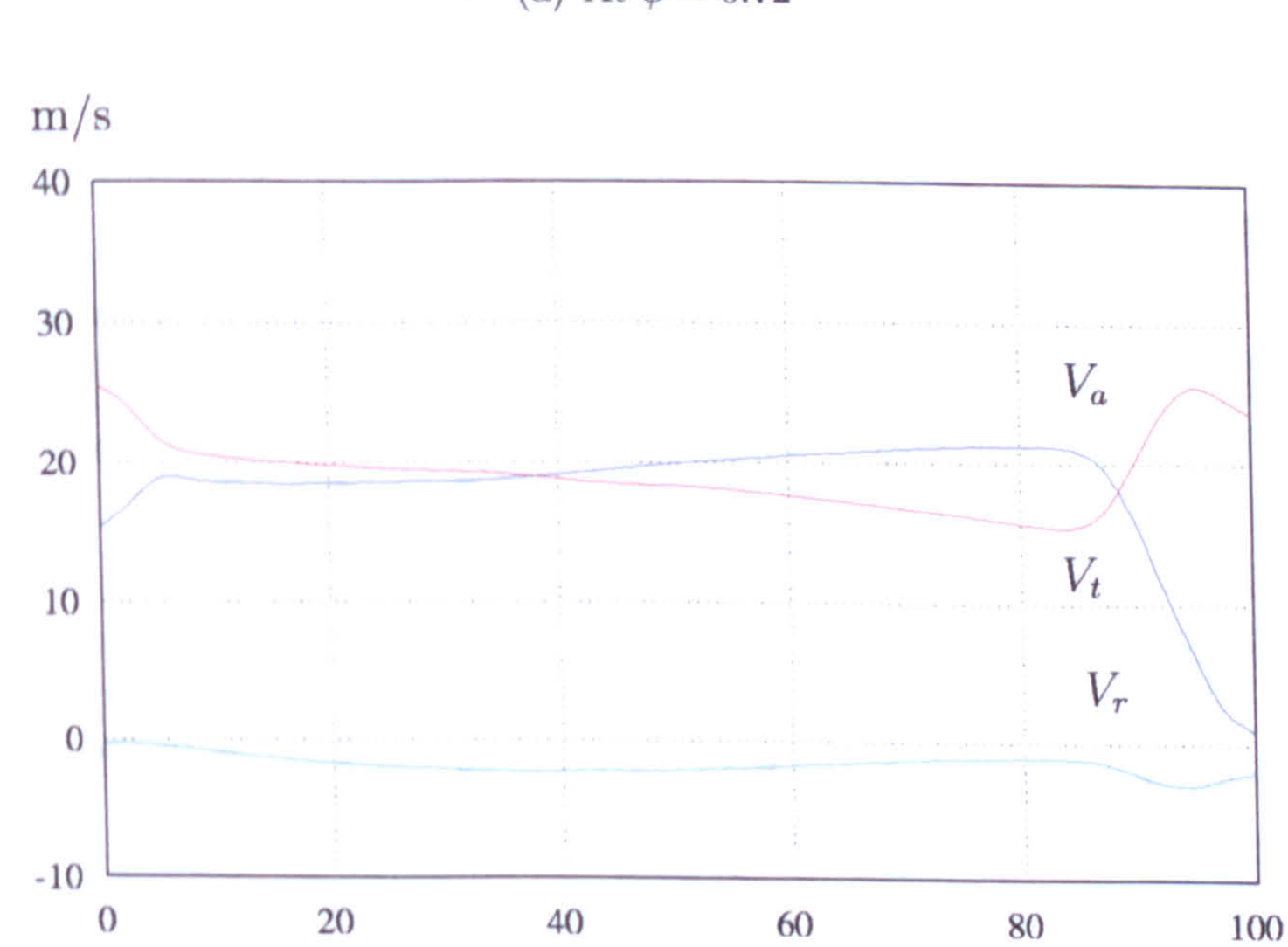

(b) At $\phi = 0.61$

Figure 6.10: Radial profile of the velocity components near the blade trailing edge

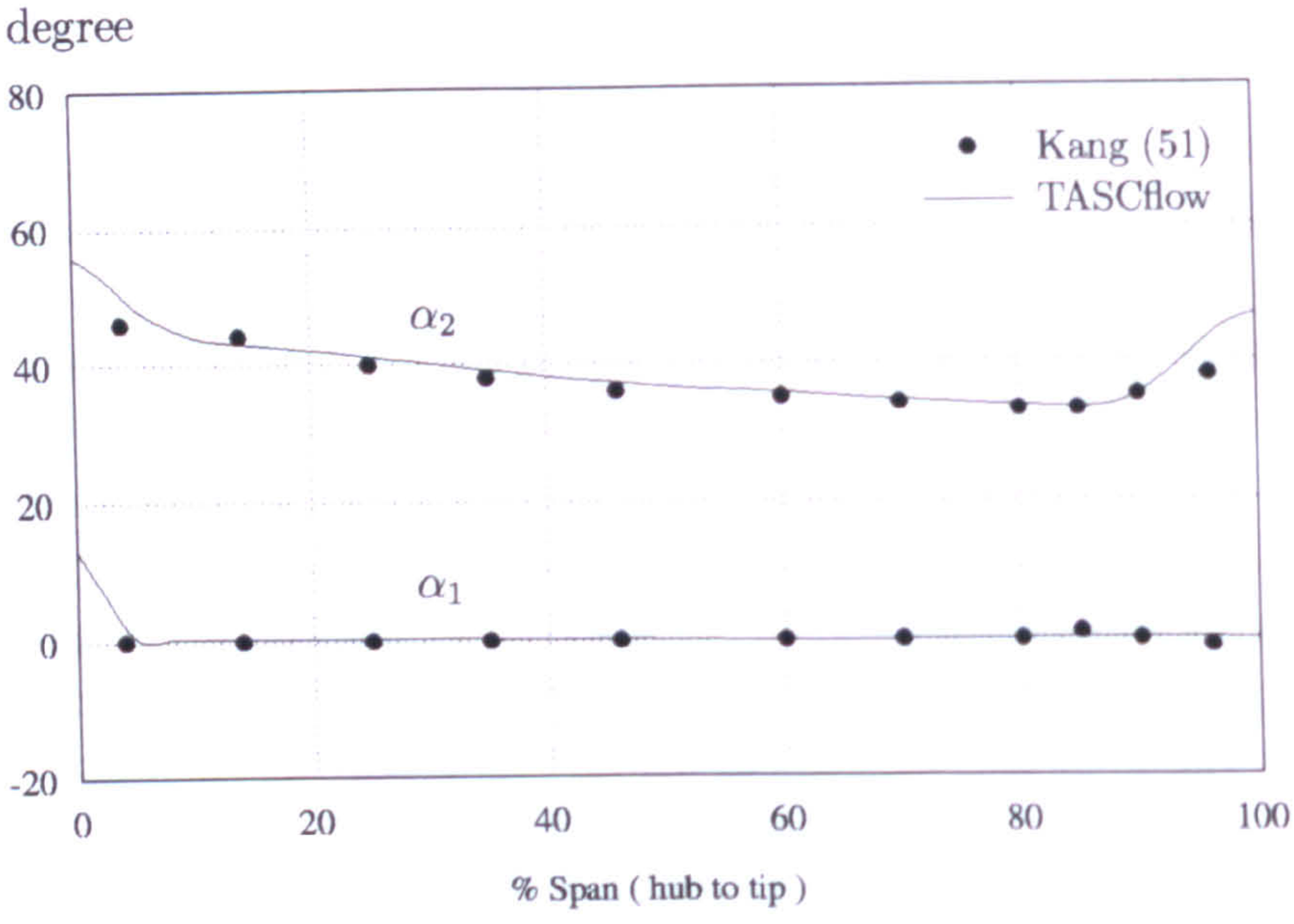

(a) At $\phi = 0.72$

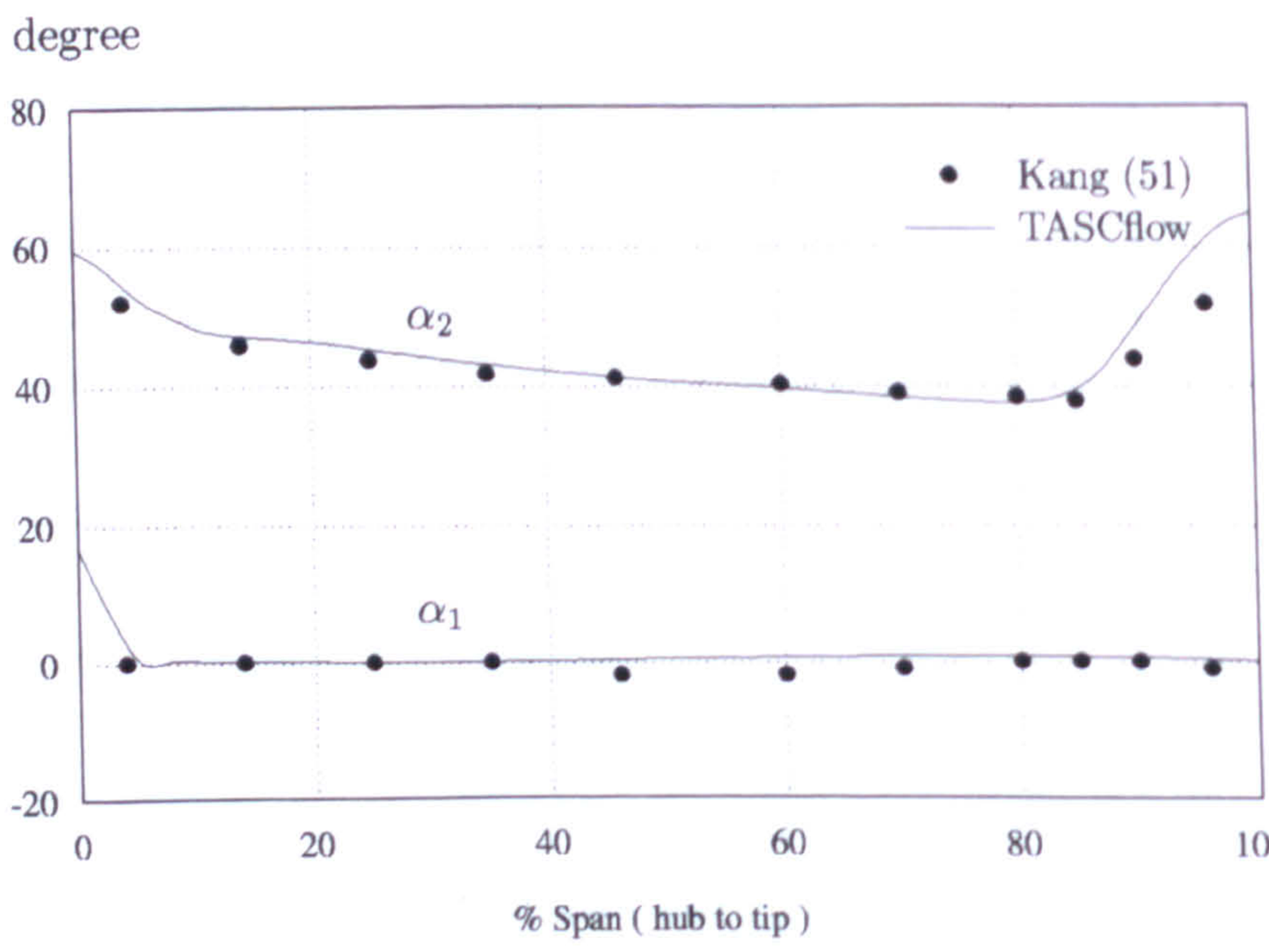

(b) At $\phi = 0.61$

Figure 6.11: Radial profile of the absolute flow angles for solid casing

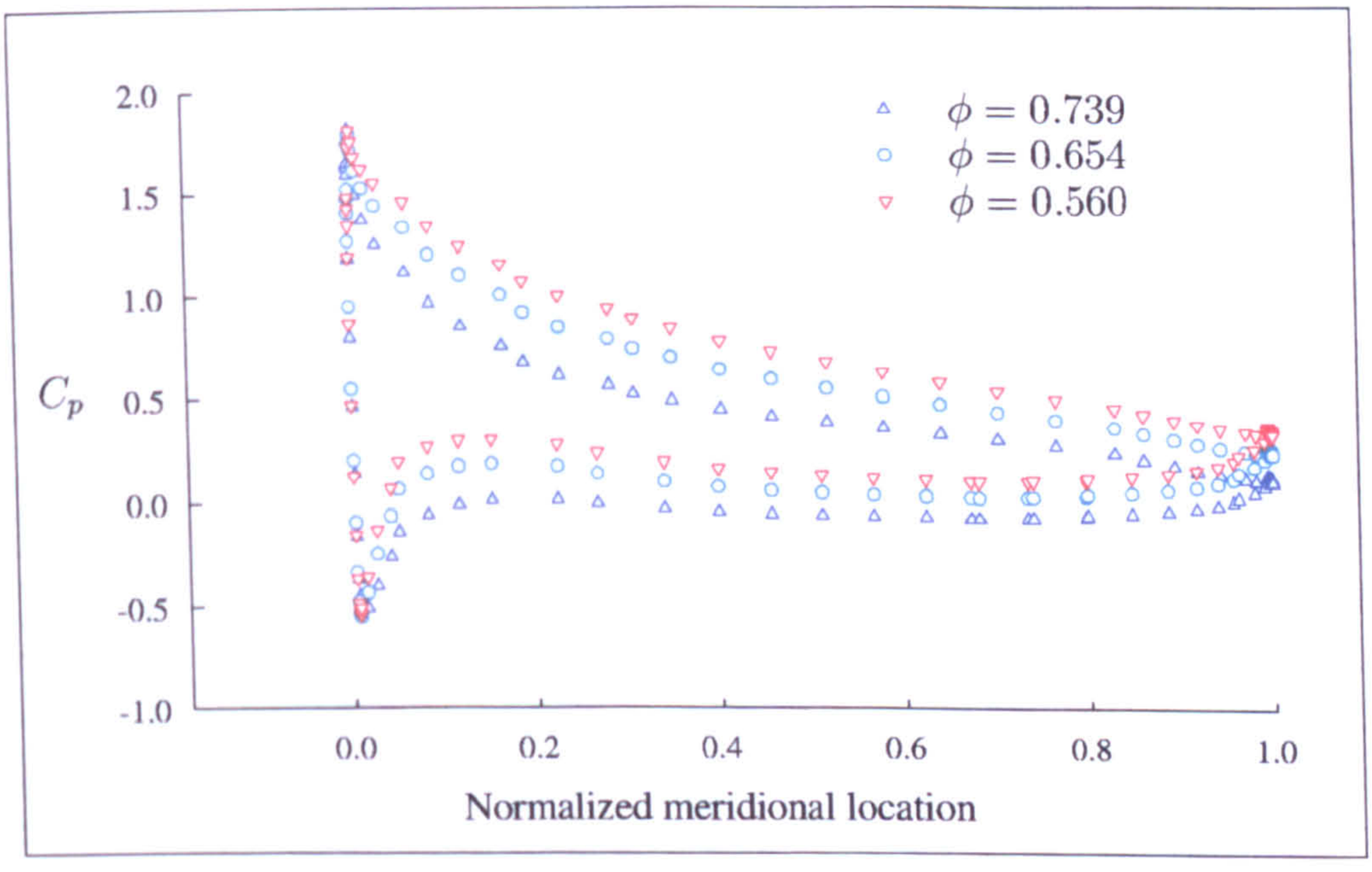

(a) Static pressure coefficient around blade at 5% span

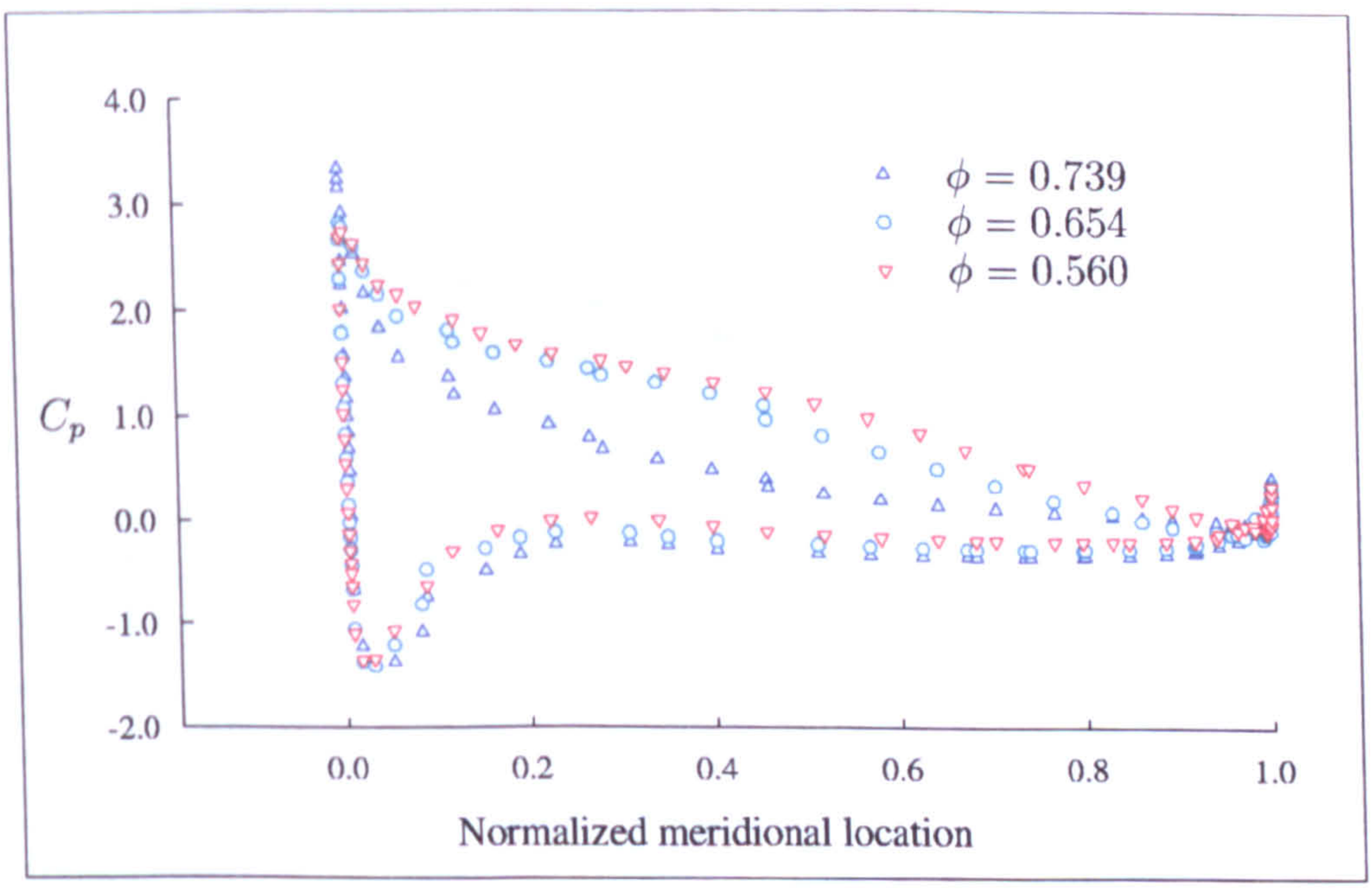

(b) Static pressure coefficient around blade at 95% span

Figure 6.12: Blade loading at different flow coefficients

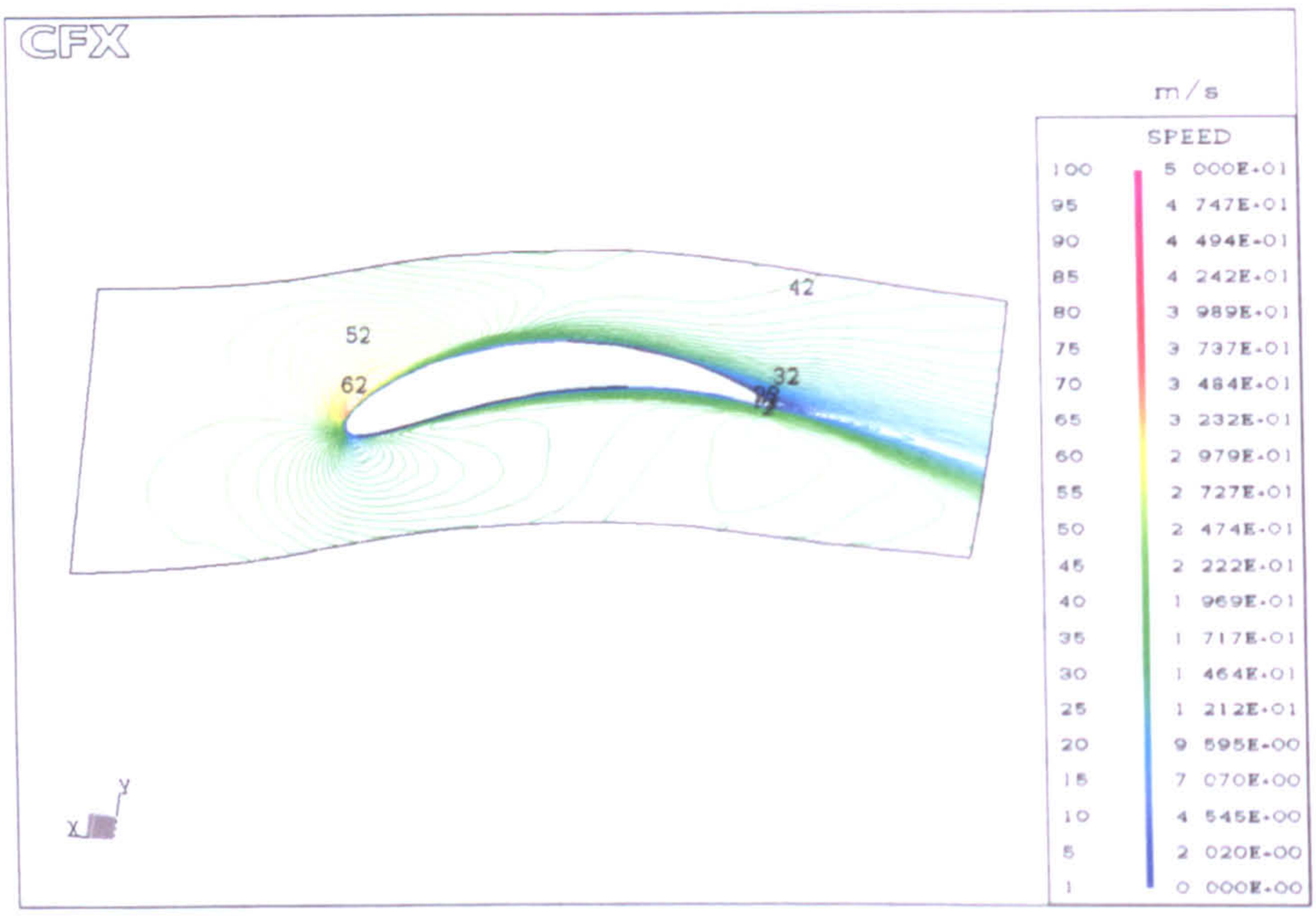

(a) At 5% span

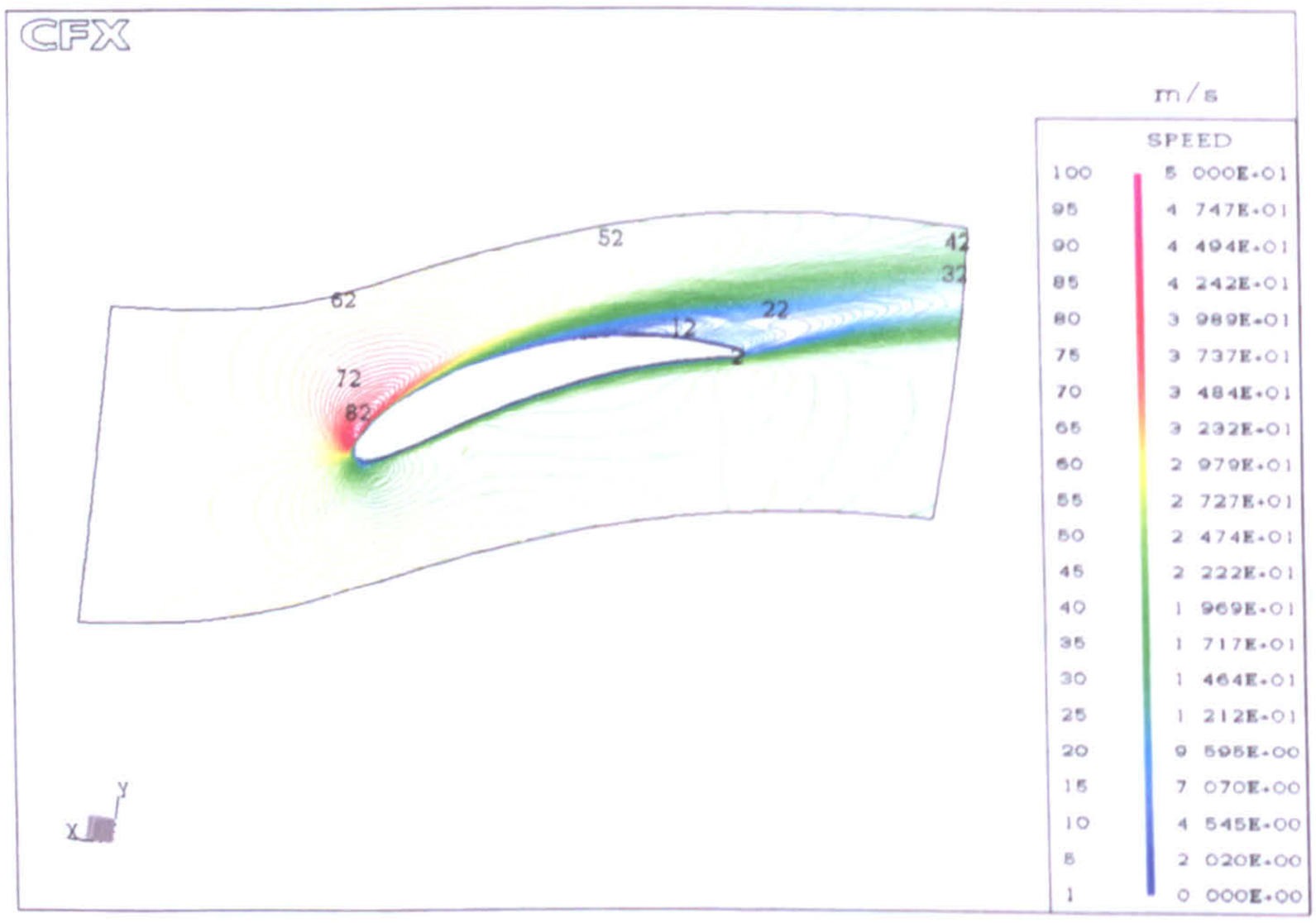

(b) At 35% span

Figure 6.13: Blade-to-blade view of speed distributions for $\phi = 0.56$

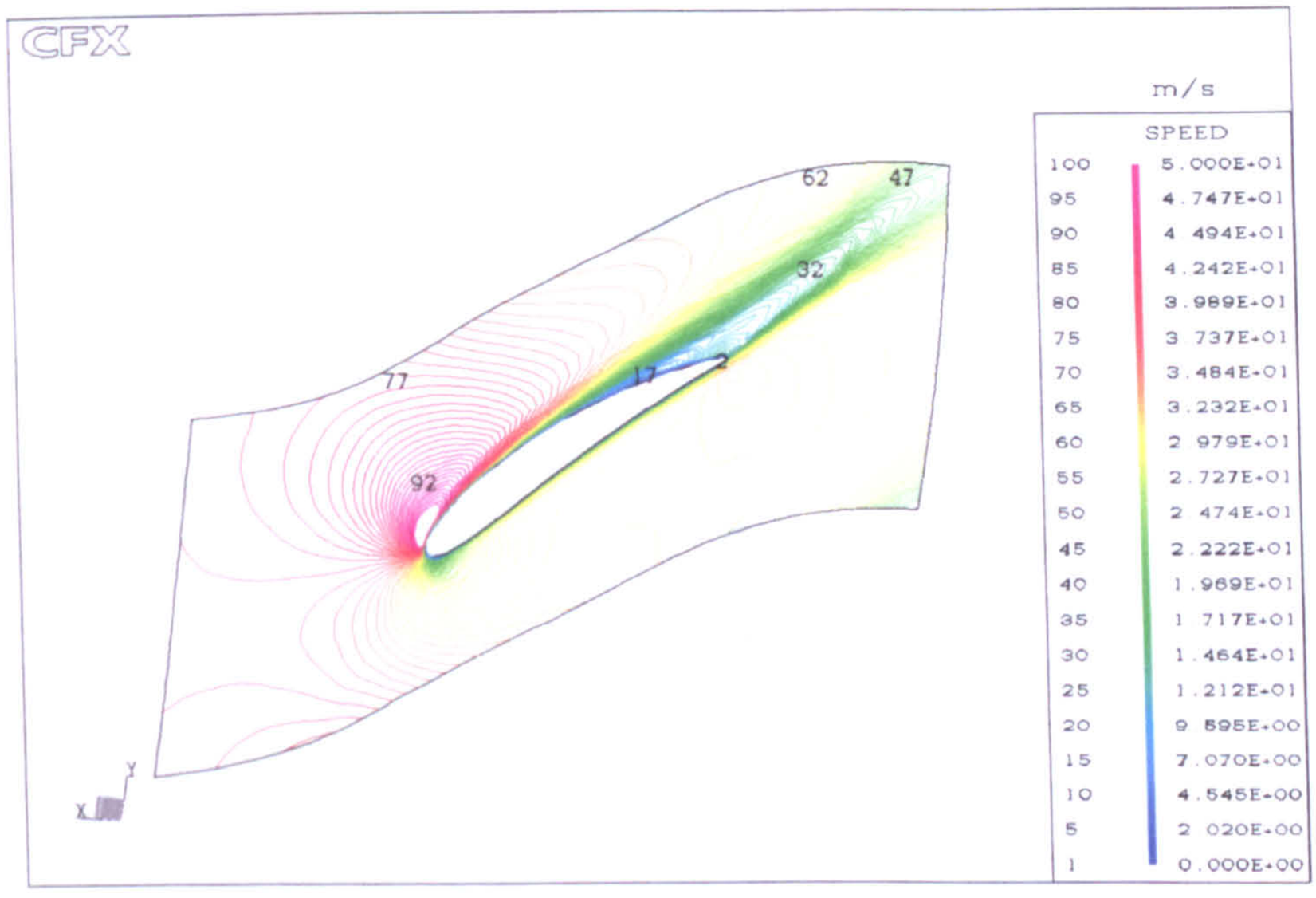

(c) At 65% span

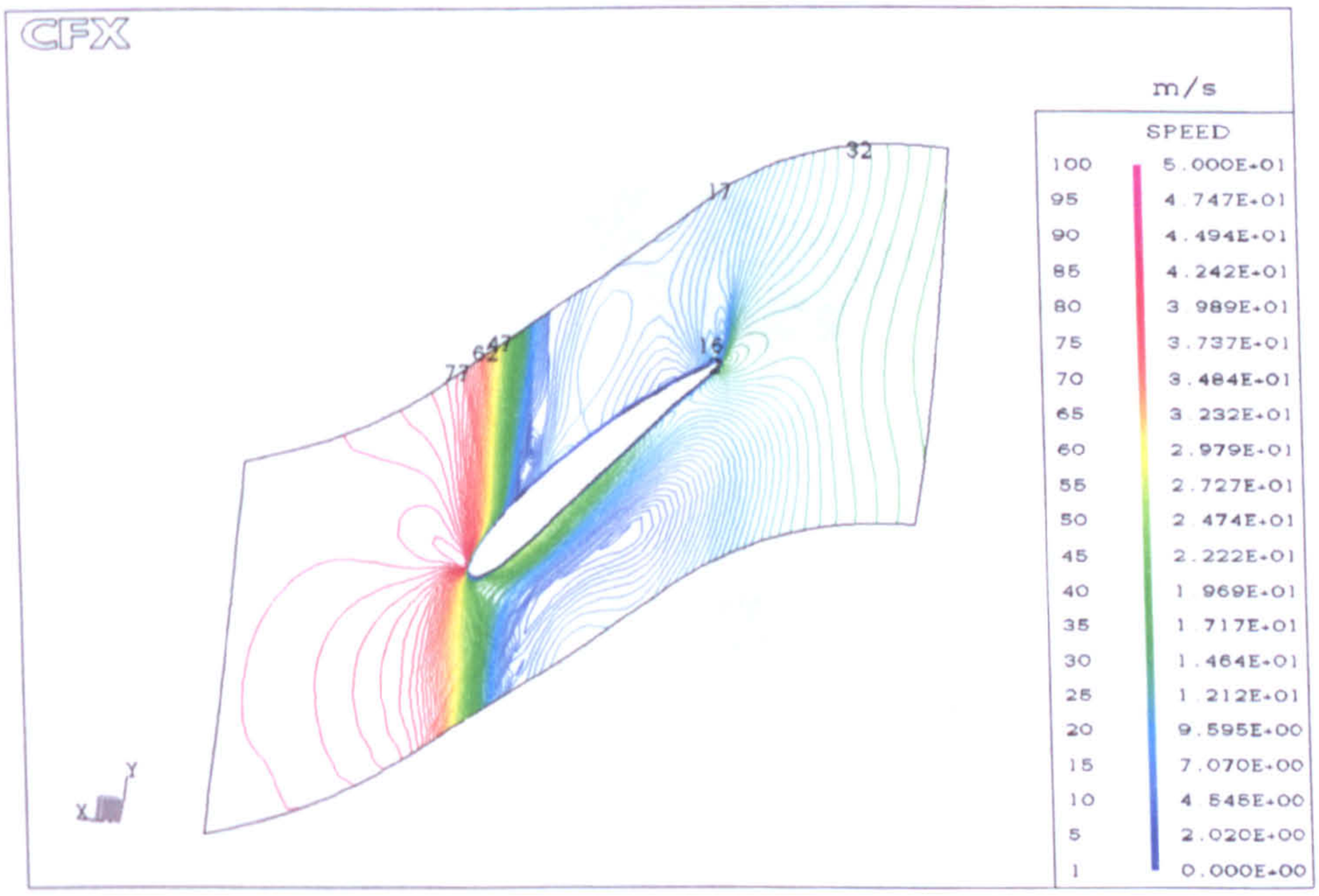

(d) At 95% span

Figure 6.13: Blade-to-blade view of speed distributions for $\phi = 0.56$ (cont.)

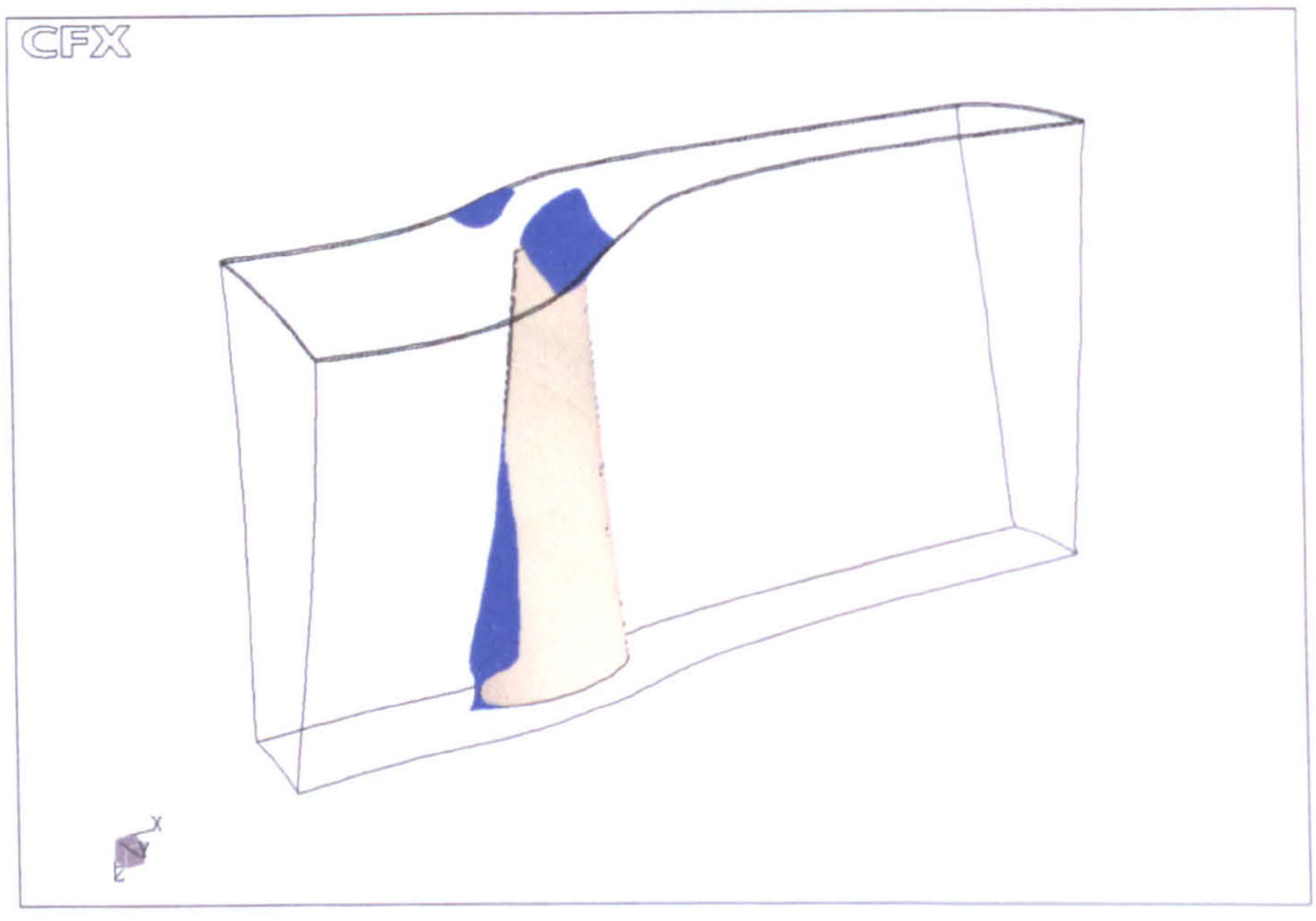

(a) At $\phi = 0.72$

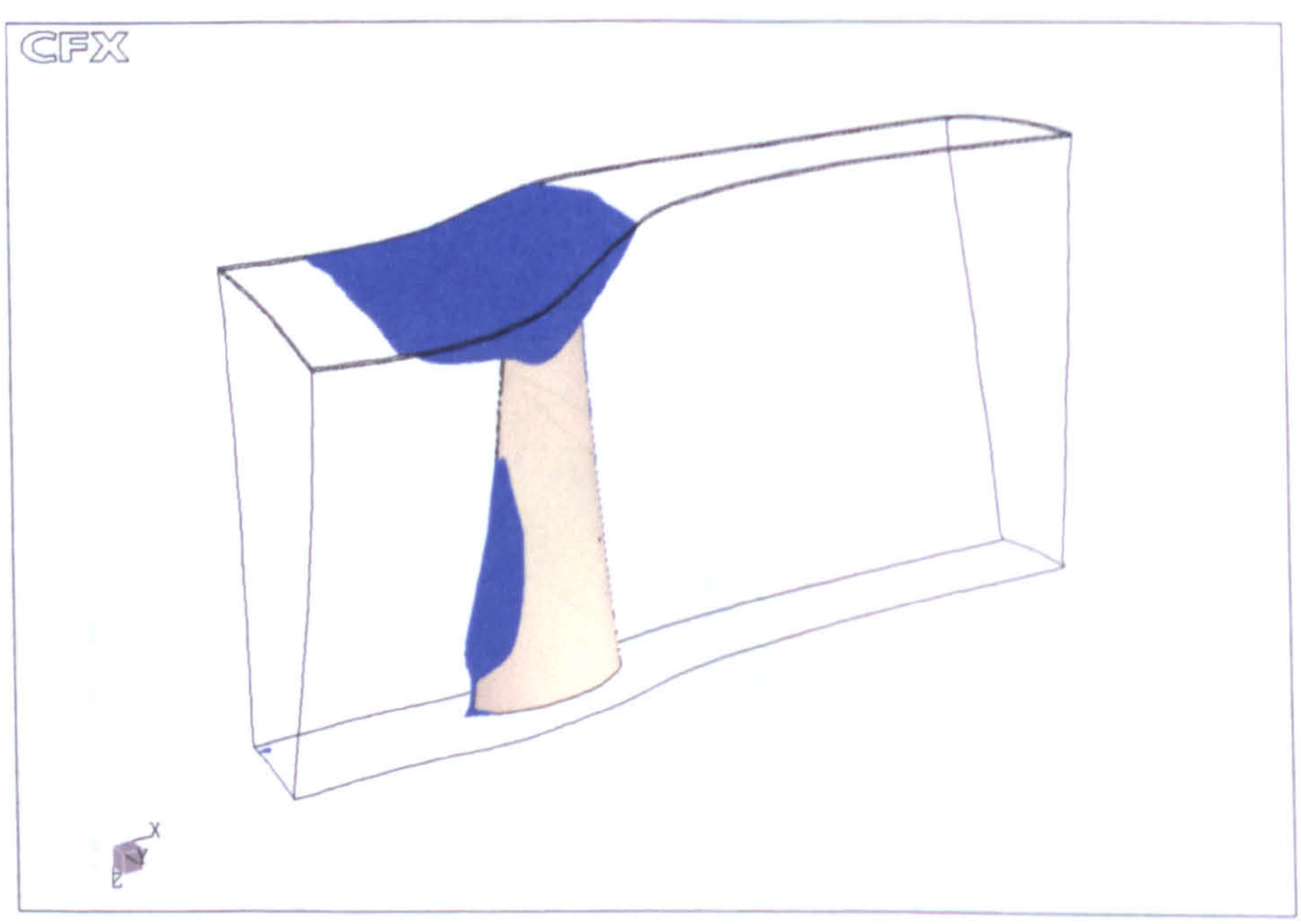

(b) At $\phi = 0.56$

Figure 6.14: Isotimic plots for solid casing at different flow coefficients

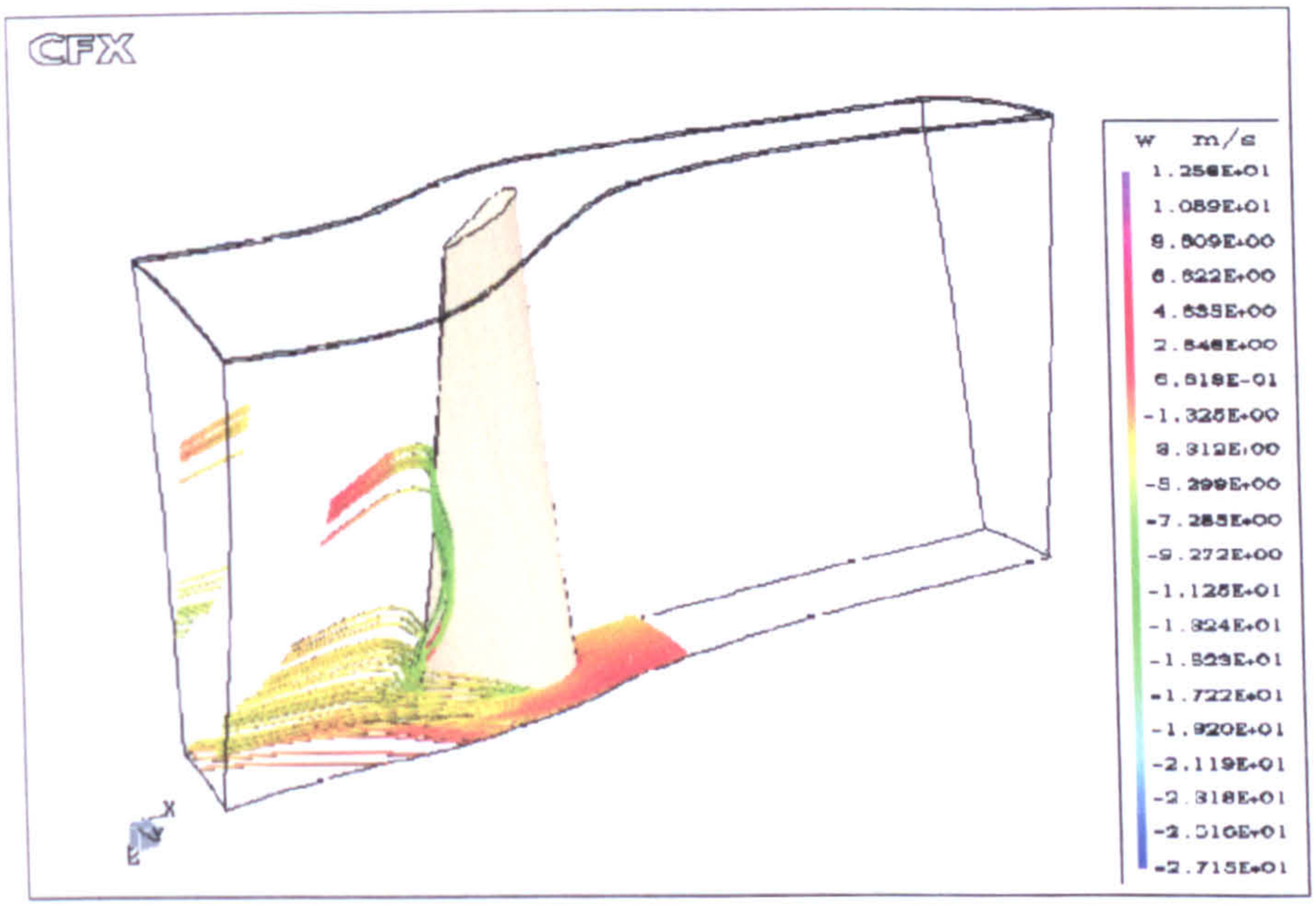

(a) At $\phi = 0.72$

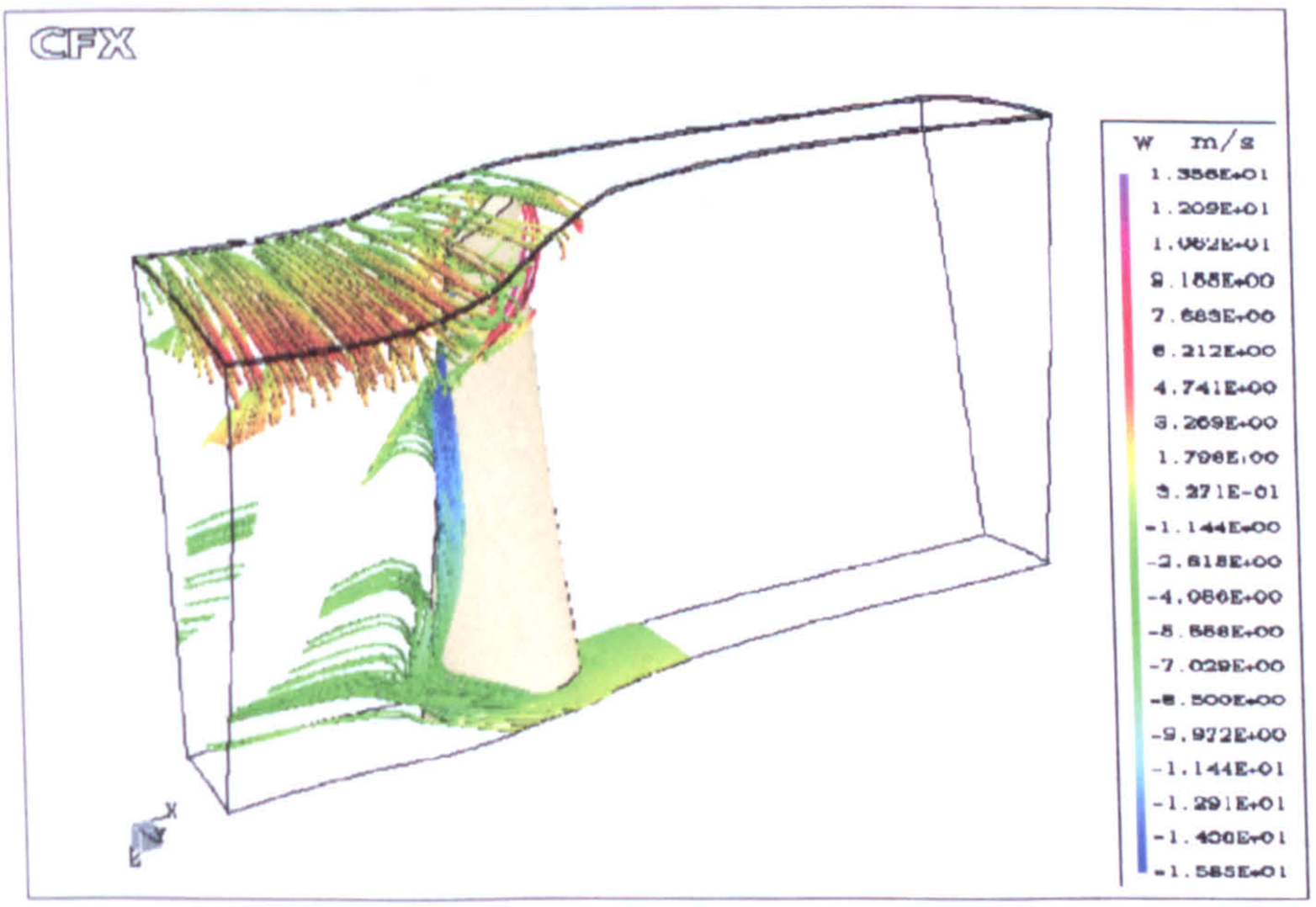

(b) At $\phi = 0.56$

Figure 6.15: Streamlines plots for solid casing at different flow coefficients

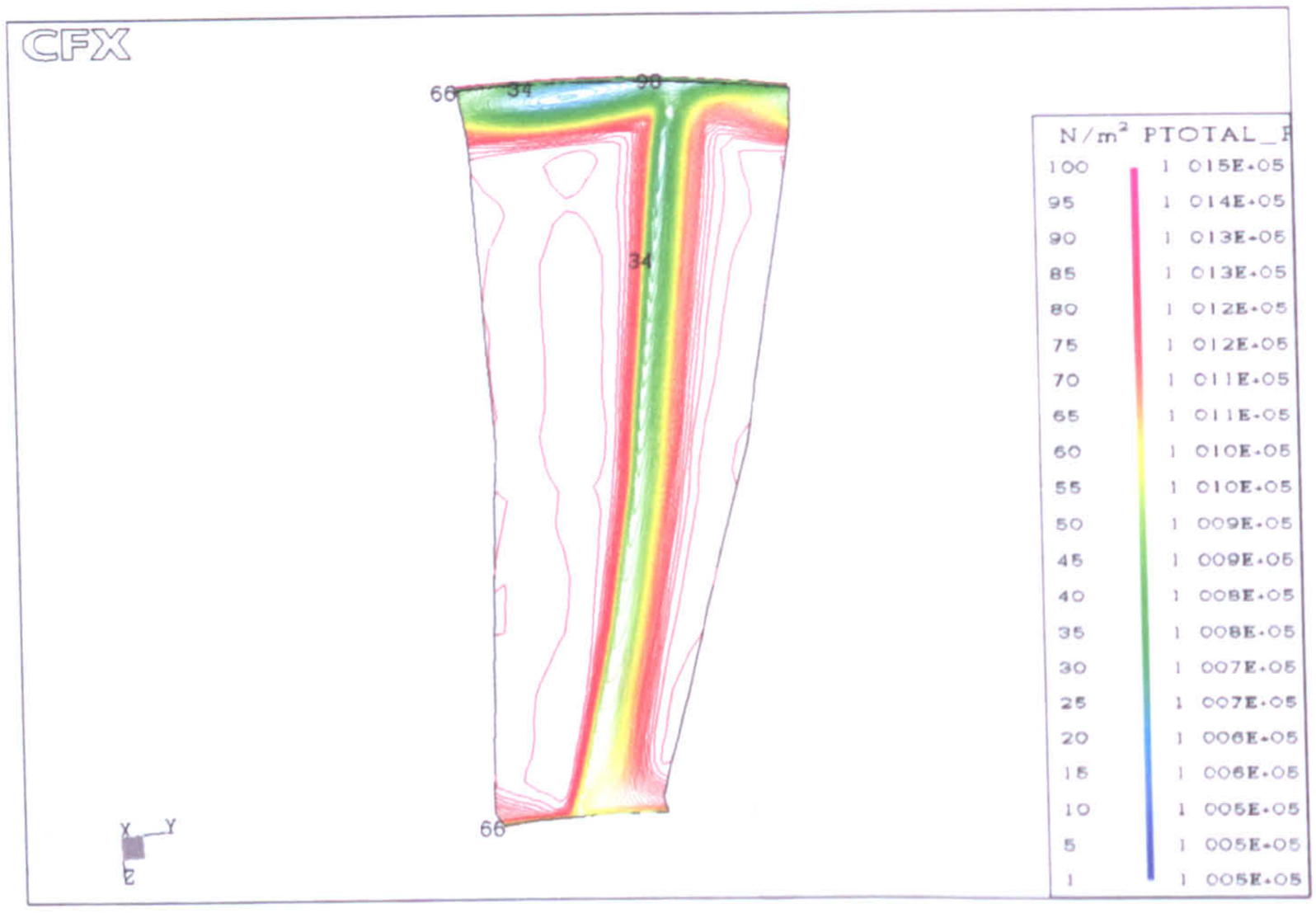

(a) At $\phi = 0.72$

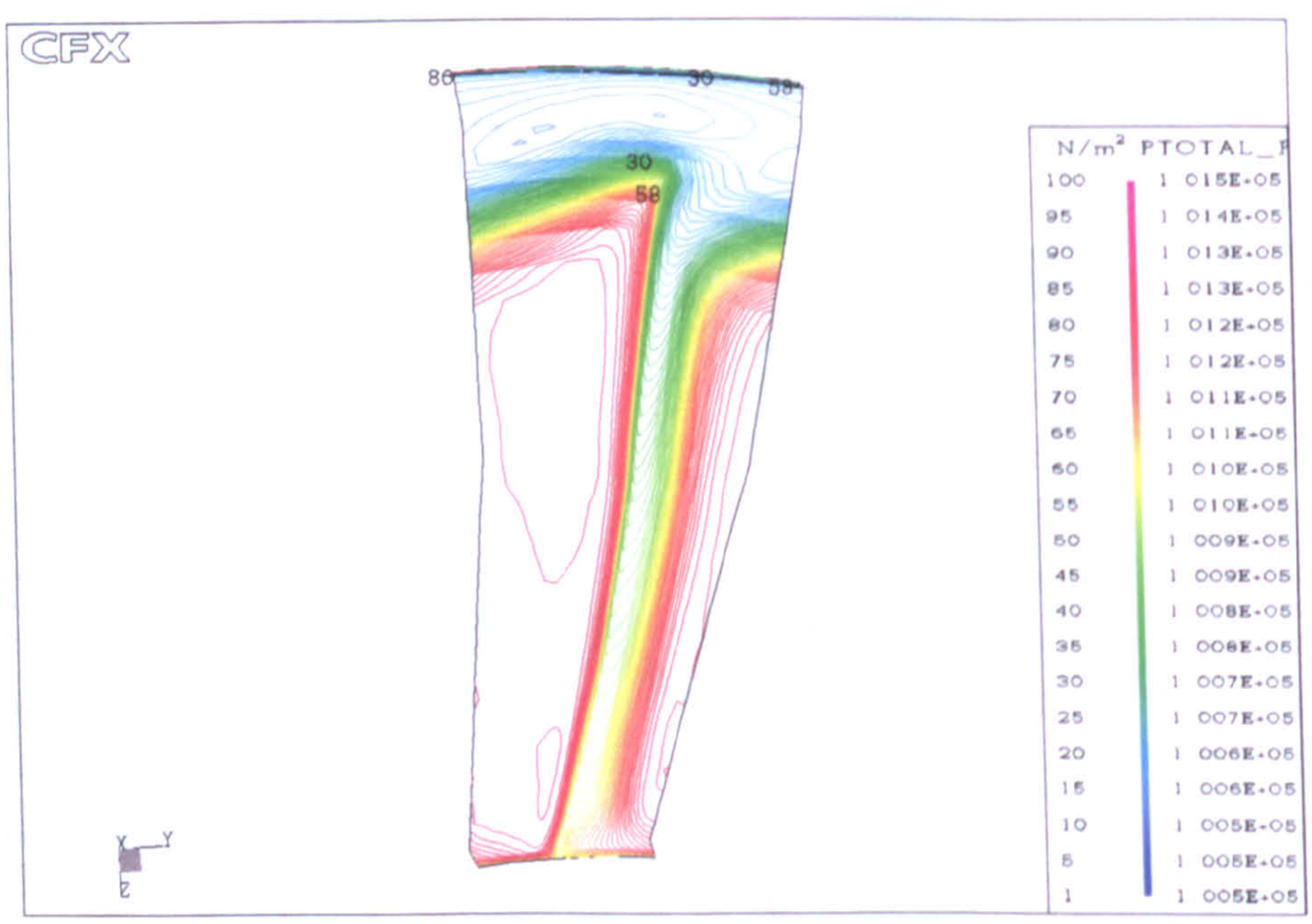

(b) At $\phi = 0.56$

Figure 6.16: Relative total pressure distributions near the blade trailing edge

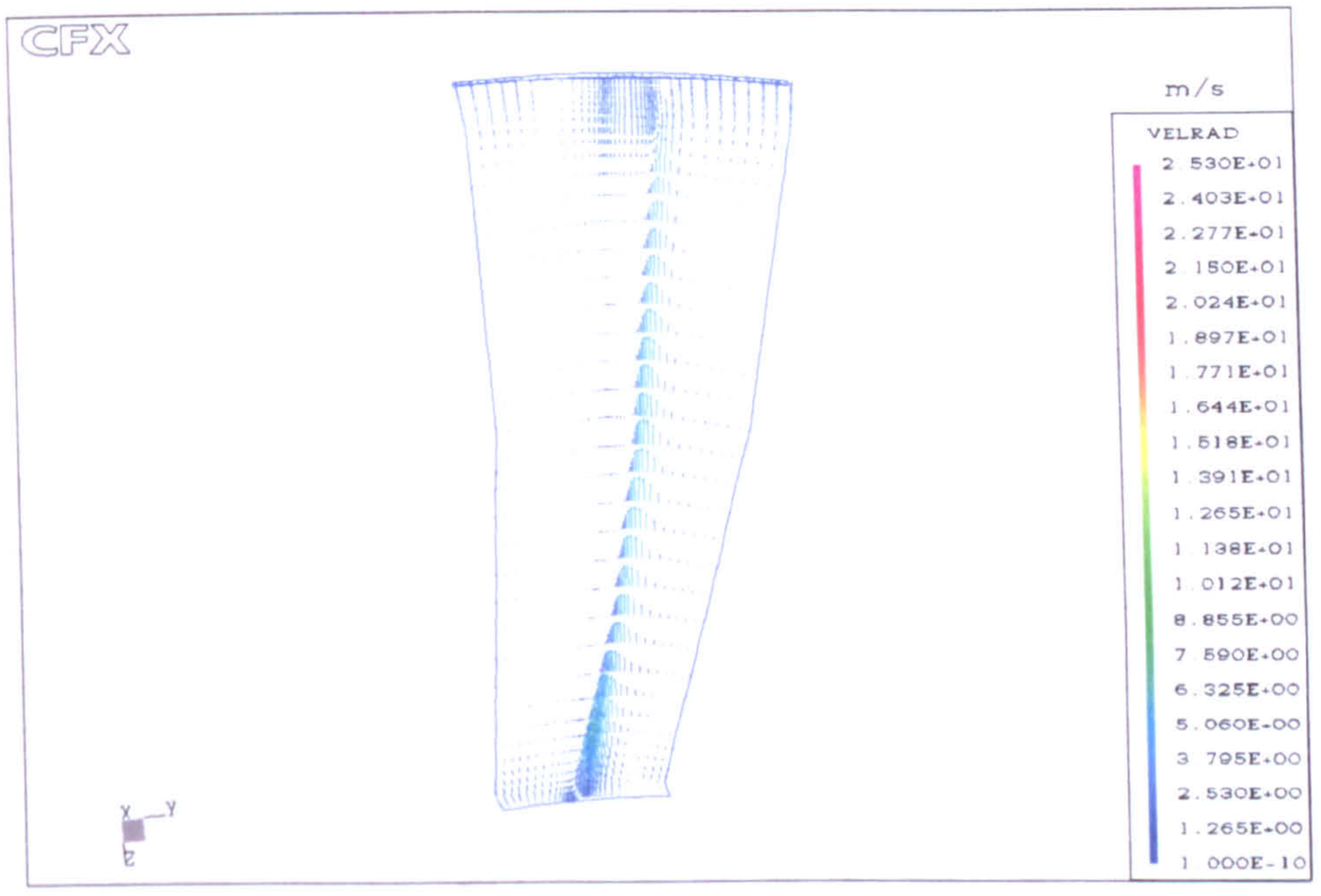

(a) At $\phi = 0.72$

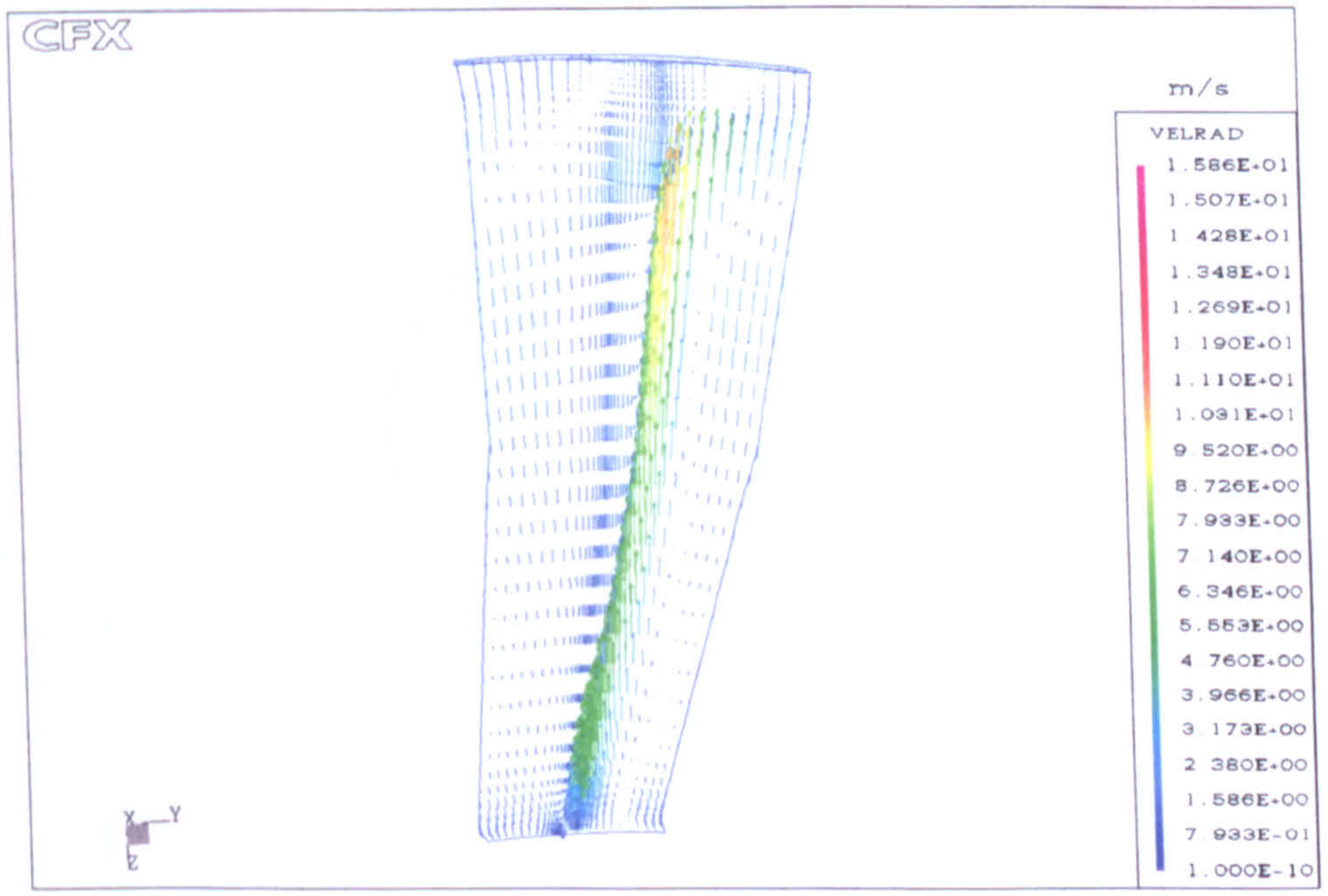

(b) At $\phi = 0.56$

Figure 6.17: Vector plot near the blade trailing edge

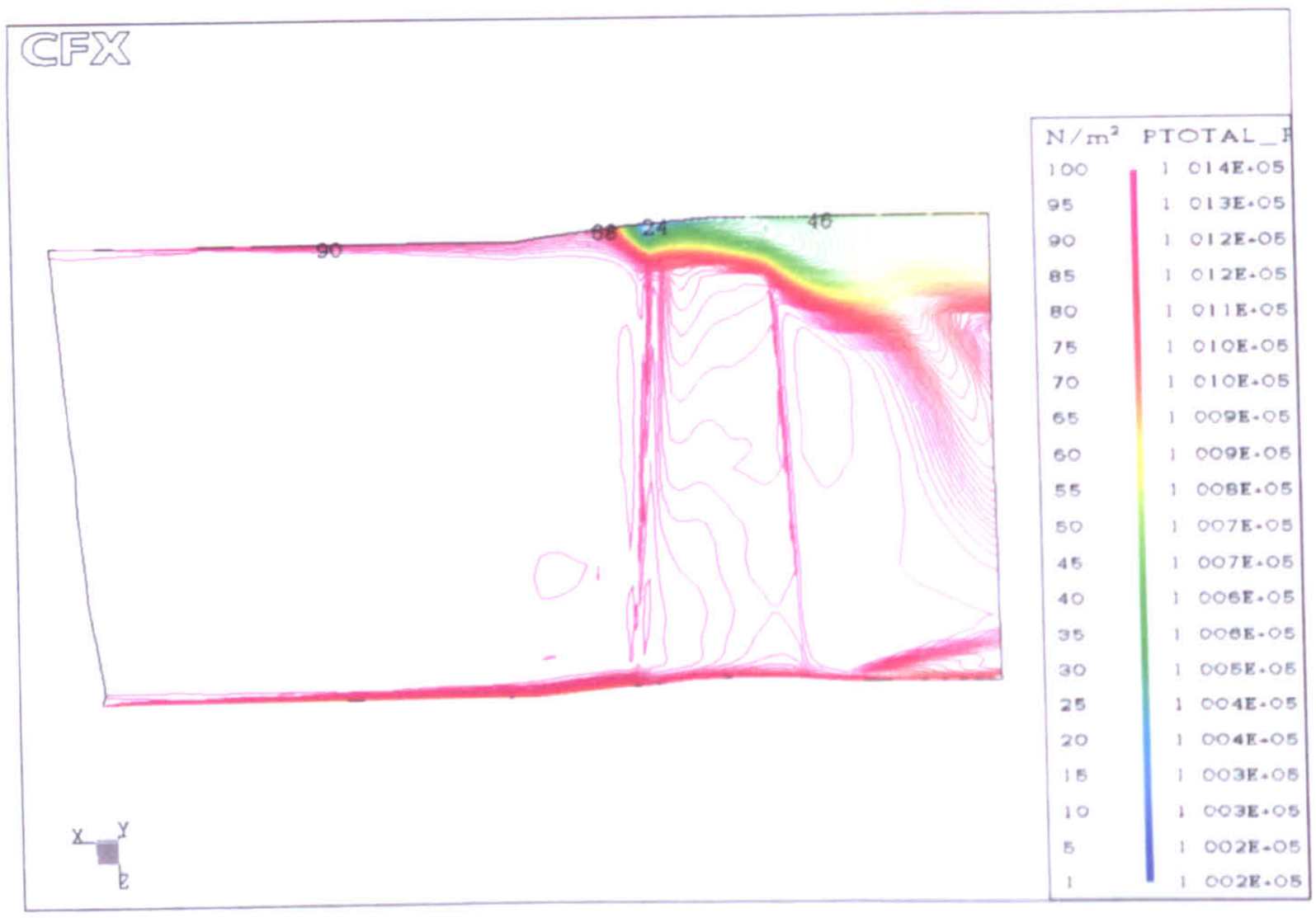

(a) At blade pressure side

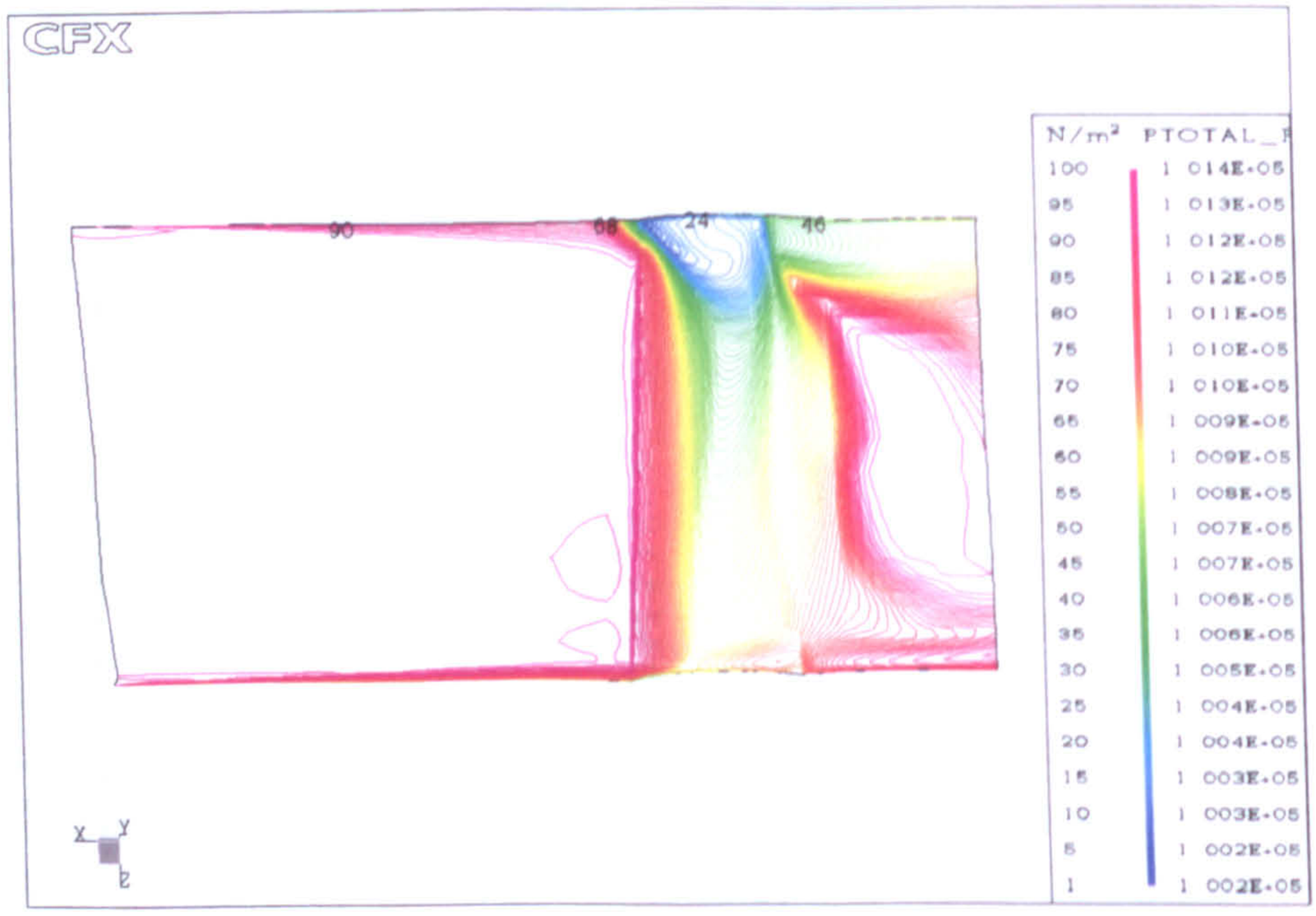

(b) At blade suction side

Figure 6.18: Meridional view of the relative total pressure at $\phi = 0.56$

7

Unsteady Simulations for Solid Casing

Practical unsteady flow measurements are complex and involve costly experimental rigs. Numerical unsteady simulations are more expensive than the steady-state ones, since they require more extensive computational resources and very large computational time. For these reasons, there are quite limited experimental and numerical results on transient unsteady flow fields. Although steady-state simulations offer a very good flow field prediction, the influence of flow unsteadiness cannot be ignored when instabilities are present.

This chapter presents two unsteady simulations for the fan with solid casing similar to that simulation carried out by März et al. (63) presented in Chapter 2, but with different boundary conditions. The first simulation was conducted on a domain with single blade passage, and the other simulation was carried out with a domain for the entire fan containing all 27 blades. For these two simulations, a transient boundary condition is specified at the domain inlet in which the total mass flow is defined as a function of time via a custom source code routine `BCDTRN` explained in Appendix B.

In this transient boundary condition the total mass flow rate is reduced by small amount from one time step to the next, starting from a value higher than the design point to a value lower than the stall point. In the simulation carried out by März et al. (63), the rotor exit pressure at the casing was gradually raised by a small

increment to obtain a flow rate lower than the stalled flow condition. One of the attractive features of this transient boundary condition of the code is the availability of dedicated files in which the flow field calculated quantities are written to individual files, one file for each time step. From these files one can investigate the flow field inside the fan domain as flow coefficient reduced.

The function, used in the source code for both simulations, is a simple linear variation of total mass flow with simulation time. This means that using a small time step will lead to a slight reduction in mass flow rate from one time step to another. The main advantage of using a small time step is that the changes in the flow field will be very small and this will reduce the number of iteration required for the simulation to converge for each time step. On the other hand, using a very small time step requires a large number of time steps to cover all the flow conditions ranging from design point to stall condition. Compromising between these two aspects, a time step of 0.001 was chosen for both simulations so that the total mass flow rate entering the domain in both simulations is reduced by 0.001 kg/s per blade passage from one time step to the next one. Even though this is a very coarse time step for unsteady simulation, the results show it is adequate to capture the related phenomena. The simulation for a single blade passage was carried out for 60 time step and the entire fan simulation for 70 time step. Table 7.1 presents the simulation time STIME, total mass flow rate $\dot{m}$, and flow coefficient ϕ at the start of selected time steps for both simulations.

Table 7.1: Transient inlet boundary conditions

(a) Single blade passage simulation

Time step	STIME	$\dot{m}$	ϕ
1	0.001	0.147	0.7497
5	0.005	0.143	0.7293
10	0.010	0.138	0.7089
20	0.020	0.128	0.6579
30	0.030	0.118	0.6069
40	0.040	0.108	0.5559
50	0.050	0.098	0.5049
60	0.060	0.088	0.4539

NB	One blade
STIME	0.148 kg/s

(b) Entire fan simulation

Time step	STIME	$\dot{m}$	ϕ
1	0.001	3.973	0.7555
10	0.010	3.730	0.7045
20	0.020	3.460	0.6535
30	0.030	3.190	0.6025
40	0.040	3.920	0.5515
50	0.050	2.650	0.5005
60	0.060	2.380	0.4495
70	0.070	2.110	0.3985

NB	27 blades
STIME	4.0 kg/s

7.1 Single blade simulation

The predicted results for the steady-state simulations of the fan with solid casing, presented in Chapter 6, highlighted the flow physics of the tip stall growth process as the mass flow is reduced. This was presented by comparing pictures of the reverse flow and its propagation at low and high flow coefficients. This phenomenon is very significant and worthwhile of further investigation by performing unsteady simulation.

7.1.1 Computational domain

The computational domain, shown in Figure 6.2, used in the steady-state simulations presented in Chapter 6 is used again for this unsteady simulation. It is a single-blade passage domain consisting of two grids, one for the main passage and a second to cover the tip region, attached together using the General Grid Interface GGI. The total number of mesh points for the domain is 200 000 points, where 100 points were used in the axial direction, 40 points in the blade-to-blade direction, and 50 points in the radial direction.

7.1.2 Boundary conditions

The average static pressure was set over the domain outlet region and a transient boundary condition was specified at the domain inlet, at which the total mass flow is defined as a function of time via a custom source code routine called `BCDTRN`. The source code is modified for this simulation so that the number of blades is fixed at `NB=1` and the initial mass flow rate at `MSTART=0.148`. Table 7.1 presents the simulation time `STIME`, total mass flow rate, and flow coefficient at the start of selective time steps.

The numerical solution is assumed to be fully converged at each time step either when the maximum residuals are less than the target value of 10^{-4} or when the number of loop iterations equals the maximum number of 50 iterations. The RNG k-ϵ turbulence model with wall functions was employed as a turbulence model, and the MLPS discretization scheme was used for the treatment of the convective term together with the PAC scheme. The shroud of the domain was made stationary in the absolute frame of reference while the rest of the domain was assumed to rotate at 1 500 rpm.

7.2 Entire fan simulation

Due to the limited resources and time consideration all the simulations carried out so far are for single blade assuming that the predicted result is the same for all the blades using the periodicity boundary condition available within the code. This is normally true at high flow rate but at low flow conditions stall cells may occur in few blades only and start to rotate in the opposite direction to the blades which is formally known as rotating stall. A powerful new machine[†] was made available at Cranfield University for a short period of time, and to utilize this machine a simulation for the entire fan with solid casing was carried out with the aim of investigating the behaviour of the flow field around fan blades near stall condition.

7.2.1 Computational domain

Since the domain used to carry out the unsteady simulation for a single blade passage consists of 200 000 node points, and using this domain to carry out unsteady simulation for the entire fan would mean a computational domain consisting of 5 400 000 nodes, which would require a high computational resource and very long time beyond the resource and time available. Hence, a new coarse grid for a single blade passage with short inlet section was generated, so that the computational domain consists of 60 000 mesh points, where 60 points are used in the axial direction, 40 points in the blade-to-blade direction, and 50 points in the radial direction.

The new grid was generated using CFX-TurboGrid software and was checked for minimum and maximum skew angle, aspect ratio and negative volume, and the necessary adjustments were made to satisfy the conditions required by the CFX-TASCflow solver. This grid was then imported to CFX-TASCbob3D 27 times, each time the new imported grid was aligned to the previous one and attached to it using the GGI interface to construct the entire fan domain with 27 blades which was consisted of 1 620 000 node points.

7.2.2 Boundary conditions

The boundary conditions used are similar to the ones used for the single blade passage unsteady simulation. The source code `BCDTRN`, used in the transient boundary

[†]Wildfire consists of 15 processors with 2 GB memory each

condition, is modified for this simulation so that the number of blades is NB=27 and the initial mass flow rate is fixed at MSTART=4.0. Table 7.1 presents the simulation time STIME, total mass flow rate, and flow coefficient at the start of selective time steps. The simulation was run for 70 time steps and each time step is completed and the numerical solution is assumed to be a fully converged either when the maximum residuals are less than the target value of 10^{-4} or when the number of iterations equals the maximum number of 40 iterations. The RNG k-ϵ turbulence model with wall functions was employed as a turbulence model, and the MLPS discretization scheme was used for the treatment of the convective term together with the PAC scheme. The shroud of the domain was made stationary in the absolute frame of reference while the rest of the domain was rotating at 1 500 rpm.

7.3 Results and discussion

Total to static pressure rise coefficient ψ for the single blade passage simulation is calculated at each time step and presented as a function of the flow coefficient ϕ in Figure 7.1. The predicted result showed a continuous increase in the pressure coefficient as the mass flow was reduced until the 41^{th} time step corresponding to flow coefficient of 0.5508, the pressure coefficient started to drop as flow coefficient is further reduced. This simulation was run for 60 time steps on a Compaq XP1000† and was completed after two days with an average 1.25 time step/hour. Even though the simulations used a coarse time step, the result of the simulation shows that it is adequate to get a converged solution as can be seen in Figure 7.2, which presents a sample from the monitor output result at midway of the single blade passage simulation. It presents the final iteration of the 29^{th} time step where the mass flow coefficient is 0.119 and the beginning of the 30^{th} time step where the simulation time, STIME, is 0.030.

The flow separation inside the domain is next discussed with isotimic plots presented in Figure 7.3. The blue shaded areas in these plots depict the presence of axial velocities, whose direction is the opposite of that of the main stream. The extent of this reversed flow as flow coefficient is reduced is clearly illustrated in the plots shown for the selected time steps. A small separated flow region at the blade tip is shown in Figure 7.3(a) near design flow coefficient of 0.7203. As mass flow rate is further reduced, Figure 7.3(b), this region is extended from just near the blade trailing to all the blade suction side at the tip. At the same flow condition another flow separation area started to grow also at the tip but from the blade pressure side.

†It has a single Digital alpha EV6 processor with 1 GB memory and 500 MHz speed.

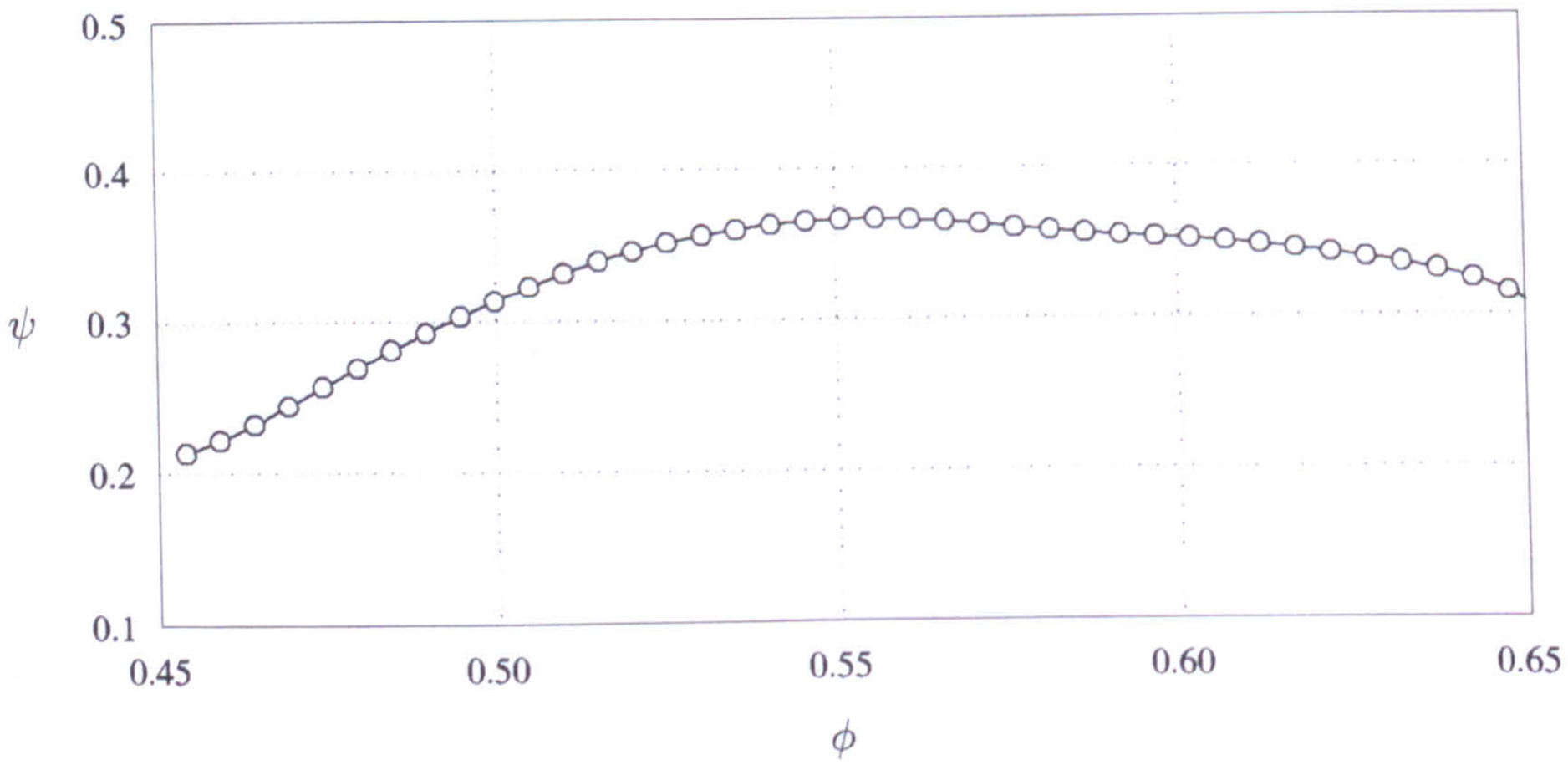

Figure 7.1: Pressure rise coefficient at selected time steps

These regions contain locally induced separation due to high blade loading and tip clearance and eventually they join together as the mass flow is further reduced as shown in Figure 7.3(c).

A new region of reverse flow start to develop at trailing edge of the blade suction side near the hub. This separated flow is continuously expanded to some three-quarters of the blade height in Figure 7.3(c) and further more in Figures 7.3(d) and 7.3(e) as the mass flow rate is reduced. A comparison between these three isotimic plots show that fairly similar amounts of flow separation are present at the tip region for these flow conditions and that near the blade trailing edge the extent of the stalled region is much more affected by the reduction in mass flow rate. Ultimately the stalled flow near the blade trailing edge reaches the blade tip, Figure 7.3(f), and combined with the separated flow already existing from the tip clearance. Any further reduction in mass flow rate will result in a drop in pressure rise coefficient and extension of the separated flow at the tip, Figure 7.3(g), until it inhabits most of the tip region over the blade and domain outlet, Figure 7.3(h).

The propagation of the reverse flow observed at blade trailing edge as mass flow rate is reduced is presented in Figure 7.4. The streamlines correspond to fluid particles released upstream of the blade root leading edge, region [25,1:40,2:3]. In the high flow rate condition, the near hub seeded fluid particles roll into a vortex extending along the blade suction side near the trailing edge. As mass flow rate is further reduced, the bulk of these particles can be seen to have been ejected towards

the outer casing and occupy this through a mechanism of radial low momentum flow transport. These plots provide evidence that the transport process is the main contributor to the very large separation observed in the shroud region, Figure 7.3(h), and the tested fan is prone to the tip stall behaviour, which characterizes tip critical machines for which the large recess casing in particularly suitable.

The pitchwise view of the radial distribution of the relative total pressure just behind the trailing edge is presented in Figure 7.5. At high flow rate condition the losses are shown at the blade tip and behind the trailing edge due to flow separation. The growth of these separated flow and losses are demonstrated with the reduction of mass flow rate in these plots. Figure 7.6 presents blade-to-blade distributions of the speed at the blade mid-span. The separated flow at blade trailing edge at high flow rate can be seen extending to some three-quarters of the blade suction side at low flow rate.

The entire fan simulation is next discussed with the total to static pressure rise coefficient ψ for the fan was calculated for each blade row and presented as a function of flow coefficient ϕ in Figure 7.7. As flow coefficient decreases the pressure coefficient increases until a flow coefficient of about 0.5. This slight increment in the pressure rise agrees with the one previously observed in the steady-state simulation results presented in Chapter 6 and shown clearly in Figure 6.3.

As flow coefficient is further reduced below the flow coefficient of 0.5, stall point, the similarity of the pressure rise coefficient distribution observed for all blades at high flow rate is no longer exist, and three distinct regimes of pressure rise can be identified in the contour plot. A very large region with very low pressure coefficient covering approximately half of the blades and another region covering one third of the blades, at which the pressure coefficient continues to rise and final region in between these two extreme regimes.

The flow separation inside the fan domain is presented in isotimic plots, Figure 7.8, in which the red shaded areas depict the presence of axial velocities, whose direction is the opposite of that of the mainstream. Similar findings to that of one-blade row simulation were observed with this simulation as flow condition changed from high flow rate to approximately flow coefficient of 0.50. For this flow range, flow separation areas at the tip of the blades and at the trailing edge of the blades suction side near the hub start to develop and expand as the flow coefficient is reduced, as shown in the consecutive Figures 7.8(a) to 7.8(c). As the flow coefficient is further reduced beyond that range, the separated flow at the trailing edge joint the separated flow already exist at the tip to inhabit the tip region of around half of the blades, Figure 7.8(d). This large separation is further expanded to two-third of the blades at very low-flow coefficient, Figures 7.8(e) and 7.8(f).

The other isotimic plots presented in Figure 7.9 describe those areas in the fan domain, in which the flow speed is less than 5 m/s. In addition to the blades and hub surfaces only a small region near the hub is shown to have low-speed at high-flow condition, Figure 7.9(a). This small region is gradually increased as flow coefficient decreased and another region with low-speed is developed and expanded at the tip of blades, Figure 7.9(b). Below flow coefficient of 0.5 the low-speed flow at the hub starts to move opposite to the blade direction and gather near the hub of half the blades and the low-speed flow at the tip also gather at only few blades, Figures 7.9(c) to 7.9(f). At low mass flow rate more flow with low-speed is transferred to those two places, Figures 7.9(g) and 7.9(h).

The extent of flow separation inside the domain demonstrated by the isotimic plots is also shown in the relative total pressure contour just behind the blades presented in Figure 7.10. At high flow condition, the plots depict the losses due to the separated flow found at the tip and behind the blade trailing edge. The reduction in mass flow cause more separation and more losses at these two regions, Figures 7.10(a) and 7.10(b). As mass flow rate is further reduced, the separated flow at the tip starts to shift towards only above few blades, Figure 7.10(c). This transport process continued with the mass flow reduction until the fan domain is divided into two regions; a stalled one with high losses and unstalled one with high total pressure, Figures 7.10(d) to 7.10(f).

```
-------------------------------------------------------------------------------
COEFFICIENT LOOP ITERATION =  21                CPU SECONDS SO FAR = 7.94E+04
-------------------------------------------------------------------------------
| Equation | Rate | RMS Res | Max Res | Max Location  |  Linear Solution  |
+----------+------+---------+---------+---------------+-------------------+
| TKE      | 0.98 | 4.9E-06 | 1.7E-04 | { 55, 16, 42} |  6.2  6.8E-03  OK |
| EPS      | 0.92 | 2.8E-06 | 2.8E-04 | { 55, 16, 41} |  6.0  4.0E-04  OK |
+----------+------+---------+---------+---------------+-------------------+
| U - Mom  | 1.00 | 2.3E-06 | 7.6E-05 | {100, 36,  2} |       1.4E-02  OK |
| V - Mom  | 1.01 | 3.7E-06 | 9.0E-05 | { 61, 28, 12} |       9.4E-03  OK |
| W - Mom  | 1.00 | 5.7E-06 | 9.8E-05 | { 95, 21, 49} |       6.5E-03  OK |
| P - Mass | 1.00 | 4.3E-08 | 5.2E-07 | {100, 36, 13} |  9.2  7.6E-03  OK |
-------------------------------------------------------------------------------
TIME STEP COMPLETED - because the maximum residuals are less than the
                      target value of "ERTIME=" 1.000E-04.
===============================================================================
-------------------------------------------------------------------------------
                    Momentum and Mass Flow Summary
-------------------------------------------------------------------------------
Boundary or source   |  X-momentum  Y-momentum  Z-momentum      Mass
-------------------------------------------------------------------------------
B.C. # 1, INFLOW     | -5.800E+02   3.613E+00  -7.565E-01   1.190E-01
B.C. # 2, OUTFLOW    |  5.823E+02  -1.640E+00  -1.243E-01  -1.190E-01
B.C. # 3, WALL       |  1.604E-02   8.028E+01   1.504E+03   0.000E+00
B.C. # 4, WALL       | -2.012E+00  -4.082E+01  -7.500E+02   0.000E+00
Coriolis+Centrifugal |  0.000E+00   5.667E-01   4.737E+00   0.000E+00
Periodic Connection  |  9.180E-04  -4.203E+01  -7.580E+02   0.000E+00
-------------------------------------------------------------------------------
Net Flow             |  2.405E-01  -2.580E-02  -4.724E-02   2.831E-06
-------------------------------------------------------------------------------
===============================================================================
TIME STEP =  30       SIMULATION TIME = 3.00E-02       CPU TIME = 7.95E+04
Wall clock time of day: Thu Aug 31 11:14:56 2000
Seconds since midnight: 40496.000
Seconds since previous:  1331.000
-------------------------------------------------------------------------------
COEFFICIENT LOOP ITERATION =  1
-------------------------------------------------------------------------------
| Equation | Rate | RMS Res | Max Res | Max Location  |  Linear Solution  |
+----------+------+---------+---------+---------------+-------------------+
| TKE      | 0.99 | 2.0E-04 | 5.0E-03 | { 62, 34, 39} |  6.1  3.3E-02  OK |
| EPS      | 0.99 | 3.4E-05 | 4.2E-03 | { 52, 14, 41} |  6.0  1.6E-03  OK |
+----------+------+---------+---------+---------------+-------------------+
| U - Mom  | 1.04 | 1.5E-04 | 2.1E-03 | { 99,  6,  2} |       4.0E-02  OK |
| V - Mom  | 0.96 | 8.5E-05 | 1.9E-03 | { 62, 33, 39} |       5.1E-02  OK |
| W - Mom  | 1.07 | 6.3E-05 | 9.9E-04 | { 63, 31, 29} |       3.6E-02  OK |
| P - Mass | 1.00 | 5.0E-07 | 1.2E-05 | {  1, 21, 30} |  9.2  4.3E-02  OK |
-------------------------------------------------------------------------------
```

Figure 7.2: Sample of the output result for the unsteady simulation

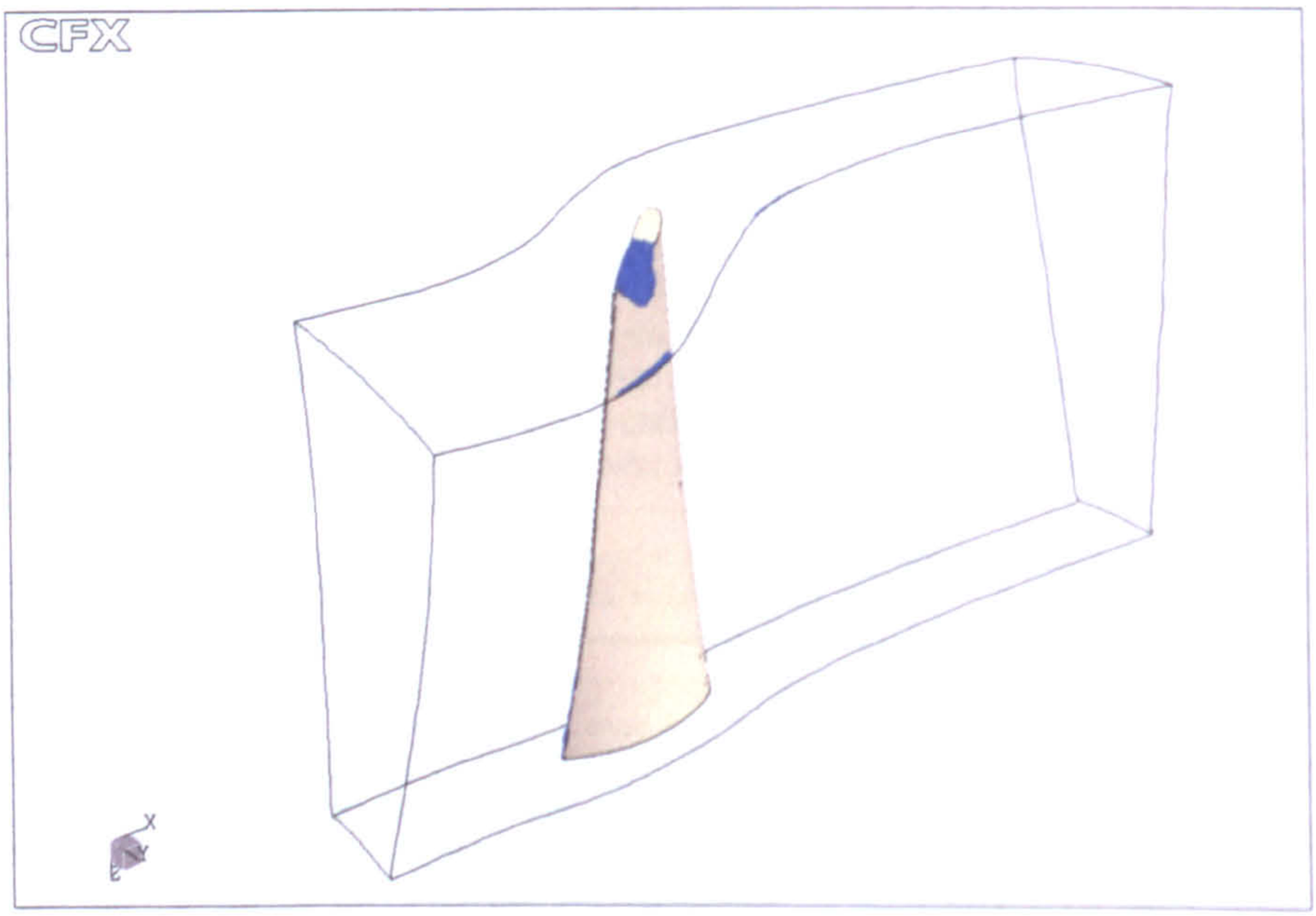

(a) At $\phi = 0.7293$ at $t = 0.006$

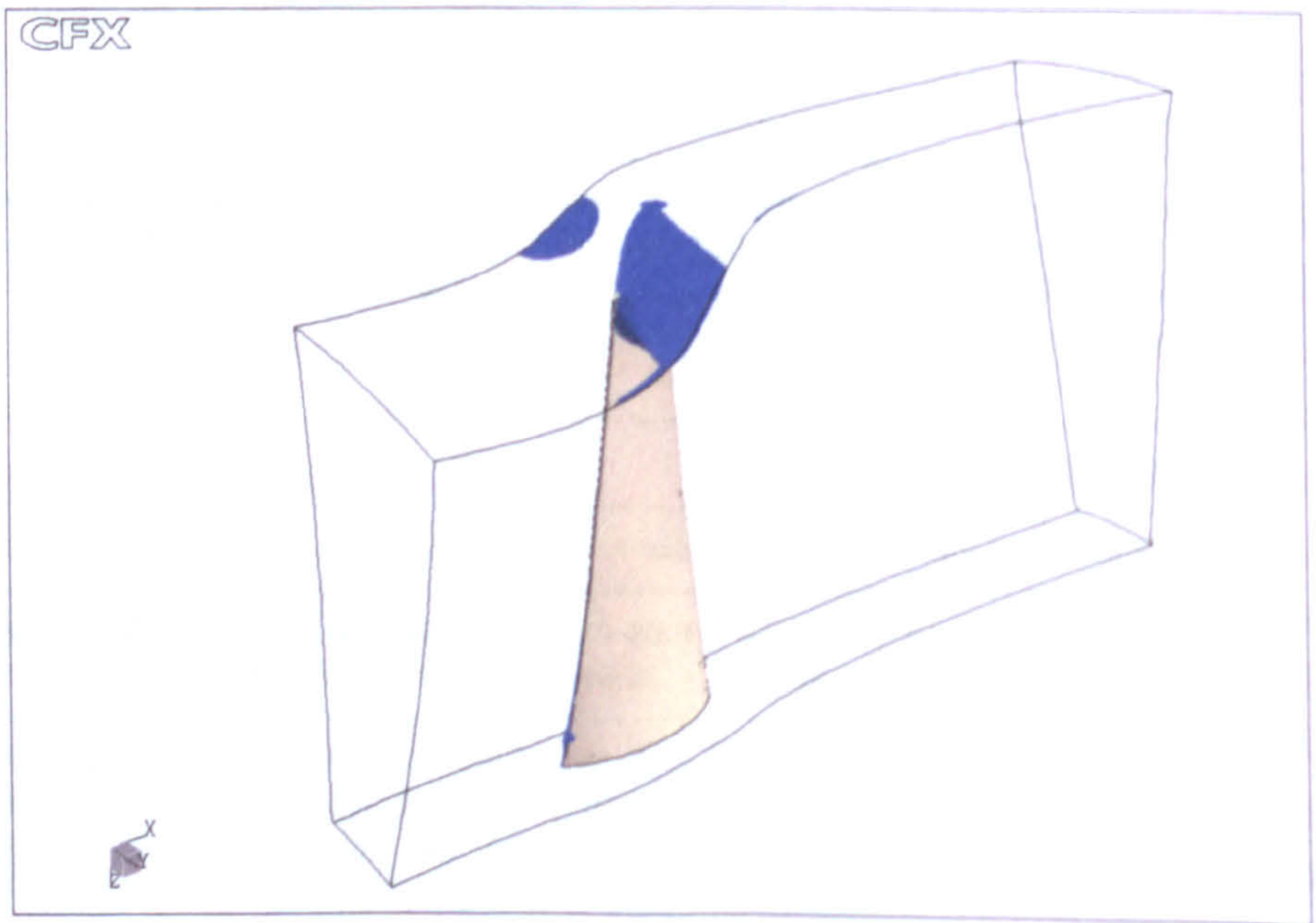

(b) At $\phi = 0.7120$ at $t = 0.009$

Figure 7.3: Flow separation from single blade passage simulation

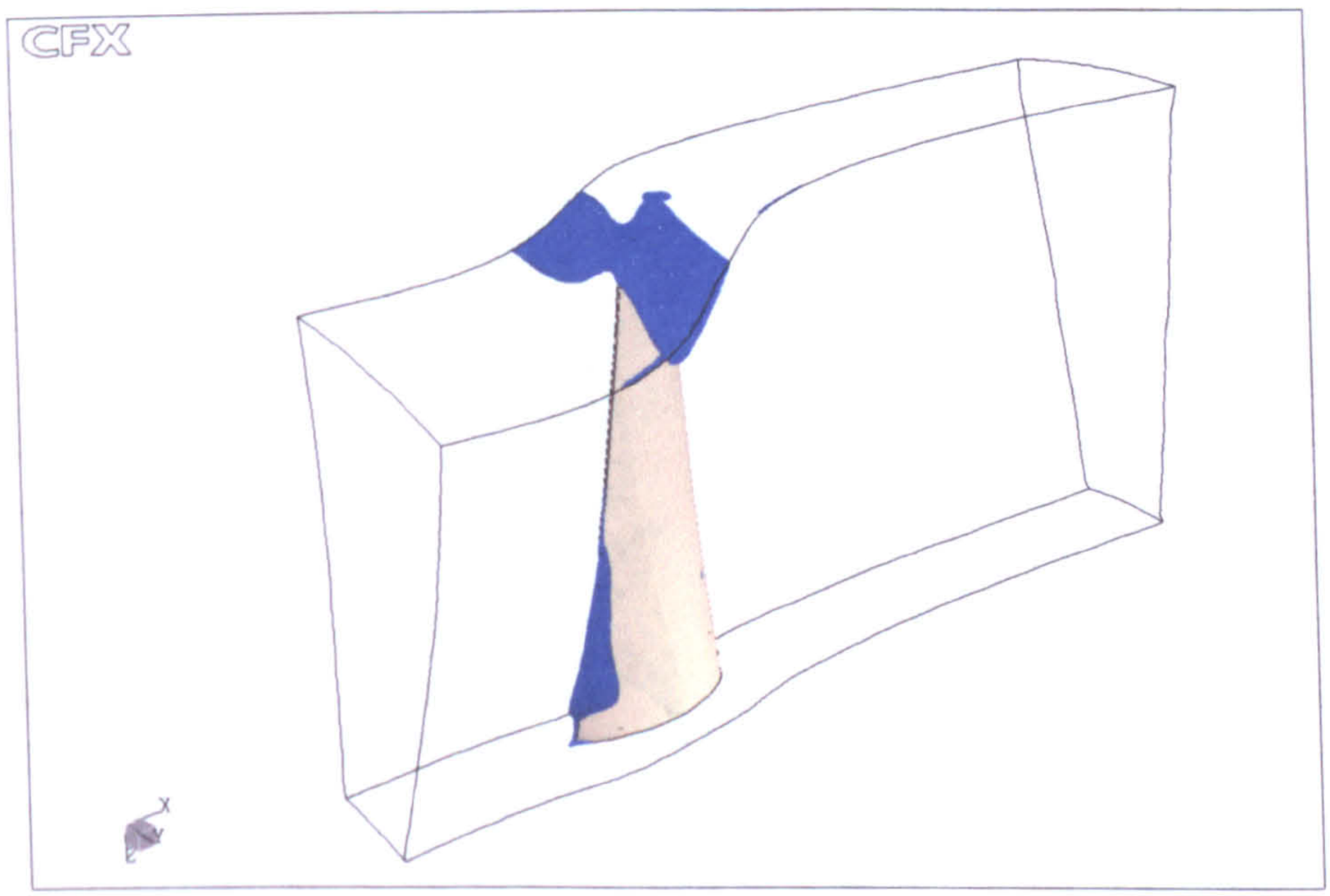

(c) At $\phi = 0.6885$ at $t = 0.014$

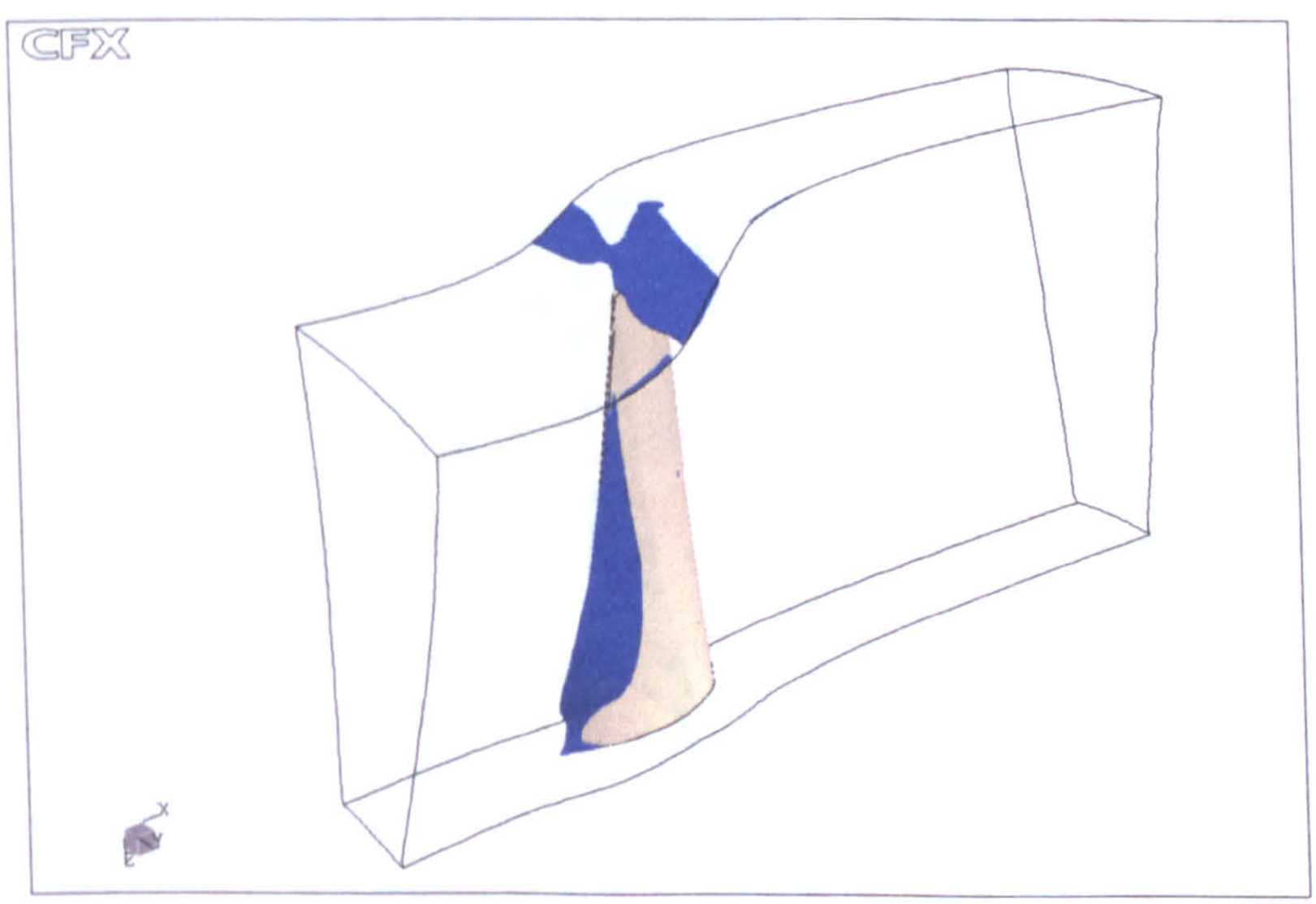

(d) At $\phi = 0.6528$ at $t = 0.021$

Figure 7.3: Flow separation from single blade passage simulation (cont.)

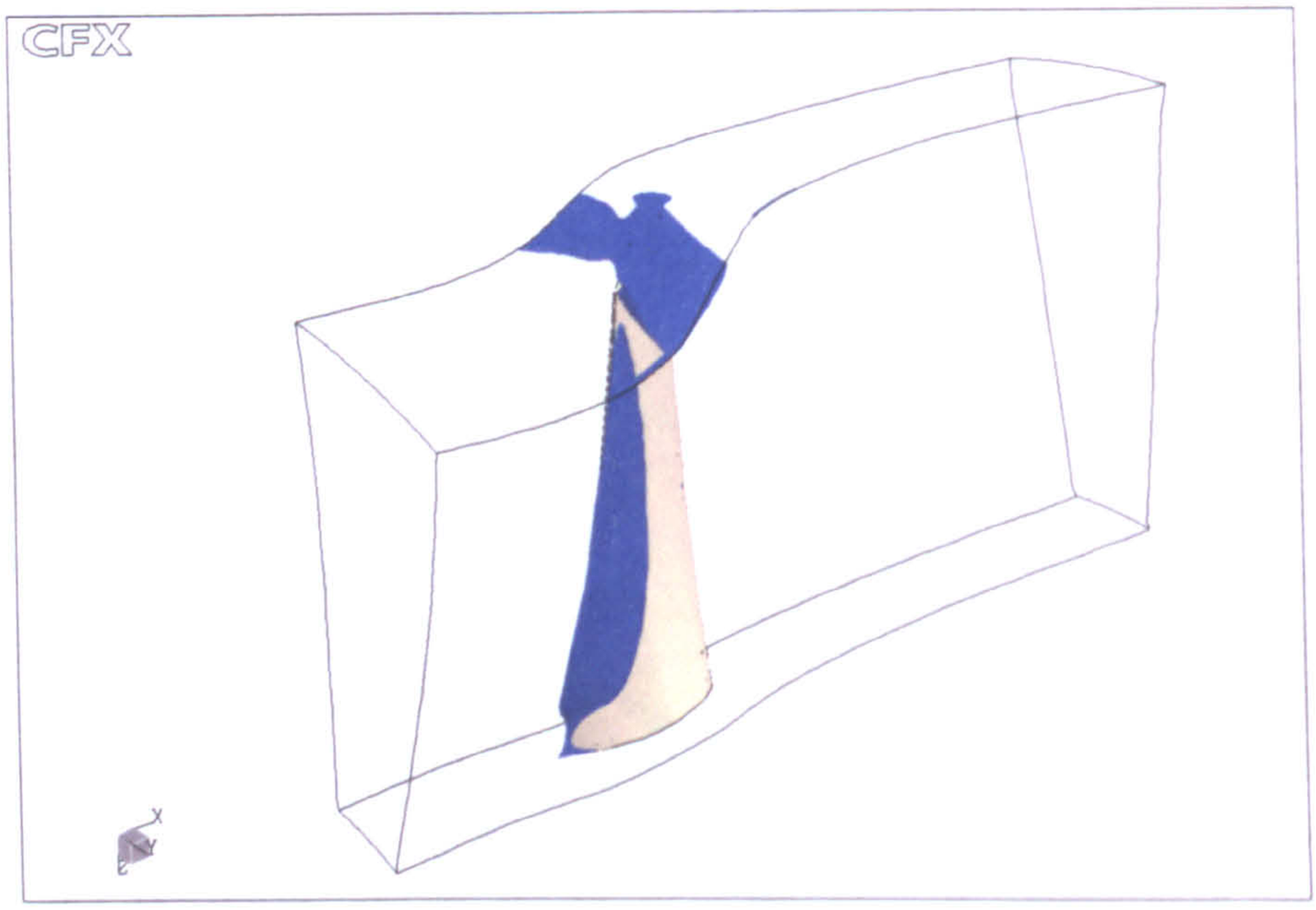

(e) At $\phi = 0.6018$ at $t = 0.031$

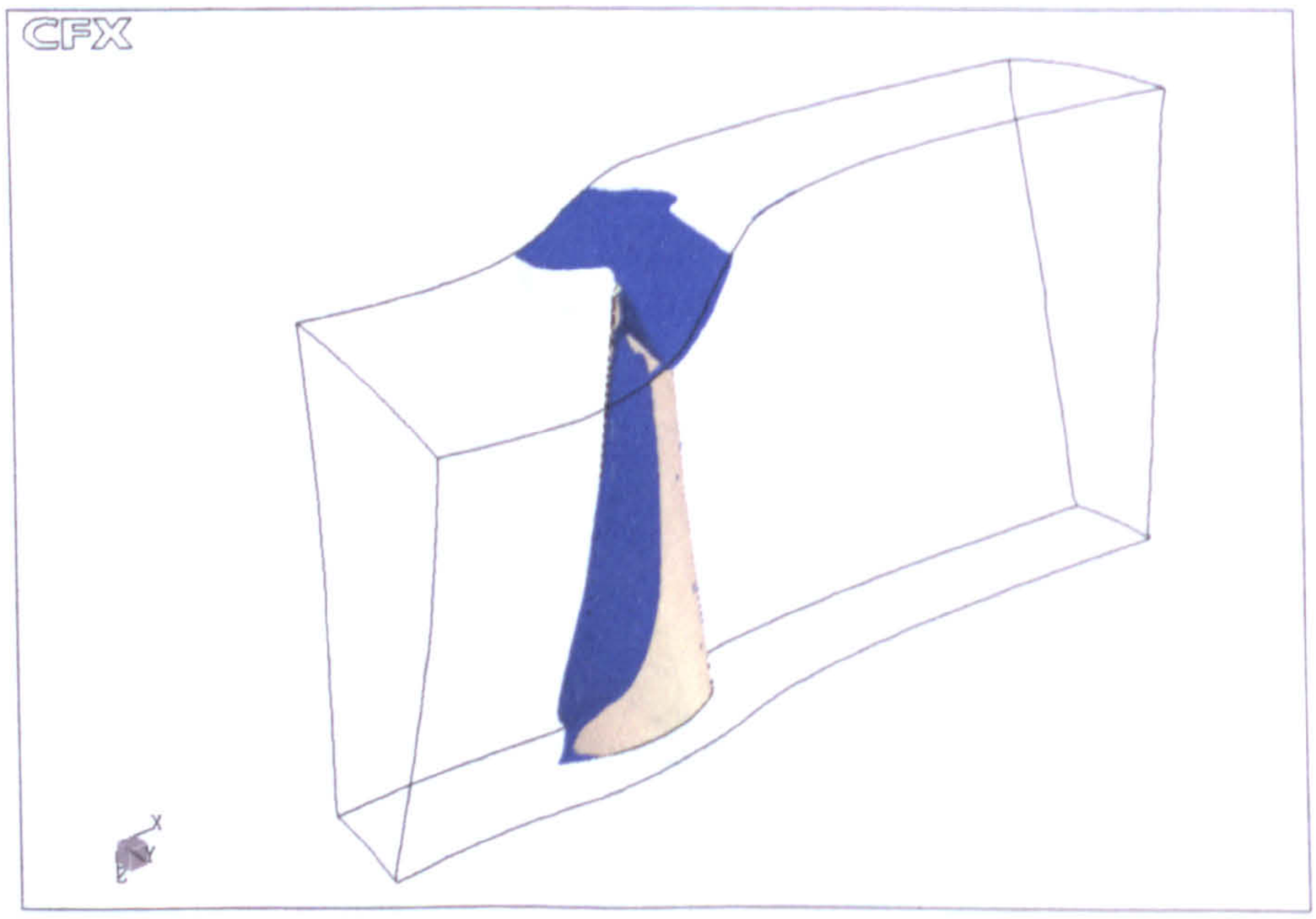

(f) At $\phi = 0.5508$ at $t = 0.041$

Figure 7.3: Flow separation from single blade passage simulation (cont.)

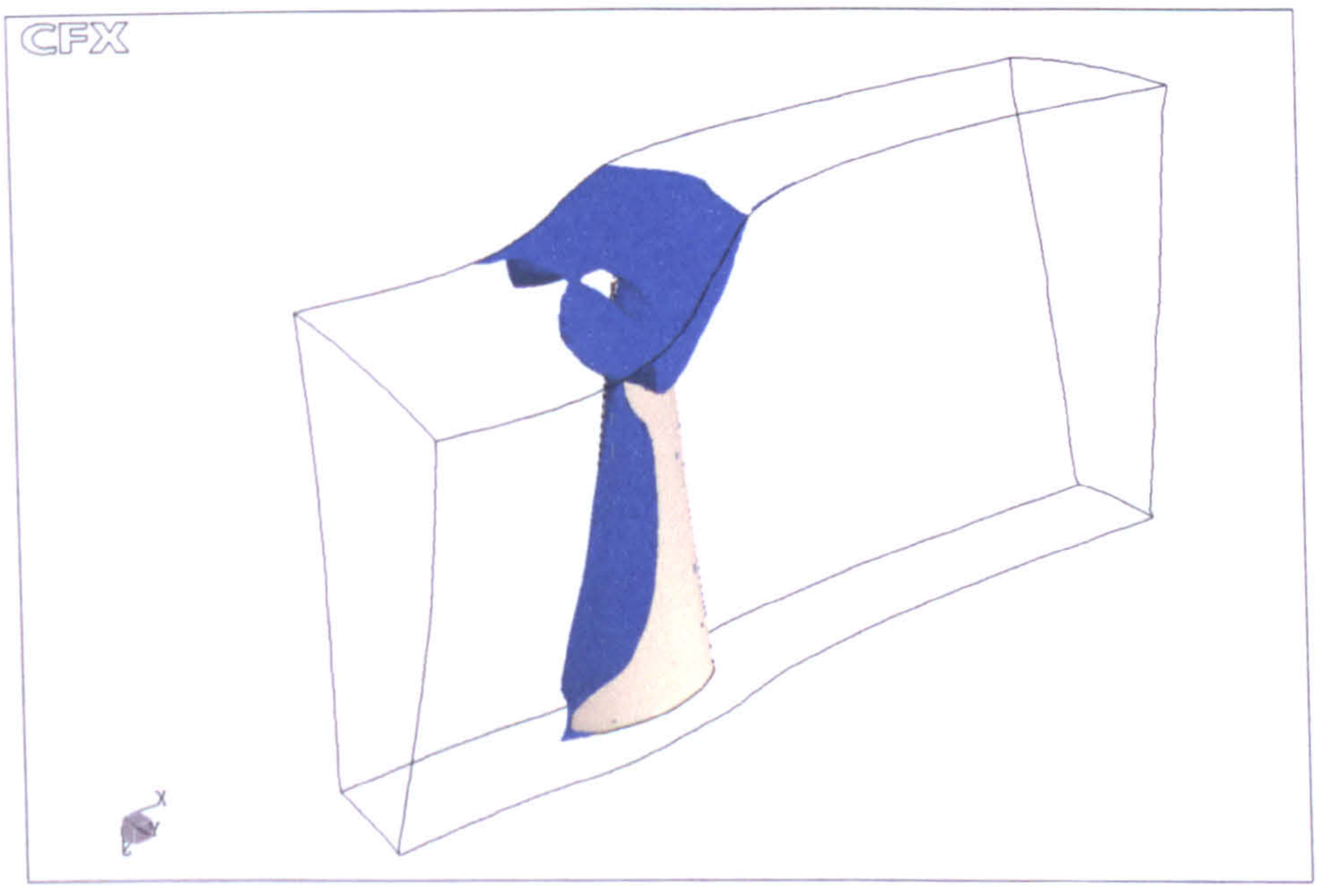

(g) At $\phi = 0.4998$ at $t = 0.051$

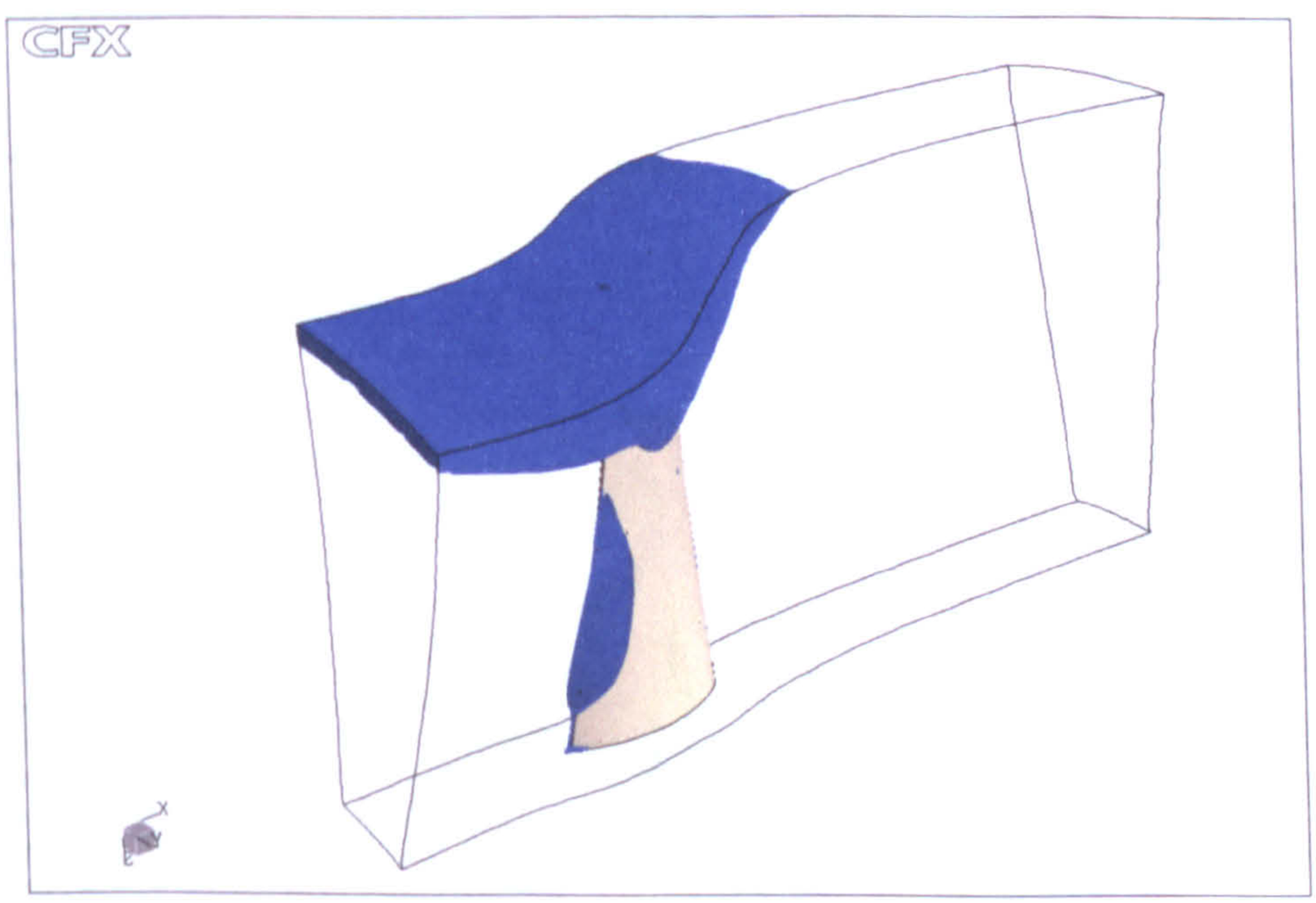

(h) At $\phi = 0.4539$ at $t = 0.060$

Figure 7.3: Flow separation from single blade passage simulation (cont.)

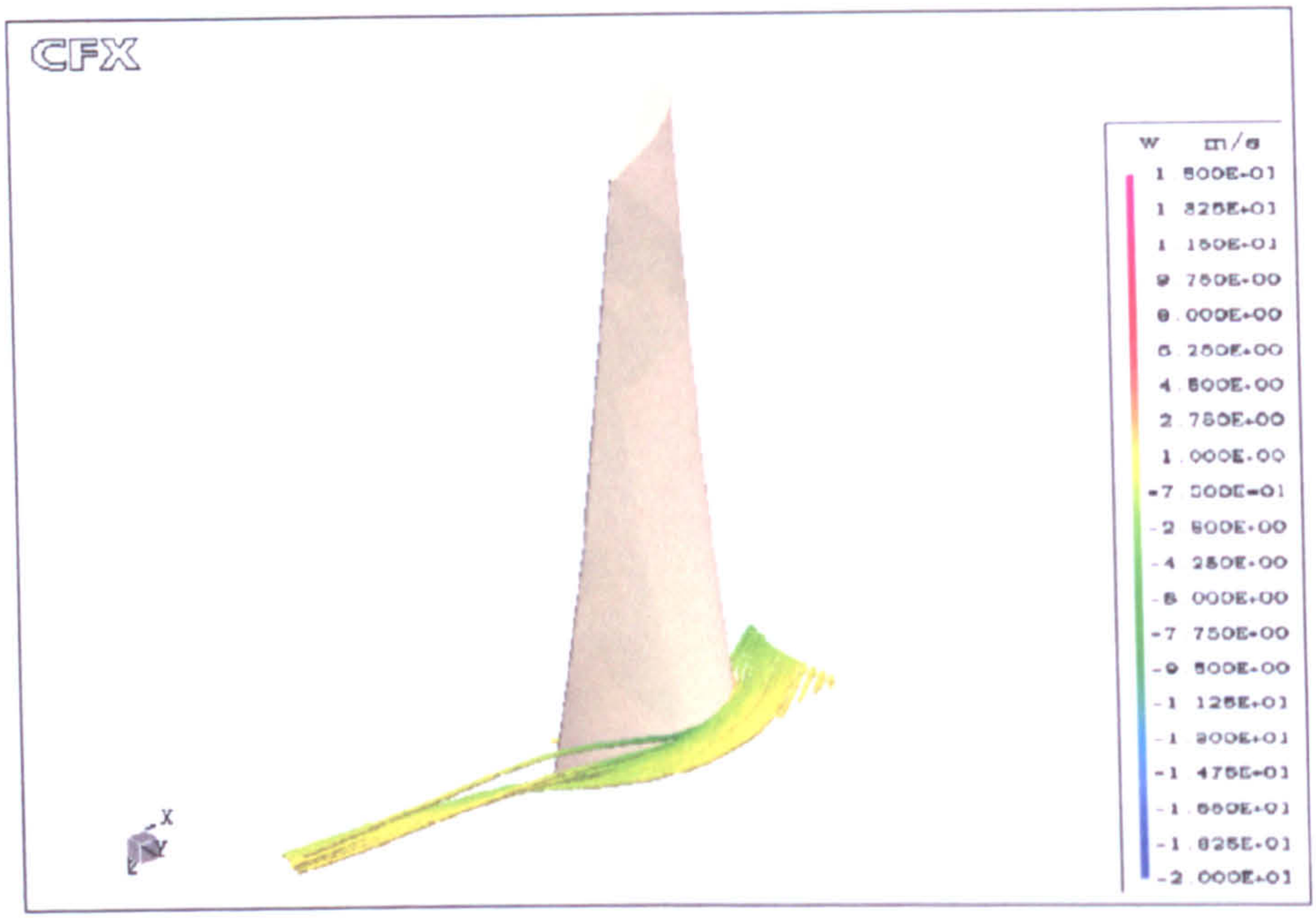

(a) At $\phi = 0.7140$ at $t = 0.009$

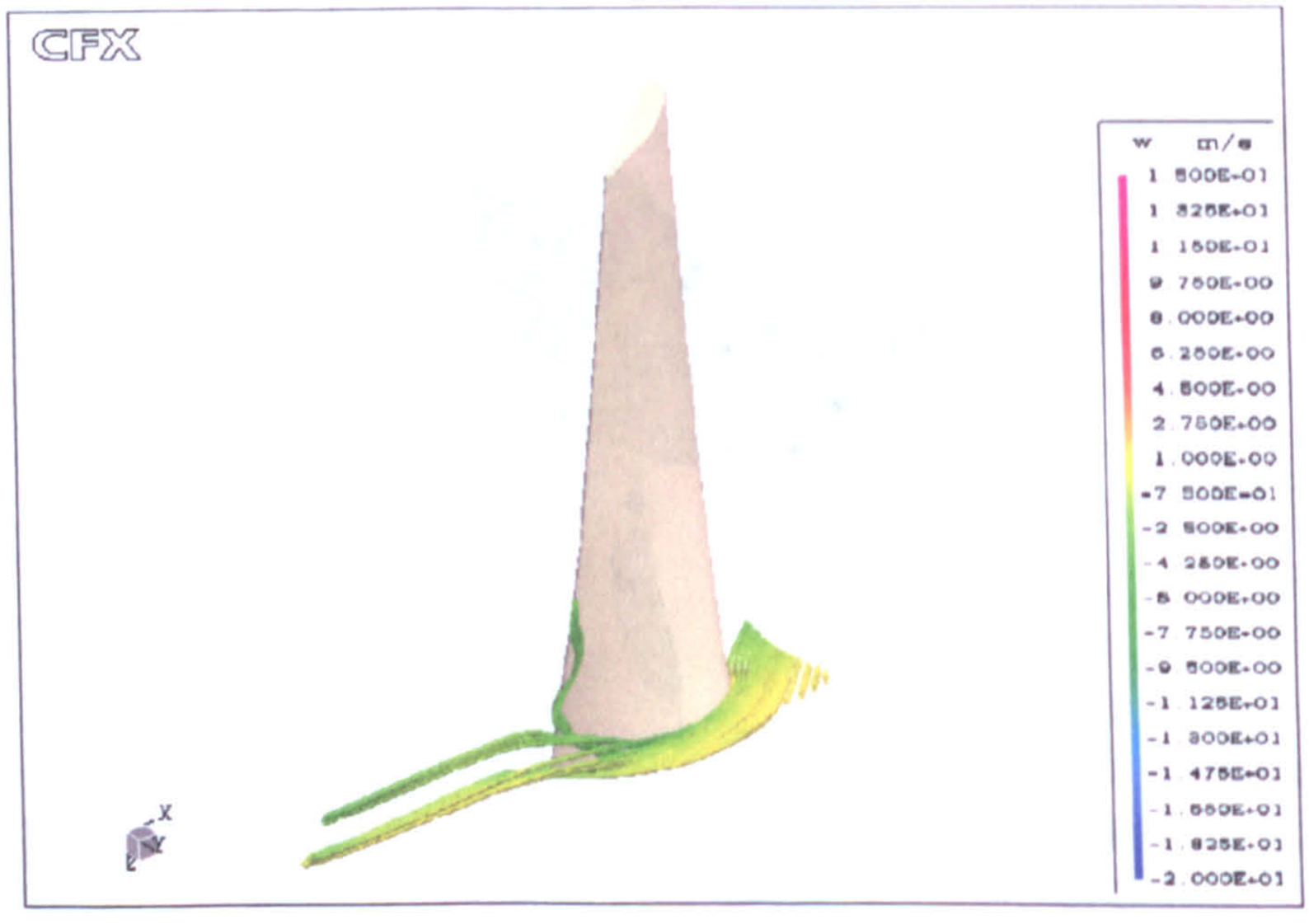

(b) At $\phi = 0.6936$ at $t = 0.013$

Figure 7.4: Streamlines plots for single blade passage simulation

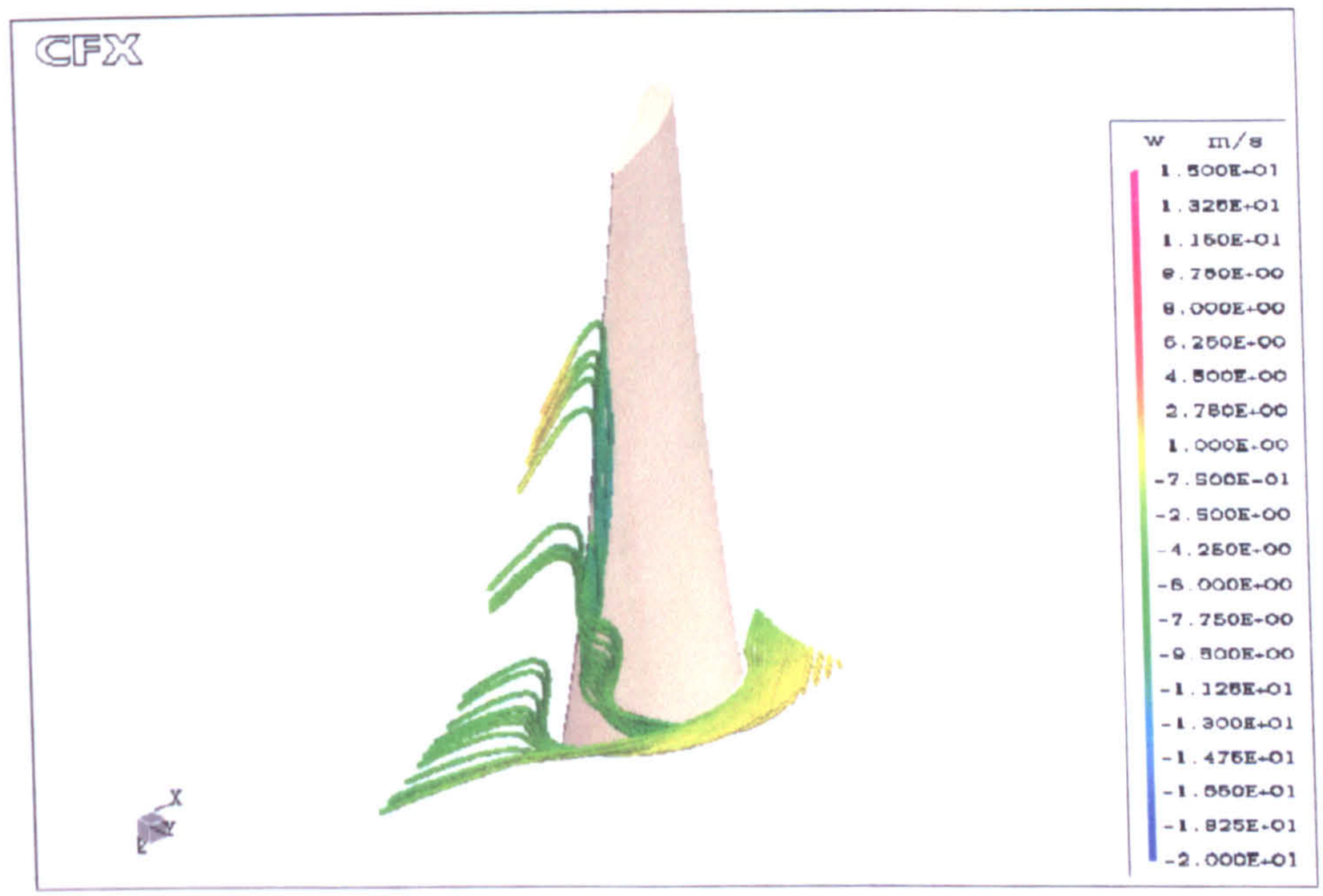

(c) At $\phi = 0.6681$ at $t = 0.018$

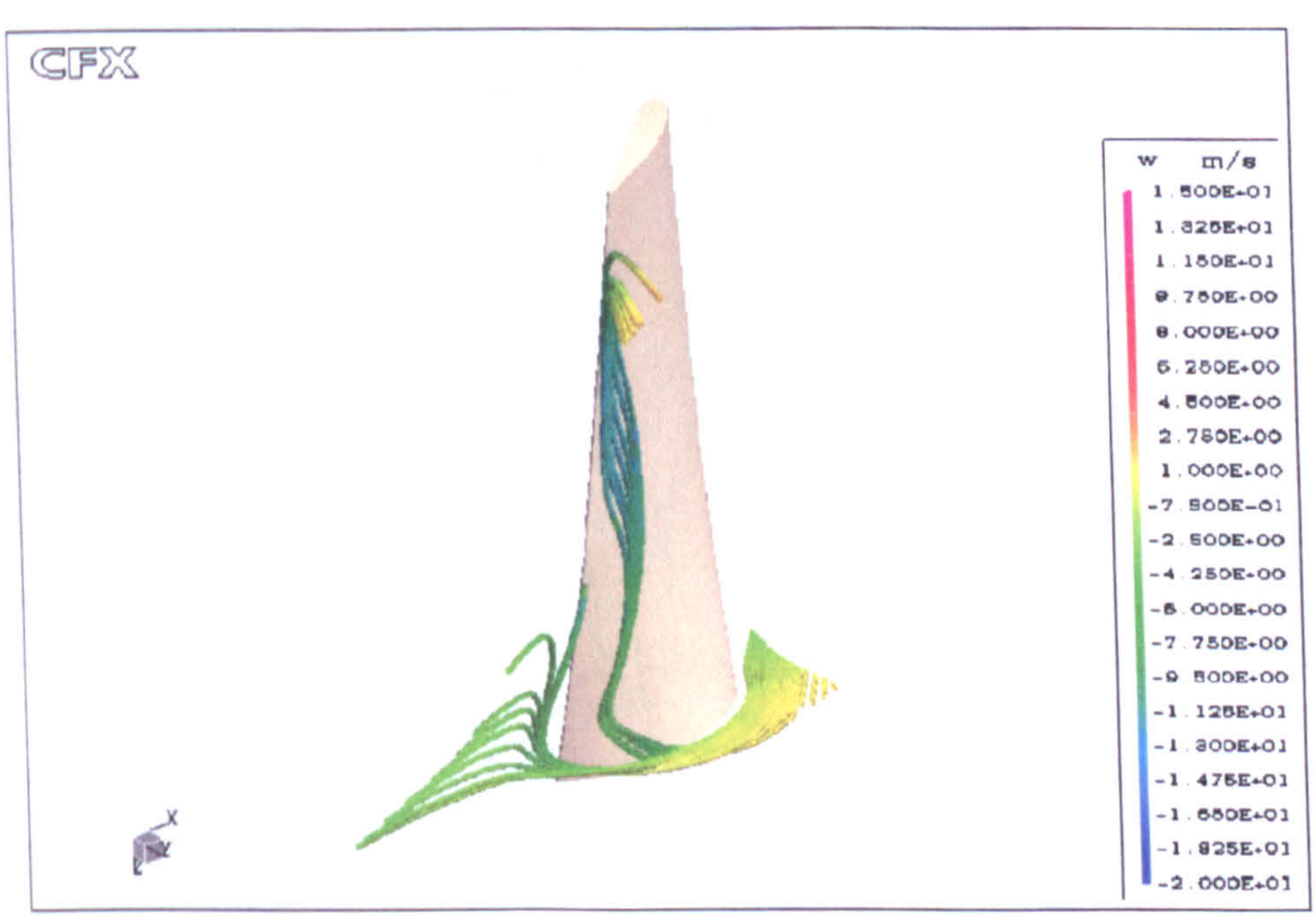

(d) At $\phi = 0.5814$ at $t = 0.035$

Figure 7.4: Streamlines plots for single blade passage simulation (cont.)

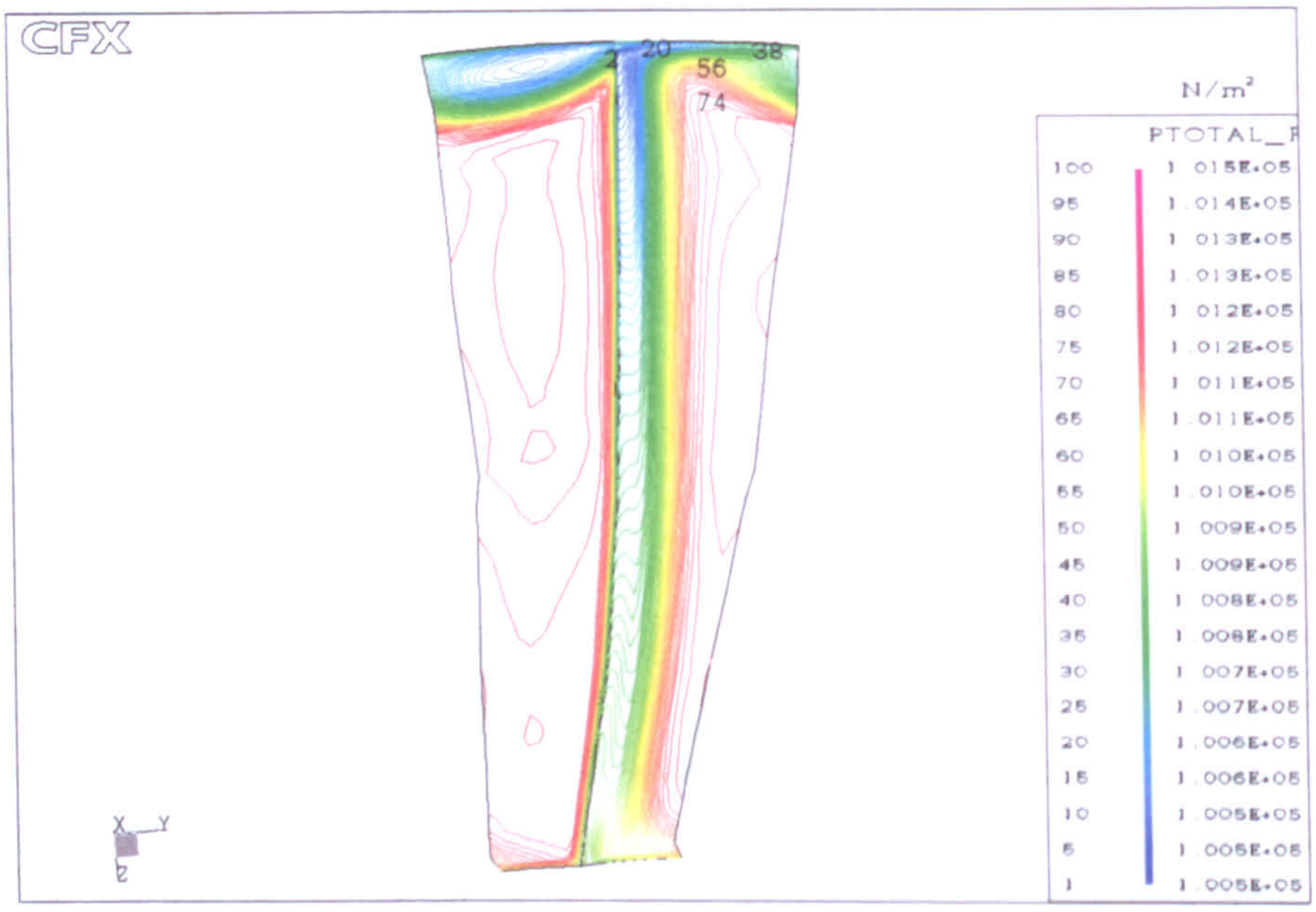

(a) At $\phi = 0.6579$ & $t = 0.020$

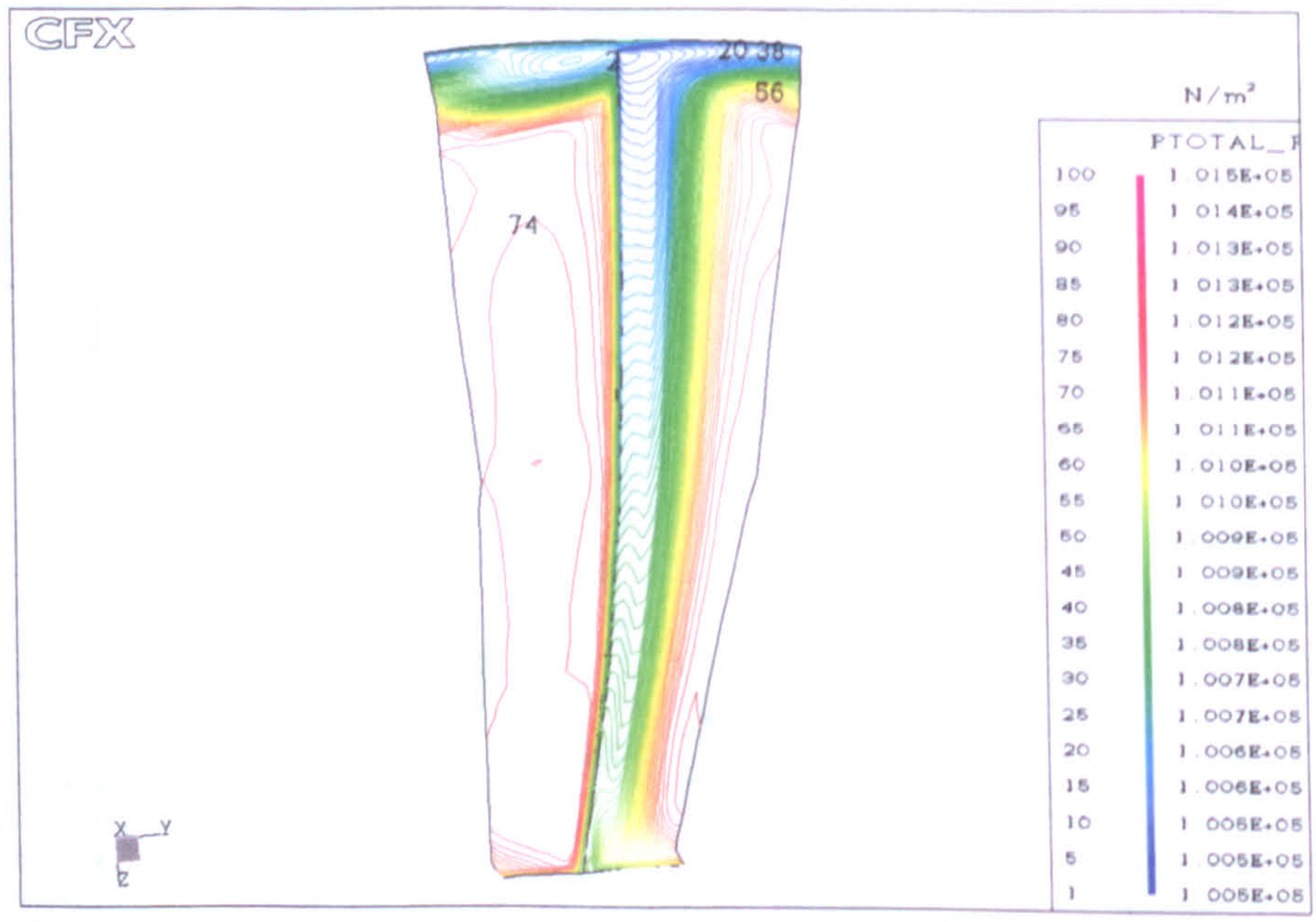

(b) At $\phi = 0.6069$ & $t = 0.030$

Figure 7.5: Relative total pressure at the blade trailing edge

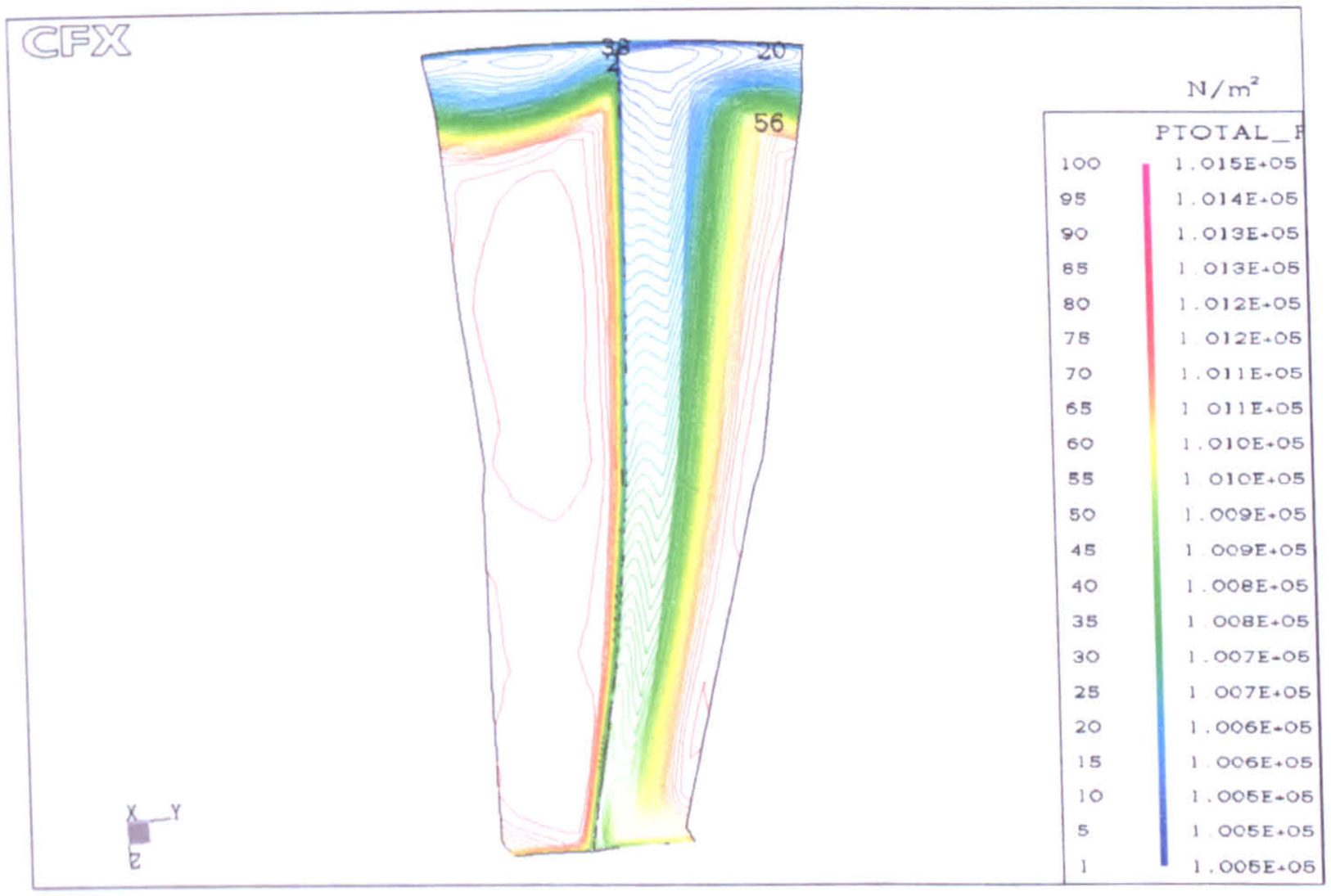

(c) At $\phi = 0.5559$ & $t = 0.040$

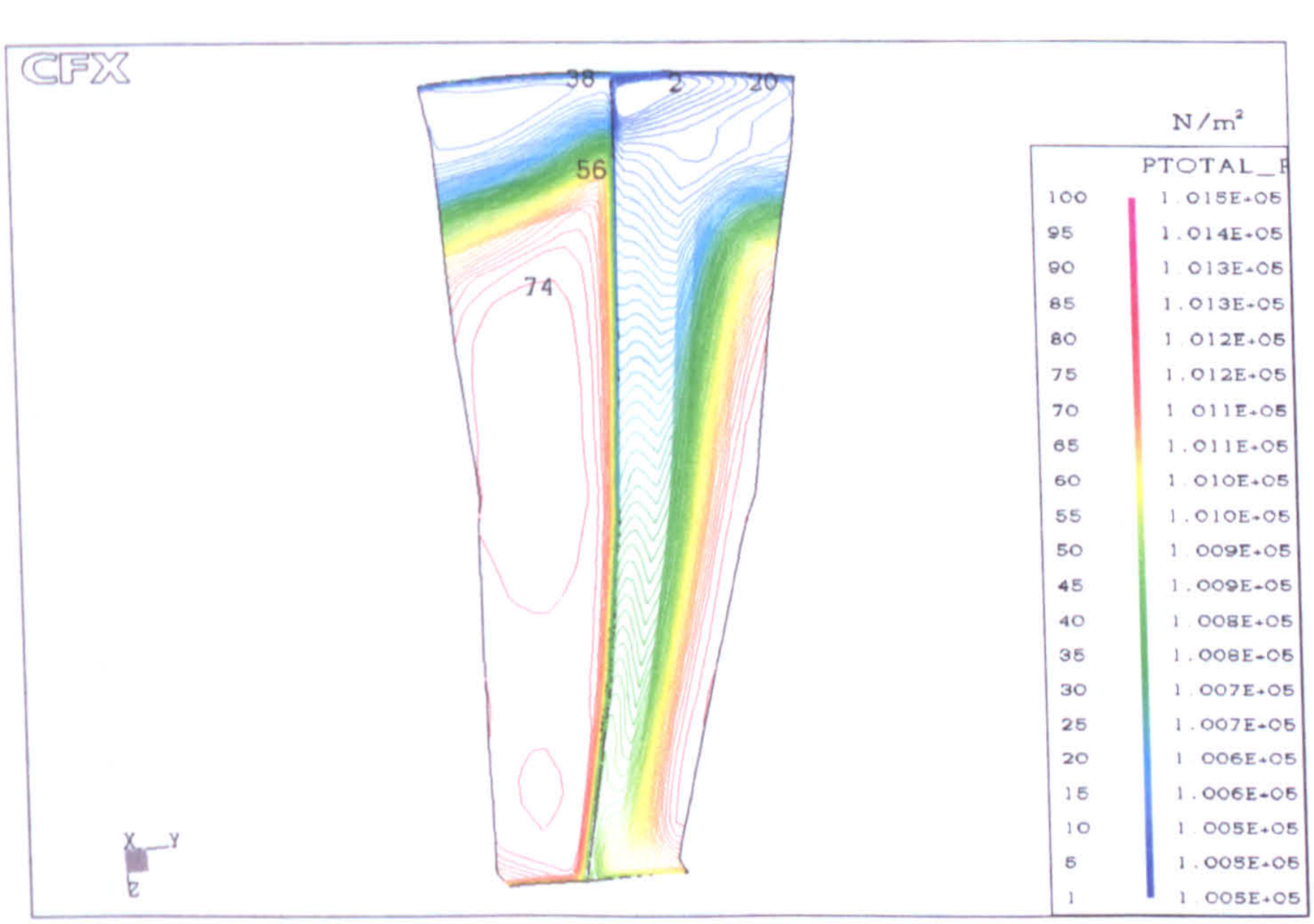

(d) At $\phi = 0.5049$ & $t = 0.050$

Figure 7.5: Relative total pressure at the blade trailing edge (cont.)

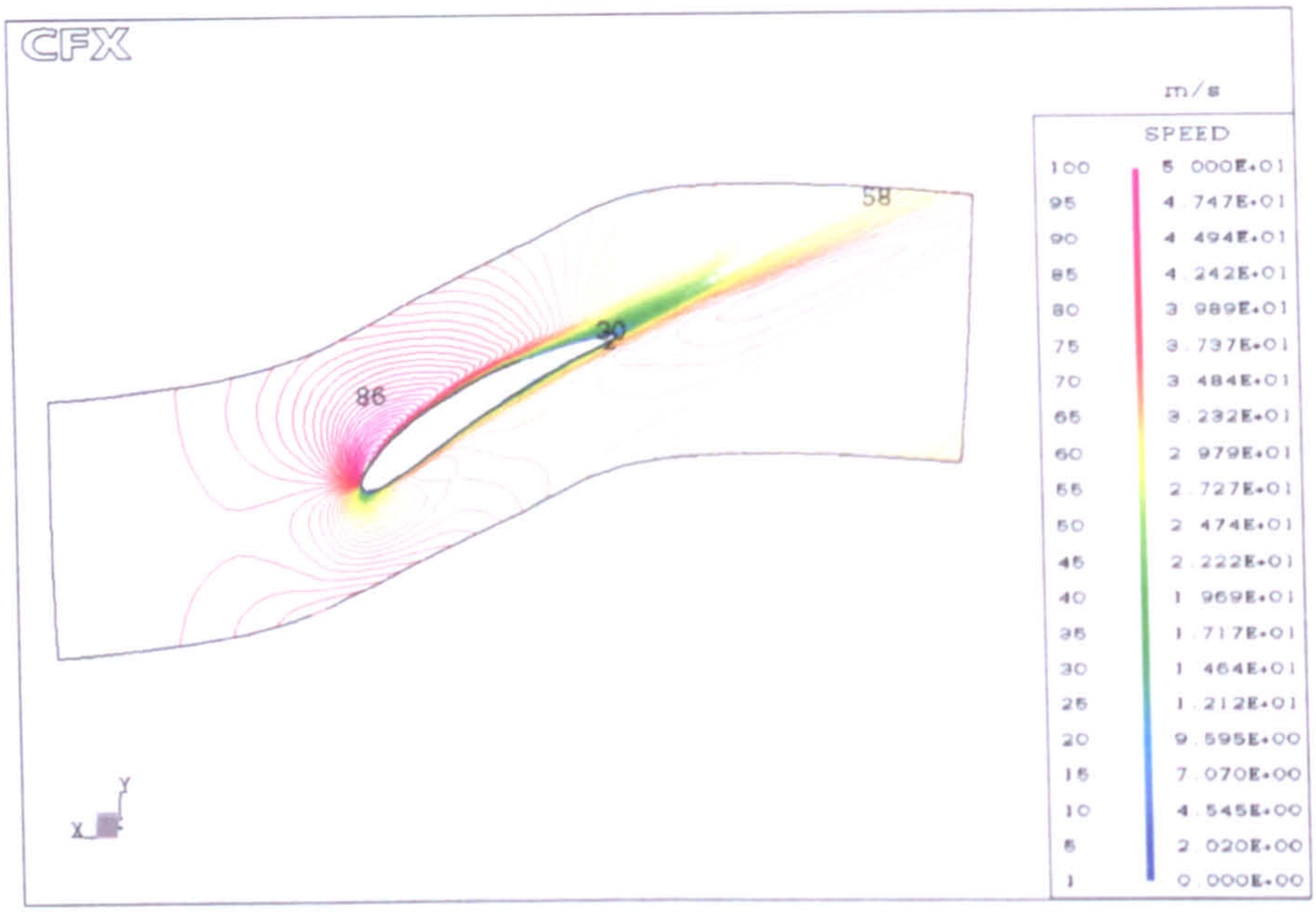

(a) At $\phi = 0.7191$ & $t = 0.080$

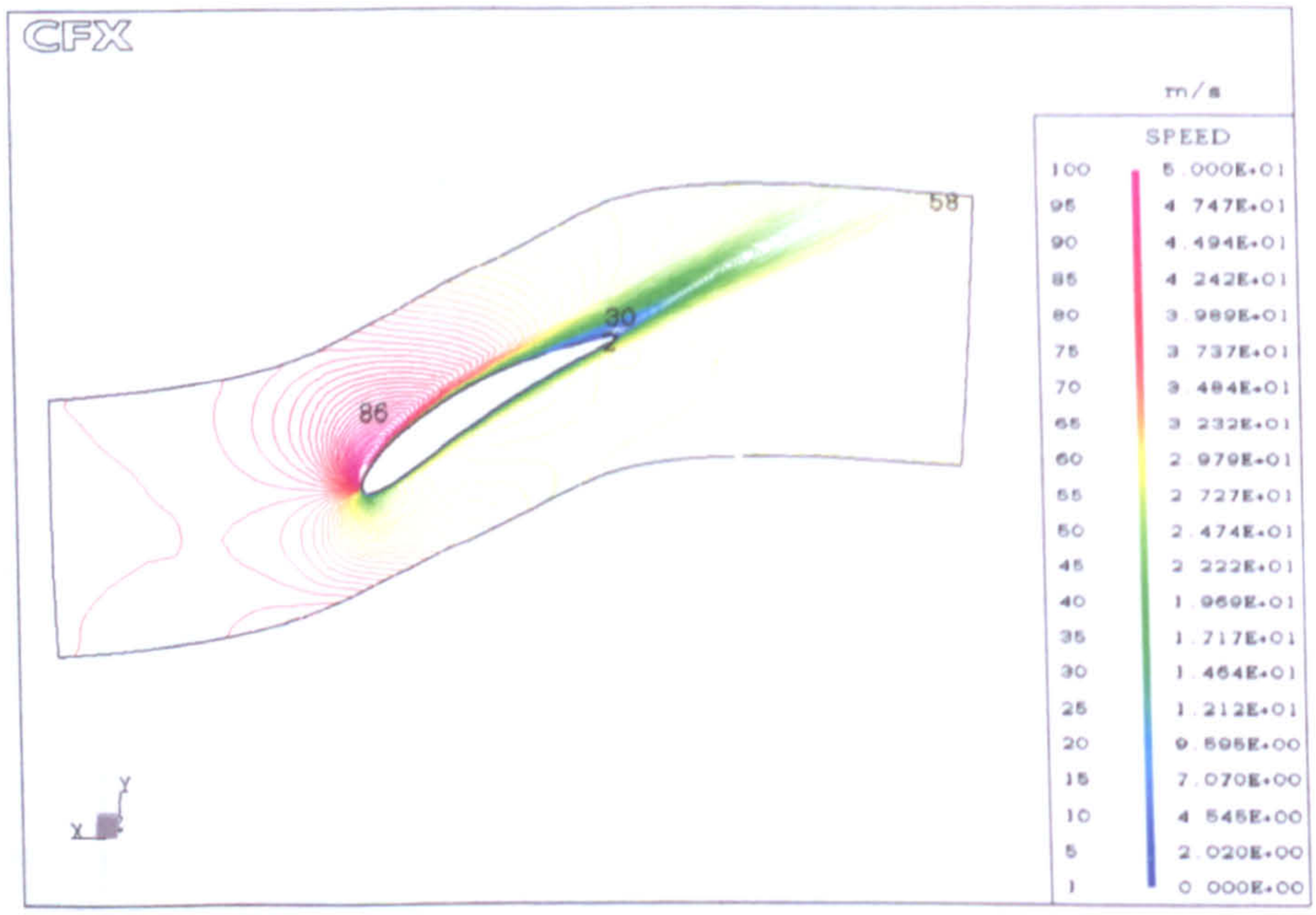

(b) At $\phi = 0.6936$ & $t = 0.013$

Figure 7.6: Velocity magnitude at mid-span for a single blade passage simulation

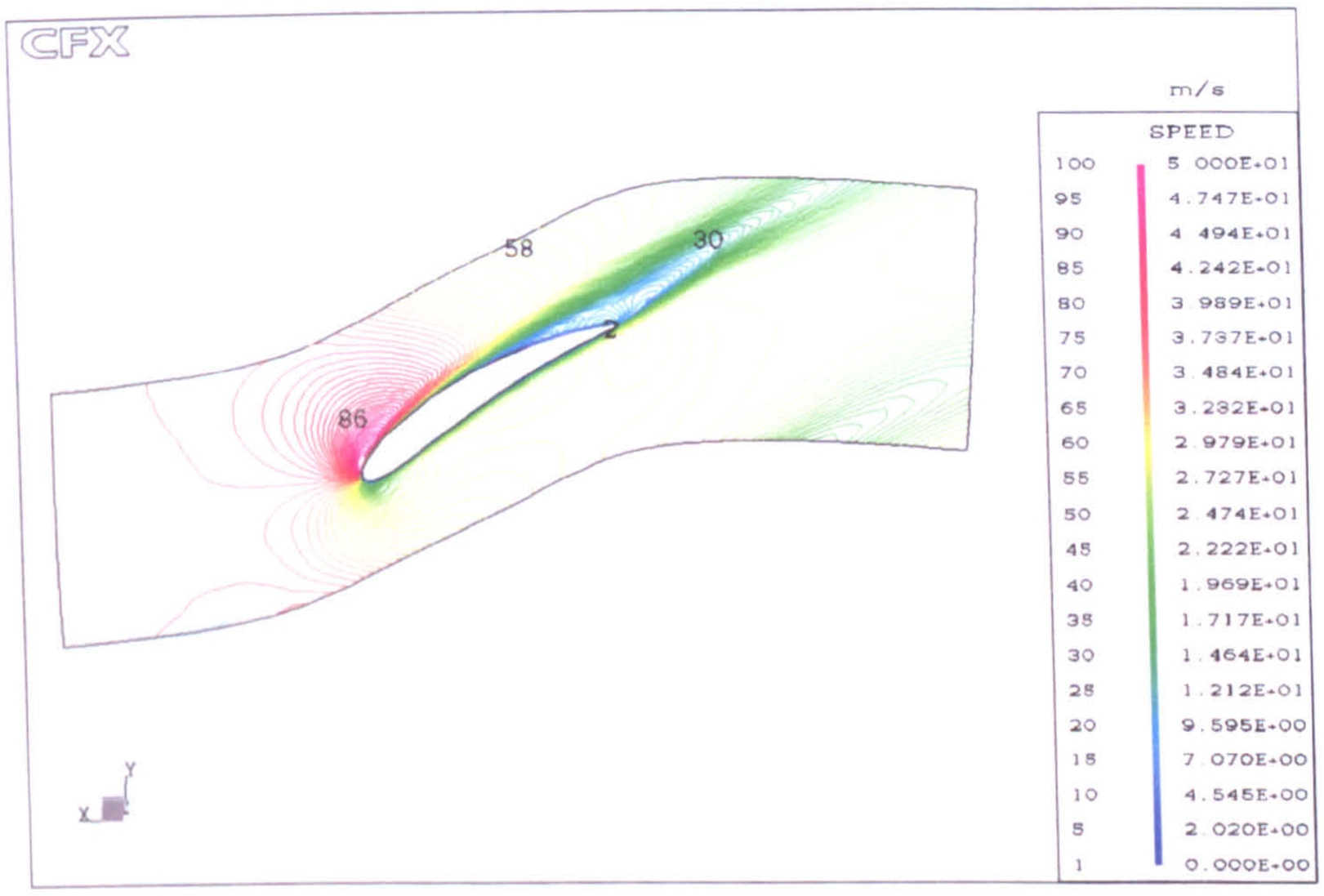

(c) At $\phi = 0.6069$ & $t = 0.030$

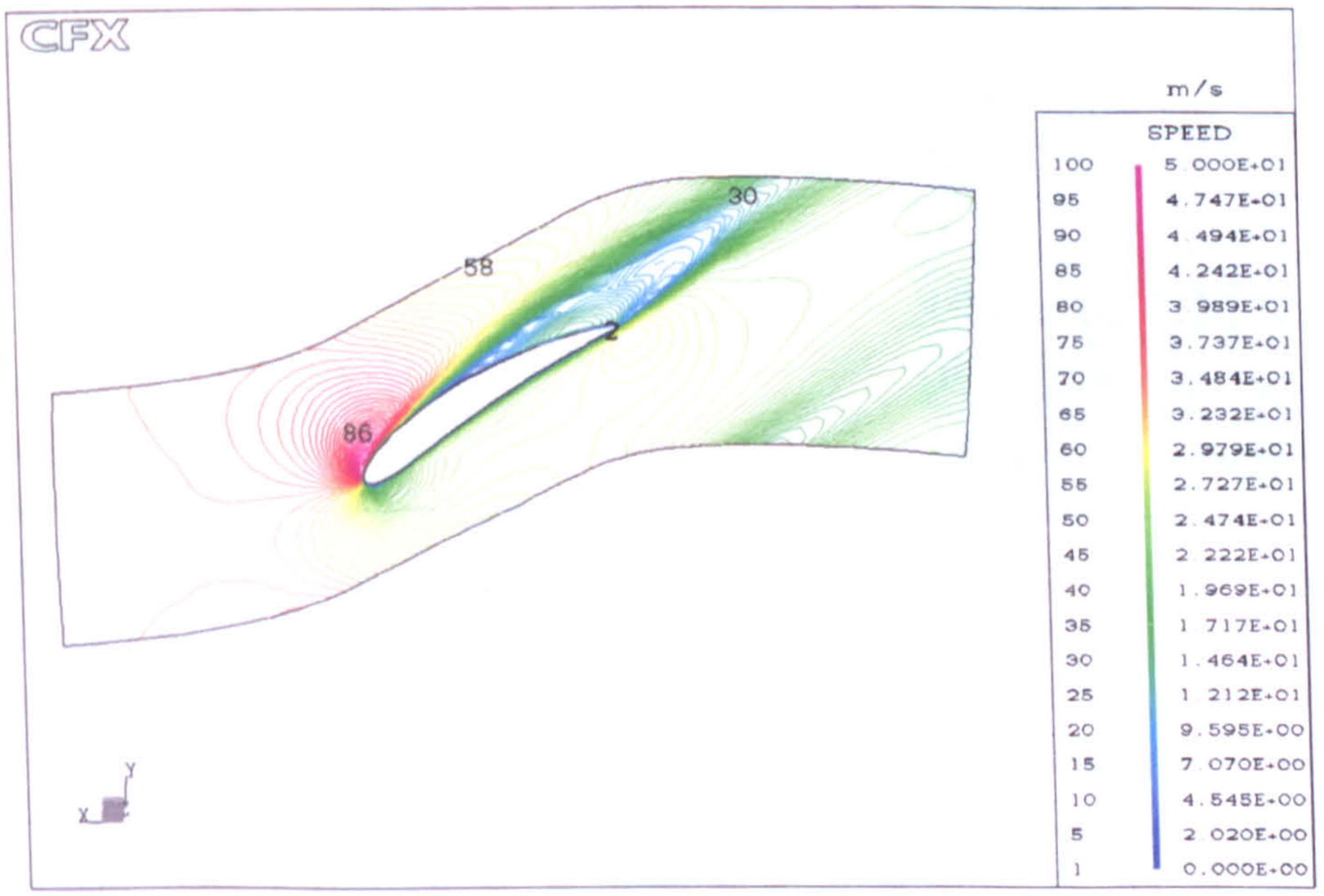

(d) At $\phi = 0.5559$ & $t = 0.040$

Figure 7.6: Velocity magnitude at mid-span for a single blade passage (cont.)

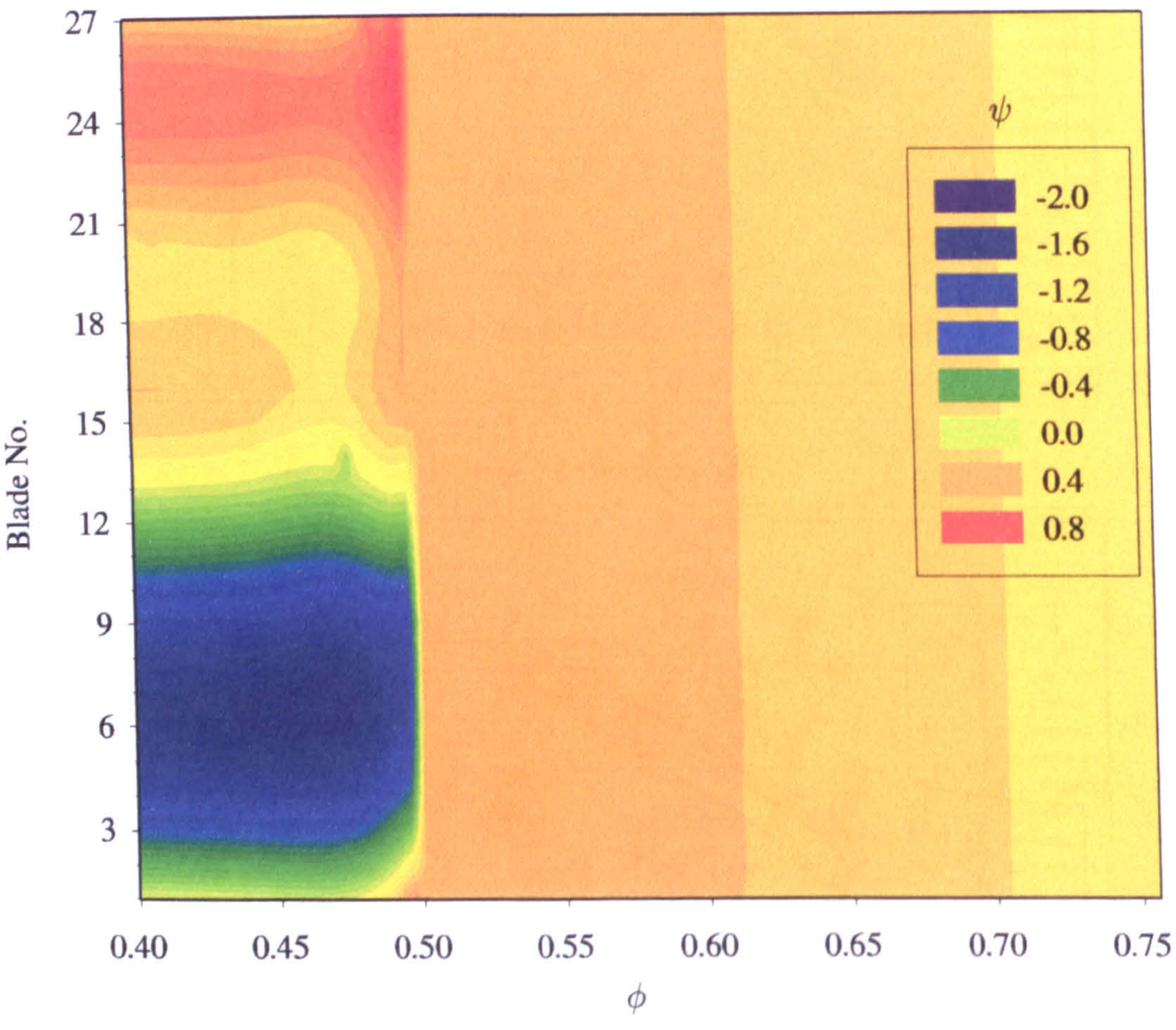

Figure 7.7: Pressure rise coefficient for the entire fan

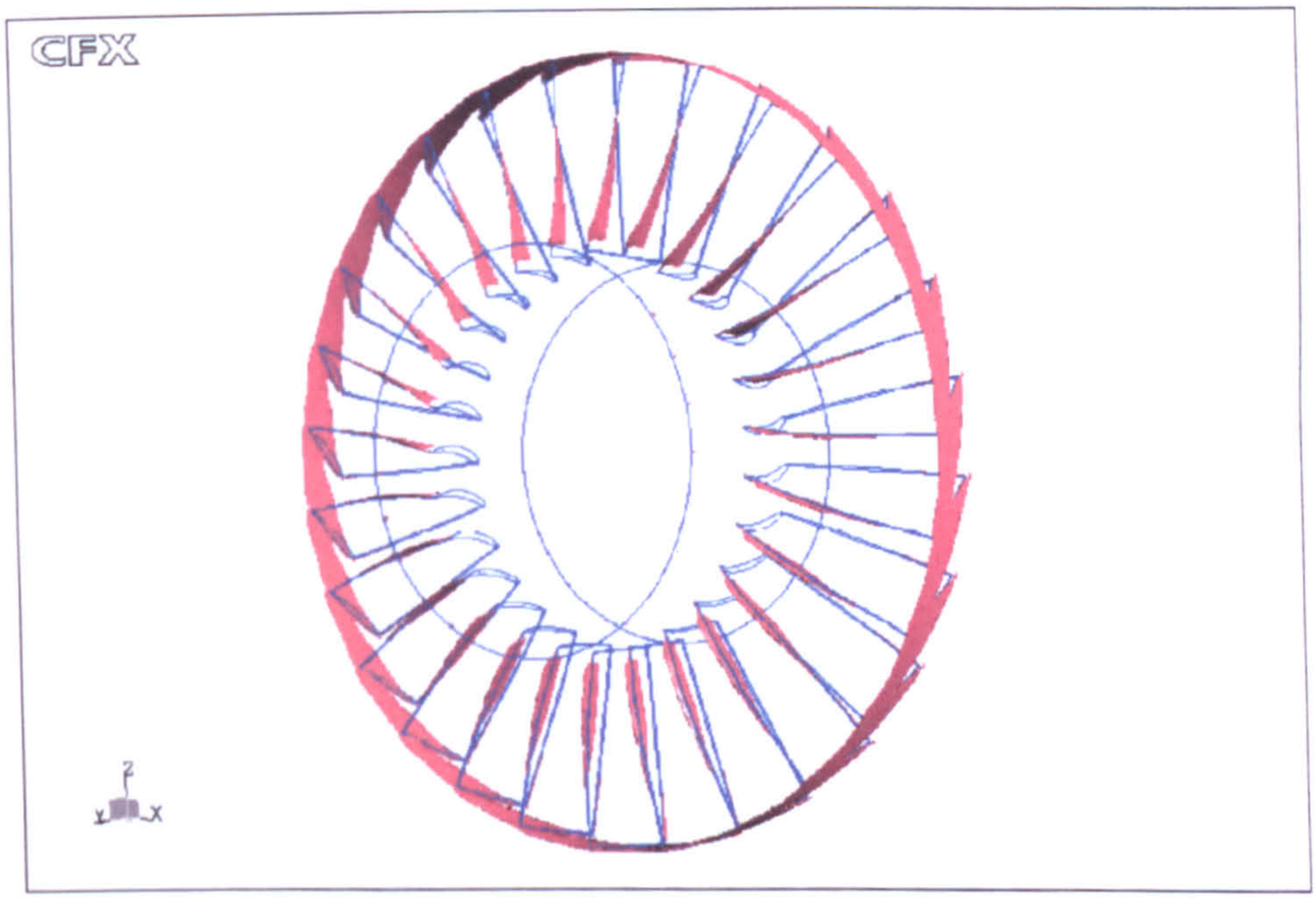

(a) At $\phi = 0.7045$ & $t = 0.010$

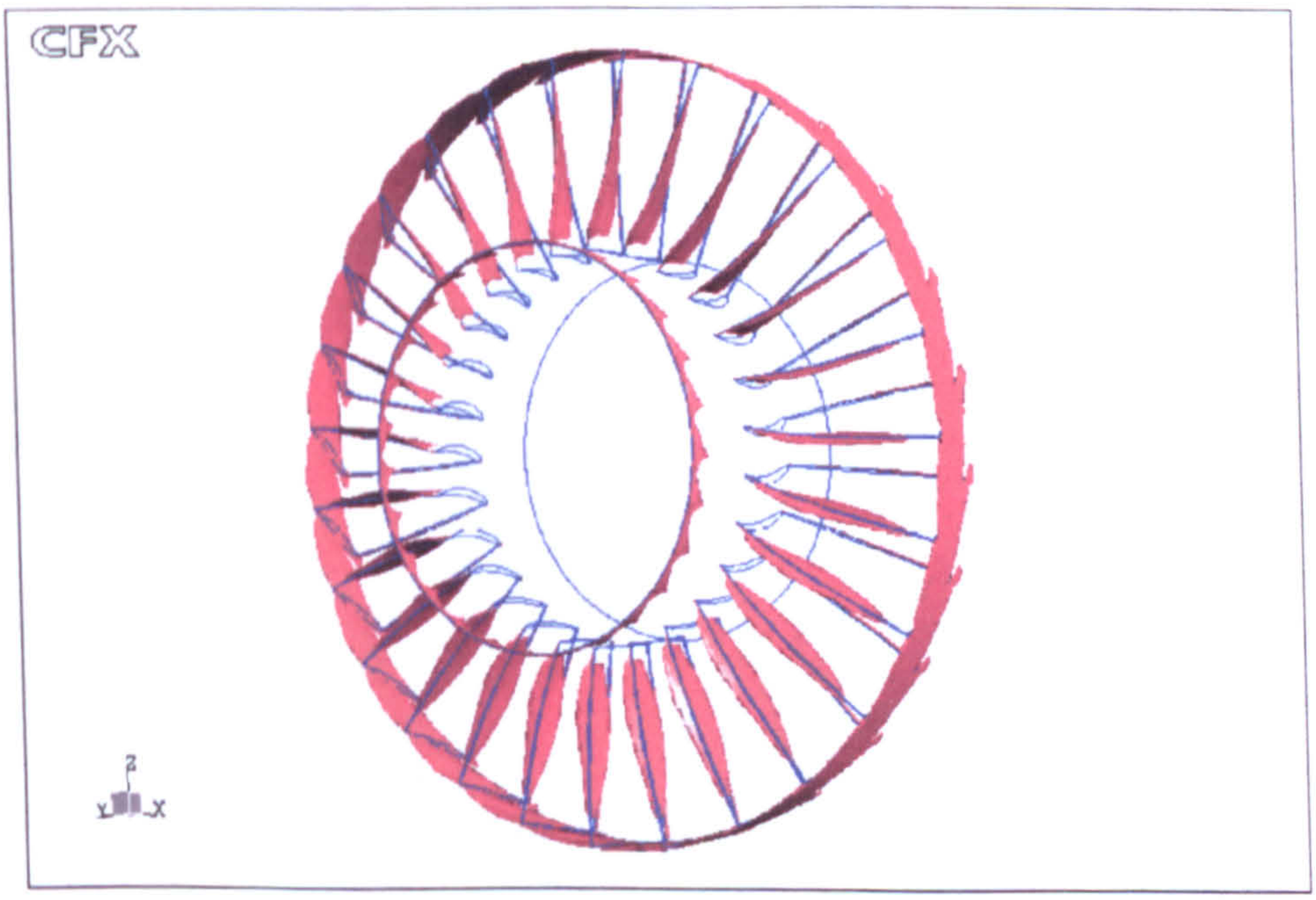

(b) At $\phi = 0.6025$ & $t = 0.030$

Figure 7.8: Flow separation from entire fan simulation

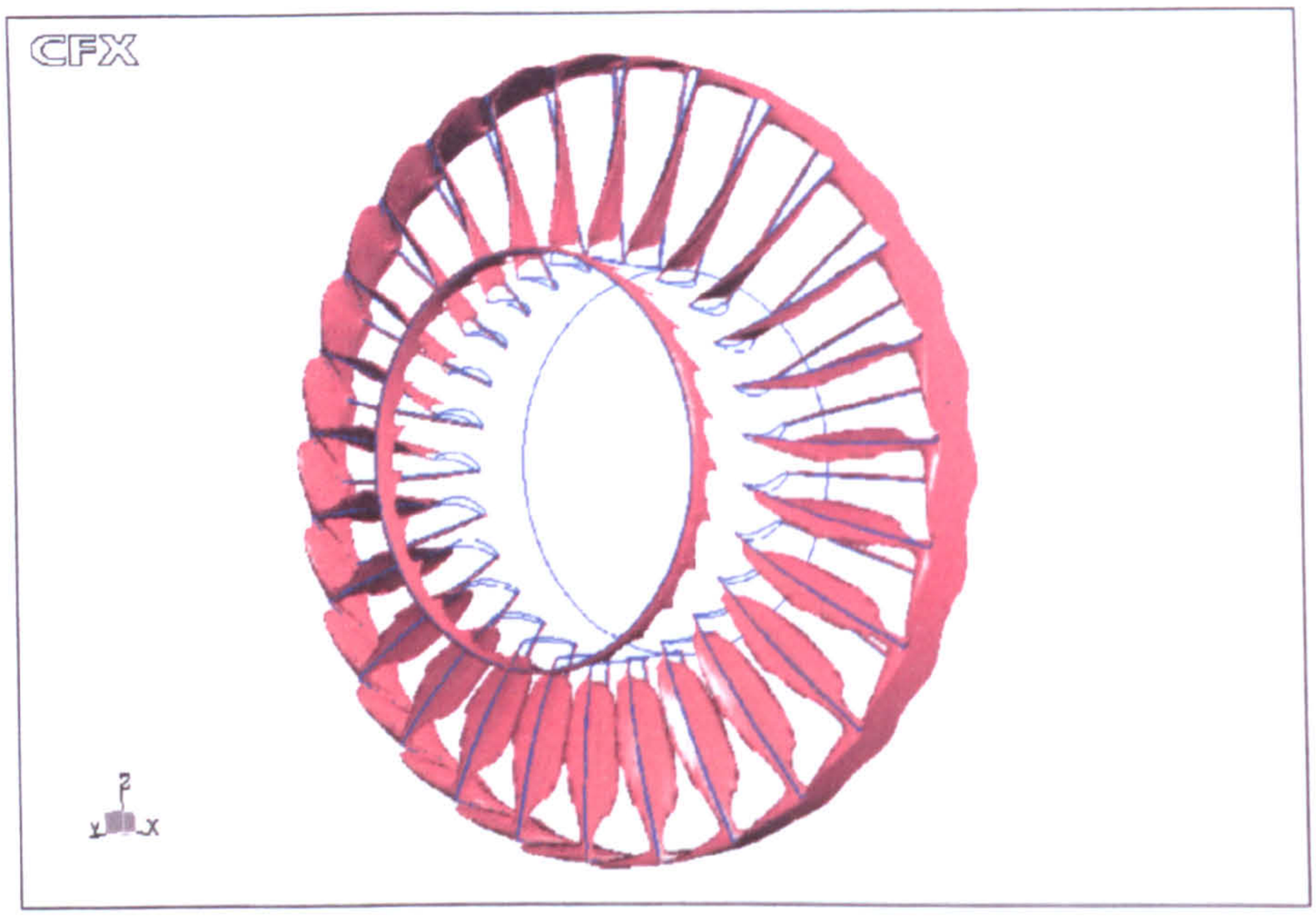

(c) At $\phi = 0.4954$ & $t = 0.051$

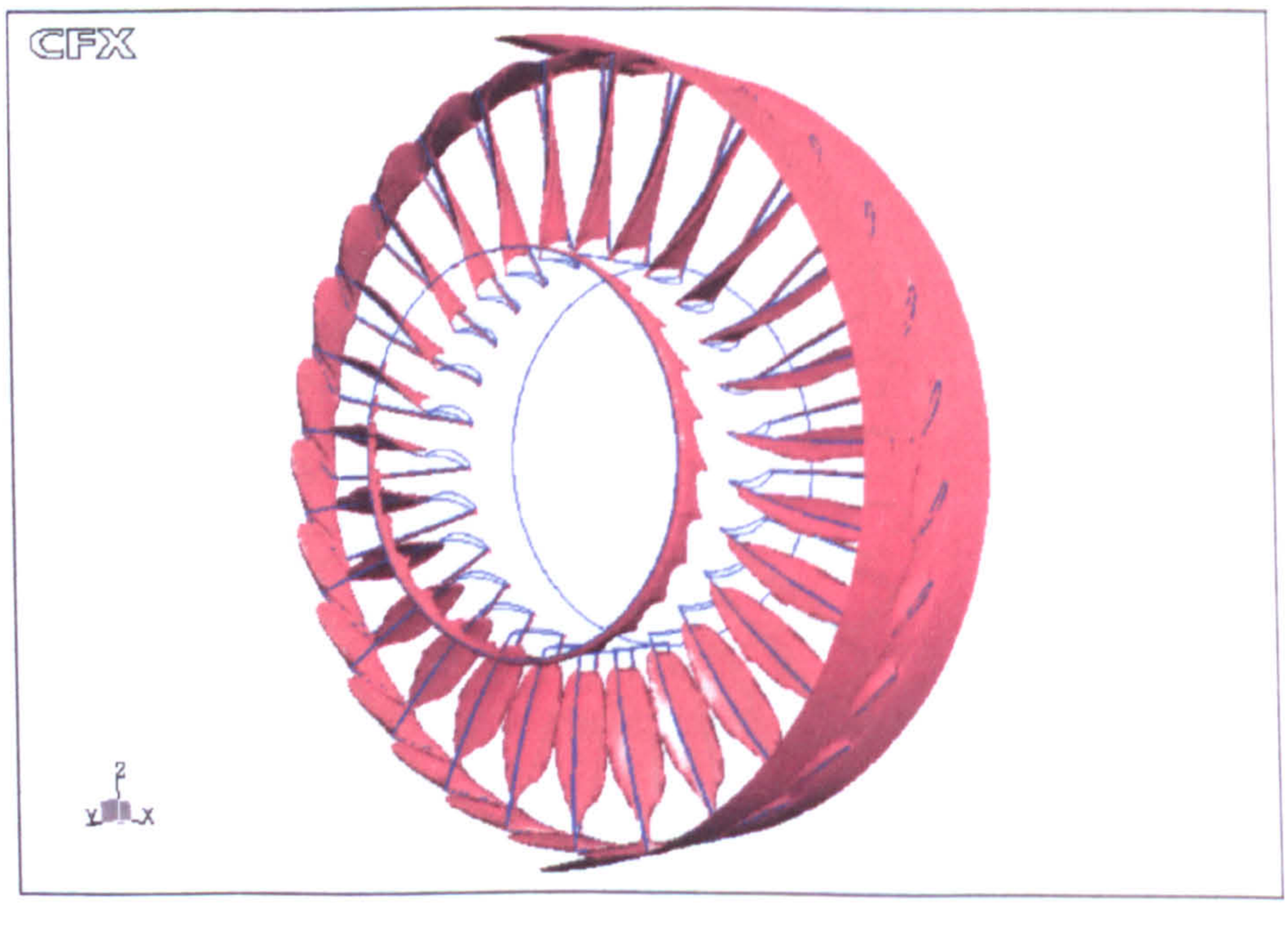

(d) At $\phi = 0.4903$ & $t = 0.052$

Figure 7.8: Flow separation from entire fan simulation (cont.)

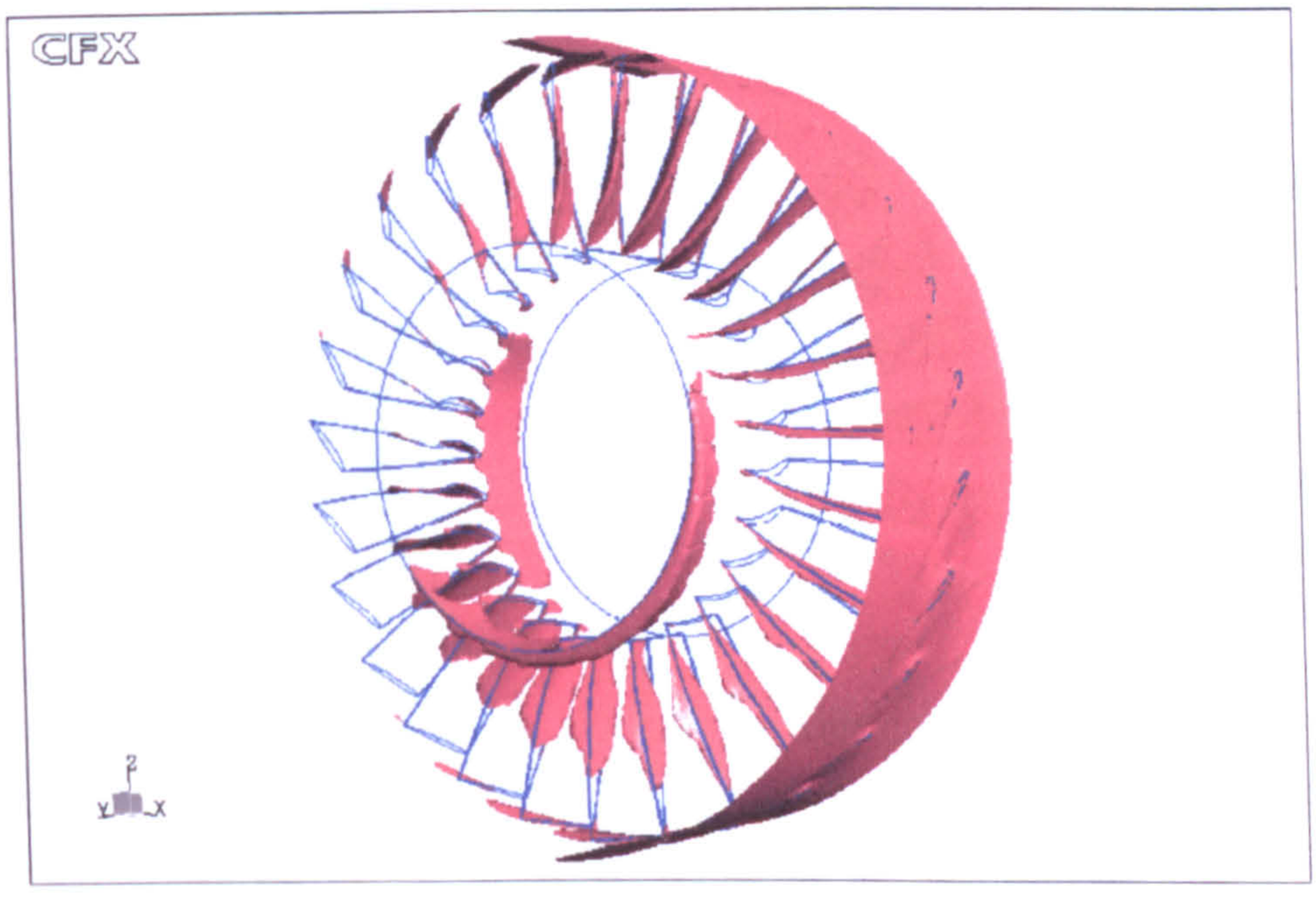

(e) At $\phi = 0.4495$ & $t = 0.060$

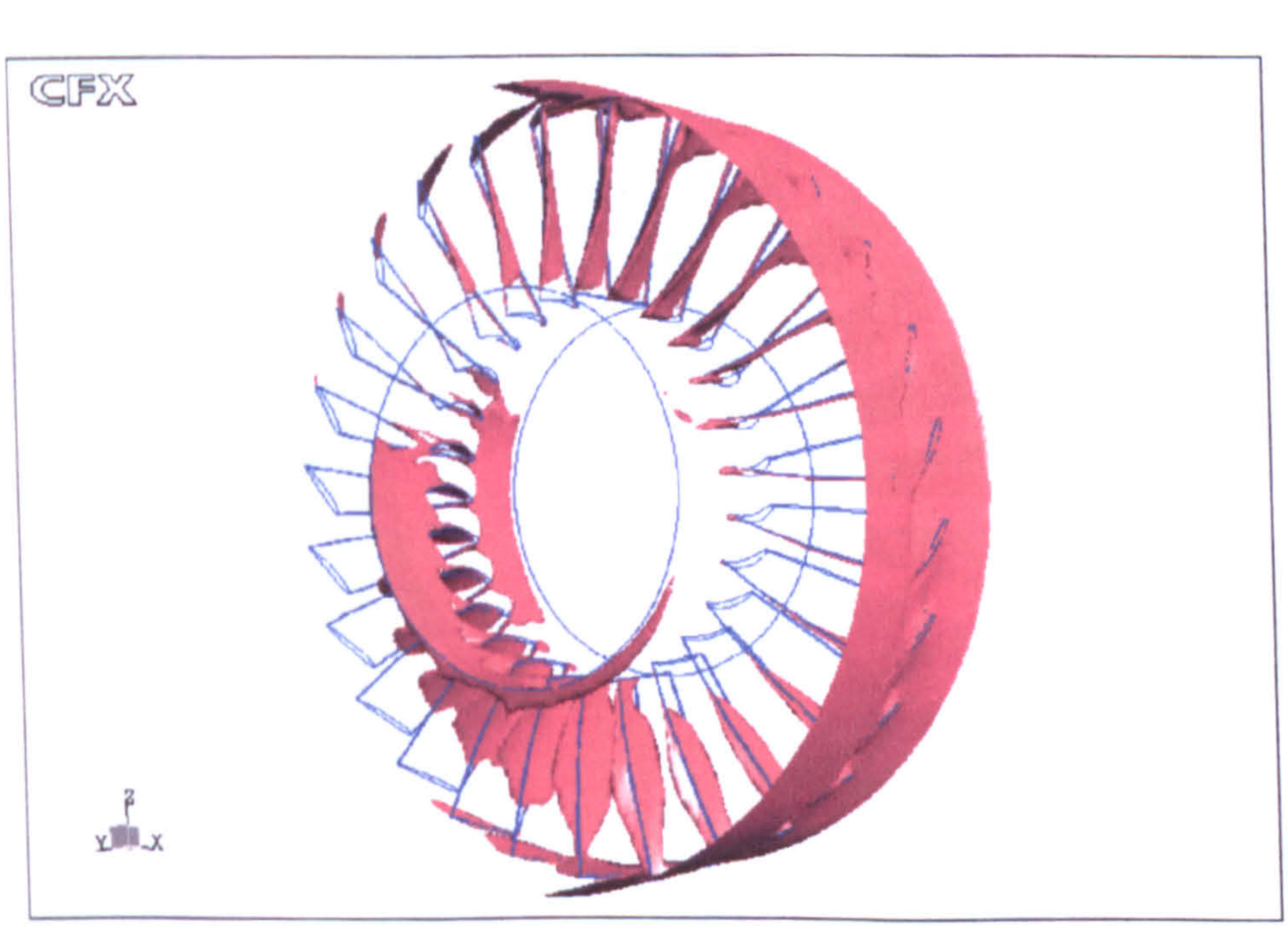

(f) At $\phi = 0.3985$ & $t = 0.070$

Figure 7.8: Flow separation from entire fan simulation (cont.)

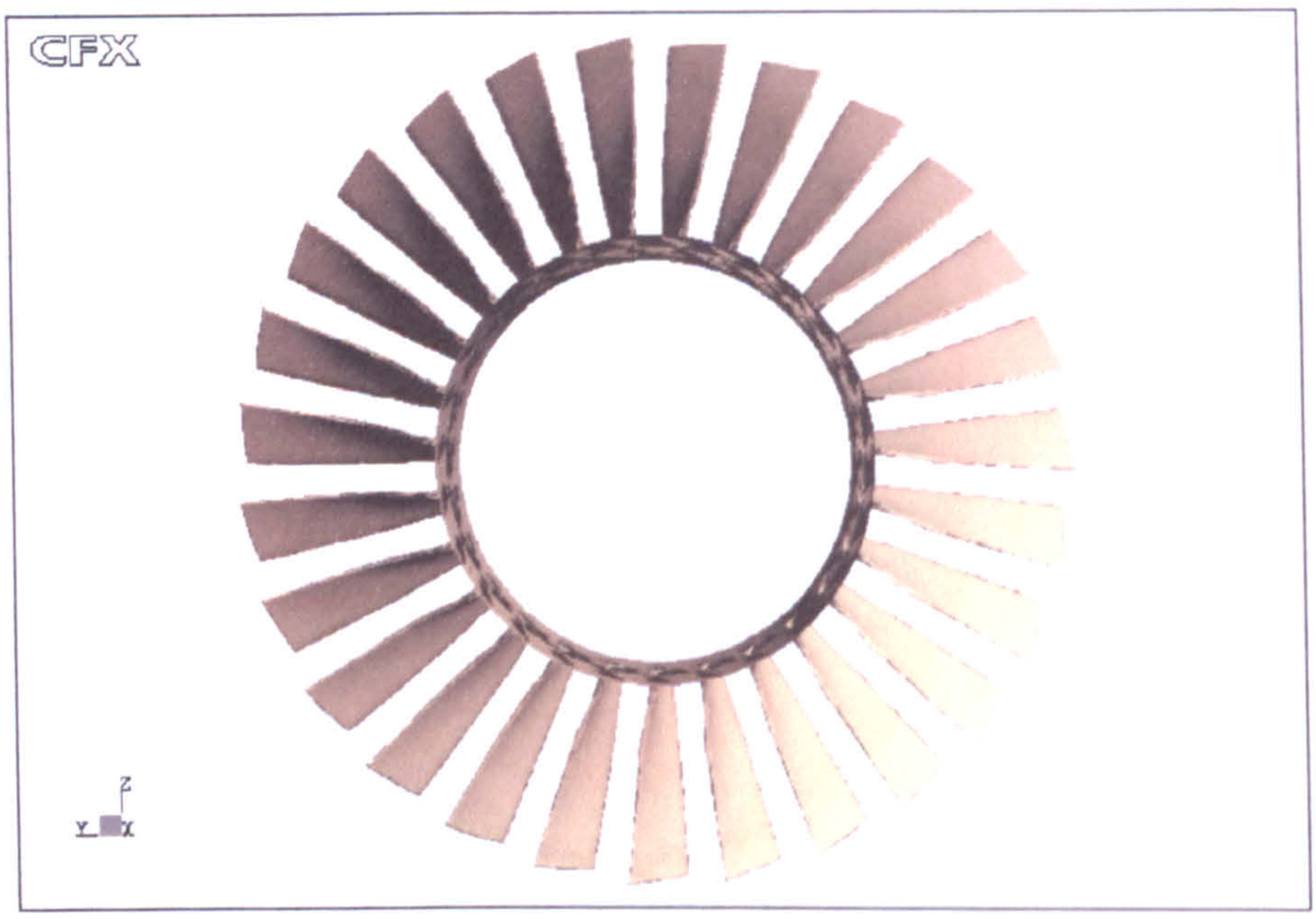

(a) At $\phi = 0.7453$ & $t = 0.002$

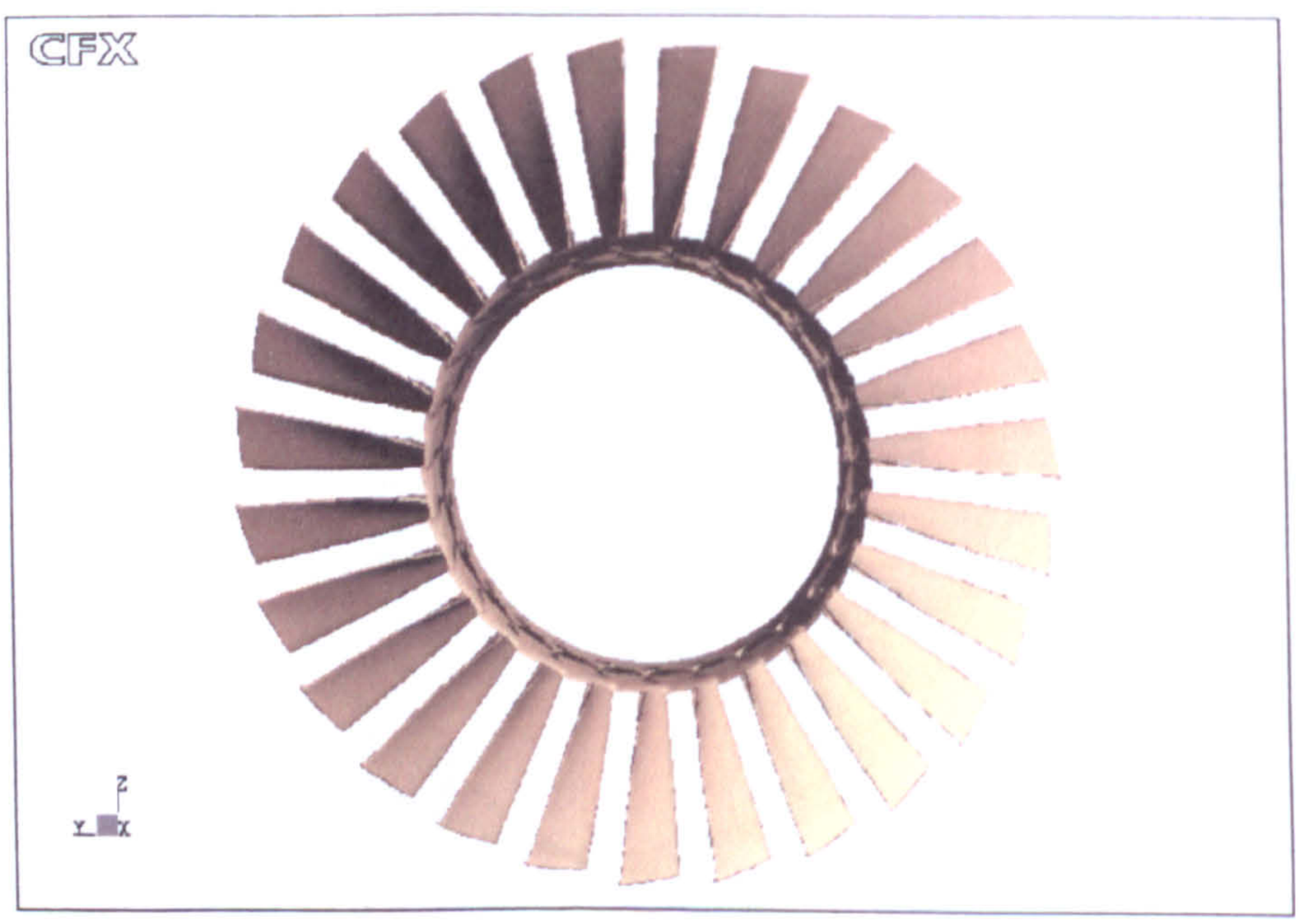

(b) At $\phi = 0.6229$ & $t = 0.026$

Figure 7.9: Isotimic plots of the low-speed regions

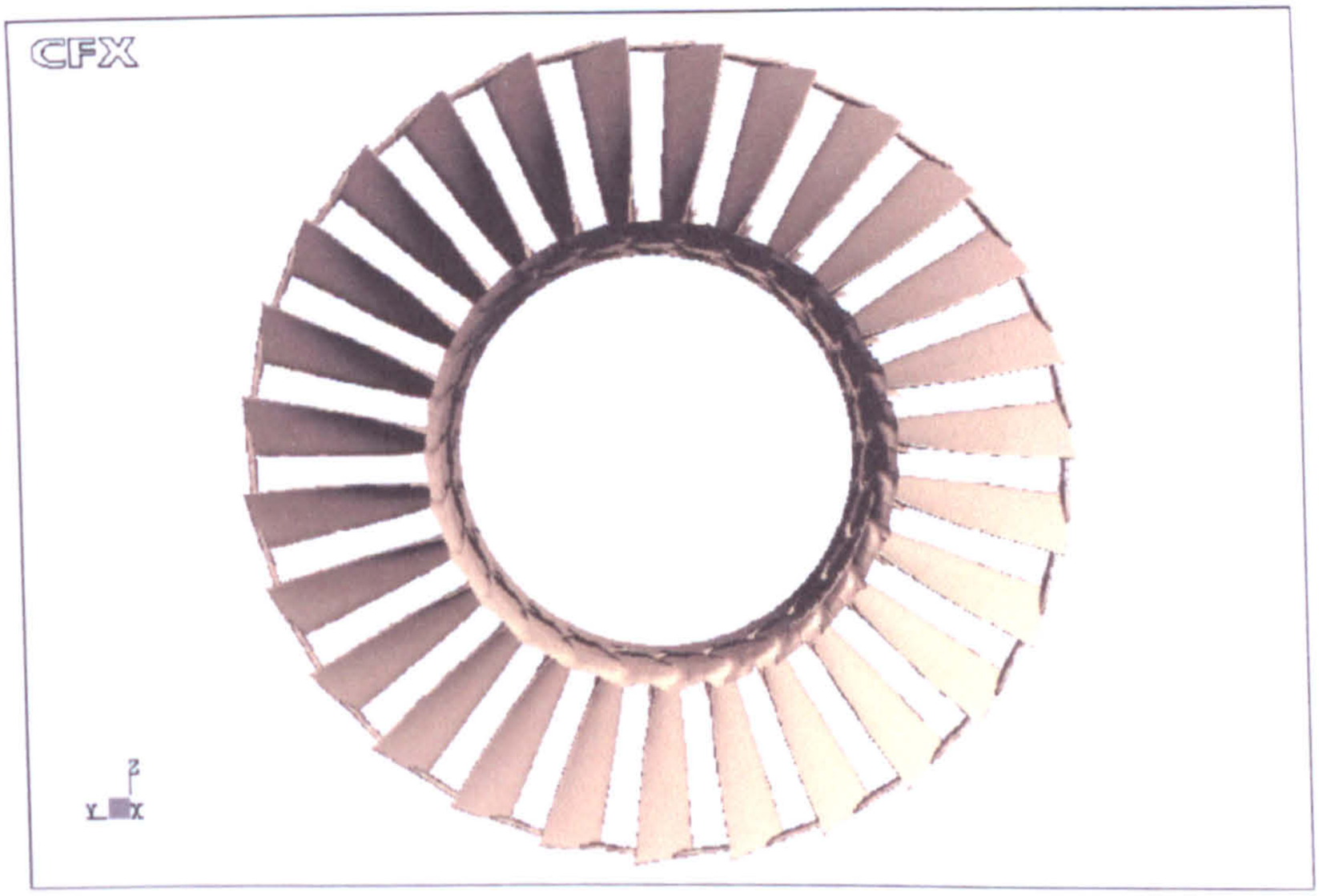

(c) At $\phi = 0.4903$ & $t = 0.052$

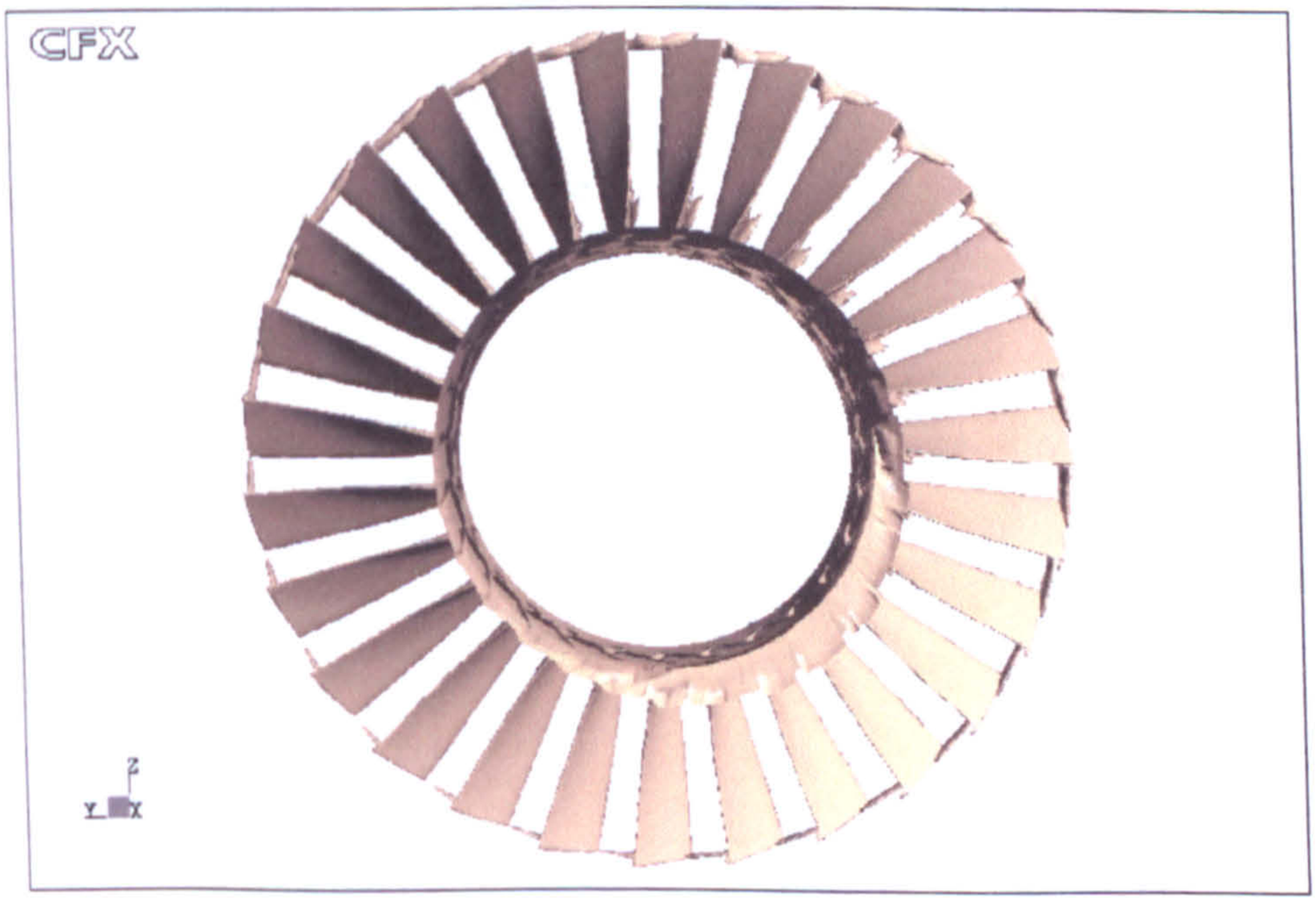

(d) At $\phi = 0.4801$ & $t = 0.054$

Figure 7.9: Isotimic plots of the low-speed regions (cont.)

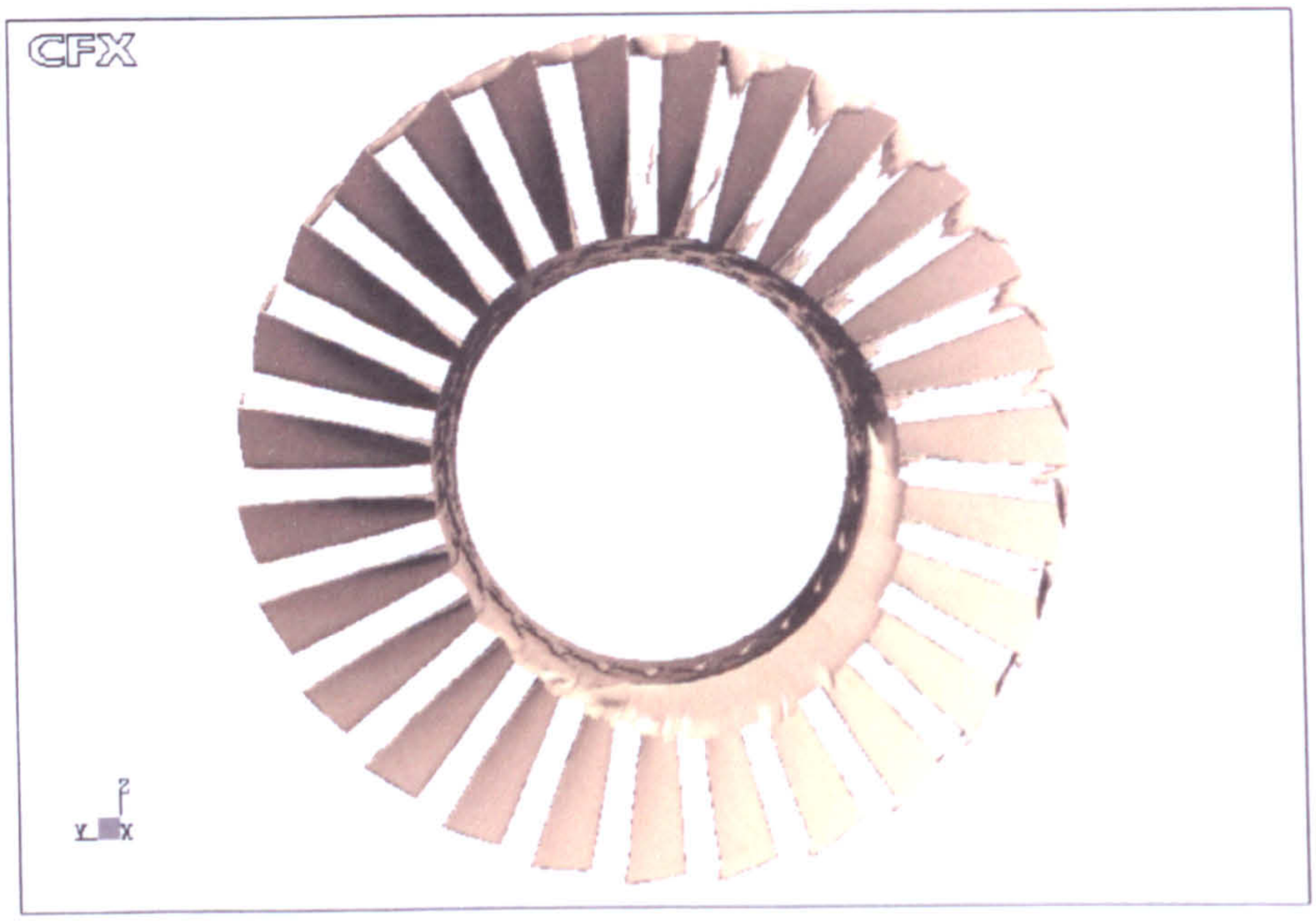

(e) At $\phi = 0.4699$ & $t = 0.056$

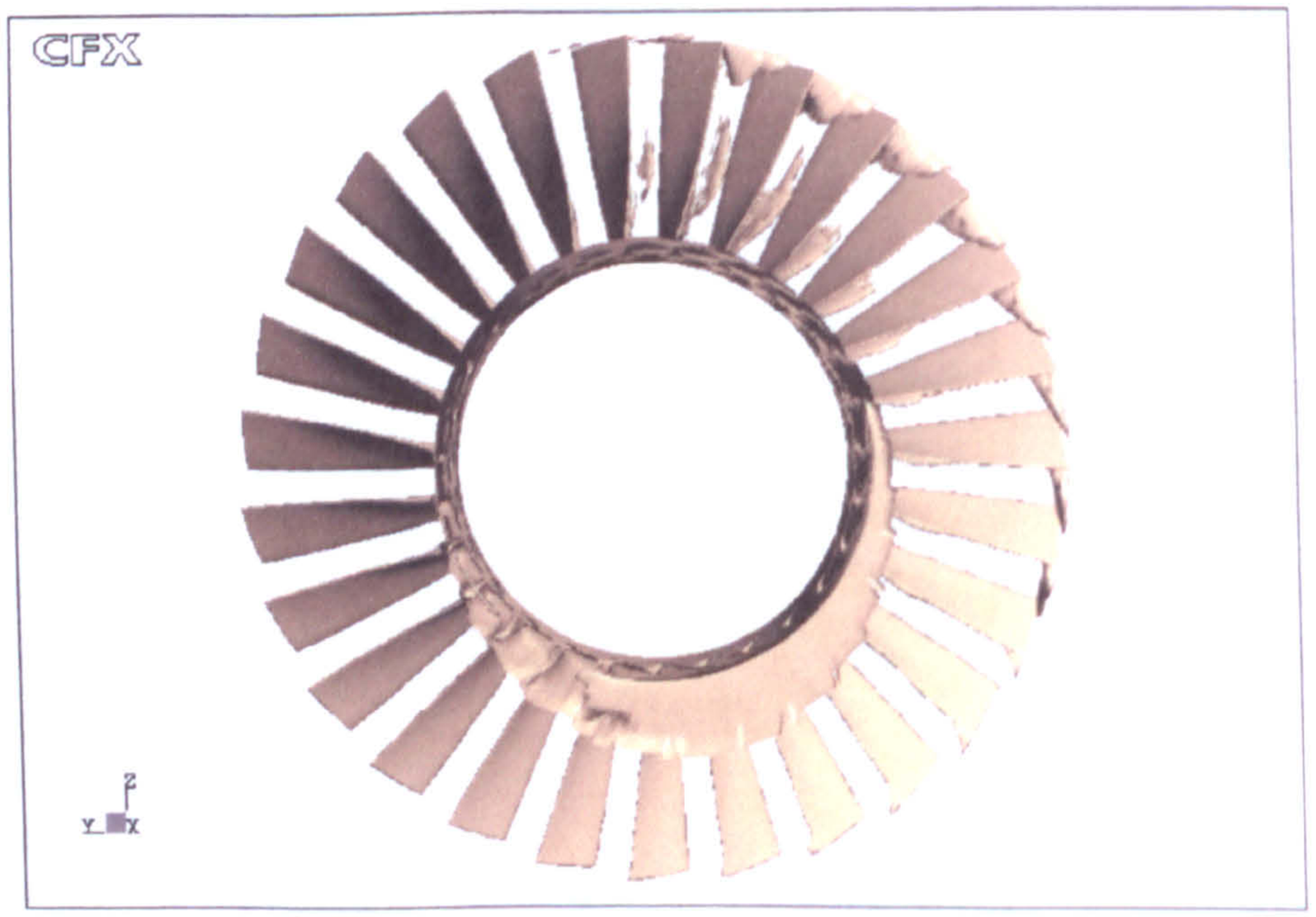

(f) At $\phi = 0.4444$ & $t = 0.061$

Figure 7.9: Isotimic plots of the low-speed regions (cont.)

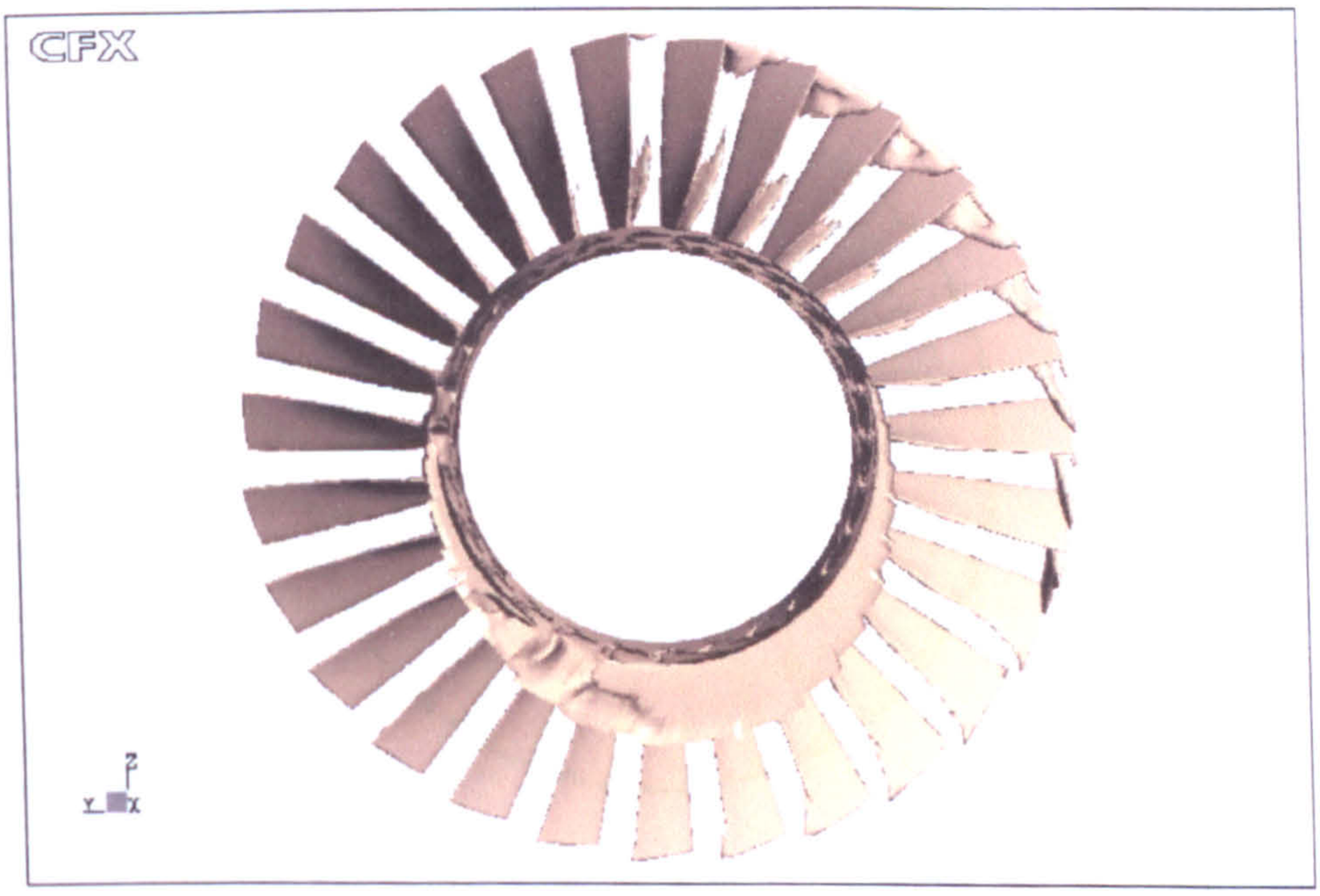

(g) At $\phi = 0.4189$ & $t = 0.066$

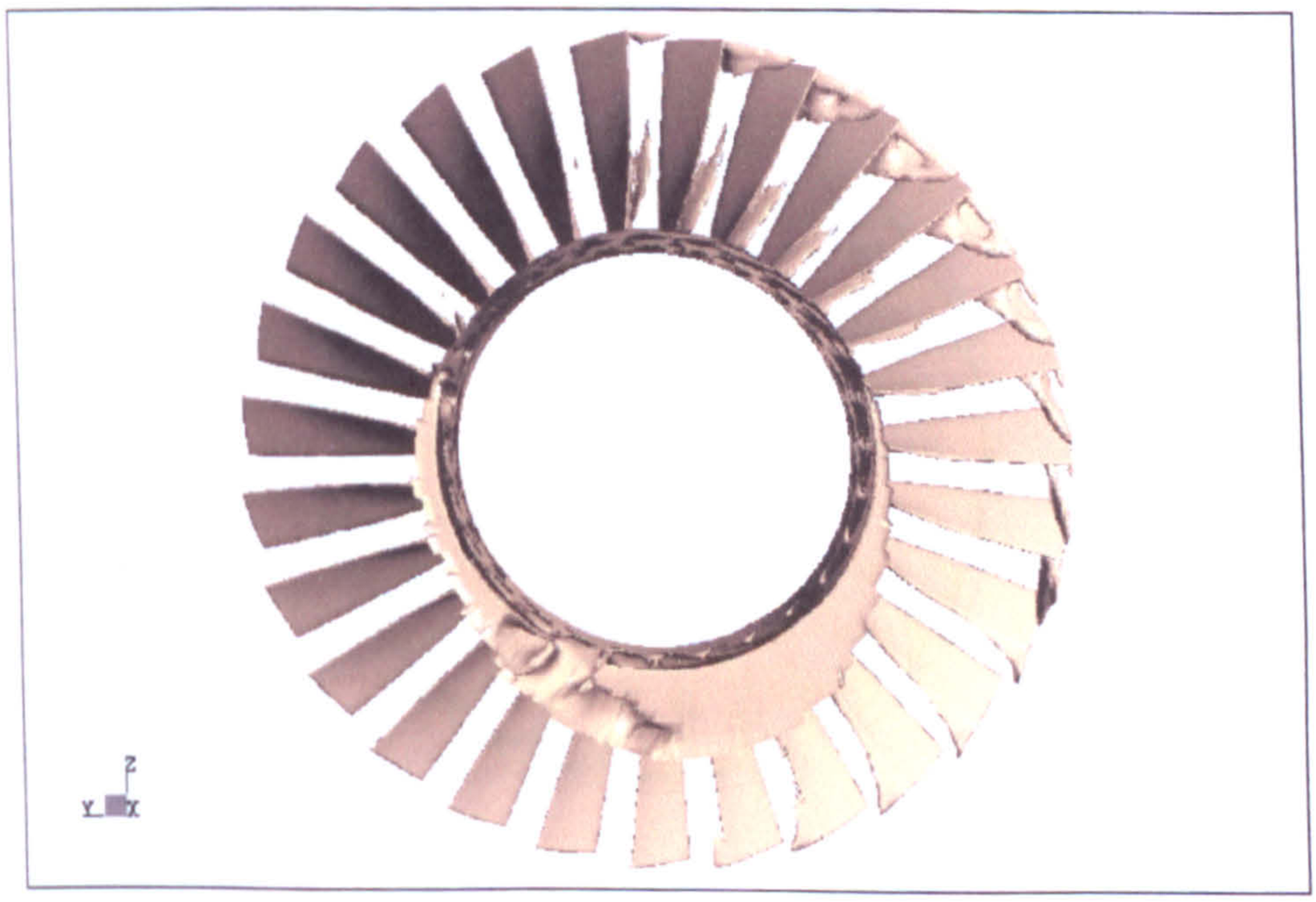

(h) At $\phi = 0.3985$ & $t = 0.070$

Figure 7.9: Isotimic plots of the low-speed regions (cont.)

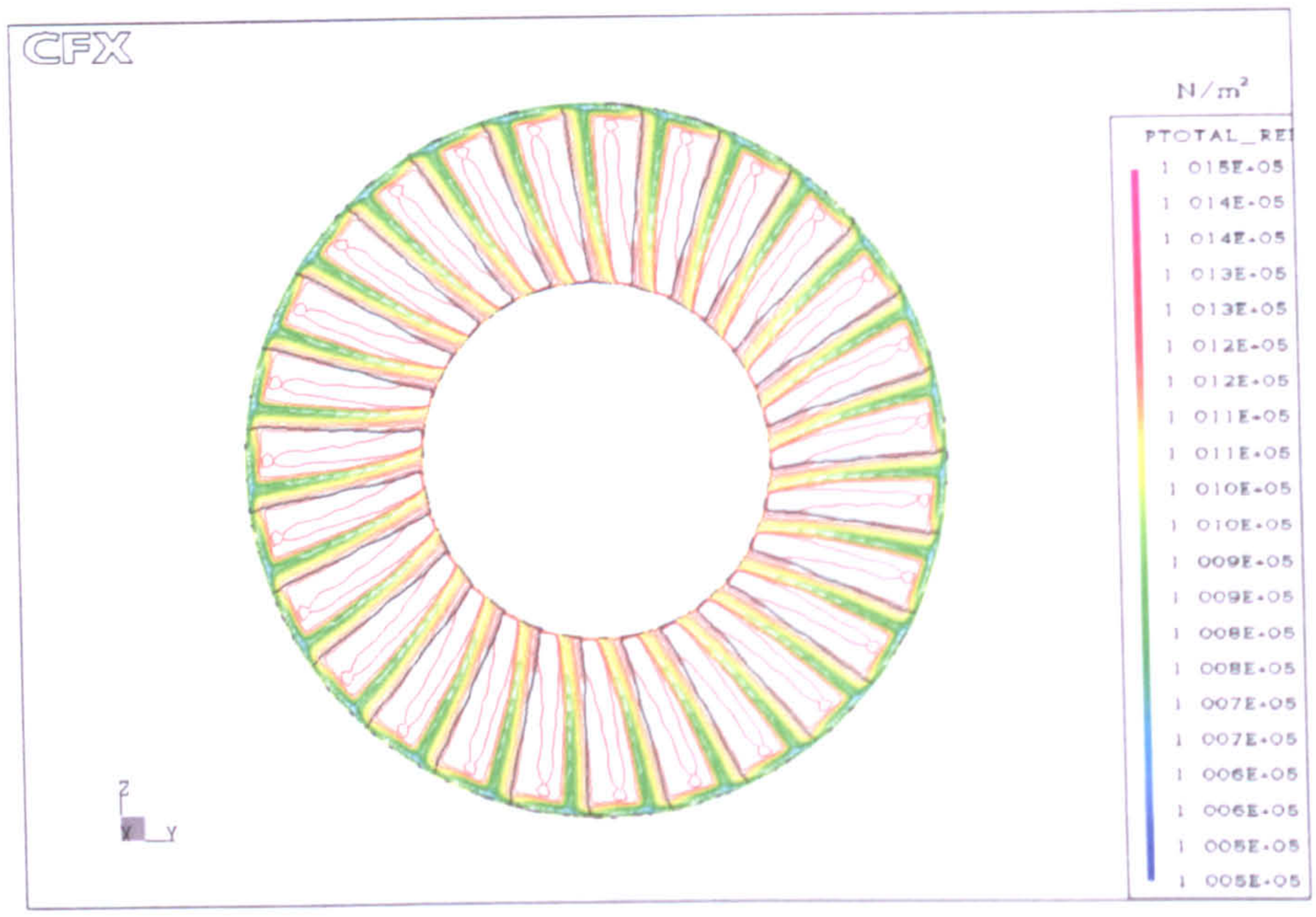

(a) At $\phi = 0.7453$ & $t = 0.002$

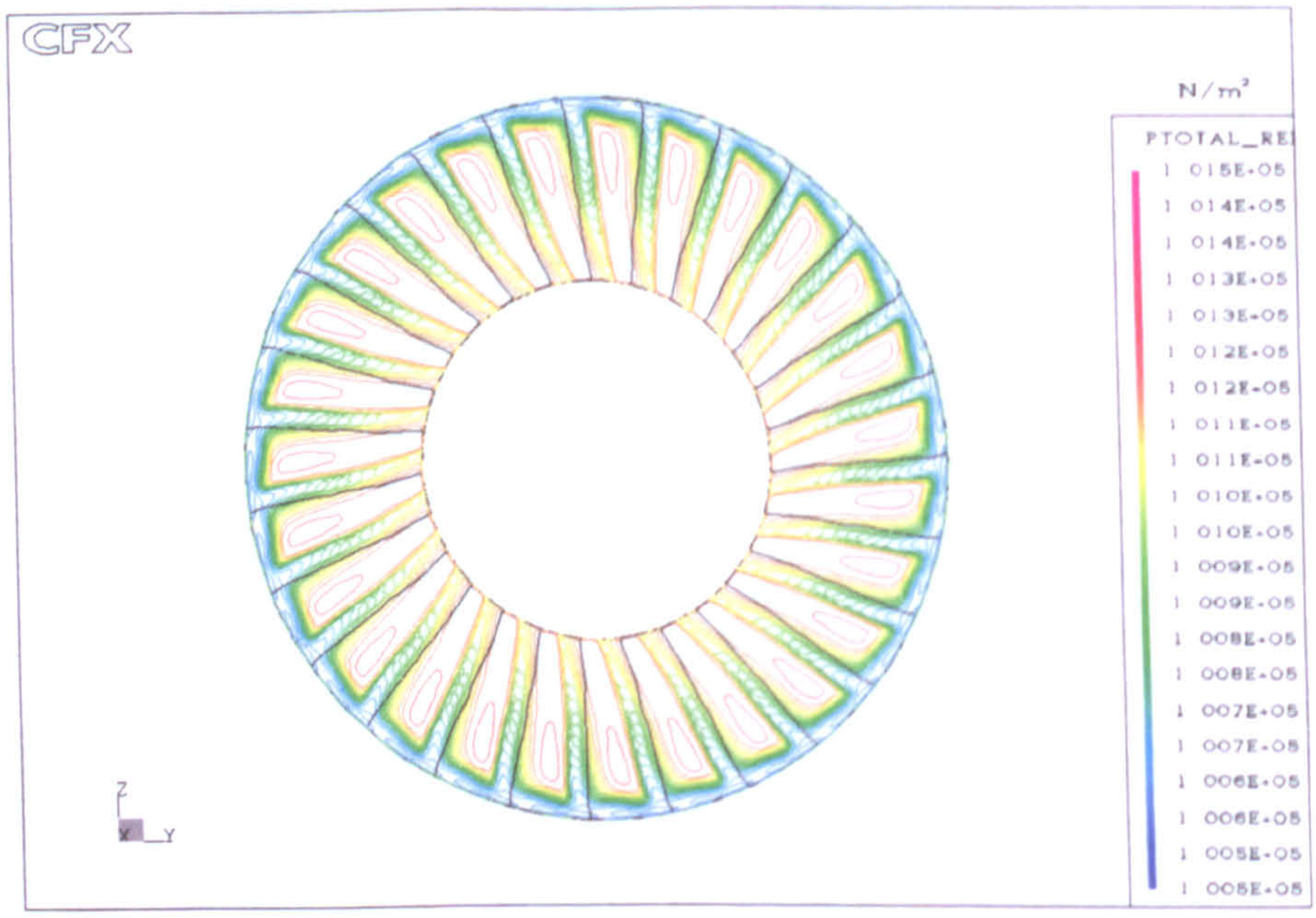

(b) At $\phi = 0.4954$ & $t = 0.051$

Figure 7.10: Blade-to-blade view of the relative total pressure distribution

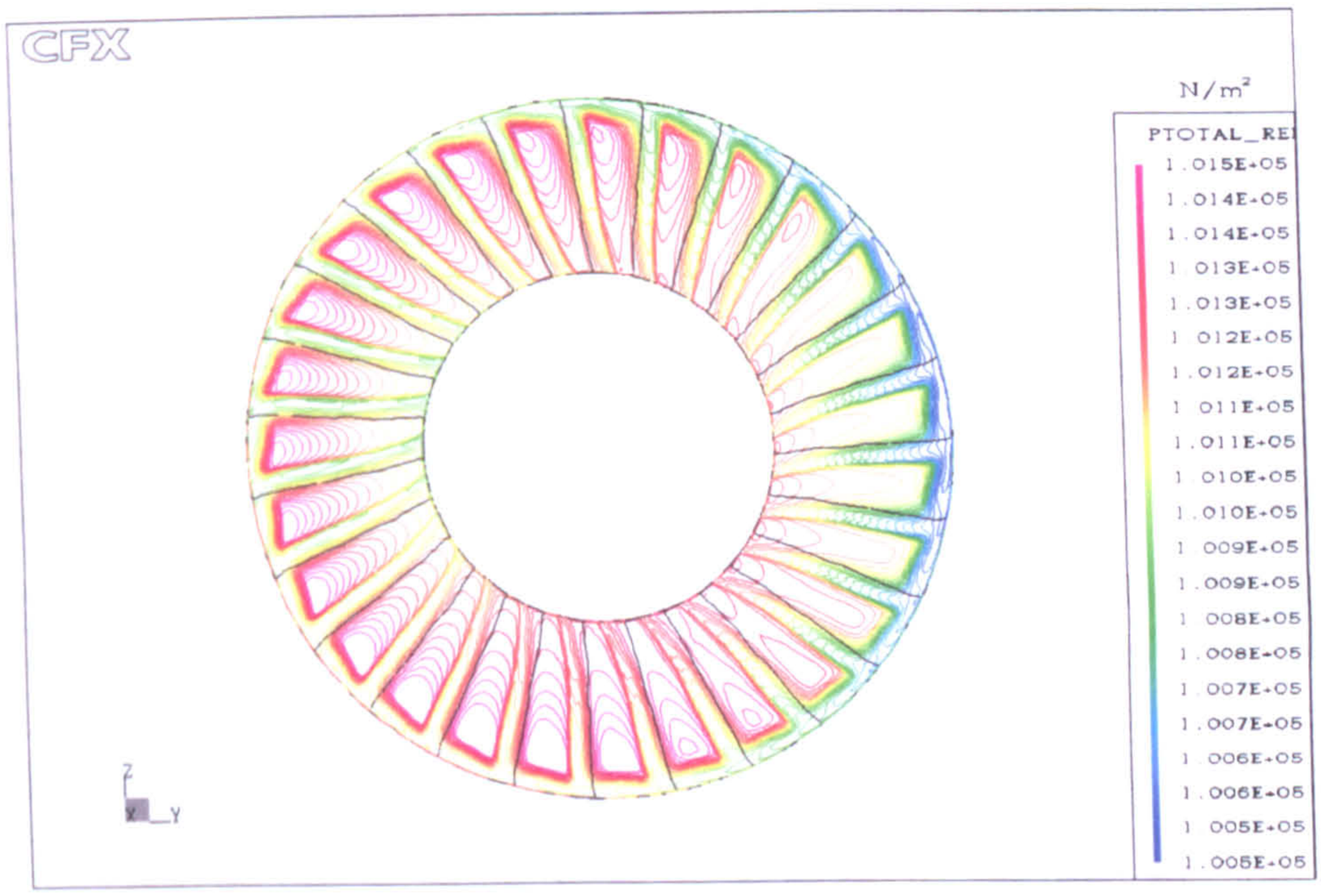

(c) At $\phi = 0.4903$ & $t = 0.052$

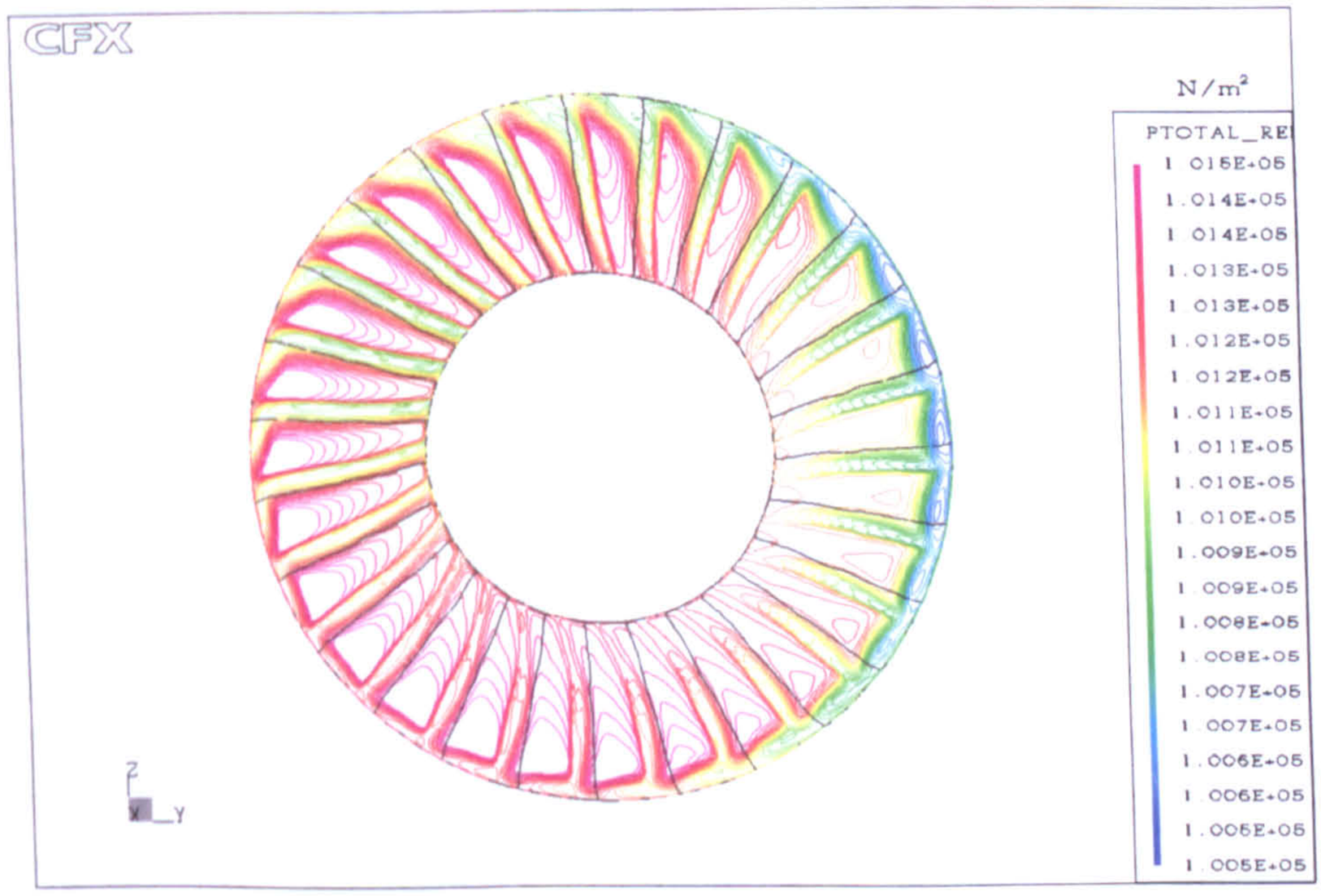

(d) At $\phi = 0.4699$ & $t = 0.056$

Figure 7.10: Blade-to-blade view of the relative total pressure distribution (cont.)

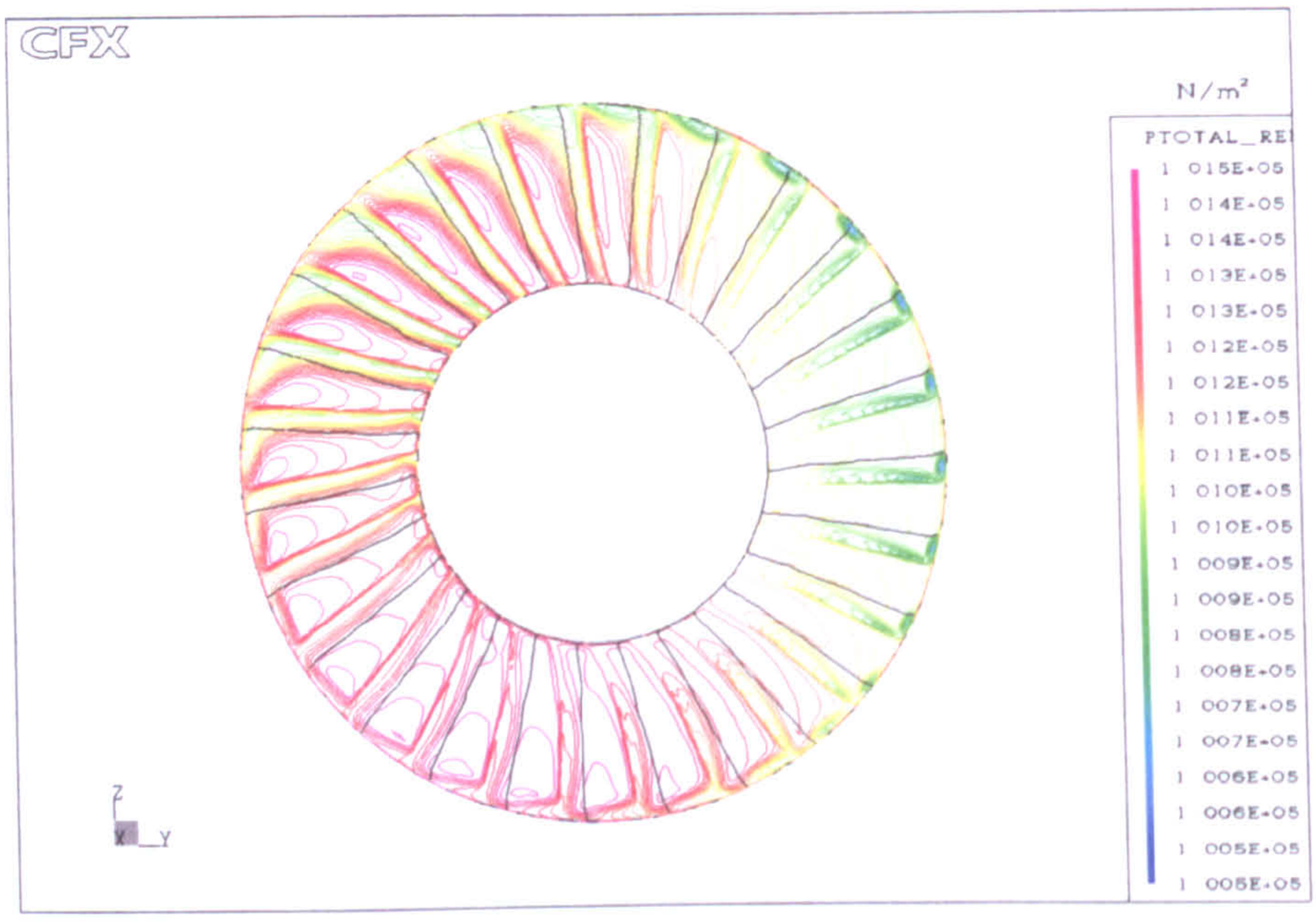

(e) At $\phi = 0.4444$ & $t = 0.061$

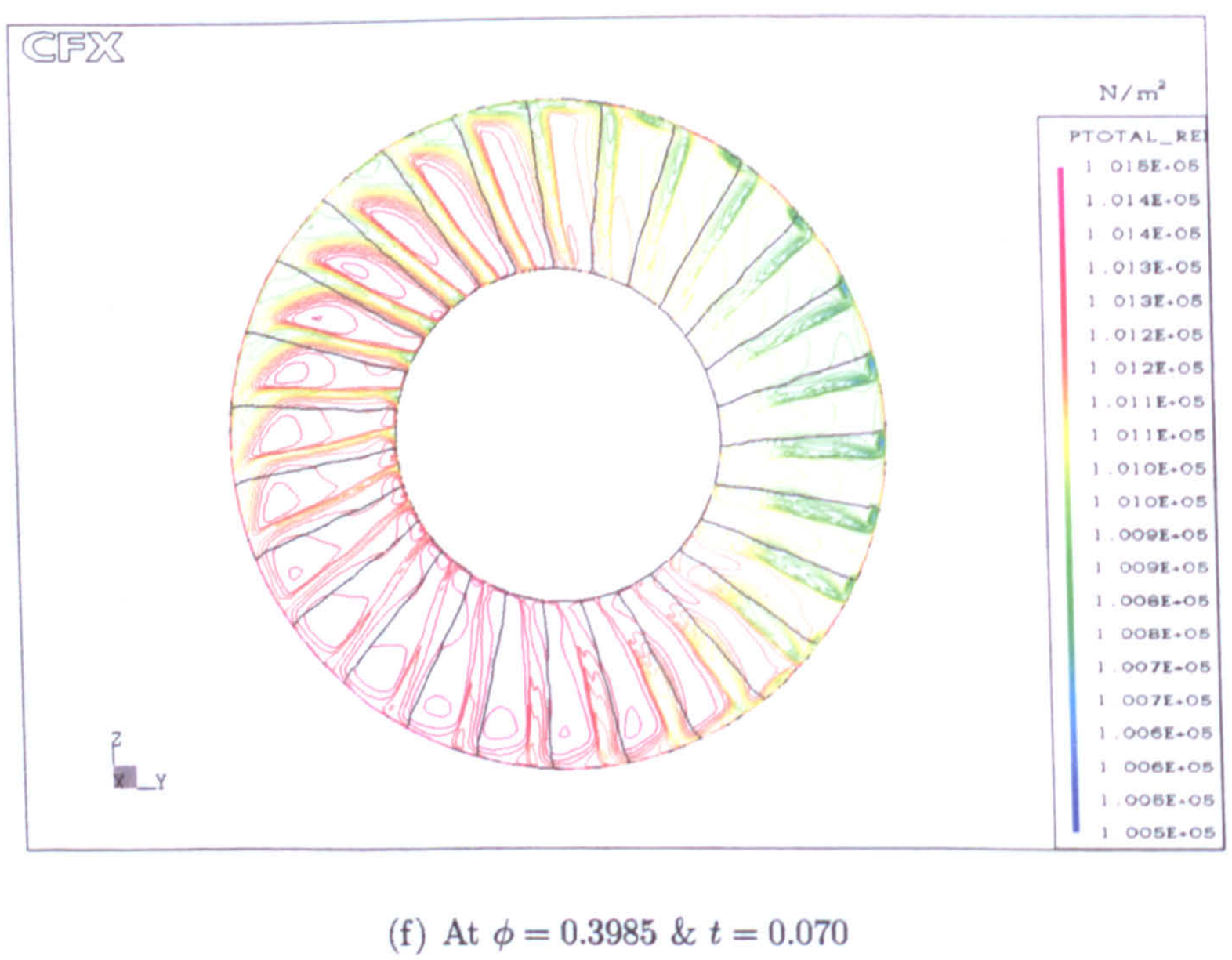

(f) At $\phi = 0.3985$ & $t = 0.070$

Figure 7.10: Blade-to-blade view of the relative total pressure distribution (cont.)

8

Steady Simulations for Treated Casing

This chapter presents the numerical simulations of the axial-fan with recess casing treatment fitted at the fan outer casing. The original solid wall casing, used in solid casing simulations presented in the last two chapters, was replaced by the recess treatment which is located partly over and upstream of the rotor blade tip and open to the flow passing through the fan. The predicted results were analyzed to investigate the effect of the recess casing treatment on stall margin improvement as well as its influence on global performance parameters. Two types of configurations were simulated, both of them have the same geometrical dimensions, but one with no vanes and one with vanes inside the casing. The effect of number of vanes inside the recess was also investigated by carrying out simulations of the fan in which the recess was equipped with double and around half of the number, 27 vanes, used originally for the vaned treated recess casing.

The overall performance of the fan in terms of pressure rise coefficient, efficiency and work-input characteristics are estimated at different flow coefficients and compared with both the solid casing predictions and the experimental work carried out at Cranfield university by Kang (51). The spanwise variation of velocity components and flow angle at the inlet and outlet of the domain were evaluated at 25 span locations and compared to the experimental data. There are no experimental data available for the pressure and velocity contours across the fan for any flow coefficient,

so the flow field inside the fan and the recess was discussed with contour plots produced numerically by the code.

8.1 Recess casing modelling

Initially the recess was numerically simulated with vaneless casing and later vanes and a shroud ring were added to the recess to simulate the vaned casing. The shroud ring is fitted to the inner edge of the vanes to separate the recess flow and main flow passage and serves as a middle reservation part between entry and exit of the recess. The recess geometry employed in the numerical simulations, Figure 8.1, adheres closely to that used by Kang, Figure 2.13(a), except that 27 instead of 24 vanes are used inside the recess. This choice of 27 vanes was dictated by the periodicity requirements of the unsteady simulations, which are to be carried out and presented later in this work. Table 8.1 presents the small geometrical difference in recess dimensions between that used in the numerical simulation and the one used by Kang.

Table 8.1: Recess and vane dimensions

Dimensions (mm)	h_r	x_{out}	x_s	x_{in}	x_e	x_r
Experimental rig*	56.00	56.00	30.00	34.00	22.00	120.00
Present work	56.00	55.44	29.69	32.85	21.65	117.98

* Test by Kang (51)

The geometry of the casing grid is designed such that it has the same periodic boundaries as the tip grid designed in Chapter 6. The amount of rotor axial chord exposed to the recess has a critical influence on the behaviour of the fan, Azimian et al. (9), and in the current study an exposure of 65% was used similar to that tested by Kang (51). The treatment grid was meshed using TASCgrid and made to be consists of 53 × 40 × 25 mesh points, of which 53 are placed in the axial direction, 40 in blade-to-blade direction, and 25 in the radial direction. The casing grid imported to CFX-TASCbob3D, the code preprocessor, and attached to the solid computational domain at the shroud surface.

A shroud ring and 27 vanes are then added to the casing grid to carry out the vaned casing simulations. To investigate the effect of the number of vanes inside the recess, the casing grid is modified to consist 54 vanes ,double the original number of vanes,

and 14 vanes, around half of the original number of vanes. Figure 8.2 presents two of the computational domains used in the numerical simulations of treated casing; the computational domain with vaneless casing in Figure 8.2(a) and the computational domain with 27 vaned casing in Figure 8.2(b).

8.2 Boundary conditions

The casing grid was attached to the tip grid using the CFX-TASCflow "Stage" interface, a mixing-plane type form of inter-blade row boundary condition, where mass and momentum are conserved across the interface. This numerical model is based on the tangential averaging of the velocity components as they are transferred from the rotating frame of reference to the stationary one. The static pressure is allowed to develop independently from both sides whereas its mean value is adjusted in a way that mass and momentum are properly conserved.

The validity of this steady model has not been fully proven but it consists the best available approach for analyzing the blade-recess interaction using a steady CFD method, Ghila and Tourlidakis (32). The numerical solution procedure is based on an iterative relaxation method and a fully convergent solution is obtained when the residual from the non-satisfaction of the discretized continuity and momentum equations falls below a very small number 10^{-5}.

The simulations were carried out for single blade passage with steady-state boundary conditions, in which the atmospheric total pressure is considered at the inlet of the domain and a different mass flow rate for each simulation is specified at the outlet of the domain. The standard k-ϵ turbulence model with wall functions, Launder and Spalding (58), was employed and the MLPS discretization method was used for the treatment of the convective term together with the PAC scheme. The vane and the shroud of the domain were made stationary while the blade, hub and the rest of the domain were rotating at 1 500 rpm.

8.3 Results and discussion

The predicted results of overall performance and work-input characteristics of the fan with treated casing were examined, and the spanwise variations of the velocity, and flow angle were evaluated and compared to the experimental data. The flow

field inside the fan was visualized and discussed with plots produced numerically by the code.

8.3.1 Fan overall performance

The predicted total to static pressure rise coefficient ψ and total to total efficiency η are presented as a function of the flow coefficient ϕ in Figure 8.3 together with the measured data given in Kang (51). The addition of the vaneless casing altered the flow behavior and appears to sustain the pressure rise coefficient down to a flow coefficient of 0.45 instead of 0.61 as for solid casing presented in Chapter 6.

In contrast with the solid casing configuration, the presence of the vaneless recess increased the peak pressure rise by about 30%. However, attaching a vaneless recess induces an attendant aerodynamic penalty in the form of a small pressure rise reduction and a slight drop in the fan efficiency at all flows. Below the flow coefficient of 0.45, the fan enters its deep stall flow regime. Even though simulations with vaneless casing were performed for flow coefficient below 0.45, no numerical results below 0.4 are presented given the uncertainty associated with these. However the numerical result for mass flow coefficient just below 0.45 showed that there were drops in pressure rise coefficient as well as efficiency due to the stall inception.

The predicted results of the numerical simulation of recess treatment with 27 vanes show that the fitting of vanes to the recess contributed to further extend the unstalled region and substantially increase the pressure rise. This rise was for the lowest simulated mass flow about some 80% of that offered by the peak rise of the vaneless recess. Furthermore the presence of vanes inside the recess modified the flow behavior to an extent that no sign of stall inception was apparent as the flow coefficient was reduced to a minimum of 0.22.

The vaned recess hardly affects the fan flow field for a flow rate higher than 0.65. This is consistent with the performance results in Figure 8.3, which show that the treatment has little effect on the performance in the high flow range. However between the flow coefficients of 0.65 to about 0.61, a point which corresponds to 45% throttle opening, there is a slight performance gain. This is due to the fact that the recess contributes to effectively reduce the whirl component and remove flow blockage found in the tip region of the solid build, and consequently increase the blade loading.

As is also apparent from Figure 8.3, the pressure rise coefficient obtained from the numerical simulation displays a very similar trend to that obtained experimentally

by Kang (51). Although the experimental work identified the stall onset for this configuration at a flow coefficient of 0.3, the numerical simulation was run down to a value of 0.22 without encountering any evidence of significant pressure drop. The predicted pressure rise is consistently higher than Kang's and this may be attributed to the fact that in the present work 27 vanes were used instead of 24 as in the experimental studies.

8.3.2 Work-input characteristics

The work-input characteristics are cast in terms of the work coefficient $\Delta H/U_m{}^2$ and are presented as function of the flow coefficient ϕ in Figure 8.4 together with the measured data given in Kang (51). The addition of both vaneless casing and recess with 27 vanes altered the flow behaviour as seen form both pressure rise coefficient and efficiency curves in Figure 8.3. The work coefficient shows excellent agreement with that of the solid casing. Quantitatively the code showed an excellent agreement with the experimental results of the work coefficient data for both vaneless and 27 vaned recess casing.

8.3.3 Effects of number of vanes

The predicted pressure rise for 27 vaned recess is consistently higher than Kang's and it was initially thought that this would be attributed to the fact that a different number of vanes are used inside the recess in both investigations. This topic is thought to deserve further investigation and so the fan was numerically simulated with the recess equipped once with double and another with around half of the number, 27 vanes, used originally. Even though the fan with 14 vanes enters its deep stall at similar flow rate to that of vaneless casing, there was no noticeable aerodynamic penalty neither in pressure rise nor in fan efficiency at high flows found in the vaneless configuration. However for the fan with 54 vanes the numerical simulation was run down to a flow coefficient value of 0.22 without encountering any evidence of significant pressure drop.

At high flow rates both simulations produced similar results in terms of pressure rise, fan efficiency and work coefficient to that of 27 vanes simulation, Figure 8.3 and Figure 8.4. As the flow rate decreases below 0.45, the fan with 14 vanes enters its deep stall flow regime, and the fan with 54 vanes predicted a slightly lower pressure rise values that produced by 27 vanes. This slight reduction in pressure

rise may result from the flow separation losses produced by the extra vanes inside the recess. Nevertheless when comparing the efficiency and work coefficient results, the discrepancy is so small and the trend so similar as to lead to the hypothesis that the flow may be largely insensitive to a small blade number variation inside the recess.

8.3.4 Absolute velocity profiles

The radial profile of the absolute axial V_a, radial V_r, and tangential V_t velocity components are presented with the measured data from Kang (51) at two different flow coefficients; design flow rate $\phi = 0.72$, and flow coefficient $\phi = 0.60$. They are presented at the inlet station in Figure 8.5 and in at the outlet station in Figure 8.6. The predicted results were area-averaged at 25 span locations at the inlet and outlet stations of the domain. The numerical simulation predicted similar velocity profiles to those experimentally reported except near the blade tip, where a slight difference can be seen. This may be caused as discussed before from the inadequacy of the k-ϵ turbulence model with wall functions used in the present work. For these two flow conditions, similar distributions of the velocity components were observed at 8 mm upstream the blade leading edge, Figure 8.7, and at 6 mm downstream the blade trailing edge, Figure 8.8.

8.3.5 Absolute flow angles

The absolute flow inlet and outlet angles of the fan are calculated at 25 span locations for both design flow rate $\phi = 0.72$, Figure 8.9(a), and for near stall flow rate $\phi = 0.60$, Figure 8.9(b). With comparison to the experimental data the code predicted similar flow angles at both flow rates specially away from the blade tip.

8.3.6 Flow field visualization

A qualitative appraisal of the stall characteristics of the fan due to the fitting of the vaneless recess is illustrated in Figure 8.10. The extent of separation present in the tip region for a flow rate $\phi = 0.50$ is substantially reduced even for a flow rate slightly below $\phi = 0.56$ corresponding to solid casing simulation in Figure 6.14(b). The separation reduction mechanism of the vaneless recess for a flow coefficient of 0.6, corresponding to near stall point in the solid build, is the subject of Figure 8.11. The

streamlines correspond to fluid particles released upstream of the blade root leading edge, are partly redirected towards the vaneless recess, effectively contributing to disperse the concentration of low momentum flow, hitherto present in the tip region.

The point of entry of the flow into the vaneless recess coincides, as seen before in the solid simulations, mainly with the location of the stalled region. This is clearly illustrated with large mass flow entering the recess above the blade tip in Figure 8.12. Inside the recess cavity, the flow adopts a slanted circulating pattern broadly aligned with the blade tip chord, Figure 8.13. Although the vaneless recess casing is by itself not a practical proposition in terms of casing treatment, the simulation of this configuration offers a valuable insight into the fundamental physics of the recess stall delaying action.

The flow behavior inside the 27 vaned configuration is subsequently analyzed for the case corresponding to flow coefficient of 0.6, Figures 8.14 to 8.18. The seeding in the streamline plots took place as for all cases upstream of the blade root leading edge. The addition of the vanes to the recess has the effect of essentially removing the whirl velocity component, Figures 8.14(a) and 8.15, while increasing the circulation in a quasi-meridional plane. Besides this swirling motion, the presence of the turning vanes induces also circulation with a near radial axis whose direction is both a function of the turning vane and of the relative motion of the blade tip, Figure 8.14(b).

The flow has a strongly dissimilar pattern on both sides of the vane as it is evident in Figure 8.16. On its concave side, Figure 8.16(a), over which most of the incoming flow impinges, the motion is characterized by the presence of a small vortex slightly ahead of the leading edge and general downthrust. In the convex side of the vane, Figure 8.16(b), the flow exhibits also a circulatory motion of larger extent located ahead of the shroud ring and there is also evidence of very low fluid transfer across the open recess. As flow jet impinges with either the vane or casing boundary, its velocity decreases accompanied with increase in the pressure as shown in Figure 8.17.

The bulk of the flow outlet from the recess cavity occurs for the mass flow coefficient of 0.6 directly above the blade tip as shown in detail in Figure 8.18 and more generally in Figures 8.14(b) and 8.16. A significant difference in the extent of blade domain re-circulation was observed for the reduced flow regime, flow coefficient 0.22, Figure 8.19(a). At this flow coefficient there is a conspicuous difference between the position where most of the flow leaves the recess to re-enter the blade domain and the corresponding position at the higher flow rate. At the flow coefficient 0.6, Figure 8.19(b), the radial flow mostly leaves the cavity ahead of the shroud ring. As the flow

coefficient is reduced, the primary outlet region on the recess is sharply displaced upstream with the zone ahead of the shroud ring fully occupied with the incoming radial flow.

This is can be seen very clearly in the mass boundary contour plots for the lower boundary of the recess casing, presented in Figures 8.20(a) and 8.20(b), corresponding to flow coefficients of 0.22 and 0.60 respectively. In these plots, the flow entering the recess is colored in red and yellow, while the green and blue colour denotes flows leaving the cavity. The mass flow enters the recess from the inlet side ahead of the shroud ring is substantially increases from 2.87% to 57.16% of the total mass flow enters the domain as the flow coefficient decreases from 0.72 to 0.22, Table 8.2. The amount of this flow leaves the recess to re-enter the blade domain from the same area is substantially decreased from 47.1% at flow coefficient of 0.60 to 0.175% to at flow coefficient of 0.22.

Table 8.2: Mass flow rate enters from the recess inlet

Flow coefficient ϕ	0.72	0.60	0.40	0.22
Total mass into the domain	0.141184	0.117653	0.078435	0.04314
Mass into the recess inlet	$4.05\text{x}10^{-3}$	$6.81\text{x}10^{-3}$	$1.64\text{x}10^{-2}$	$2.47\text{x}10^{-2}$
Inlet recess/total mass	2.87%	5.79%	20.97%	57.16%

The radial extent of the flow redistribution is next shown in the meridional plots of speed, Figures 8.21(a) and 8.21(b) for the flow coefficients of 0.6 and 0.22 respectively. Besides the swirling effect due to the recess, a sizeable region of low momentum flow is seen to have developed around the blade trailing edge near the hub with the reduction in the flow coefficient. This is consistent with Kang's experimental findings for the low mass condition "It is difficult to gain any further improvement of the rig by casing treatment and it seems that the hub stall or separation sets a new limit to the operating range".

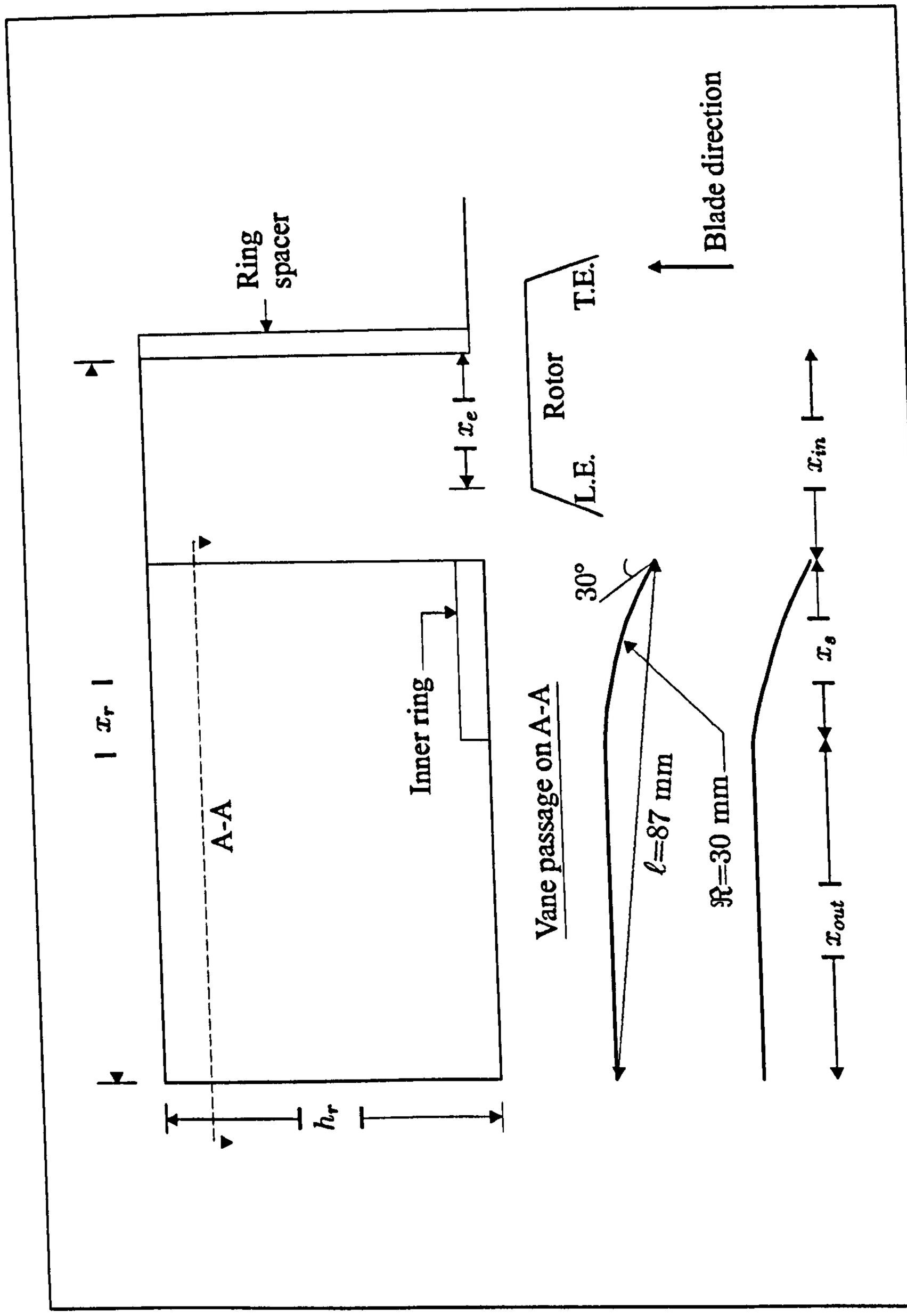

Figure 8.1: Sketch of the recess casing and vane geometry

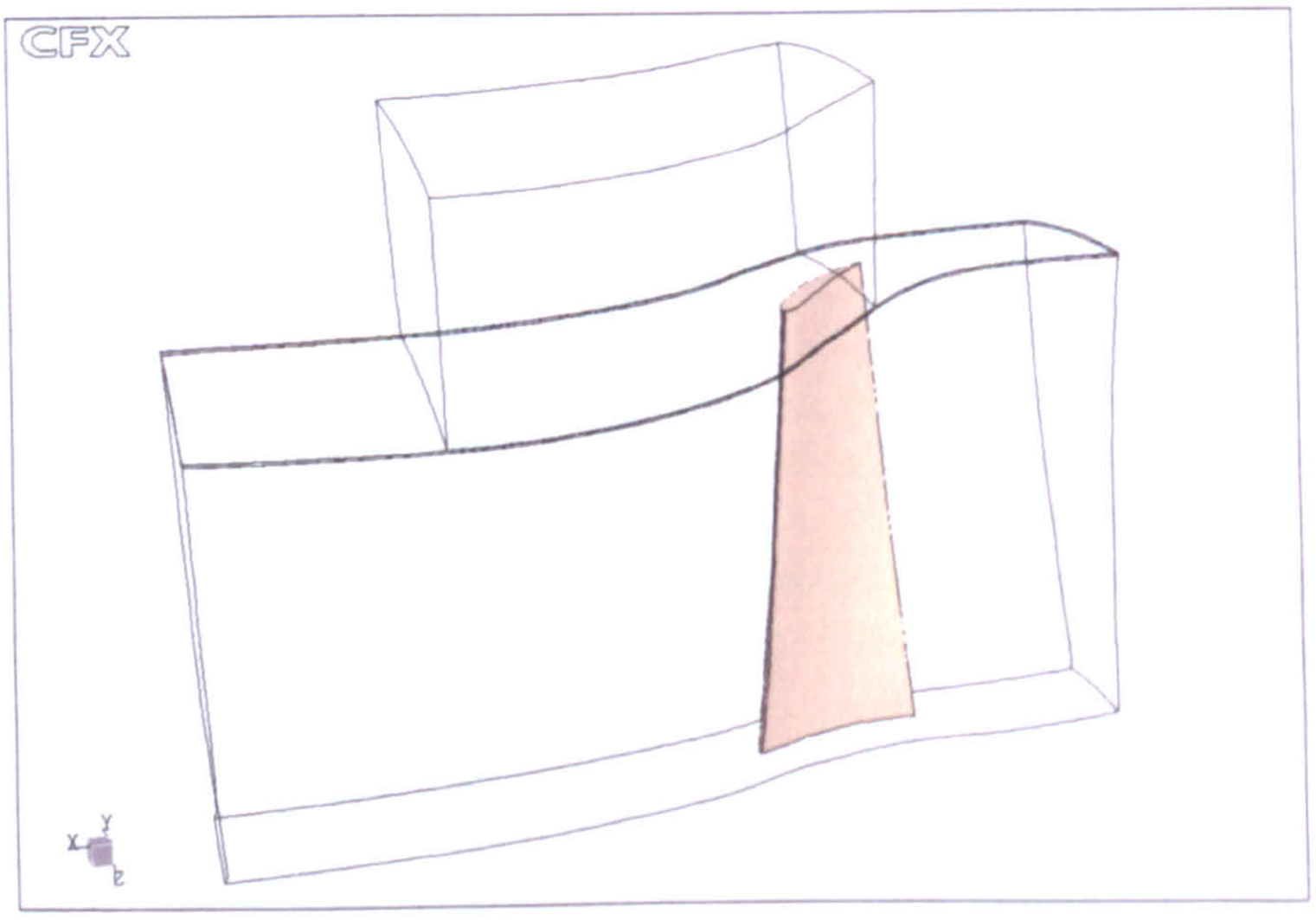

(a) With vaneless recess

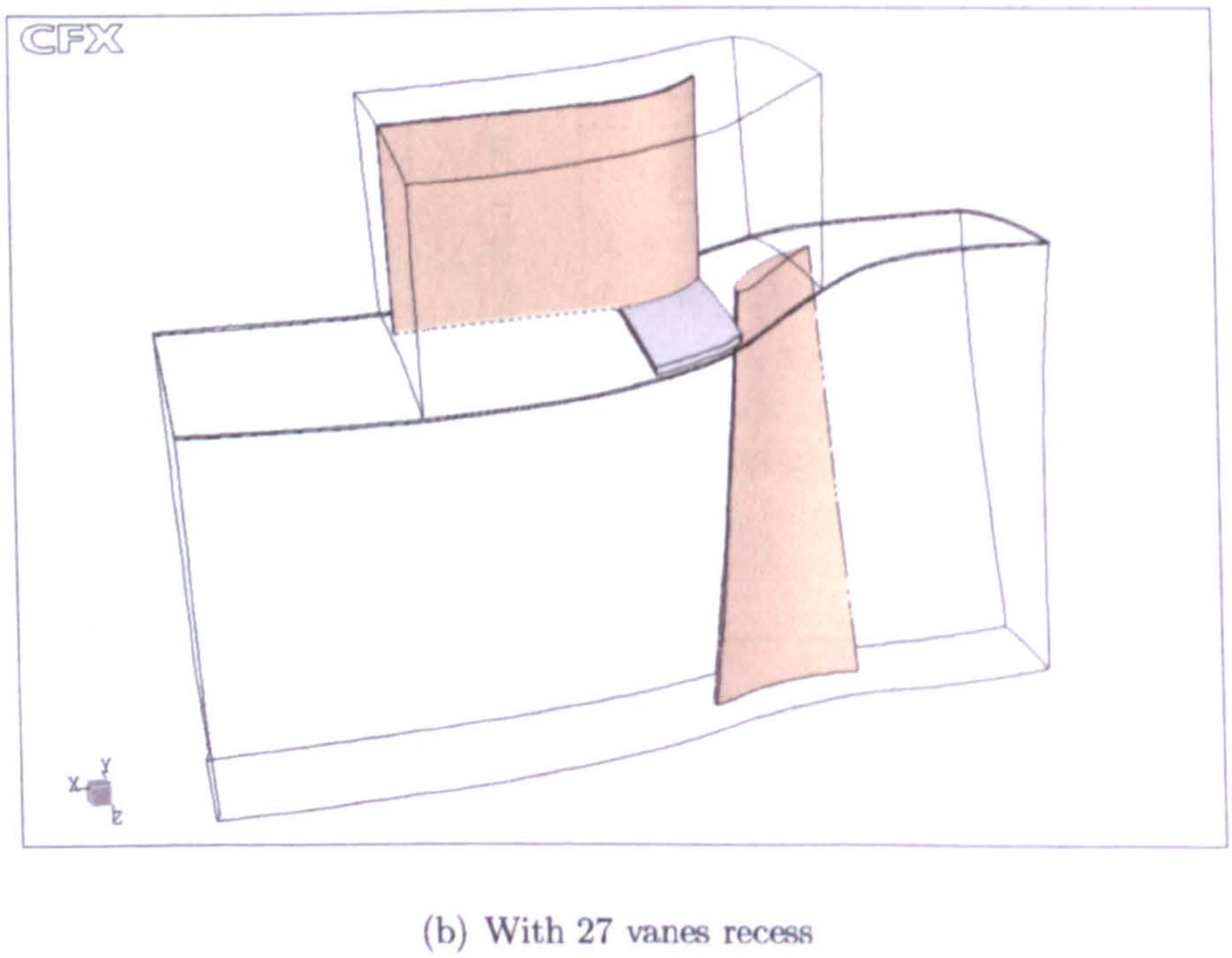

(b) With 27 vanes recess

Figure 8.2: Computational domains for treated casing

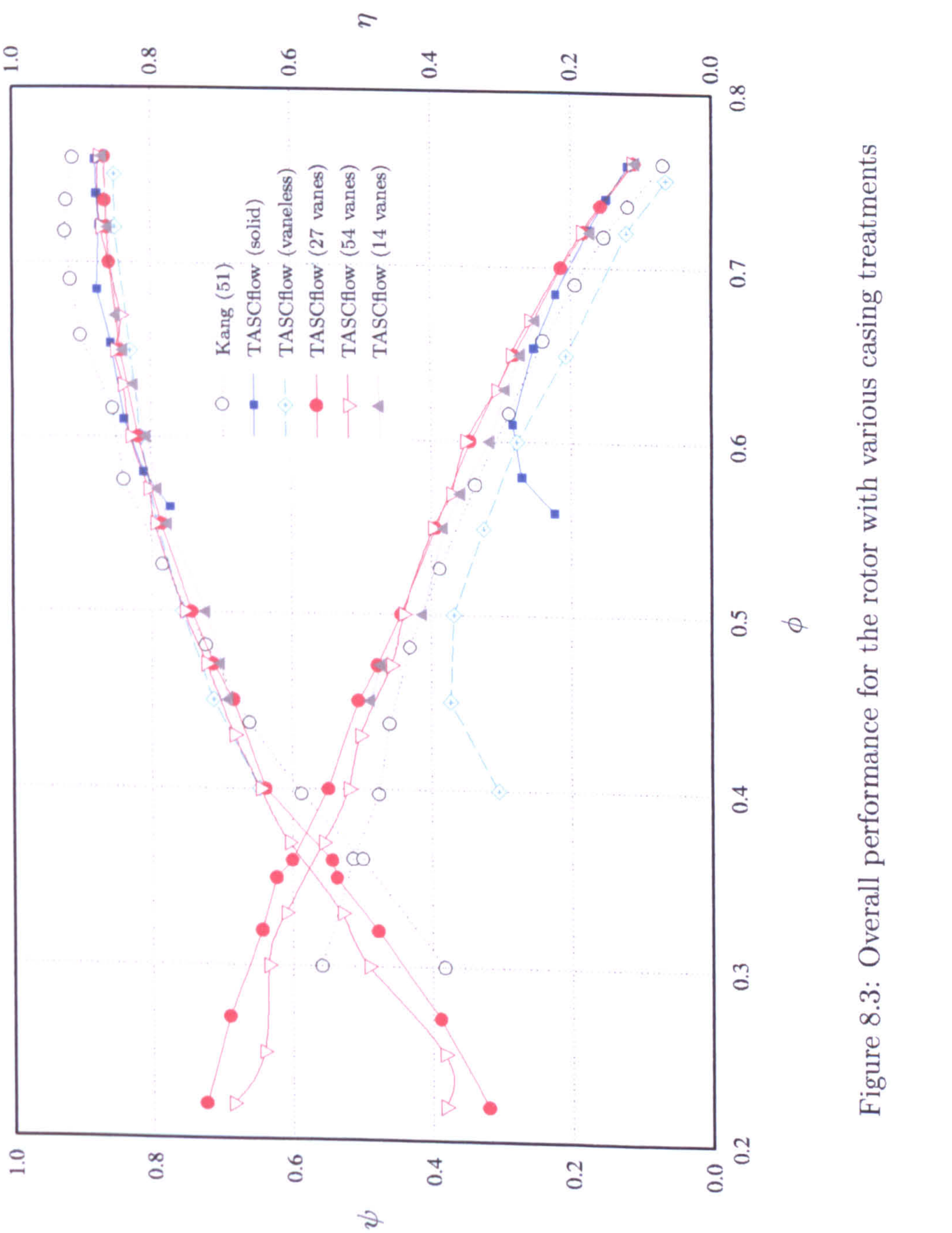

Figure 8.3: Overall performance for the rotor with various casing treatments

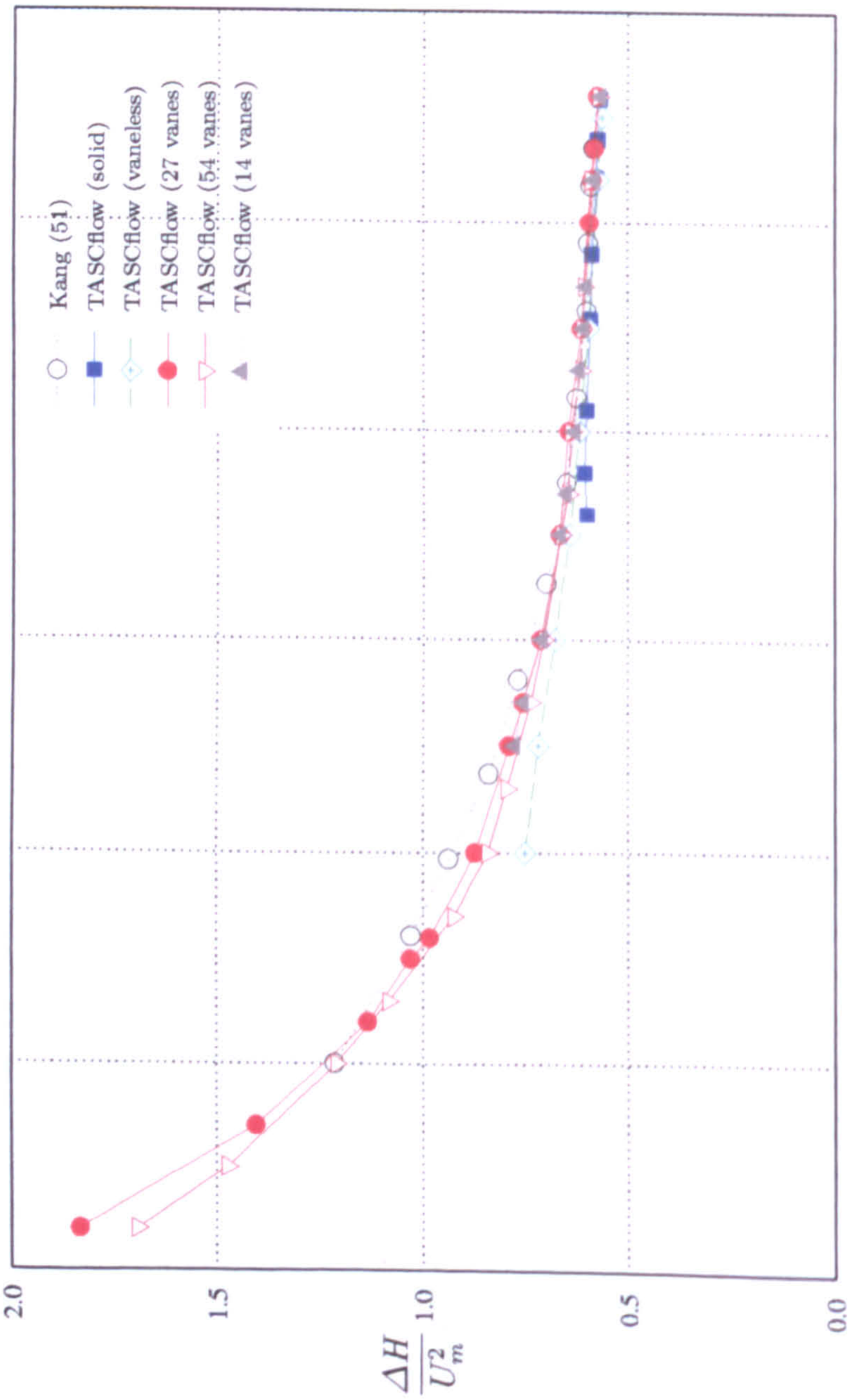

Figure 8.4: Work-input characterstics for the rotor with various casing treatments

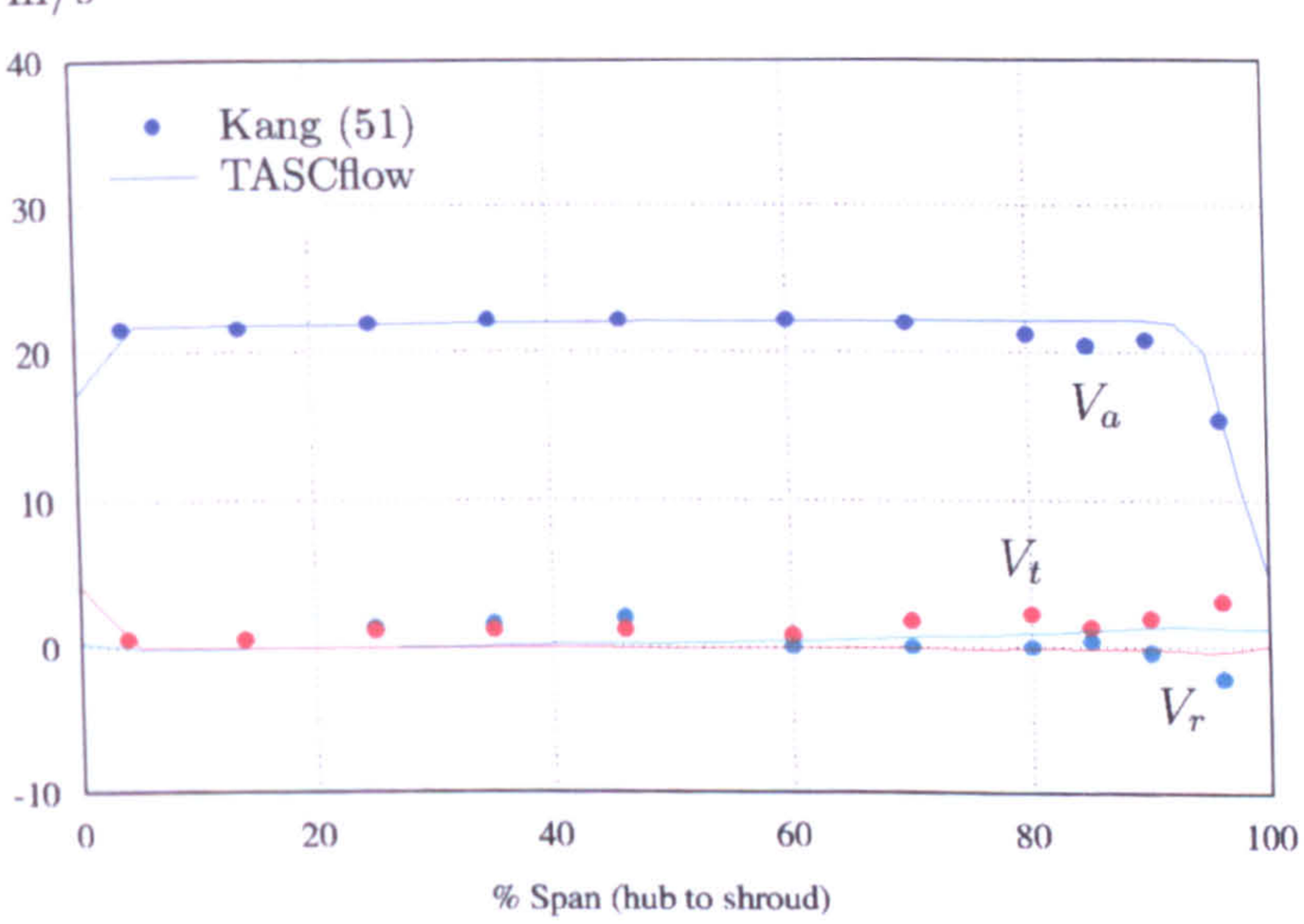

(a) At $\phi = 0.72$

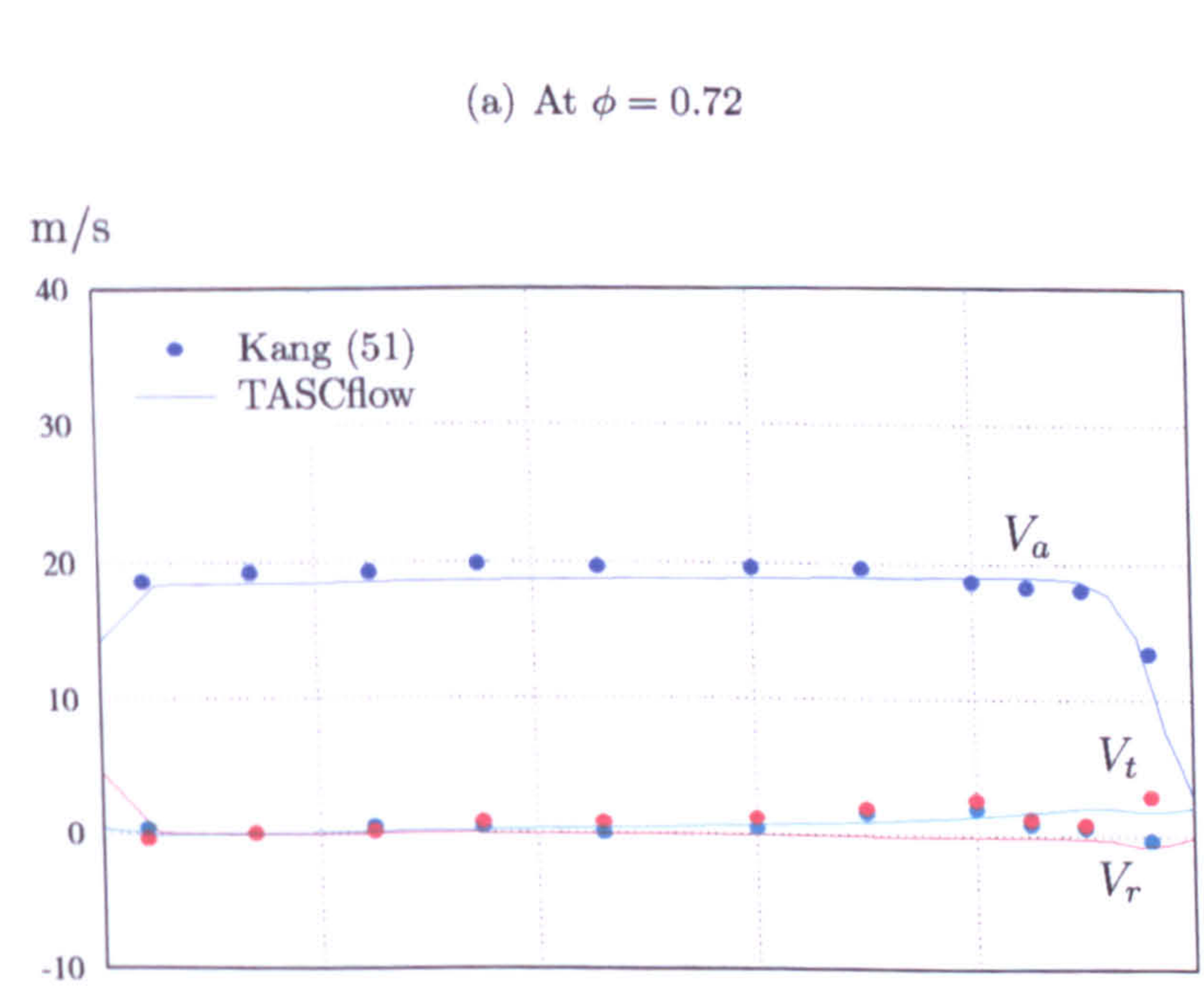

(b) At $\phi = 0.60$

Figure 8.5: The spanwise distributions of the velocity components at the inlet

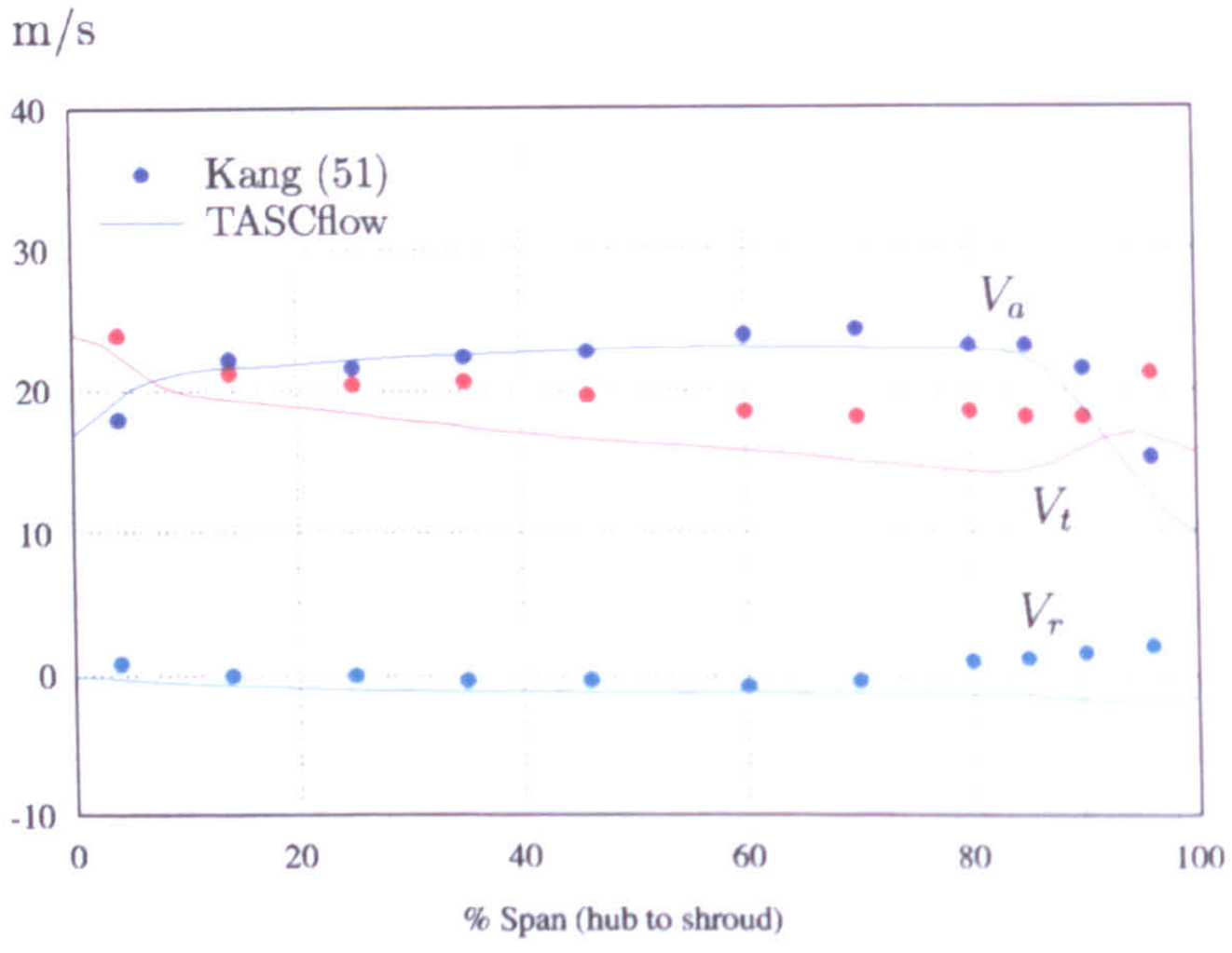

(a) At $\phi = 0.72$

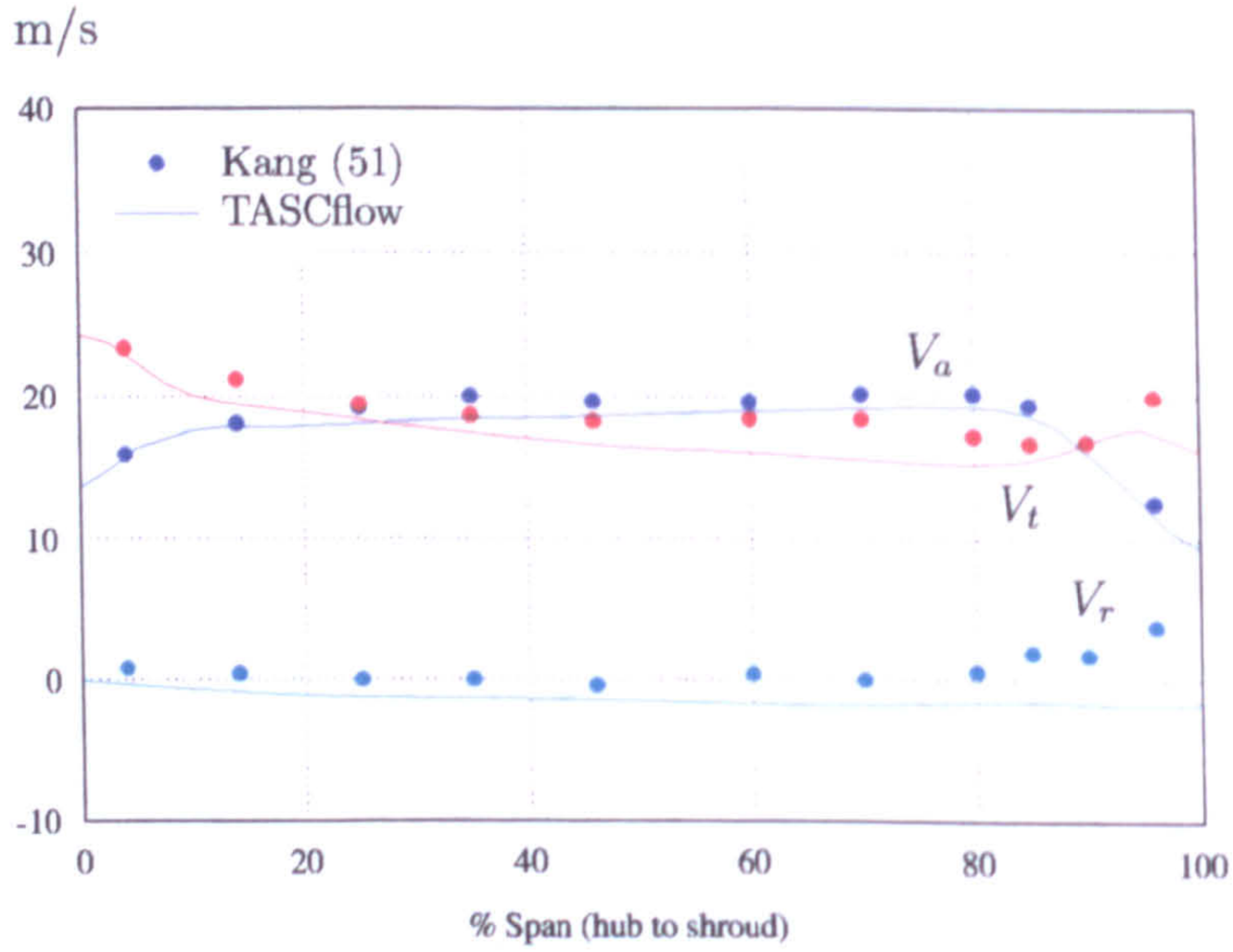

(b) At $\phi = 0.60$

Figure 8.6: The spanwise distributions of the velocity components at the outlet

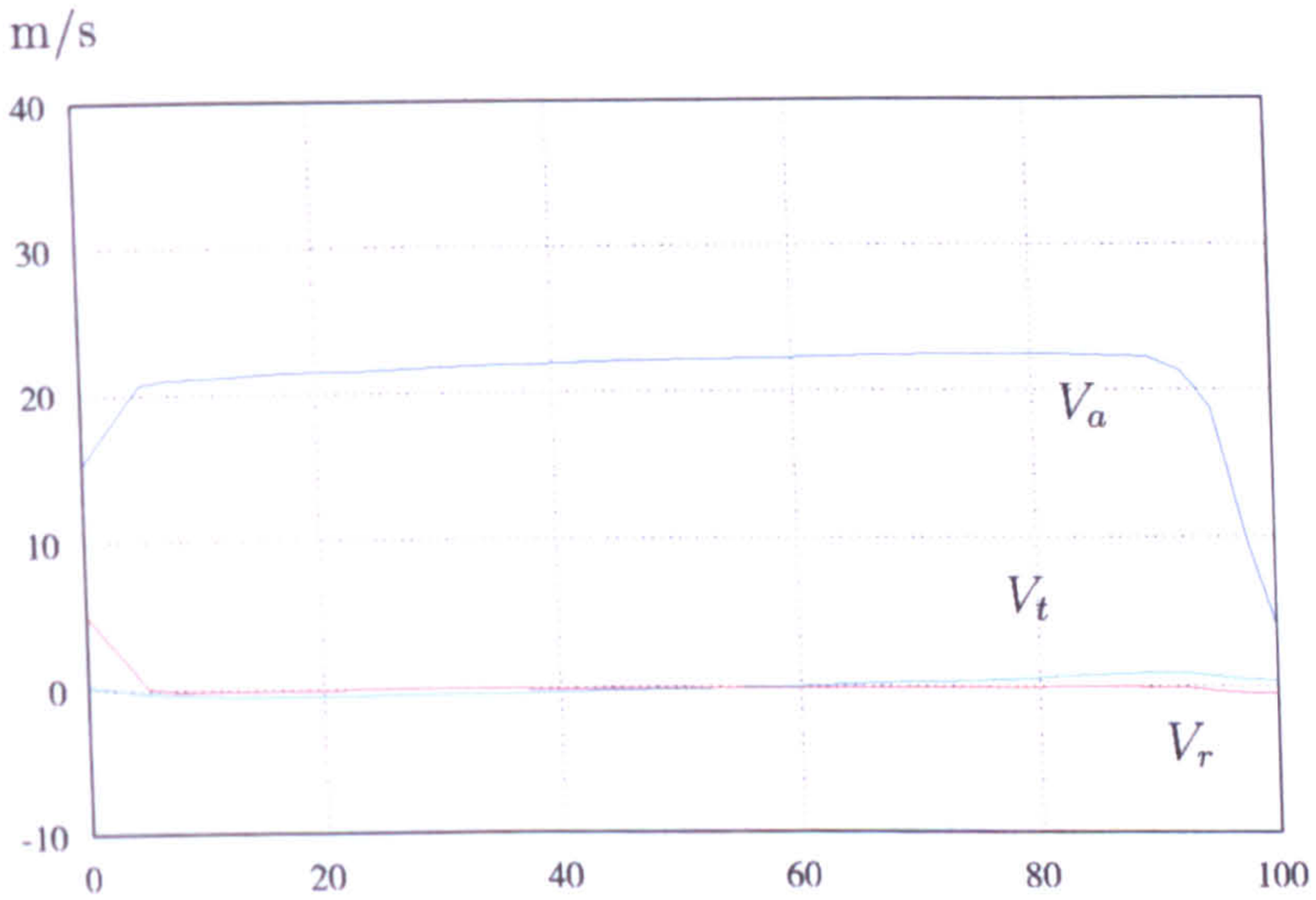

(a) At $\phi = 0.72$

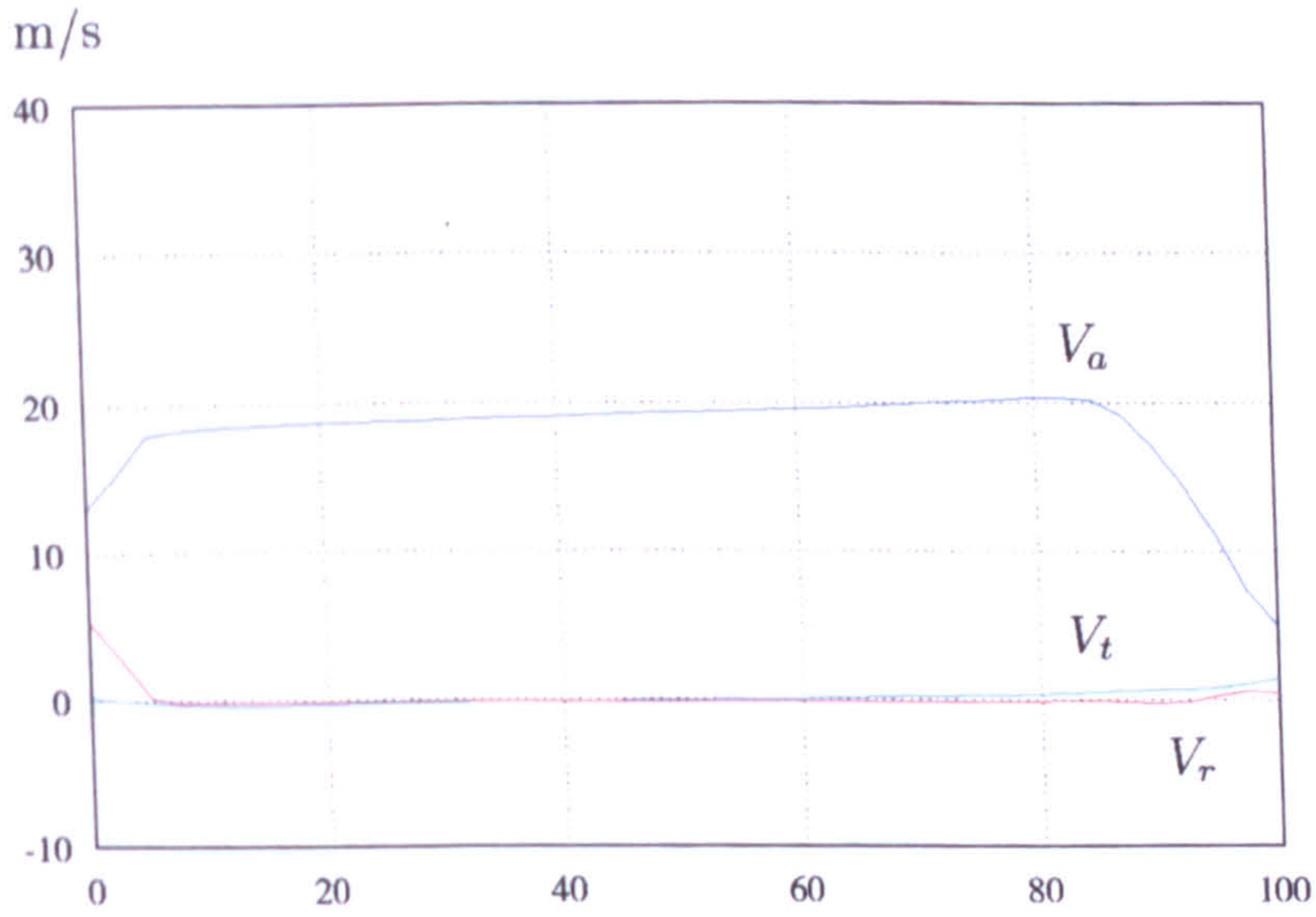

(b) At $\phi = 0.60$

Figure 8.7: The spanwise velocity components near the blade leading edge

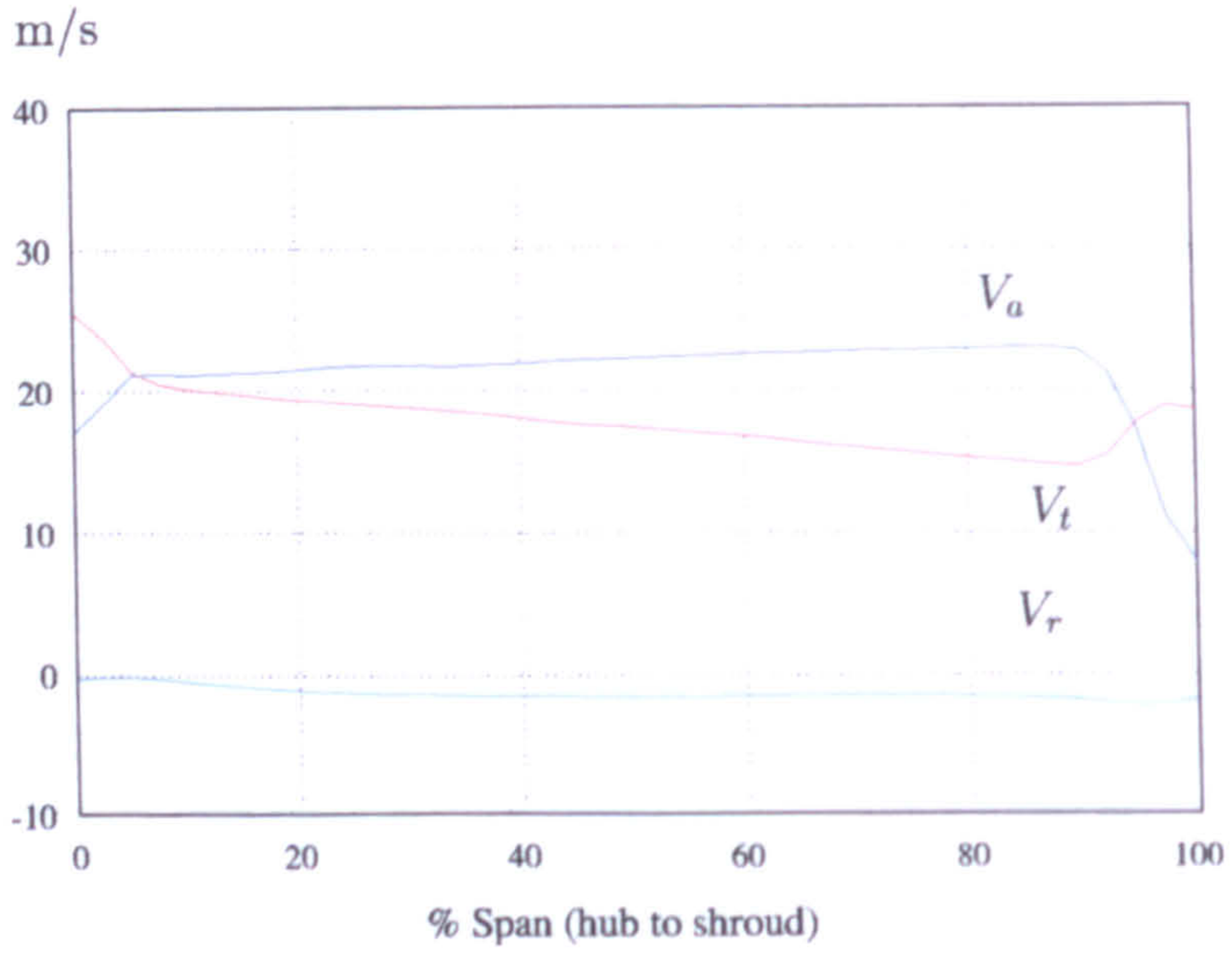

(a) At $\phi = 0.72$

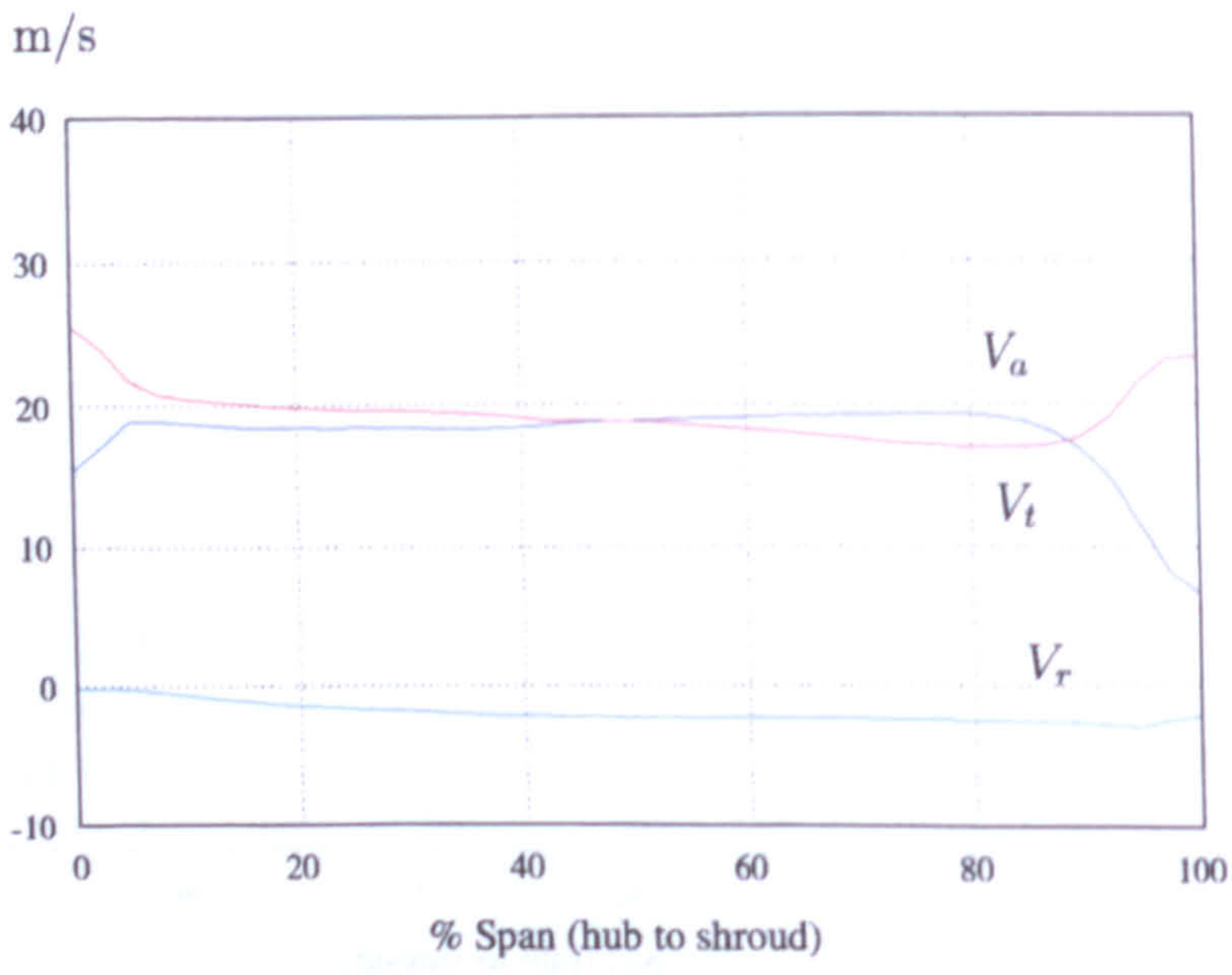

(b) At $\phi = 0.60$

Figure 8.8: The spanwise velocity components near the blade trailing edge

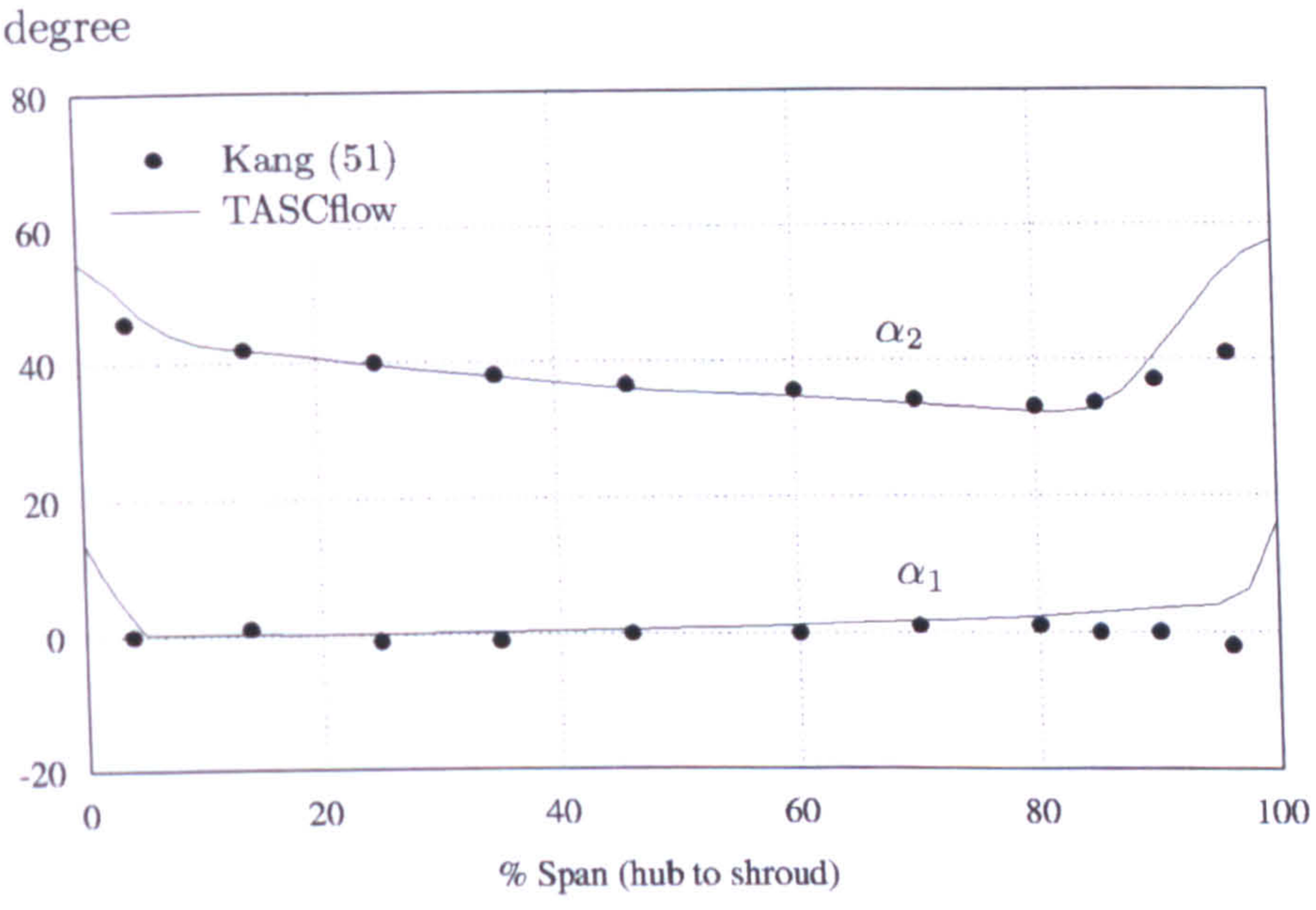

(a) At $\phi = 0.72$

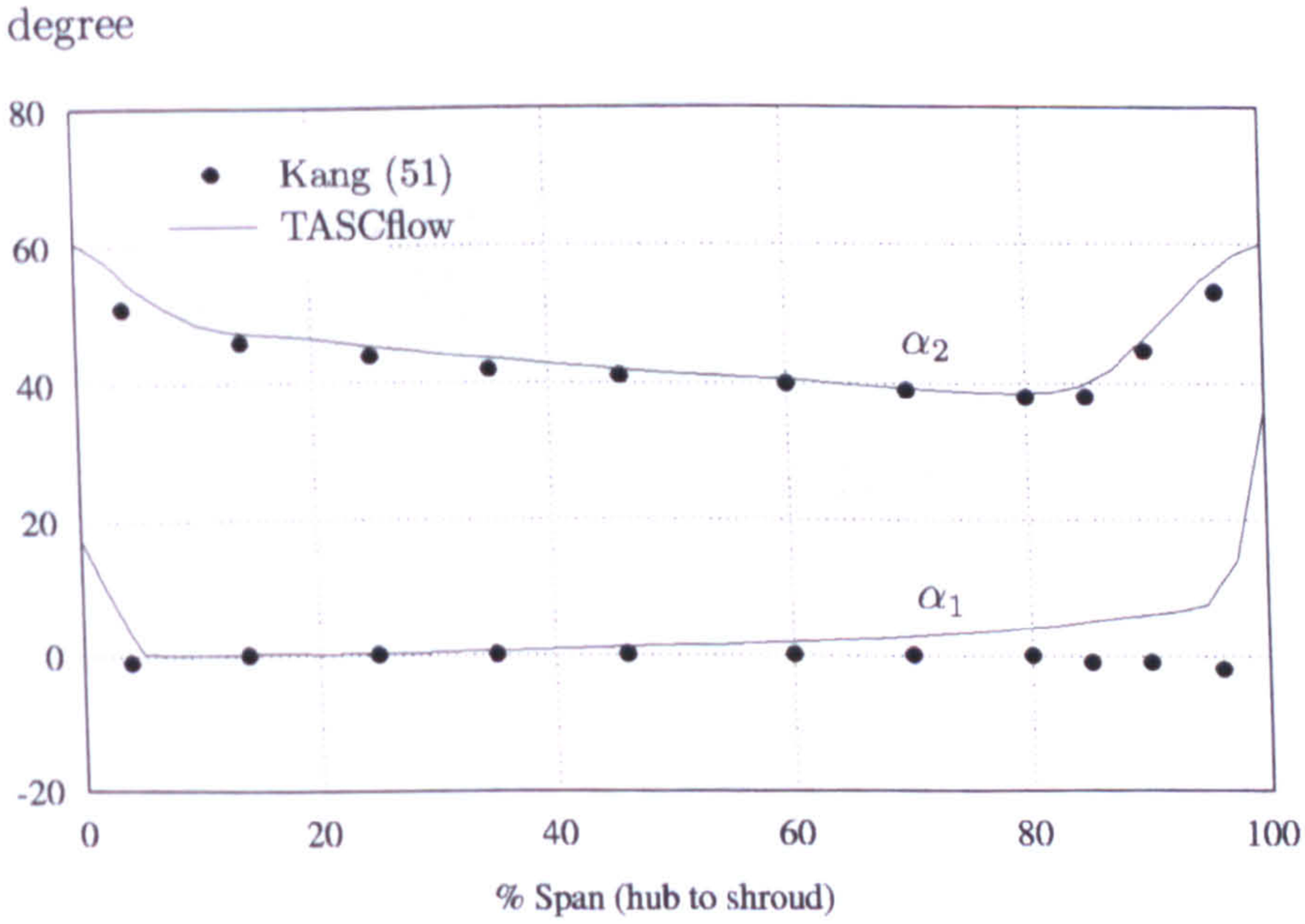

(b) At $\phi = 0.60$

Figure 8.9: Absolute flow angles with treated casing

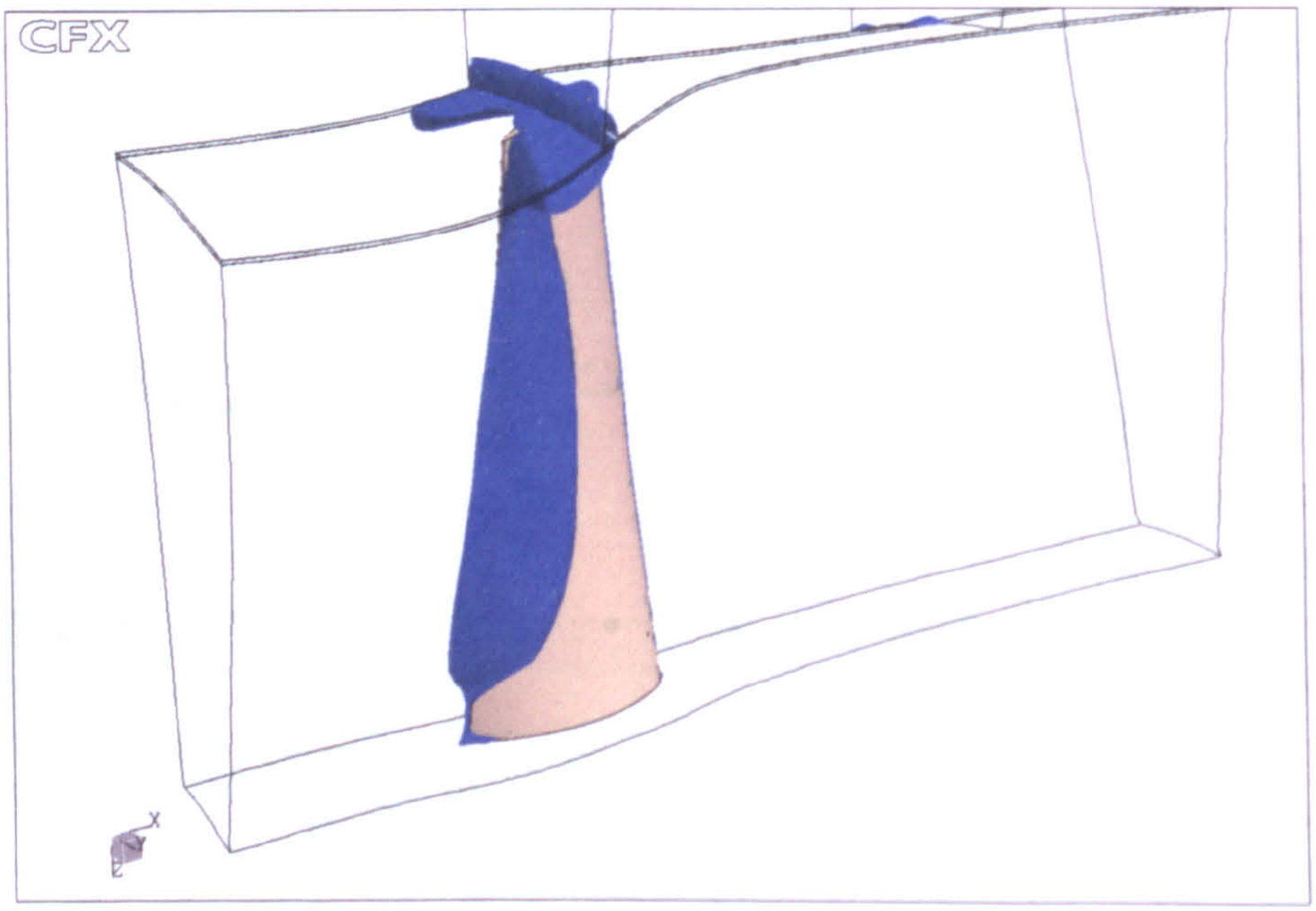

Figure 8.10: Isotimic plot for vaneless casing at $\phi = 0.50$

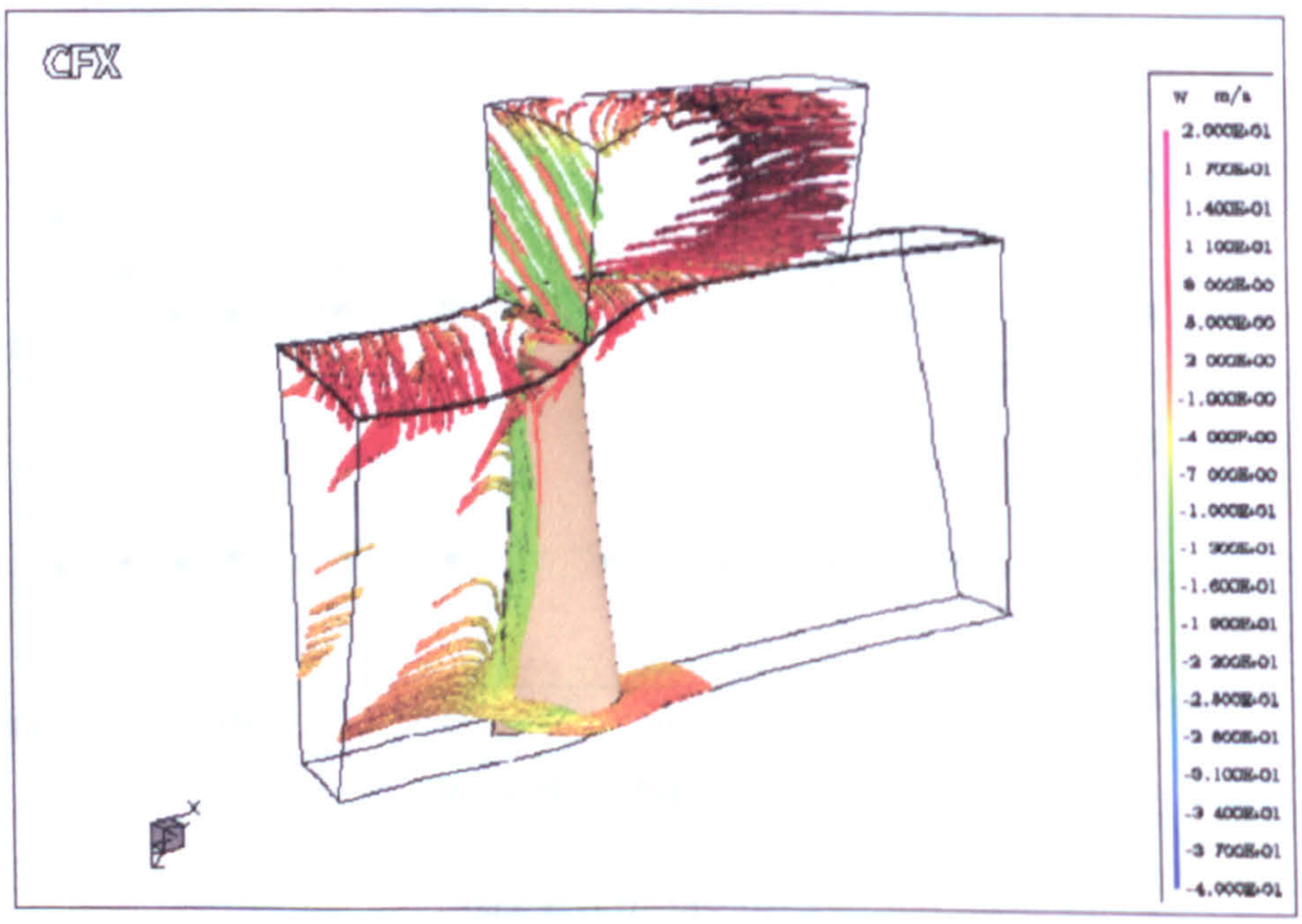

Figure 8.11: Streamlines plot for vaneless casing at $\phi = 0.60$

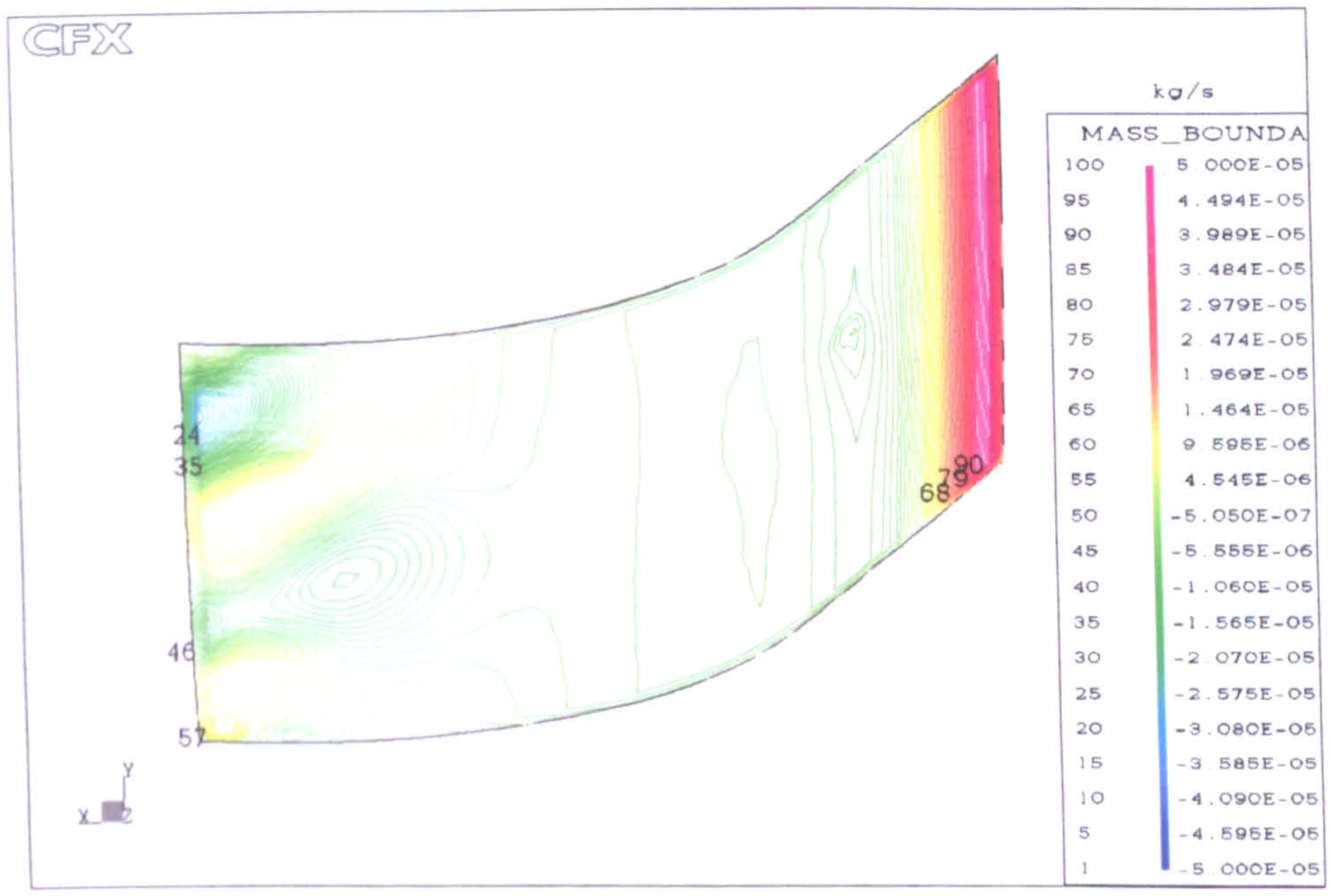

Figure 8.12: Mass at the bottom of vaneless casing for $\phi = 0.60$

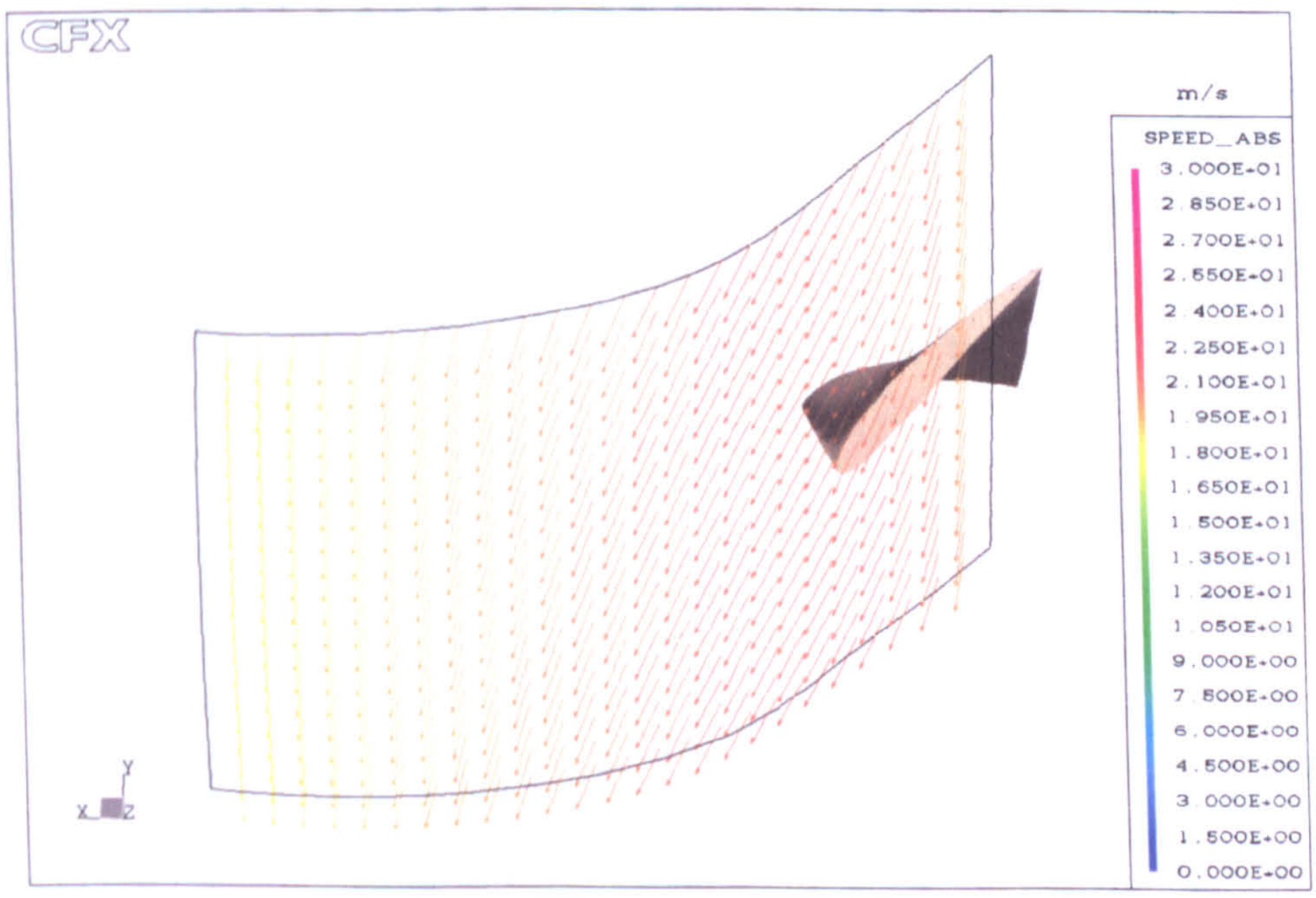

Figure 8.13: Vector plot at the top of vaneless casing for $\phi = 0.60$

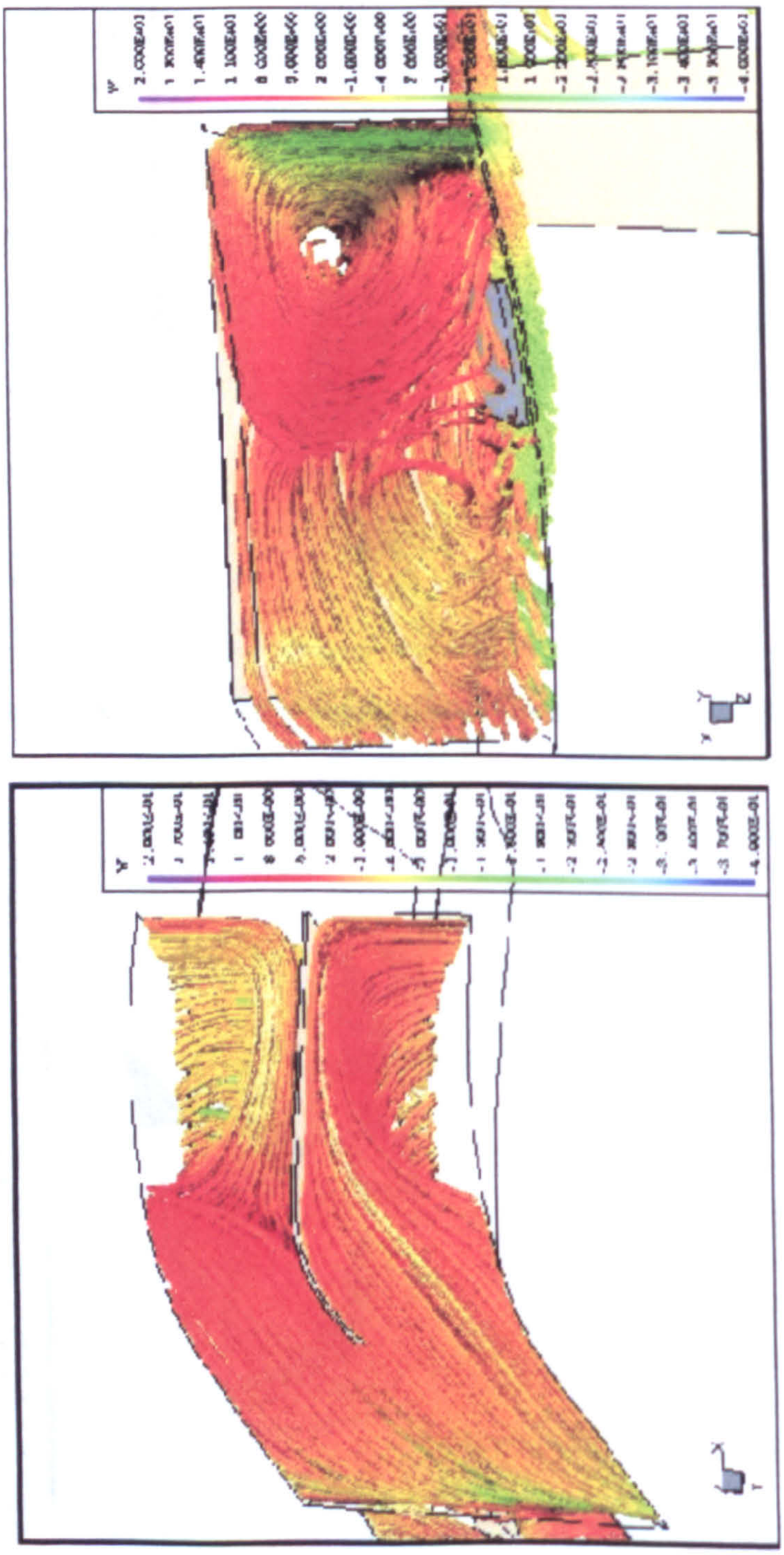

(a) Blade-to-blade view

(b) Meridional view

Figure 8.14: Streamlines plots inside the recess vaned at $\phi = 0.60$

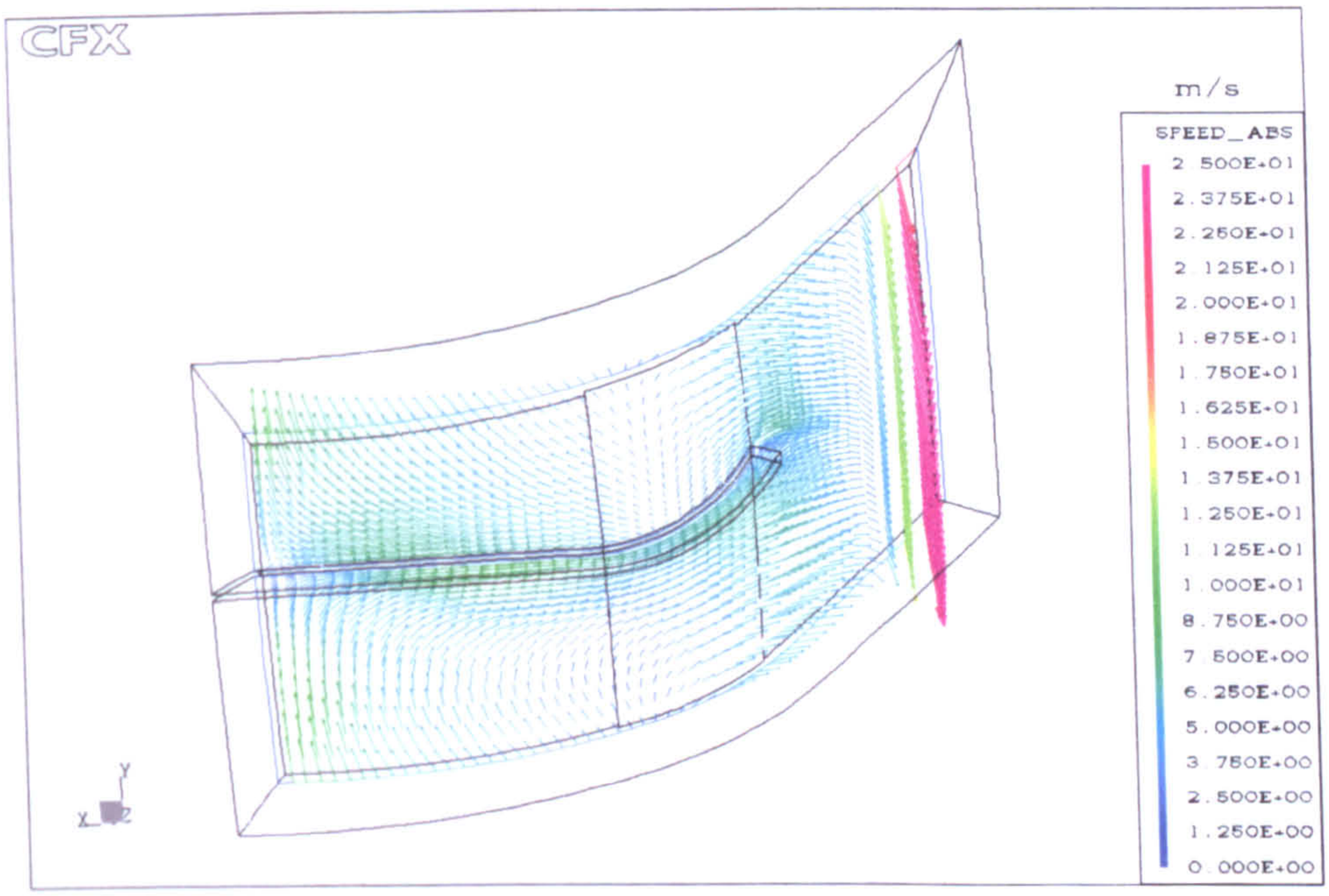

(a) At the casing bottom

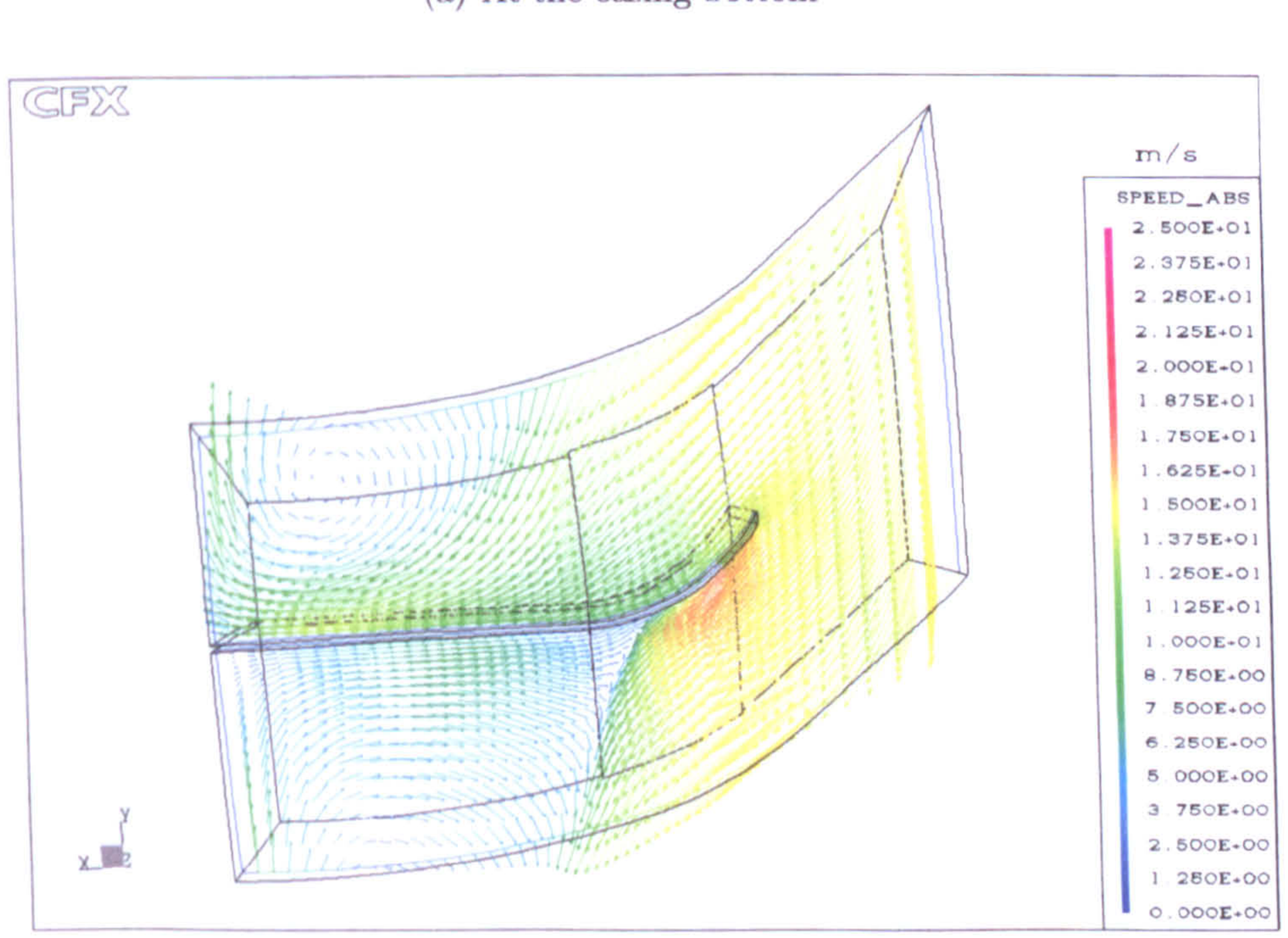

(b) At the casing top

Figure 8.15: Blade-to-blade view vector plots of the flow in the casing at $\phi = 0.60$

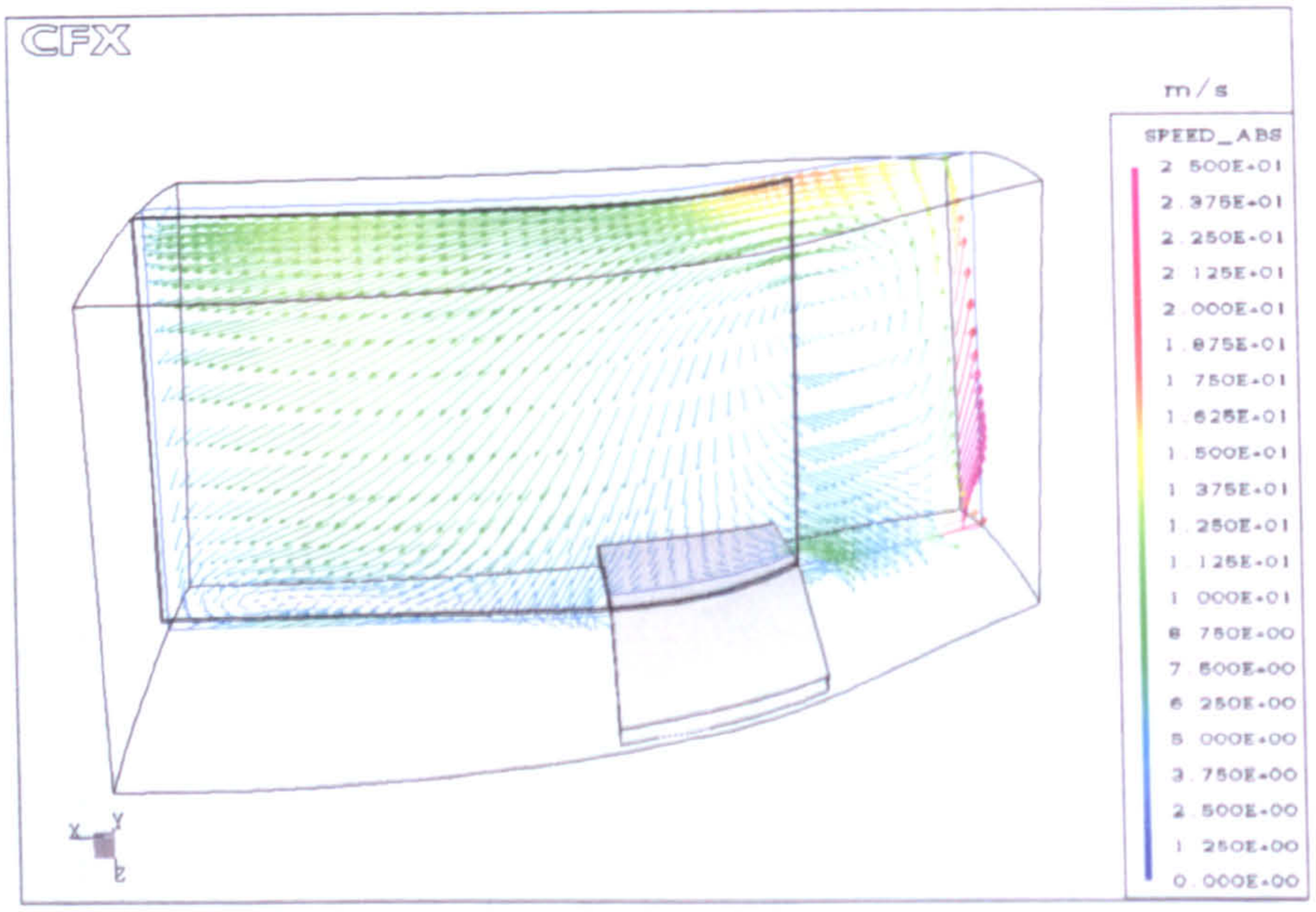

(a) At vane concave side

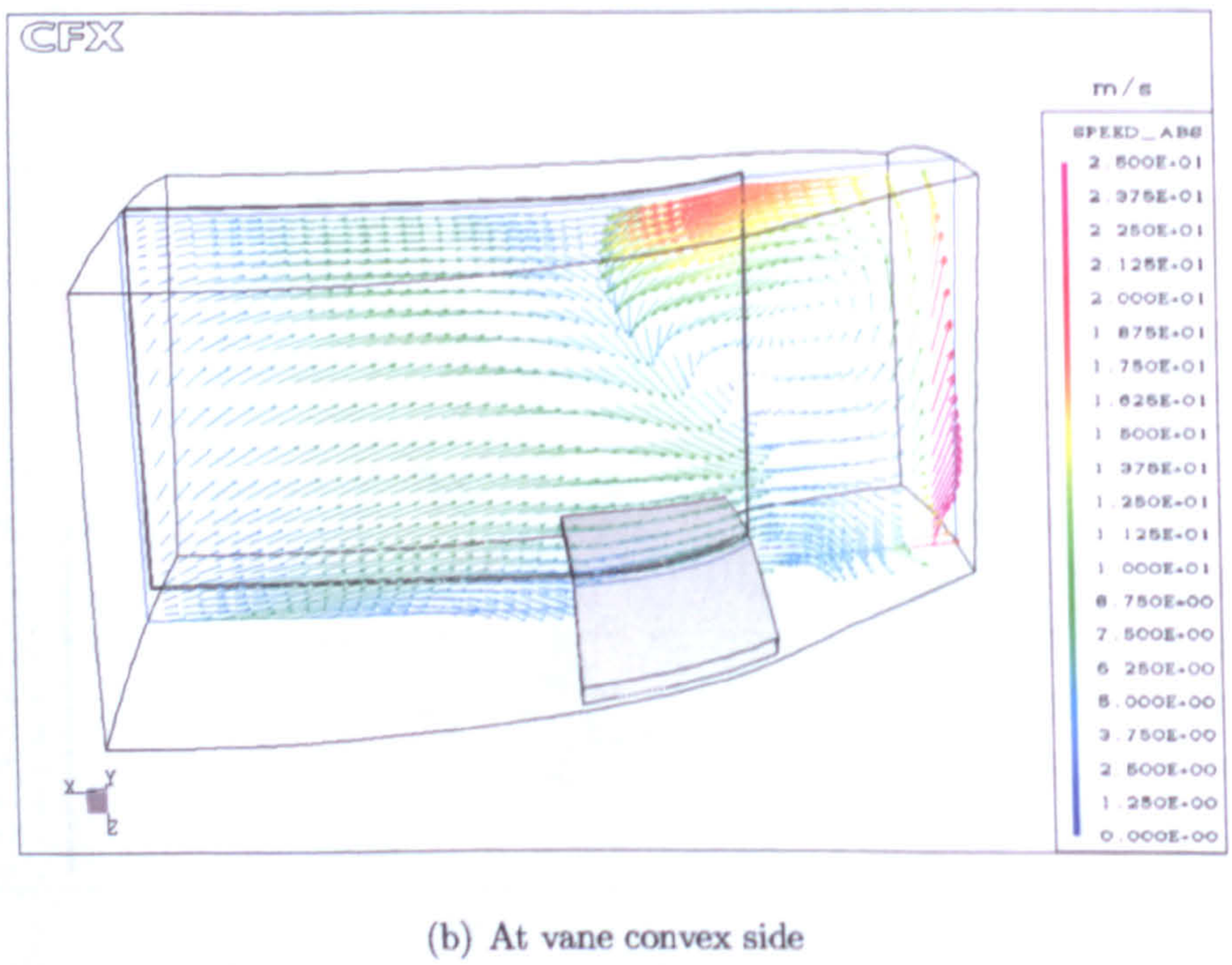

(b) At vane convex side

Figure 8.16: Meridional view of vector plots of the flow in the casing at $\phi = 0.60$

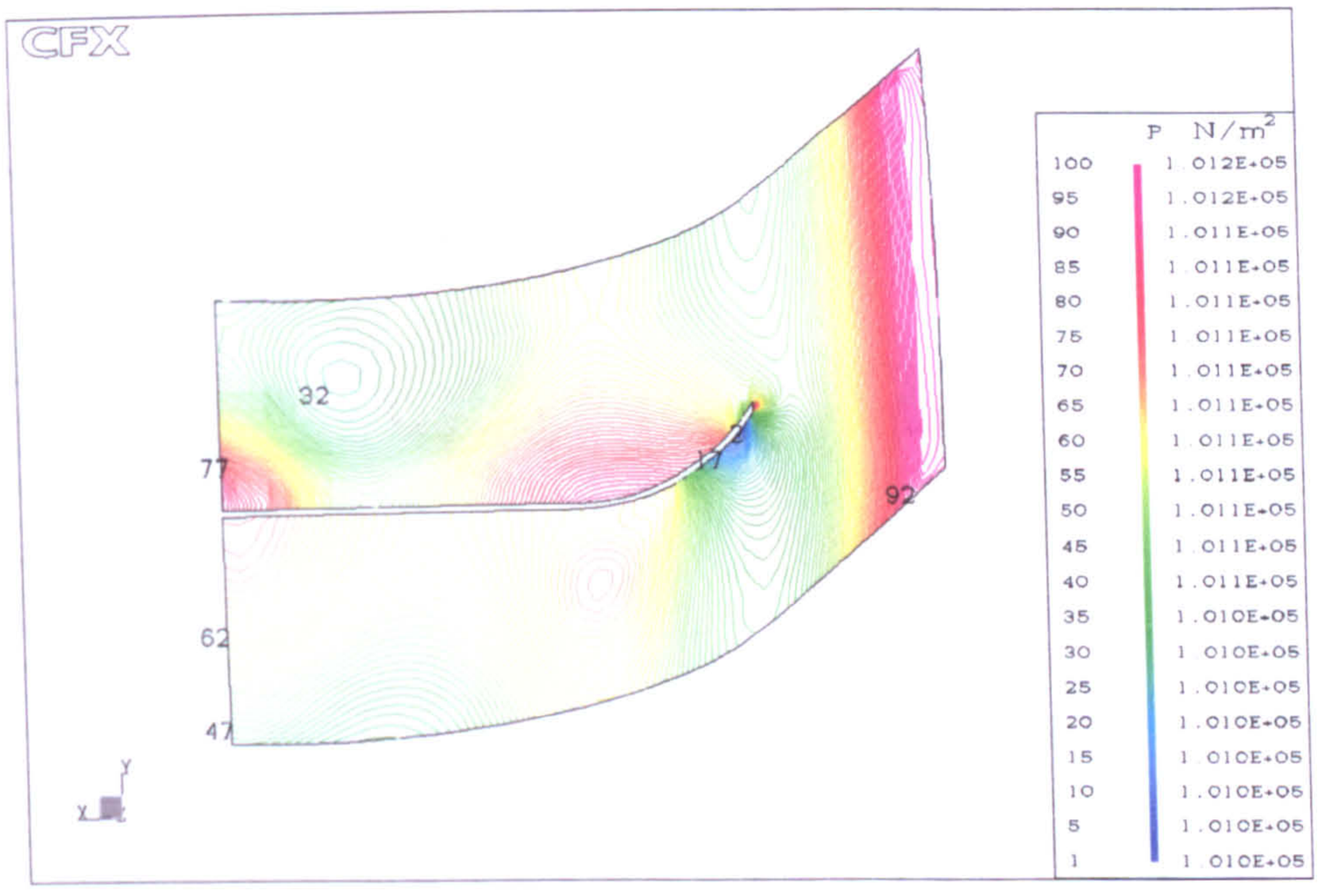

Figure 8.17: Pressure contour near the casing tip at $\phi = 0.60$

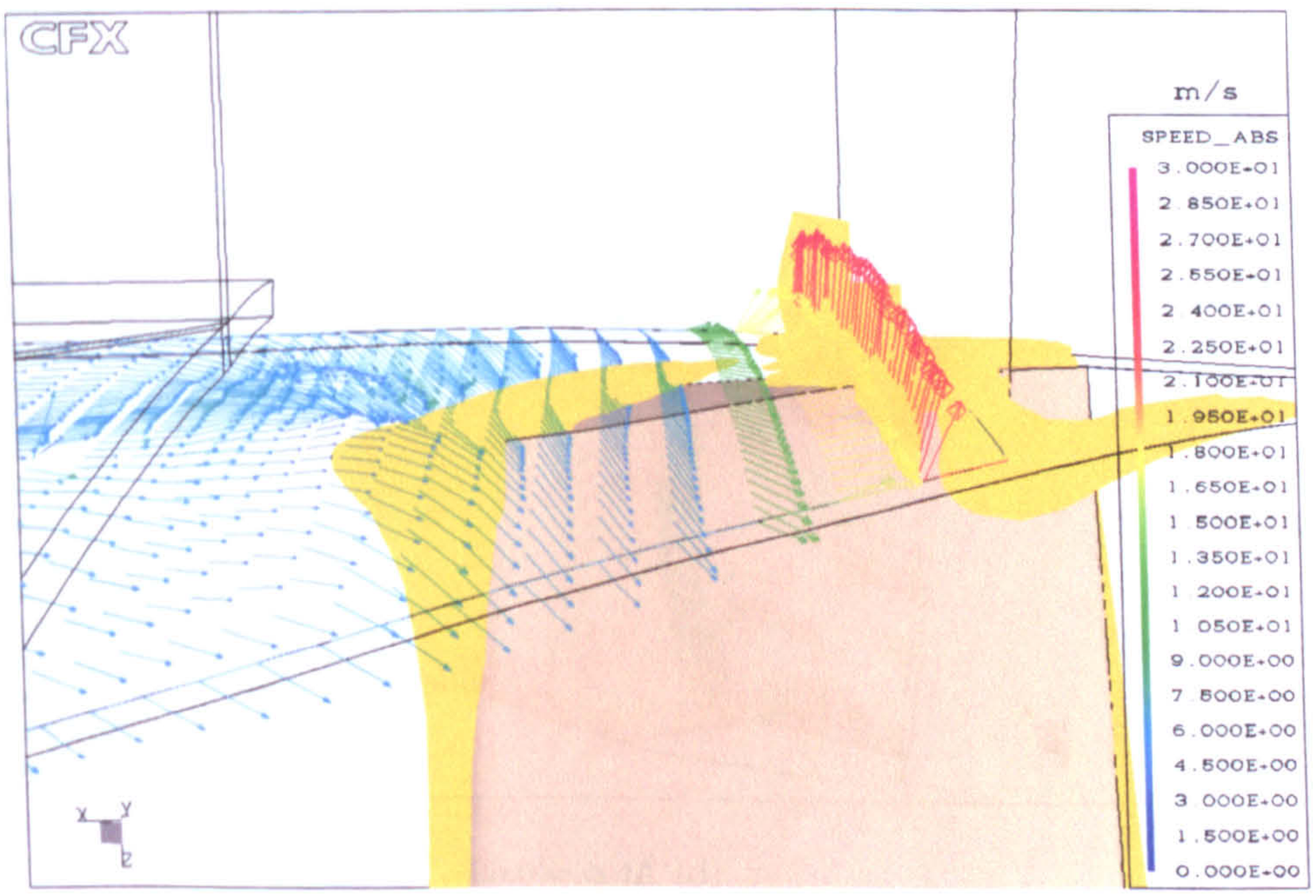

Figure 8.18: Flow at the casing entry section for $\phi = 0.60$

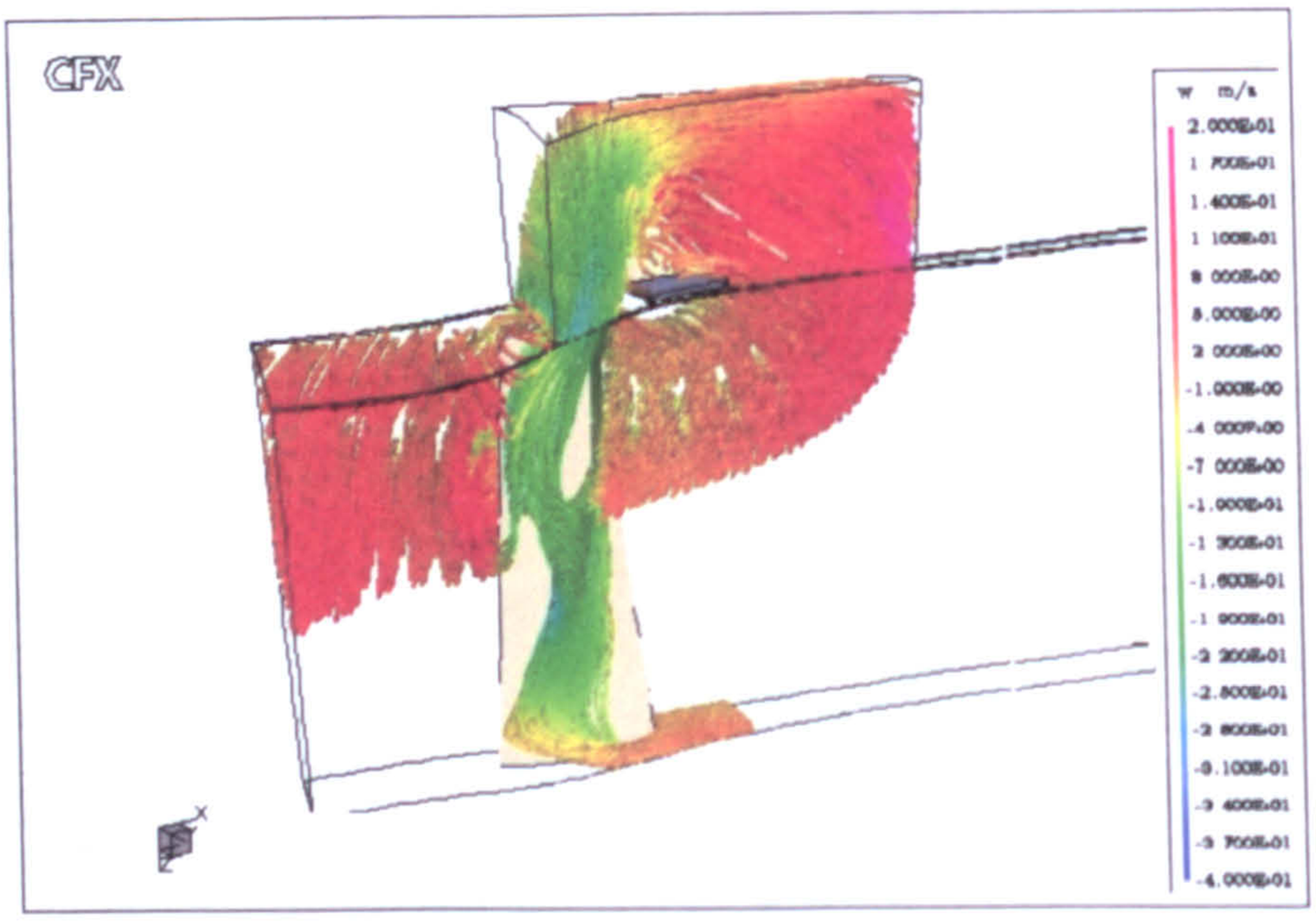

(a) At $\phi = 0.22$

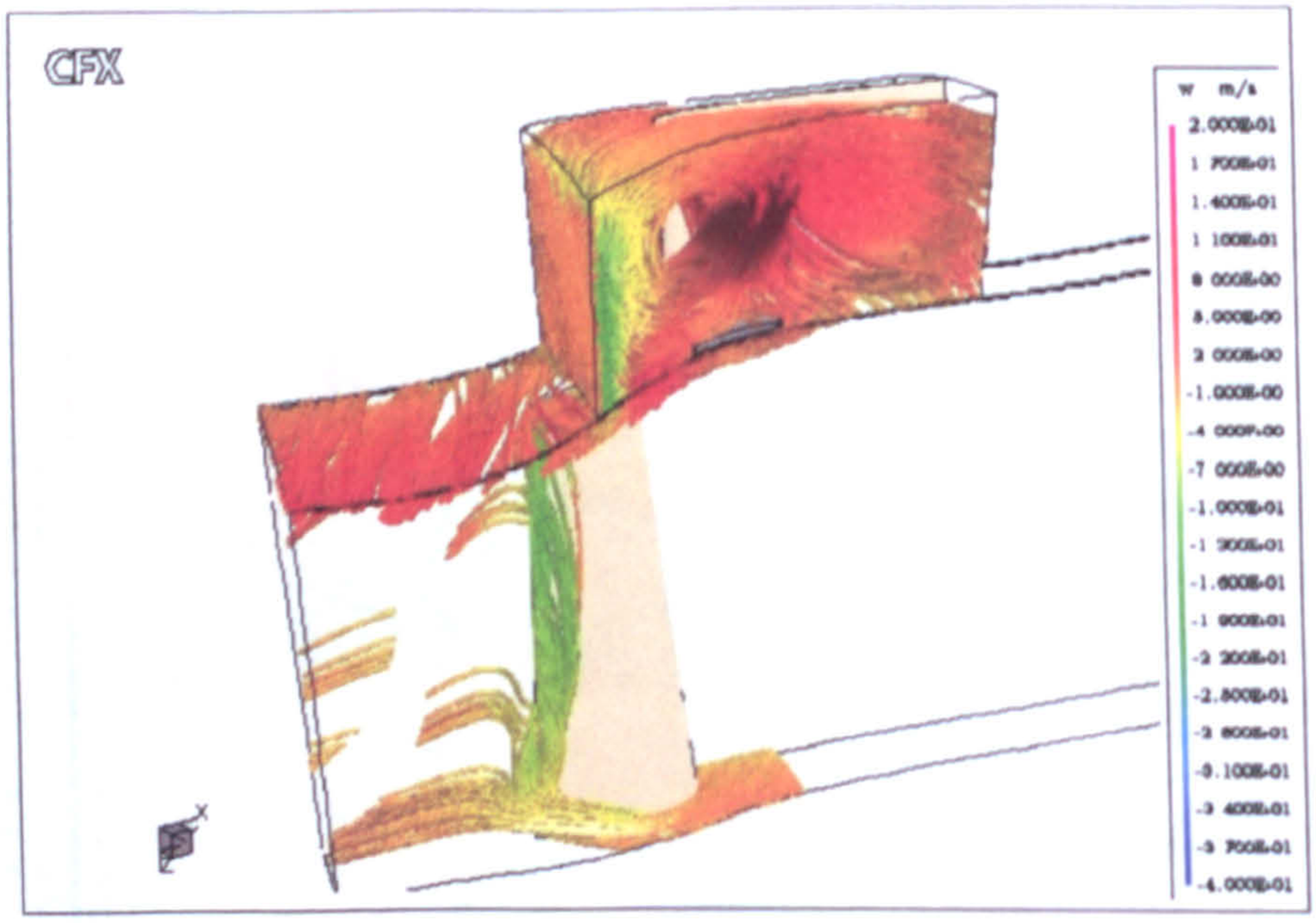

(b) At $\phi = 0.60$

Figure 8.19: Streamlines plots in the domain for the vaned casing

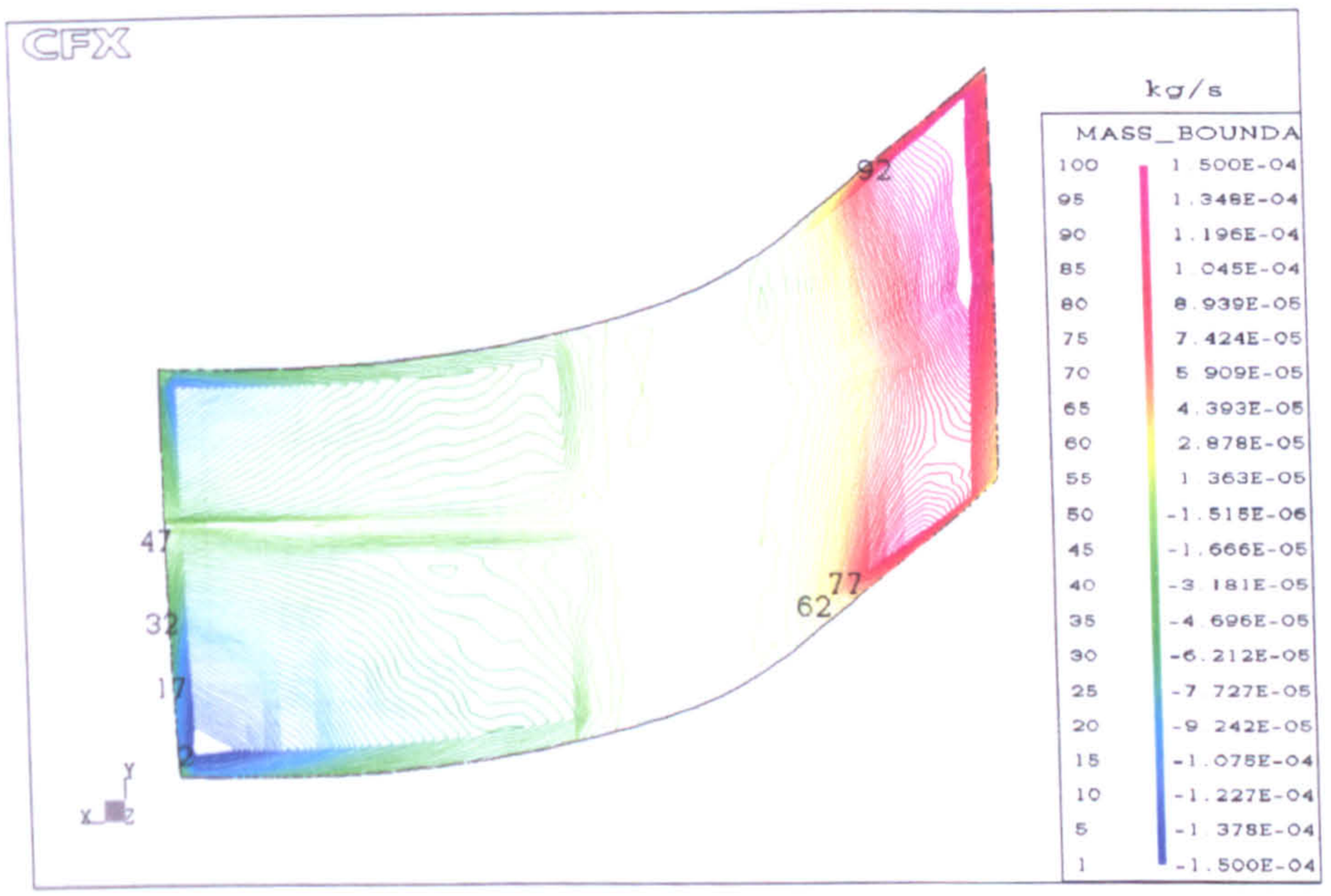

(a) At $\phi = 0.22$

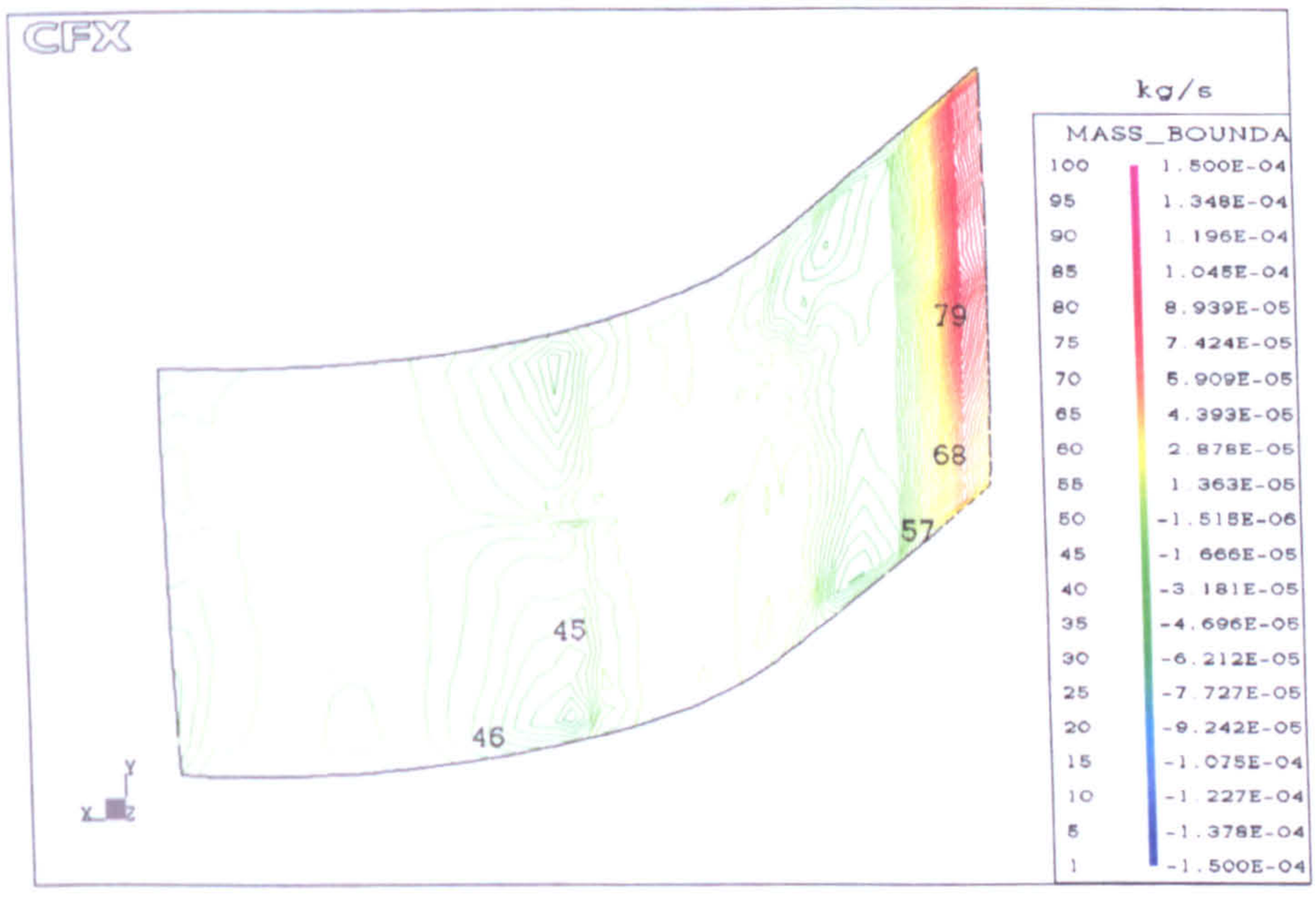

(b) At $\phi = 0.60$

Figure 8.20: Mass at the bottom boundary of the vaned casing

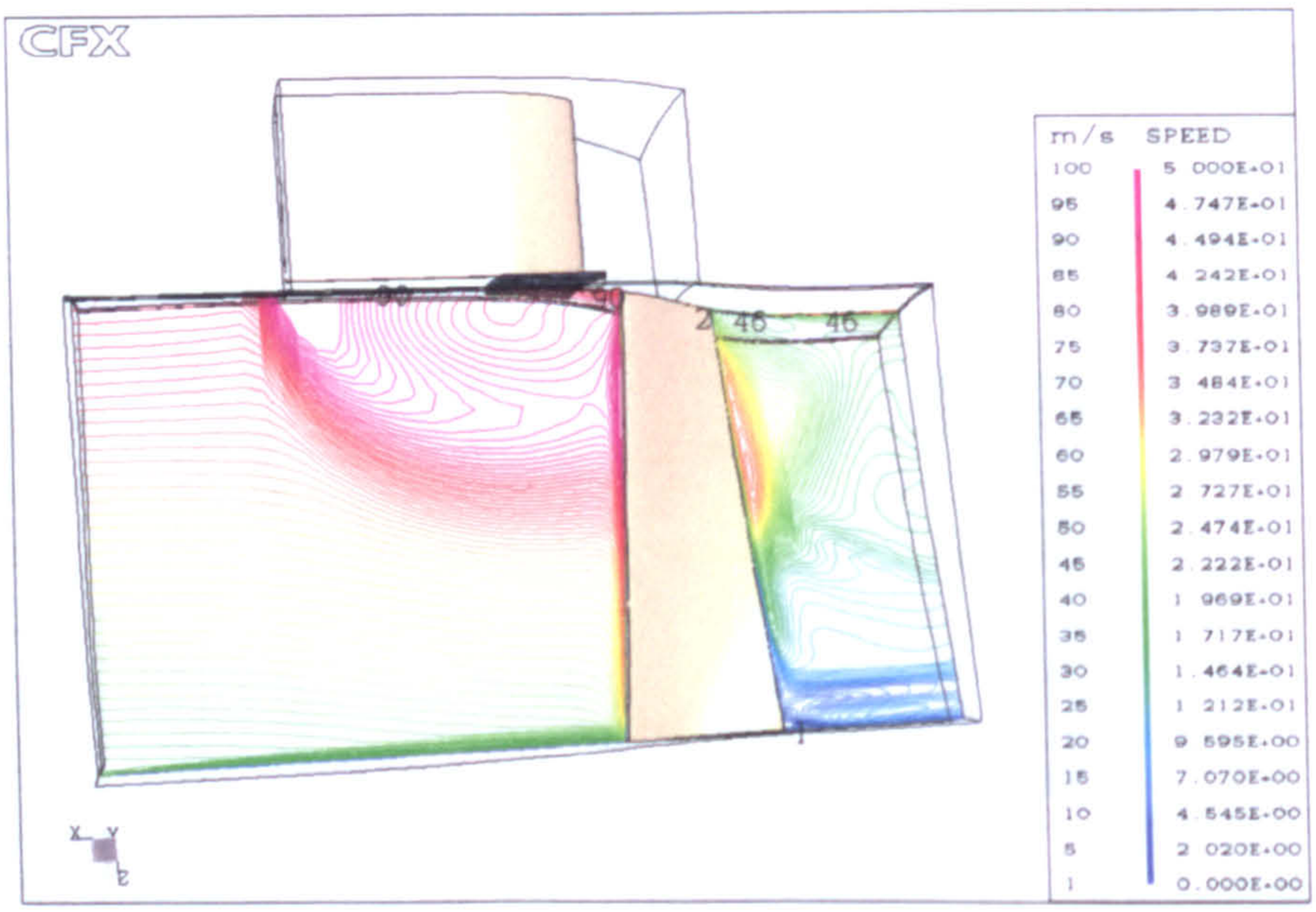

(a) At $\phi = 0.22$

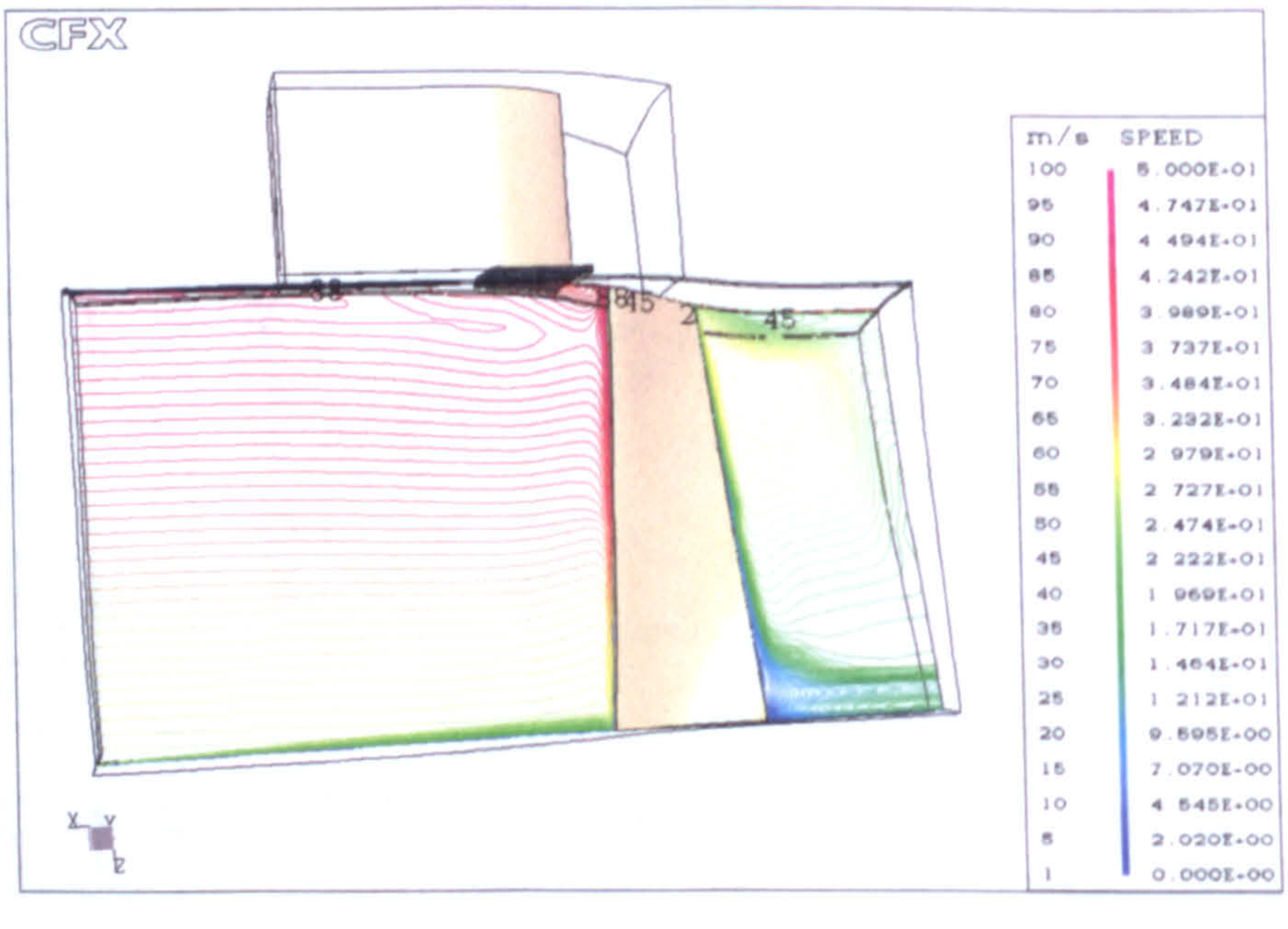

(b) At $\phi = 0.60$

Figure 8.21: Meridional view of speed contour with vaned casing

9

Unsteady Simulations for Treated Casing

Unsteady simulations are nowadays very much the source of information about the flow unsteadiness and its influence on the fan or compressor performance. In centrifugal compressors unsteady simulation is carried out to investigate the interaction between the impeller and diffuser, He (43). It is also used to investigate the interaction between the rotor and stator blades in single or multi-stage axial flow compressors, Teixeira (94). In the present work unsteady simulation could be very useful in investigating the interaction between the rotor blades and the vanes inside the recess which will be regarded as the stator. This chapter presents the predicted results of unsteady simulations of the fan with recess treatment. The predicted results were compared to the results that were produced by the steady-state simulations presented in Chapter 8.

9.1 Unsteady simulation parameters

The solution procedure of unsteady simulation is usually carried out by calculating the flow field at a large number of time steps, each of which corresponds to a different relative angular displacement of the rotating component in respect with the stationary one. To ensure an accurate transient solution, the fluid equations must

be adequately solved at each time step. This requires that a coefficient iteration loop be used, so within each individual time step a number of iterations have to be performed in order to resolve the new flow field that is consistent with the updating of the transient geometry of the fan.

Although it is possible to start a transient rotor/stator computation from a simple initial guess, or from an existing prediction, it is far more economic in time and resources to first obtain a steady-state sliding interface solution using Frozen Rotor interface between components. This solution will contain most of the overall flow features and should "converge" to the desired transient simulation in the fewest transient cycles. As was mentioned in Chapter 4, in a Frozen-Rotor connection of two grids the relative motion between the components is suspended and the numerical interface plane acts purely as a transparent connection, through which the flow of information in both directions is freely exchanged.

One of the attractive features of the unsteady implementation of the code is the availability of dedicated files in which the time histories of the primary calculated quantities are written to individual files, one file for each time step. To monitor the solution, the operator needs to nominate a corresponding node which the code designates as monitor point "MP". It is possible to select up to 100 such points. These will be used to track the progress of the solution from one time step to the next and to determine if a steady cycle has been obtained. This is achieved by evaluating the dependent variables u, v, w, and p at each time step.

Time step is a very important parameter in any unsteady simulation. Its size is not subject to any specific limitation other than the need to resolve the flow fields associated with the relative change in position of the rotating components. Hence, choosing a small time step means a more accurate solution with a large CPU time and vice versa. The setting of the time step was done by considering the time scale or cycle time, the passing period of one blade, which is in the present work is equal to 1/27 of a revolution divided by the rotation of speed N of the rotor resulting in a cycle time of 0.001 48 seconds. This cycle time is then divided by the discrete number of time steps selected for the completion of a single blade sweep.

9.2 Boundary conditions

The computational domain presented in Chapter 8 used for the steady state simulation of the fan with treated casing, is used to carry out these unsteady simulations. In this domain, shown in Figure 8.2(b), the treatment has 27 vanes, which is equal

to the number of rotor blades and this feature ensures the equal pitch required by the code in the unsteady simulation. The casing grid was attached to the tip grid using the CFX-TASCflow Rotor/stator "sliding" interface explained in Chapter 4.

For these simulations the atmospheric total pressure is set at the inlet of the domain and the mass flow rate corresponding to the flow coefficient is specified at the outlet of the domain. The vane and the shroud of the domain were made stationary, while the blade, hub and the rest of the domain were set as rotating at 1 500 rpm. The standard k-ϵ turbulence model with wall functions was employed and the MLPS discretization method was used for the treatment of the convective term together with PAC scheme. To ensure an accurate unsteady solution, the convergence criterion for the maximum residual at each time step was chosen to be 10^{-5} and for monitoring the solution 75 monitor points "MP" were defined at different positions in the computational domain.

For smoother unsteady simulation start up, a converged solution of a steady-state simulation using the "Frozen-Rotor" interface was used as an initial guess for these simulations. The boundary conditions of the "Frozen Rotor" simulation are similar to those used to conduct a steady-state simulation in Chapter 8, except that the "Frozen-Rotor" interface is specified for the attachment between the casing and tip grids instead of the "Stage" interface.

Initially, runs making use of 10 and 25 time steps per pitch sweep, corresponding to an individual time step of 14.815×10^{-5} and 5.926×10^{-5} respectively, were carried out for different flow coefficients. No repeating time history patterns were obtained for any of the independent variables with these two time steps. As a consequence, the time steps were halved to 50 corresponding to an individual time step of 2.963×10^{-5} seconds. Also in these initial simulations, the variation of the number of iterations per time step, from a minimum of 10 up to 30 showed a better convergence with the higher number of iterations. As a result the maximum number of coefficient iterations was set to be 30. This means that the solver will proceed to the next time step if the maximum residuals are below 10^{-5} or if the number of coefficient iterations is equal to 30.

An unsteady simulation for the flow coefficient of 0.72 was carried out with the above mentioned boundary conditions. The plot of Figure 9.1 displays the time history of the axial velocity at two monitor points, MP21 located at the blade mid-span ahead of the blade leading edge as shown in Figure 9.2(a), and MP72 located at the mid-span of the recess grid at the entry side as shown in Figure 9.2(b).

To give a measure of the computational cost involved in the production of a simulation capable of producing a flow time history, such as that shown in Figure 9.1,

approximately three days were needed to finish one blade sweep, 50 time steps, when the simulation was run on a Compaq XP1000 machine. The size of the individual time step calculation files, denoted in the code as say trn.1 for the first time step, was for this case 8.76 Mb per file corresponding thus to 3.504 Gb for the 8 blade sweeps. This has then to be stored for the purpose of assembling a time history such as that presented in Figure 9.1.

The availability of the steady-state solution presented in Chapter 8, which employs exactly the same grid platform and differs only in the mode of treatment of the blade-recess interface, enables a direct comparison between the results obtained by both methods, and also identifies the sources and locations of the differences in the results. A subroutine "UNSTEADY", presented in details in Appendix C, was written to calculate some useful parameters of the unsteady simulation results such as the average flow properties, equation (C.2), their standard deviation, equation (C.3), in addition to the variation of these averaged results from the steady-state ones, equation (C.1).

9.3 Initial runs post-processing remarks

The initial post-processing of the unsteady simulation result using the "UNSTEADY" macro shows unrealistic flow distribution inside the domain. This is clearly demonstrated in Figure 9.3, which presents the averaged value of the static pressure from the unsteady results at the blade mid-span. This picture shows a very low average static pressure especially near the domain outlet. Consequently, Figure 9.4 represents the difference between the steady and the averaged unsteady results, shows a higher value of pressure difference around $-600\,N/m^2$ at the outlet of the domain. The negative sign means that the averaged unsteady results are lower than the steady state ones as shown in equation (C.3).

Further investigation of the flow field result from this unsteady simulation at each time step shows that pulses of low-pressure propagate from the domain outlet at a few time steps in each blade sweep. An example of these pulsations is shown for time step 13 in Figure 9.5, which represents the static pressure distribution near the blade tip. This pulsation was found to be independent of the relative position of the blade to the vane inside the casing, where some sweeps have only one pulsation and others have two or more. This non-linear pulsation was caused by imposing a steady boundary condition for unsteady simulation at the outlet of the computational domain, where the position of the outlet boundary is very near to the blade and hence it affects the flow solution inside the computational domain.

To investigate further this conclusion, similar simulations were run, firstly with different flow coefficients $\phi = 0.60$ and $\phi = 0.40$, and secondly with different outlet boundary conditions, in which the static pressure was specified at the outlet instead of the initially specified mass flow rate. The same phenomena were found in all these simulations, which clearly indicates that the low-pressure pulsation found near the domain outlet is directly caused from specifying of a steady state boundary condition too close to the blade, and that this in turn affects the flow solver.

9.4 Computational domain modification

The strategy adopted to prevent this pulsation involved the displacement of the steady-state outlet boundary condition away from the outlet station shown in Figure 5.1. This was done by adding another grid to extend the computational domain further away from the outlet station of the domain. This extra grid was generated with an H-type mesh using TASCgrid, and consists of $40 \times 40 \times 50$ mesh points, where 40 points were used in the axial direction, 40 points in the blade-to-blade direction, and 50 points in the radial direction.

This outlet grid was imported into CFX-TASCbob3D and attached to the original computational domain using the GGI interface, described in Chapter 4, in order to build the computational domain employed in the unsteady simulations as shown in Figure 9.6. This domain has in total 333 000 mesh points, of which 180 000 mesh points are in the blade grid, 20 000 mesh points are in the tip grid, 53 000 mesh points are in the casing grid, and 80 000 mesh points are in the outlet grid.

9.5 Extended domain simulation

The simulation of a single point corresponding to flow coefficient $\phi = 0.60$ was carried out while employing the extended computational domain described above. The sclection of the particular flow coefficient was dictated by the considerations of both the computational resources available and the large requirements of unsteady simulations as well as the relative importance of the chosen flow point. As was shown in Chapter 6, the flow coefficient of $\phi = 0.60$ point is the nearest one to stall for which a corresponding steady-state simulation is also available and this fact, plus the notion that any dissimilarity between steady and unsteady computations will be greatest at lower flow rates, led to this choice of flow condition to simulate.

The boundary conditions prescribed for the extended domain simulation were similar to those employed in the computation previously described, namely absolute total pressure at inlet and mass flow coefficient at the outlet. The observation of the results of the initial run showed an absence of a strict repeating pattern in the plotted values of the main computed variables, the Cartesian velocity components as well as static pressure. In order to enforce this repeatability the time step was halved to 1.48×10^{-5}, corresponding thus to 100 time steps per pitchwise sweep, according to the principle illustrated above in boundary conditions. This change in time step value achieved the desired repeating pattern and the solution was considered to have been achieved after 15 sweeps with 100 time steps each and 30 iterations per time step. The overall computation time was about 24 days based on 4.5 days per sweep while the code was run on a Compaq XP1000 processor.

9.6 Computational results and discussion

The first post-processing output of the unsteady simulation is presented in the form of blade-to-blade plots of the static pressure, radial velocity and speed vectors taken at the bottom of the casing treatment domain, Figures 9.7 to 9.9, respectively. All these figures contain four plots each corresponding to four different angular locations spaced at 25 time steps or 3.33 degrees and 0.000 37 seconds at 1 500 rpm.

The static pressure plots, Figure 9.7, illustrate the effects of blade passage upon the pressure field of the recess vane and this can clearly be seen to present a very small change with the passing of the blade. Although there is a well defined low-pressure region associated with the blade tip this is hardly seen to impact on the pressure distribution inside the vane passage of the casing recess.

The analysis of the equivalent radial velocity plots, Figure 9.8, paints a similar picture but one which deserves a more detailed comment. In these plots the flow entering the recess has, due to the orientation of the local coordinates, a negative radial velocity and is coloured in blue or green while yellow and red denotes the parts of the flow leaving the cavity into the rotor domain. It is worth pointing out that although only one blade is actually shown in the plots, in some of these the effects of the adjacent blade are also present such as in Figures 9.8(c) and 9.8(d).

As was the case for the static pressure plots there is no large scale interaction between the rotor tip and the region of the recess vane and shroud ring in the radial velocity and vector plots, Figures 9.8 and 9.9. At this flow coefficient $\phi = 0.60$ the radial flow mostly leaves the cavity ahead of the shroud ring, as was previously seen in Chapter

8, but the availability of unsteady results enables to further understand the physics of this mechanism. In all of the radial velocity and vector plots the higher values of radial flow are found in a small region near the rotor blade pressure side. This amounts the pushing of the flow with the pressure surface of the blade and although the process is visible in an average form elsewhere in Chapter 8, for example Figures 8.18 and 8.20(b), this is particularly highlighted in the unsteady computations.

Although the examination of the unsteady simulation of the recess treatment cavities does not offer a picture of large scale unsteady activity, this is on itself quite significant and enables the drawing of an important conclusion namely that large casing treatments rely primarily on a steady-state flow process. The corollary of this conclusion is of course that a steady-state simulation should then be sufficient to capture the essential flow features of a recess treatment configuration. This point is further explored in the following section below.

9.7 Steady-unsteady computations Comparison

The comparisons between steady and unsteady results are assisted by the employment of exactly the same grid in the two models, the only difference between the two being the mode of treatment of the interface between the two grid components. The plots used for the steady/unsteady results evaluation are pitchwise distributions of cylindrical velocity components and blade-to-blade contour plots of Cartesian velocity components, overall speed and static pressure.

9.7.1 Wake plots

For the pitchwise distributions, the averaging of the unsteady simulation results was carried out on the three cylindrical coordinate rotor relative velocity components V_a, V_r and V_t and these were taken immediately downstream of the rotor blade trailing edge. The results corresponding to two radial locations, 10% and 90% of the span, are presented in Figures 9.10 and 9.11 respectively, where each of the plots shows a trace obtained though the time-averaging of the unsteady simulation and its equivalent due to the steady-state computation.

In all three pictures corresponding to the first of these figures, Figure 9.10 taken in the near hub region, an almost coincidence of the plots obtained from the two solution methods is readily apparent. This is not surprising given the distance of this

data collection region from the sector more intuitively associated with the periodic instability caused by the rotor/recess vane cyclic interaction.

The plots related to the tip region, Figure 9.11, show a lesser degree of agreement between the traces due to the two approaches although even here the magnitude of the discrepancies are at all times fairly small irrespective of the particular velocity component. A noteworthy feature of this particular average of the unsteady/steady comparison is the presence of unsteady average wakes which show velocity defects which are wider and deeper than those due to the steady-state simulations.

The rationale of this disagreement between the wake shapes given by the two methods is of course due primarily to the presence of interaction effects between rotating and stationary components although local component-relative unstable flow features can also contribute particularly in near stall flow regimes. In the presence of the periodic disturbances due to a relatively-rotating component, either predominantly viscous in origin, as is the case of downstream acting wakes, or mostly of a potential nature, as happens with the upstream action of downstream components, the blade-relative main flow features, wakes, boundary layers and tip clearance flows, oscillate about a mean position. Given this unsteady environment it is therefore not surprising that the average width of a spatially unsteady wake will be greater than that computed from the flow field described by a steady-state simulation.

The absence of a typical rotor/stator arrangement must certainly contribute, in the present case, to a lessening of this form of steady/unsteady results disagreement but the essential of the mechanism described in the previous section is nevertheless quite apparent in all the plots of Figure 9.11.

9.7.2 Contour plots

The evaluation of the differences between the two computation average forms is very usefully performed in a qualitative way through the comparison of a set of contour plots of the main calculated quantities at the computational domain mid-span and near the blade tip as illustrated in Figure 9.12. These quantities include the axial, tangential and radial velocity components, speed and static pressure.

The blade-to-blade plots of Figures 9.13 and 9.14 display the axial velocity at the computational domain mid-span region and near the blade tip for the flow coefficient of 0.60 with Figure 9.13 corresponding to steady-state simulation and Figure 9.14 denoting the time-averaged unsteady results. There are slight differences between the two plots where the plot of the unsteady calculation exhibits a slightly wider

wake. Nevertheless, a better way to establish the magnitude and the locations of the variance between the two distributions is to plot the difference at a nodal level calculated using the previously discussed "UNSTEADY" macro.

As had been seen in the pitchwise distribution plots described above, the differences between the results due to the two methods are quite small and not easily identifiable in the blade-to-blade plots. A surer way to establish the magnitude and the location of the variance between the two distributions is to plot the difference at a nodal level as is done in Figure 9.15. This plot shows that the dominant variation is predominantly located in the suction side of the blade. While it is important to retain the notion that the absolute magnitude of these differences is quite small it is still worthwhile to note that the blade wake and hence its suction side boundary layer are the feature which primarily are the subject to a different characterization by the two computational methods.

The pattern of the differences is consistent with an unsteady loading regime which acts essentially in the vicinity of the suction surface of the blade. In terms of magnitude, the maximum difference between the two results is small representing around 6% of the maximum freestream value. This plot confirms that there is in general a quasi absence of variation in axial velocity between the two models. This is not altogether unexpected, given that the stage interaction effects are intuitively more likely to affect the tangential and radial velocity components than the axial one.

However the examination of the corresponding plots of the tangential and radial velocity components in Figures 9.16 to 9.21 respectively, confirms that both average formulations are very well matched in the computational domain mid-span. For each velocity component the contours in the two plots presenting the steady result and time-averaged unsteady ones follow closely the same trends to such an extent as to make the identification of disparities between the two particularly difficult. Therefore use is made again of the plotting of nodal differences, Figures 9.18 and 9.21. In terms of magnitude, the maximum difference between the two results is very small for both velocity components with typical values of 7 and 6% of the maximum tangential and radial velocity respectively.

The same situation was confirmed to exist in the plots of Figures 9.22 to 9.27 representing the distributions of both the static pressure and velocity magnitude respectively. The plots of these figures demonstrated that both methods of averaging are very similar and well matched at the mid-span of the computational domain. The nodal differences between the two formulations presented in Figure 9.24 for the static pressure and Figure 9.27 for the velocity magnitude, show a very small

difference between the two results. In terms of magnitude the maximum difference is 0.2 and 0.05 of the maximum static pressure and flow speed respectively at the mid-span region.

The standard deviation tells how spread out a distribution is, and how tightly the values of the distribution is clustered around the average of those same values. It's a measure of dispersal, or variation, in a distribution. In other words, if the values of a distribution is close to the average of those values, then we may expect to see a low standard deviation. In contrast, if the values is spread across a greater range, it may present a high standard deviation. Figure 9.28 represents the standard deviation of the flow velocity magnitude in the computational domain. The plot shows that the maximum standard deviation is around 0.1 at the suction side of the blade. This low standard deviation value would likely be an indicator of stability. In comparison, higher standard deviation is often interpreted as higher volatility.

9.8 Summary

In this particular case of studying the interaction between the rotor and the vanes inside the recess, the rotor and stator are aligned in the radial direction unlike the common case in axial compressors in which the rotor and stator are aligned in the direction of the streamwise direction. As shown in the steady-state simulations of the fan with the recess, Chapter 8, a very small mass flow enters the recess compared to the total mass flow rate through the fan. In addition, the radial speed of the flow entering the recess is much smaller than the axial speed of the flow leaving the domain from the outlet. Hence the interaction between the rotor and the recess vane passages is found to be very small as compared to the interaction between the rotor and stator in a single stage fan, with one rotor and one stator rows.

This weak coupling was found to cause numerical problems in the unsteady simulation which was required to run for a large number of time steps in order to establish a proper repeating pattern. In addition, the specification of a steady boundary condition at the domain outlet during an unsteady analysis was found to be very problematic and led to a significant extension of the flow domain with an associated considerable increase in the required computational resources to carry out the analysis.

(a) Monitoring point 21

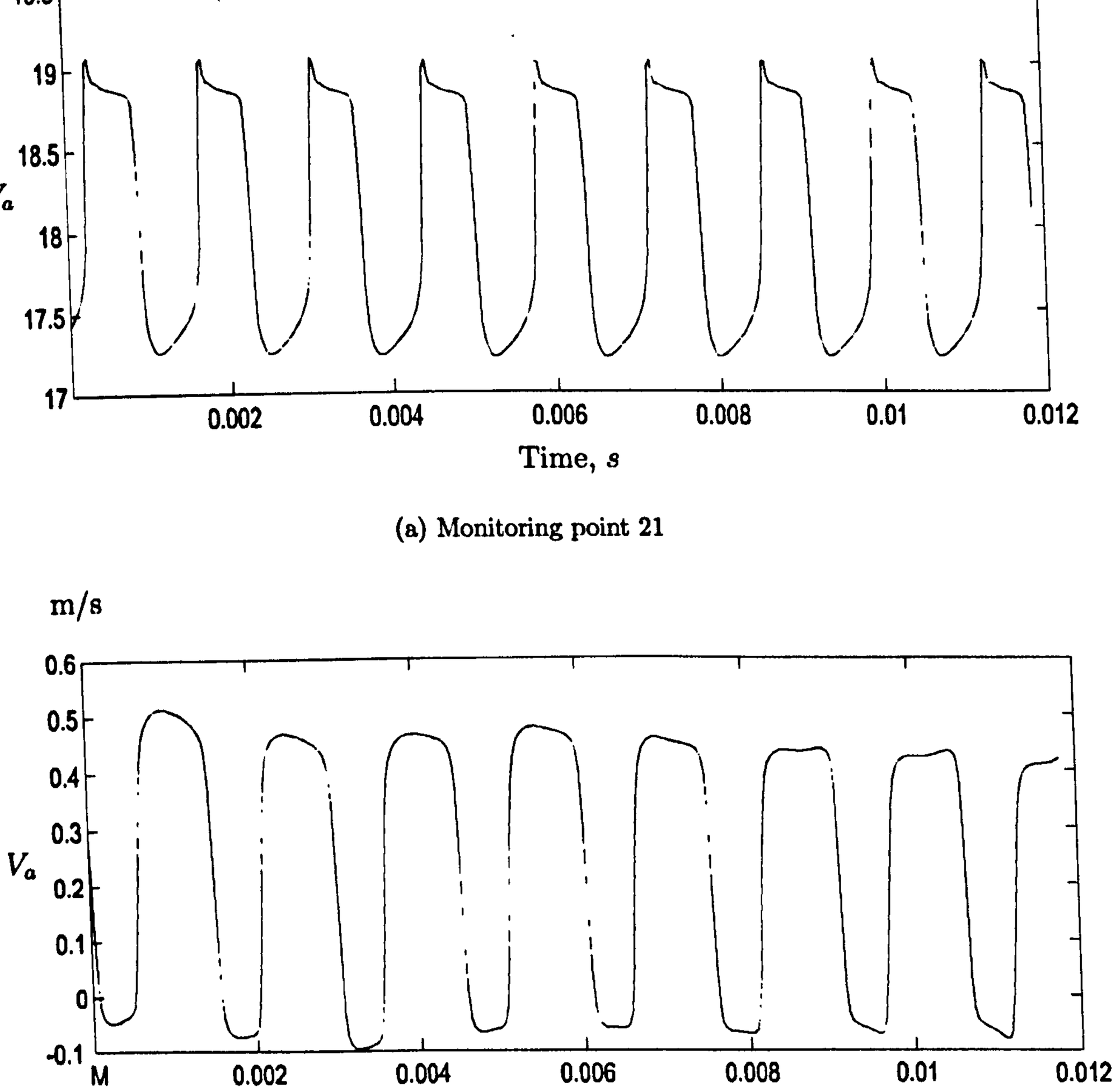

(b) Monitoring point 72

Figure 9.1: Axial velocity time history at flow coefficient $\phi = 0.72$

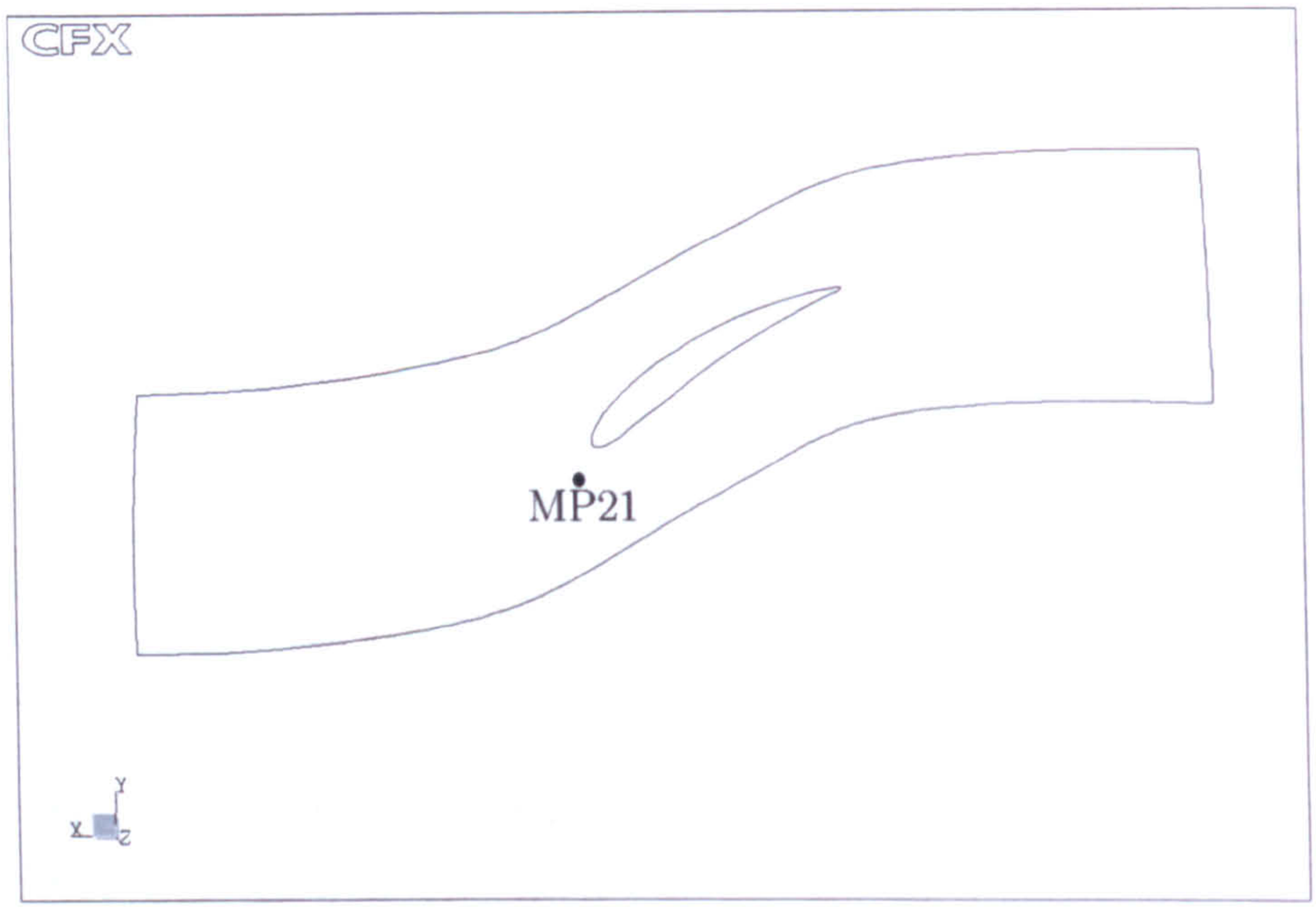

(a) Mid-span of the blade grid

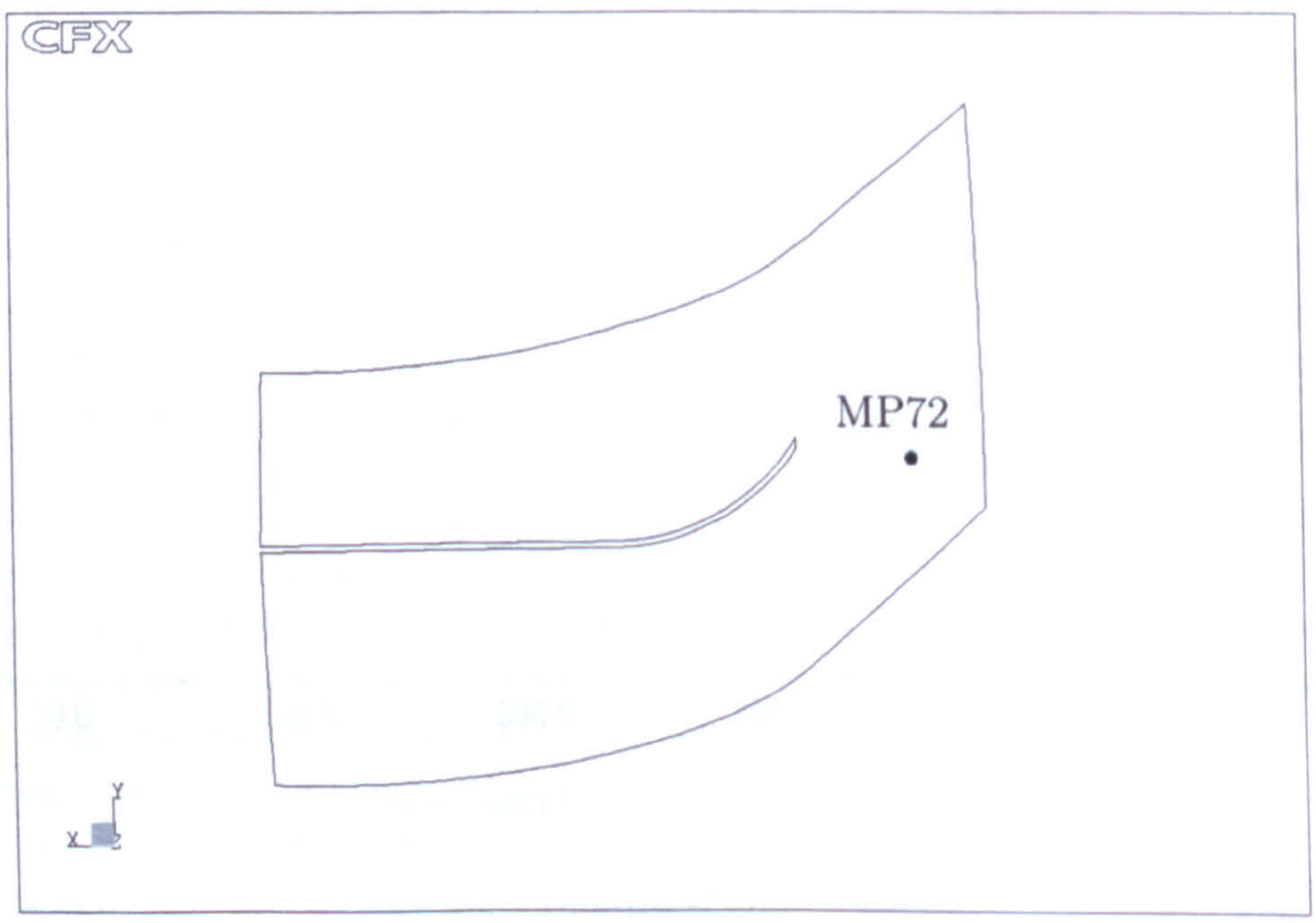

(b) Mid-span of the casing grid

Figure 9.2: Axial velocity time history at flow coefficient $\phi = 0.72$

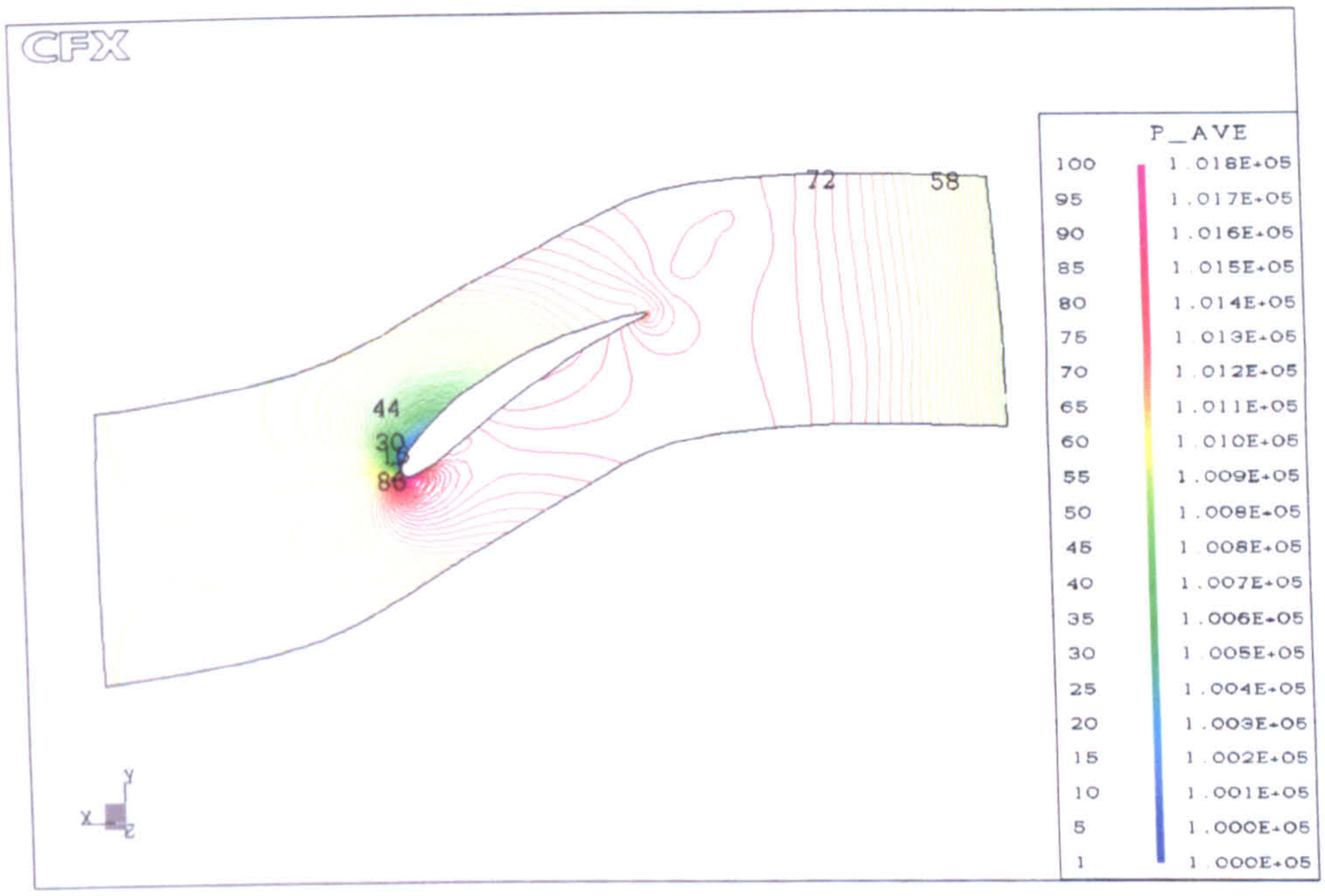

Figure 9.3: Average static pressure distribution at mid-span

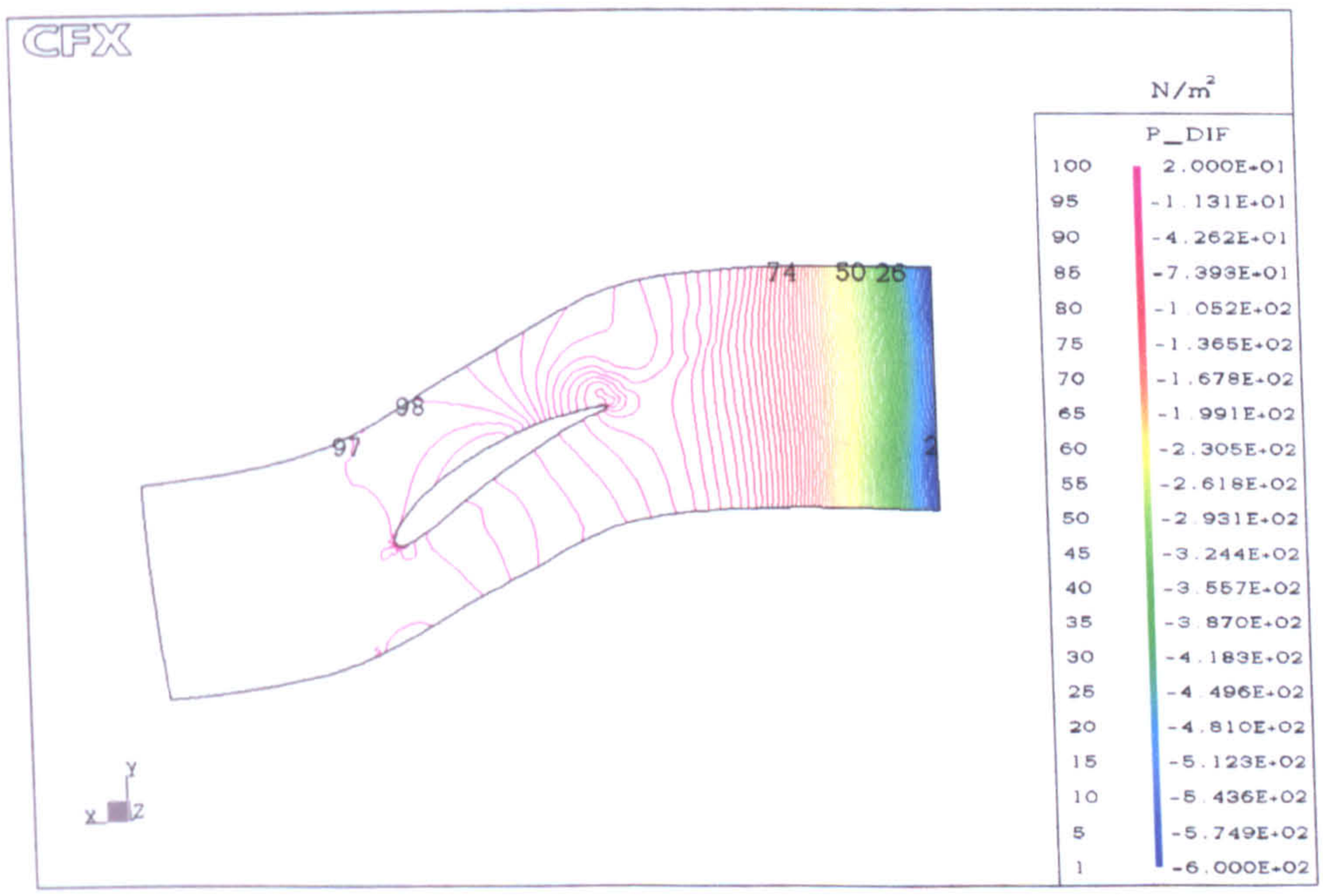

Figure 9.4: Static pressure comparison between steady and unsteady results

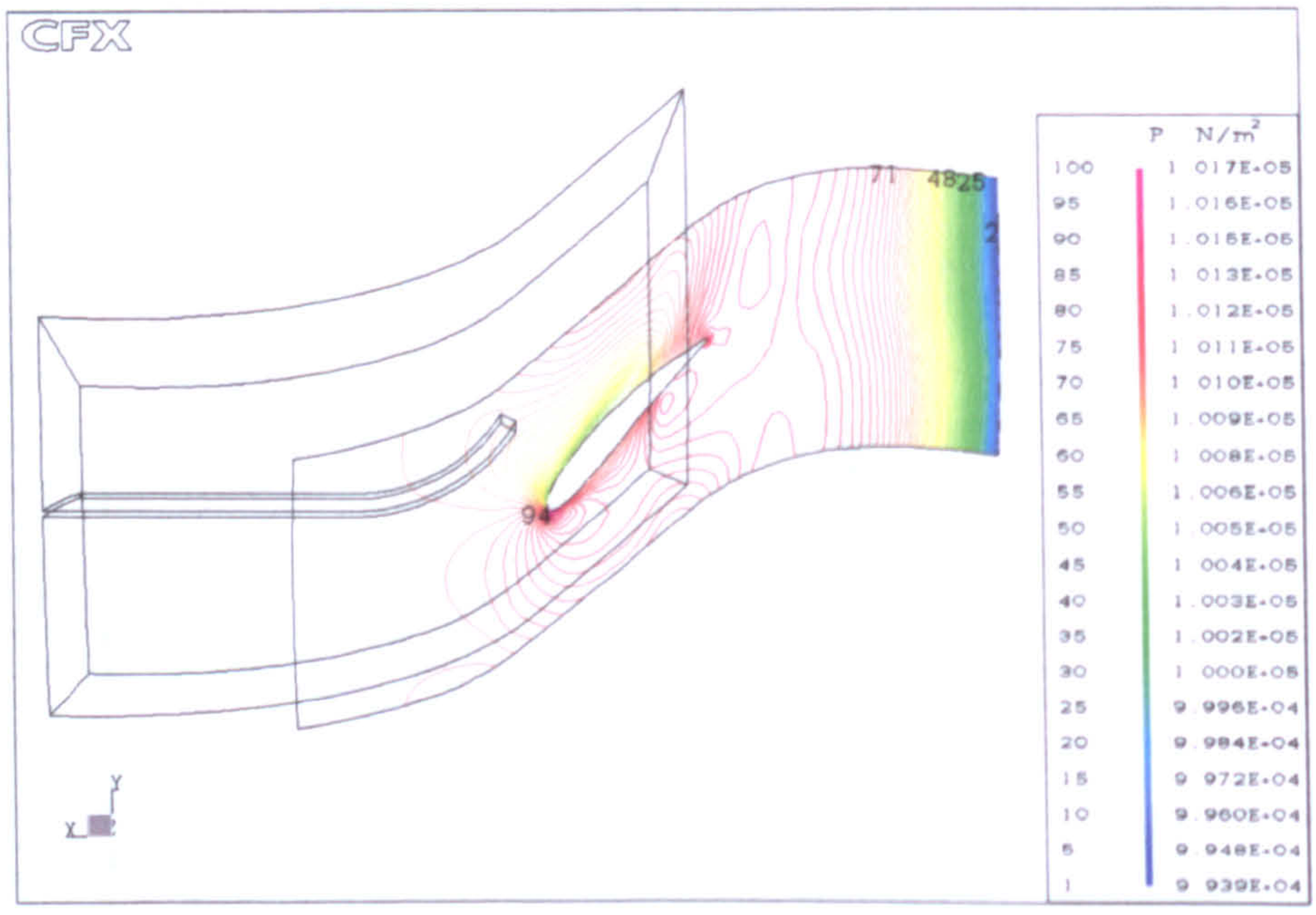

Figure 9.5: Static pressure distribution near the blade tip at time step 13

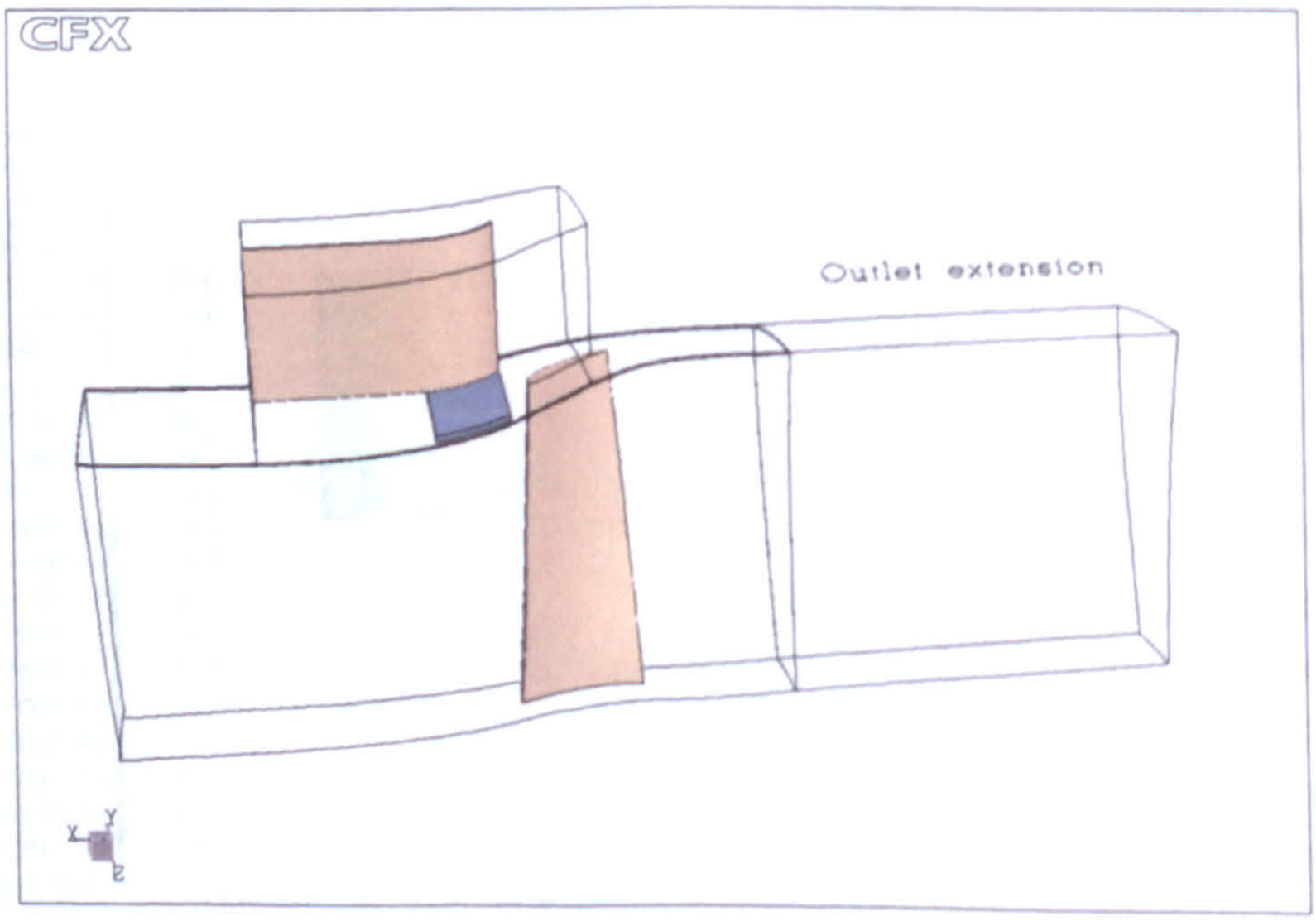

Figure 9.6: Computational domain for unsteady simulation

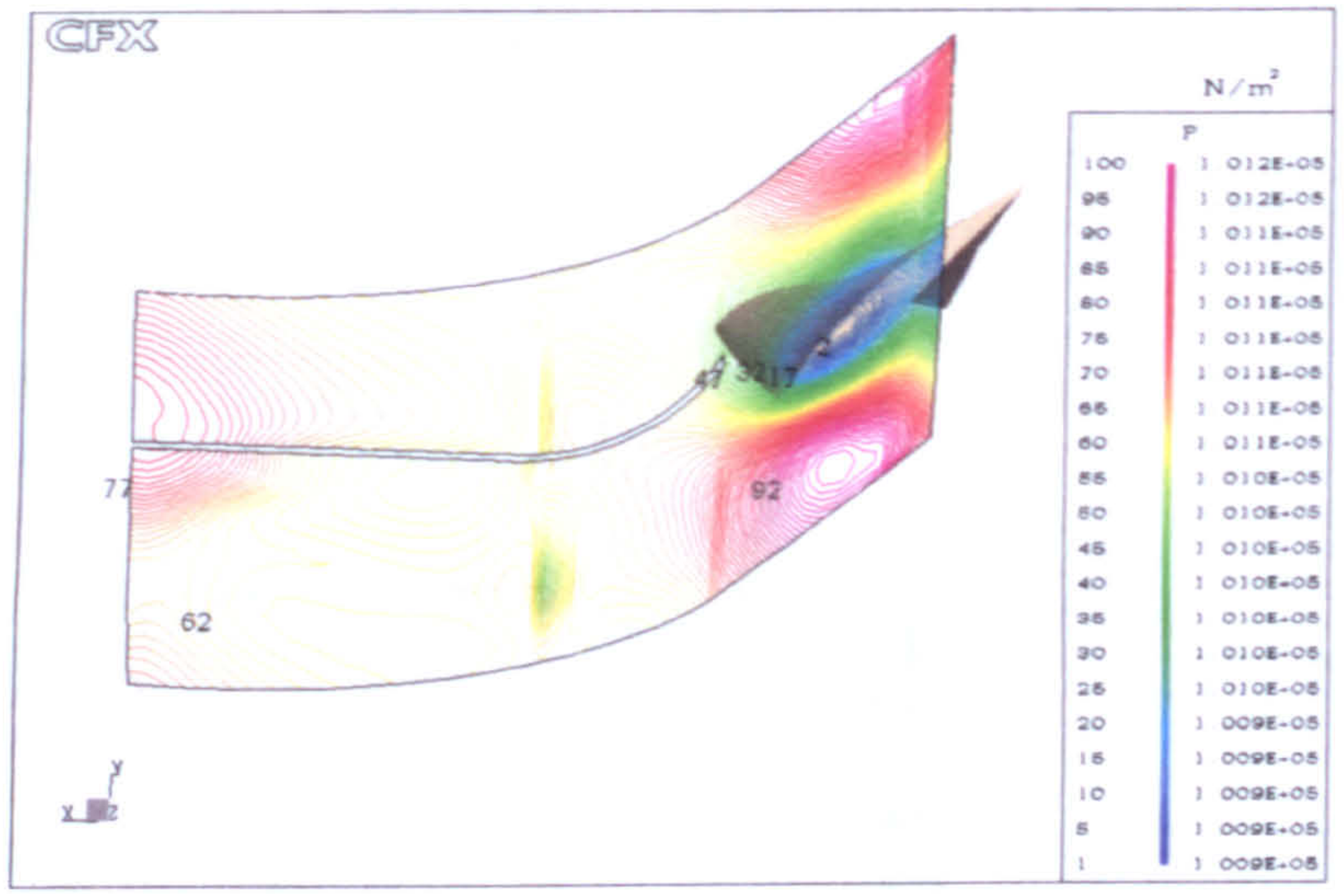

(a) 1st time step

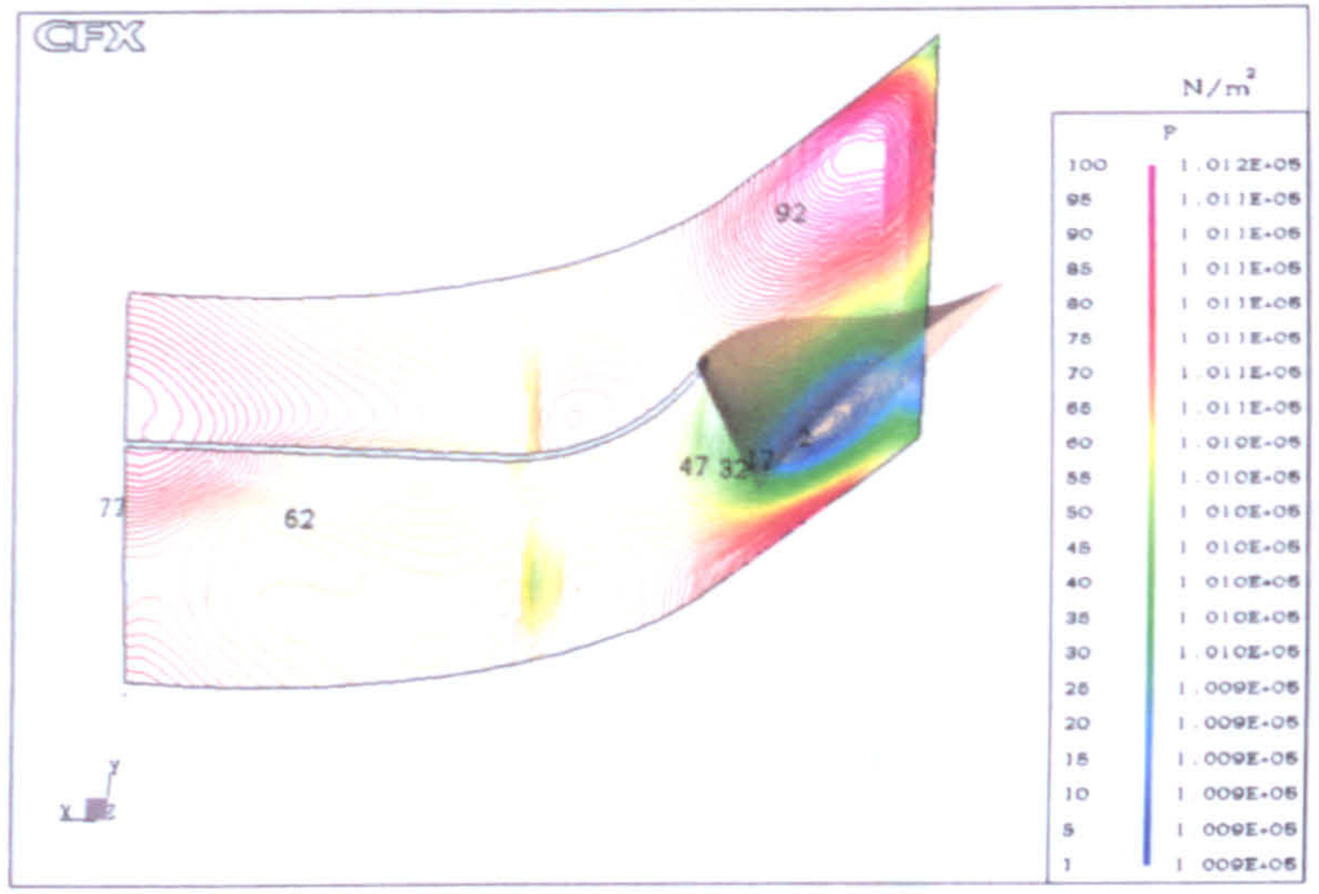

(b) 25th time step

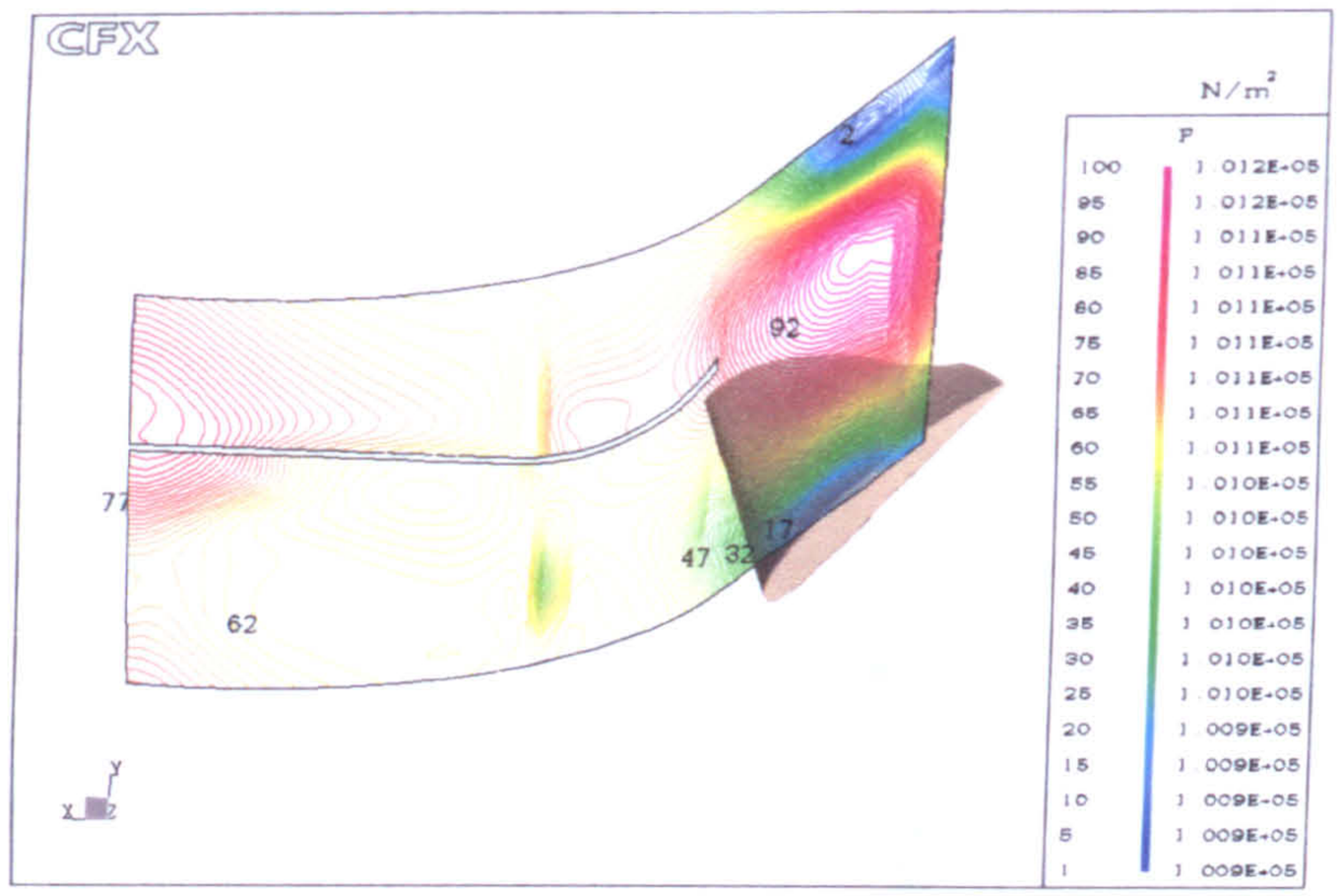

(c) 50th time step

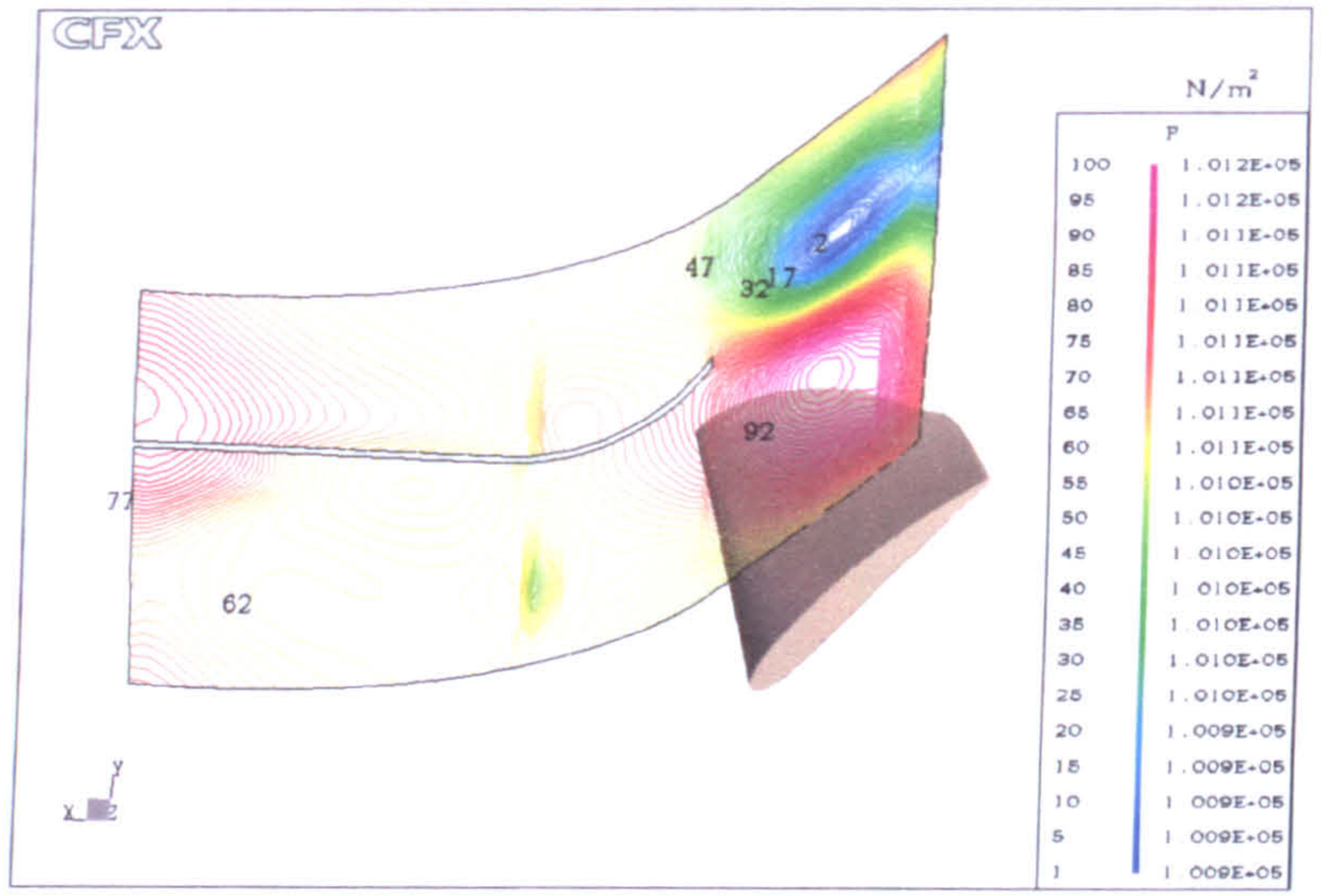

(d) 75th time step

Figure 9.7: Static pressure at the casing bottom for different time steps

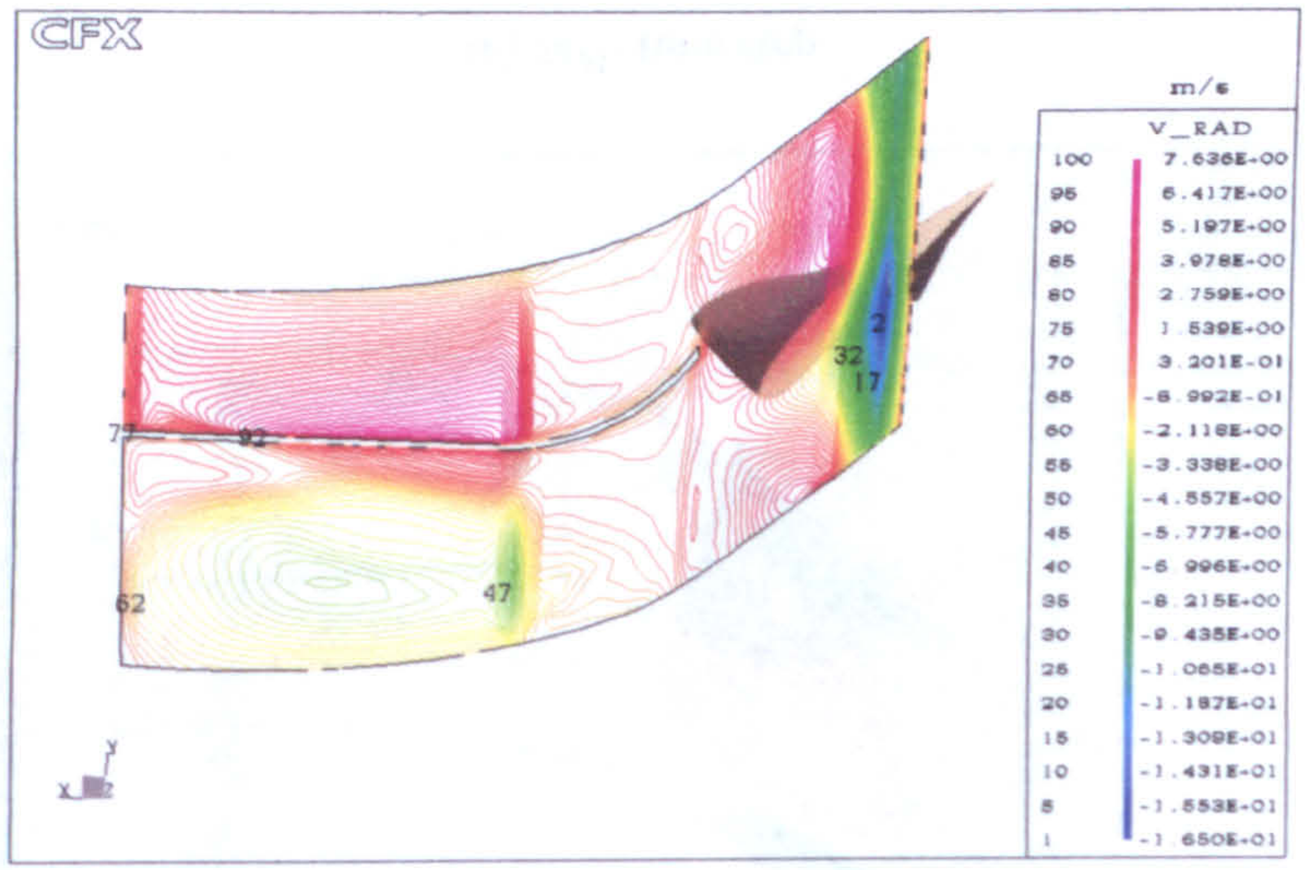

(a) 1st time step

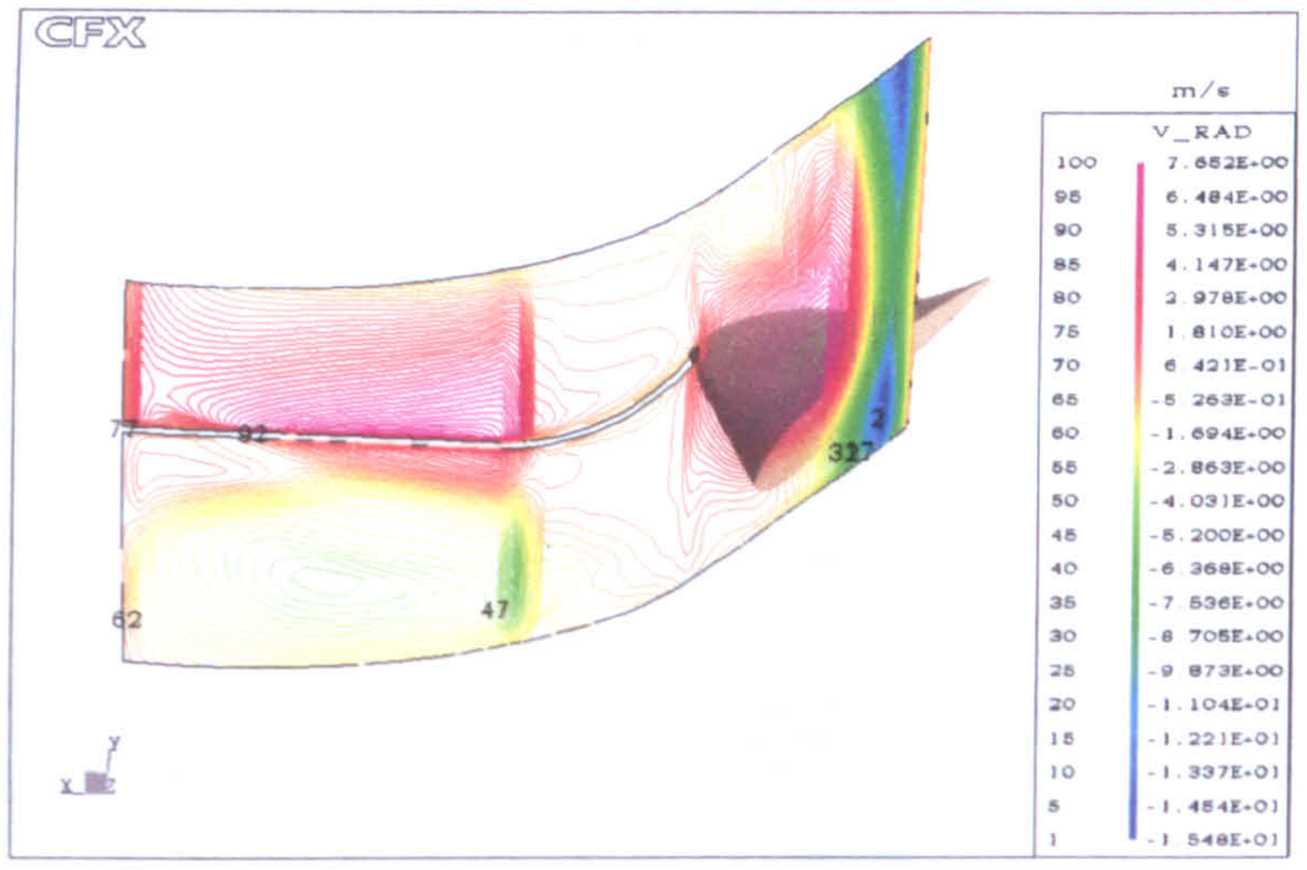

(b) 25th time step

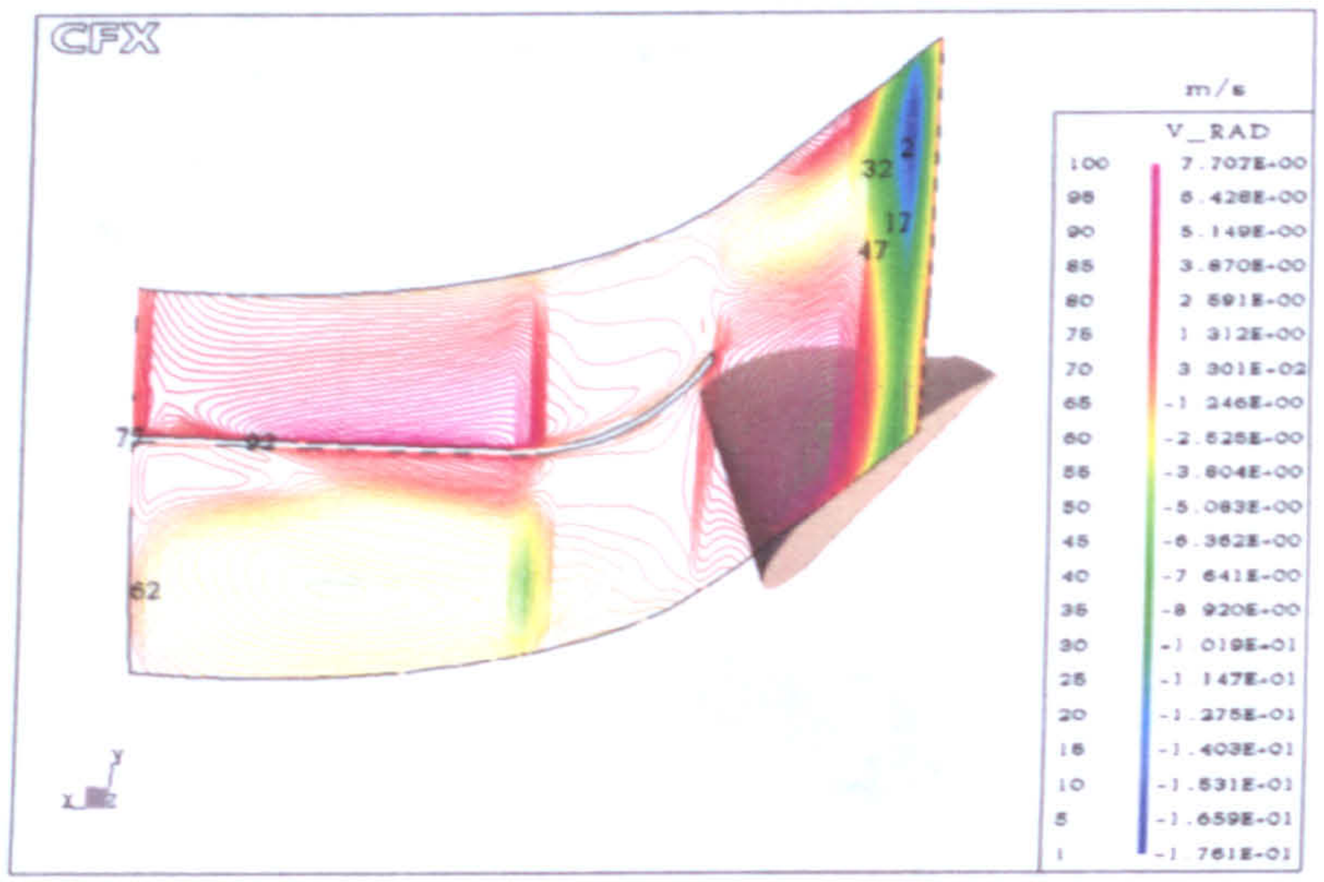

(c) 50th time step

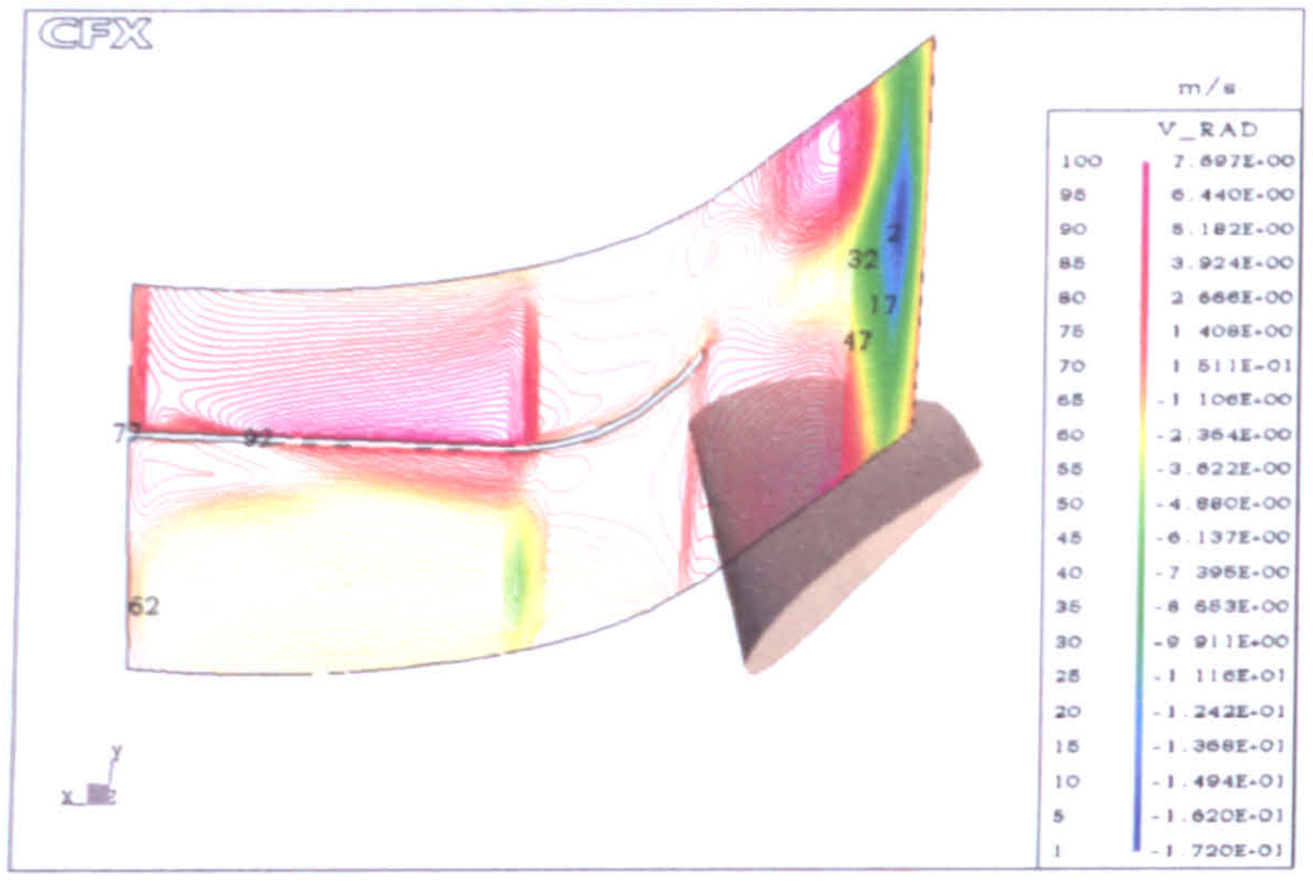

(d) 75th time step

Figure 9.8: Radial velocity near the casing bottom for different time steps

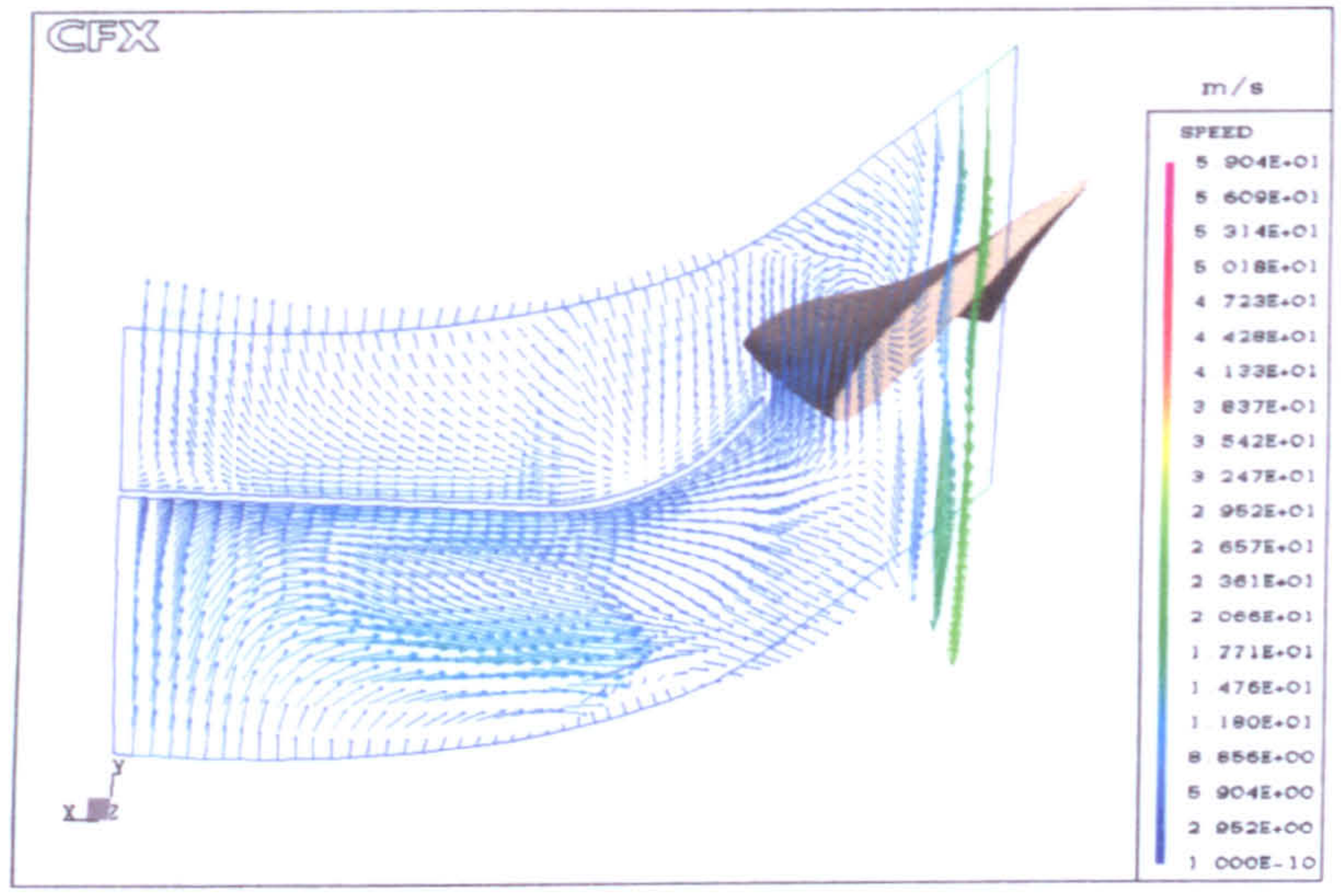

(a) 1st time step

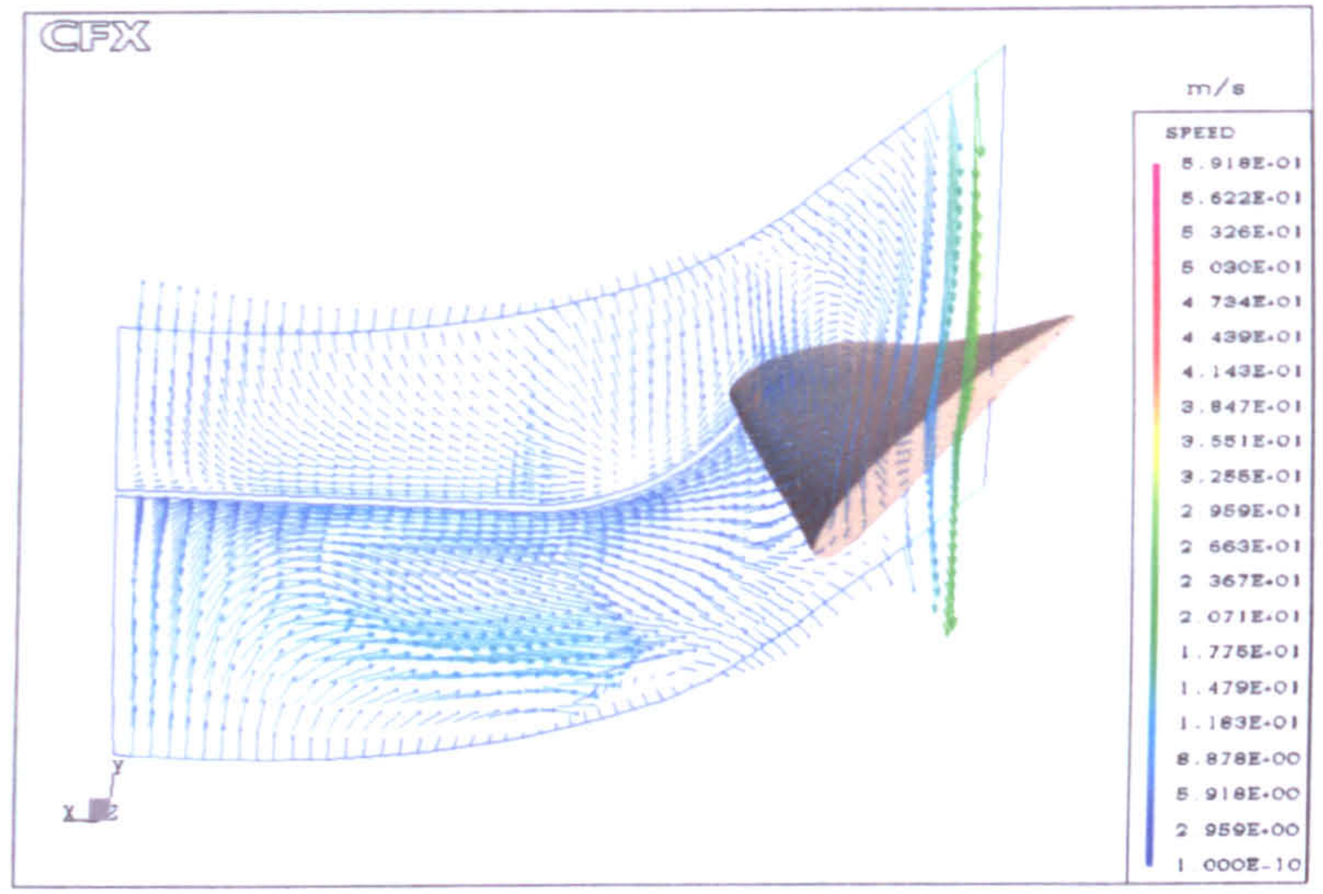

(b) 25th time step

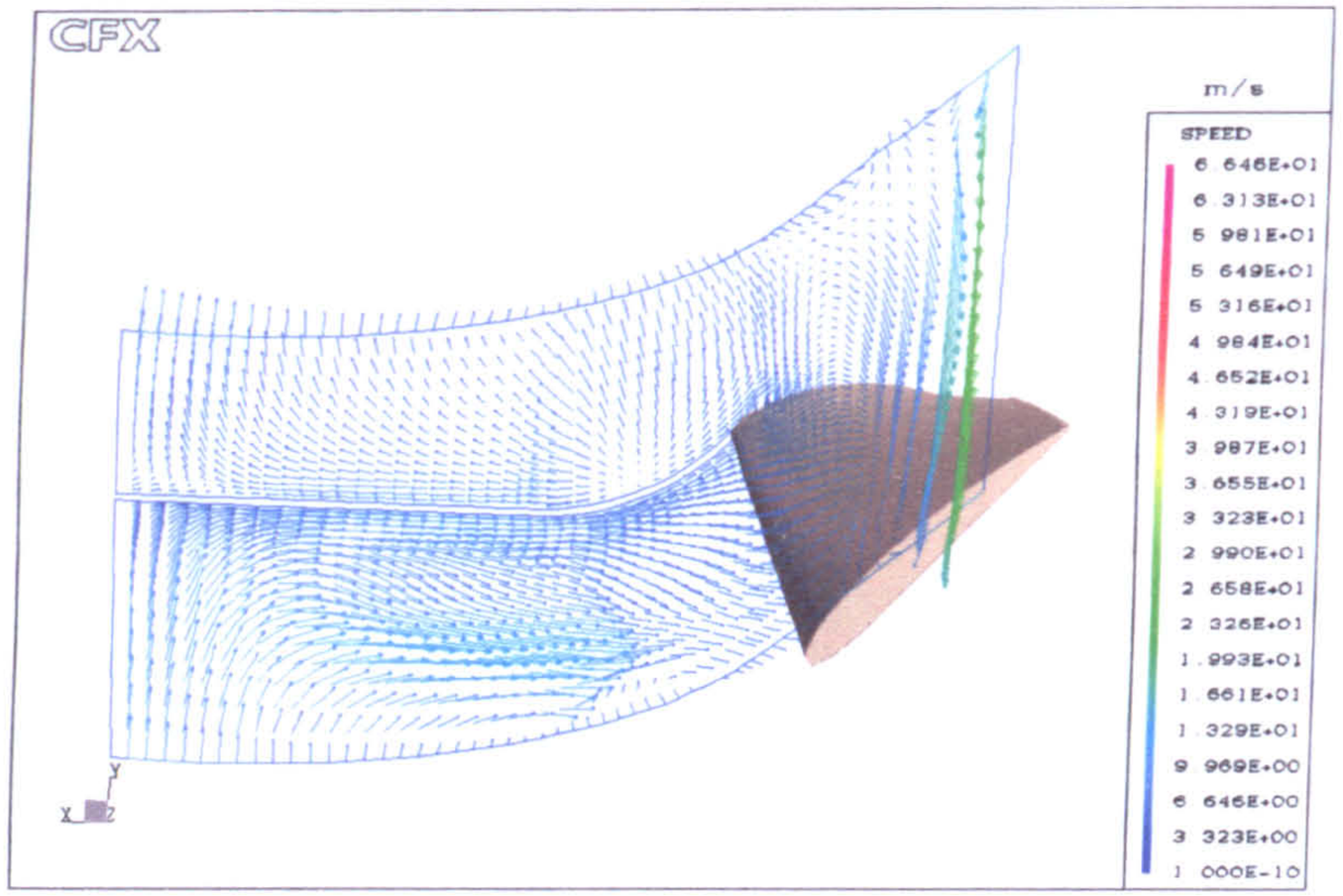

(c) 50th time step

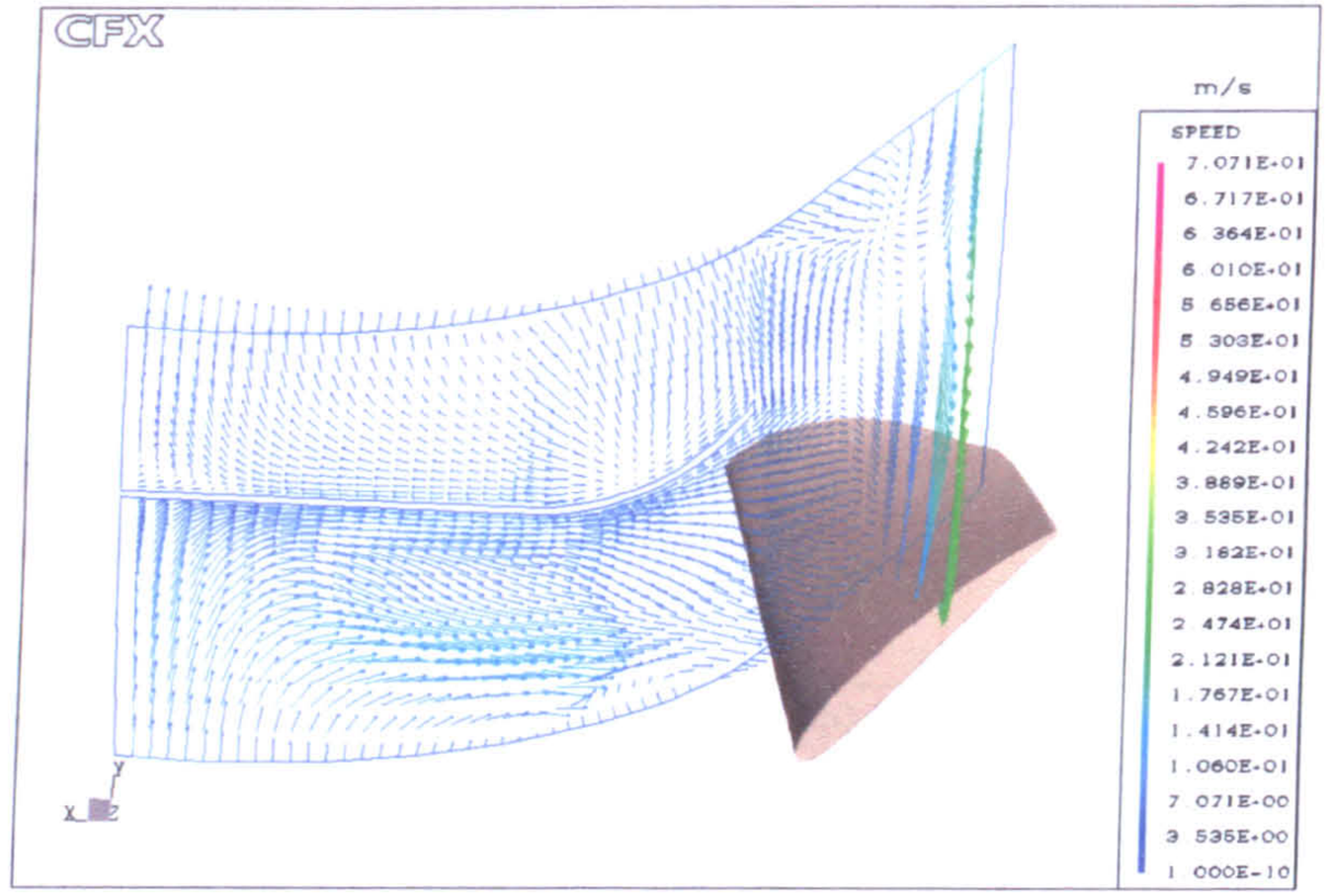

(d) 75th time step

Figure 9.9: Vector plot near the casing bottom for different time steps

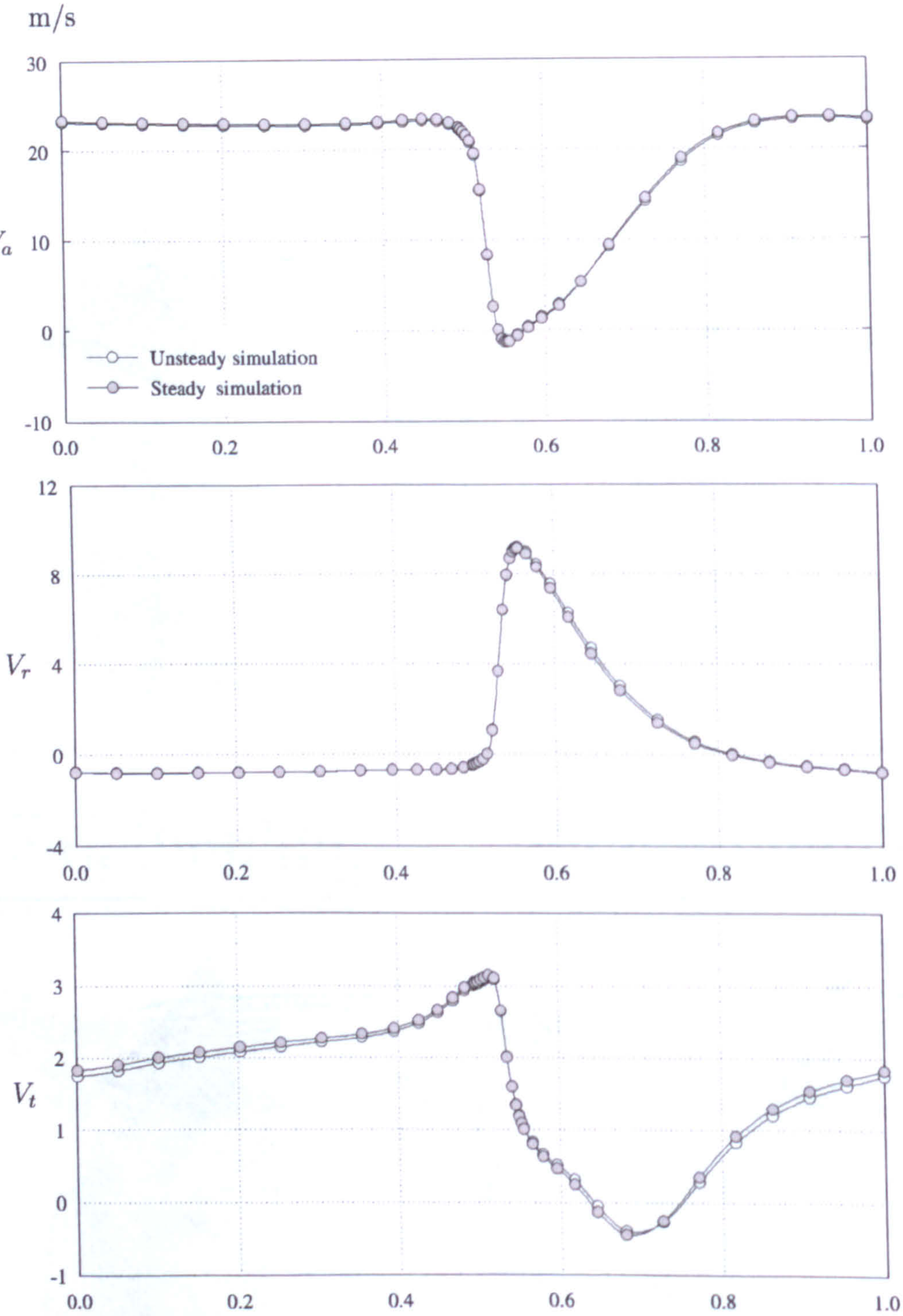

Figure 9.10: Pitchwise variation of velocity component at 10% span

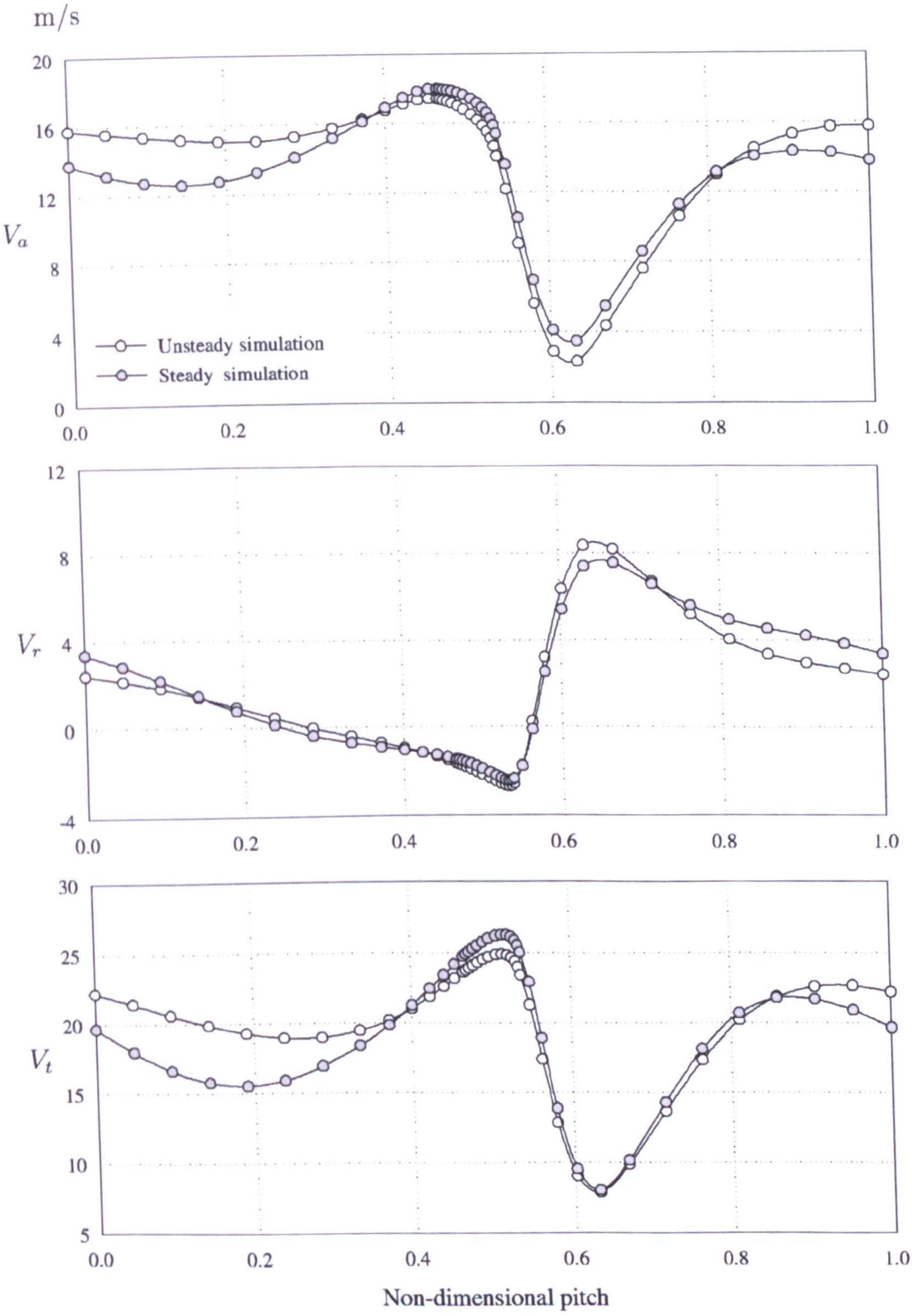

Figure 9.11: Pitchwise variation of velocity component at 90% span

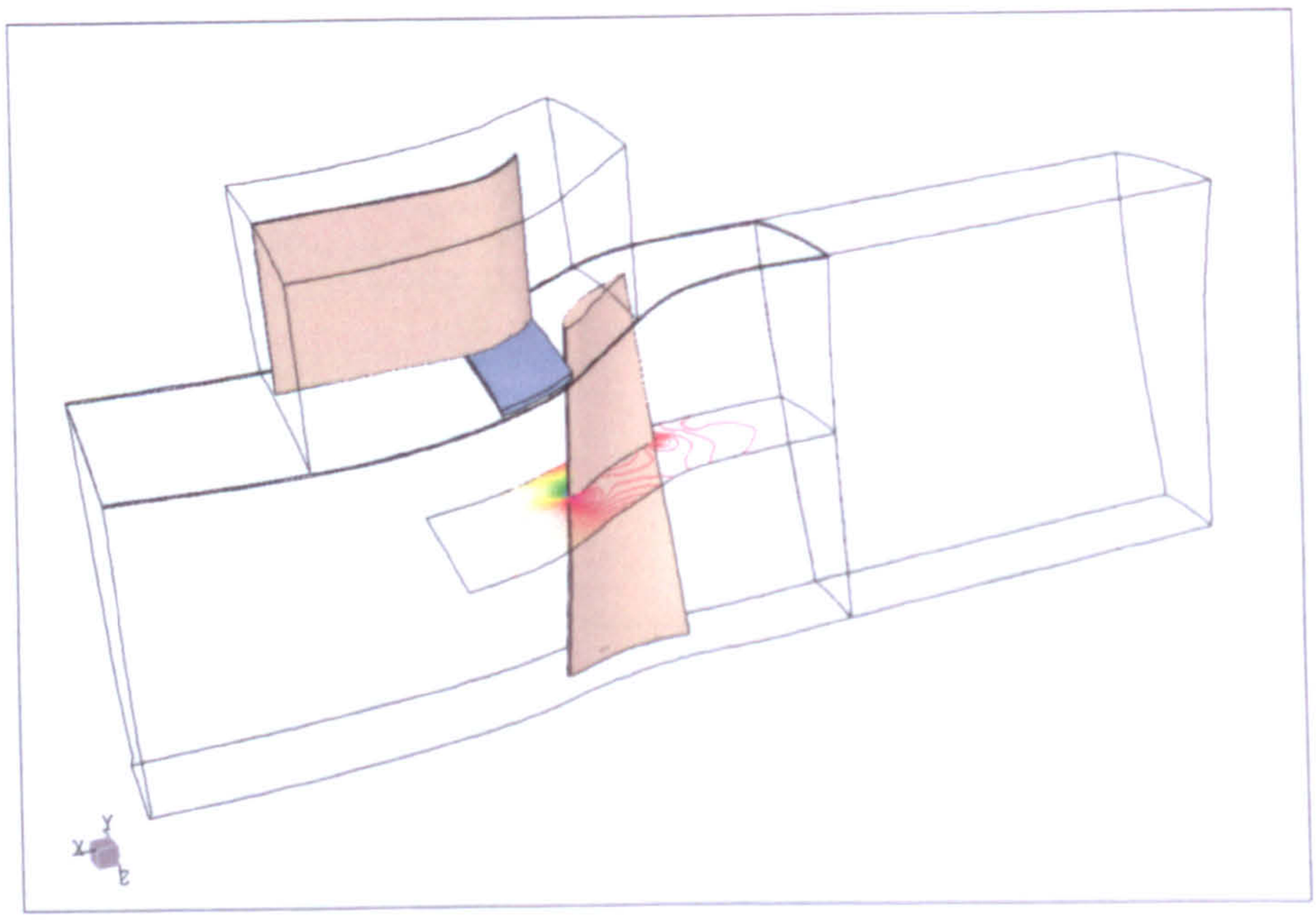

(a) At blade mid-span

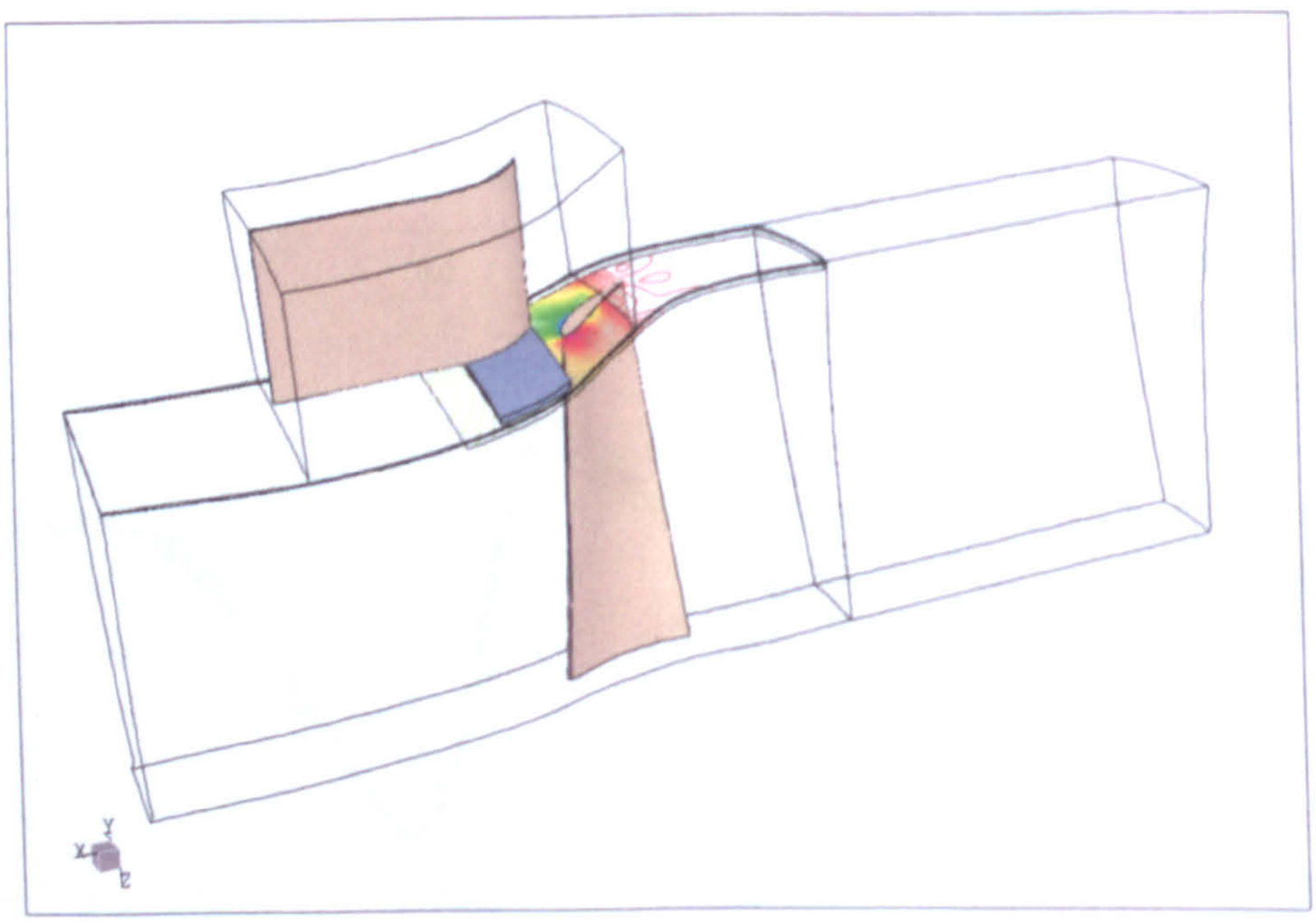

(b) Near the blade tip

Figure 9.12: Comparison locations on the computational domain

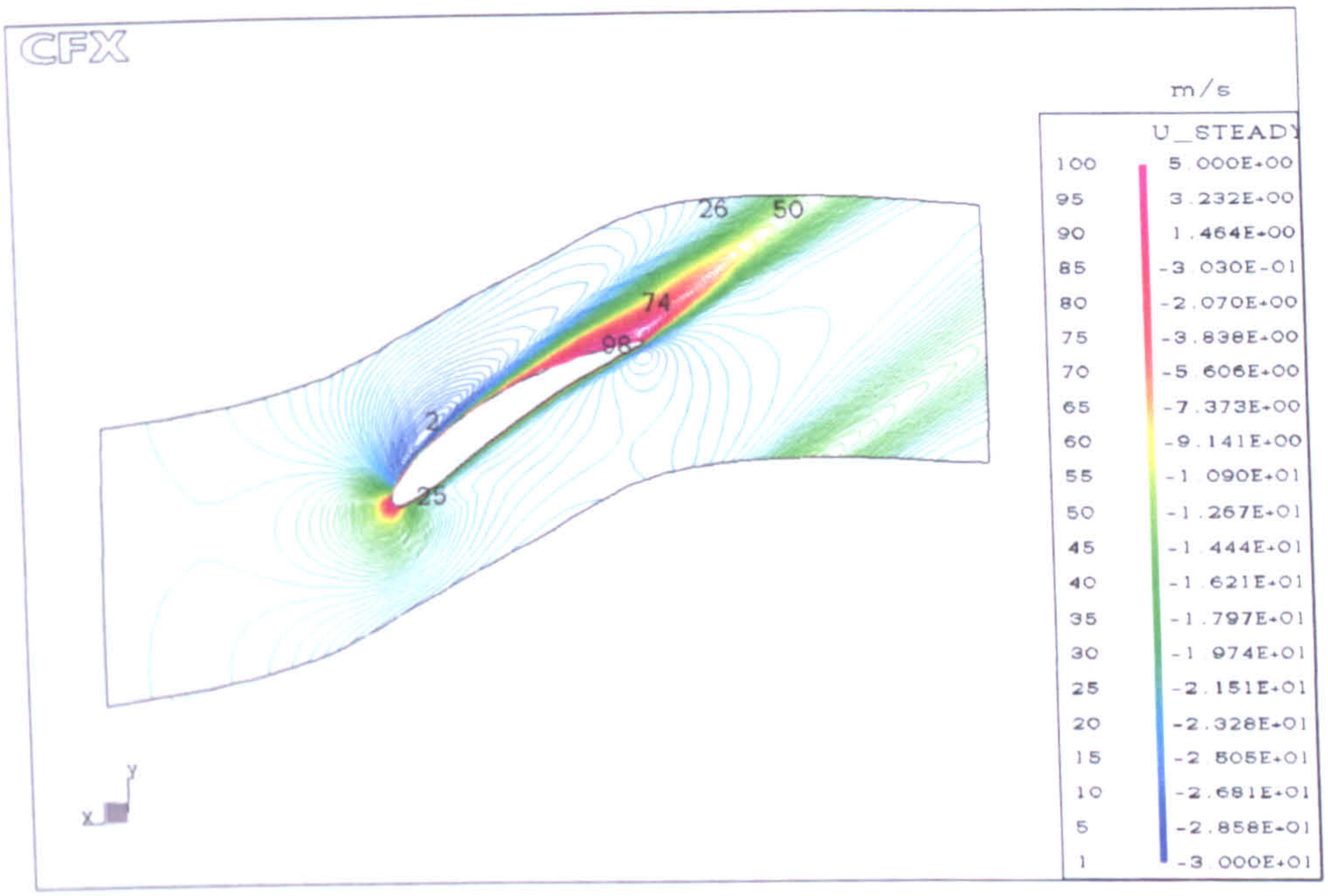

(a) At the blade mid-span

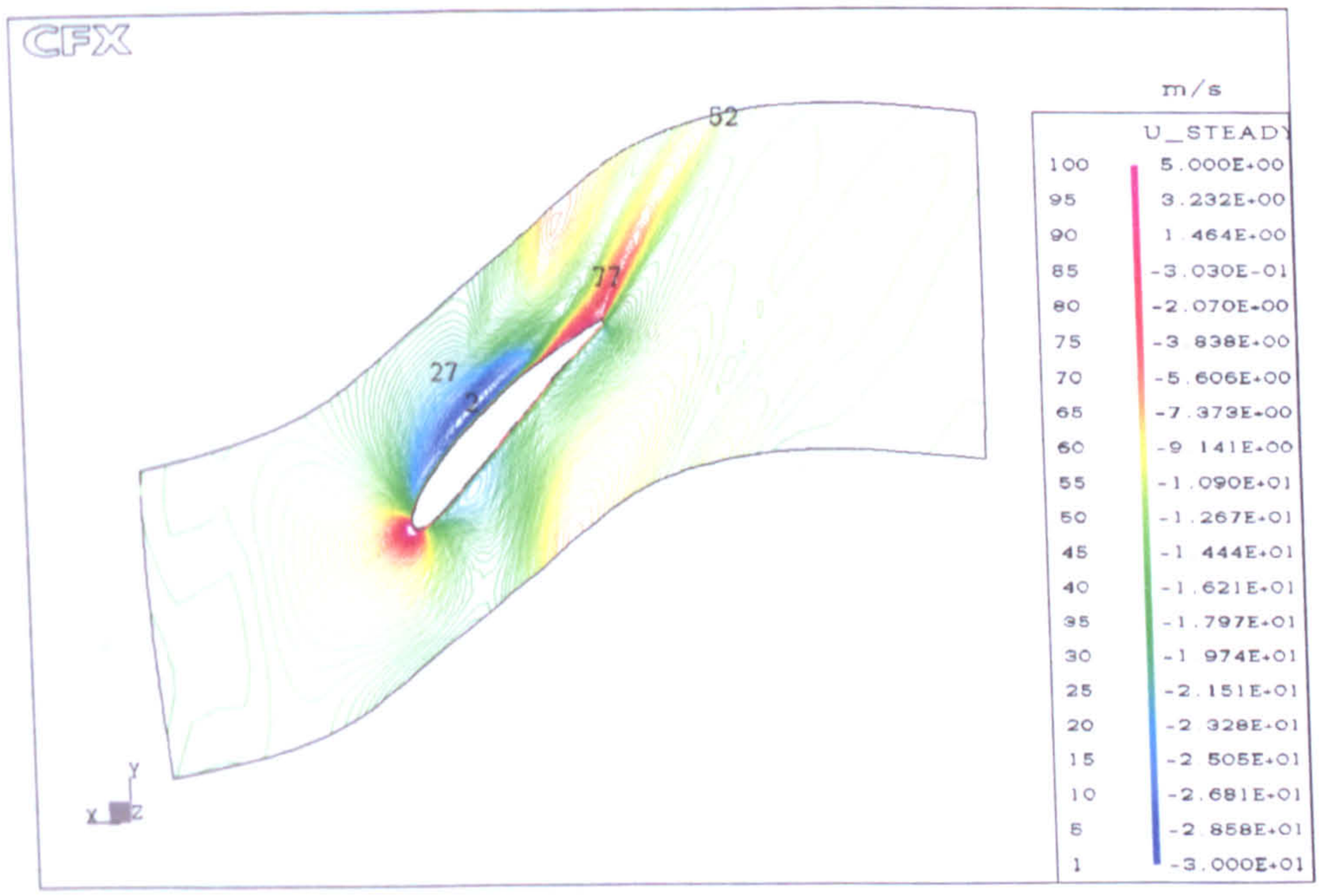

(b) Near the blade tip

Figure 9.13: Steady-state result of the axial flow velocity

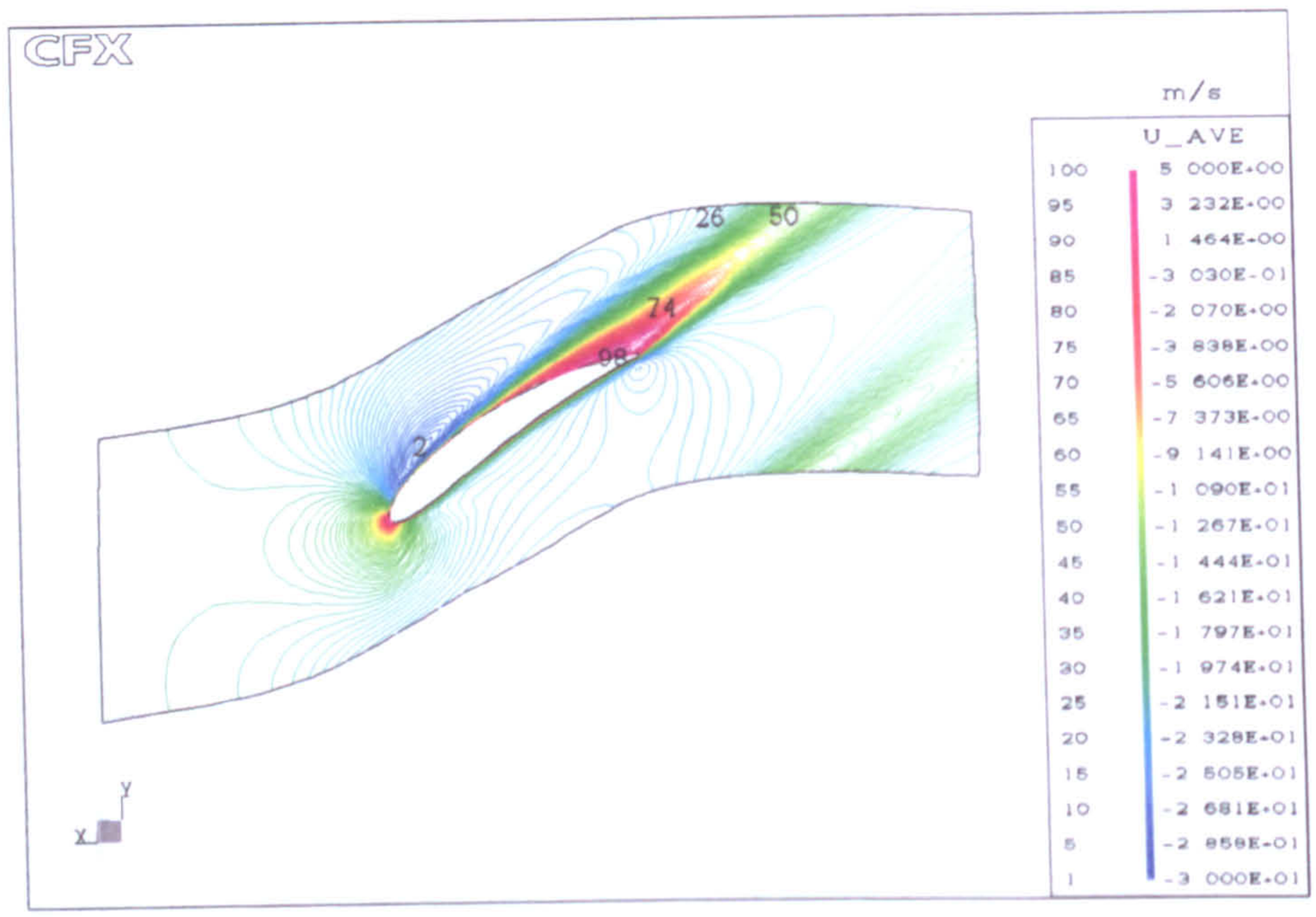

(a) At the blade mid-span

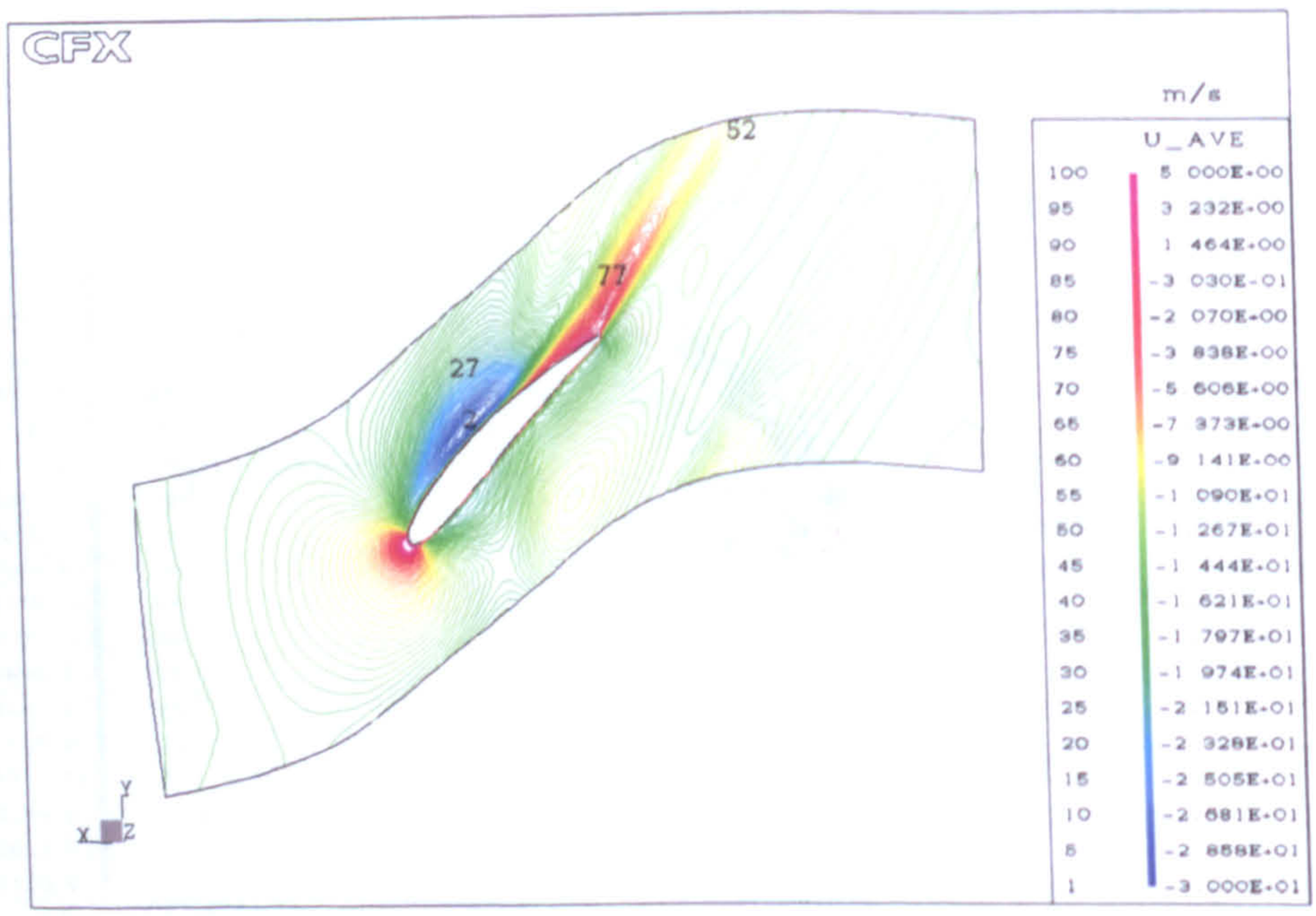

(b) Near the blade tip

Figure 9.14: Time-averaged unsteady result of the axial flow velocity

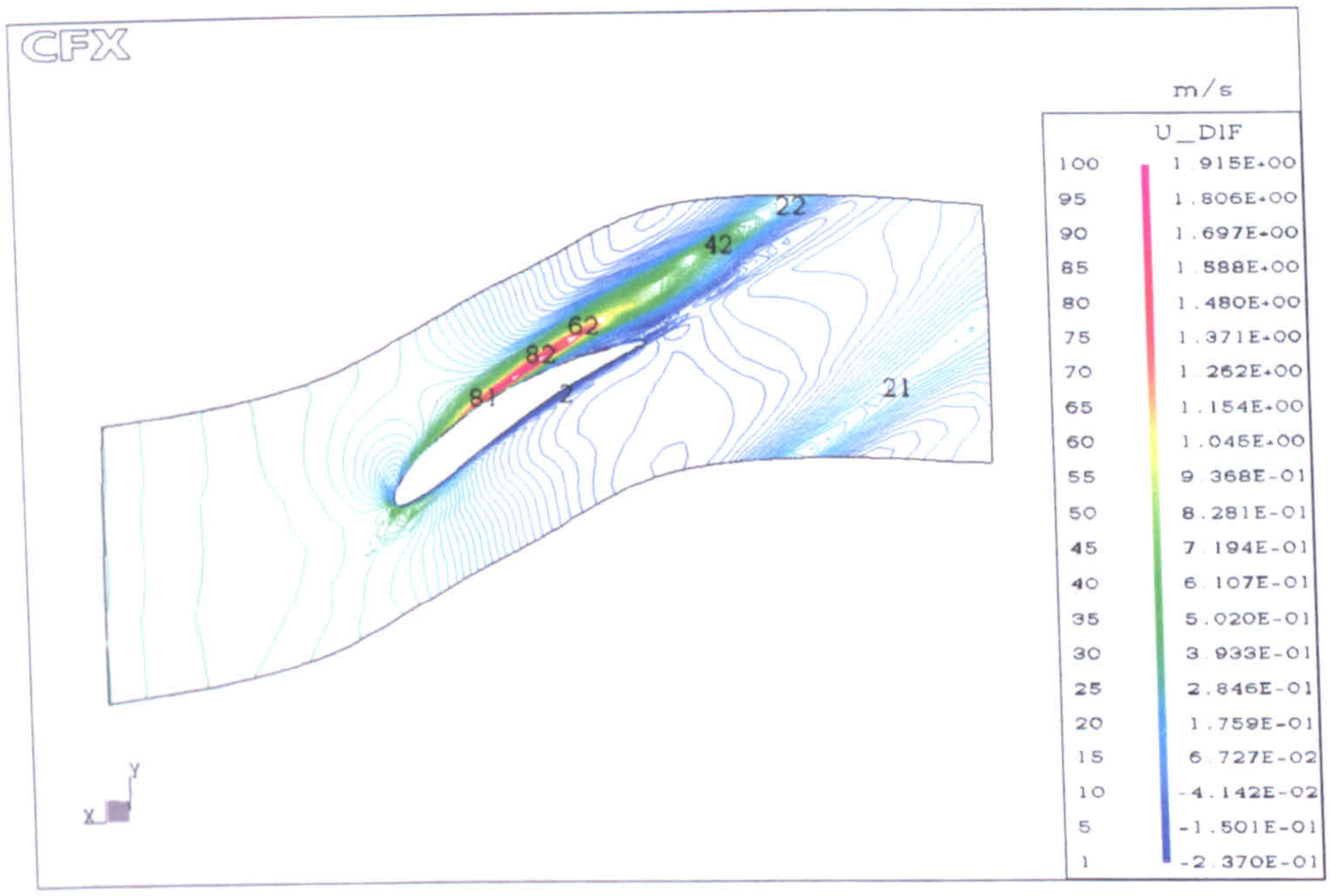

(a) At the blade mid-span

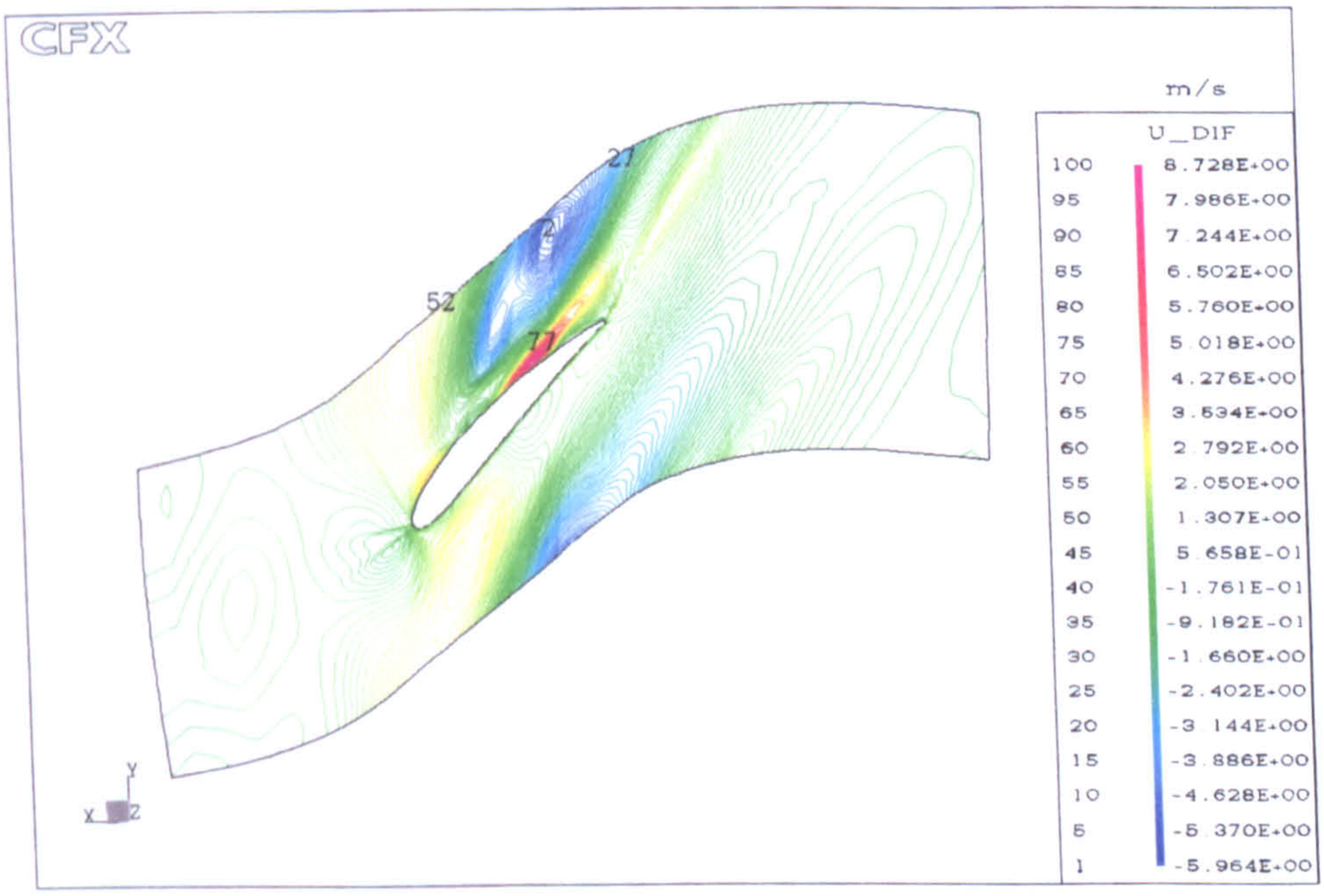

(b) Near the blade tip

Figure 9.15: The flow axial velocity difference between the two formulations

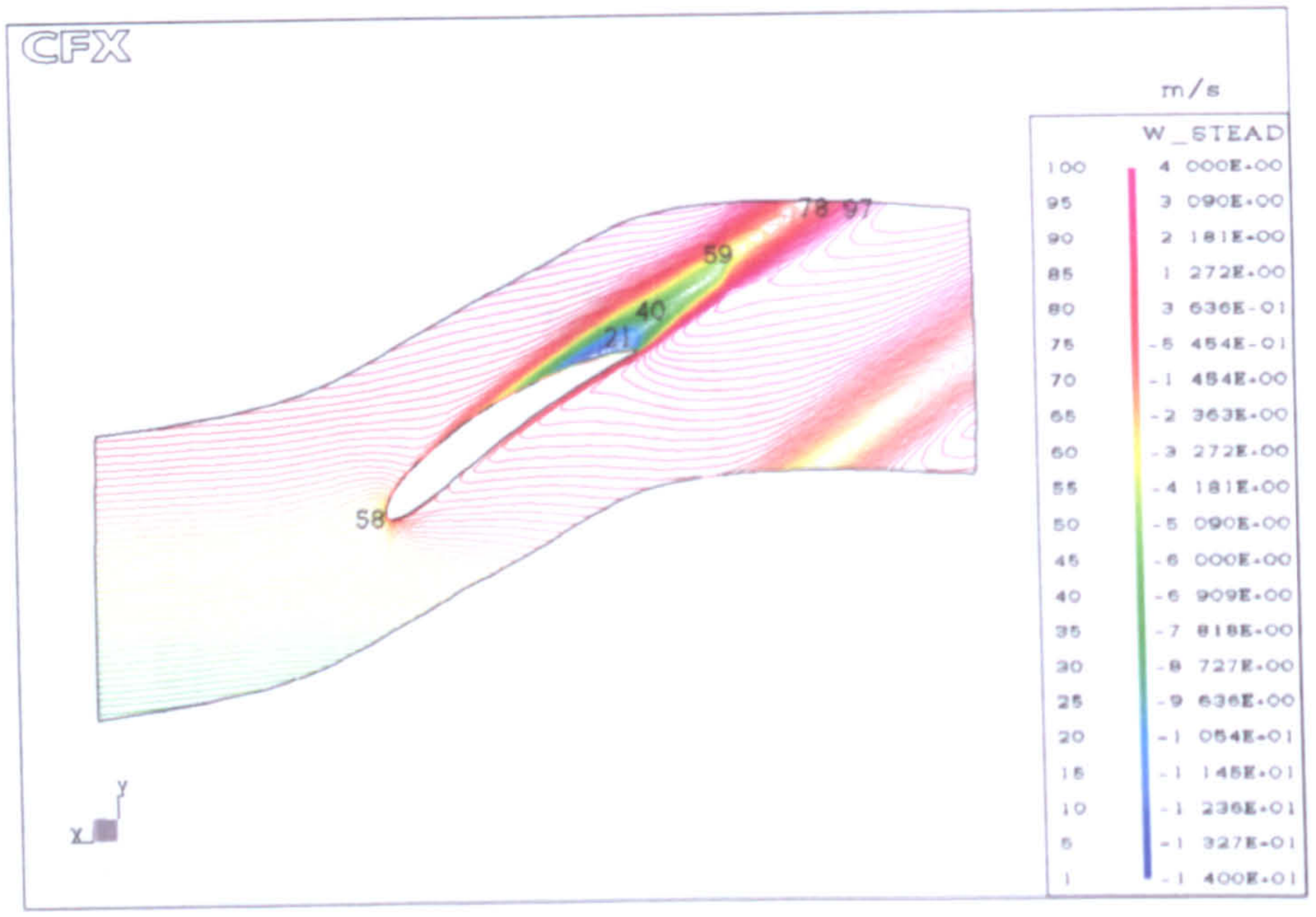

(a) At the blade mid-span

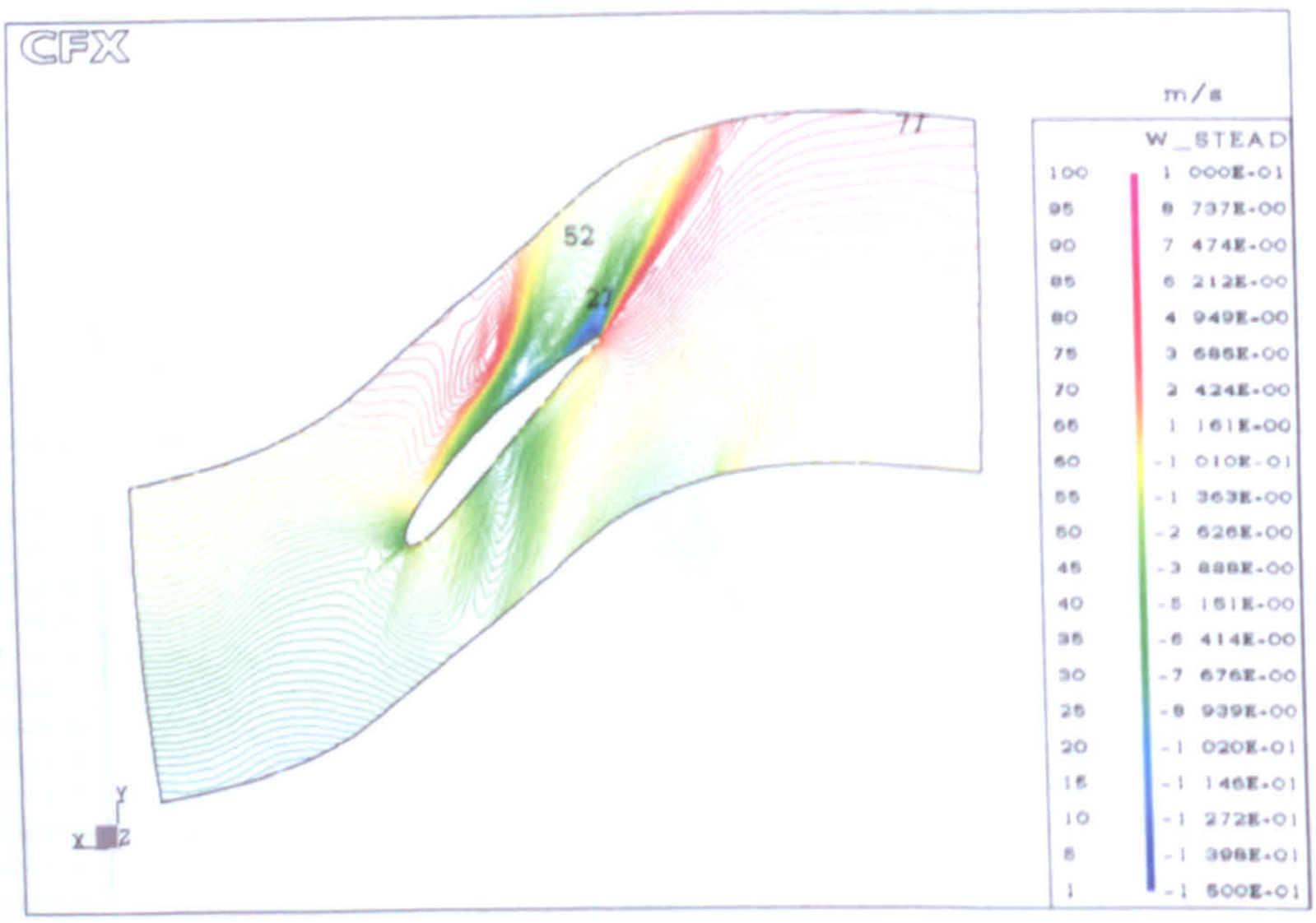

(b) Near the blade tip

Figure 9.16: Steady-state result of the tangential flow velocity

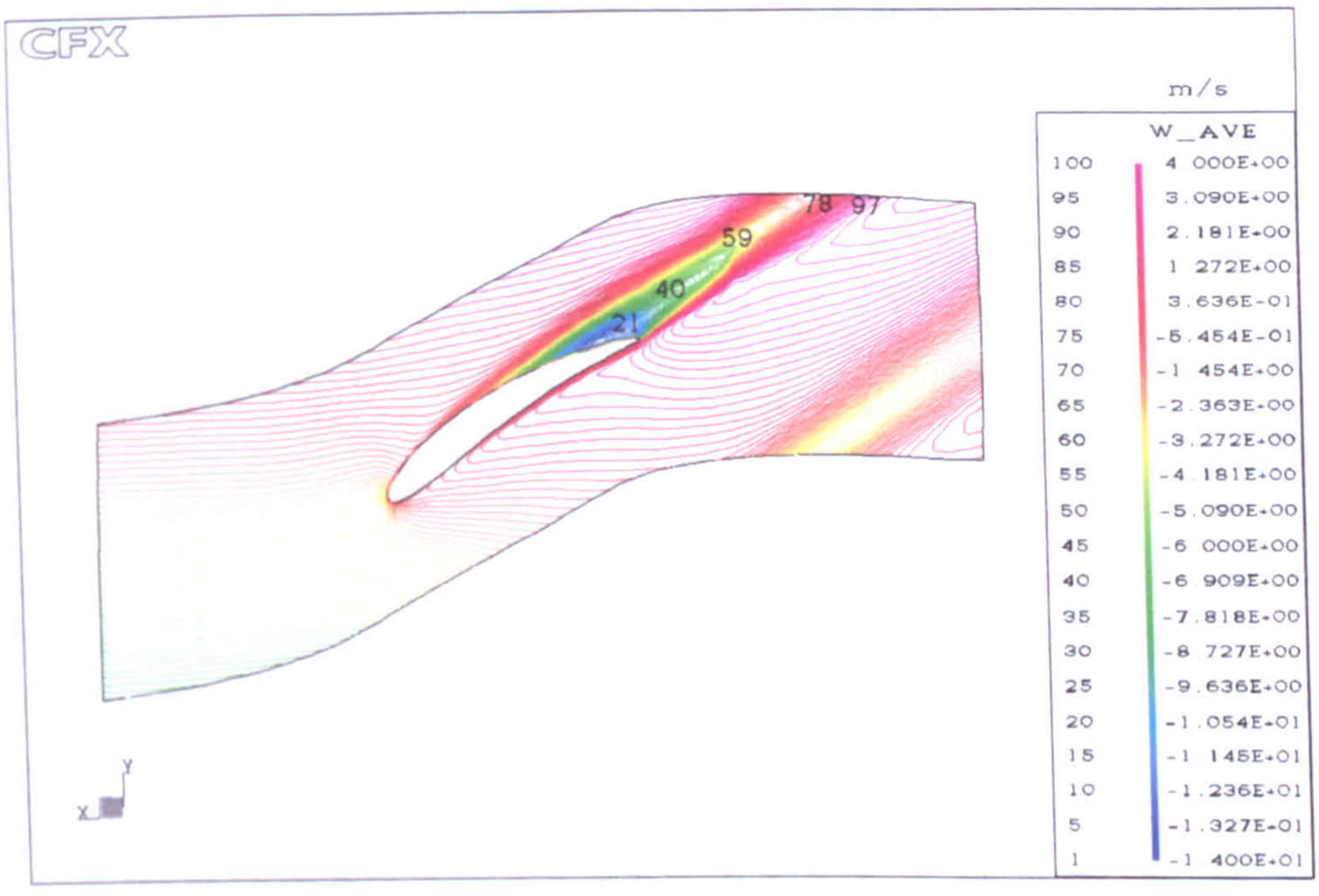

(a) At the blade mid-span

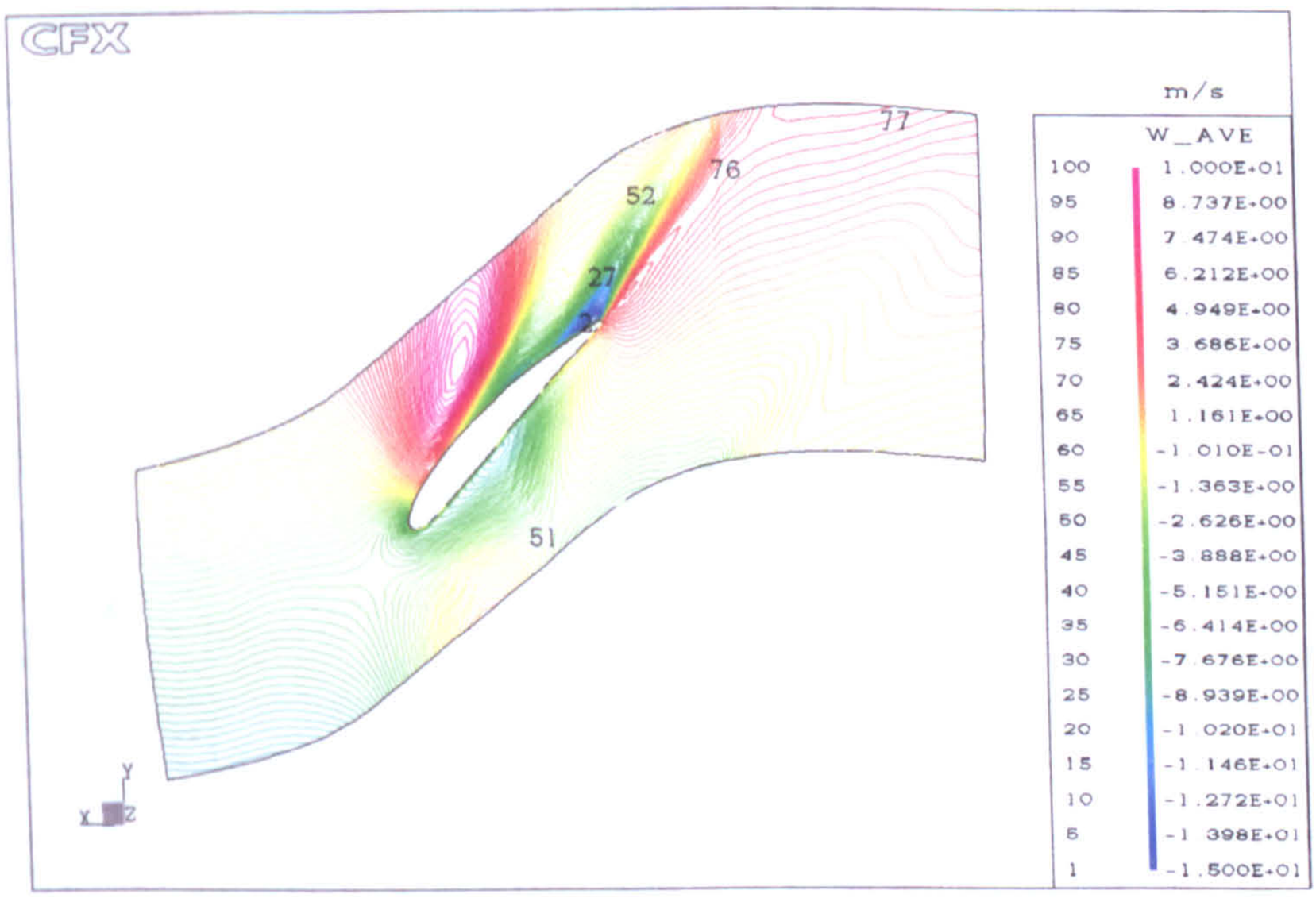

(b) Near the blade tip

Figure 9.17: Time-averaged unsteady result of the tangential flow velocity

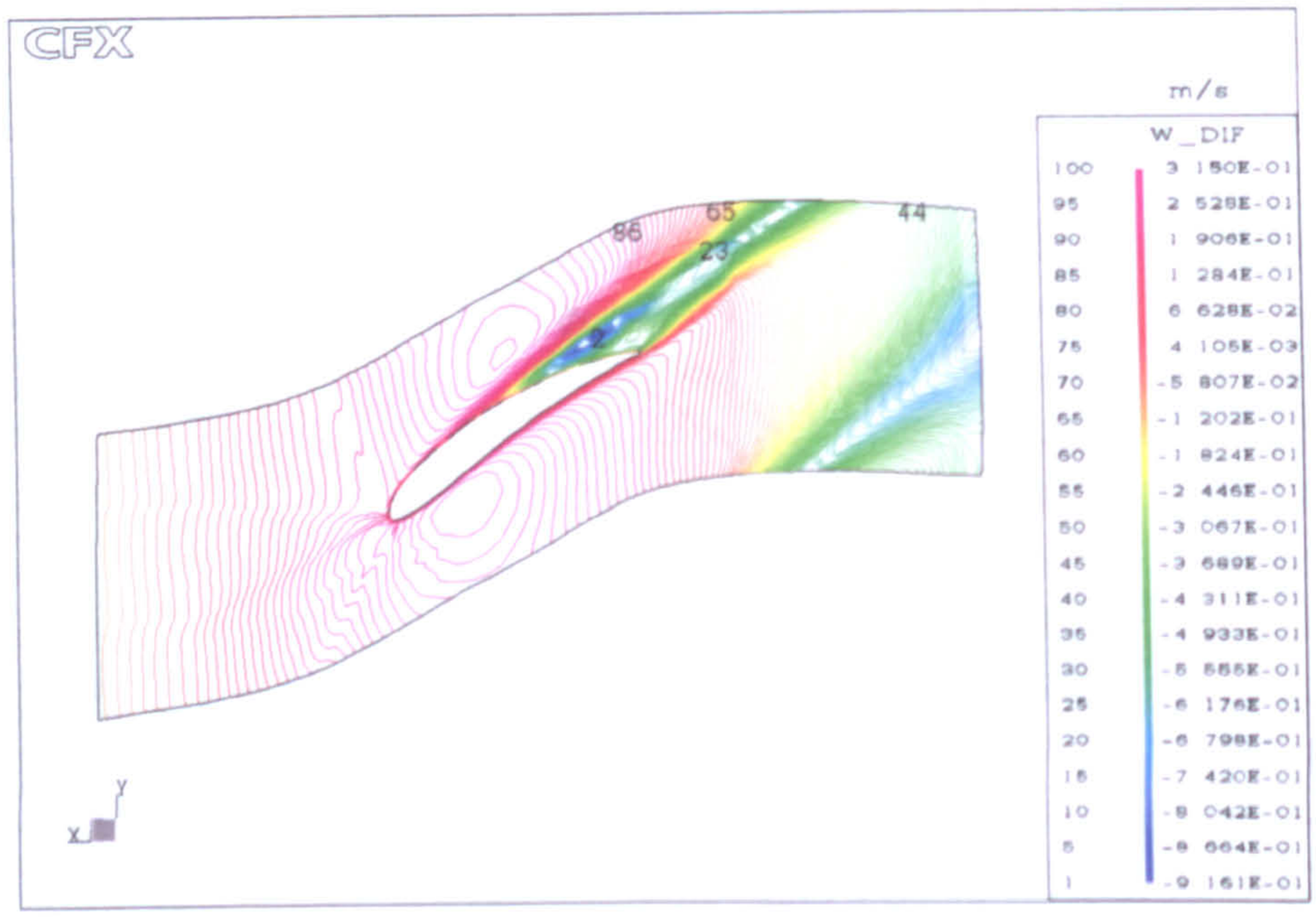

(a) At the blade mid-span

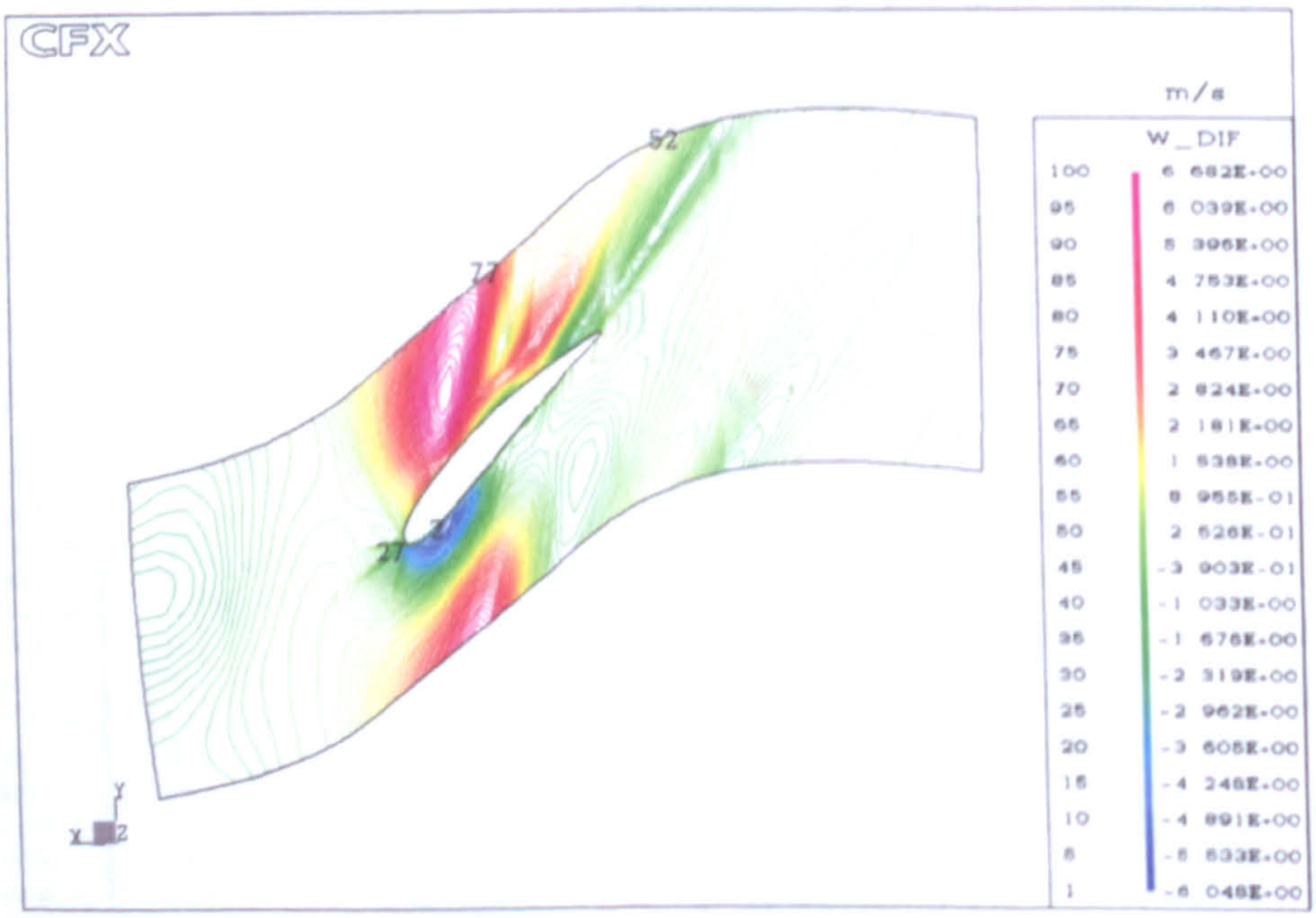

(b) Near the blade tip

Figure 9.18: The flow tangential velocity difference between the two formulations

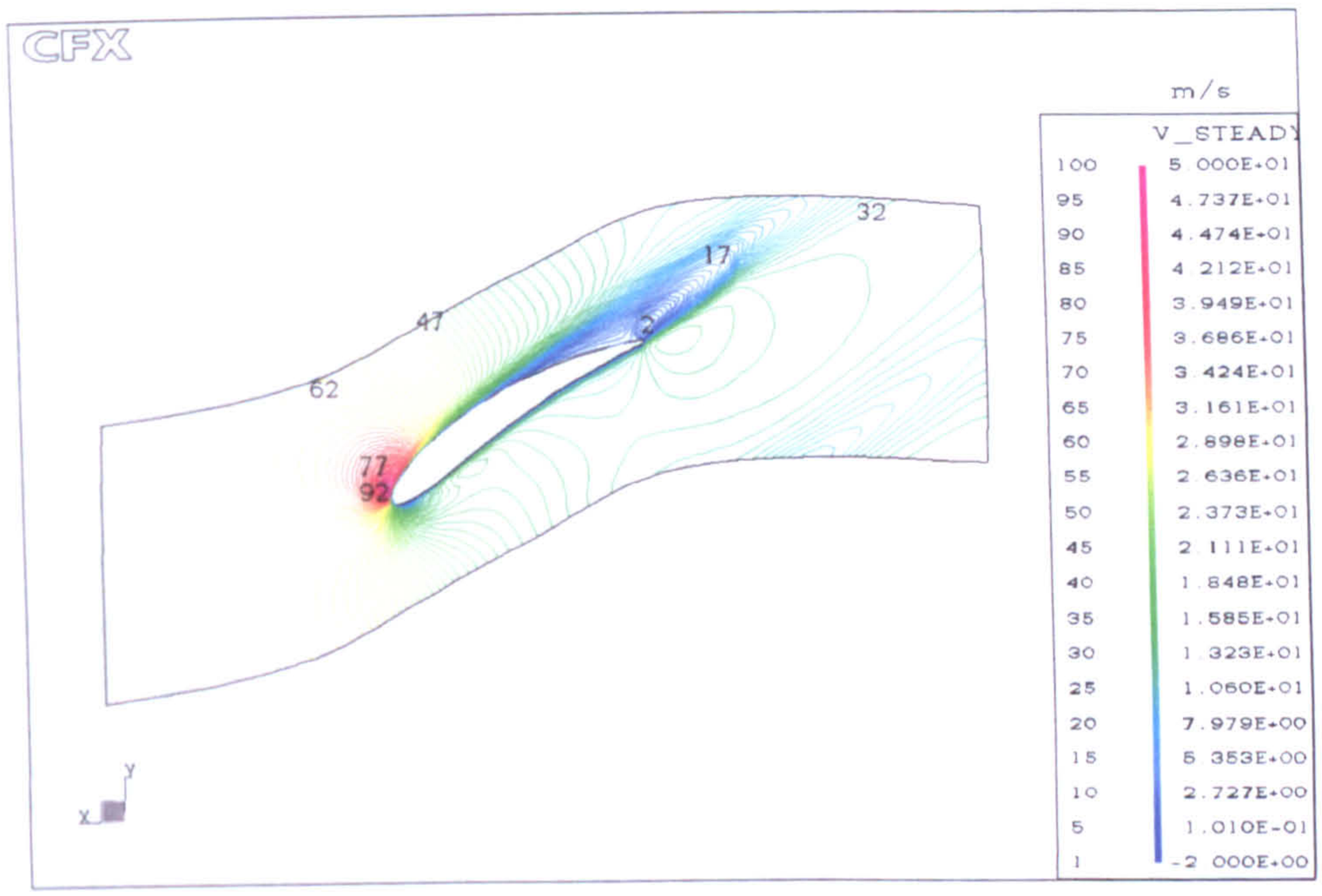

(a) At the blade mid-span

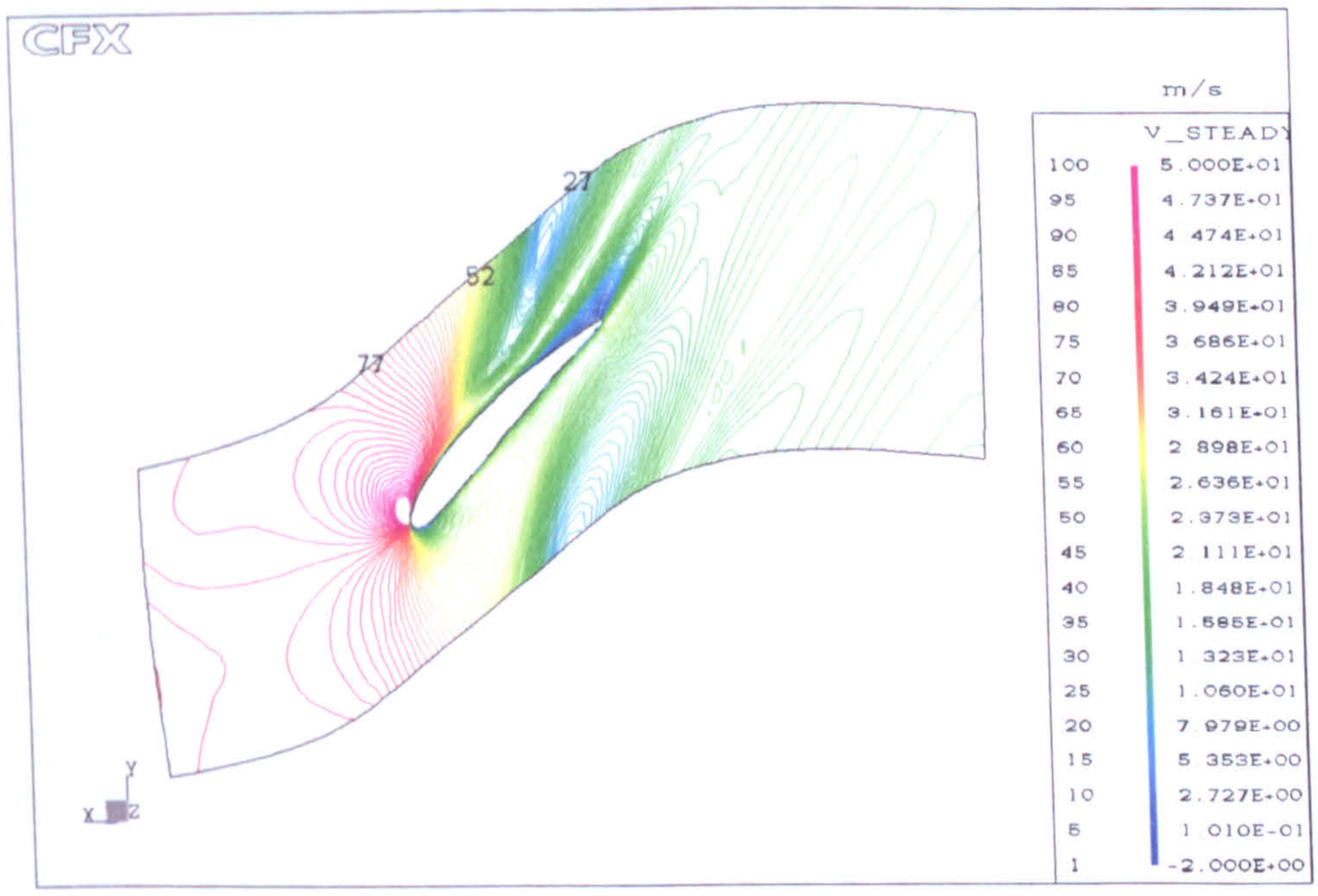

(b) Near the blade tip

Figure 9.19: Steady-state result of the radial flow velocity

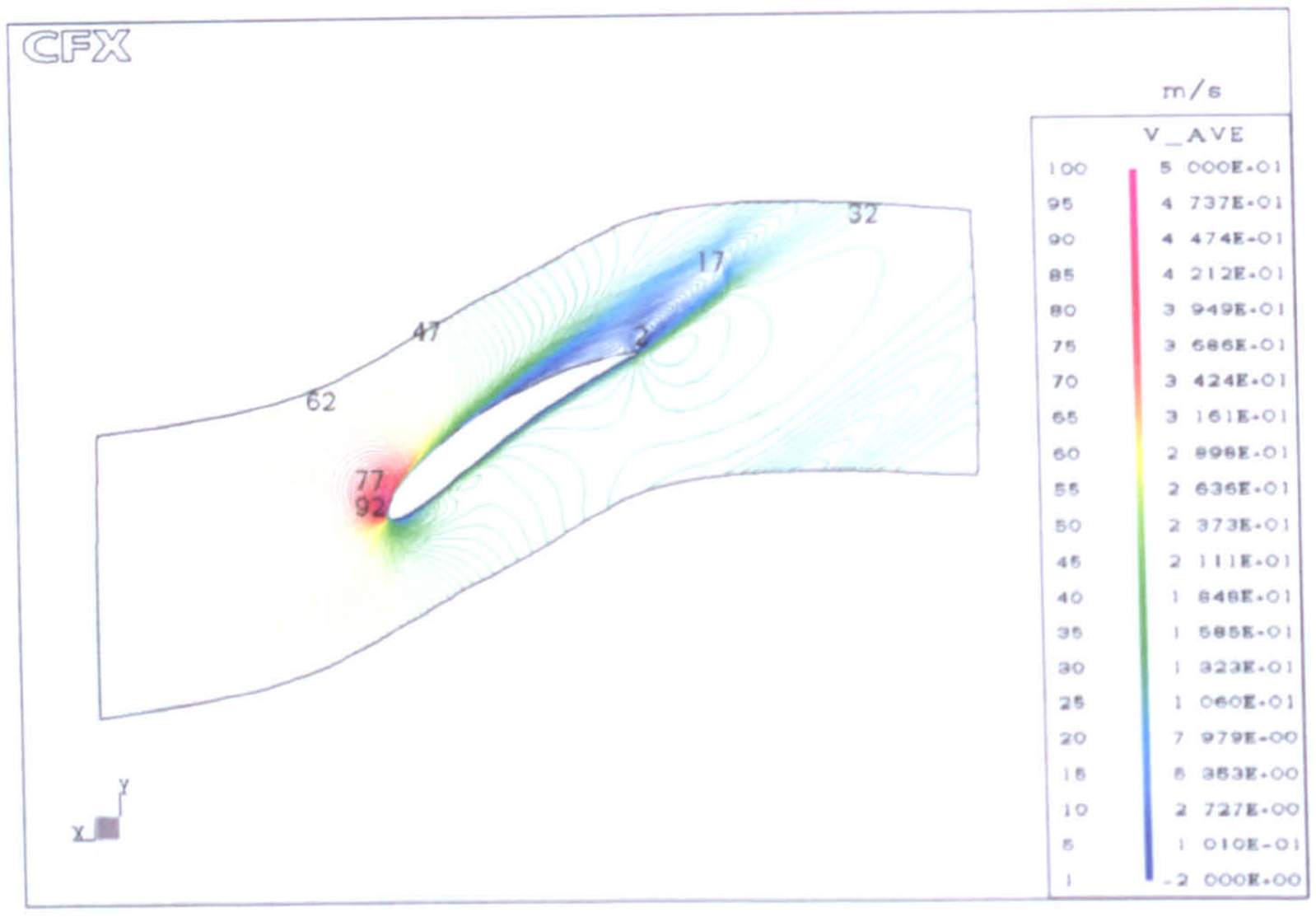

(a) At the blade mid-span

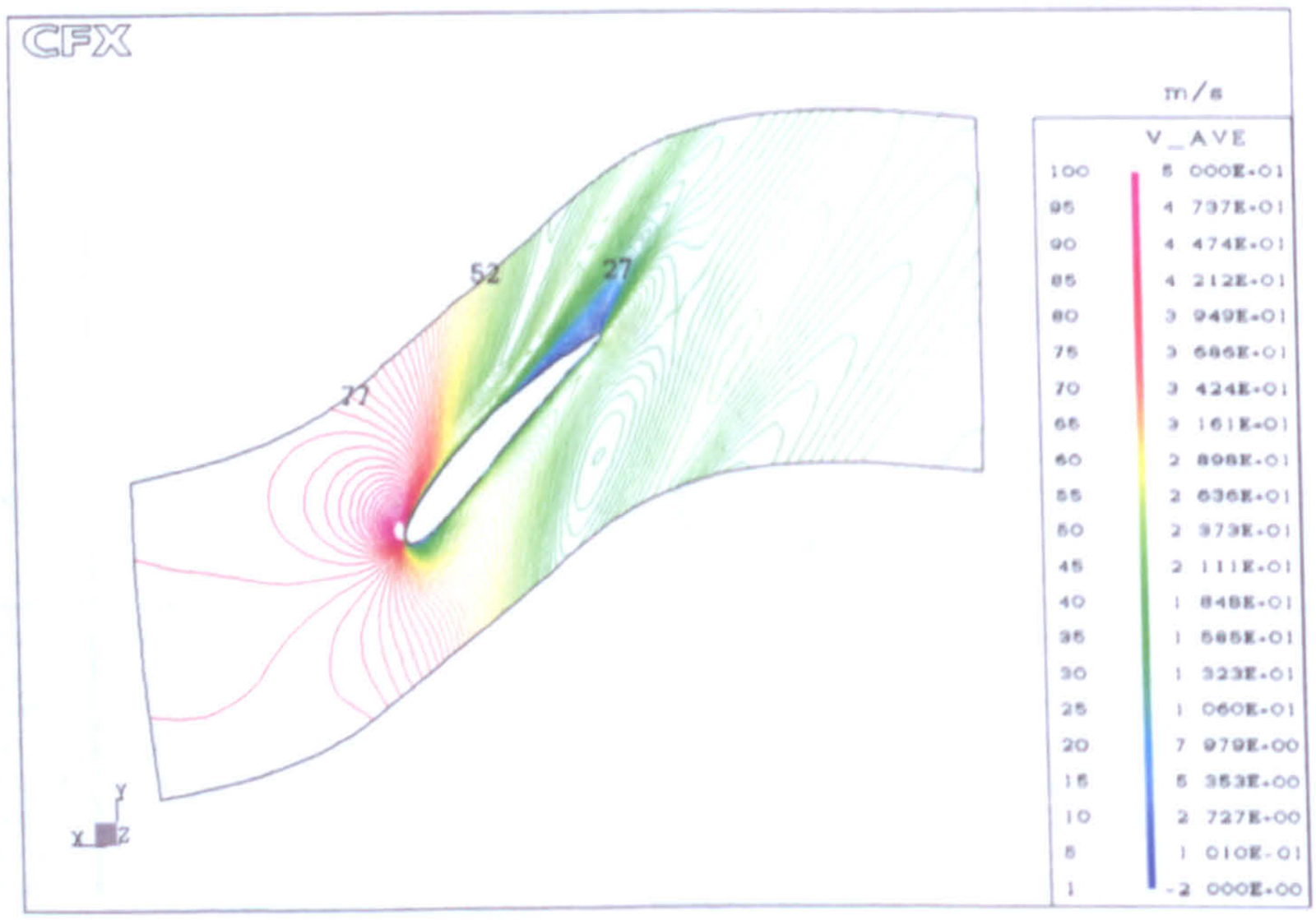

(b) Near the blade tip

Figure 9.20: Time-averaged unsteady result of the radial flow velocity

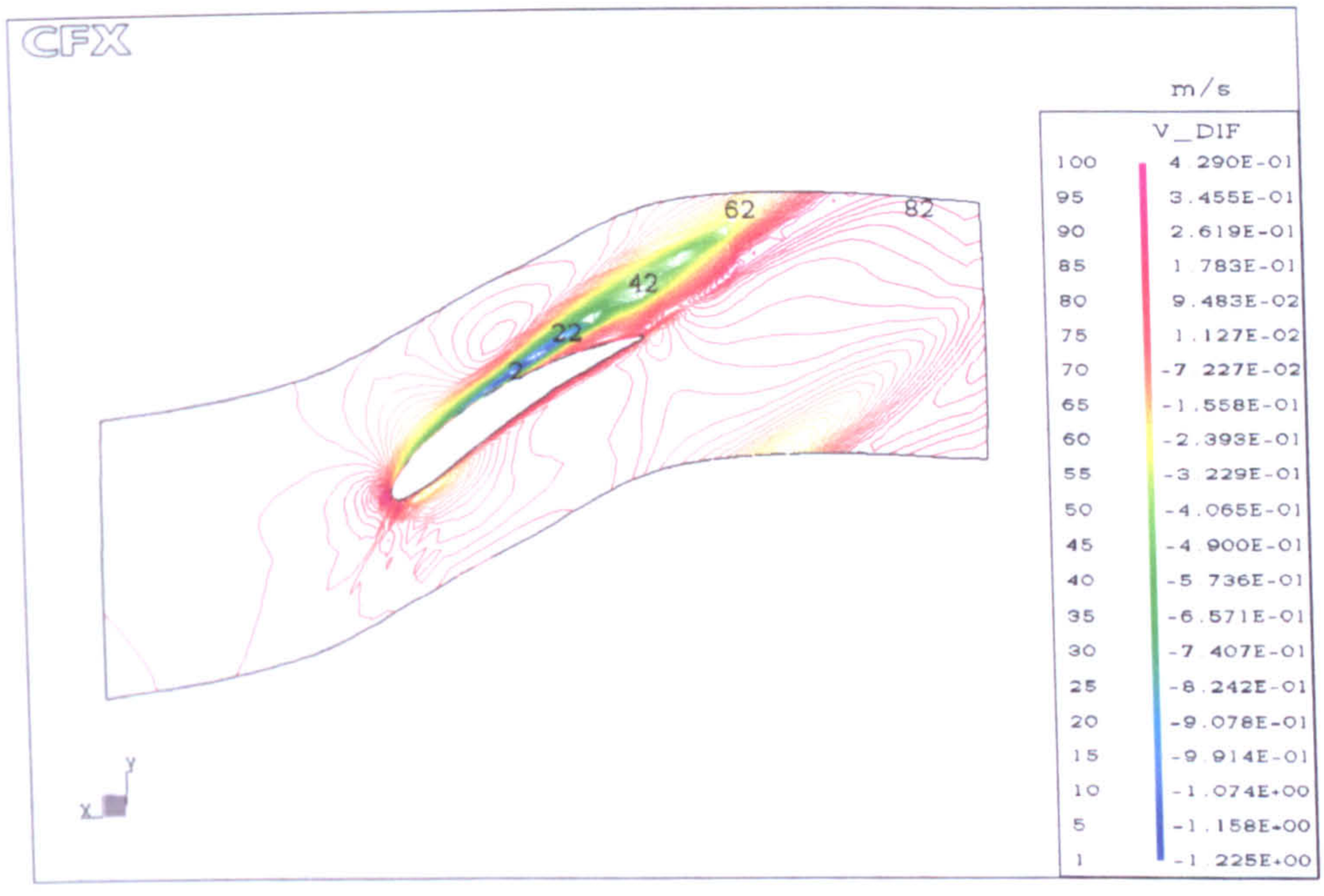

(a) At the blade mid-span

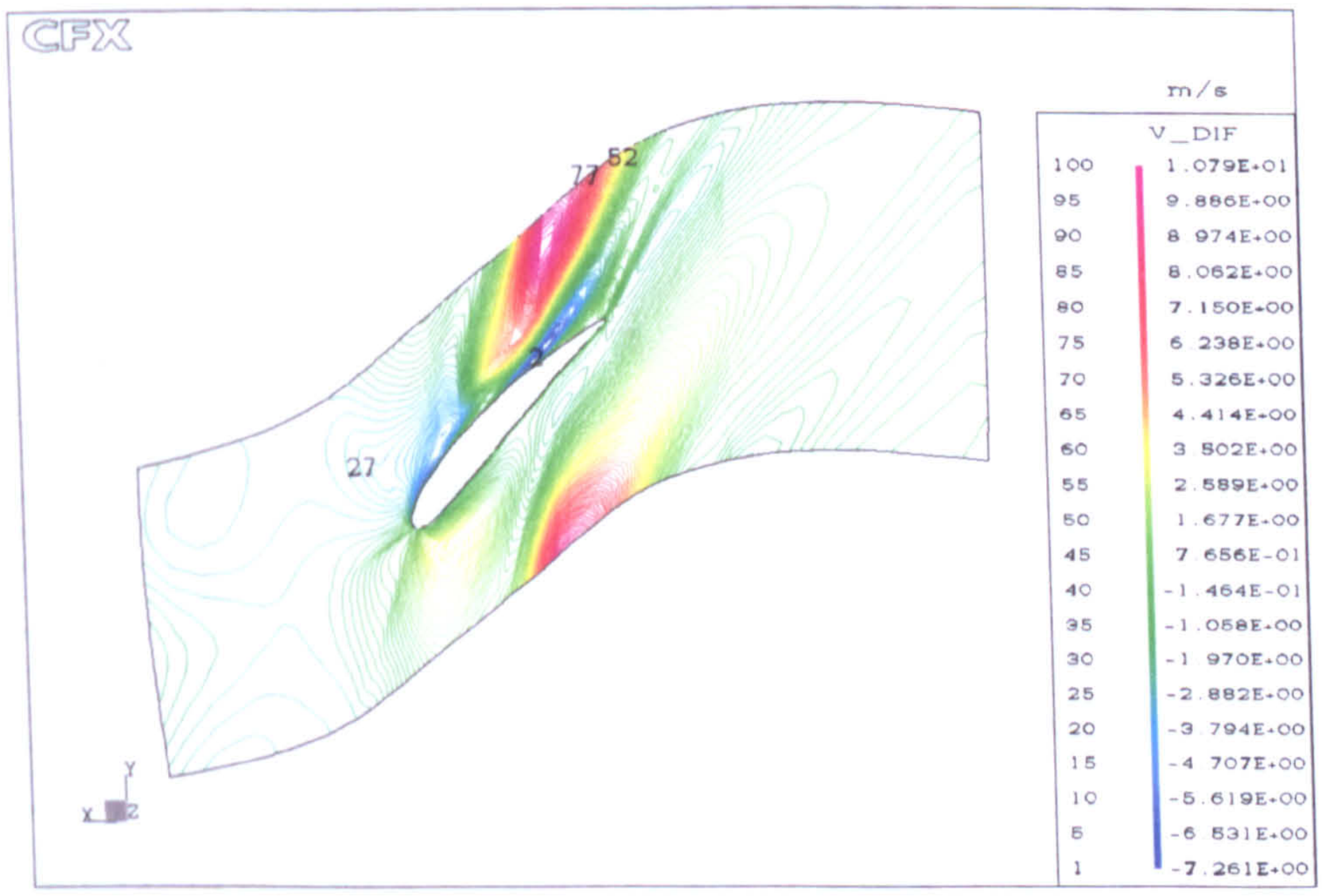

(b) Near the blade tip

Figure 9.21: The flow radial velocity difference between the two formulations

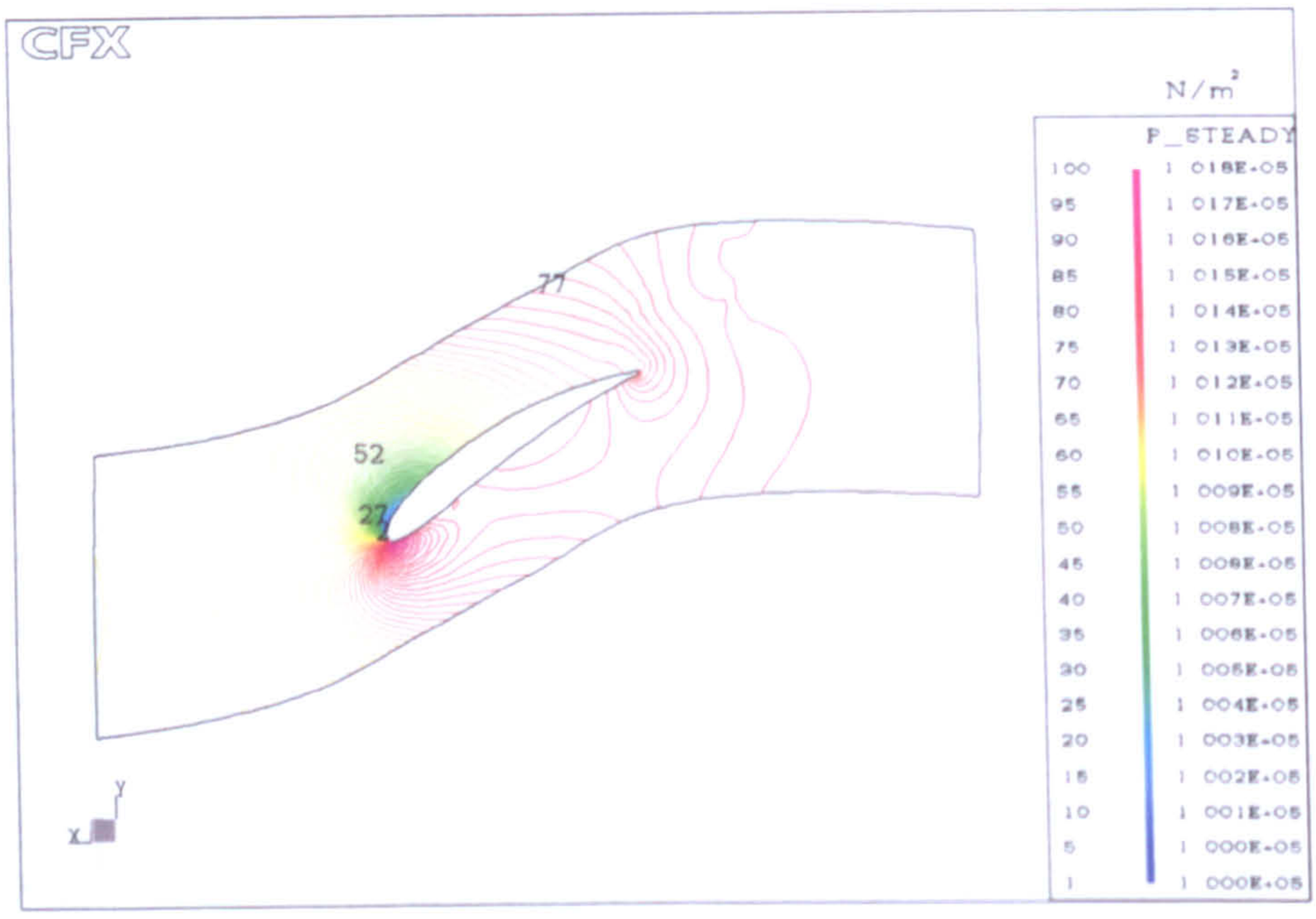

(a) At the blade mid-span

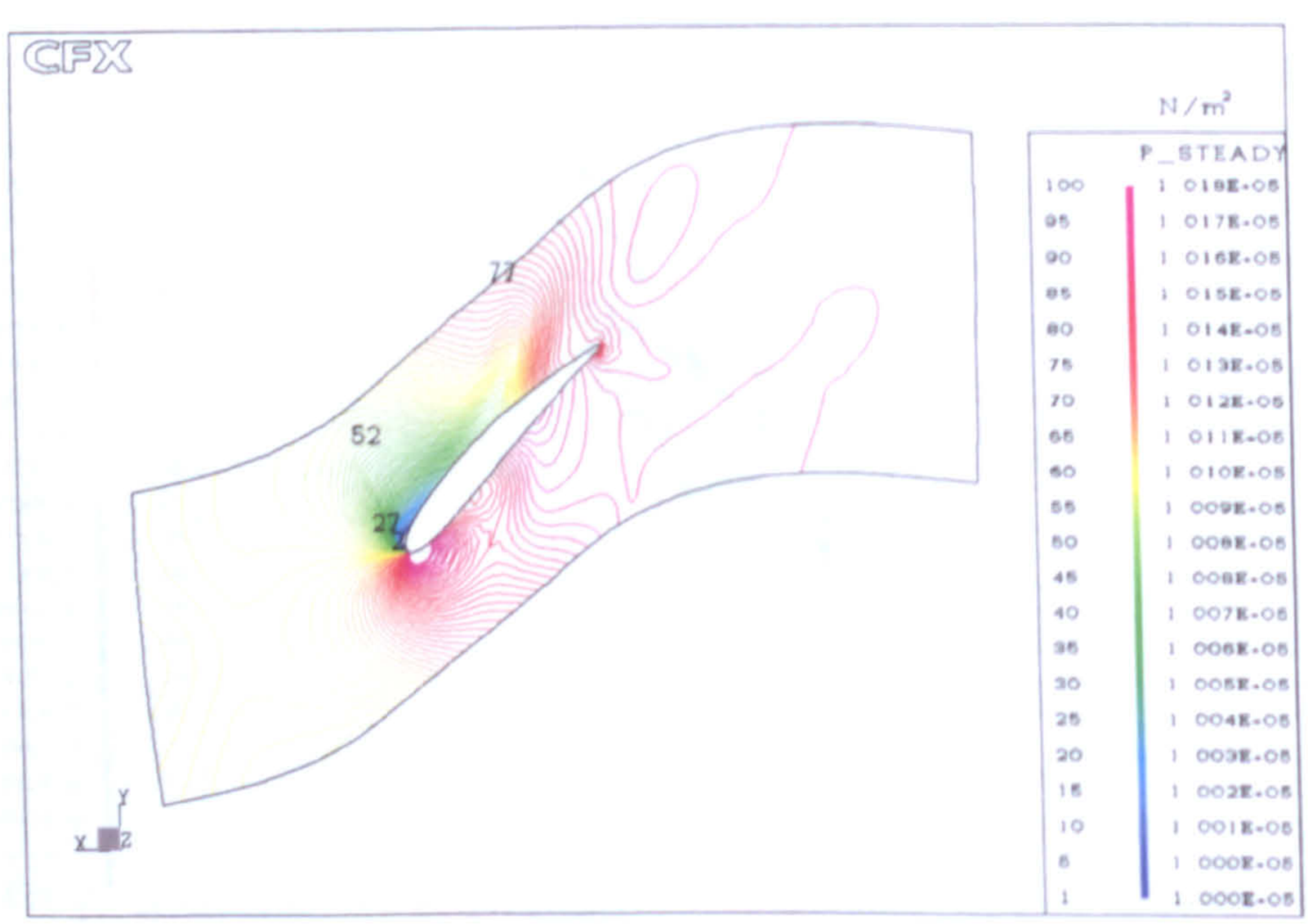

(b) Near the blade tip

Figure 9.22: Steady-state result of the static pressure

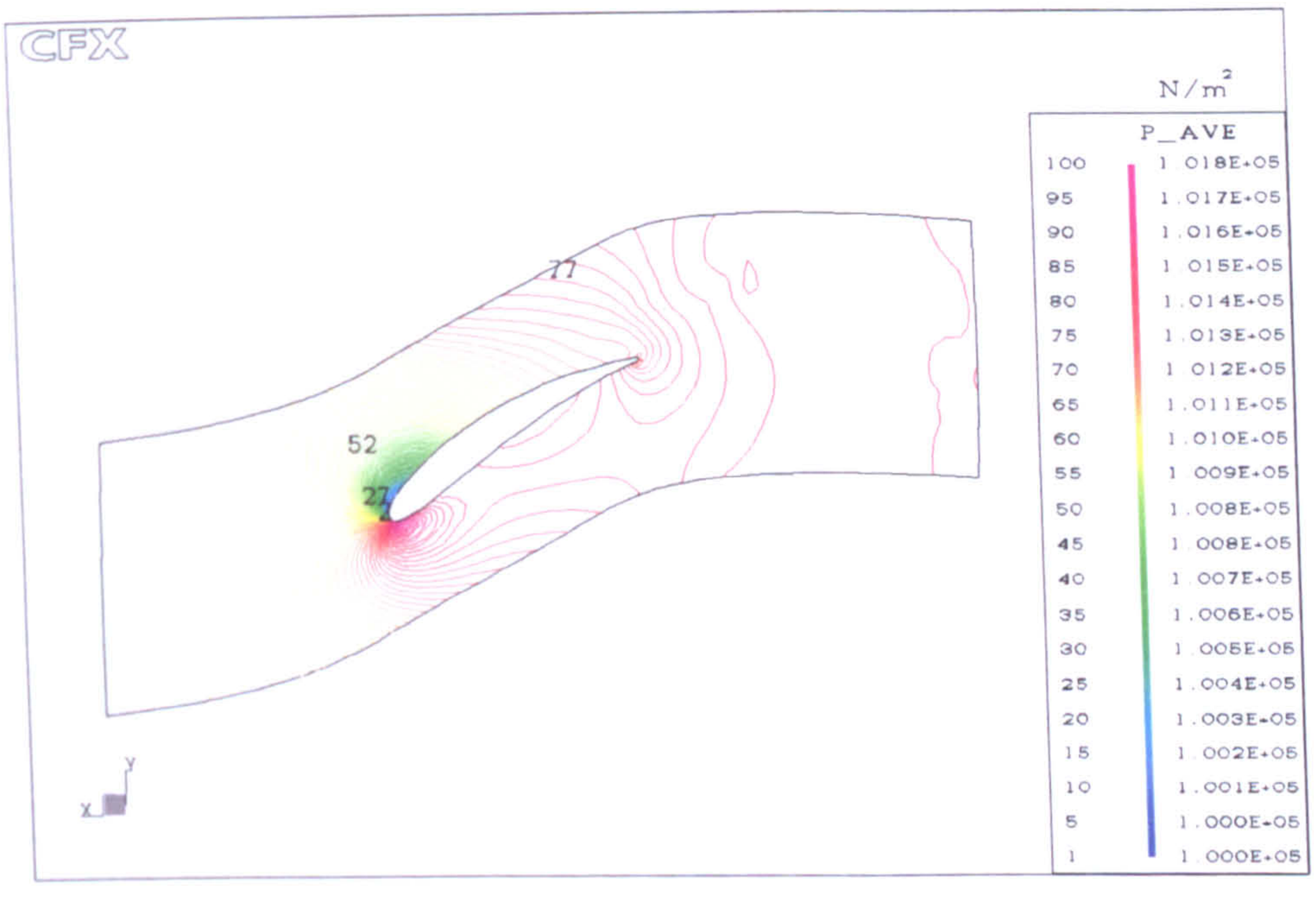

(a) At the blade mid-span

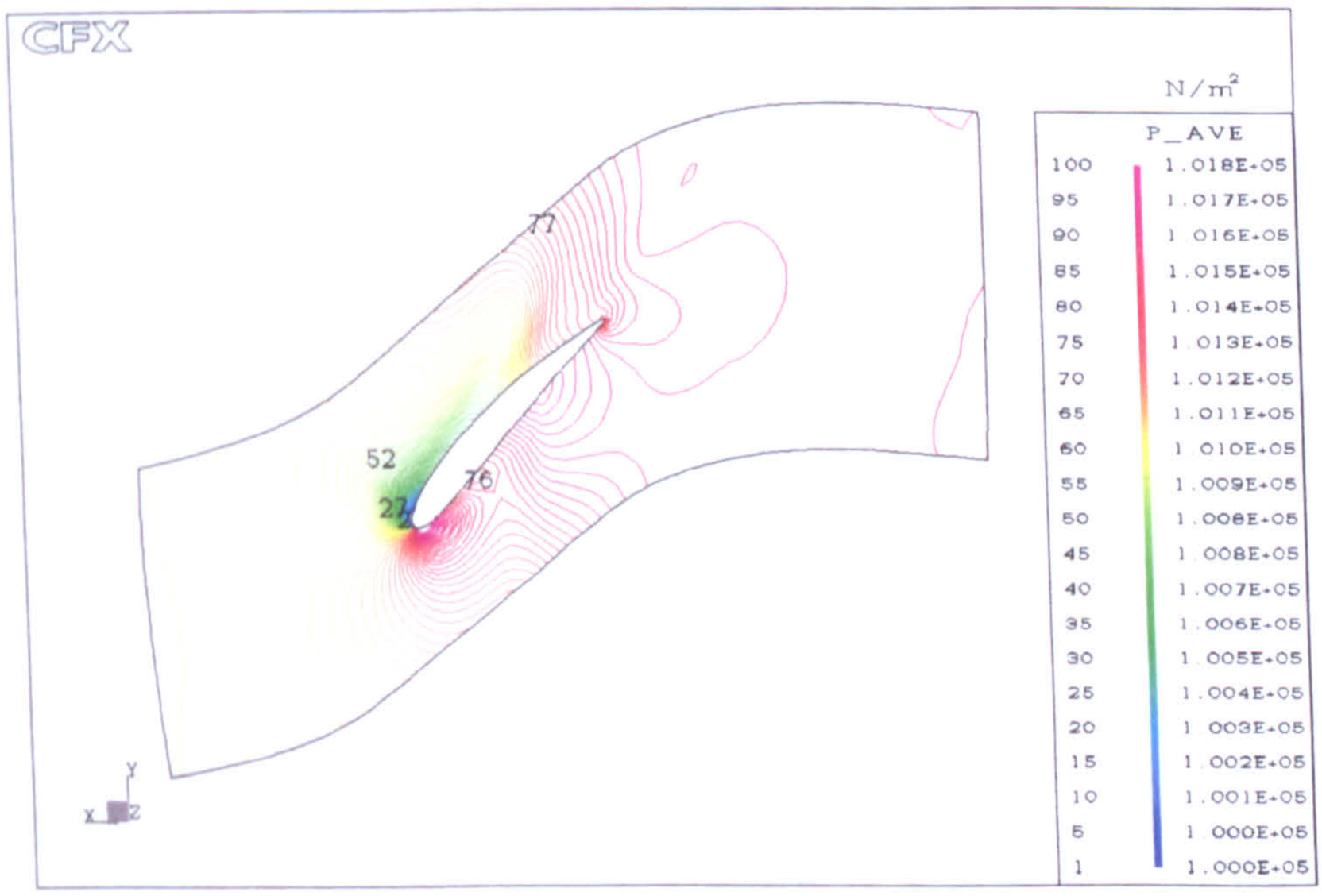

(b) Near the blade tip

Figure 9.23: Time-averaged unsteady result of the static pressure

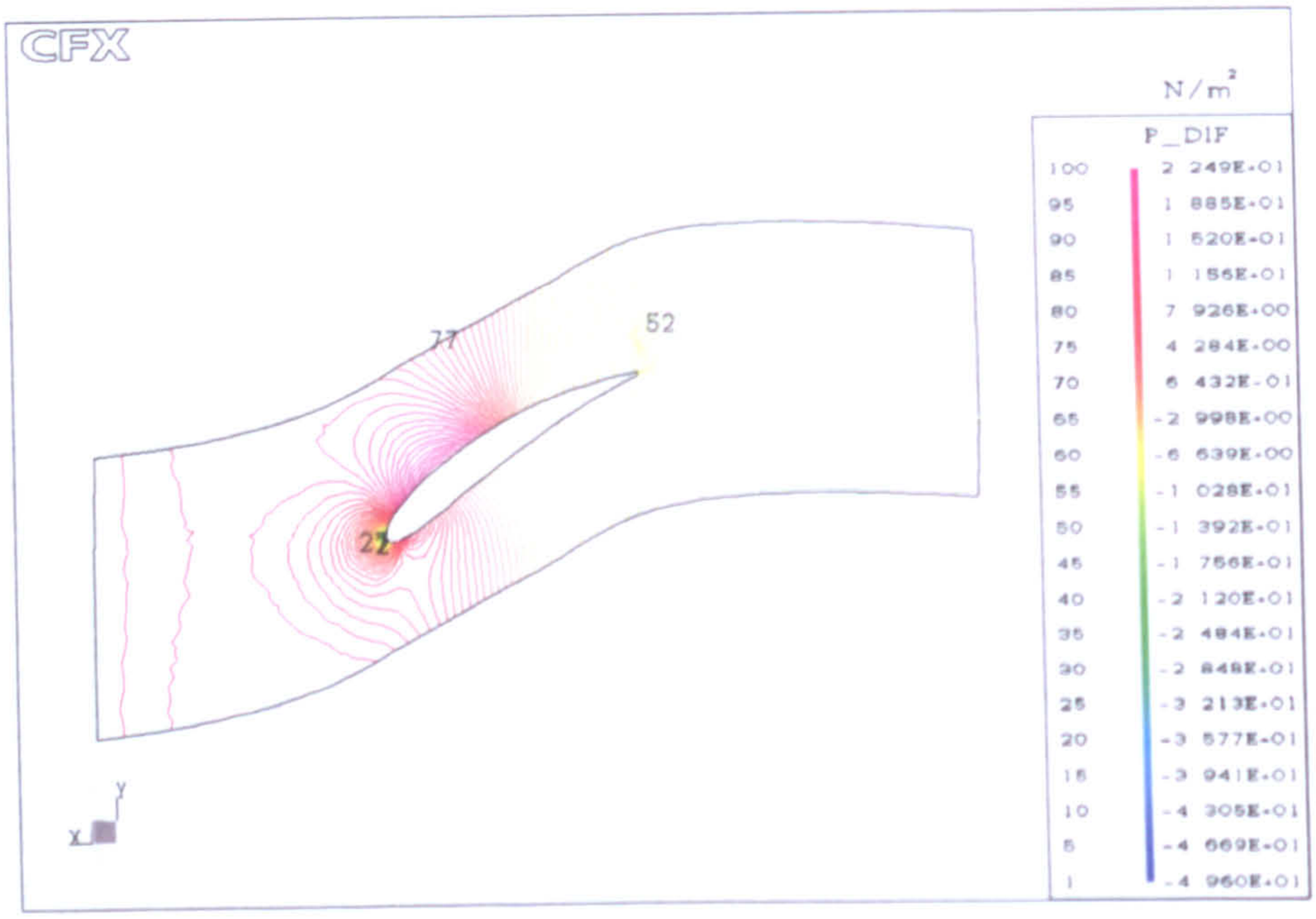

(a) At the blade mid-span

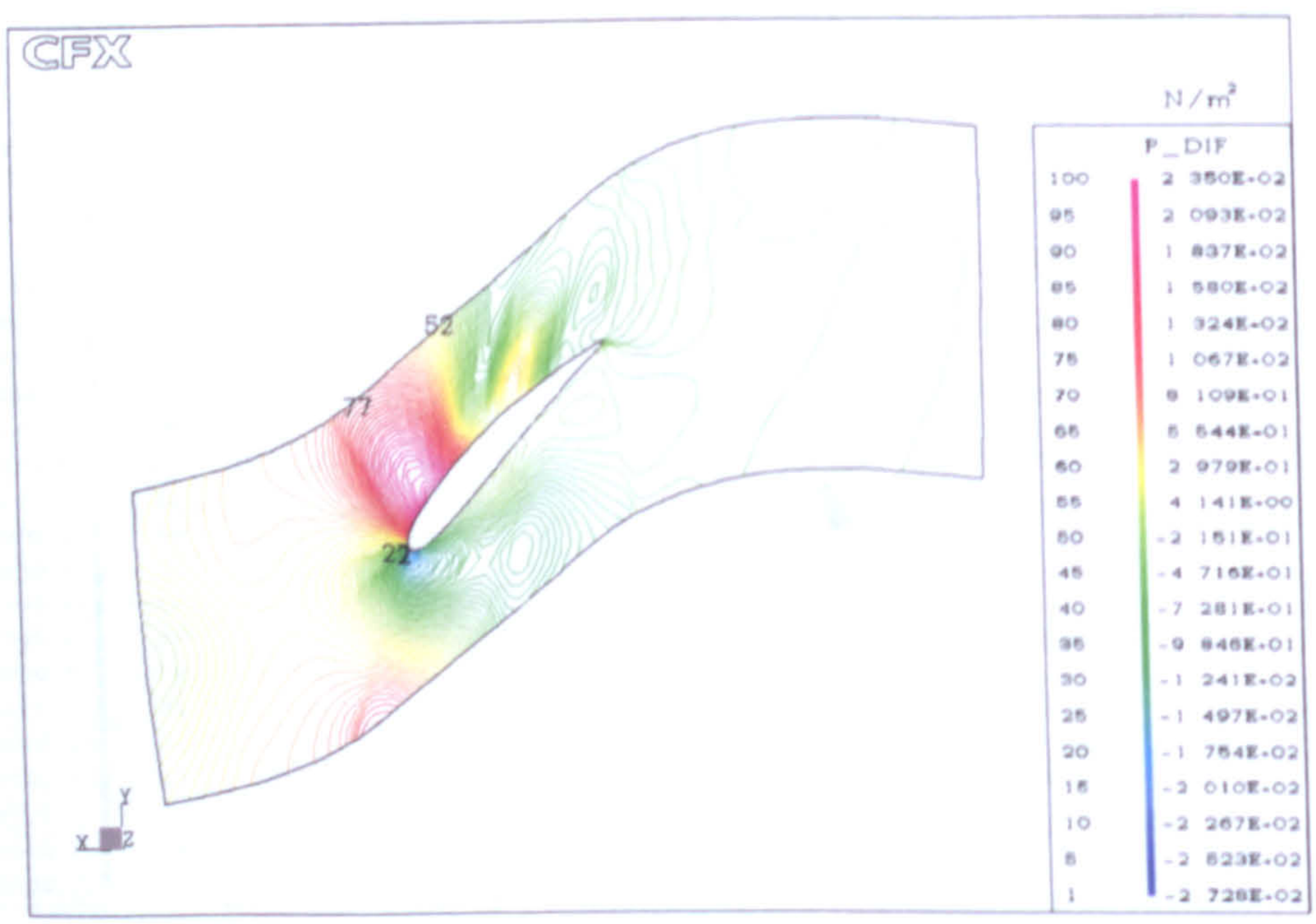

(b) Near the blade tip

Figure 9.24: The static pressure difference between the two formulations

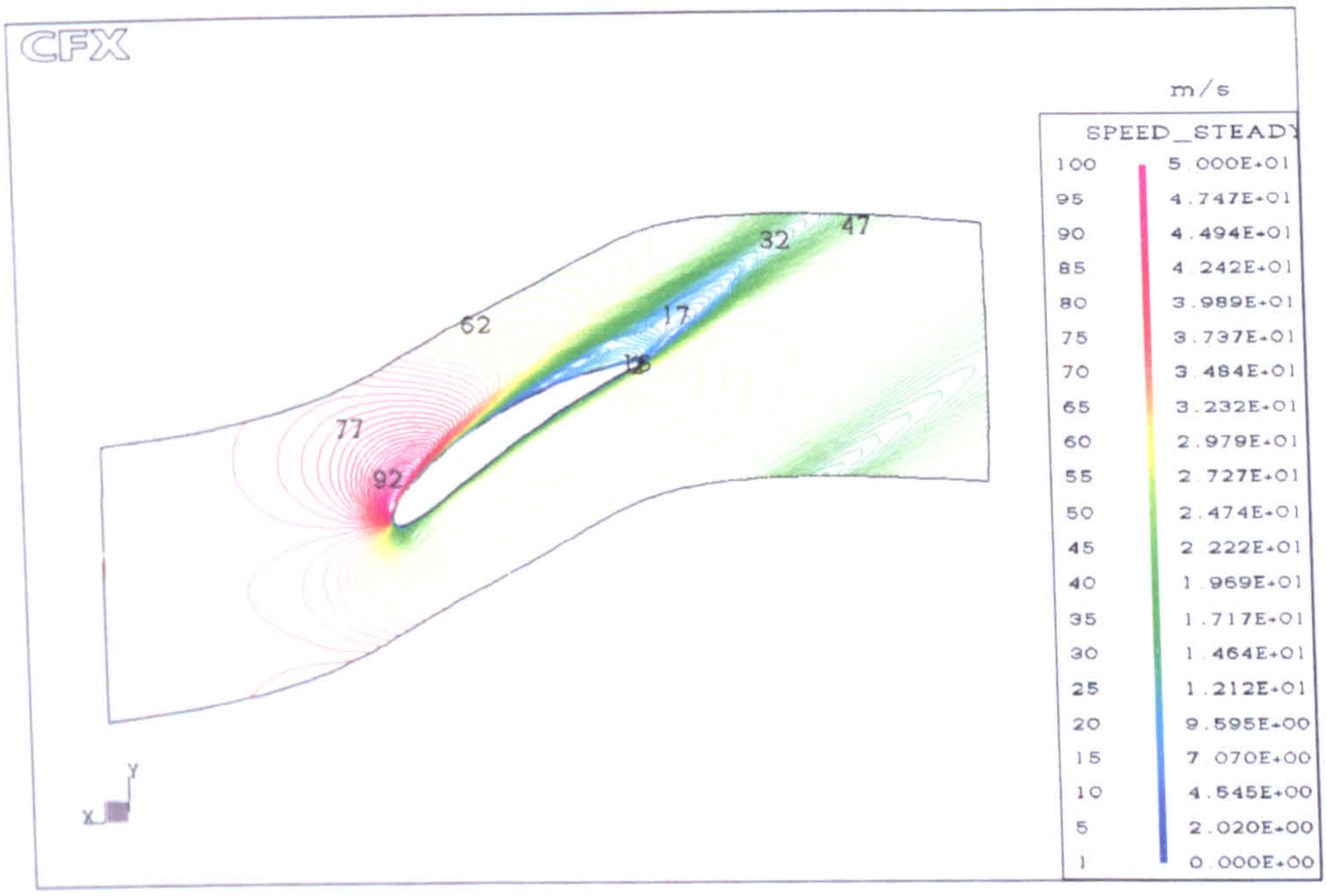

(a) At the blade mid-span

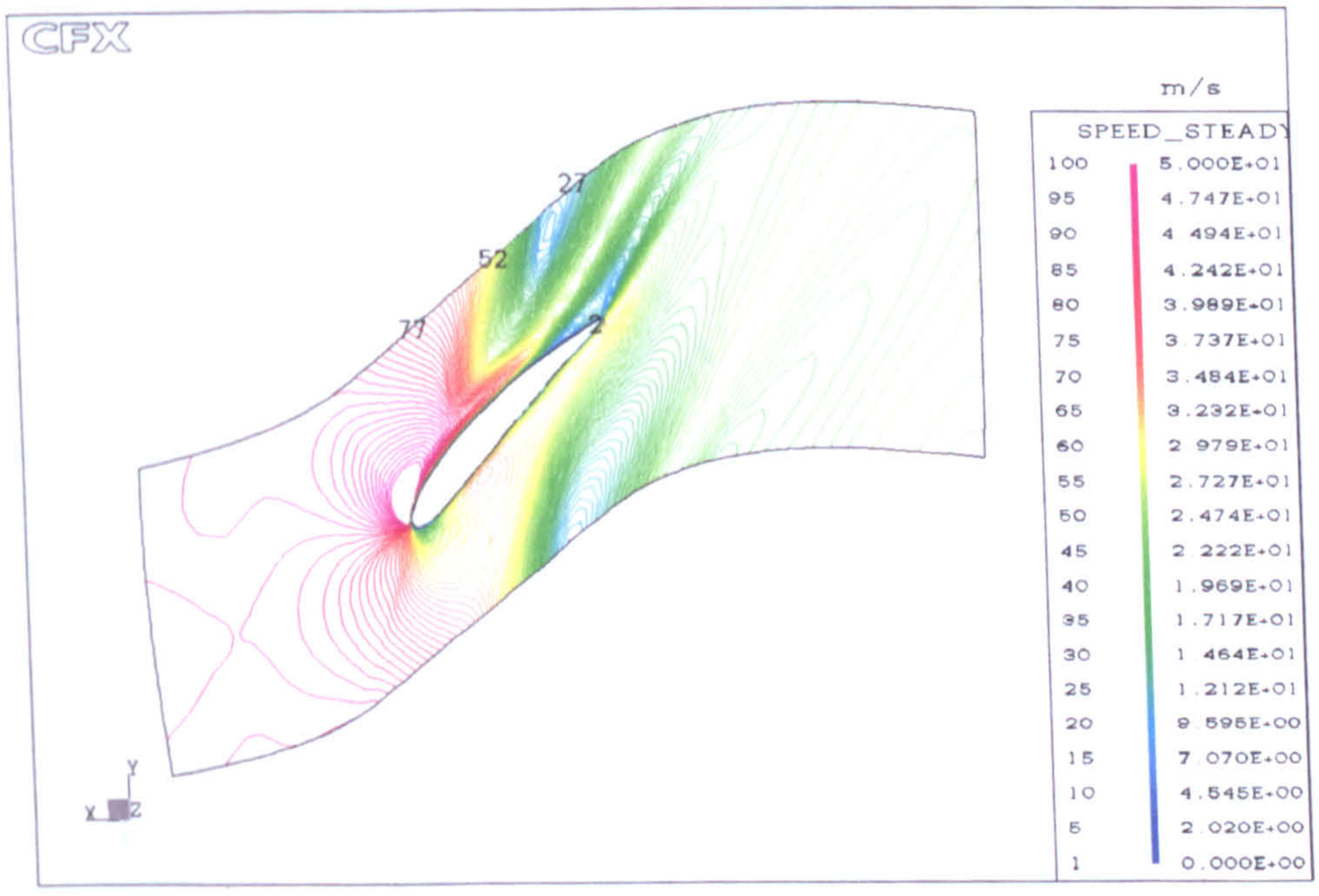

(b) Near the blade tip

Figure 9.25: Steady-state result of the velocity magnitude

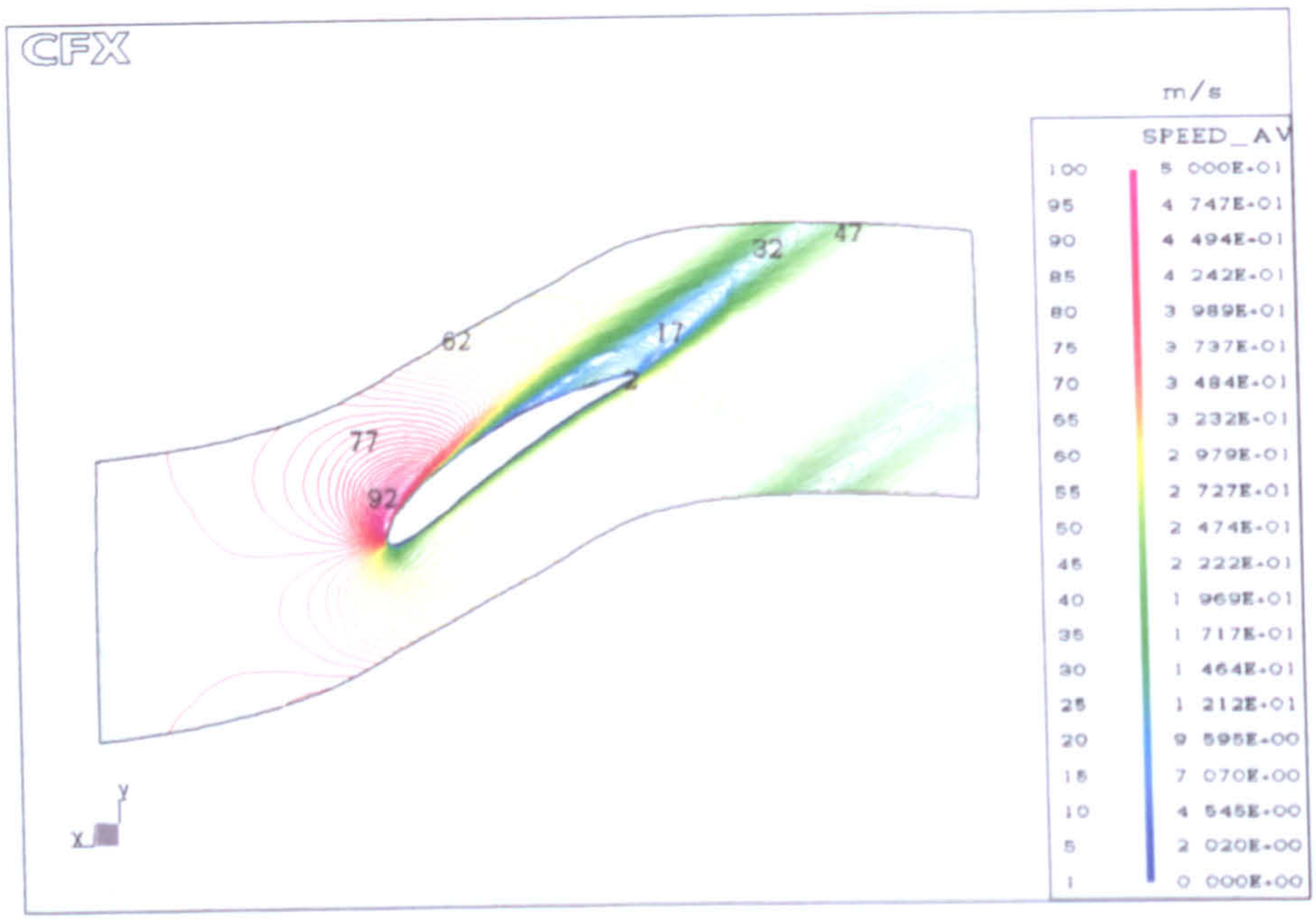

(a) At the blade mid-span

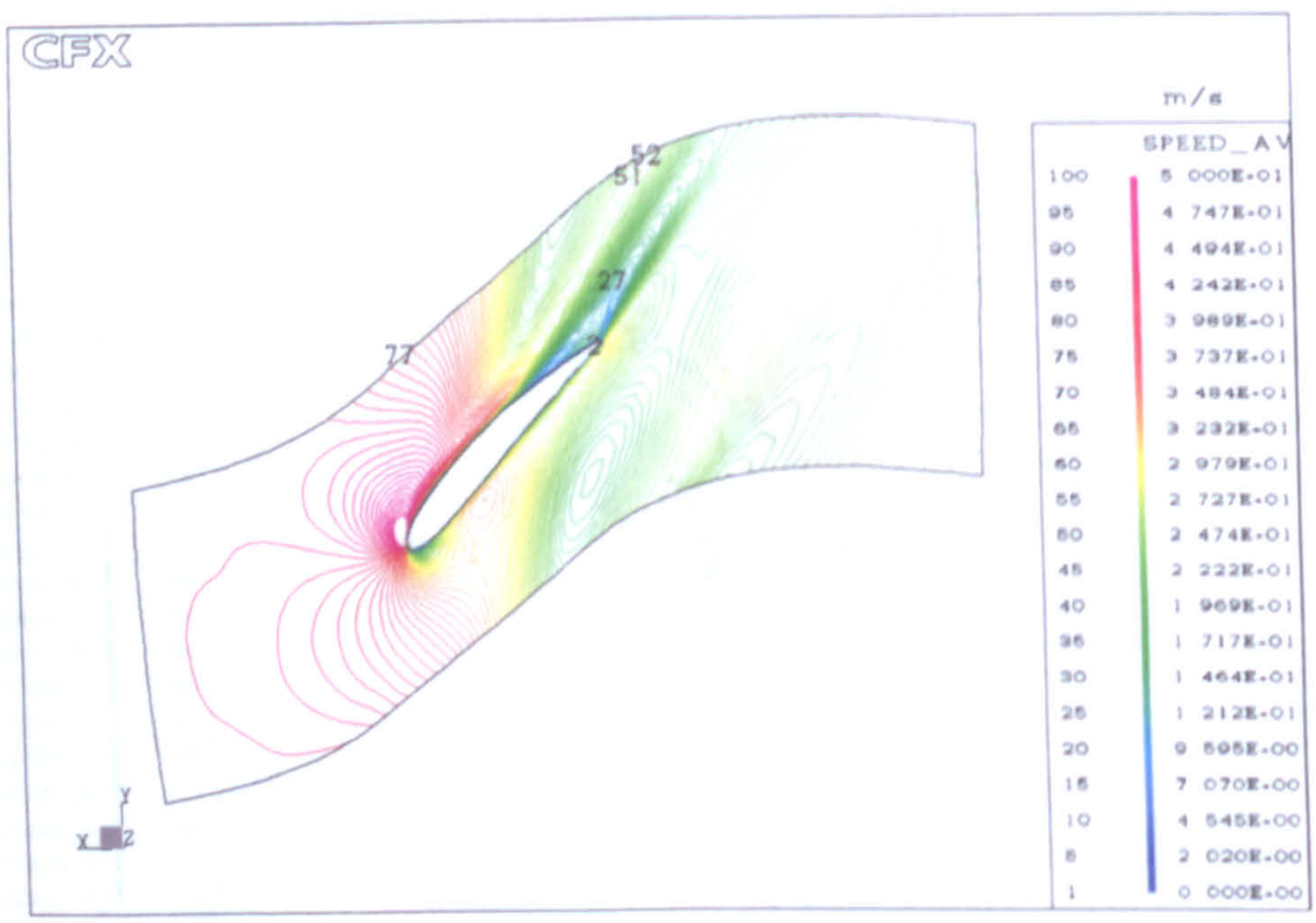

(b) Near the blade tip

Figure 9.26: Time-averaged unsteady result of the velocity magnitude

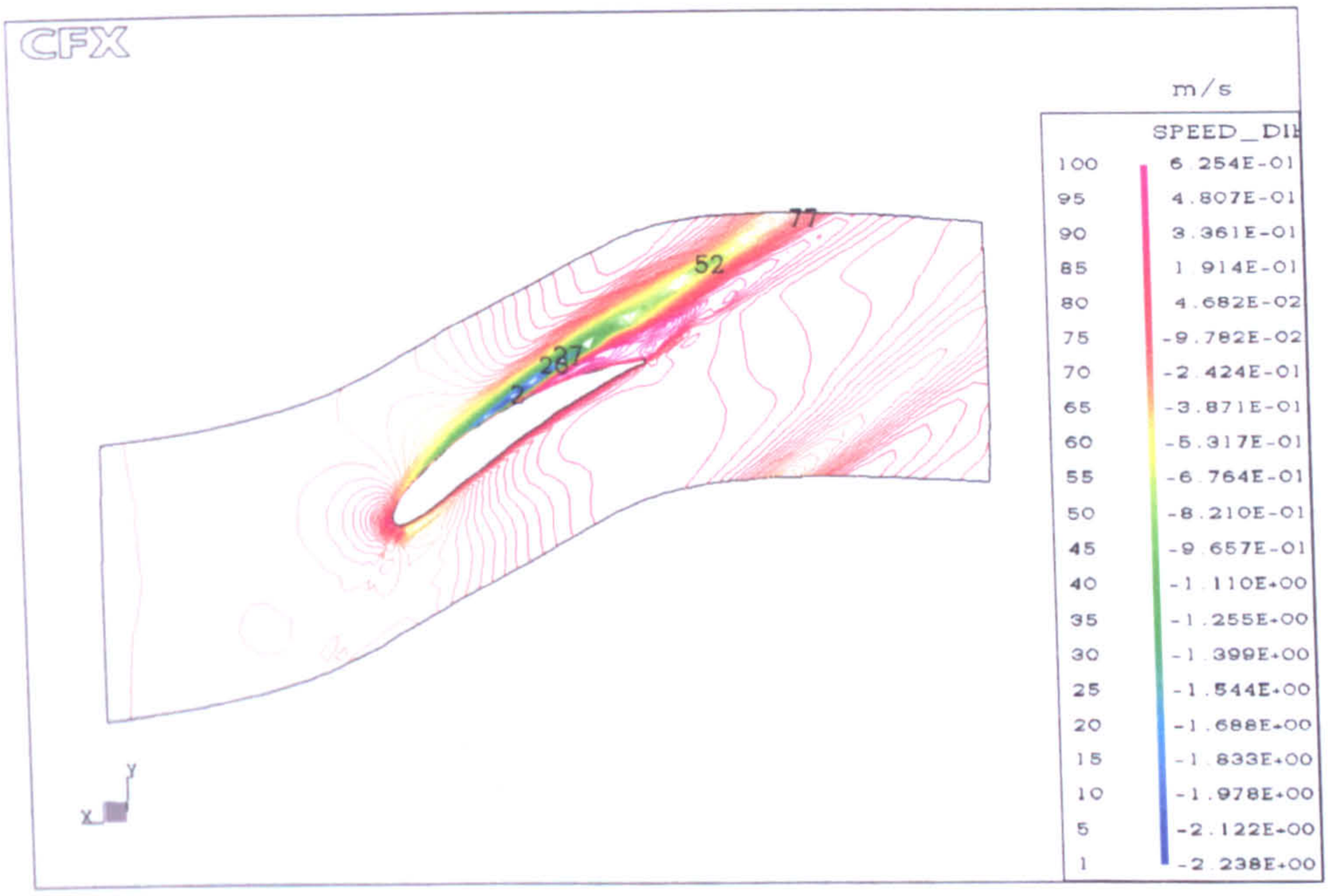

(a) At the blade mid-span

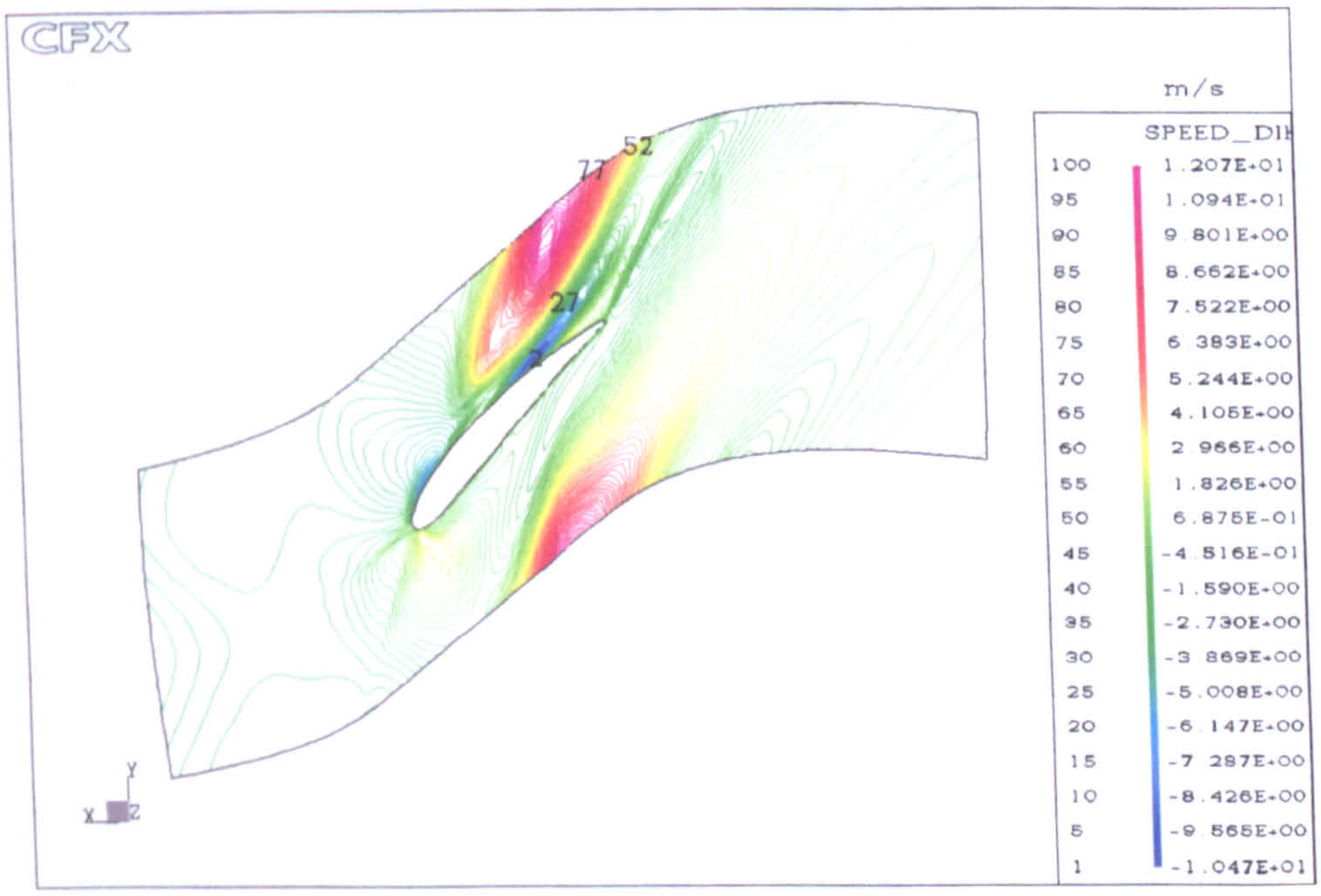

(b) Near the blade tip

Figure 9.27: Velocity magnitude difference between the two formulations

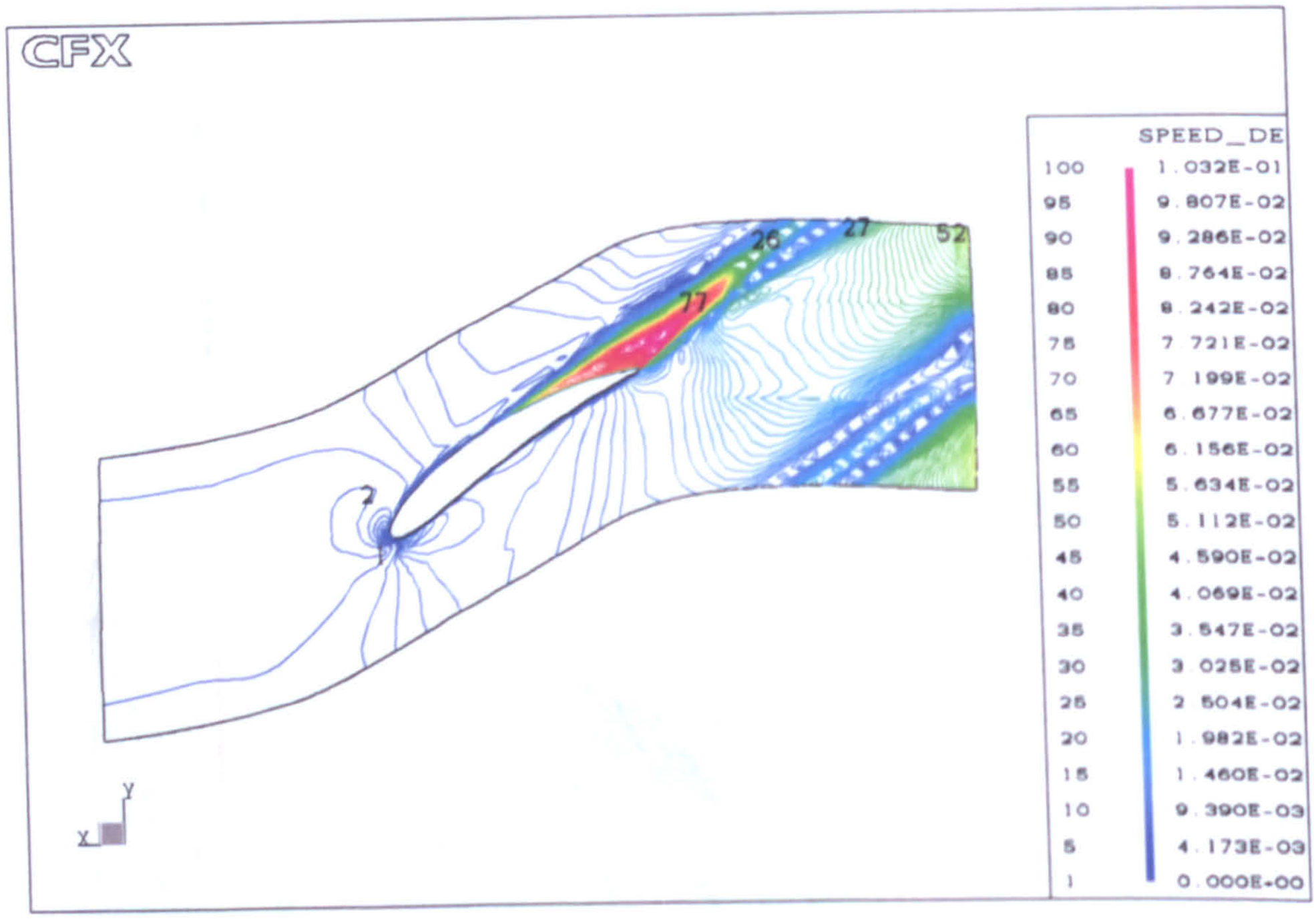

Figure 9.28: Standard deviation of velocity magnitude at blade mid-span

10

Conclusions and Future Work Suggestions

The current research work offered a detailed numerical investigation of the flow in a single axial-flow fan with and without recess casing treatment. It analysed the effects of this passive stall control device on stall margin improvement as well as its influence on global performance parameters. Both steady-state and unsteady simulations were carried out for the fan with solid and treated casing. The results of these simulations offered a valuable contribution to the understanding of the physical processes occurring when approaching stall and the working mechanism by which recess casing treatments improve the stall margin.

Several treatment configurations were numerically simulated including vaneless and vaned recess with different number of vanes inside the cavity. The predicted results of the overall performance, efficiency and work-input characteristics of the fan were found to agree very well with the previously reported experimental work carried out at Cranfield University.

A Reynolds-Averaged Navier-Stokes CFD code, CFX-TASCflow, was used for the analysis. It is a 3-D RANS solver based on a fully implicit pressure correction scheme. The problem being investigated in the present work is a low-speed case in which the flow can be considered incompressible. Hence, the code was set to solve the RANS equations for the conservation of mass and momentum in terms of the independent variables velocity and pressure for steady-state and unsteady problems.

The study cases carried out with different turbulence models and discretization schemes produced no major difference in the predicted results. The two-equation turbulence models are very widely used especially for incompressible flows, as they offer a good compromise between numerical effort and computational accuracy. Hence, the standard k-ϵ turbulence model with wall functions was used as a turbulence model, and the MLPS discretization scheme was used for the treatment of the convective term together with the PAC scheme.

10.1 Conclusions

The steady-state simulations of the solid casing build showed that for the unstalled region the predicted results and the experimental work exhibit similar trends in the pressure rise as well as the efficiency characteristics. Quantitatively the code showed an excellent agreement with the experimental results of the work coefficient data. The spanwise variation of the predicted pressure coefficients, velocity component and flow angles at both inlet and outlet of the domain agreed very well with experimental results.

There is no reliable method to define the stall point using a steady RANS solver based on physical criteria. Usually the numerical procedure becomes unstable or diverges when approaching stall and this usually consists an indication of stall based on purely numerical basis. However the numerical result for mass flow coefficient just below 0.61 showed that there were drops in pressure rise coefficient as well as efficiency due to the stall inception. The numerical simulations were performed beyond the unstalled region into the stalled region but as is to be expected from the limitation of a steady code, these were accompanied by increasing convergence difficulties.

The steady-state simulations depicted the presence of a large amount of separated flow in the computational domain. The extent of the stalled region at the tip was much more affected by the reduction in mass flow rate than the one observed behind the blade trailing edge in the near hub. In fact, this large separated flow at the shroud responsible for the stall of the fan was shown to be due to the locally induced separation at the rotor tip and to a large extent the ejection of a reversed flow from the blade trailing edge near the hub towards the outer casing.

In addition to these steady-state simulations, the unsteady results of both single blade passage and entire fan simulation of solid casing confirmed these flow physics of the tip stall growth process as mass flow decreases through streamlines plots

which highlighted the ejection of flow particles, seeded near the hub, towards the outer casing. This phenomenon provides evidence that the tested fan is prone to the tip stall behaviour, which characterizes tip critical machines for which this type of passive stall devices in particularly suitable. A significant contribution to the growth of the stalled region commonly found near the tip region of the blade is made by the strong radial flow of low momentum fluid originated from the already stalled hub section of the blade.

The total to static pressure rise coefficient calculated from the entire fan simulation agreed very well with the one observed in the steady-state simulation results. Unlike the steady-state simulation the unsteady simulation for the entire fan defined the stall point at a flow coefficient of 0.5. At higher than the stall flow rate, the pressure rise coefficient agreed very well with the one previously observed in the steady-state simulation. As the flow coefficient is reduced below the stall point, the similarity of the pressure rise distribution observed for all blades at high flow rate does no longer exist, and a very large stalled region covering approximately half of the blades can be identified.

Numerical simulations of the axial fan with recess casing treatment were presented. Vaneless and vaned configurations were adopted, with different number of vanes inside the vaned recess. The simulations were carried out with a steady-state boundary condition using a "Stage" interface between the recess casing and the main blade domain. The validity of this steady model has not been fully proven but it consists the best available approach for analysing the blade-recess interaction using a steady CFD method. The predicted results provided a clear insight to the mechanism by which the recess improves the stall margin without any significant penalty in fan efficiency.

The addition of the vaneless casing altered the flow behaviour and appears to sustain the pressure rise coefficient down to a flow coefficient of 0.45 instead of 0.61 as for solid casing. In contrast with the solid casing configuration, the presence of the vaneless recess increases the peak pressure rise by about 30%. However, attaching a vaneless recess induces an attendant aerodynamic penalty in the form of a small pressure rise reduction and a slight drop in the fan efficiency at all flows.

Although the vaneless recess casing is by itself not a practical proposition in terms of casing treatment, the simulation of this configuration offers a valuable insight into the fundamental physics of the recess stall delaying action. The extent of separation present in the tip region is substantially reduced even for a flow rate below the stall point corresponding to the solid build. The separation reduction mechanism of the vaneless recess is due to the redirection of the separated flow in the tip region

towards the vaneless recess, effectively contributing to disperse the concentration of low momentum flow, hitherto present in the tip region.

The vaned casing treatment improves the stall margin while more than doubling the maximum pressure rise without incurring a significant efficiency penalty. The predicted results of pressure rise, efficiency and work-input display very similar trends to that obtained experimentally. The results show that the fitting of vanes to the recess contributed to further extending the unstalled region and substantially increase the pressure rise. Furthermore the presence of vanes inside the recess modified the flow behaviour to an extent that no sign of stall inception was apparent as the flow coefficient was reduced to a minimum of 0.22. This is due to the fact that the recess contributes to effectively reduce the whirl component and remove flow blockage found in the tip region of the solid build, and consequently increase the blade loading.

The fan was also numerically simulated with the recess equipped once with double and another with around half of the number, 27 vanes, used originally. Even though the fan with 14 vanes enters its deep stall at similar flow rate to that of vaneless casing, there was no noticeable aerodynamic penalty neither in pressure rise nor in fan efficiency at high flows found in the vaneless configuration. However for the fan with 54 vanes the numerical simulation was run down to a very low flow rate without encountering any evidence of significant pressure drop.

At high flow rates both simulations produced similar results in terms of pressure rise, fan efficiency and work coefficient to that of 27 vanes simulation. At low-flow rates, the fan with 14 vanes enters its deep stall flow regime, and the fan with 54 vanes predicted a slightly lower pressure rise values that produced by 27 vanes. This slight reduction in pressure rise may result from the flow separation losses produced by the extra vanes inside the recess. Nevertheless when comparing the efficiency and work coefficient results, the discrepancy is so small and the trend so similar as to lead to the hypothesis that the flow may be largely insensitive to a small blade number variation inside the recess.

Although the examination of the unsteady simulation of the recess treatment cavities does not offer an image of large scale unsteady activity at the flow condition investigated, this is on itself quite significant and enables the drawing of an important conclusion namely that recess casing treatments rely primarily on a steady-state flow process. The corollary of this conclusion is of course that a steady-state simulation should then be sufficient to capture the essential features of the recess treatment at least for design purposes.

However, in this case the rotor and stator are aligned in the radial direction unlike

the common case in axial compressors in which the rotor and stator are aligned in the direction of the flow field. As shown in the steady-state simulation of the fan with the recess, a very small mass flow enters the recess compared to the total mass flow through the fan at this flow condition. Also the radial speed of the flow entering the recess is much smaller than the axial speed of the convective flow exiting the domain from the outlet. Hence the interaction between the rotor and the recess vane will be very small compared to the interaction between the rotor and stator in a single stage fan.

On the mechanism of stall delay, the simulations of all recess treatment configurations offer a valuable insight into the fundamental physics of the recess stall delaying action. Fitting the recess effectively reduced the whirl component and removed flow blockage found in the tip region of the solid build. The presence of the turning vanes diffuses the rotational element of the flow and during this process raises the static pressure above the mainstream, thus permitting it to return to the mainstream in a quasi-axial sense. The result of this process is that in the blade tip region a larger amount of axial flow will be present thus offering a contribution to maintaining the stability of the flow.

At high flow rates the flow was found to leave the cavity to re-enter the blade domain mostly ahead of the shroud ring. As the flow coefficient is reduced, the primary outlet region on the recess is sharply displaced upstream with the zone ahead of the shroud ring fully occupied with the incoming radial flow.

The CFX-TASCflow code proved to be an appropriate numerical platform to successfully model recess casing treatments as expressed by the consistently good agreement found between the numerical and experimental results. Moreover the presented simulations highlighted the practicability of employing such a CFD code to expediently and economically conduct an array of parametric studies on the effects of casing treatment design modifications in opposition to the lengthy and costly alternative of assembling, instrumenting and running physical test rigs.

10.2 Future work suggestions

The work described in this thesis gives the general picture for the application of the recess casing treatment to an industrial axial-flow fan. However further work remains to be done and this section highlights some areas that require additional investigation.

The vaned recess casing treatment simulated throughout this work was one of the three design configurations tested by Kang (51), which consists of a flat inner ring and vanes which are cambered only in the flow direction. Previous studies by Basharhagh (15) and Kang (51) have used various design configurations for both the ring and vane with some small improvements noted. It would be interesting to simulate some of these design modifications.

In addition to the provision of variable geometry to the entire casing treatment set up, the present work suggests that a number of contending vaned recess designs warrant further study. These investigations ought to include detailed numerical simulations designed to identify the correct dimensions of the treatment such as the optimum of the vane count, amount of blade exposure, and the variation of the turning and/or the provision of lean to the vanes.

The time span of the research work saw the introduction of a number of improvements in CFX-TASCflow code namely the addition of an LES capability and the extension of the solution to a parallel architecture. These with the expansion of the computational resources available in the university, will enable a new and further investigation of some of the cases presented in this work, such as:

(i) The treatment simulated in the present work was applied to a low-speed axial-flow fan and it would be worth trying to study the effect of this type of treatment on high-speed machines including multistage compressors.

(ii) Further detailed investigation to the stall process using LES and in the future DNS. Also more realistic simulation of the transient stalling process using a valve closing simulation.

(iii) An investigation to study the effect of inlet distortion on the flow behaviour.

(iv) Experimental work to identify unsteady interactions and especially radial flows from hub.

(v) Aeroelastic computations to take into account the structure behaviour of the fan blades.

(vi) Further numerical development of an interface appropriate for radial coupling of axial flow turbomachinery, where the amount of flow passing is at a minimum.

A

Rotor Blade Geometry

This appendix presents the procedure and calculations performed by a FORTRAN code developed to compute the cylindrical coordinate (r, θ, z) of the C4 blade profile from the geometrical data available in Table 5.1. The steps are explained for one profile, as shown in Figure A.1, which are extended to include all 8 profiles, one at each cross-section. The chord of the profile C is calculated from its radius r and space to chord ratio S/C taken form Table 5.1,

$$C = \frac{2\pi\, r}{27\,(S/C)} \tag{A.1}$$

where 27 is the number of blades. The maximum thickness of the profile t_{max} can then be calculated by:

$$t_{max} = 0.12\, C \tag{A.2}$$

where 12% is the maximum thickness by chord ratio. The camber radius r_c of the

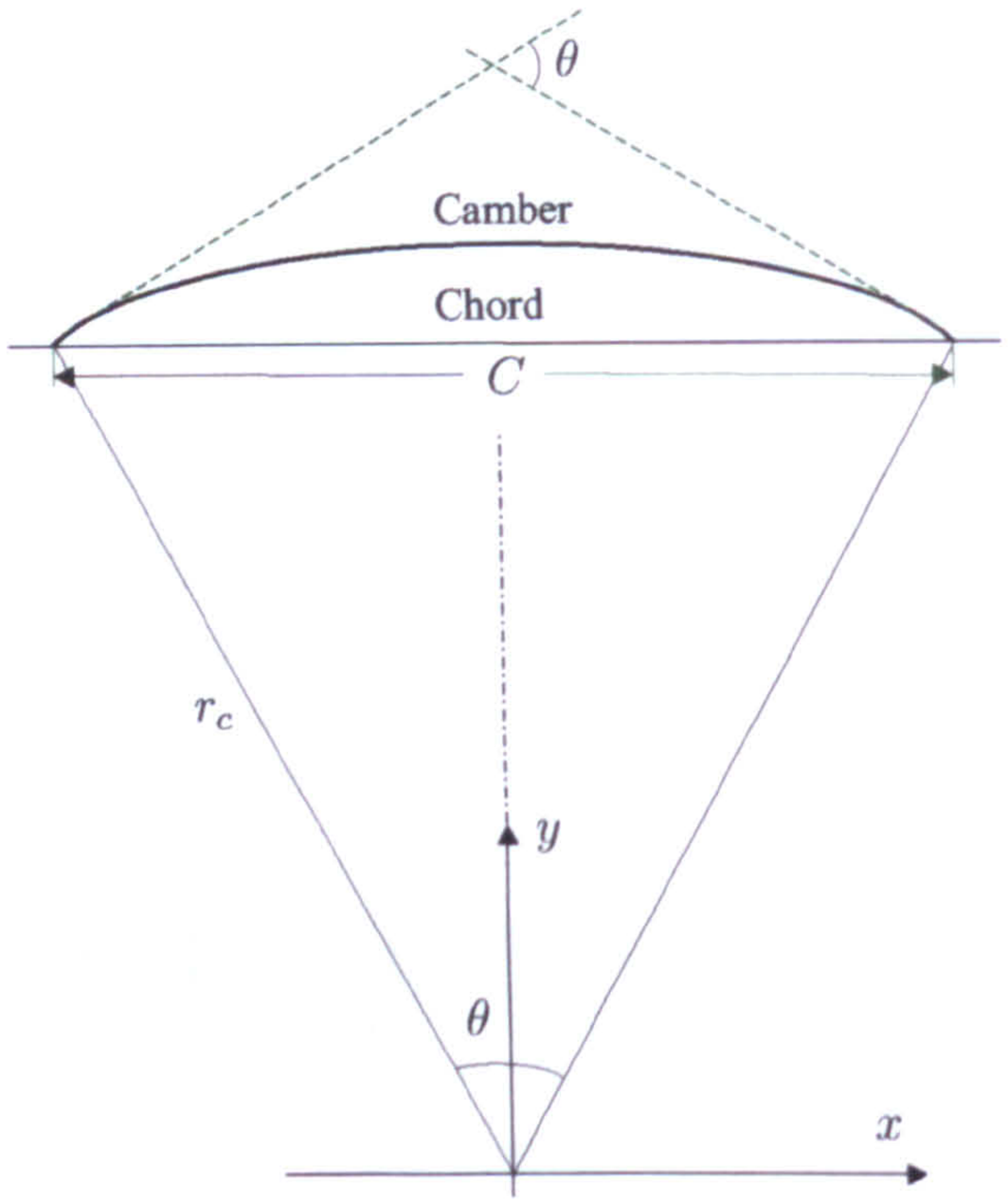

Figure A.1: Sketch of blade profile geometry

profile is calculated by

$$r_c = \frac{C/2}{\sin(\theta/2)} \tag{A.3}$$

where θ is the camber angle taken for each profile from Table 5.1. The thickness distribution of the profile is estimated from analytical relations as a function of the designed maximum blade thickness t_{max} and a fractional distance f from the leading edge to the trailing edge along the camber line of the blade, Tourlidakis (96). These relations are:

$$t = \begin{cases} 2\left(28.110f^3 - 25.281f^2 - 6.563f + 15.492f^{\frac{1}{2}}\right)\dfrac{t_{max}}{10} & f < 0.3 \\ 2\left(3.448f^3 - 14.632f^2 - 7.848f + 3.869\right)\dfrac{t_{max}}{10} & f \geqslant 0.3 \end{cases} \tag{A.4}$$

The radius of each point on the profile r_p is calculated from the camber radius r_c and the thickness t. This done by adding half of the thickness to the camber radius for points on the suction side, and subtracting half of the thickness from the camber radius for points on the pressure side.

$$r_p = r_c \pm \frac{t}{2} \tag{A.5}$$

The camber angle θ is also divided into the same number of fractional distance $(n-1)$, resulting in all fractional distances have an equal fractional angle:

$$\delta\theta = \frac{\theta}{n-1} \tag{A.6}$$

where n is the total number of points on the profile. This mean that each point on the profile has an angle θ_p with respect to x-axis:

$$(\theta_p)_j = \frac{\pi - \theta}{2} + \underset{1 \rightarrow n}{j}\, \delta\theta \tag{A.7}$$

Then, the 2-D Cartesian coordinate (x, y) for each point in the profile can be calculated from its radius and angle, calculated from equation (A.5) and equation (A.7) respectively by:

$$x_p = r_p \cos\theta_p \tag{A.8}$$

$$y_p = r_p \sin\theta_p \tag{A.9}$$

The resulting profile has to be stagger around its center area by the stagger angle ξ given in Table 5.1. This is done by dividing the profile into a number of small triangles m. For each triangle, the area A_k and its center (x_k, y_k) are calculated. Then, the center of the profile (x_c, y_c) is calculated by:

$$x_c = \frac{\sum_{k=1}^{m} A_k x_k}{\sum_{k=1}^{m} A_k} \tag{A.10}$$

$$y_c = \frac{\sum_{k=1}^{m} A_k y_k}{\sum_{k=1}^{m} A_k} \tag{A.11}$$

Then each profile coordinate (x_p, y_p) is transferred so that its center area is the same as origin of the coordinate by:

$$x_t = x_p - x_c \tag{A.12}$$

$$y_t = y_p - y_c \tag{A.13}$$

Then the profile is staggered around the origin $(0,0)$ by an angle ξ given for each profile in Table 5.1 using:

$$\begin{bmatrix} x_s \\ y_s \end{bmatrix} = \begin{bmatrix} \cos\xi & \sin\xi \\ -\sin\xi & \cos\xi \end{bmatrix} \begin{bmatrix} x_t \\ y_t \end{bmatrix} \tag{A.14}$$

Figure A.2 presents an example of these three steps for the profile at the hub, where:

Actual Profile: is the coordinate of the profile (x_p, y_p)

Profile center: is the center coordinate of the profile (x_c, y_c)

Transferred profile: is the transferred coordinate of the profile (x_t, y_t)

staggered profile: is the staggered coordinate of the profile (x_s, y_s)

Finally the cylindrical coordinates (r, θ, z) required by CFX-TurboGrid to generate the grid for the blade are calculated by:

$$z = x_s \tag{A.15}$$

$$\theta = \sin^{-1}\left(\frac{y_s}{r}\right) \tag{A.16}$$

The cylindrical coordinate for the profiles at the hub, mid-span and shroud are presented in Figure A.3.

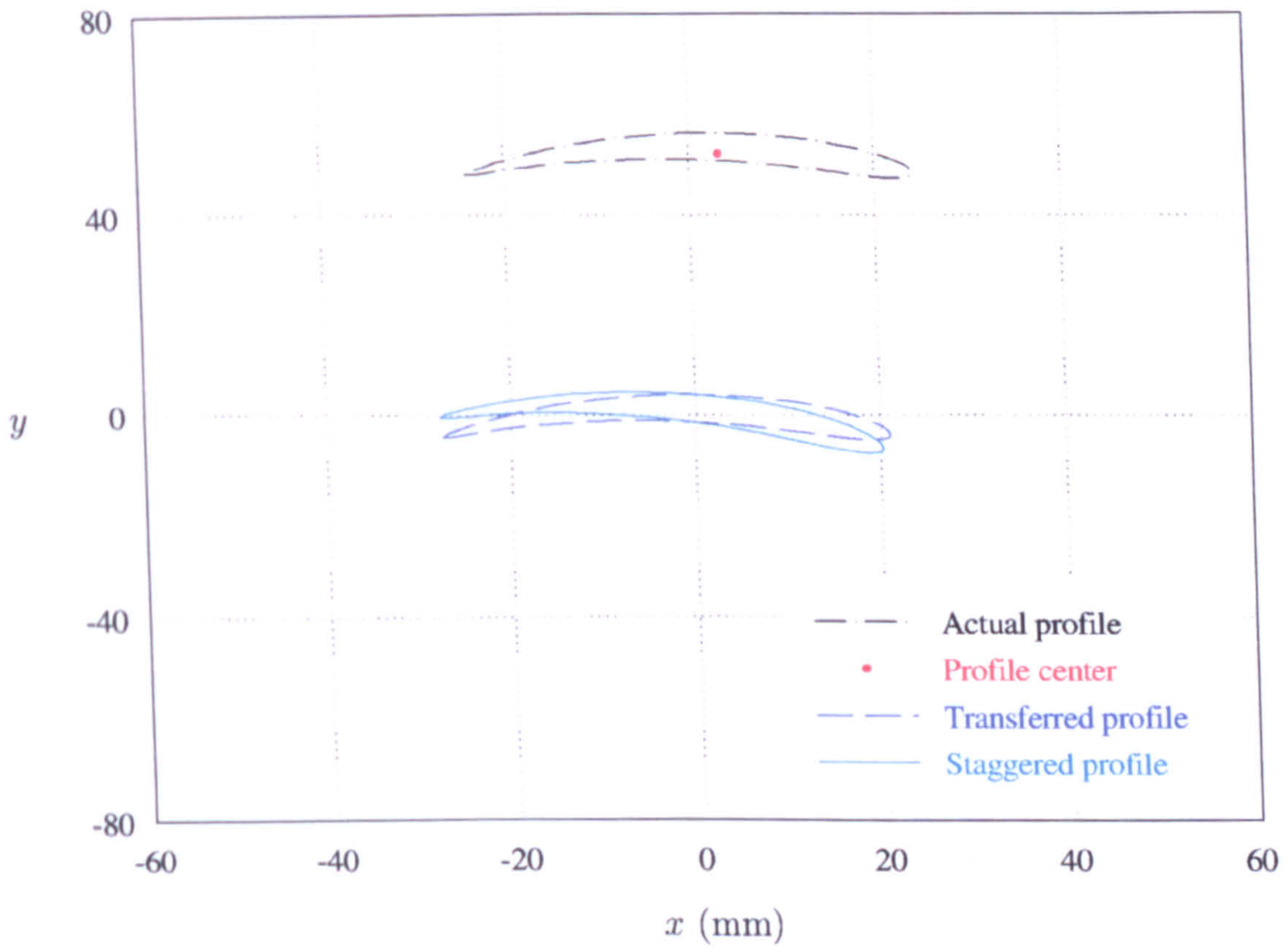

Figure A.2: Cartesian coordinate of the profile at the blade hub

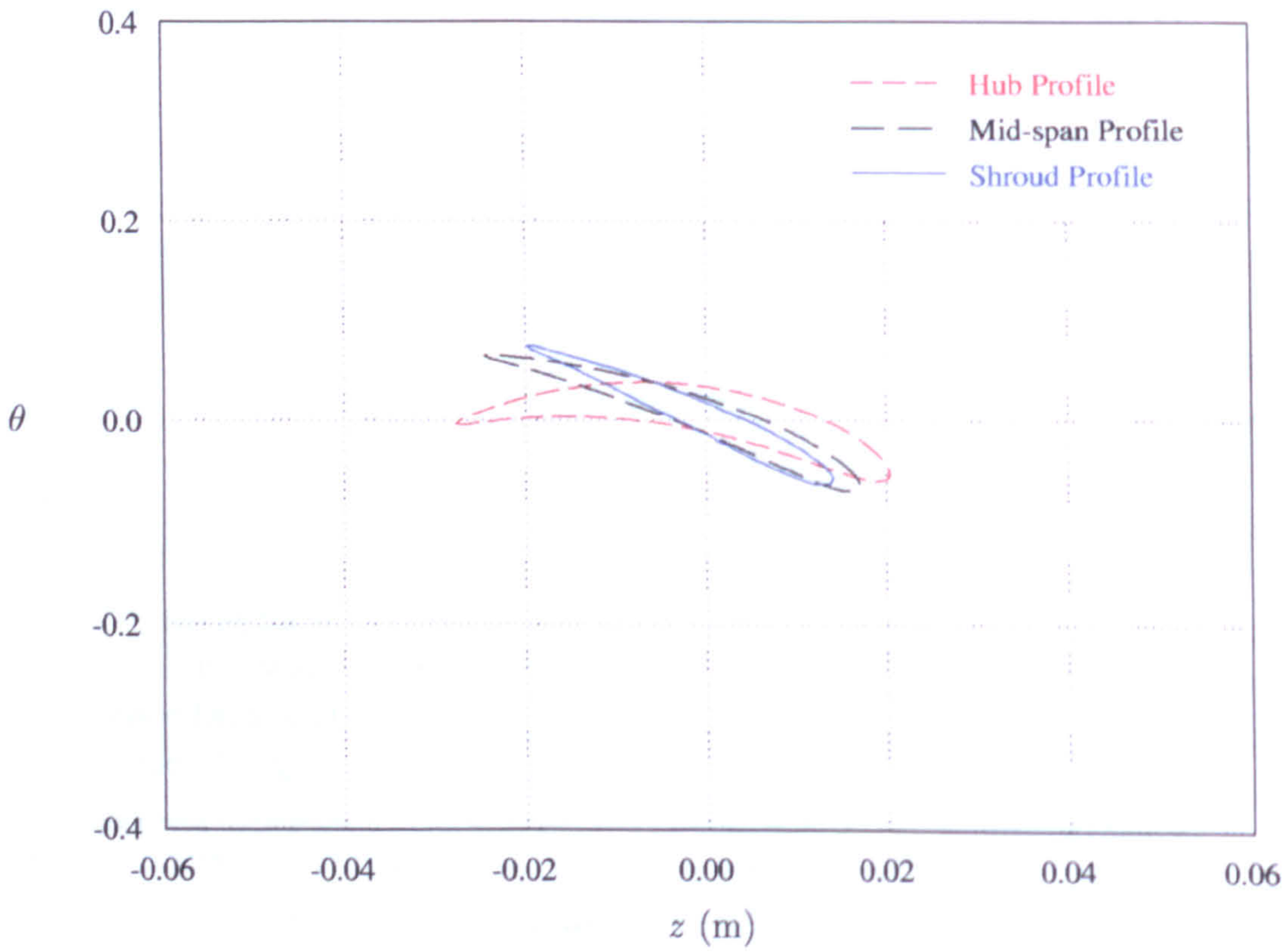

Figure A.3: Cylindrical coordinate of some blade profiles

B

Subroutine BCDTRN

This subroutine is used in conjunction with the specification of a variety of transient boundary conditions. This routine can be used to specify different transient boundary conditions in the one simulation providing that each transient boundary condition has a unique key number "KEY". This number is useful in the "BCDTRN" routine when you are defining different transient functions for more than one boundary condition specification. The BCDTRN routine has the following argument list:

```
C
      SUBROUTINE BCDTRN(LABEL,VAL,STIME,KEY)
C
```

where "LABEL" is passed into the routine and is the name of the variable for which you need to specify a value. LABEL will be one of U, V, W, T or user defined scalar variable names. "VAL" is the specified transient value and KEY is the unique key number for the boundary condition. The "STIME" is the cumulative simulation time for the entire run. In the present study a linear variation function is used to calculate the total mass flow rate, LABEL, each time step:

$$\dot{m}_n = \dot{m}_o - t \tag{B.1}$$

where $\dot{m}_n$ and $\dot{m}_o$ are mass flow for the new and old time steps respectively and t is the total simulation time, STIME. In CFX-TASCbob3D, a transient boundary condition is defined for the domain inlet and is given the unique key '999'. The BCDTRN routine is then copied to a local working directory and then compiled and linked locally to the CFX-TASCflow solver. The BCDTRN used in the one-blade simulation is as follows:

```
C
      SUBROUTINE BCDTRN(LABEL,VAL,STIME,KEY)
C
C ---------------------------------------------
C
      CHARACTER*(*) LABEL
      REAL VAL,STIME
      INTEGER KEY
C     VAL    = 0.0
      NB     = 1
      MSTART = 0.148
      IF(KEY.EQ.999.AND.LABEL.EQ.'MASS') VAL= MSTART- (NB*STIME)
C
      RETURN
      END
C
```

where NB is the number of blades and MSTART is the mass flow rate at the start of the simulation. These two quantities are then changed for the entire fan simulation to 27 blades and 4.0 kg/s respectively.

C

Subroutine UNSTEADY

This routine was developed for post-processing the predicted results of the unsteady simulations for the fan with treated casing in order to calculate the standard deviation of flow variables as well as to compare the predicted results from both steady and unsteady simulations. Standard deviation is the square root of the variance, which is a measure of how spread out a distribution of a variable is. In the present work it was used to calculate the level of the unsteadiness of the flow field variables such as speed, static pressure, relative total pressure, and velocity components inside the computational domain.

The variation of a variable ϕ_{var} between its values from the steady and unsteady simulations is calculated by:

$$\phi_{\text{var}} = \bar{\phi} - \phi_{\text{ss}} \tag{C.1}$$

where ϕ_{ss} is the steady state simulation value and $\bar{\phi}$ is the average value of the

unsteady simulation which is calculated by:

$$\bar{\phi} = \frac{1}{n}\sum_{i=1}^{n}\phi_i \tag{C.2}$$

where n is the number of time steps in one cycle, ϕ_i is the value of ϕ at time step i. A control chart of the subroutine for calculating the average value of the variable ϕ is illustreated in Figure C.1.

The standard deviation $\widehat{\phi}$ of the variable ϕ is calculated by:

$$\widehat{\phi} = \sqrt{\frac{1}{n}\sum_{i=1}^{n}\left(\phi_i - \bar{\phi}\right)^2} \tag{C.3}$$

A control chart for the calculation of the variation of a variable ϕ between the steady and unsteady predicted values as well as its standard derivation is illustreated in Figure C.2.

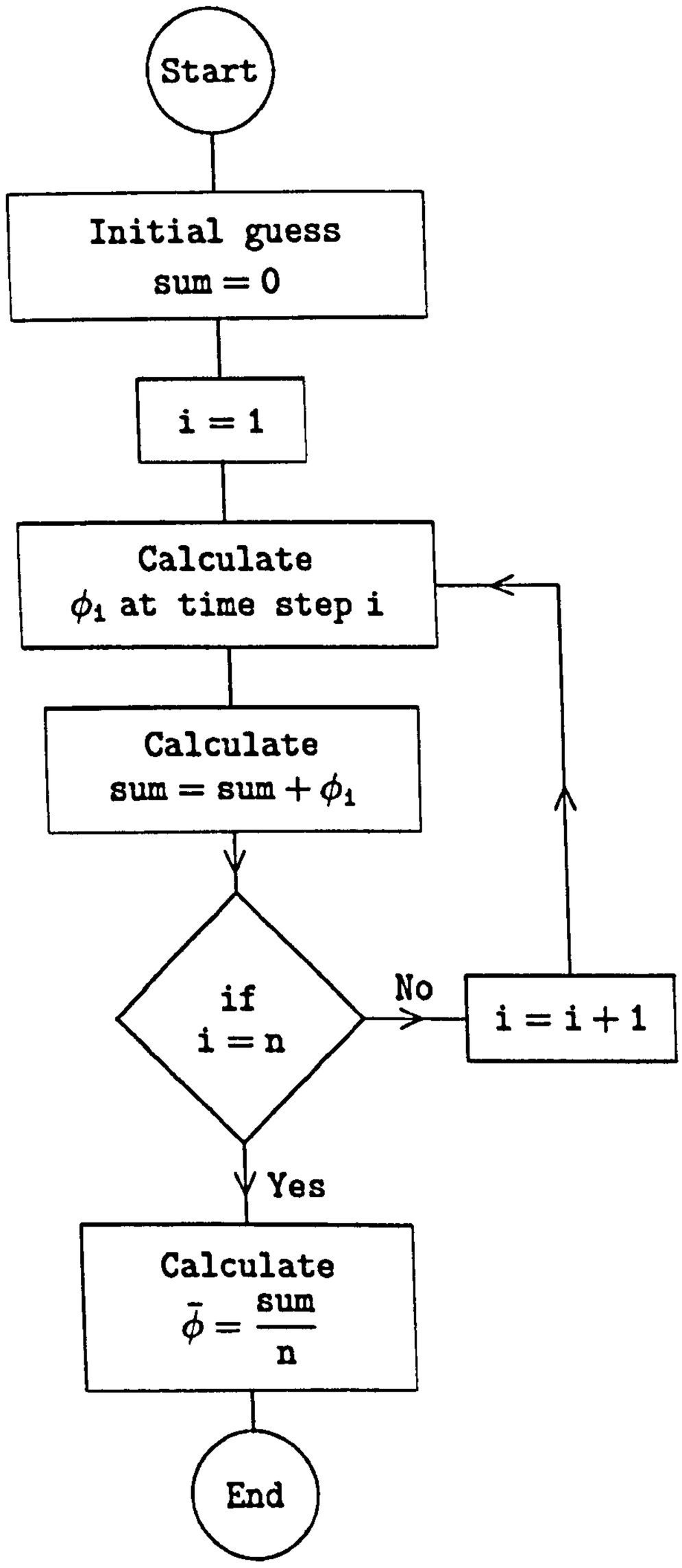

Figure C.1: A control chart for calculating the average value of a variable

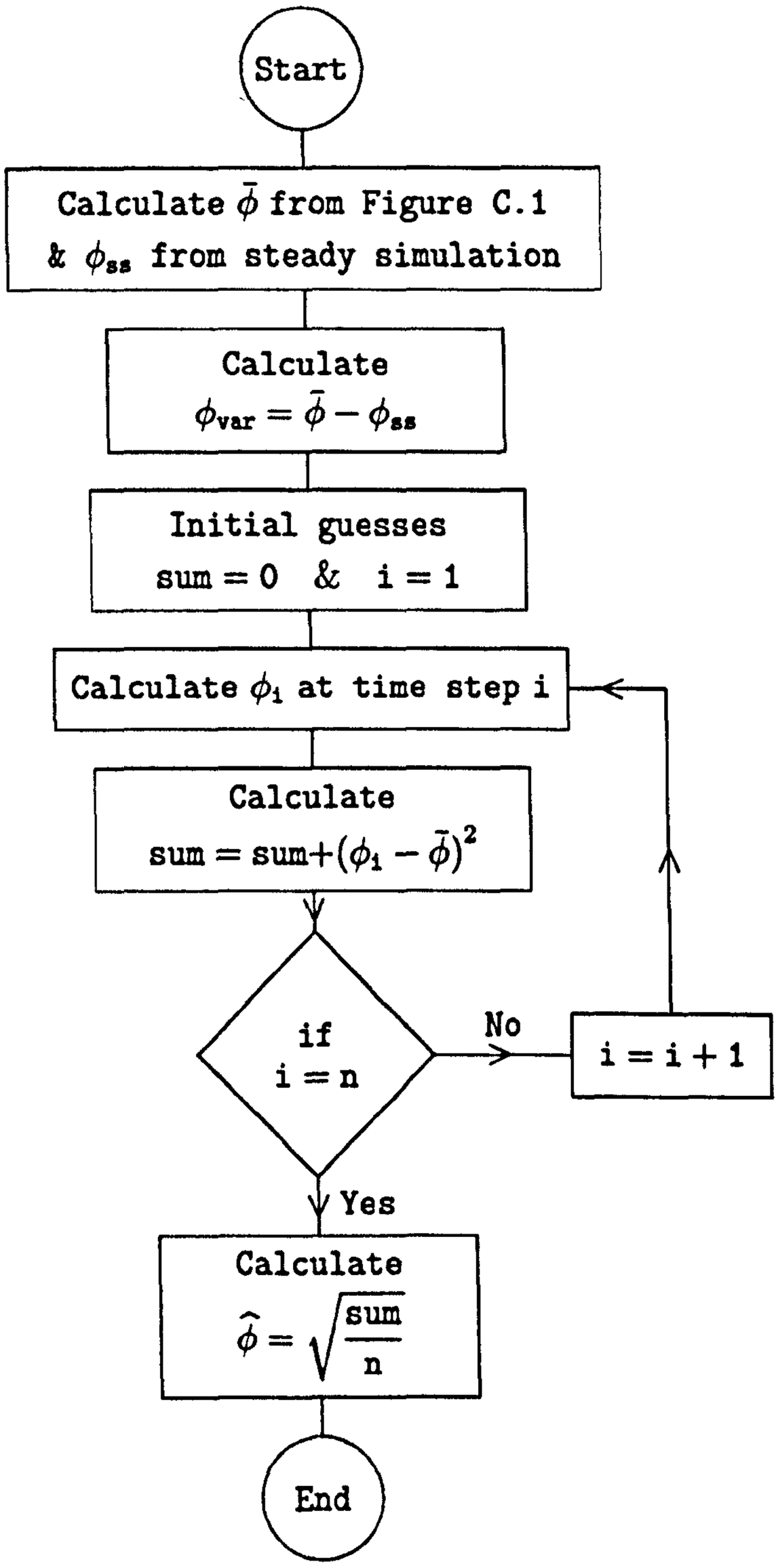

Figure C.2: A control chart for calculating the standard deviation

D

Thesis editing

I am not a TEX expert and writing this work with LATEX 2_ε given me great respect for those who created it. Many thanks to those TEXperts, Diller (23), Grätzer (34), Kopka and Daly (55) and Lamport (57) who their material made writing this thesis much easier. I would like also to express my deepest appreciation and heartfelt thanks to all who gave their time so generously to develop and improve LATEX 2_ε, who their packages[†] helped me get it into its present shape. Of course, the responsibility is mine for all the mistakes remaining in this thesis.

[†]Available from CTAN at `http://www.ctan.org/`

References

(1) AEAT. CFX-TASCflow User Documentation, Version 2.8. AEA Technology Engineering Software Limited. Waterloo, Ontario, Canada, January 1999.

(2) AEAT. CFX-TASCflow User Documentation, Version 2.10. AEA Technology Engineering Software Limited. Waterloo, Ontario, Canada, January 2000.

(3) AEAT. CFX-TurboGrid Software Documentation, Version 1.5. AEA Technology Engineering Software Limited. Waterloo, Ontario, Canada, January 2000.

(4) M. Akhlaghi. *Application of a Vaned-Recesed Tubular-passage Casing Treatment to a Multistage Axial-Flow Compressor.* PhD thesis, Cranfield University, UK, 2001.

(5) C. A. Amann, B. E. Nordenensen, and G. D. Skellenger. Casing Modification for Increasing the Surge Margin of a Centrifugal Compressor in an Automotive Turbine Engine. *ASME, Journal of Engineering for Power*, 97:329–336, 1975.

(6) J. D. Anderson. *Computational Fluid Dynamics: the basics with applications.* McGraw Hill, New York, 1995.

(7) A. R. Azimian. *Application of Recess Vaned Casing Treatment to Axial Flow Compressors.* PhD thesis, Cranfield University, UK, 1987.

(8) A. R. Azimian, R. L. Elder, and A. B. Mckenzie. A Tip Treatment for Axial Flow Fans and Compressors. Industrial Fans-Aerodynamics Design Siminar, IMechE, April 1987.

(9) A. R. Azimian, R. L. Elder, and A. B. Mckenzie. Application of Recess Vaned Casing Treatment to Axial Flow Fans. *ASME, Journal of Turbomachinery*, 112:145–150, 1989.

Missing pages are unavailable

(10) E. E. Bailey. Effects of Grooved Casing Treatment on the Flow Range Capability of a Single Stage Axial Flow Compressor. NASA TM X–2459, 1972.

(11) E. E. Bailey and C. H. Voit. Some Observations of Effects of Porous Casing on Operating Range of a Single Axial-Flow Compressor Rotor. NASA TM X–2120, 1970.

(12) B. S. Baldwin and H. Lomax. Thin-Layer Approximation and Algebraic Model for Separated Turbulent Flows. *AIAA*, (78–257), 1978.

(13) H. Bard. The Stabilisation of Axial Fan Performance. Installation Effects Ductes Fan System Siminar, IMechE, 1984.

(14) H. Bard. Fan Stability by Anti-stall in Tunnels and Industrial Process Ventilation. Turbo-Compressor and Fan Stability Siminar, IMechE, April 1993.

(15) M. Z. Basharhagh. *Recess Vane Passive Stall Control for Axial Flow Fans.* PhD thesis, Cranfield University, UK, 1992.

(16) M. Z. Basharhagh, A. B. McKenzie, and R. L. Elder. A Study of Casing Treatment Stall Margin Improvement Phenomena. ASME 92–GT–36, 1992.

(17) E. Blanco-Marigorta, R. Ballesteros-Tajadura, and C. Santolaria. Hot-wire Measurements During Rotating Stall in a Variable Pitch Axial Flow Fan. ASME 96–GT–441, 1996.

(18) P. Cheng, M. E. Prell, E. M. Greitzer, and C. S. Tan. Effects of Compressor Hub Treatment on Stator Stall and Pressure Rise. *Journal of Aircraft*, 21(7): 469–475, 1984.

(19) L. J. Cheshire. The Design and Development of Centrifugal Compressors for Aircraft Gas Turbines. IMechE, War Emergency Issue No. 12, 1945. Reprinted in US by ASME, January 1947.

(20) A. J. Crook, E. M. Greitzer , C. S. Tan, and J. J. Adamczyk. Similarity Analysis of Compressor Tip Clearance Flow Structure. *ASME, Journal of Turbomachinery*, 115:501–512, 1993.

(21) N. A. Cumpsty. *Compressor Aerodynamics.* Longman Group UK Limited, 1989.

(22) L. J. Day. *Axial Compressor Stall.* PhD thesis, University of Cambridge, UK, 1976.

(23) A. Diller. *LaTeX: LINE BY LINE Tips and Techniques for Document Processing.* John Willy & Sons, New York, 1995.

(24) J. P. Van Doormaal, A. Turan, and G. D. Raithby. Evaluation of New Techniques for the Calculation of Internal Recirculating Flows. AIAA–87–0059, 1987.

(25) H. W. Emmons, C. F. Pearson, and H. P. Grant. Compressor Surge and Stall Propagation. *Transactions of the ASME*, 5:204–211, 1955.

(26) E. E. Fabri and J. Reboux. Effect of Outer Casing Treatment and Tip Clearance on Stall Margin of a Supersonic Rotating Cascade. ASME 75–GT–95, 1975.

(27) J. Fabri. Rotating Stall in Axial Flow Compressors. In *Symposium on Turbomachinery.* IMechE, London, 1970.

(28) C. A. J. Fletcher. *Computational Techniques for Fluid Dynamics, Volumes I & II.* Springer-Verlag, Berlin, 1991.

(29) H. Fujita and H. Takata. A Study on Configurations of Casing Treatment for Axial Flow Compressors. *Bulletin of the JSME*, 27(230):1675–1681, 1984.

(30) P. F. Galpin and G. D. Raithby. Numerical Solution of Problems in Incompressible Fluid Flow: Treatment of the Temperature-Velocity Coupling. *Numerical Heat Transfer*, 10:105–129, 1986.

(31) V. H. Garnier, A. H.Epstein E. M., and Greitzer. Rotating Waves as a Stall Inception Indication in Axial Compressors. *ASME, Journal of Turbomachinery*, 113:290–302, 1991.

(32) A. Ghila and A. Tourlidakis. Computational Analysis of Passive Stall Delay Through Vaned Recess Treatment. ASME 2001–GT–0342, June 2001.

(33) H. P. Grant. Hot-wire Measurements of Stall Propagation and Pulsation Flow in an Axial Flow Induced Centrifugal Impeller System. Technical Report No. 133, Pratt and Whitney Research, 1951.

(34) G. Grätzer. *Math into LaTeX: An Introduction to LaTeX and AMS-LaTeX.* Birkhäuser Boston, 1996.

(35) E. M. Greitzer. Review: Axial Compressor Stall Phenomena. *Transactions of ASME, Journal of Fluids Engineering*, 102:134–151, 1980.

(36) E. M. Greitzer, J. P. Haddad, R. S. Mazzawy, and H. D. Joslyn. A Fundamental Criterion for the Application of Rotor Casing Treatment. *ASME, Journal of Fluids Engineering*, 101:237–243, 1979.

(37) R. G. Griffin and L. H. Smith. Experimental Evaluation of Outer Case Blowing or Bleeding of Single Stage Axial Flow Compressor: Part I; Design of Rotor and Bleeding and Blowing Configrations. NASA–CR–54587, 1966.

(38) E. J. Hall, A. J. Crook, and R. A. Delaney. Aerodynamic Analysis of Compressor Casing Treatment with a 3-D Navier-Stokes Solver. AIAA–94–2796, 1994.

(39) E. J. Hall, D. A. Topp, and R. A. Delaney. Task 7: ADPAC User's Manual; Final Report. NASA–CR–195472, 1996.

(40) E. J. Hall, D. A. Topp, N. J. Heidegger, G. S. McNulty, K. F. Weber, and R. A. Delaney. Task 7: Endwall Treatment Inlet Flow Distortion Analysis; Final Report. NASA–CR–195468, 1996.

(41) K. Hanjalic. *Two-dimensional Asymmetric Turbulent Flow in Ducts.* PhD thesis, University of London, UK, 1970.

(42) F. H. Harlow and C. W. Hirt. Generalised Transport Equations of Anisontropic Turbulence. Los Alamos Science Laboratory, University of California, Report LA 4086, 1969.

(43) N. He. *Impeller-Diffuser Interactions in High Speed Centrifugal Compressors.* PhD thesis, Cranfield University, UK, 2001.

(44) S. D. R. Hill. *Casing Treatment for an Industrial Axial Flow Fan.* PhD thesis, Cranfield University, UK, 1998.

(45) K. A. Hoffmann and S. T. Chiang. *Computational Fluid Dynamics for Engineers, Volumes I & II.* A Publication of Engineering Education System, Kansas, USA, 1993.

(46) M. C. Huppert and W. A. Benser. Some Stall and Surge Phenomena in Axial-Flow Compressors. *Journal of Aeronautical Science*, 20(12):835–845, 1953.

(47) B. R. Hutchinson and G. D. Raithby. A Multigrid Method Based on the Additive Correction Strategy. *Numerical Heat Transfer*, 9:511–537, 1986.

(48) T. Iura and W. D. Rannie. Experimental Investigations of Propagation Stall in Axial Flow Compressors. *Transactions of the ASME*, 76:463–471, 1954.

(49) S. K. Ivanov, V. E. Dudkin, V. P. Peredery, and V. V. Molchanov. Axial Flow Ventilation Fan. U. K. Patent Application (19) GB (11) 2 124 303A, 1984.

(50) M. C. Johnson and E. M. Greitzer. Effects of Slotted Hub and Casing Treatments on Compressors Endwall Flow Fields. *ASME, Journal of Turbomachinery*, 109:380–387, 1987.

(51) C. S. Kang. *Casing Treatment for an Industrial Axial Flow Fan.* PhD thesis, Cranfield University, UK, 1996.

(52) C. S. Kang, R. L. Elder, and A. B. Mckenzie. Recessed Casing Treatment Effects on Fan and Flow Field. ASME 95–GT–197, 1995.

(53) M. Kato and B. E. Launder. The Modelling of Turbulent Flows Around Stationary and Rotating Cylinders. The 9th Turbulent Shear Flow Symposium, Kyoto, Japan, 1993.

(54) C. C. Koch and L. H. Jr. Smith. Experimental Evaluation of Outer Case Blowing or Bleeding of Single Axial Stage Single Flow Compressor. NASA CR–54587–54590, 1968.

(55) H. Kopka and P. W. Daly. *A Guide to LaTeX: Document Preparation for Beginners and Advanced Users.* Addison-Wesley, 1999.

(56) B. Lakshminarayana, M. Pouagare, and R. Davino. Three-dimensional Flow Field in the Tip Region of a Compressor Rotor Passage - Part I: Mean Velocity Profiles and Annulus Wall Boundary Layer; Part II: Turbulence Properties. *ASME, Journal of Engineering for Power*, 104:760–771, 1982.

(57) L. Lamport. *LaTeX, A Document Preparation System: User's Guide and Reference Manual.* Addison-Wesley, 1994.

(58) B. E. Launder and D. B. Spalding. The Numerical Computation of Turbulent Flows. *Journal of Computer Methods in Applied Mechanics and Engineering*, 3:269–289, 1974.

(59) N. K. Lee. Effects of Compressor Endwall Suction and Blowing on Stability Enhancement. *ASME, Journal of Turbomachinery*, 112:133–144, 1990.

(60) B. P. Leonard. A Stable and Accurate Convective Modelling Procedure Based on Qudratic Upstream Interpolation. *Journal of Computer Methods in Applied Mechanics and Engineering*, 19:59–98, 1979.

(61) V. D. Liseikin. *Grid Generation Methods.* Springer-Verlag Berlin Heidelberg, 1999.

(62) F. E. Marble. Propagation of Stall in a Compressor Blade Row. *Journal of Aeronautical Sciences*, 22, 1955.

(63) J. März, C. Hah, and W. Neise. An Experimental and Numerical Investigation into The Mechanism of rotating Instability. ASME 2001–GT–0536, June 2001.

(64) J. Mathieu and J. Scott. *An Introduction to Turbulent Flow.* Cambridge University Press, 2000.

(65) N. M. McDougall. *Stall Inspection in Axial Compressors.* PhD thesis, Cambridge University, UK, 1988.

(66) A. B. McKenzie. Axial Flow Fans and Compressors; Aerodynamic Design and Performance. Cranfield Series on Turbomachinery Technology, 1997.

(67) F. R. Menter. Zonal Two-Equation k-ω Turbulence Models for Aerodynamic Flows. AIAA–93–2906, 1993.

(68) F. R. Menter. Two-Equation Eddy-Viscosity Turbulent Models for Engineering Application. *AIAA Journal*, 32(8), 1994.

(69) Y. Miyake, T. Inaba, and T. Kato. Improvement of Unstable Characteristics of an Axial Flow Fan by Air-Separator Equipment. *Trans. ASME, Journal of Fluids Engineering*, 109:36–40, 1987.

(70) F. K. Moore and E. M. Greitzer. A Theory of Post-Stall Transients in Axial Compression Systems: Part I - Development of Equations, Part II - Application. *ASME, Journal of Engineering for Gas Turbine and Power*, 108, 1986.

(71) R. D. Moore, G. Kovich, and R. J. Blade. Effect of Casing Treatment on Overall and Blade-Element Performance of a Compressor Rotor. NASA TN-D-6538, 1971.

(72) O. Niestroj and P. M. Came. Three-Dimensional Flow Predictions in Axial-Flow Turbine Cascades. ASME 98-GT-325, 1998.

(73) W. M. Osborn, G. W. Lewis, and L. J. Heidelberg. Effect of Several Porous Casing Treatment on Stall Limit and on Overall Performance of an Axial Compressor Rotor. NASA TN–D–6537, 1971.

(74) W. M. Osborn and R. D. Moore. Effect of Casing Treatment on Overall Performance of Axial Flow Transonic Fan Stage with Pressure Ratio of 1.7 and Tip Solidity of 1.5. NASA TM–X–3477, 1977.

(75) S. V. Patankar. *Numerical Heat Transfer and Fluid Flow.* Series in Computational Methods in Mechanics and Thermal Sciences. Hemisphere Publishing Corporation, Tayler & Francis Group, New York, 1980.

(76) Z. Ping, L. Ya-Jun, L. Bao-Ju, and F. Yu-Chen. An Experimental Inestigation on the Mechanism of Stall Margin Improvement of Casing Treatment. ASME 85–IGT–102, 1985.

(77) U. Piomelli. Large-Eddy Simulation: Present State and Future Perspectives. AIAA–98–0534, 1998.

(78) D. C. Jr. Prince, D. C. Wisler, and D. E. Hilvers. A Study of Casing Treatment Stall Margin Improvement Phenomena. ASME 75–GT–60, 1975.

(79) G. D. Raithby. Skew Upstream Differencing Schemes for Problems Involving Fluid Flow. *Journal of Computer Methods in Applied Mechanics and Engineering*, 9:153–164, 1976.

(80) G. D. Raithby and G. E. Schneider. Numerical Solution of Problems in Incompressible Fluid Flow: Treatment of the Velocity-Pressure Coupling. *Numerical Heat Transfer*, 2:417–440, 1979.

(81) G. D. Raithby and K. E. Toorance. Upstream-Weighted Differencing Schemes and Their Application to Elliptic Problems Involving Fluid Flow. *Computers & Fluids*, 8(12):191–206, 1974.

(82) W. Rodi. Eperience with Two-Layer Models Combining the k-ϵ Model with a One-Equation Model Near the Wall. AIAA–91–0216, 1991.

(83) B. Roy and L. Agrawal. Casing Boundary Layer Control by Recess Vaned Casing for a Twin-Rotor Contra-Rotating Axial Flow Fan Unit. ASME 94–GT–478, 1994.

(84) P. Rubini. Numerical Methods for Turbulent Flows. Lecture Notes, Cranfield University, UK, 1996.

(85) B. A. Russell and A. A. Mahmoud. Sall–Free Axial Flow Fan. UK Patent Application (19) GB(11) 2 101685 B, 1984.

(86) C. T. Shaw. *Using Computational Fluid Dynamics.* Prentice Hall International UK Ltd., 1992.

(87) W. M. Shulze, J. R. Erwin, and W. R. Westphal. Investigation of an Impulse Axial Flow Compressor Rotor over a Range of Blade Angles. NASA RM–L50F27A, 1950.

(88) G. D. J. Smith and N. A. Cumpsty. Flow Phenomena in Compressor Casing Treatment. *ASME, Journal of Engineering for Gas Turbine and Power*, 106: 532–541, 1984.

(89) R. W. Snyder and R. J. Blade. Analytical Study of Effect of Casing Treatment on Performance of Multi-stage Compressor. NASA TN–D–6917, 1972.

(90) M. Soundranayagam and R. L. Elder. A Study of Stall in a Low Hub-Tip Ratio Fan. *ASME, Journal of Turbomachinery*, 115:10–18, 1993.

(91) P. Spalart and S. Allmaras. A One–Equation Turbulence Model for Aerodynamic Flows. *AIAA*, (92–0439), 1992.

(92) S. Takata and Y. Tsukuda. Stall Margin Improvement by Casing Treatment; Its Mechanism and Effectivness. *ASME, Journal of Engineering for Power*, 99:121–133, 1977.

(93) S. Tanaka and S. Murata. On the partial flow performance axe flow compressor and rotating stall. *Bulletin of the JSME*, 18(25):1277–1284, 1975.

(94) J. Teixeira. *Computational Analysis of Hig-Speed Axial-Flow Compressors Using Two Deterministic Stress Models.* PhD thesis, Cranfield University, UK, 2002.

(95) M. E. Thomas, N. R. Shimp, M. J. Raw, P. F. Galpin, and G. D. Raithby. The Development of an Efficient Turbomachinery CFD Analysis Procedure. AIAA/ASME/SAE/ASEE 25th Joint Propulsion Conference, Monterey, CA, July 1989.

(96) A. Tourlidakis. *Numerical Modelling of Viscous Turbomachinery Flows with Pressure Correction Method.* PhD thesis, Cranfield University, UK, 1992.

(97) R. C. Turner, J. Reith, and D. W. Sparkes. A Low-Speed Investigation into the Compressor Windmilling and Turbine Characteristics of Several Compressor Stages. NGTE aerodynamic Note No. 679, 1960.

(98) D. C. Urasek and G. W. Jr. Lewis. Effect of Casing Treatment on Performance of an Inlet Stage for a Transonic Multi-stage Compressor. NASA TM X–3347, 1976.

(99) K. A. Ushakov. Removal of unstable operation of axial flow fan by means of separators. *Industrial Aerodynamics*, 24:9–14, 1962.

(100) S. Venkateswaran and C. L. Merkle. Efficiency and Accurarcy Issues in Contemporary CFD Algorithms. AIAA–2000/2251, 2000.

(101) H. K. Versteeg and W. Malalasekera. *An Introduction to Computational Fluid Dynamics, the Finite Volume Method.* John Wiley & Sons, New York, 1995.

(102) J. R. Viegas and M. W. Rubesin. Wall-Function Boundary Conditions in the Solution of the Navier-Stockes Equations for Complex Compressible Flows. AIAA–83–1694, 1983.

(103) J. F. Wendt, editor. *Computational Fluid Dynamics, An Introduction.* Springer-Verlag, New York, 1992.

(104) A. J. Wennerstom. Low Aspect Ratio Axial Flow Compressor - Why and What It Means. The 3rd Elliot Garett Turbomachinery Award Lecture, SP683, 1986.

(105) F. M. White. *Viscous Fluid Flow.* McGrew-Hill, New York, 1991.

(106) D. S. Whithead, N. Hall, and A. Poursartip. Gerry Casing Treatment. Cambridge University Engineering Department, 1980. CUED/A-Turbo/TR-101.

(107) D. C. Wilcox. A Multiscale Model for Turbulent Flows. AIAA 24th Aerospace Sciences Metting, 1986.

(108) D. C. Wilcox. A Two-Equation Turbulence Model for Wall-Bounded and Free-Shear Flows. AIAA–93–2905, 1993.

(109) D. C. Wisler and D. E. Hilvers. Stator Hub Treatment Study. NASA CR–134729, 1974.

(110) V. Yakhot, S. A. Orszag, S. Thangam, T. B. Gatski, and C. G. Speziale. Development of Turbulence Models for Shear Flows by a Double Expansion Technique. *Physics of Fluids*, 7(4):1510–1520, 1992.

(111) H. Yu and A. B. Mckenzie. Stall in Low Hub-Tip Ratio Fans. IMechE, Paper No. C401/010, 1990.